PROCEEDINGS OF SAIP2017

62nd ANNUAL CONFERENCE OF THE SOUTH INSTITUTE OF PHYSICS

EDITED BY:
Prof. JAPIE ENGELBRECHT

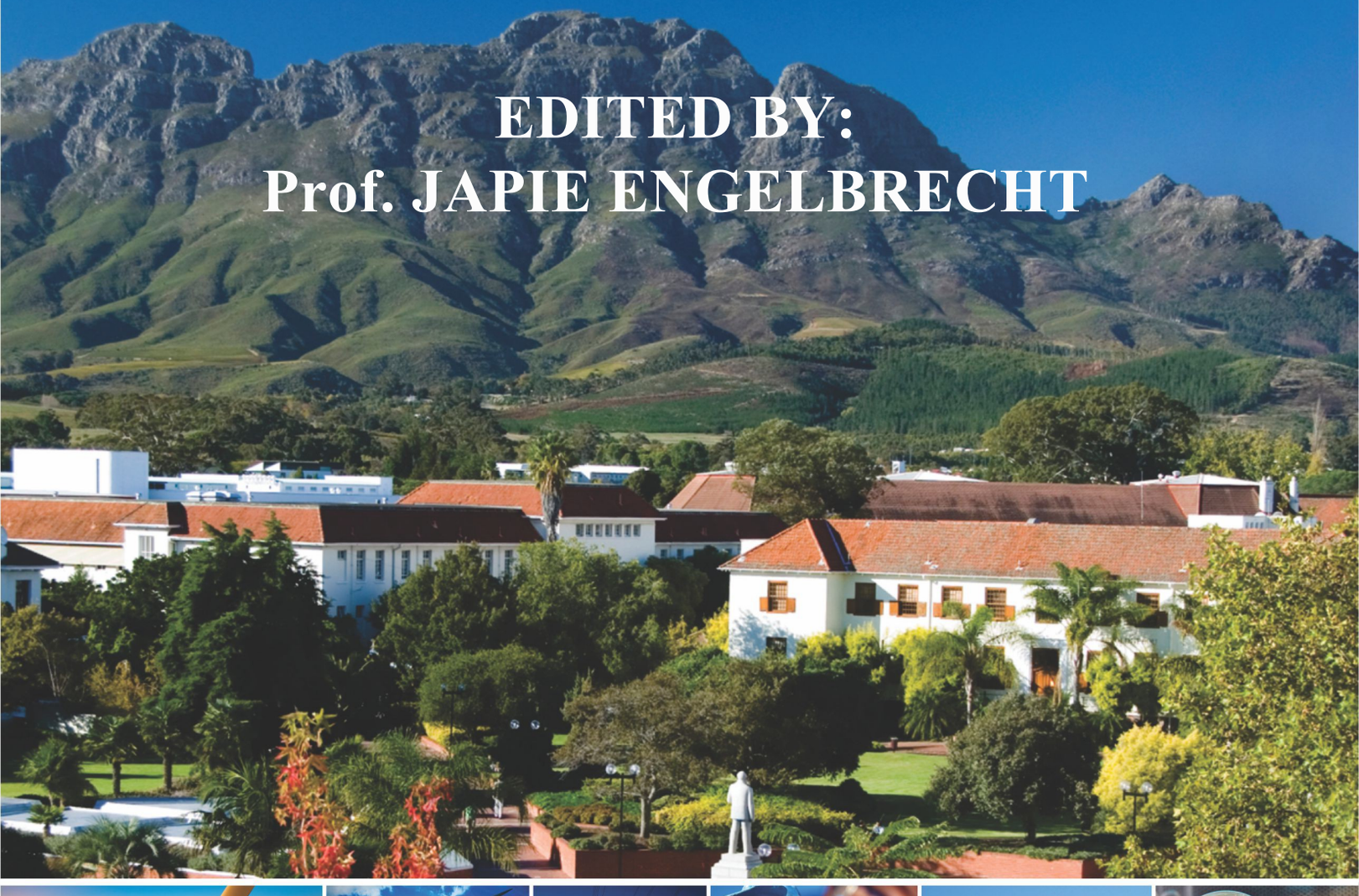

WWW.SAIPCONFERENCE.CO.ZA

UNIVERSITEIT STELLENBOSCH UNIVERSITY

1903 2003
FISIKA · STELLENBOSCH · PHYSICS

SOUTH AFRICAN INSTITUTE OF PHYSICS

PROCEEDINGS EDITOR: Prof. Japie Engelbrecht

PUBLISHER: The South African Institute of Physics (SAIP)

The Proceedings of SAIP2017, the 62nd Annual Conference of the South African Institute of Physics (SAIP) will only be available electronically on the SAIP website:
www.saip.org.za.

ISBN: 978-0-620-82077-6

SAIP2017

Proceedings of SAIP2017,
the 62nd Annual Conference of the South African Institute of Physics

Hosted by the Departments of Physics of Stellenbosch University

3 July to 7 July 2017
Stellenbosch University, Stellenbosch, South Africa

Edited By
Prof. Japie Engelbrecht

TABLE OF CONTENTS

Conference Chairs and Committees . . . . . *xi*
Message from the Chair . . . . . *xii*
Message from the Editor . . . . . *xiii*
List of Reviewers . . . . . *xiv*

FULL RESEARCH PAPERS

Division A - Division for Physics of Condensed Matter and Materials

Investigation of Thermoelectric Properties of $CH_3NH_3PbI_3$: Density Functional Theory and Boltzmann Transport Calculations **2**
I O Abdallah, D P Joubert and M S H Suleiman

First-principles investigation of lattice thermal conductivity and structural stability of $CH_3NH_3PbI_3$ **8**
I O Abdallah, D P Joubert and M S H Suleiman

The role of the pre-exponential factor in the segregation profiles of Cu(111)-SnSb and Cu(100)-SnSb ternary alloys **14**
J K O Asante and W D Roos

Quasiparticle band structure and optical properties of alpha-MnO_2: a beyond density functional theory investigation **19**
M Chepkoech, D P Joubert and G O Amolo

Intermediate valence behavior in the new ternary compound $Yb_{13}Pd_{40}Sn_{31}$ **25**
R F Djoumessi, A M Strydom, F Gastaldo, I Curlik; M Reiffers and M Giovannini

Mechanical milling effect on the structural and magnetic properties of sintered $La_{0.67}Sr_{0.33}MnO_3$ **30**
I P Ezekiel, T Moyo and S Dlamini

Predicting the Mo substitution and vacancy-complex induced electrical defect levels in Ge **36**
E Igumbor, O Olaniyan, R E Mapasha, H T Danga and W E Meyer

Analysis of the structure, particle morphology and photoluminescent properties of green emitting $BaB_8O_{13}:Ce^{3+}$ phosphor **41**

M A Lephoto, K G Tshabalala, S J Motloung and O M Ntwaeaborwa

First-principles stability study of olivine $NaMPO_4$ (M: Mn, Fe,Co) **47**

N L Lethole, H R Chauke and P E Ngoepe

Optimisation of inorganic-organic photoactive hybrid thin films **54**

S S Magubane, T F G Muller, C J Oliphant and C J Arendse

Structural and thermodynamic properties of Zr-Nb-Co compound. **60**

M M Malebati, P E Ngoepe and H R Chauke

The structural and sensing properties of cobalt and indium doped zinc oxide nanopowders synthesised through high energy ball milling technique **65**

M F Manamela, T E Mosuang and B W Mwakikunga

Mechanical properties and temperature dependence of B_{19} $Ti_{50-x}Zr_xPt_{50}$ shape memory alloys **71**

M P Mashamaite, H R Chauke and P E Ngoepe

Bias enhanced nucleation and growth for improving the optomechanical properties of diamond-like carbon films **77**

W M Mbiombi, B A Mathe, D Wamwangi, R Erasmus and D G Billing

Atomistic simulation of the structure and elastic properties of pentlandite structure (Ir_9S_8) **83**

M A Mehlape, D Tanzwani and P E Ngoepe

Computational modelling study of the $Ti_{50}Pt_{50-x}Cu_x$ shape memory alloys **89**

R Modiba, H Chikwanda and P E Ngoepe

The effect of thiol collectors on nickel-rich (110) pentlandite surface using density functional theory **95**

P P Mkhonto, H R Chauke and P E Ngoepe

Gas-Sensing Properties of TiO_2 Nanoparticles Double Doped with Ag and Cu **101**

O O Nubi and T E Mosuang

Investigation of the magnetic ground state of $PrRu_2Ga_8$ compound **107**

M O Ogunbunmi and A M Strydom

Numerical simulation of structural, electronic and optical properties of vanadium diselenide (VSe_2) **113**

E Rugut, D Joubert and G Jones

Elastic properties of chalcogenide based phase change memories by surface Brillouin scattering **119**

D Wamwangi, B Mathe, M Baloi, D G Billing, C Persch, M Salinga and M Wuttig

Thermoelectic properties of $Sm_3Rh_4Ge_{13}$ **125**

S P Xhakaza, B M Sondezi and A M Strydom

Division B - Nuclear, Particle and Radiation Physics

Measurements of natural radioactivity in soil using an array of cerium doped lanthanum bromide scintillator detectors **131**

M Bashir, R T Newman and P Jones

Investigating the diffusion of Xe implanted into glassy carbon **135**

M Y A Ismail, J B Malherbe, O S Odutemowo, T T Hlatshwayo, E G Njoroge and E Wendler

Calculation of the energy produced from radiative capture in SAFARI-1 . . . . . **140**

L Jurbandam, O M Zamonsky

The impact of an extended Inner Detector tracker on the W+-W+-jj measurement in pp collisions at the High-Luminosity LHC with the upgraded ATLAS detector. **146**

C Lee, R van Tonder and S Yacoob

High-fidelity modelling of the ETRR-2 research reactor **152**

M Mashau, S A Groenewald and F A van Heerden

Assessing the impact of rock phosphate storage on uranium and thorium concentration in soil samples from Richards Bay using neutron activation analysis. **158**

F B Masok, P L Masiteng, R D Mavunda, P P Maleka and H Winkler

Composite Scintillators - A new type of radiation hard scintillator **164**

J E Mdhluli, Yu I Davydov, V Baranov, S Mthembu, R Erasmus, H Jivan, B Mellado, E Sideras-Haddad, A Boyarintsev, T Nepokupnaya, Y Onufriyev and I Vasiliev

Geometrical validation of New Small Wheel simulation software. **170**

C Mwewa, V Cairo, A Dell'Acqua, A Hamilton, V Martinez and S Yacoob

Reconstruction of missing energy in events with two photons at the ATLAS detector in Large Hadron Collider **176**

K G Tomiwa, X Ruan, S Liao and B Mellado

Performance of various event generators in describing multijet final states at the LHC **182**

S von Buddenbrock

Production of the Madala boson in association with top quarks **187**

S von Buddenbrock

Division C - Photonics

Cell death induced by combination of Phthalocyanine photosensitizer and Doxorubicin on MCF-7 breast carcinoma cells. **194**

E C Aniogo, B P George and H Abrahamse

Photobiomodulation activates the JAK/STAT signalling pathway in diabetic wounded cells in vitro **199**

S W Jere, H Abrahamse and N N Houreld

Characterization of the spectral irradiance lamps at NMISA **204**

M Mkabela, P Du Toit, R Sieberhagen and W Meyer

Analysis and Performance of a closed loop external cavity diode laser control system **210**

V Opeolu, K Govender, A Wyngaard, O Nemraoui, G De Jager and J Scarrott

Experimental study of the weak field Zeeman spectra of ^{85}Rb and ^{87}Rb **216**

A Wyngaard, G De Jager, C Steenkamp and K Govender

Division D1 - Astrophysics

Structure formation with causal bulk viscosity **223**

G Acquaviva, A John and A Pénin

Exploring the potential of the dark matter candidate from the Madala hypothesis with multi-frequency indirect detection **228**

G Beck and S Colafrancesco

Spectral analysis of Fermi-LAT gamma-ray bursts with known redshift and their potential use as cosmological standard candles **234**

F F Dirirsa, S Razzaque and F Piron

Optimization of galaxy identification algorithms in large Hi surveys **240**

T Gqaza, R C Kraan-Korteweg, B Frank, M Ramatsoku, T H Jarrett, E Elson and A C Schroeder

Reverberation mapping of a $z \sim 0{:}375$ active galactic nucleus **246**

M S Hlabathe, E Romero-Colmenero, S M Crawford and LCO AGN Key collaboration

Modelling the hardening of gamma-ray spectra by extragalactic background light **252**

A M Kudoda and A Faltenbacher

Probing quantum gravity through strong gravitational lensing **257**

S Marongwe and M Mafu

Quasi-Newtonian scalar-tensor cosmologies **263**

H Sami and A Abebe

Division D2 - Space Science

Ensemble Estimation of Network Parameters: A Tool to Improve the Real-time Estimation of GICs in the South African Power Network **270**

M J Heyns, S I Lotz, P J Cilliers and C T Gaunt

Division E - Education

Influence of guided inquiry on first-year students' attitudes to laboratory activities and performance in physics **277**

V M Baloyi, W E Meyer, E Gaigher and M A Graham

Students' explanation of motion in real-life context **283**

P Molefe and M N Khwanda

First year university physics students' understanding of units and measurements **289**

S Ramaila and L Reddy

First year university physics students' perceptions of teaching methods **294**

S Ramaila and L Reddy

Soweto Science Centre as a flagship community engagement initiative **300**

S Ramaila and L Reddy

How do undergraduate students respond to early research? **306**

B M Sondezi

Division F - Applied Physics

Simulation of Ground Level Spectral Solar Irradiance in Rwanda using LibRadtran. **312**

M C Cyulinyana and H Winkler

A new D-T neutron facility at UCT **324**

T Hutton and A Buffler

Testing the scattering distribution of a photon in a turbid medium using Monte Carlo simulations. **331**

T Mabhengu, M C Cyulinyana and H Winkler

Computational comparison of a novel cavity absorber for parabolic trough solar concentrators **337**

K Mohamad and P Ferrer

Numerical modelling of control rod calibrations and fuel depletion at the OPAL research reactor. **344**

R Mudau, D Botes and F A Van Heerden

The proposed improvements of the hydrometer calibration system using Cuckow's method at NMISA **350**

B Ndlovu, R T Mautjana and D J Mabena

The MinPET diamond discovery technique. **355**

T Nemakhavhani, D Unwuchola, R C Andrew, M N H Cook, S H Connell, S E Ballestrero, U Uggerhoj, S Pape Moller, P Aggerholm, N Hertel and J A Swartz

Calculation of direct and di use solar irradiance components using a Slob Algorithm model in Gauteng conditions. **361**

L C Nethwadzi and H Winkler

An investigation of synchronisation techniques for a handheld QKD device **367**

S Pillay, M Mariola and F Petruccione

System control applications of low-power radio frequency devices **373**

R M van Rensburg, B Mellado and C J Sandrock

Division G - Theoretical and Computational Physics

How quantum is bird migration: A review **380**

B Adams, I Sinayskiy and F Petruccione

Entanglement and gravity **385**

J M Hartman, S H Connell, C Engelbrecht and F Petruccione

Heavy flavor tagged photon bremsstrahlung from AdS/CFT **391**

W A Horowitz

Matrix logarithmic quantum wave equation **397**

M Znojil and K G Zloshchastiev

Conference Chairs and Committees

SAIP2017 Division Chairs

Division for Physics of Condensed Matter and Materials:
Prof. Japie Engelbrecht (Nelson Mandela Metropolitan University)
Division for Nuclear, Particle and Radiation Physics:
Dr. Simon Mullins (iThemba LABS)
Division for Photonics:
Prof. Andrew Forbes (University of the Witwatersrand)
Division for Astrophysics
Dr. Christo Venter (North-West University)
Division for Space Science:
Dr. Du Toit Strauss (North-West University)
Division for Physics Education:
Prof. Sam Ramaila (University of Johannesburg)
Division for Applied Physics:
Prof. Ernest van Dyk (Nelson Mandela Metropolitan University)
Division for Theoretical and Computational Physics:
Prof. Kristian Müller-Nedebock (Stellenbosch University)

SAIP2017 Conference Committee

Prof. Erich Rohwer - Chairperson
Prof. Piet Walters
Dr. Christine Steenkamp
Dr. Pieter Neethling
Prof. Paul Papka
Prof. Kristian Müller-Nedebock
Dr. Hermann Uys
Dr. Richard Newman
Dr. Gurthwin Bosman

Proceedings Editorial Committee

Editor: Prof. Japie Engelbrecht (Nelson Mandela Metropolitan University)
Committee Members: Prof. Deena Naidoo & Dr. John Habarulema
Compilation & Online Publishing: Dr. Roelf Botha & Mr. Juan Grey

Proceedings Review Panel

Prof. Japie Engelbrecht - Editor
Prof. Deena Naidoo - Education and Condensed Matter
Dr. John Habarulema - Astro & Space
Dr. Phil Ferrer - Applied Physics
Dr. Ernest E. Van Dyk - Applied Physics
Dr. Simon Mullins - Nuclear Particle and Radiation
Prof. Simon Connell - Nuclear Particle and Radiation
Prof. Kristian Müller-Nedebock - Theoretical
Dr. Will Horowitz - Theoretical

Message From The Conference Chair

Dear SAIP 2017 delegate,

The physics department at Stellenbosch University would like to extend a hearty welcome to you, in the hope that the conference program will live up to your expectations. We trust that the academic program will be enlightening, and that the social program will be conducive to network-building and making good friends.

The Physics Department at Stellenbosch was founded in 1903 and has a proud tradition of contributing to the South African Institute of Physics and its activities. We have the pleasure of hosting the SAIP annual conference again as we have done successfully in the past. As a physics department we focus on theoretical physics, nuclear physics and photonics. We acknowledge the assistance and contribution of our collaborators from iThemba LABS, the CSIR National Laser Centre and the National Institute for Theoretical Physics to the activities of our department and, particularly, their support for this conference. We thank the plenary speakers who accepted the invitation and have travelled to address the 2017 Annual Conference of the SAIP, and we thank the various sponsors who have made their participation possible. In hosting this conference we embrace the opportunity to facilitate engagement of all the various disciplines in physics participating at the conference. We hope to serve the broader physics community to develop its identity as a professional institute, representing all physicists.

We trust that the workshops will have a positive effect on our younger researchers, and that the plenary presentations will broaden our horizons. Last, but not least, it is our wish that you also enjoy the social activities offered during the week and that you leave Stellenbosch inspired and refreshed.

Prof. EG Rohwer
Head of Physics Department
Chair of the LOC

Message from the Editor

It took me a while to consider the request by Prof Deena Naidoo to become the Editor of the SAIP 2017 Conference Proceedings. However, the more I thought about it, the more it made sense: I am retired, one person will deal with all aspects and will coordinate the process and so on. In my mind's eye I saw delivery of the Proceedings on the expected date, i.e. before the next conference. "After all" (I thought) what could go wrong?" (with apology to the insurance company advertisement on TV).

The production of a journal or a proceedings involves a large number of people: the editorial committee, authors submitting articles, two reviewers for each article and finally the editor. If any of the cogs in this "machine" fails, the whole process slows down and is being delayed. Non the less, the review process cannot be hurried along, as eventually the SAIP expects a Proceedings of a standard comparable to that of international journals. We therefore are hugely indebted to the Content Reviewers for their time and due diligence in the review process.

A total of 116 articles were received. Rejection of articles were due to not complying with the required layout, scientific value or not addressing the concerns and suggested corrections of the Reviewers. This was done with the goal of ensuring maintenance of a standard comparable to that of international journals.

I appeal to all students, supervisors and promoters to take much more care in future upon submission of articles to be considered for publication in the Conference Proceedings, to take a greater responsibility in ensuring that articles adhere to the required Layout, and to ensure that articles are proofread before submission to cut down on grammatical and typographical errors. All this will speed up the editorial process, and ensure that the Proceedings can be published timeously.

I wish to SINCERELY thank the following persons for their help and assistance:

- The Editorial Committee under the leadership of Prof Deena Naidoo
- Tebogo Mokhine, whose IT skills carried the day – without him I would have thrown in the towel long ago!
- Mr Brian Masara, CEO of SAIP and John Basco Habarulema, Council member for SAIP Conference matters
- Division Chairs for identifying reviewers, especially those who stepping up to help at the end.
- All content reviewers who participated and who helped to keep the standard of accepted articles of a high standard.
- Dr. Roelf Botha for managing the proceedings compilation and online publishing.

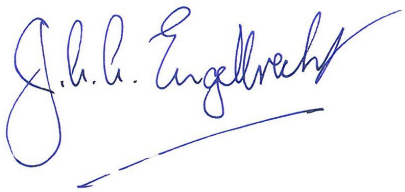

Prof. Japie Engelbrecht
Editor: SAIP 2017 Conference Proceedings

List of Reviewers

Prof.	ABEBE, Amare	North-West University
Dr.	ALBERS, Claudia	University of Witwatersrand
Prof.	ALLIE, Saalih	University of Cape Town
Dr.	ASANTE, Joseph	Tshwane University of Technology
Prof.	ADAMIAK, Daniel	University of Cape Town
Dr.	BARK, Robert	iThemba LABS
Prof.	BASSON, Ilsa	University of South Africa
Prof.	BECK, Geoffrey	University of the Witwatersrand
Dr.	BIETENHOLZ, Michael	Hartebeesthoek Radio Astronomy Observatory
Mr.	BLYTH, S. L.	University of Cape Town
Dr.	BOSMAN, Gurthwin	Stellenbosch University
Prof.	BOTHA, André E.	University of South Africa
Prof.	BOTHA, Johannes R.	Nelson Mandela Metropolitan University
Prof.	BOTTCHER, Markus	North-West University
Prof.	BRAUN, Moritz	University of South Africa
Dr.	BUTHELEZI, Zinhle	iThemba LABS
Dr.	CARLESCHI, Emanuela	University of Johannesburg
Prof.	CHINAKA, Eric	University of Johannesburg (Necsa)
Prof.	CHITHAMBO, Makaiko	Rhodes University
Dr.	CLERK, Douglas	University of the Witwatersrand
Prof.	CLEYMANS, Jean	University of Cape Town
Prof.	COLAFRANCESCO, Sergio	University of the Witwatersrand
Prof.	CONNELL, Simon	University of Johannesburg
Prof.	CORNELL, Alan	University of Witwatersrand
Dr.	CROZIER, Jacqui	Nelson Mandela Metropolitan University
Mr.	DE BEER, Frikkie	South African Nuclear Energy Corporation
Prof.	DE MELLO KOCH, Robert	University of Witwatersrand
Prof.	DEJENE, Francis	University of the Free State
Prof.	DELION, Doru S.	National Institute for Physics and Nuclear Engineering
Prof.	DERRY, Trevor	University of Witwatersrand
Prof.	DHLAMINI, Mokhotjwa S.	University of South Africa
Prof.	DIETEL, Thomas	University of Cape Town
Dr.	DOYLE, Bryan	University of Johannesburg
Dr.	DUNSBY, Peter	University of Cape Town
Mr.	DZHUNUSHALIEV, Vladimir	Kyrgyz-Russian Slavonic University
Mr.	EGGERS, Hans	Stellenbosch University
Prof.	ELLIS, George	University of Cape Town
Prof.	ENGELBRECHT, Christian	University of Johannesburg
Prof.	ENGELBRECHT, Japie	Nelson Mandela Metropolitan University
Prof.	ERASMUS, Rudolph	University of Witwatersrand
Prof.	FAANHOF, Arnaud	North-West University
Prof.	FANG, Yaquan	Institute for Higher Education Policy
Prof.	FERRER, Phil	University of Witwatersrand
Prof.	FISH, Derek	University of Zululand

Prof.	FÖRTSCH, Siegfried	iThemba LABS
Prof.	GEYER, Hendrik	Stellenbosch University
Dr.	GOLDSTEIN, Kevin	University of the Witwatersrand
Prof.	GRAYSON, Diane	University of Pretoria
Prof.	HABARULEMA, John Bosco	South African National Space Agency
Dr.	HARRIS, Richard	University of the Free State
Prof.	HEARNE, Giovanni	University of Johannesburg
Dr.	HERBERT, Mark	University of the Western Cape
Prof.	HOROWITZ, William	University of Cape Town
Mr.	HUSTON, Joey	Michigan State University
Dr.	JANSE VAN VUUREN, Arno	Nelson Mandela Metropolitan University
Prof.	JOHN, Anslyn	Rhodes University
Prof.	JOHN, Ignatius	Cape Peninsula University of Technology
Dr.	JONES, Pete	iThemba LABS
Prof.	JOUBERT, Daniel	University of the Witwatersrand
Prof.	KAR, Deepak	University of the Witwatersrand
Prof.	KARATAGLIDIS, Steven	University of Johannesburg
Mr.	KASTBERG, Anders	Institute of Physics of Nice
Prof.	KEARTLAND, Jonathan	University of the Witwatersrand
Dr.	KNAPPE, Svenja	University of Colorado Boulder
Prof.	KOSCH, Michael	South African National Space Agency
Dr.	KOTZE, Pieter	South African National Space Agency
Prof.	KROON, R. E.	University of the Free State
Prof.	KRÜGER, Tjaart	University of Pretoria
Prof.	LEE, Mike	Nelson Mandela Metropolitan University
Dr.	LEMMER, Miriam	North-West University
Prof.	LEUSCHNER, F. Wilhelm	University of Pretoria
Prof.	LIPPSTREU, Luke	University of Cape Town
Prof.	LINDSAY, Robert	University of the Western Cape
Dr.	MADHUKU, Morgan	iThemba LABS
Prof.	MADJOE, Reggie	University of the Western Cape
Dr.	MALEKA, Peane	iThemba LABS
Prof.	MALHERBE, Johan	University of Pretoria
Dr.	MANOLA, Marco	University of Kwa-Zulu Natal
Dr.	MAPASHA, Edwin	University of Pretoria
Prof.	MAPHANGA, Rapela	Council for Scientific and Industrial Physics
Mr.	MASARA, Brian	South African Institute of Physics
Dr.	MASITENG, Paulus	University of Johannesburg
Dr.	MATTHEWS, Alan	University of Kwa-Zulu Natal
Prof.	MEDVED, Allan Joseph	Rhodes University
Prof.	MEINTJES, Pieter	University of the Free State
Prof.	MELLADO, Bruce	University of the Witwatersrand
Prof.	MEYER, Edson	University of the Free State
Dr.	MEYER, Walter	University of Pretoria
Dr.	MOHANTY, Pankaj	University of Johannesburg
Prof.	MOHR, Peter	Germany Institute for Nuclear Physics
Mr.	MOKHINE, Tebogo	South African Institute of Physics
Dr.	MOLEPO, Mahlaga	University of South Africa
Dr.	MOLOI, Sabata	University of South Africa

Prof.	MOTHUDI, Bakang M.	University of South Africa
Dr.	MSIMANGA, Mandla	Tshwane University of Technology
Prof.	MURONGA, Azwinndini	University of Johannesburg
Prof.	MÜLLER-NEDEBOCK, Kristian	Stellenbosch University
Prof.	NAIDOO, Deena	University of the Witwatersrand
Prof.	NEETHLING, Johannes	Nelson Mandela Metropolitan University
Prof.	NEETHLING, Pieter	Stellenbosch University
Prof.	NEETHLING, Jan	Nelson Mandela Metropolitan University
Prof.	NETSHISAULU, Thomas	University of Limpopo
Prof.	NEWMAN, Richard	Stellenbosch University
Prof.	NGOEPE, Phuti	University of Limpopo
Dr.	NOTHNAGEL, Gabriel	South African Nuclear Energy Corporation
Dr.	NTOAHAE, Peter S.	University of Limpopo
Prof.	NTWAEABORWA, Odireleng	University of the Free State
Dr.	O'CONNEL, Jacques	Nelson Mandela Metropolitan University
Prof.	PAPKA, Paul	Stellenbosch University
Dr.	PELLEGRI, Luna	University of the Witwatersrand
Dr.	PENNY, Clement	University of the Witwatersrand
Dr.	PETERSON, Stephen	University of Cape Town
Dr.	QUANDT, Alex	University of the Witwatersrand
Prof.	RAYNER, Jonathan	University of Sedgefield
Dr.	REDDY, Leelakrishna	University of Johannesburg
Prof.	RICHTER, Werner	Stellenbosch University
Dr.	ROBERTSON, Cherie	University of Johannesburg
Prof.	ROOS, Wiets	University of the Free State
Dr.	RORO, Kittessa	Council for Scientific and Industrial Physics-NLC
Prof.	ROUX, F. Stef	Stellenbosch University
Prof.	SCHOLTZ, Frederik	National Institute for Theoretical Physics
Mr.	SCHULTZ, Ross	Nelson Mandela Metropolitan University
Prof.	SHARPEY-SCHAFER, John F.	University of Western Cape
Prof.	SMITS, Derck	University of Johannesburg
Dr.	SOO KIM, Jong	University of the Witwatersrand (NITheP)
Dr.	STEENKAMP, Christine	University of Stellenbosch
Prof.	STRYDOM, Andre	University of Johannesburg
Prof.	SWART, Hendrik	University of the Free State
Prof.	TAME, Mark	University of Kwa-Zulu Natal
Dr.	TAYLOR, Dale	University of Cape Town
Prof.	TERBLANS, JJ (Koos)	University of the Free State
Dr.	THANTSHA, Nicolas	Tshwane University of Technology
Prof.	THERON, Chris	University of Pretoria
Mrs.	TIBANE, Malebo	University of South Africa
Prof.	TRIAMBAK, Smarajit	University of Western Cape
Dr.	TSHABALALA, K. George	University of the Free State
Dr.	URGESSA, Zelalem N.	Nelson Mandela Metropolitan University
Dr.	USMAN, Iyabo	University of the Witwatersrand
Prof.	VALLABHAPURAPU, Vijaya S.	University of South Africa
Dr.	VAN DER HEYDEN, Kurt	University of Cape Town
Prof.	VAN DYK, Ernest	Nelson Mandela Metropolitan University
Prof.	VAN SOELEN, Brian	University of the Free State

Prof.	VENTER, André	Nelson Mandela Metropolitan University
Dr.	VICKEY, Trevor	University of the Witwatersrand
Dr.	VORSTER, Frederik	Nelson Mandela Metropolitan University
Dr.	WADIASINGH, Zorawar	North-West University
Mr.	WANG, Renjie	CERN
Prof.	WATTERSON, John	University of the Witwatersrand
Prof.	WEIGEL, Herbert	Stellenbosch University
Dr.	WELTMAN, Amanda	University of Cape Town
Dr.	WESTRAADT, Johan	Nelson Mandela Metropolitan University
Ms.	WESTRAADT, Lindsay	Nelson Mandela Metropolitan University (CHRTEM)
Dr.	WHEATON, Spencer	University of Cape Town
Dr.	WIEDEKING, Mathis	iThemba LABS
Prof.	WINKLER, Helmut	University of Johannesburg
Prof.	WYNGAARDT, Shaun	Stellenbosch University
Dr.	YACOOB, Sahal	University of Cape Town
Prof.	ZACHARIAS, Michael	North-West University
Prof.	ZNOJIL, Miloslav	Institute of Nuclear Physics

DIVISION A – DIVISION FOR PHYSICS OF CONDENSED MATTER AND MATERIALS

Investigation of Thermoelectric Properties of $CH_3NH_3PbI_3$: Density Functional Theory and Boltzmann Transport Calculations

Ibrahim Omer Abdallah[1,2], Daniel P Joubert[1], and Mohammed S H Suleiman[1,3]

[1] The National Institute for Theoretical Physics, School of Physics and Mandelstam Institute for Theoretical Physics, University of the Witwatersrand, Johannesburg, Wits 2050, South Africa.
[2] Department of Scientific Laboratories, Sudan University of Science and Technology, Khartoum, Sudan.
[3] Department of Basic Sciences, Imam Abdulrahman Bin Faisal University, P. O. Box 1982, Dammam, KSA.

E-mail: ibraphysics@gmail.com

Abstract. Mixed organometal perovskite $CH_3NH_3PbI_3$ has recently emerged as a promising candidate for low cost, high-efficiency solar cells. The materials' thermoelectric properties which are key to the solar thermoelectric applications have not been investigated extensively. In this paper, the thermoelectric properties of organic-inorganic halide perovskite $CH_3NH_3PbI_3$ were studied by solving the semiclassical Boltzmann transport equation on top of density functional theory (DFT) calculations using maximally-localised Wannier functions (MLWFs). Electronic transport properties were evaluated within the constant relaxation time approximation at different temperatures: 50 K, 100 K and 150 K. The Seebeck coefficient (S), electrical conductivity (σ), electronic thermal conductivity (κ_e), power factor ($S^2\sigma$) and figure of merit (ZT) as function of chemical potential are analysed. The maximal figure of merit is found to be 0.06 and 0.122 at 100 K and 150 K, respectively.

1. Introduction

Organic-inorganic perovskites ABI_3 (A = CH_3NH_3 or NH_2CHNH_2; B = Sn, Pb), have been specified as light harvesting materials [1]. In addition, they were treated as new thermoelectric materials with a large Seebeck coefficient and low thermal conductivity [2, 3], implying that these materials might be potential candidates for thermoelectric applications [4]. The efficiency of thermoelectric devices is characterized by a dimensionless figure of merit ZT[1] $= S^2\sigma T/\kappa$, where S, σ, T and κ are Seebeck coefficient, electrical conductivity, temperature and total thermal conductivity, respectively [6]. Both phonons and electrons are heat carriers, therefore the total thermal conductivity has two contributions, the lattice thermal conductivity component κ_l and the electronic thermal conductivity component κ_e. Thermoelectric materials with a large thermoelectric figure of merit can convert heat to electricity via the Seebeck effect. To have a

[1] "The expressions for figure of merit , Z and ZT, are used interchangeably in the field of TE. Z is the figure of merit with units of 1/K (1/T), and ZT is the standard notation for the dimensionless figure of merit" [5].

large figure of merit one needs a large power factor $S^2\sigma$ and low thermal conductivity κ. In the present work, we studied the thermoelectric properties of the $CH_3NH_3PbI_3$ in an orthorhombic system from a combination of semiclassical Boltzmann transport equation and density functional theory calculations using maximally-localised Wannier functions (MLWFs). $CH_3NH_3PbI_3$ is orthorhombic at low temperature (space group Pnma, 62), with the unit cell shown in Figure 1. Section 2 describes the methodology used in the investigation. Section 3 presents the results and discussion. Finally, we shall give our conclusion in section 4.

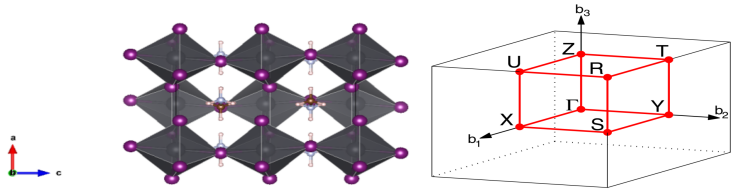

Figure 1. (Color online) The crystal structure of orthorhombic $CH_3NH_3PbI_3$ (left) and its corresponding Brillouin zone (right). Filled red circles are the high symmetry points, while the red bold lines indicate segments of the high symmetry path ($\Gamma - X - S - Y - \Gamma$).

2. Methodology

In this work, the investigation of the electronic structure properties was performed using the Vienna Ab-initio Simulation Package (VASP) [7, 8] based on Density Functional Theory (DFT) [9, 10]. The Projector-Augmented Wave (PAW) [11] method was employed to treat electron-ion interactions. To describe the electrons' exchange and correlation effects, we used the Generalized Gradient Approximation (GGA) as parametrized and revised by Perdew, Burke and Ernzerhof (PBEsol) [12]. $4 \times 4 \times 2$ Monkhorst-Pack meshes were used in sampling the Brillouin zone with an energy cut-off of 520 eV. The atomic positions were fully optimized until all components of the forces were less than 1 meV/atom.

The thermoelectric and electronic transport properties were calculated by solving the semiclassical Boltzmann transport equations in the constant relaxation-time approximation (here $\tau = 10^{-14}$ s) as implemented in the BoltzWann code [13]. The code uses a maximally-localized Wannier functions (MLWFs) [14] basis set to interpolate the bandstructure obtained from the above-mentioned DFT calculations. After using $6 \times 4 \times 4$ k-points for the construction of the MLWFs, a $40 \times 40 \times 40$ was utilized to calculate the electronic transport properties such as Seebeck coefficient S, electrical conductivity σ, electronic thermal conductivity κ_e and the power factor $S^2\sigma$. The computation of MLWFs has been performed within WANNIER90 package [15].

3. Results and discussion

3.1. Bandstructure and density of states

The bandstructure of the structurally optimized $CH_3NH_3PbI_3$ was calculated along the high symmetry points of the Brillouin zone (BZ) using the generalized gradient approximation (GGA) for solids (PBEsol). The calculated electronic bandstructure of $CH_3NH_3PbI_3$ is shown in Figure 2, together with total (TDOS) and projected (PDOS) density of states. Both the valence band maximum (VBM) and conduction band minimum (CBM) were found to be located at the Γ point of the Brillouin zone (BZ), hence the investigated material has a direct band-gap semiconductor character at the gamma Γ point. The calculated band gap according to PBEsol without including spin orbit coupling was found to be 1.57 eV in good agreement with the experimental result of 1.61 eV [16] and with other theoretical predictions [17, 18, 19]. Density of states around the fundamental band gap show that, only iodine I and lead Pb contribute to the DOS.

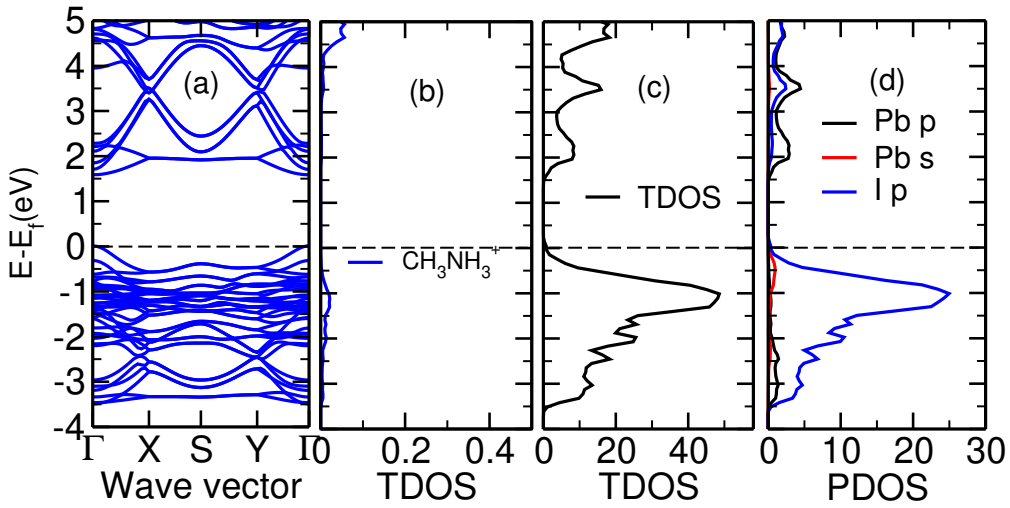

Figure 2. (Color online) DFT calculated electronic structure for $CH_3NH_3PbI_3$: (a) band structure; (b) $CH_3NH_3^+$ (TDOS); (c) total density of states (TDOS), (d) partial density of states (PDOS) (arb. units) using PBEsol.

3.2. Thermoelectric properties

The calculated properties are plotted in Figures 3-7 as functions of the chemical potential μ at temperatures: 50 K, 100 K and 150 K.

The Seebeck coefficient S, is defined as the ratio of the electric field to the temperature gradient when the electrical current is zero. The calculated Seebeck coefficients as a function of chemical potential μ at different temperatures are presented in Figure 3. It is clear that Seebeck coefficient of $CH_3NH_3PbI_3$ has positive values at chemical potential $\mu = 0$, indicating that it is a p-type semiconductor. In the z-direction the maximum values of the Seebeck coefficient S almost remained constant from 50 to 150 K.

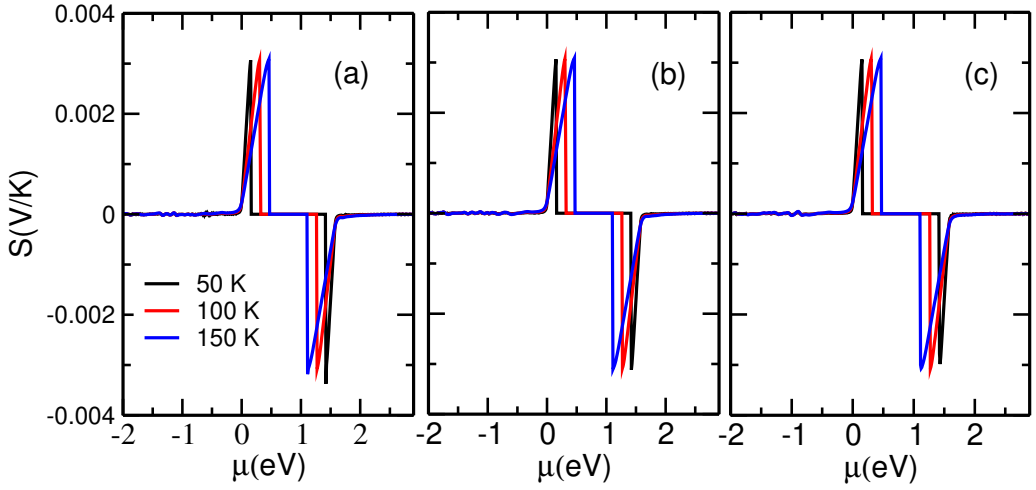

Figure 3. (Color online) Variation of Seebeck coefficient with respect to chemical potential at different temperatures in the (a) x-direction, (b) y-direction, and (c) z-direction.

The calculated electrical conductivity σ as a function of chemical potential at different temperatures are presented in Figure 4. Electrical conductivity was found to be almost

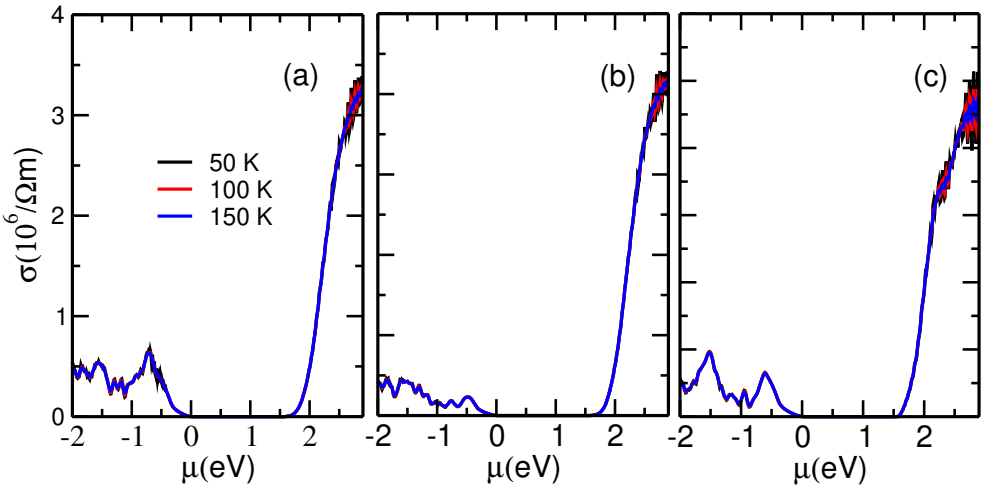

Figure 4. (Color online) Variation of electrical conductivity with respect to chemical potential at different temperatures in the (a) x-direction, (b) y-direction, and (c) z-direction.

temperature independent in the considered temperature range. This trend was observed in SnSe [20] and ScRhTe [21]. In general, the value of electrical conductivity increases with increase in absolute value of the chemical potential at all temperatures with the highest value 4.58×10^6 $\Omega^{-1}\mathrm{m}^{-1}$ in the z-direction at chemical potential 2.84 eV.

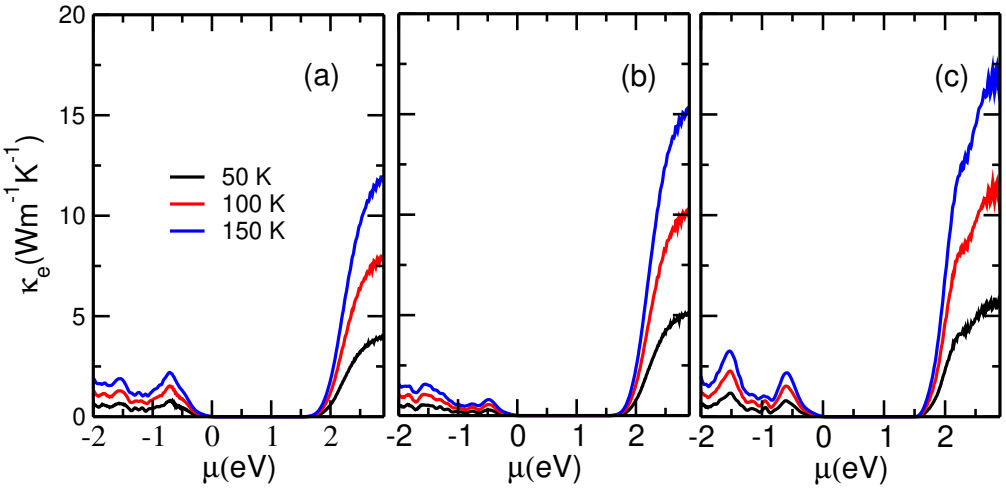

Figure 5. (Color online) Electronic thermal conductivity as a function of chemical potential at different temperatures in the (a) x-direction, (b) y-direction, and (c) z-direction.

The electronic thermal conductivity κ_e as a function of chemical potential at different temperatures are plotted in Figure 5. At chemical potential 2.84 eV the maxima of the electronic thermal conductivity in z-direction increases from 5.8 $\mathrm{Wm}^{-1}\mathrm{K}^{-1}$ at 50 K to 17.3 $\mathrm{Wm}^{-1}\mathrm{K}^{-1}$ at 150 K.

The power factor $S^2\sigma$ as a function of chemical potential at different temperatures is shown in Figure 6. At chemical potential 1.96 eV, the maximum calculated value of the power factor was found to be 0.00042 $\mathrm{Wm}^{-1}\mathrm{K}^{-2}$ and 0.00072 $\mathrm{Wm}^{-1}\mathrm{K}^{-2}$ in z-direction at 100 K and 150 K, respectively.

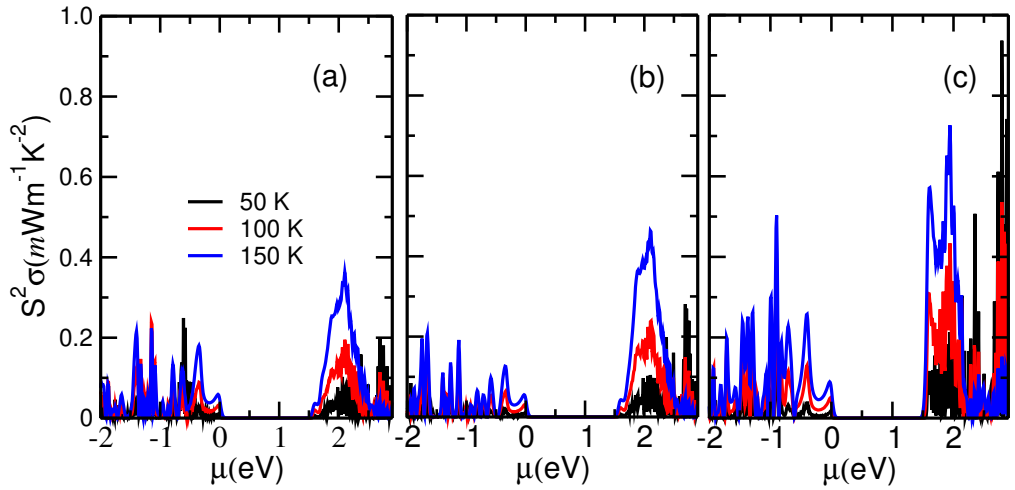

Figure 6. (Color online) Calculated power factor as a function of chemical potential at different temperatures in the (a) x-direction, (b) y-direction, and (c) z-direction.

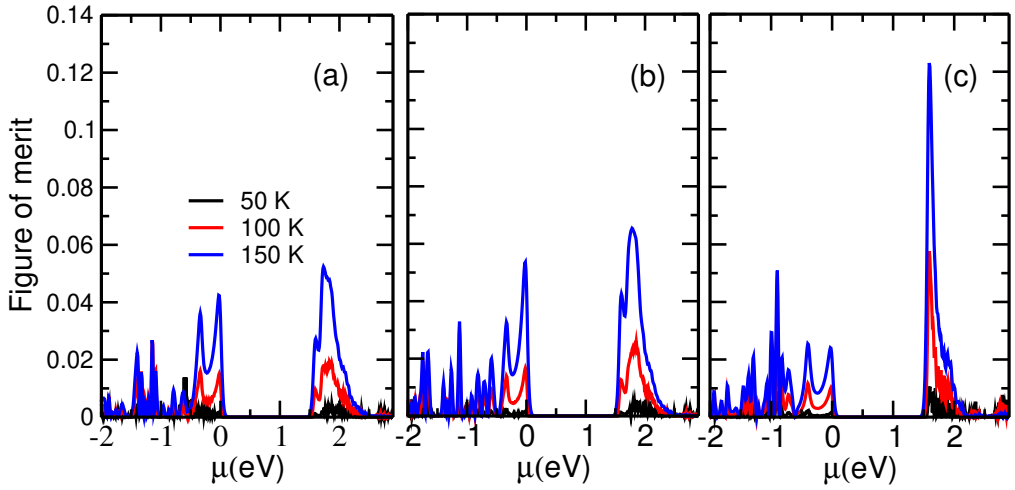

Figure 7. (Color online) Calculated figure of merit as a function of chemical potential at different temperatures in the (a) x-direction, (b) y-direction, and (c) z-direction.

Using the calculated transport coefficients, and the calculated lattice thermal conductivities K_L from Ref. [22], the figure of merit as a function of chemical potential at low temperatures along x-, y- and z-directions is obtained as shown in Figure 7. We can see that the values of ZT increase with increasing temperature. The maxima of the ZT in the z-direction increases from 0.06 at 100 K to 0.122 at 150 K.

From the presented figures, it is evident that the obtained Seebeck coefficient (Figure 3) and figure of merit (Figure 7) are nearly isotropic; while the electrical conductivity (Figure 4), the electronic thermal conductivity (Figure 5), and the power factor (Figure 6) are highly anisotropic with their optimal values in the z-direction.

4. Conclusion

We have carried out a detailed theoretical study of the thermoelectric properties of $CH_3NH_3PbI_3$ in an orthorhombic system for the first time based on density functional theory combined

with the Boltzmann transport theory within the constant relaxation time approximation as implemented in BoltzWann code. Based on the results, we show that the optimum ZT values of the orthorhombic $CH_3NH_3PbI_3$ was found to be 0.06 at 100 K and 0.122 at 150 K in the z direction.

Acknowledgements
IOAA would like to acknowledge the support he received from NRF-TWAS for funding, and Sudan University of Science and Technology (SUST). We also wish to acknowledge the Centre for High Performance Computing (CHPC), South Africa, for providing us with computing facilities.

References

[1] Lee C, Hong J, Stroppa A, Whangbo M H and Shim J H 2015 *RSC Advances* **5** 78701–78707
[2] Stoumpos C C, Malliakas C D and Kanatzidis M G 2013 *Inorganic chemistry* **52** 9019–9038
[3] Pisoni A, Jaćimović J, Barišić O S, Spina M, Gaál R, Forró L and Horváth E 2014 *arXiv preprint arXiv:1407.4931*
[4] He Y and Galli G 2014 *Chemistry of Materials* **26** 5394–5400
[5] Tritt T M and Subramanian M 2006 *MRS bulletin* **31** 188–198
[6] Goldsmid H, Nolas G and Sharp J 2001 Thermoelectrics: Basic principles and new materials developments
[7] Kresse G and Hafner J 1993 *Physical Review B* **47** 558
[8] Kresse G and Hafner J 1994 *Physical Review B* **49** 14251
[9] Hohenberg P and Kohn W 1964 *Physical review* **136** B864
[10] Kohn W and Sham L J 1965 *Physical review* **140** A1133
[11] Kresse G and Joubert D 1999 *Physical Review B* **59** 1758
[12] Perdew J P, Ruzsinszky A, Csonka G I, Vydrov O A, Scuseria G E, Constantin L A, Zhou X and Burke K 2008 *Physical Review Letters* **100** 136406
[13] Pizzi G, Volja D, Kozinsky B, Fornari M and Marzari N 2014 *Computer Physics Communications* **185** 422–429
[14] Souza I, Marzari N and Vanderbilt D 2001 *Physical Review B* **65** 035109
[15] Mostofi A A, Yates J R, Lee Y S, Souza I, Vanderbilt D and Marzari N 2008 *Computer physics communications* **178** 685–699
[16] Baikie T, Fang Y, Kadro J M, Schreyer M, Wei F, Mhaisalkar S G, Graetzel M and White T J 2013 *Journal of Materials Chemistry A* **1** 5628–5641
[17] Wang Y, Gould T, Dobson J F, Zhang H, Yang H, Yao X and Zhao H 2013 *Physical Chemistry Chemical Physics* **16** 1424–1429
[18] Brivio F, Frost J M, Skelton J M, Jackson A J, Weber O J, Weller M T, Goni A R, Leguy A M, Barnes P R and Walsh A 2015 *Physical Review B* **92** 144308
[19] Ali I O A, Joubert D P and Suleiman M S H 2018 *Materials Today: Proceedings* **5** 10570–10576
[20] Wang F Q, Zhang S, Yu J and Wang Q 2015 *Nanoscale* **7** 15962–15970
[21] Kaur K and Kaur J 2017 *Journal of Alloys and Compounds* **715** 297–303
[22] Ali I O A, Joubert D P and Suleiman M S H 2018 *The European Physical Journal B* **91** 263 ISSN 1434-6036

First-principles investigation of lattice thermal conductivity and structural stability of $CH_3NH_3PbI_3$

Ibrahim Omer Abdallah[1,2], Daniel P Joubert[1], and Mohammed S H Suleiman[1,3]

[1] The National Institute for Theoretical Physics, School of Physics and Mandelstam Institute for Theoretical Physics, University of the Witwatersrand, Johannesburg, Wits 2050, South Africa.
[2] Department of Scientific Laboratories, Sudan University of Science and Technology, Khartoum, Sudan.
[3] Department of Basic Sciences, Imam Abdulrahman Bin Faisal University, P. O. Box 1982, Dammam, KSA.

E-mail: ibraphysics@gmail.com

Abstract. Hybrid halide perovskites have recently emerged as new materials for solar cell applications leading to a new class of hybrid semiconductor photovoltaic cells, with very recent results demonstrating a 20.1% efficiency. Here, we investigate the structural stability, elastic constants, vibrational properties and lattice thermal conductivity of the orthorhombic $CH_3NH_3PbI_3$ using first-principles density functional theory calculations. The relaxed system is dynamically stable, while the equilibrium elastic constants satisfy all the mechanical stability criteria for orthorhombic crystals, showing stability against the influence of external forces. The non-isotropic lattice thermal conductivity of $CH_3NH_3PbI_3$ was calculated with the single-mode relaxation-time approximation and a full solution of the linearized phonon Boltzmann equation from first-principles anharmonic lattice dynamics calculations. Our results show that lattice thermal conductivity is anisotropic, and the calculated lattice thermal conductivity at 150 K was found to be 0.189, 0.138, and 0.530 $Wm^{-1}K^{-1}$ in the directions x, y and z, respectively

1. Introduction

Hybrid organic-inorganic perovskites have recently attracted strong interest as photo absorbers in solar cells, due to their high absorption coefficient, high carrier mobility, long diffusion lengths and ease of fabrication [1, 2]. Methyl ammonium lead iodide $CH_3NH_3PbI_3$ is one of the most relevant for photovoltaic applications in the perovskite family. Depending on temperature and on atomic sizes of the chemical constituents, perovskites can possess cubic, tetragonal or orthorhombic structural phases. For temperatures below 160 K, the $CH_3NH_3PbI_3$ perovskite structure presents an orthorhombic crystal symmetry with space group Pnma (62) [3]. Brevio F. et al., [4] and Feng [5] have identified the lattice dynamics, vibrational spectra and the mechanical properties of the cubic, tetragonal and orthorhombic phases. However, to the best of our knowledge, the vibrational and elastic properties of $CH_3NH_3PbI_3$ have not been investigated extensively. The theoretical study using density functional theory (DFT) by Xin Qian et al. [6] found a very low thermal conductivity (0.59 W/mK) for the tetragonal phase at room temperature, and higher thermal conductivity for the pseudocubic phase (1.80 W/mK) at 330 K. We systematically studied the elastic constants, vibrational properties and lattice

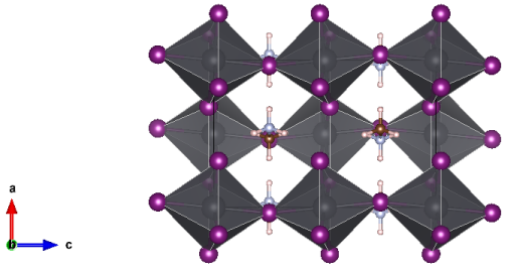

Figure 1. The crystal structure of the orthorhombic phase.

thermal conductivity of the $CH_3NH_3PbI_3$ in an orthorhombic system using density functional theory. The unit cell of the orthorhombic $CH_3NH_3PbI_3$, space group 62 (Pnma), with the unit containing 48 atoms is shown in Figure 1. The computational methodology of this study are elaborated in Section 2. Results and discussions are summarized in Section 3, and conclusions appear in Section 4.

2. Methodology

In this work, the investigation of the electronic structure properties was performed using the Vienna Ab-initio Simulation Package (VASP) [7, 8], based on Density Functional Theory (DFT) [9, 10]. The Projector-Augmented Wave (PAW) [11] method was employed to treat electron-ion interactions. To describe the electron exchange-correlation, we used the Generalized Gradient Approximation (GGA) as parameterized by Perdew, Burke and Ernzerhof for solids PBEsol [12]. $4 \times 4 \times 2$ Monkhorst-Pack meshes were used in sampling the Brillouin zone with an energy cut-off of 520 eV. The atomic positions were fully optimized until all components of the forces were less than 1 meV/atom.

To determine the stability of $CH_3NH_3PbI_3$ we examine its elastic constants. The elastic constants can be obtained by calculating the total energy as a function of the appropriate lattice deformation by first principles calculations. The elastic strain energy density is given by [13]

$$U = \frac{\Delta E}{V_0} = \frac{1}{2}\sum_{i}^{6}\sum_{j}^{6} C_{ij} e_i e_j, \tag{1}$$

where ΔE is the energy difference between the deformed and equilibrium structures; V_0 is the volume of cell; C_{ij} are the elastic constants; e_i and e_j are strains.

For an orthorhombic system, the nine independent elastic constants are C_{11},C_{12}, C_{13}, C_{22}, C_{23}, C_{33}, C_{44}, C_{55}, and C_{66}. In terms of these constants, the Born conditions for mechanical stability [13] are

$C_{11} > 0$; $C_{11}C_{22} > C^2_{12}$; $C_{11}C_{22}C_{33}$ +2 $C_{12}C_{13}C_{23}$ - $C_{11}C^2_{23}$ - $C_{22}C^2_{13}$ - $C_{33}C^2_{12}$ >0; $C_{44} > 0$; $C_{55} > 0$; and $C_{66} > 0$.

Bulk elastic properties: bulk modulus B_V, Young's modulus E and shear modulus G_V were calculated from the elastic constants by the Voigt method [14] using the following formulas for an orthorhombic crystal

$$B_V = \frac{1}{9}[c_{11} + c_{22} + c_{33}] + \frac{2}{9}[c_{12} + c_{13} + c_{23}] \tag{2}$$

$$G_V = \frac{1}{15}[c_{11} + c_{22} + c_{33} - c_{12} - c_{13} - c_{23}] + \frac{3}{5}[c_{44} + c_{55} + c_{66}] \tag{3}$$

The Young's modulus E, and Poisson's ratio, ν can be given by

$$E = \frac{9BG}{3B+G} \tag{4}$$

$$\nu = \frac{3B-2G}{2(3B+G)} \tag{5}$$

Phonon properties were computed using a finite displacement method. Force constants were computed from a $2 \times 2 \times 2$ supercell expansion and analyzed using the Phonopy code [15] with VASP as force calculator. For the phonon density of states, the Brillouin zone (BZ) integrations were performed with $36 \times 36 \times 36$ meshes.

In general the thermal conductivity has two contributions, the electronic thermal conductivity κ_e and the lattice thermal conductivity κ_L. The lattice thermal conductivities were calculated with the single-mode relaxation-time (SMRT) approximation and linearized phonon Boltzmann equation as implemented in Phono3py [16]. For the third-order interatomic force constants a $2 \times 2 \times 2$ supercell was built containing 384 atoms, and reciprocal spaces of the supercells were sampled by $2 \times 2 \times 2$ meshes. To compute lattice thermal conductivity, the reciprocal spaces of the primitive cells were sampled using $8 \times 8 \times 8$.

3. Results and discussion

3.1. Elastic stability

The mechanical stability for $CH_3NH_3PbI_3$ orthorhombic crystal was obtained by checking that all the elastic constants are positive and satisfy the Born conditions for mechanical stability [13]. The computed elastic constants using PBEsol approximations are shown in Table 1. From the obtained results, one can confirm that the structure is mechanically stable against the influence of external forces in both approximations. Comparing our results from Table 1, with the values calculated from other work [5]. The differences in the values presented in Table 1 are due to the different approximation used.

Table 1. PBEsol calculated independent elastic constants for an orthorhombic system in (GPa)

Method	c_{11}	c_{12}	c_{13}	c_{22}	c_{23}	c_{33}	c_{44}	c_{55}	c_{66}
PBEsol	28.37	12.63	11.35	21.00	09.73	37.67	05.37	04.95	11.16
Other [5]	27.8	11.7	17.4	20.5	20.2	24.8	03.0	09.8	06.3

Table 2. Calculated bulk modulus B_V, Young's modulus E, shear modulus G_V, Poisson's ratio ν and B/G ratio

Method	B_V(GPa)	E(GPa)	G_V(GPa)	ν	B/G
PBEsol	17.16	20.44	7.85	0.30	2.19
Other [5]	18.10	15.00	3.60	0.36	3.30

According to equations (2-5), the bulk modulus B, Young's modulus E, shear modulus G, Poisson's ratio ν and B/G ratio are presented in Table 2 with other theoretical results [5]. Our results show that the elastic constant C_{11} is smaller than C_{33} and larger than C_{22} for $CH_3NH_3PbI_3$, implying the anisotropy of its elasticity.

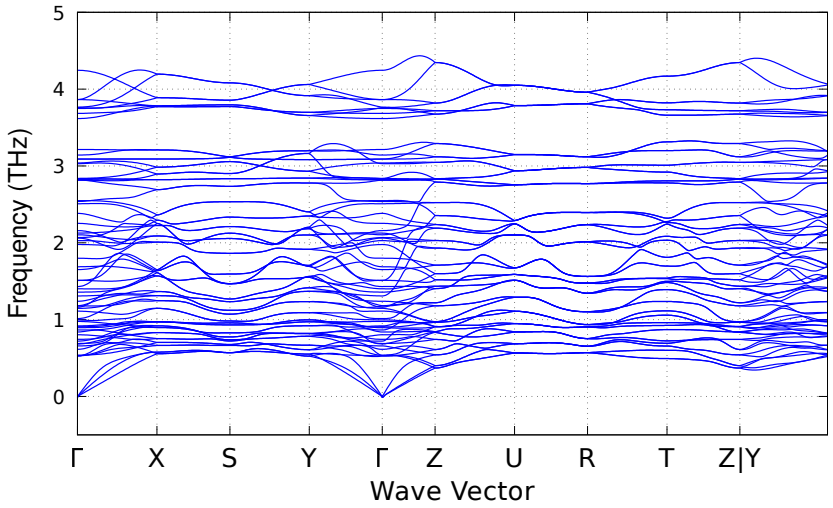

Figure 2. (Color online) Phonon dispersion relation graph calculated using PBEsol
.

3.2. Dynamical stability

Figure 2 shows the calculated phonon bandstructure curve of $CH_3NH_3PbI_3$ in an orthorhombic system. It can be seen from this figure that all phonon modes are positive in the Brillouin zone of the structure, therefore, the relaxed system is dynamically stable.

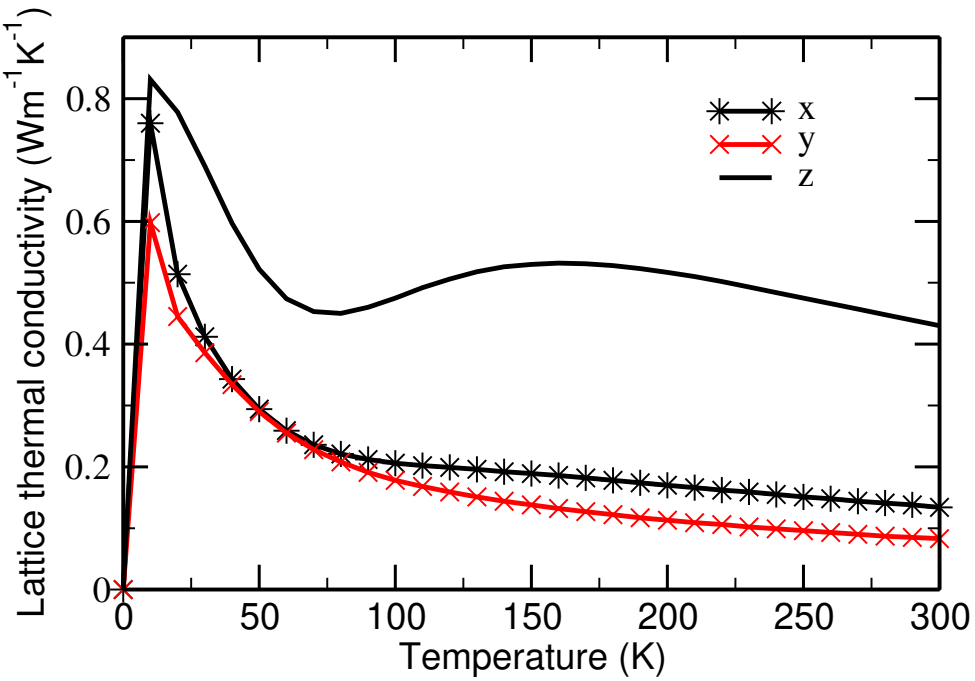

Figure 3. (Color online) Lattice thermal conductivity of $CH_3NH_3PbI_3$ as a function of temperature along $x-$, $y-$ and $z-$ axes.

3.3. Lattice thermal conductivity

The lattice thermal conductivity κ_L is very important which as it significantly affects thermoelectric material performance. Figure 3 shows the temperature-dependent lattice thermal conductivity κ_L of $CH_3NH_3PbI_3$ along $x-$, $y-$ and $z-$ directions. the calculated lattice thermal conductivities are found to be very low and anisotropic. For example, the calculated κ_L at 150 K a long $x-$, $y-$ and $z-$ directions are 0.189, 0.138, and 0.530 $Wm^{-1}K^{-1}$, respectively. As temperature increases to room temperature k_L reduces to 0.134, 0.083, and 0.43 $Wm^{-1}K^{-1}$ a long x, y and $z-$ directions, respectively. The obtained value on z direction is significantly larger than those values on the $x-$ and $y-$ directions. Table 3 shows the calculated lattice thermal conductivity for $CH_3NH_3PbI_3$ in an orthorhombic phase between 50 K and 150 K in the $x-$, $y-$ and $z-$directions with the corresponding average values. At 150 K, the ratios $\kappa_L(z)/\kappa_L(y)$ = 3.84 and $\kappa_L(z)/\kappa_L(x)$ = 2.80, indicate high anisotropic behavior of the structure.

Table 3. The calculated lattice thermal conductivity ($Wm^{-1}K^{-1}$) in the $x-$, $y-$ and z-directions with the corresponding average values.

T (K)	$\kappa_L(a)$	$\kappa_L(b)$	$\kappa_L(c)$	κ_L(avg)
50	0.294	0.290	0.522	0.340
100	0.206	0.178	0.475	0.286
150	0.189	0.138	0.530	0.286

4. Conclusion

The structural stability, elastic constants, vibrational properties and lattice thermal conductivity of the orthorhombic $CH_3NH_3PbI_3$ have been calculated using a generalized gradient approximation as parametrized by Perdew, Burke and Ernzerhof PBEsol. The relaxed system is dynamically stable, and the equilibrium elastic constants satisfy all the mechanical stability criteria for an orthorhombic crystal, showing stability against the influence of external force. The calculated lattice thermal conductivity at 150 K was found to be 0.189, 0.138, and 0.530 $Wm^{-1}K^{-1}$ in the directions along $x-$, $y-$ and $z-$ axes, respectively. Our results confirmed the very low thermal conductivity.

Acknowledgements

IOAA would like to acknowledge the support he received from NRF-TWAS for funding, and Sudan University of Science and Technology (SUST). We also wish to acknowledge the Centre for High Performance Computing (CHPC), South Africa, for providing us with computing facilities.

References

[1] Green M A, Ho-Baillie A and Snaith H J 2014 *Nature Photonics* **8** 506–514

[2] Chen Q, De Marco N, Yang Y M, Song T B, Chen C C, Zhao H, Hong Z, Zhou H and Yang Y 2015 *Nano Today* **10** 355–396

[3] Baikie T, Fang Y, Kadro J M, Schreyer M, Wei F, Mhaisalkar S G, Graetzel M and White T J 2013 *Journal of Materials Chemistry A* **1** 5628–5641

[4] Brivio F, Frost J M, Skelton J M, Jackson A J, Weber O J, Weller M T, Goni A R, Leguy A M, Barnes P R and Walsh A 2015 *Physical Review B* **92** 144308

[5] Feng J 2014 *APL Materials* **2** 081801

[6] Qian X, Gu X and Yang R 2016 *Applied Physics Letters* **108** 063902

[7] Kresse G and Hafner J 1993 *Physical Review B* **47** 558

[8] Kresse G and Hafner J 1994 *Physical Review B* **49** 14251
[9] Hohenberg P and Kohn W 1964 *Physical review* **136** B864
[10] Kohn W and Sham L J 1965 *Physical review* **140** A1133
[11] Kresse G and Joubert D 1999 *Physical Review B* **59** 1758
[12] Perdew J P, Ruzsinszky A, Csonka G I, Vydrov O A, Scuseria G E, Constantin L A, Zhou X and Burke K 2008 *Physical Review Letters* **100** 136406
[13] Mouhat F and Coudert F X 2014 *Physical Review B* **90** 224104
[14] Voigt W 1928 *Ann Arbor, Mich*
[15] Togo A and Tanaka I 2015 *Scr. Mater.* **108** 1–5
[16] Togo A, Chaput L and Tanaka I 2015 *Physical Review B* **91** 094306

The role of the pre-exponential factor in the segregation profiles of Cu(111)-SnSb and Cu(100)-SnSb ternary alloys

JKO Asante[1] and WD Roos[2]

[1]Department of Physics, Tshwane University of Technology, Pretoria, South Africa
[2]Department of Physics, University of the Free State, Bloemfontein, South Africa.

E-mail: Asantejko@tut.ac.za

Abstract. Cu(111) and Cu(100) were thermally doped with the same concentrations of Sn (0.14 at%) and Sb (0.12 at%) in both crystals. Auger electron spectroscopy was used to measure the segregation profiles. The segregation parameters of Sn and Sb were extracted by comparing simulated profiles with the experimental data. The segregation profiles in the two crystals were compared and it was found that the profiles of both Sn and Sb in Cu(111) shifts to lower temperatures than those in Cu(100) samples. The quantified segregation parameters were used to explain the shift. It is argued that changes in the pre-exponential diffusion factors, rather than the activation energies, were the main contributing parameter.

1. Introduction

It has become known from binary alloy studies that an impurity that has lower surface energy, larger atomic size as well as having attractive inter-atomic interaction with the host element, will segregate to the grain boundaries or surfaces towards total energy minimization of the alloy [1,2].

Impurity segregation to the grain boundaries of alloys could cause these alloys to become brittle and fail during use. The effects of undesirable low concentration impurities could be neutralised by introducing other impurities that have higher interaction energy, but have no tendency to segregate due to a low segregation energy. The need to understand and quantify segregation parameters is thus necessary for theoretical considerations, designing and manufacturing.

The energetics involved in impurity segregation in ternary and multi-component alloys as well as other segregation parameters have been discussed theoretically and quantified experimentally [3-5]. Besides the bulk concentration, the parameters that account for kinetics segregation of impurity atoms are the activation energy and pre-exponential diffusion factor [6]. In a recent study, Jafta *et al*. [6] have shown that the pre-exponential factor, in the diffusion coefficient of Sb segregating in Cu, is dependent on the surface orientation of a crystal. In this case the authors considered a binary system of a Sb doped Cu(111/110) bi-crystal.

The current study compare the kinetic segregation behaviours of two elemental impurities (Sn and Sb) in two low index surface orientations of Cu and argued that the orientation dependency, in the temperature range studied, is mainly because of a change in the vacancy formation entropy.

2. Experimental

A thin layer of Sn, about 50 kÅ, was evaporated onto pure 99.999 at.% Cu(100) and Cu(111) single crystals. The crystals were sealed in quartz tubes filled with Ar gas and annealed at 920 ºC for 44 days to ensure a homogeneous distribution of the elements. The procedures were repeated for Sb (35 kÅ) on the same samples. Atomic adsorption spectroscopy was used to determine the bulk concentrations as 0.14 at.% Sn and 0.12 at.% Sb.

A method of ramping the sample temperature at a constant rate (0.05 K/s) from 400 K to 900 K and at the same time, using AES to measure the surface concentrations in the form of Sn($M_5N_{45}N_{45}$), Sb($M_5N_{45}N_{45}$) and Cu($L_3M_{45}M_{45}$) peaks was followed. Each sample was mounted onto the same resistance heater in a vacuum with base pressure $< 4.0 \times 10^{-9}$ Torr. The temperature was measured with a chromel-alumel thermocouple on the back of the sample.

The measured segregation profiles were simulated with a modified Darken model [7], yielding the segregation parameters.

3. Results and discussion

Figures 1 and 2 show the experimental results and model fits for Sn and Sb segregation in Cu(100) and Cu(111) at a linear temperature ramp of 0.05 K/s. The values of the fitting parameters used are given in Table 1.

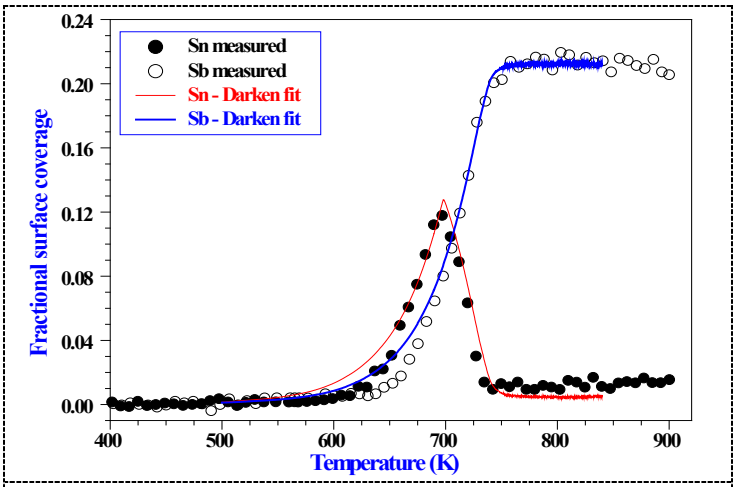

Figure 1. Measured Sn and Sb segregation profiles (solid and opened circles resp.) in Cu(100)SnSb at a heating rate of 0.05 Ks^{-1} and fits (solid lines)

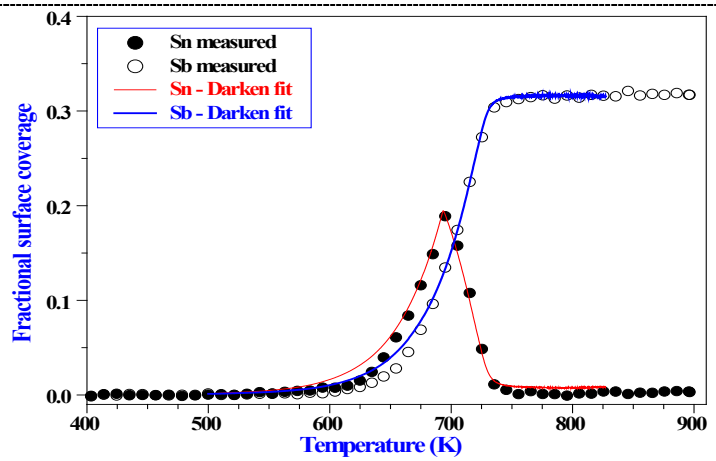

Figure 2. Measured Sn and Sb segregation profiles (solid and opened circles resp.) in Cu(111)SnSb at a heating rate of 0.05 Ks^{-1} and fits (solid lines)

Table 1. Summary of Sn and Sb segregation parameters in Cu(100) and Cu(111).

Orientation	Segregating species	D_o (m^2s^{-1})	E ($kJmol^{-1}$)	ΔG ($kJmol^{-1}$)	$\Omega_{Cu\text{-}i}$ ($kJmol^{-1}$)	$\Omega_{Sn\text{-}Sb}$ ($kJmol^{-1}$)
Cu(100)	Sn	$(6.3 \pm 0.7) \times 10^{-6}$	175 ± 4	65 ± 5	3.4 ± 0.2	
	Sb	$(2.8 \pm 0.3) \times 10^{-5}$	186 ± 3	84 ± 4	15.9 ± 0.3	-5.4 ± 0.5
Cu(111)	Sn	$(9.3 \pm 0.5) \times 10^{-4}$	196 ± 5	68 ± 4	3.6 ± 0.2	
	Sb	$(3.4 \pm 0.6) \times 10^{-3}$	206 ± 4	86 ± 5	16.2 ± 0.3	-5.3 ± 0.5

Both figures 1 and 2 clearly show that Sn segregates first, attained some maximum concentration, depending on the orientation, and is then replaced from the surface by Sb [8]. This replacement is because of the lower Sn segregation energy, compared to Sb, as well as the repulsive interaction ($\Omega_{Sn\text{-}Sb}$) between the two segregates. The temperature where Sn reaches a maximum coverage on the surface of both orientations is the same and confirms the same bulk concentrations of Sn.

It is well known from thermodynamic segregation theory that the kinetic region of segregation is controlled by the diffusion coefficient of the species. For vacancy diffusion, the activation energy E is the sum of the migration enthalpy, E_m, and the vacancy formation enthalpy E_v. The vacancy formation energy, E_v is defined as the difference between the bulk cohesive and the surface cohesive energies. In a fcc lattice, the vacancy created by a bulk Cu atom has a coordination number of twelfth. On the surface of (100) and (111) orientations the coordination numbers are four and three respectively. The surface cohesive energies of Sn in (100) surface is therefore higher than for the (111) surface. The difference in activation energy between the (100) and (111) orientations for both Sn and Sb is the same (about 20 kJ/mol) see Table 1 indicating that the creation of vacancies is mainly due to Cu atoms. The migration energy is thus a bulk phenomenon and independent of the surface orientations [6]. The two orientations will have different E_vs and are thus orientation dependant. The change in the activation energies between the orientations, is thus because of the change in vacancy formation enthalpies.

The activation energies suggests that, other segregation parameters being equal, the (100) profiles shift to higher temperatures for higher activation energy. However, from the segregation plots of Sn in the two orientations, figure 3, Sn in the Cu(111) profile with $E_{Cu(111)}$ = 196 kJ/mol lies at lower temperatures than the Sn profile in the Cu(100) with $E_{Cu(100)}$ = 175 kJ/mol. Similarly, Sb in Cu(111) lies at lower temperatures as compared to Sb in Cu(100). The plausible explanation therefore lies in the differences in the pre-exponential factors.

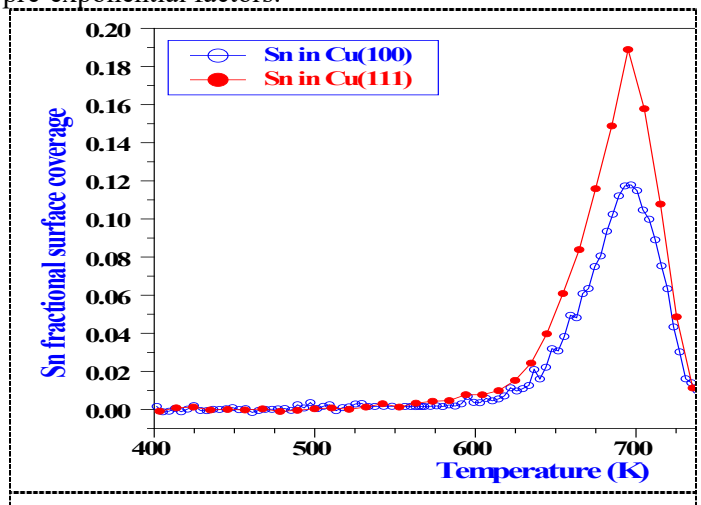

Figure 3. Measured Sn segregation profiles in Cu(100)SnSb and in Cu(111)SnSb under the same experimental conditions. The samples heating rate was 0.05 K/s.

The pre-exponential factors, D_os, depend on the change in entropy of both vacancy formation and migration Gibbs free energies as well as the frequency of vibrations [6]. The values in Table 1, indicate a similar change in entropy between the orientations. This is evident in the ratios of the D_os. D_o(Sn:111)/D_o n: 00 D_o(Sb:111)/D_o(Sb:100) resulting in differences in entropy changes of 4.99 k_B and 4.79 k_B respectively (here k_B = Boltzmann's constant). The entropy change is therefore greater in Cu(111) than in Cu(100). Consequently, Sn in Cu(111) has a higher D_o (= 9.3 x 10^{-4} m^2s^{-1}) than in Cu(100) with D_o = 6.3 x 10^{-6} m^2s^{-1}. Noting the same bulk concentration of Sn in the two orientation, the effect of the D_os, which is two order of magnitude higher, of Sn in Cu(111) than in Cu(100), could be the plausible way to explain the lower temperature kinetic profile of Sn in Cu(111) as compared to that of Sn in Cu(100). A plot of the diffusion coefficient versus temperature, using the parameters in Table 1, (see figure 4) further confirms the dominant role of the D_os in the diffusion coefficient in this temperature region. The same is true for Sb.

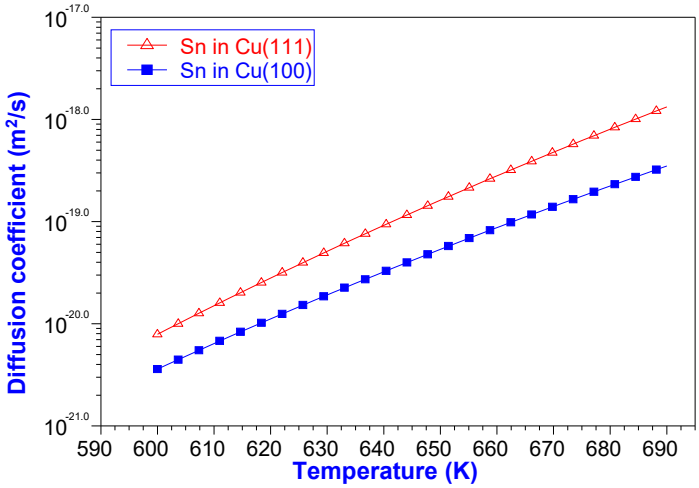

Figure 4. The diffusion coefficients of Sn in Cu(100) and Cu(111) in the kinetic region

4. Conclusion

It has been confirmed experimentally that the segregation parameters of ternary alloys of Cu are orientation dependant if vacancy diffusion plays a role in the kinetics. The changes in diffusion parameters describing the segregation profiles of Sb and Sn in (111) and (100) orientations, proved that the differences are due to different vacancy formation entropies. The changes in the vacancy formation energies are reflected in the changes in activation energies as well as changes in the pre exponential diffusion terms. Both Sn and Sb profiles lie at lower temperatures in Cu(111)SnSb as compared to their profiles in Cu(100)SnSb. In the kinetic temperature range these changes are mainly due to the vacancy formation entropy term differences in the D_os which is found to be about 4.8 k_B and yielding a higher diffusion coefficient.

References

[1] Nyéki J, Girardeaux C, Erdélyi Z, Langer G A, Erdélyi G, Beke D L and Rolland A 2001 *Surf. Sci.* **495** 200
[2] Yan S L, Lin M and Wang J Y 2013 *Appl. Phy.* A **113(2)** 423
[3] Madito M J, Swart H C and Terblans J J 2012 *Proceedings of* 57th *SAIP Conf*. UP Pretoria
[4] Bozzolo G, Farrente J, Noebe R D, Good B, Honecy F S and Abel P 1999 *Comp.Mat. Sci.***15(2)** 169
[5] Ardell A J and Bellon P 2016 *Cur. Opin. in Sol. Stat. and Mat.Sci.* **20(3)** 115
[6] Jafta C J, Roos W D, Terblans J J, Asante J K O and Ozoemena K I 2011 *Proceedings of* 56th *SAIP Conf*. UNISA Pretoria
[7] Du Plessis J 1990 *Surface Segregation Diffusion and Defect Data*, Sci-Tech, Brookfield
[8] Asante J K O and Roos W D 2012 *Surf. Rev. and Lett.* **19(1)** 1250006-1

Quasiparticle band structure and optical properties of α-MnO_2: a beyond density functional theory investigation

M Chepkoech[1], D P Joubert[1] and G O Amolo[1,2]

[1]The National Institute for Theoretical Physics, School of Physics and Mandelstam Institute for Theoretical Physics, University of the Witwatersrand, Johannesburg Wits 2050, South Africa

[2]Department of Physics and Space Science, The Technical University of Kenya, P.O. Box 52428-00200, Nairobi, Kenya

E-mail: chepkoechmirriam@gmail.com

Abstract. The quasi-particle band structure and the optical properties of spin polarized bulk α-MnO_2 have been investigated by means of many body perturbation theory within an *ab initio* framework. As a starting point the electronic band structure obtained from Density Functional Theory with a Hubbard correction (DFT+U, $U = 2.4$ eV) shows that bulk α-MnO_2 is a semiconductor with a band gap of 1.284 eV. The quasiparticle band structure at the $scGW_0$ many body perturbation level of approximation yields a fundamental band gap of 2.20 eV. Moreover, for the optical properties calculations, two particle excitations have been included through solving the Bethe-Salpeter equations (BSE). From our results, the α-MnO_2 exhibits strong optical absorption in the visible region along all the crystallographic directions. The optical anisotropy in this material is analyzed by means of the dielectric function as well as the optical absorption coefficients along different principal axes. The optical absorption spectrum predicts strongly bound excitons that lie below the calculated quasiparticle band gap with binding energies of 0.60 and 0.07 eV in bulk α-MnO_2.

1. Introduction

The demand for clean and sustainable energy has emerged to be a driving force in the search of alternative energy sources and efficient storage devices. To mitigate this energy crisis, solar cell technology has attracted great attention promising to replace the fossil-fuel based energy production. This can be realized through the use of lightweight, environmentally friendly and relatively cheap materials in the development of the solar cells. Manganese dioxide (MnO_2) is a transition metal oxide semiconductor which exhibits unique chemical and physical properties due to its complex and flexible crystal structure and morphology. MnO_2 has numerous applications ranging from catalysts, ion sieves in industries, electrode material for rechargeable batteries to energy storage devices [1-4]. It has also attracted considerable attention in many areas of research such as portable electronics, optoelectronics, photovoltaic cells and supercapacitors due to its relative abundance, low toxicity, low cost as well as unique power and energy densities. It exists in various polymorphs namely α, β, γ, λ that differ from one another in the way the MnO_6 octahedral units are packed. Their band gaps fall in the infra red and visible regions of the absorption spectrum and are therefore potential candidates for solar cell applications.

The excited electronic states properties of semiconductors are of great importance since they play a crucial role in physical properties such as electrical conductivities and optical absorption. Computational design of the solar energy materials requires accurate description of the ground-state and excited-state properties. It is known that density functional method [5] provide accurate ground state properties but fails to describe the excited state properties of materials [6]. Thus the main aim of this work is to investigate the quasiparticle band structure and optical properties of bulk α-MnO_2 using the Density Functional Theory (DFT) with a Hubbard correction (U) and many-body Green's function perturbation theory methods. The electronic and the magnetic properties of this compound have been studied extensively [7]. However, we are not aware of any experimental or theoretical studies of excited states properties of bulk α-MnO_2. Ramajanickam *et. al* have experimentally studied the structural and optical properties of 1-dimensional α-MnO_2 nanowires and β-MnO_2 nanofibres [8]. This paper is organized as follows. In Section 2, we briefly describe the computational techniques adopted in this work. In Section 3, we present the results and discussions of the structural, electronic and optical properties of α-MnO_2. Finally, a summary and conclusion is provided in Section 4.

2. Computational methods

Due to the failure of the standard (DFT) to correctly predict the physical properties of strongly correlated materials, we have used DFT plus effective Coulomb interaction (U) and the post-DFT many-body perturbation theory techniques as implemented in the Vienna *ab initio* Simulation Package (VASP) [9-14] to investigate the electronic and optical properties of bulk α-MnO_2. The Projector Augumented Wave method [11, 15] was used to describe the interactions between the core and the valence electrons. The Generalized Gradient exchange correlation approximation (GGA) was employed in the form of Perdew, Burke and Ernzerhof [16] with a Hubbard correction (PBE+U) [17-19]. The PBE+U approximation has been demonstrated to give a good description of electronic properties of manganese oxides. PBE+U calculations were carried out following the version of Dudarev *et al.* approach [20] as implemented in the VASP code [17-19]. We applied the U on the $3d$ states of Mn atoms. We used several U values until we obtained band gap values that were in good agreement with the experimental values. A Hubbard parameter $U = 2.4$ eV was adopted in this study. The GW type of pseudopotentials supplied through VASP (v.52) were adopted in our calculations. A plane wave basis set with kinetic energy cut-off of 300 eV was employed. Brillouin zone integration was performed using an $8\times8\times2$ k-point grid centered on Γ to ensure convergence of the Kohn-Sham eigenvalues. Starting from the (PBE+U) eigenfunctions and eigenenergies, we calculated the quasiparticle energy correction by adopting the partially self consistent $scGW_0$ level of approximation [21, 22]. In this approximation the wavefunctions and the quasi-particle energies are updated while the screened Coulomb interaction is kept at the DFT level of approximation. Four cycles were needed for convergence. To study the excitonic effects, optical properties were investigated within the BSE level of approximation. All the BSE calculations were performed by employing the Tamm-Dancoff approximation [23-25]. In order to converge the optical excitations that lie in the low frequency regime, we considered the 24 highest valence bands and 24 lowest conduction bands.

3. Results and discussions

3.1. Structural properties

α-MnO_2 crystallizes in a body centered tetragonal structure belonging to the 14/m space group (No. 87). It consists of double chains of MnO_6 which form 2×2 tunnels along the c axis. Experimentally [26], it is known to possess antiferromagnetic ordering at low temperatures. The antiferromagnetic ordering displayed in Figure 1(a) have been used throughout our entire calculations. The primitive and the conventional unit cells of α-MnO_2 are shown in Figure 1(a) and (b). We present the calculated cohesive energies and primitive cell volumes fitted to the

third-order Birch Murnaghan Equation of State in Figure 1(c). For each volume the atoms were allowed to relax till the forces were less than 5 meV/Å. The calculated structural properties, i.e., the lattice constants a and c, unit-cell volume (Ω), cohesive energy (E_{coh}) and bulk modulus (B) of α-MnO_2 are summarized in Table 1 together with other theoretical and experimental data. Our computed lattice parameters are in good agreement with the experimental values.

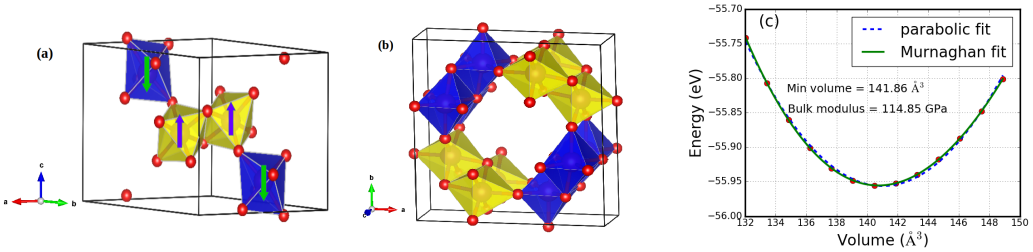

Figure 1. (a) Primitive unit cell showing spin orientations of the Mn atoms in the oxygen octahedra. The green arrows show Mn atoms with spin down magnetic moments whereas the purple arrows show Mn with spin up magnetic moments. (b) Conventional unit cell of α-MnO_2. (c) Calculated cohesive energies vs. primitive cell volumes of α-MnO_2.

Table 1. Experimental data and calculated structural parameters for α-MnO_2.

Structural parameters	a(Å)	c(Å)	Ω(Å^3)	E_{coh}(eV/atom)	B(GPa)
PBE+U ($U = 2.4$)	9.869	2.913	283.83	−4.42	114.85
Expt.[27]	9.750	2.861	271.97	-	-
Expt.[28]	9.784	2.863	274.07	-	-
Ref.[29]	9.887	2.920	285.03	-	-

3.2. Quasiparticle spectrum

The quasiparticle band structure of α-MnO_2 was studied by using many body perturbation theory. The Brillouin zone of the body centered tetragonal crystal of α-MnO_2 is shown in Figure 2 [Left]. The band structure of α-MnO_2 calculated from DFT+U and scGW$_0$ approximations along high symmetric directions in the Brillouin zone is presented in Figure 2 [Middle]. The top of the valence band has been shifted to zero for both calculations. The scGW$_0$ band structure displays an indirect band gap with the valence band maxima located at M and the conduction band minima located at X which is in agreement with our PBE+U results and those obtained by Yusuke *et al.* [29] who found an indirect band gap of 1.40 eV using PBE+U. Our predicted band gap value for α-MnO_2 using PBE+U was found to be 1.284 eV which is in excellent agreement with the experimental measured value, $E_g = 1.32$ eV [30]. The scGW$_0$ calculations shift the band gap from 1.284 eV to 2.20 eV as expected [31]. In order to understand the nature of the electronic band structures, the density of states of α-MnO_2 and the projected density of states of Mn and O elements calculated by scGW$_0$ are displayed in Figure 2 [Right]. It is observed that the valence bands are mainly occupied by the O 2p states with a mixture of Mn 3d states, while the conduction bands are dominated by Mn 3d states with a mixture of O 2p states. This mixture implies presence of hybridization between Mn 3d and O 2p states.

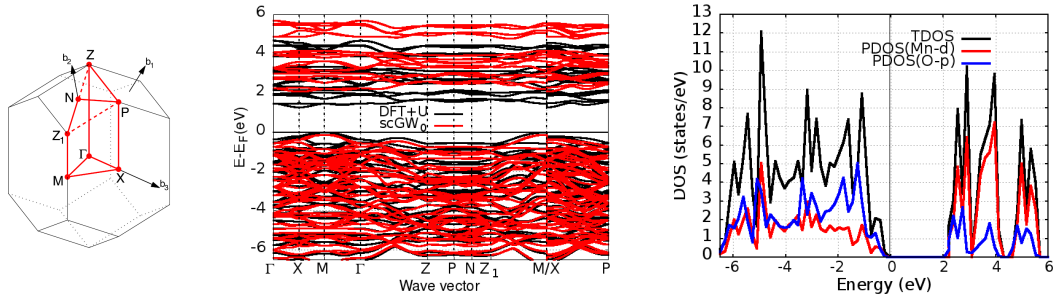

Figure 2. [Left]Brillouin zone of the body centered tetragonal crystal of α-MnO_2, [Middle] band structure calculated using DFT+U (black solid lines) and $scGW_0$ (red solid lines) and [Right] total and projected density of states using the $scGW_0$ approximation.

3.3. Optical properties

To obtain the optical excitons which are not given by the GW level of approximation, BSE calculations were done on top of the partially self consistent $scGW_0$ approximation. Optical properties of α-MnO_2 were investigated by means of a complex dielectric function $\varepsilon(\omega)$ which is expressed as $\varepsilon_1(\omega)+i\varepsilon_2(\omega)$ where $\varepsilon_1(\omega)$ and $\varepsilon_2(\omega)$ are the real and the imaginary parts of the dielectric function. Since α-MnO_2 has a tetragonal symmetry, we have evaluated the dielectric function for two independent principle components i.e. $\varepsilon_a(\omega)$ and $\varepsilon_c(\omega)$ which correspond to light polarized parallel and perpendicular to the c axis. Due to the symmetry, we have compared our optical related constants in two directions. The imaginary and the real parts of the dielectric function as a function of the photon energy along the a and c directions are depicted in Figure 3(a) and (b). The imaginary part of the dielectric function, $\varepsilon_2(\omega)$ show various peaks at different photon energies i.e. the main peaks occurs between energy values 2.5-3.4 eV, which correspond to interband transitions from the valence bands to the conduction bands. The prominent peaks in $\varepsilon_1(\omega)$ are situated at 2.25(2.54) eV along the $a(c)$ directions, which are located in the visible range of the spectrum. The static real parts of the dielectric function $\varepsilon(0)$ along the $a(c)$ axes are 6.56(8.81) respectively. Unfortunately, experimental data are unavailable for comparison.

Related constants such as absorption coefficients $\alpha(\omega)$, optical reflectivity $R(\omega)$, refractive index $n(\omega)$ and energy loss $L(\omega)$ were determined from the values of $\varepsilon(\omega)$. The absorption coefficient as a function of photon energy is presented in Figure 3(c). For the $\alpha(\omega)$ spectrum, the

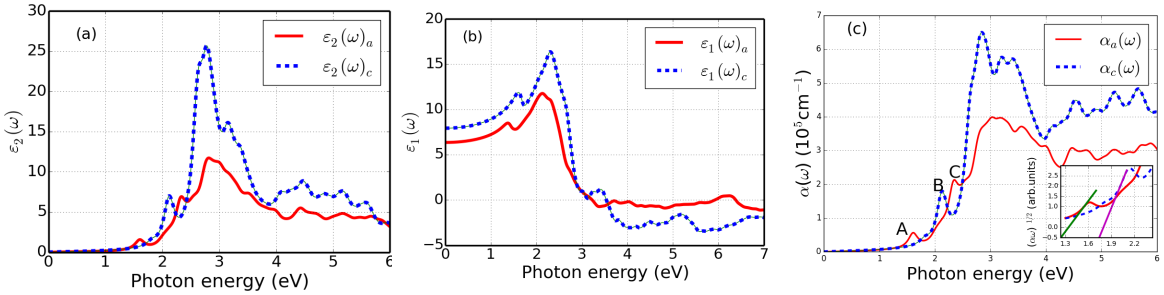

Figure 3. (a) Imaginary part of the dielectric function $\varepsilon_2(\omega)$, (b) real part of the dielectric function $\varepsilon_1(\omega)$ and (c) optical absorption spectrum $\alpha(\omega)$ of α-MnO_2 as a function of photon energy within the BSE level of approximation.

highest absorption peaks are situated in the visible region and are consistent with the interband transitions between the high symmetric k-points in the electronic band structure. For instance, the first peak corresponds to the transition from the valence band maximum located at M to the

conduction band minimum located at the X point. Additionally, it is observed that the main peaks in $\alpha_c(\omega)$ are higher than those in $\alpha_a(\omega)$ which clearly shows that the absorption is greater in the c axis than in the a axis. It should be pointed out that this compound may be a good absorber in the visible region. To obtain the optical absorption band edges, we used Tauc method proposed by Tauc *et al.* [32]. Here, the optical absorbance data are plotted with respect to the energy. Our Tauc plot is shown in the inset Figure 3(c). From the Tauc plot, it is clear that the absorption band edge occurs at 1.35(1.78) eV in the $a(c)$-directions. This significant difference in the absorption edge implies that α-MnO_2 exhibits anisotropic behaviour. Meanwhile, in the low frequency regime, the optical absorption spectrum predicts bound excitons that lie below the quasiparticle band gap. The approximate binding energies of excitons are determined by finding the difference in energy between the quasiparticle band gap and the peaks of the BSE absorption spectrum. We estimated the energies of the excitons in the low lying frequency regions of the absorption spectrum and compared these with the calculated quasiparticle band gap. The binding energies of the excitons are presented in Table 2. Positive and negative values of binding energies imply the presence of bound and resonant excitons respectively at a given energy. Figure 4(a) shows a refractive index of α-MnO_2. At first glance, one may notice a

Table 2. BSE calculated positions of A, B and C peaks and the corresponding binding energies of excitons in eV for α-MnO_2.

Peaks	E^A	E^B	E^C
	1.60	2.13	2.34
Binding energies	0.60	0.07	-0.14

similarity between the line shape of $n(\omega)$ and that of $\varepsilon_1(\omega)$ which is due to the $n(\omega) = \sqrt{\varepsilon_r}$ relation. We also noticed considerable anisotropic behaviour throughout the spectra. It is also clear that the refractive index of this compound is high in the optical region i.e 1.65-3.1 eV and gradually decreases beyond this point. The static refractive index $n(0)$ along the $a(c)$ directions were found to be 2.56(2.97) respectively and show that the light polarized along the a-axis is less refracted than along the c direction. The calculated optical reflectivity $R(\omega)$ as a function of photon energy is illustrated in Figure 4(b). We obtained a maximum value of reflectivity of around 61(49)% respectively along the $a(c)$ axes and occurs at the visible region. The energy loss function $L(\omega)$ spectra is presented in Figure 4(c). This quantity describes theoretical energy loss of a fast electron transversing in a material. The peaks in the $L(\omega)$ spectra display characteristics features associated with the plasma resonance [33] and the corresponding frequencies are referred to as plasma frequencies. The $L(\omega)$ spectra peaks show trailing edges in the reflection spectra.

4. Conclusion

In conclusion, the electronic properties of α-MnO_2 were investigated using spin polarized Density Functional Theory with a Hubbard correction U. We obtained a DFT+U band gap of 1.284 eV which is in good agreement with the experimental values whereas the calculated quasi-particle fundamental band gap is 2.20 eV and occurs between the M→X high symmetry directions. We also studied the optical properties of α-MnO_2 where we included the electron-hole interaction on top of partially self consistent $scGW_0$ through solving the Bethe-Salpeter equations which produced an optical band gap of 1.35 eV, which is in excellent agreement with the experimentally observed value of E_g = 1.32 eV [30]. We observed that the optical absorption spectra exhibit anisotropic behaviour which strongly depends on the polarization direction of the incident light. It was noted that α-MnO_2 absorbs violet light as evidenced by the main peak in the absorption

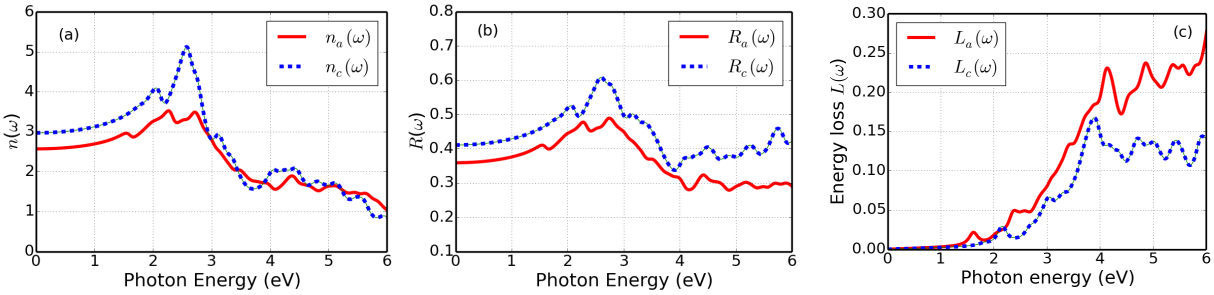

Figure 4. Calculated (a) refractive index $n(\omega)$, (b) optical reflectivity $R(\omega)$ and (c) energy loss L(ω) spectrum of α-MnO_2 as a function of photon energy.

spectrum. Moreover, optical absorption spectra predict the existence of bound excitons in the low lying frequency regions.

Acknowledgments

We wish to acknowledge the financial support from AIMS-DAAD. We are also grateful to the Centre for High Performance Computing, South Africa, for providing us with the computational facilities.

References

[1] Kumar R, Sithambaram S and Suib S 2009 *J. Catal.* **262** 304
[2] Wang L, Meng C, Han M and Ma W 2008 *J. Colloid Interface Sci.* **325** 31
[3] Thackeray M M 1997 *Prog. Solid State Chem.* **25** 1-71
[4] Cheng F, Zhao J, Song W, Li C, Ma H, Chen J and Shen P 2006 *Inorg. Chem.* **45** 2038
[5] Hohenberg P and Kohn W 1965 *Phys. Rev.* **140** 1133
[6] Aulbur W, Jönsson L. and Wilkins J 1999 *Solid State Physics* **54** 1-218
[7] Franchini C, Podloucky R, Paier J, Marsman M and Kresse G 2007 *Phys. Rev.* B **75** 195128
[8] Rajamanickam N, Ganesan P, Rajashabala S and Ramachandran K 2014 *AIP Conf. Proc.* **1591** 267-269
[9] Kresse G and Hafner J 1993 *Phys. Rev.* B **47** 558
[10] Kresse G and Furthmuller J 1996 *Comput. Mater. Sci.* **6** 15
[11] Kresse G and Joubert D 1999 *Phys. Rev.* B **59** 1758
[12] Furthmuller J, Cappellini G, Weissker H C and Bechstedt F 2002 *Phys. Rev.* B **66** 155208
[13] Shishkin M and Kresse G 2006 *Phys. Rev.* B **74** 035101
[14] Shishkin M and Kresse G 2007 *Phys Rev.* B **75** 235102
[15] Blochl P E 1994 *Phys. Rev.* B **50** 17953
[16] Perdew J P, Burke K and Ernzerhof M 1996 *Phys. Rev. Lett.* **77** 3865
[17] da Silva J L F, Ganduglia-Pirovano V, Sauer J, Bayer V and Kresse G 2007 *Phys. Rev.* B **75** 045121
[18] Franchini C, Bayer V, Podloucky R, Paier J and Kresse G 2005 *Phys. Rev.* B **72** 045132
[19] Franchini C, Podloucky R, Paier J, Marsman M and Kresse G 2007 *Phys. Rev.* B **75** 195128
[20] Dudarev S L, Botton G A, Savrasov S Y, Humphreys C J and Sutton A P 1998 *Phys. Rev.* B **57** 1505
[21] Hedin L 1965 *Phys. Rev.* **136** A796
[22] Hedin L and Lundqvist S 1970 *Solid state Phys.* **23** 1-181
[23] Salpeter E and Bethe H A 2001 *Phys. Rev.* **86** 6
[24] Albrecht S, Reining L, Del Sole R and Onida G 1998 *Phys. Rev. Lett.* **80** 4510
[25] Rohlfing M and Louie S G 1998 *Phys. Rev. Lett.* **81** 2312
[26] Yamamoto N, Endo T, Shimada M and Takada T 1974 *Jpn. J. Appl. Phys.* **13** 723
[27] Yang J B, Zhou X D, James W J, Malik S K and Wang C S 2004 *Appl. Phys. Lett.* **85** 3160
[28] Fritsch S, Post J E, Suib S L and Navrotsky A 1998 *Chem. Mater.* **10** 474
[29] Yusuke N, Kaoru O and Shinichiro N 2016 *Phys. Chem. Chem. Phys.* **18** 13294-13303
[30] Gao T, Fjellvag H and Norby P 2009 *Anal. Chim. Acta* **648** 235
[31] Kobayashi S, Nohara Y, Yamamoto S and Fujiwara T 2008 *Phys. Rev.* B **78** 155112
[32] Tauc J, Grigorovici R and Vancu A 1966 *Phys. Status Solidi* **15** 627-637
[33] Fox M 1972 *Optical Properties of Solids*, Academic Press, New York

Intermediate valence behavior in the new ternary compound $Yb_{13}Pd_{40}Sn_{31}$

R.F. Djoumessi[1], A.M. Strydom[1], F. Gastaldo[2], I. Čurlík[3,] M. Reiffers[3], and M. Giovannini[2]

[1] Highly Correlated Matter Research Group, Physics Department, University of Johannesburg, PO Box 524, Auckland Park 2006, South Africa
[2] Department of Chemistry, University of Genova, Via Dodecaneso 31, 1-16146 Genova, Italy
[3] Faculty of Humanities and Natural Sciences, University of Prešov, 17. Novembra 1, SK 081 16 Prešov, Slovakia

E-mail: amstrydom@uj.ac.za

Abstract. The new compound $Yb_{13}Pd_{40}Sn_{31}$ crystallizes in a hexagonal structure of space group P6/mmm (number 191). Magnetic susceptibility shows a non-regular temperature dependence for a local-magnetic moment system. The inverse magnetic susceptibility does not obey Curie-Weiss law throughout the measured temperature range (400 K - 2 K). This behavior is unexpected for Yb in its magnetic Yb^{3+} state and suggests that the system is subject to valence instabilities such as c-f hybridization. We find that the magnetism in $Yb_{13}Pd_{40}Sn_{31}$ is well described by the interconfiguration fluctuation (ICF) model, having an unstable valence for the Yb ion. The temperature dependent electrical resistivity shows that the compound becomes superconducting below 2.3 K. Specific heat analysis shows a peak at 2.3 K indicative of bulk superconductivity, and that the anomaly at 2.3 K survives even in 1 T but becomes suppressed in B = 4 T. As an important discovery, we observe that, aside from the peak at T_c, there is an enormous upturn in the electronic specific heat well below T_c which may be precursor effect of very low-lying magnetic order.

1. Introduction

Rare-earth intermetallic based materials are the most intriguing and thoroughly studied among the strongly correlated electron systems. The proximity of the 4f shell to the Fermi level leads to peculiar phenomena such as heavy fermion behavior, non-Fermi liquid behavior, Kondo effect, valence fluctuation and superconductivity to name a few. Those characteristics are mainly believed to arise due to a variable hybridization between the localized 4f-electrons and the delocalized conduction electrons. In particular and in contrast to cerium, ytterbium-based intermetallics are much less studied due to the high vapor pressure of elemental ytterbium making the sample preparation extremely difficult therefore limiting discovery of new materials; but their correlated electron physics are no less exciting. The most intensively studied systems of the intermediate valence state are cerium based. The Yb compound of this work is an extension to the series of already known Yb-based intermediate valence systems [1, 2]. We report on the magnetic and physical properties of the new ternary intermetallic compound $Yb_{13}Pd_{40}Sn_{31}$ obtained as part of the investigation of the isothermal section of the Yb-Pd-Sn system at 600°C [3].

2. Synthesis and experimental details

Stoichiometric amounts of the reactants Yb (99.9 wt-%), Pd (99.95 wt-%) and Sn (99.999 wt-%) were mixed together to form a polycrystalline sample of $Yb_{13}Pd_{40}Sn_{31}$ by induction melting in a sealed tantalum crucible under a stream of pure argon. To improve the homogeneity, the obtained sample was then wrapped in Ta foil, placed in an evacuated quartz tube and annealed in a furnace at 600°C for 14 days. It was subsequently quenched in cold water. The microstructure of the sample was obtained from the semiquantitative analysis using quantitative Electron Probe MicroAnalysis (EPMA) and Scanning Electron Microscopy (SEM). X-ray diffraction was used for phase identification of crystalline materials and to establish microscopic details such as chemical phase purity, crystallographic lattice parameters as well as details of the atomic coordinates in the structural unit cell. The experiment was carried out on an X'Pert MPD diffractometer and the collected data analyzed using the Powder-Cell [4] program.

Magnetic susceptibility and magnetization measurements were performed on a 7 T SQUID magnetometer (MPMS XL, Quantum Design, San Diego) in the temperature range of 1.7 K - 400 K. Electrical resistivity measurements in the temperature range between 1.8 and 300 K were performed based on the four-probe method using the Electrical Transport Option (ETO) available on the commercial Physical Property Measurement System (PPMS) from the same manufacturer. This latter facility was used also for the heat capacity measurements based on the quasi-adiabatic time relaxation method.

3. Results and Discussion

The powder X-ray diffraction pattern indicated that the obtained sample was single-phase, and crystallizes in a hexagonal structure, similar to hP168-$Y_{13}Pd_{40}Sn_{31}$ as already reported in [3]. The magnetic and physical properties of $Yb_{13}Pd_{40}Sn_{31}$ are investigated for the first time and reported in this work. The magnetic susceptibility will be analyzed in two temperature regions, using two different models, which is justified due to the temperature evolution of χ that is non-monotonous.

Figure 1 shows the DC-magnetic susceptibility measured in a field-cooling mode in an applied magnetic field of 0.01 T. Between 400 K and 60 K, $\chi(T)$ is found to be only very weakly temperature dependent. Most importantly, there is no Curie-Weiss behavior as we would expect if the Yb ion was in its stable magnetic Yb^{3+} state. This effect could be intrinsic and due to a magnetic moment instability of the Yb^{3+} ions, such as what Ce and Yb correlated electrons systems are prone to. The origin of this can be a crystalline electric field (CEF) effect or a strong and temperature dependent moment screening effect known as Kondo effect. However, the inverse magnetic susceptibility ranging from about 10 K down to the lowest measured temperature can be adequately described by a modified Curie-Weiss law as shown in the inset of figure 1 given by the expression:

$$\chi(T) = \frac{N_A \mu_{eff}^2}{3k_B(T - \theta_P)} + \chi_0, \tag{1}$$

where N_A is the Avogadro number and k_B the Boltzmann constant. μ_{eff} and θ_P are respectively the effective magnetic moment and the Weiss temperature and χ_0 is the temperature-independent susceptibility. The least-squares fit of equation 1 leads to $\theta_P = -0.70(2)$ K, $\chi_0 = 1.6 \times 10^{-3}(3)$ emu/mol.Yb and $\mu_{eff} = 0.50\ \mu_B$/Yb. While the negative value of the Weiss temperature suggests the presence of some weak antiferromagnetic interactions, the strongly reduced value of the effective moment compared to the value of the free $Yb^{3+} = 4.54\ \mu_B$ suggests a strong hybridization between the 4f and conduction electrons. Evidently below$\sim$10 K, this system achieves a stable but strongly renormalized magnetic moment. The higher-temperature situation is described below.

The mid-to higher temperature region magnetic behavior of the Yb ions can be well understood

in terms of the Interconfiguration fluctuation (ICF) model [2, 5] between $4f^{13}$ and $4f^{14}$ states of Yb described by the equation:

$$\chi_{\rm ICF}(T) = \frac{{\rm N_A}\mu_{\rm eff}^2(1-\nu(T))}{3{\rm k_B}(T+T_{\rm sf})}, \qquad \text{with} \qquad \nu(T) = \frac{1}{1+8\exp[-E_{ex}/{\rm k_B}(T+T_{\rm sf})]}, \tag{2}$$

where $\nu(T)$ is the fractional occupation of the $4f^{14}$ electronic ground state of the Yb compounds. E_{ex} represents the energy difference between respectively the ground state ($4f^{14}$, Yb^{2+}) and the excited state ($4f^{13}$,Yb^{3+}). $T_{\rm sf}$ is the spin fluctuation temperature that gives an estimation of the width of the 4f-level after the hybridization process with the conduction electrons. $\nu(T)$ describes the $4f^{13} \rightleftharpoons 4f^{14}$ valence instability in the Yb ion as a conduction electron effectively jumps into the 4f-shell momentarily due to the electron affinity to fill the shell. This is permitted to happen as a consequence of overlapping wave functions. The ground state ($4f^{14}$, Yb^{2+}) has both zero angular momentum and effective magnetic moment and the excited state ($4f^{13}$,Yb^{3+}) corresponds to the total angular momentum $J = 7/2$ and an effective magnetic moment $\mu_{\rm eff} = 4.54\ \mu_{\rm B}$. The least-squares fit of the data in the temperature range 10 to 400 K can be done by the following formula:

$$\chi(T) = \chi_{\rm ICF}(T) + \chi_{\rm imp}(T) + \chi_0, \tag{3}$$

where $\chi_{\rm imp}(T) = C_{\rm imp}/(T+\theta_{\rm imp})$ is the Curie-Weiss impurity and χ_0 comes from the temperature-independent contributions that is the Van Vleck paramagnetism and the core electron diamagnetism. This produces results as shown by the fit in figure 2. The least-squares

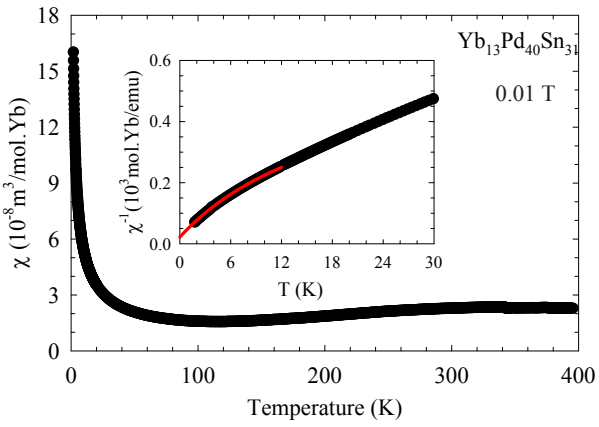

Figure 1. Temperature dependence of the magnetic susceptibility $\chi(T)$ measured up to 400 K. The inset represents the least-squares fit of equation 1 to the low-region of $\chi(T)$ with parameters as discussed in the text.

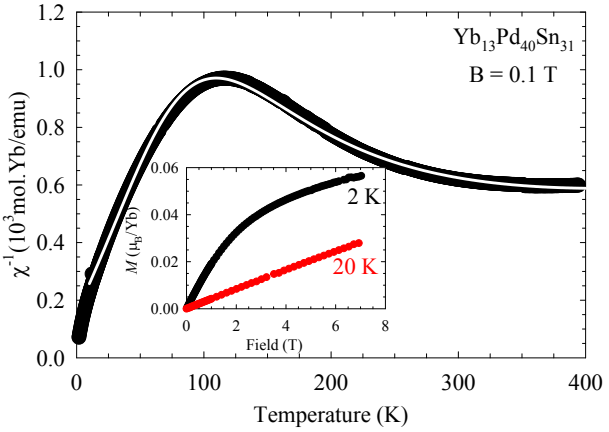

Figure 2. Temperature dependence of the inverse magnetic susceptibility $\chi^{-1}(T)$. The solid line represents the ICF fit of equation 3 as discussed in the text. Inset: magnetization isotherms in fields up to 7 T.

fit leads to the parameters: $C_{\rm imp} = 0.128$ emu.K/Yb.mol; $\theta_{\rm imp} = -18.9$ K; $E_{\rm ex} = 1306$ K; $T_{\rm sf} = 173$ K and $\chi_0 = 6.33 \times 10^{-4}$ emu/mol.Yb. The value of the spin fluctuation temperature is in qualitative agreement with the position of the peak on the experimental data. In the inset of figure 2, the isothermal magnetization has been measured in fields up to 7 T for two different temperatures, 2 and 20 K. At 2 K, the magnetization shows a curvature as B increases together with a tendency to saturate at high fields while at 20 K, we observe a linear in B behavior as expected for a paramagnetic system with $T < T_{\rm sf}$. From these measurements, there is no

evidence of a magnetic phase transition down to the lowest measured temperature.
The temperature dependence of the electrical resistivity in zero applied magnetic field is presented in figure 3. The compound reveals a quasi-metallic like behavior in a broad temperature range. A superconducting phase transition is observed at about 2.2 K with a critical field of ≈ 50 mT when $T = 0.4$ K (not shown here). However, the bulk character of this superconductivity behavior has not been fully proven yet and more susceptibility measurements are planned. Below about 10 K, the data follows the Fermi-liquid relation where the electron-phonon scattering is taken into account as shown in the following equation:

$$\rho(T) = \rho_0 + \rho_{ee}T^2 + \rho_{ep}T^5, \tag{4}$$

where ρ_0 is the residual resistivity, ρ_{ee} and ρ_{ep} the parameters that account respectively for the electron-electron and the electron-phonon scattering. The least-squares fit as shown in

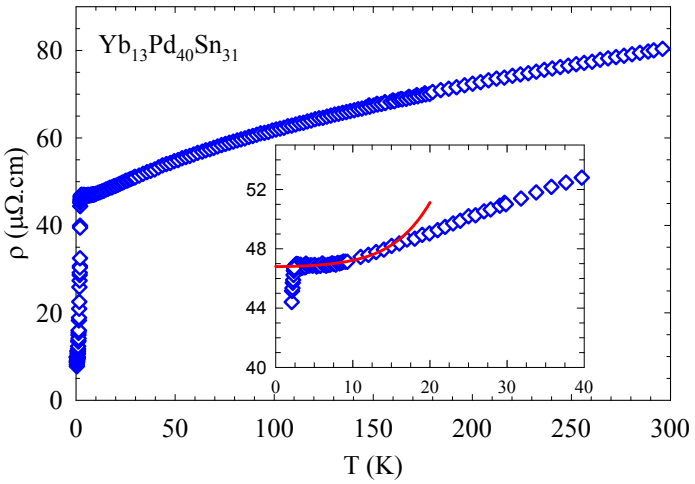

Figure 3. Temperature dependence of electrical resistivity. Inset: Low temperature region with a least-squares fit of the Fermi-liquid relation.

the inset yields to the parameters $\rho_0 = 46.80$ $\mu\Omega$.cm, $\rho_{ee} = 3.3 \times 10^{-3}$ $\mu\Omega$.cm. K^{-2} and $\rho_{ep} = 9.4 \times 10^{-7}$ $\mu\Omega$.cm K^{-5}.
Figure 4 shows the temperature dependence of heat capacity. As observed in figure 4(a), the superconducting phase transition observed in the electrical resistivity is also present here and moreover, it appears that the anomaly at ≈ 2.2 K survives even in 1 T but becomes completely suppressed in 4 T. This suggests a field driven dynamic besides the superconductivity. Quite aside from the peak at the transition, there is an enormous upturn in $C_p(T)/T$ towards lowest temperature that could be at a first thought a form of nuclear entropy originating from a hyperfine splitting. It is noted that among the highest natural abundance, the ^{171}Yb isotope has a I = 1/2 nuclear spin while ^{173}Yb isotope has a I = 5/2. However, the behavior in a field of 1 T is not consistent with the evolution of the tail at low temperature in the case of a nuclear contribution to the heat capacity. The entropy was estimated from the relation:

$$S(T) = \int_0^T \frac{C_P(T')}{T'} dT' \tag{5}$$

The data as represented in (b) shows no tendency to saturation in the entropy and a rather weak field dependence associated with a power law behavior. As presented in (c), the low-temperature data of $C_P(T)/T$ data shows a linear dependence in T^2 corresponding to the

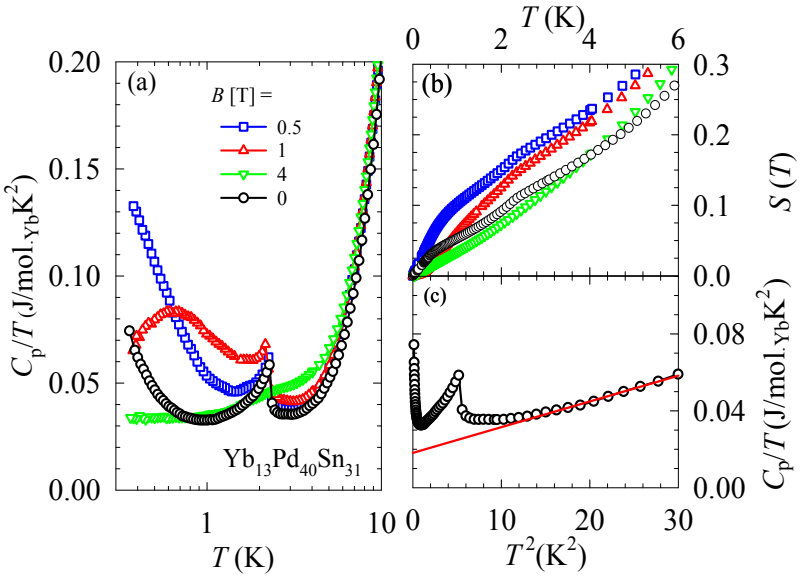

Figure 4. (a): Temperature dependence of the heat capacity for different applied magnetic fields. (b): Calculated entropy in different applied fields. (c): Low temperature region of the C_p/T vs T^2 dependence in zero field with a fit of the most linear region as discussed in the text.

electronic contribution to the specific heat. This gives an estimate of the Sommerfeld coefficient that is found to be $\gamma = 18.1$ mJ/mol.K^2. From this value we can say that the effective mass $m^* \simeq 3m_e$(free electron mass) [6], which is a slightly enhanced value indicating the presence of some electronic correlations but it is still low to classify the compound $Yb_{13}Pd_{40}Sn_{31}$ as a heavy fermion system where the effective mass can be up to thousand times more than the mass of a free electron [6].

4. Conclusion

In summary, the new Yb ternary compound $Yb_{13}Pd_{40}Sn_{31}$ that crystallizes in hexagonal structure is found here to be a new intermediate valence system with no magnetic ordering from the magnetic susceptibility, electrical resistivity and heat capacity results. Moreover, a superconducting behavior that remains to be investigated is also consistently found in the low-temperature measurements of the electrical resistivity and heat capacity.

Acknowledgments

RFD thanks UJ for a scholarship and both the research group members and Dr. M. Falkowski from the Charles University in Prague for their help and fruitful discussions. AMS thanks the FRC/URC of UJ and the SA NRF (93549) for financial assistance.

References

[1] Kaczorowski D, Gribanov A, Rogl P and Dunaev S 2016 *J. Alloys Comp.* **685** 957–961

[2] Kowalczyk A, Falkowski M and Toliński T 2010 *J. Appl. Phys.* **107** 123917

[3] Gastaldo F, Giovannini M, Strydom A, Djoumessi R, Čurlík I, Reiffers M, Solokha P and Saccone A 2017 *J. Alloys Comp.* **694** 185–192

[4] Kraus W and Nolze G 1996 *J. Appl. Cryst.* **29** 301–303

[5] Sales B and Wohlleben D 1975 *Phys. Rev. Lett.* **35** 1240

[6] Kittel C 1996 *Introduction to Solid State Physics* (Wiley, New York)

Mechanical milling effect on the structural and magnetic properties of sintered $La_{0.67}Sr_{0.33}MnO_3$

Itegbeyogene P. Ezekiel[1], **Thomas Moyo and Sanele Dlamini**
School of Chemistry and Physics, University of KwaZulu-Natal, P/Bag X5401, Durban 4000, South Africa

E-mail: itegbeyogene@gmail.com

Abstract. We report structural and temperature dependence of magnetization properties of the as-sintered and milled $La_{0.67}Sr_{0.33}MnO_3$ oxides. The refined X-ray diffraction data show that all samples are single phase and crystallize in rhombohedral symmetry. The crystallite sizes decreased from 46 nm to 11 nm after milling the as-sintered sample for 1, 3, 6 and 12 hours. The surface morphology of the samples shows significant changes at the surface of all the samples. The saturation magnetization M_S is observed to follow Bloch's law. M_S decreases from 52 emu/g to 7 emu/g at 300 K and from 80 emu/g to 40 emu/g at 2 K due to particle size reduction. We use core-shell model to investigate changes in M_S as function of particle size and estimate a dead layer thickness of the nanoparticles to be about 0.96 nm. The results show increased coercive fields with reduction in temperature and particle size. The coercive field at 2 K show a significant increase from 170 Oe to 870 Oe in the sample milled for 12 hours. We also report the effects of zero field cooling and field cooling on the magnetisation of the samples.

1. Introduction

The possible application of perovskite manganites in solid-state refrigeration and their colossal magnetoresistance have contributed to several studies of these materials [1-3]. The double exchange interaction that exists between the Mn^{3+}-O-Mn^{4+} bonds in the manganite structure of $A_{1-x}B_xMnO_3$ where A is a rare-earth element and B is divalent element [4-6], influences the properties. In particular, La-Sr-manganites have shown promising potential applications near room temperature. The $La_{1-x}Sr_xMnO_3$ perovskites, at the composition $x = 0.33$ has attracted much attention because its Curie temperature is about 370 K and has a large magnetic moment [1]. This makes it a good candidate for magnetocaloric effect applications near room temperature. A study of $La_{0.9}Sr_{0.1}MnO_3$ synthesized by the citrate-gel method reveals how the magnetic properties of these materials can significantly change due to surface effects. The sample initially had a Curie temperature T_C of 250 K, which decreased with increase in grain size [3]. The synthesis process and surface spins appear to also play important roles in determining the final properties. The interest in this study is to investigate the particle size and surface effects on the structural and magnetic properties of mechanically milled $La_{0.67}Sr_{0.33}MnO_3$ perovskites initially synthesized by solid-state reaction process.

2. Experimental details

$La_{0.67}Sr_{0.33}MnO_3$ was synthesised by the pre-sintering of a pellet of a well-mixed high purity La_2O_3, SrO and MnO_2 powders at 1200 °C for 15 hours. The pellet was ground in an agate mortar and pestle into powder and another pellet was prepared for further sintering at 1350 °C for 15 hours. This is a double sintering process. We re-ground the final pellet in an agate mortar and pestle, denoted as sample S0. The effects of mechanical milling on the magneto-structural properties of S0 was studied on samples S1, S3, S6 and S12 after S0 was mechanically milled in a Retsch PM 400 planetary ball mill at a ball to mass ratio of 20:1 and speed of 250 rpm for 1, 3, 6, and 12 hours respectively. Appropriate amounts of samples about 0.5 g were available for X-ray diffraction (XRD) with a Cu radiation source. A Zeiss ultra plus high-resolution scanning electron microscope (HRSEM) was used to study the surface morphology. Each sample was held fixed in a Perspex cone sample holder by a piece of cotton wool for the magnetization measurements in a Cryogenic Ltd 5 Tesla mini cryogen free measurement system. This avoids torque during the measurements.

3. Results and discussion

The XRD patterns of the samples shown in Figure 1 were analysed using Fullprof-Suite [1]. All the samples have rhombohedral structure that belongs to the space group $R3C$ [3]. The values of the refined lattice parameters and the cell volumes presented in Table 1 are in close agreement with reported values [1, 6]. The significant shift observed in the S12 pattern towards higher values of 2θ is associated with a reduction in lattice parameters caused by high surface deformation and strain due to prolonged milling. Figure 2 shows estimates of the strain and average crystallite sizes from the Williamson-Hall plot [7] and the Scherrer formula [8] respectively. High-energy mechanical ball milling is an effective technique for achieving reduction in particle sizes due to the grinding effect of the balls [9]. Figure 2 shows the results. The slight increase in the crystallite size for S12 appears to be due to a thermal annealing effect because of prolonged high-energy ball milling. In this case, further particle size reduction does not occur due to limited sizes of the grinding balls but instead the mechanical energy goes into heating the sample. This caused sample S12 to exhibit a different trend.

The HRSEM images in Figure 3 show the milling effect on the surface morphology of the samples. The images clearly show a variation in the surface texture with a more compacted surface for S12. Considering the high percentage of atoms at the surface of nanomaterials [10], we expect a modification of the magnetic properties of the samples due to such variations. Nanoparticles usually have high percentage of its atoms at the surface of the core [10]. Therefore, as the size of the core of the nanoparticle reduces, the surface to core volume ratio increases.

Figures 4 and 5 show magnetic hysteresis loops measured at 300 K and 2 K respectively. The loops are typical of ferromagnetic order having a sigmoidal shape with noticeable hysteresis as shown in Figure 6. The coercive field $H_C = \left|H_{C1} + H_{C2}\right|/2$ was estimated from the hysteresis loops where H_{C1} and H_{C2} are the values of the negative and positive coercive fields respectively [11]. Figure 7 shows the temperature T dependence of the saturation magnetization M_S which were deduced by using the law of approach to saturation [12]. The M_S dependence on T in Figure 7 follows the modified Bloch's law $M_S(T) = M_S(0)\left(1 - \frac{T}{T_0}\right)^{\beta}$ [12] with fit parameters given in Table 2. The characteristic temperature T_0 where the magnetization becomes zero decreases continuously as a function of milling time. The Bloch's exponent β values are in the range of reported values [13]. The solid line in the H_C dependence on T is a guide to the eye. The decrease in T_0 and M_S is attributed

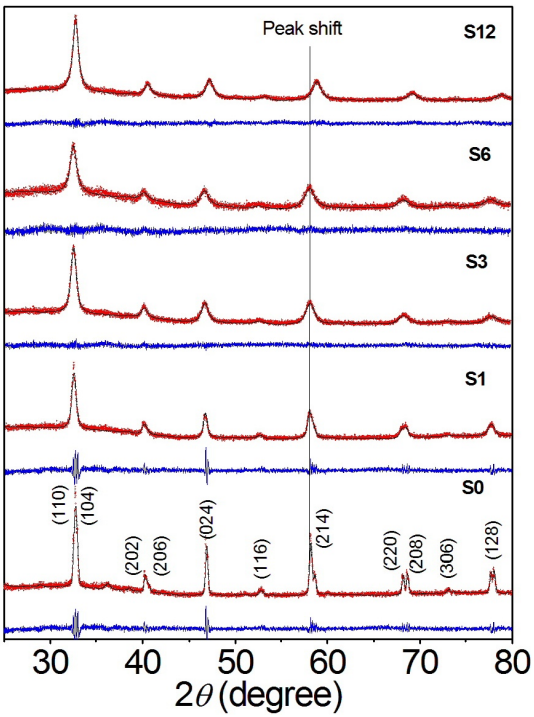

Figure 1. Refined XRD patterns for as-sintered sample (S0) and milled samples for 1, 3, 6 and 12 hours.

Table 1. Lattice parameters a, b, c, cell volume V and goodness of χ^2 as obtained from Rietveld refinements of as-sintered sample S0 and the milled samples.

	$a = b$ (Å) ±0.006	c (Å) ±0.002	V (Å^3) ±0.079	χ^2
S0	5.499	13.344	349.448	3.32
S1	5.503	13.366	350.559	2.41
S3	5.495	13.417	350.875	2.25
S6	5.497	13.469	352.424	2.39
S12	5.485	13.412	349.383	2.18

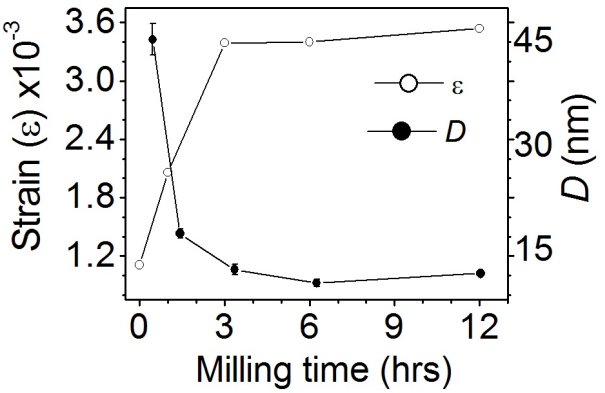

Figure 2. Average crystallite size D and the strain ε as a function of milling time.

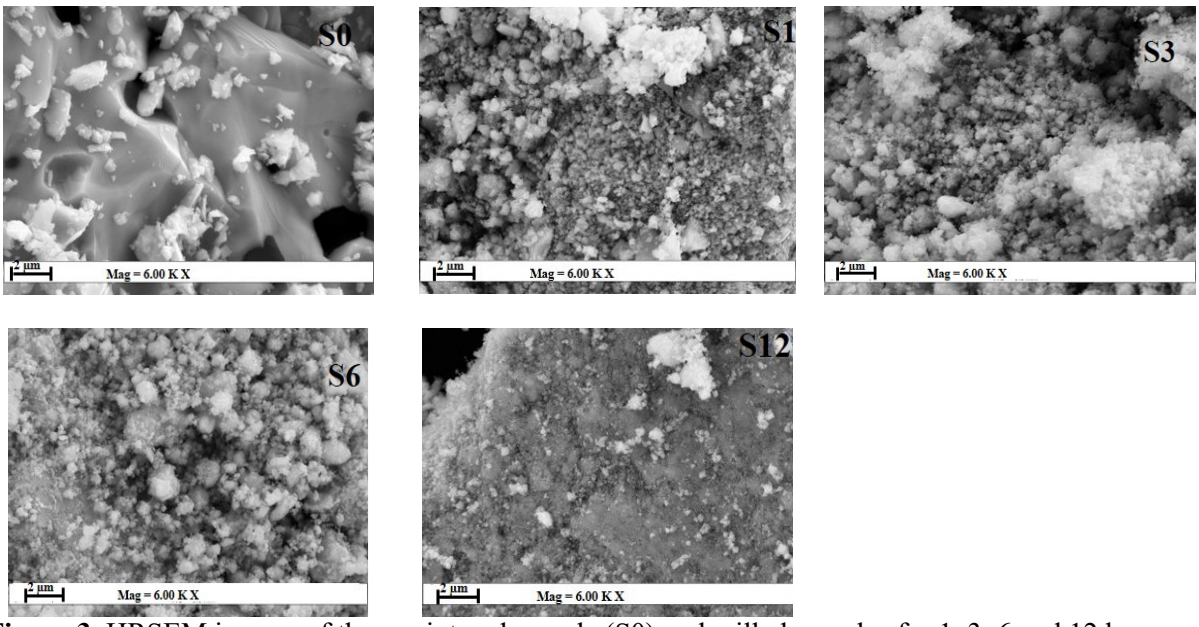

Figure 3. HRSEM images of the as-sintered sample (S0) and milled samples for 1, 3, 6 and 12 hours.

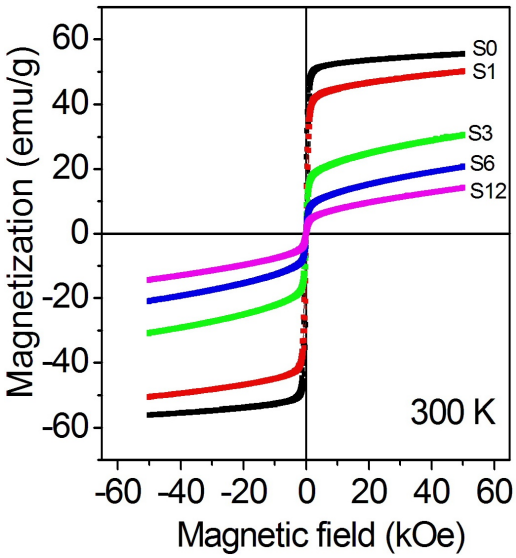

Figure 4. Magnetic hysteresis loops measured at 300 K.

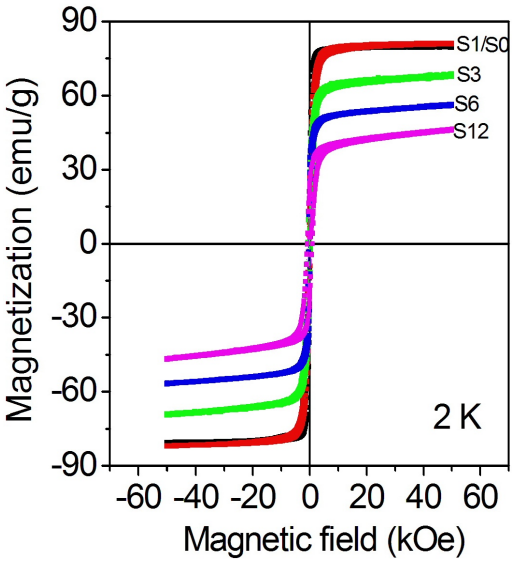

Figure 5. Magnetic hysteresis loops measured at 2 K.

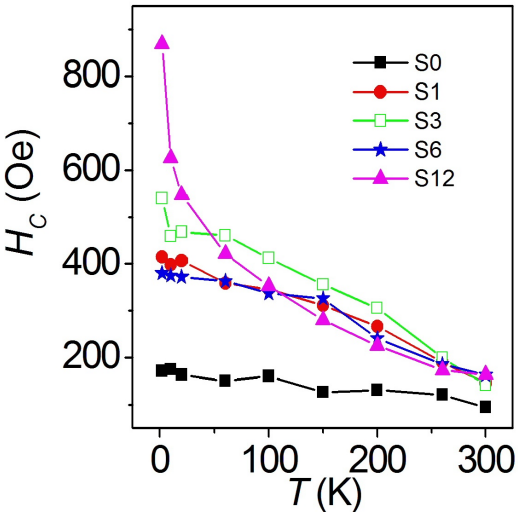

Figure 6. Temperature dependence of coercive field H_C.

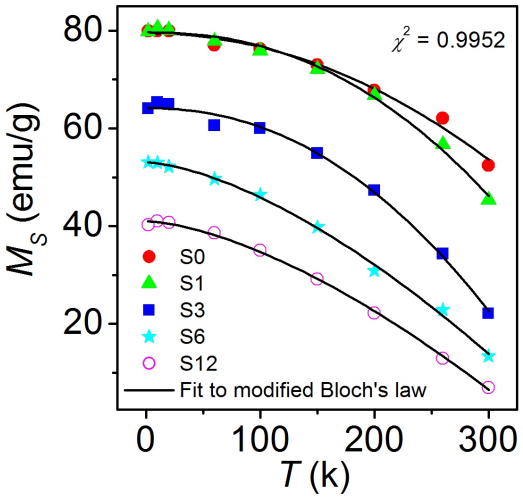

Figure 7. Temperature dependence of saturation magnetization, M_S.

Table 2. Saturation magnetization $M_S(0)$, characteristic temperature T_0, Bloch's exponent β and the goodness of fit χ^2.

Sample	$M_S(0)$ (emu/g) ±0.5	T_0 (K) ±14	β ±0.1	χ^2
S0	79	522	2.0	0.989
S1	79	440	2.3	0.995
S3	64	367	2.2	0.995
S6	53	365	1.5	0.998
S12	41	335	1.6	0.999

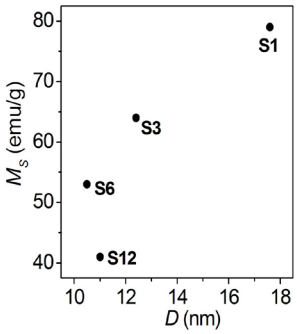

Figure 8. Dependence of saturation magnetization on the crystallite size.

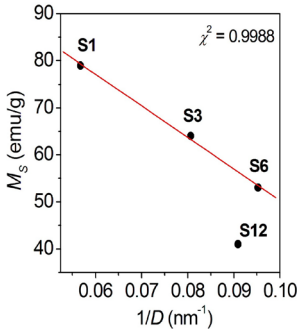

Figure 9. A fit to estimate M_S(bulk) and the thickness dead layer d.

to a disordered surface spin called the "magnetic dead layer" as earlier shown in the surface morphology changes in the HRSEM and the decrease in particle size as measured from the XRD results. This can best be described by the core shell model [1, 14]. The shell (layer) consists of disordered moments with an ordered core. The magnetization decreases as the milling time increases. This explains the decrease in M_S as the core decreases as shown in Figure 8. The dead layer thickness d = 0.96±0.01 nm is estimated from the dependence of M_S on the inverse of crystallite size D using formula $M_S = M_S(\text{bulk})\left[1-\frac{6d}{D}\right]$ [1, 14, 15]. Figures 9 shows a very strong correlation ($\chi^2 = 0.9988$) between M_S and D^{-1} for samples S1, S3 and S6. The M_S(bulk) was estimated be 117±3 emu/g. The sample S12 appears not to be part of this set consistent with XRD data in Figure 1. For S1-S6, the thickness of the layer does not significantly change [1] with the milling time. However, the degree of disorder in the dead layer could vary.

Figure 10 shows the zero-field cooled (ZFC) and field cooled (FC) magnetizations of samples S0, S1, S6 and S12 which are used to investigate changes in the blocking temperature T_B and the irreversibility temperature T_{irr}. The results show significant differences between ZFC and FC magnetizations. The step in the ZFC and FC at 43 K for S0 is due to the inhomogeneous nature of the ferromagnetic clusters. This decreases in the FC curve of S1 and disappears completely on further milling. Below the freezing temperature of T_f = 43 K, the moments are frozen therefore the FC curve remains unchanged. In Figure 11, T_B significantly drops from 280 K for S0 to 122 K for S12, while T_{irr} drops from 312 K to 256 K. This shows strong dependence of T_B and T_{irr} on particle size.

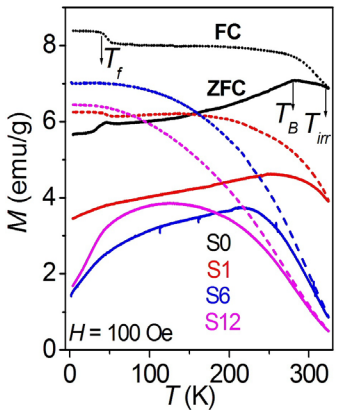

Figure 10. ZFC-FC magnetization curves.

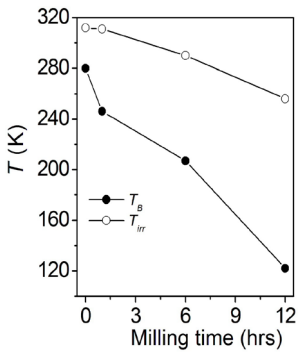

Figure 11. Blocking temperature T_B and irreversibility temperature, T_{irr}.

4. Conclusions

We have investigated the particle size and surface effects on the structural and magnetic properties of double sintered and subsequently milled samples of $La_{0.67}Sr_{0.33}MnO_3$ oxides. The XRD data shows all samples in single phase and crystallized in rhombohedral structure. The crystallite sizes decreased as a function of milling time except for the S12 sample, which increased slightly due to suspected thermal annealing effect caused by prolonged milling. In this case, particle size reduction appears less effective at the lowest particle size. In all the samples, the temperature dependence of the saturation magnetization M_S follows the Bloch's law. The evolution of M_S with reduction in particle size follows the core-shell model except for the S12 sample, which appears not to be part of the set. Using the core-shell model, we have determined the thickness of the disordered surface layer for milled samples S1, S3 and S6 to be 0.96 nm. All the samples show significant ZFC and FC effects, which we attribute to ferromagnetic clusters at the core surrounded by disordered surface layers.

Acknowledgments

The authors are thankful to the National Research Foundation of South Africa and the University of KwaZulu-Natal for research grants.

References

[1] Rostamnejadi A, Venkatesan M, Kameli P, Salamati H and Coey J M D 2011 *J. Magn. Magn. Mater*. **323** 2214.
[2] Giri S K, Dasgupta P, Poddar A, Nigam A K and Nath T K J 2014 *J. Alloys Comp*. **582** 609.
[3] Baaziz H, Tozri A, Dhahri E and Hilil E K 2015 *Ceramics Int*. **41** 2955.
[4] Skini R, Khlifi M, Dhahri E and Hilil E K 2014 *J. Supercond. Nov. Magn.* **27** 247.
[5] Ho T A, Lim S H, Tho P T, Phan T L and Yu S C 2017 *J. Magn. Magn. Mater* **426** 18.
[6] Rocco D, Coelho A A, Gama S and Santos M C 2013 *J. Appl. Phys*. **113** 113907.
[7] Zak A, Khorsand W H, Majid Abd, Abrishami M E and Yousefi R 2011 *Sol. Stat. Sci.* **13** 251.
[8] Abdallah H M I, Moyo T, Itegbeyogene E P and Osman N S E 2014 *J. Magn. Magn. Mater*. **365** 83.
[9] Yadav T P, Yadav R M and Singh D P 2012 *J. Nanosci. Nanotechnol*. **2(3)**, 22.
[10] Kodama R H 1999 *J. Magn. Magn. Mater*. **200** 359.
[11] Ramudu M and J Gerhard 2013 *J. Appl. Phys. Lett*.**102** 232406.
[12] Andreev S V, Bartashevich M I, Pushkarsky V I, Maltsev V N, Pamyatnykh L A, Tarasov E N, Kudrevatykh N V and Goto T 1997 *J. Alloys Comp*. **260** 196.
[13] Maaz K, Mumtaz A, Hasanain S K and Bertino M F 2010 *J. Magn. Magn. Mater.* **322** 2199.
[14] Sarkar T, Raychaudhuri A K, Bera A K and Yusuf S M 2010 *New J. Phys*. **12** 123026.
[15] Vázquez-Vázquez C, López-Quintela M A, Buján-Núñez M C and Rivas J 2011 J. *Nanopart. Res*. **13** 1663.

Predicting the Mo substitution and vacancy-complex induced electrical defect levels in Ge

E. Igumbor[1,2], O. Olaniyan[1], R. E Mapasha[1], H. T. Danga[1], W. E. Meyer[1]

[1] Department of Physics, University of Pretoria, Pretoria 0002, South Africa
[2] Department of Mathematical and Physical Sciences, Samuel Adegoyega University, Km 1 Ogwa-Ehor Rd. Ogwa Edo State Nigeria

E-mail: wmeyer@up.ac.za; elgumuk@gmail.com

Abstract. In this report, results based an *ab initio* calculation of Mo substitution and vacancy−complex induced electrical levels in the Ge were presented. Density functional theory with the Heyd, Scuseria and Ernzerhof (HSE06) hybrid functional was used to calculate the total energies of Mo vacancy-complexes of Ge ($V_{Ge}Mo_{Ge}$) and Mo substitution in Ge (Mo_{Ge}). Formation and minimum energies of the first nearest neighbour (N1), second nearest neighbour (N2) and third nearest neighbour (N3) configurations of the $V_{Ge}Mo_{Ge}$ and the Mo_{Ge} were obtained for charge states −2, −1, 0, +1 and +2. The calculated formation energies for the $V_{Ge}Mo_{Ge}$ resulted in positive binding energies for the N1, N2 and N3 configurations. For the neutral charge state, the N2 configuration is the most energetically favourable with energy of formation and binding energy of −0.14 and 0.06 eV, respectively. The Mo_{Ge} in the neutral charge state had a formation energy of −2.99 eV and induced electrically active level which exhibits a negative-U ordering within the band gap of Ge. The (+2/−1) transition state induced by the Mo_{Ge} is a deep level lying at $E_V + 0.31$ eV.

1. Introduction

Experimental or theoretical studies of defects in germanium (Ge) have been on the increase recently due to the potential application of Ge in microelectronics [1]. The investigation of Ge as a possible promising material for optoelectronic applications and complementary metal−oxide−semiconductor (CMOS) field−effect transistor devices has been on the increase [1]. Ge is a semiconductor that has a narrow indirect band gap of 0.78 eV at 0 K [2]. Furthermore, due to Ge relatively high electron-hole mobility, it has the potential to be considered as a superior material than silicon for the development of metal-oxide−semiconductor field−effect−transistors (MOSFETs) [3]. Defects are known to influence Ge either positively or negatively. Defects that influence Ge positively, enhances its performance, for example the p− or the n−type dopant which are responsible for the change of the majority carrier type are always desired. Several defects in Ge have been investigated using experimental techniques such as deep level transient spectroscopy (DLTS) [3, 4, 5] or perturbed angular correlation spectroscopy (PACs) [6]. Theoretically, few of these defects have been predicted owing to the shortfall of the density functional theory (DFT) [7] with either local density approximation (LDA) or generalised gradient approximations (GGA) of Perdew, Burke, and Ernzerhof (PBE) [8] in predicting accurately the band gap of Ge. But since the advent of the Heyd, Scuseria and Ernzerhof

(HSE) [9] hybrid functional, this limitation has been eliminated. Amongst the defects in Ge predicted are self, di-interstitials [10], mono or multi-vacancies and recently, rare earth related defects [11, 12, 13]. Experimental or theoretical results have revealed or predicted, that dopants in Ge are known to form clusters with lattice vacancies [14] as a result of defect−complexes in Ge such as vacancy−complexes, interstitial-complexes. Recently it has been shown that negative-U ordering could arise from a Tm defect-complexes in Ge [15].

In this report, the electrical levels induced by Mo vacancy-complexes ($V_{Ge}Mo_{Ge}$) and Mo substitution (Mo_{Ge}) in Ge are presented with a view of providing experimental insight for the engineering of these defects for better industrial or laboratory applications. The density functional theory with the HSE06 hybrid functional was used for all calculations. The formation and minimum energies of the first nearest neighbour (N1), second nearest neighbour (N2) and third nearest neighbour (N3) configurations for the $V_{Ge}Mo_{Ge}$ and the Mo_{Ge} were obtained for charge states -2, -1, 0, $+1$ and $+2$.

2. Computational details

All calculations were carried out using HSE06 within the framework of DFT as implemented in the VASP 5.3 code [16]. The projector-augmented wave method [17, 18] was used to separate the valence from the core electrons. Based on the HSE06 approach, the short-range exchange potential was calculated by mixing a 25 percent fraction of nonlocal Hartree-Fock exchange with the GGA-PBE. The HSE06 functional gives accurate predictions of the electronic band gap and improve charge state transition properties for several defects in a semiconductor material [2, 10]. For the modelling of the defects, an initial 64 atom supercell was used for the pristine, while for the Mo_{Ge} a Ge atom was replaced by a Mo atom in the initial 64 atoms supercell. For the $V_{Ge}Mo_{Ge}$, a vacancy was created from the Mo_{Ge} system to yield Mo vacancy-complex system. A $2 \times 2 \times 2$ Monkhorst-Park [19] mesh scheme for generating the k-points was used to sample the Brillouin zones. Geometric relaxation was performed until the Hellmann-Feynman forces on each atom and the final change in the total energy were less than 0.001 eV/Å and 10^{-5} eV, respectively. Spin orbit coupling was taken into account for all caculations. While formation energies of the $V_{Ge}Mo_{Ge}$ and Mo_{Ge} were calculated using the method of Refs [1, 11], the binding energies for the N1, N2 and N3 configurations of the $V_{Ge}Mo_{Ge}$ were calculated based on the method of Refs [15, 20]. The effect of using a supercell and its image repetitions gives rise to spurious interactions. Futhermore, the introduction of a charge state in the defect, causes electrostatic interaction probmens between the periodic cell containing the defect giving rise to errors. These errors where properly corrected using the FNV method as stated in Refs [1, 11]. The band gap of 0.78 eV for Ge as reported by Igumbor *et al* [10] was used for this present report.

3. Results and Discussion

Figs 1 and 2 display the fully relaxed geometric structures of the Mo_{Ge} and $V_{Ge}Mo_{Ge}$, respectively. The effects of the defect on the structural properties of both $V_{Ge}Mo_{Ge}$ and Mo_{Ge} were examined. Based on a previous report, the experimental and theoretical results of the nearest neighbour Ge−Ge bond length and Ge−Ge−Ge bond angle after structural relaxation were 2.46 Å and 109.40° [14, 20], respectively. For the Mo_{Ge}, the Mo formed bond length of 2.49 Å with its nearest neighbour Ge atom. The smallest angle formed by two nearest neighbour Ge atoms with Mo is 109.5°. The bond length of Mo−Ge was 1.20% higher than that of the Ge-Ge, and the bond angle of Ge−Mo−Ge was 0.10% higher than that of the Ge−Ge−Ge. This is expected as the atomic radius of the Mo atom is higher than that of the Ge atom. The bond length formed by Ge−Mo and bond angle formed by Ge-Mo-Ge for N1 (N2) were 2.50 (2.47) Å and 108.14° (108.52°), respectively. The bond length of the nearest Ge-Mo and the smallest bond angle of the nearest Ge-Mo-Ge for the N3 configuration are similar to that of the

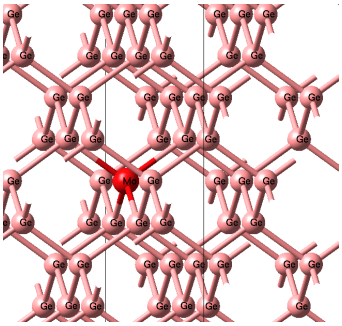

Figure 1. Fully relaxed geometric structures of Mo_{Ge}.

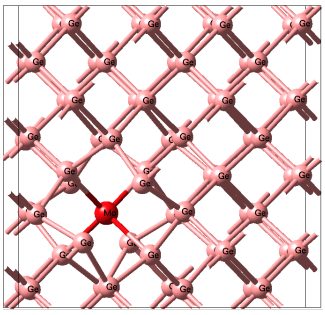

Figure 2. Fully relaxed geometric structures of $V_{Ge}Mo_{Ge}$ for the N1 configuration.

N1 configuration. Based on the amount of strain induced by the dopant in the system, it is expected that the Mo_{Ge} will induce smaller strain in the system compared to the $V_{Ge}Mo_{Ge}$.

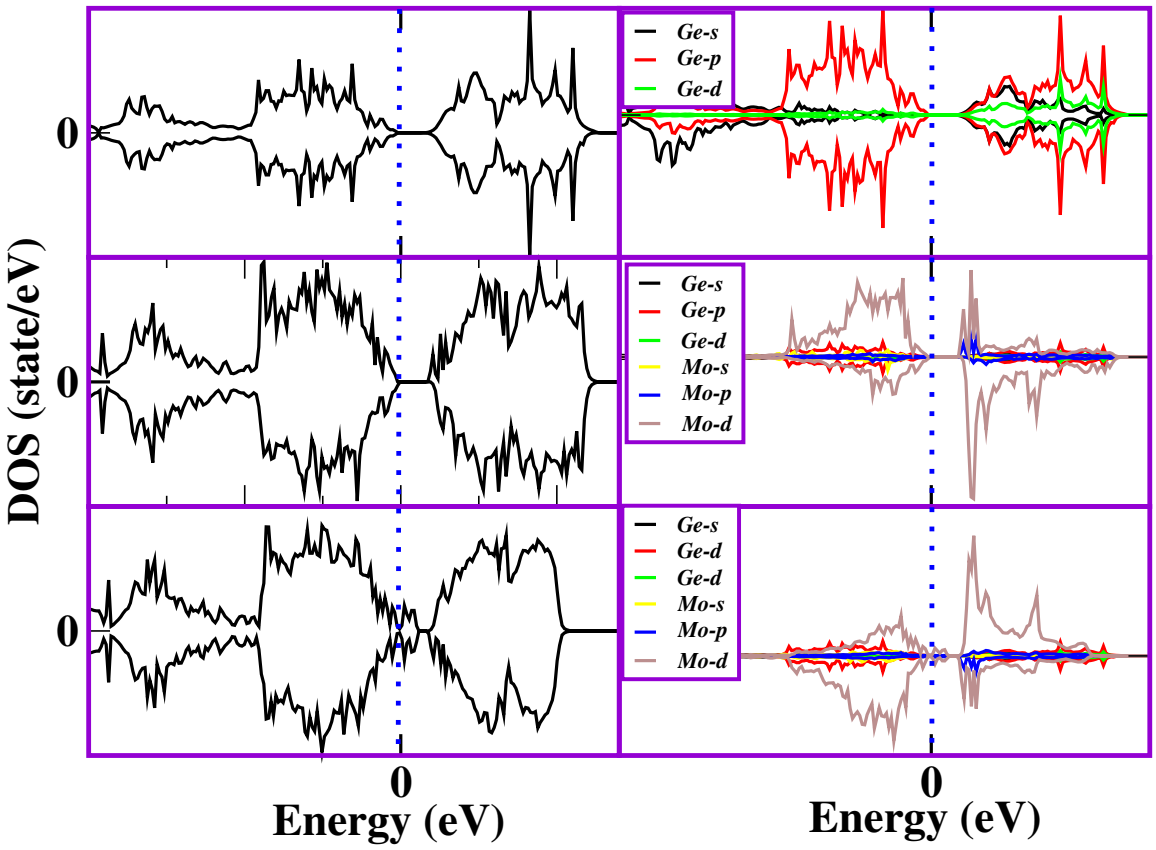

Figure 3. The plots of the total density of states (left) and partial density of states (right) for the pristine Ge (upper panel), Mo_{Ge} (middle panel) and $V_{Ge}Mo_{Ge}$ (lower panel) complex for the N1 configuration.

Fig. 3 displays the plots of the total density of states (TDOS) and partial density of states (PDOS) of the pristine Ge, Mo_{Ge} and $V_{Ge}Mo_{Ge}$ complex (we only displayed the TDOS and

PDOS for the N1 configuration, since the other configurations have similar DOS and PDOS). The TDOS and PDOS for the N2 and N3 configurations are similar to that of the N1 and hence we did not display them. As expected, the $p-$orbital is dominant in the band structure for the pristine Ge. The Mo_{Ge} as a result of the $d-$orbital from the Mo atom has its ground states orbital densely populated at the valence band maximum. This resulted in the band gap of the pristine Ge reduced by 0.20 eV. The effect of the s and $p-$orbitals of the Mo atom is minimal at the valence band maximum. Another interesting feature observed from the Mo_{Ge} is the presence of strong orbital hybridization between the $p-$orbital of Ge and $d-$orbital of Mo (see the middle panel of Fig. 3). Both the TDOS and PDOS of the $V_{Ge}Mo_{Ge}$ are displayed at the lower panel of Fig. 3. The $V_{Ge}Mo_{Ge}$ electrons induced states in the band gap of Ge. These states are about 0.58 eV above the Fermi level. This behaviour is attributed to the influence of the germanium vacancy on the band gap of Ge. The orbital ground states were mainly contributed by the $d-$orbital of Mo atom. This led to a reduction in the band gap of Ge by 0.23 eV. The $V_{Ge}Mo_{Ge}$ exhibited strong orbital hybridization between the $p-$orbital of Ge and the $d-$orbital of Mo.

The formation energies of the Mo_{Ge} for -2, -1, 0, $+1$ and $+2$ were -1.97, -2.83, -2.99, -3.45 and -2.81 eV, respectively. While the formation energies of the $V_{Ge}Mo_{Ge}$ for N1, N2 and N3 in the neutral charge state were -0.06, -0.14 and -0.05 eV, respectively. Under equilibrium conditions, the N2 amongst other complexes is the most energetically favourable with a formation energy of -0.12 eV. The binding energies (0.06, 0.14 and 0.05 eV of the N1, N2 and N3, respectively) for the $V_{Ge}Mo_{Ge}$ have been calculated to predict if the defect$-$complex is stable without dissociating into non-interacting defects. It turns out that all the calculated binding energies for the N1, N2 and N3 were positive and hence stable. The implication is that the defect complex system of the $V_{Ge}Mo_{Ge}$, remain as cluster defects without dissociating into a non-interacting defect except at the expense of higher energy.

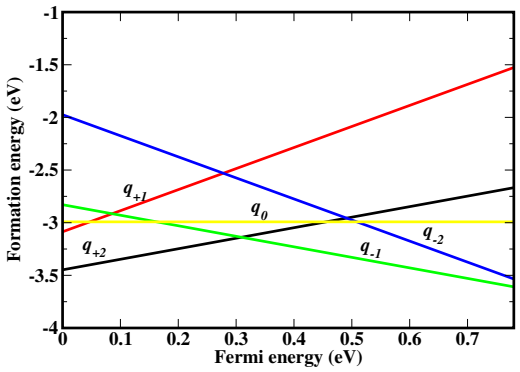

Figure 4. Plot of formation energy as a function of the Fermi energy for (a) Mo_{Ge}.

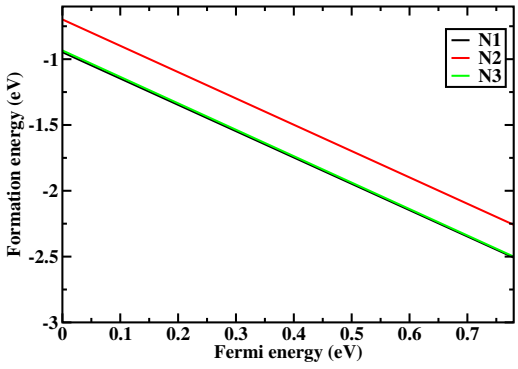

Figure 5. Plot of formation energy as a function of the Fermi energy for $V_{Ge}Mo_{Ge}$.

Figs 4 and 5 show the plot of the formation energy as a function of the Fermi energies for the Mo_{Ge} and $V_{Ge}Mo_{Ge}$, respectively. The electrically active levels induced by Mo dopant were investigated for both the $V_{Ge}Mo_{Ge}$ and Mo_{Ge}. For any given Fermi energy, it is important to note that a system is assume to reached thermodynamic equilibrium at the lowest energy charge state. For the $V_{Ge}Mo_{Ge}$ no sign of induced electrical level in the band gap of Ge was observed for all configurations. However, the -2 charge states was most thermodynamically stable for all Fermi energies in all configurations. Furthermore, for the Mo_{Ge}, as the Fermi energy is varied, the dopant introduced deep electrically active level in the band gap of Ge. The deep level introduced by the Mo_{Ge} is 0.31 eV above the valence band maximum. Another

interesting feature of Mo_{Ge} is the $(+2/-1)$ charge state transition level which is a negative−U. Using the method of Ref. [21], we predicted a negative−U ordering with an energy of -3.28 eV. This negative−U is attributed to the large lattice distortion experienced by the defect system. Additional notable thermodynamic charge states transition levels induced in the band gap of Ge due to its doping by Mo are $(+2/-1)$ and $(0/-1)$. However, these levels were thermodynamically accessible but not stable.

4. Summary

The Mo substitution (Mo_{Ge}) and vacancy-complexes ($V_{Ge}Mo_{Ge}$) induced electrical levels in Ge were presented. The HSE06 hybrid functional within the framework of DFT was used for all calculations. The formation energy for the neutral charge state of the Mo_{Ge} is -2.99 eV. The Mo_{Ge} induced deep level in the band gap of Ge. The Mo_{Ge} exhibits negative-U ordering for the $(+2/-1)$ transition. The formation energy result for the $V_{Ge}Mo_{Ge}$ show that under equilibrium conditions, the N2 configuration is the most energetically favourable. The $V_{Ge}Mo_{Ge}$ did not induce any thermodynamically stable transition charge state level in the band gap of Ge.

Acknowledgments

This work is based on the research supported partly by National Research foundation (NRF) of South Africa (Grant specific unique reference number (UID) 98961). The opinions, findings and conclusion expressed are those of the authors and the NRF accepts no liability whatsoever in this regard.

Reference

[1] Igumbor E and Meyer W E 2016 *Materials Science in Semiconductor Processing* **43** 129–133
[2] Deák P, Aradi B, Frauenheim T, Janzén E and Gali A 2010 *Phys. Rev. B* **81** 153203
[3] Claeys C and Simoen E 2011 *Germanium-based technologies: from materials to devices* (Elsevier)
[4] Auret F, Coelho S, Myburg G, van Rensburg P J and Meyer W 2009 *Physica B: Condensed Matter* **404** 4376–4378
[5] Markevich V P, Hawkins I D, Peaker A R, Litvinov V V, Murin L I, Dobaczewski L and Lindstrm J L 2002 *Applied Physics Letters* **81** 1821–1823
[6] Igumbor E 2017 *Hybrid functional study of point defects in germanium* Ph.D. thesis University of Pretoria
[7] Hohenberg P and Kohn W 1964 *Phys. Rev.* **136** B864–B871
[8] Perdew J P, Burke K and Ernzerhof M 1996 *Phys. Rev. Lett.* **77** 3865–3868
[9] Heyd J, Scuseria G E and Ernzerhof M 2006 *The Journal of Chemical Physics* **124**
[10] Igumbor E, Ouma C, Webb G and Meyer W 2016 *Physica B: Condensed Matter* **480** 191–195
[11] Igumbor E and Andrew R Cand Meyer W E 2017 *Journal of Electronic Materials* **46** 1022–1029
[12] Igumbor E, Omotoso E, Danga H, Tunhuma S and Meyer W 2017 *Nuclear Instruments and Methods in Physics Research Section B: Beam Interactions with Materials and Atoms* **409** 9 – 13
[13] Igumbor E, Omotoso E, Tunhuma S, Danga H and Meyer W 2017 *Nuclear Instruments and Methods in Physics Research Section B: Beam Interactions with Materials and Atoms* **409** 31 – 35
[14] Chroneos A, Uberuaga B P and Grimes R W 2007 *Journal of Applied Physics* **102** 083707
[15] Igumbor E, Mapasha R E, Andrew R and Meyer W E 2016 *Computational Condensed Matter* **8** 31–35
[16] Kresse G and Furthmüller J 1996 *Computational Materials Science* **6** 15 – 50
[17] Kresse G and Furthmüller J 1996 *Phys. Rev. B* **54** 11169–11186
[18] Blochl P E 1994 *Phys. Rev. B* **50** 17953–17979
[19] Monkhorst H J and Pack J D 1976 *Phys. Rev. B* **13** 5188–5192
[20] Igumbor E and Mapasha R Eand Meyer W E 2016 *Journal of Electronic Materials* 1–8
[21] Igumbor E, Obodo K and Meyer W E 2015 *Solid State Phenomena* **242** 440–446

Analysis of the structure, particle morphology and photoluminescent properties of green emitting $BaB_8O_{13}:Ce^{3+}$ phosphor

MA Lephoto[1], KG Tshabalala[1], SJ Motloung[1] and OM Ntwaeaborwa[2]
[1]Department of Physics, University of the Free State (Qwa Qwa Campus), Private Bag X13, Phuthaditjhaba, 9866, South Africa
[2]School of physics, University of the Witwatersrand, Private Bag 3, Wits, 2050, South Africa

E-mail: ntwaeab@gmail.com

Abstract. BaB_8O_{13}: Ce^{3+} powder phosphors were synthesized by the solution combustion method for general lighting applications. Powder X-ray diffraction pattern confirmed the formation of orthorhombic structure of BaB_8O_{13} and the crystallite sizes estimated with Scherrer's equation and Hall-Williamson's plot were in the nanometre scale. Scanning electron microscopy micrographs showed that the particles have irregular shapes and were agglomerated together. The bands in the Fourier transform infrared spectra in the range of 650 – 1600 cm^{-1} confirmed the formation of borate host. The $BaB_8O_{13}:Ce^{3+}$ powder phosphors showed emission at around 515 nm ascribed to the $5d^1$ - $4f^1$ transition of Ce^{3+} after excitation at 270 nm using a monochromatized xenon lamp. A standard CIE diagram derived from relative emissions from the powder phosphors suggested a unique emission concentrated in the green region, thus the phosphor serve as a potential source of green light in light emitting devices.

1.Introduction

Oxide materials such as borate compounds are excellent hosts for luminescent dopant ions because of their good optical properties, such as high damage threshold and good non-linearity. They also have good chemical and thermal stability, low synthesis temperature and they can be synthesized cost effectively [1]. Barium octaborate BaB_8O_{13} is considered as an excellent host material for luminescent dopant ions. Its structure consists of two separated interlocking three dimensional infinite network as alternating triborate and pentaborate groups, which forms BO_3 triangles and BO_4 tetrahedral units [2]. Ce^{3+} ions have been widely used as activators in various fluoride and oxide materials. The preparation of rare earth doped phosphor materials for application in advanced illumination technologies has been the subject of intense research for many decades. This type of research has been encouraged by the need to increase the efficiency of white light emitting solid state devices which can serve as an alternate source of lighting [3].

In most Ce^{3+} doped phosphors, parity allowed 5d - 4f emission ranging from ultra-violet to red color has been demonstrated and it is dependent on the host lattice and the site size, and the size symmetry and coordination number. In fact, the emission color of Ce^{3+} can be from the ultraviolet to visible region of the electromagnetic wave spectrum due to dependence of the 5d level of Ce^{3+} on the crystal field strength of the host lattice [4]. Different methods including wet chemistry and solid state

have been used to prepare different types of phosphors. Among these methods, the solution combustion has been widely used due to versality, easy of incorporation of dopant ions, cost effectiveness and relatively short reaction time. Depending on the type of precursors, as well as conditions used for the process, the solution combustion may occur as either volume or layer-by-layer propagating combustion modes. This process may not only yield nanosized materials but also uniform (homogeneous) doping of traces of rare-earth impurity ions in a single step [5]. In the current study, $BaB_8O_{13}:Ce^{3+}$ powder phosphors were synthesized by the solution combustion method. The photoluminescent properties, structure and particle morphology of these phosphors are reported.

2. Experimental

Powder samples of BaB_8O_{13}: xCe^{3+} (x = 0.03, 0.05, 0.07, 0.09 and 0.11) were synthesized by a solution combustion method. The following precursors all in analytical purity were used: Barium nitrate [$Ba(NO_3)_2$], boric acid [H_3BO_3], Cerium nitrate [$CeN_3O_9.6H_2O$] ,ammonium nitrate [NH_4NO_3] and urea [NH_2CONH_2]. In this preparation, NH_4NO_3 was used as an oxidizer and NH_2CONH_2 was used as a fuel. The stoichiometric amounts of reactants were mixed in a beaker with 10 mL of de-ionized water and stirred vigorously using a magnetic stirrer on a hot plate maintained at a temperature of 70 ^oC for 30 min. The resulting solution was then transferred to a crucible and was introduced into a muffle furnace preheated to 600 ºC. Within a few minutes, the solution boiled and ignited to produce a self-propagating flame. The entire combustion process was complete in less than 5 min but the crucible was left in the furnace for 10 min to ensure that decomposition was complete. After 10 min the crucible was removed from the furnace and allowed to cool to room temperature. The combustion ashes of the powder samples were ground gently into fine powders using pestle and mortar. The powders were post annealed at 800 ^oC for 5 hours in a muffle furnace. The structure, particle morphology and photoluminescent properties of the synthesized powder phosphors were examined by means of X-ray diffraction (XRD), Fourier transform spectroscopy (FTIR), scanning electron microscopy (SEM), Elemental energy dispersive analysis (EDS) and photoluminescence spectroscopy (PL emission and PL excitation).

3. Results and Discussion

Figure 1(a) shows the powder X-ray diffraction (XRD) patterns of BaB_8O_{13}: xCe^{3+} (x = 0.03, 0.05, 0.07, 0.09 and 0.11) powder phosphors. The XRD patterns of the powder phosphors were indexed to orthorhombic structure with cell parameters a = 8.550 Å, b = 17.350 Å and c = 13.211 Å according to JCPDS card no: 20-0097 [2]. The patterns show some extra peaks marked with asterisks (*) which may be attributed to the unreacted precursors during the combustion reaction. The presence of other phases or some of the precursors is attributed to the fact that the combustion wave is not uniform and portion of the precursors might not react completely during the combustion process [6]. The patterns also show a shift of peaks towards the lower angle as shown in figure 1(b). The observed XRD peak shifts might be caused by the lattice strain or lattice defects [7]. The average crystallite sizes of the phosphors were estimated by using Scherrer's equation [8]. The estimated average crystallite sizes of BaB_8O_{13}: xCe^{3+} powder phosphors were found to be 32, 36, 39, 43 and 40 nm for x = 0.03, 0.05, 0.07, 0.09 and 0.11, respectively. The crystal structure of BaB_8O_{13} host matrix is shown in figure 1(c). It is observed from the crystal structure that BaB_8O_{13} consists of both tetrahedron (BO_4) and triangular (BO_3) groups. Looking at the ion bond between Ba, B and O ions, it is observed that B and Ba are connected via O ions. According to our calculations, the average bond lengths between B-O and Ba-O were 1.415 Å and 2.713 Å, respectively. The average bond angles between O-B-O, B-O-B and Ba-O-B were calculated to be 111.34º, 128.47º and 115.57º, respectively.

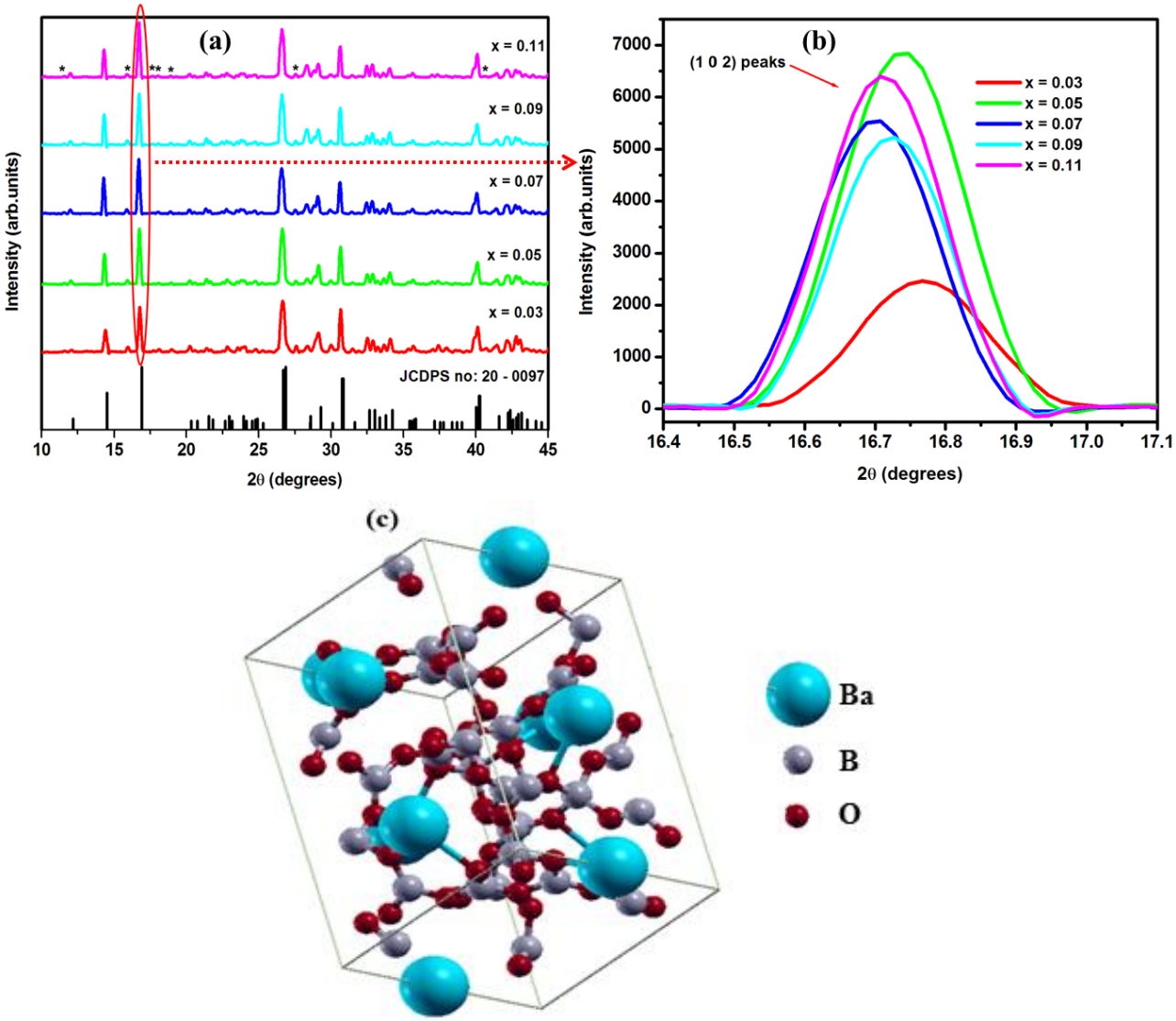

Figure 1. (a) Room temperature XRD pattern of BaB_8O_{13}:$x$$Ce^{3+}$ powder phosphors, (b) magnified view of (102) plane for BaB_8O_{13}:$x$$Ce^{3+}$ powder phosphors and (c) crystal structure of BaB_8O_{13} host (blue, grey and red balls represent barium, boron and oxygen atoms, respectively).

Figure 2 shows the Fourier Transform Infrared (FTIR) spectrum of BaB_8O_{13}:0.05Ce^{3+} powder phosphor. The FTIR spectrum was recorded in the spectral range of 650 - 3000 cm^{-1}. The spectrum exhibits some broad bands in the range 650 - 1600 cm^{-1}. The bands at 698, 730, 775, and 799 cm^{-1} are assigned to the out-of-plane bending mode of the group BO_3. The in-plane bending modes of the BO_3 group are shown by the bands at 871, 928, 980, 1101 and 1138 cm^{-1}. The bands peaking at 1235, 1270, 1319, 1363 and 1408 cm^{-1} are assigned to the asymmetric stretching vibration of the BO_3 group [1].

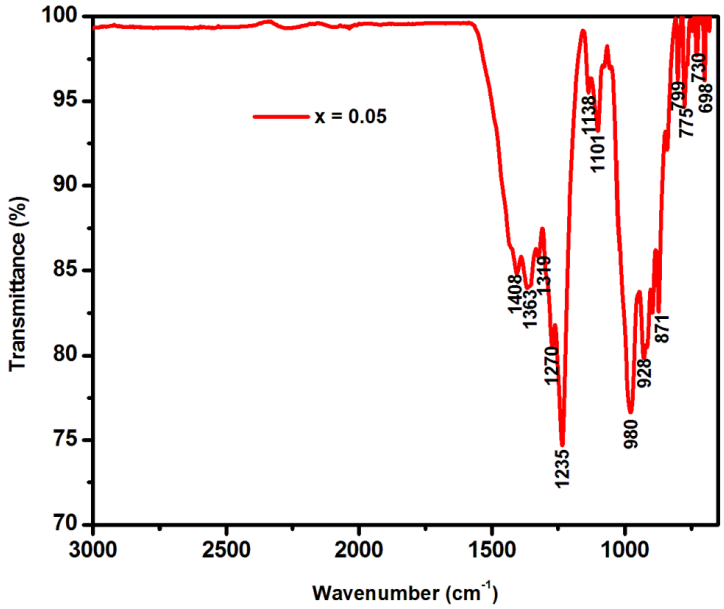

Figure 2. Room temperature FTIR spectrum of BaB_8O_{13}:0.05Ce^{3+} phosphor.

The scanning electron microscope (SEM) micrograph of BaB_8O_{13}:0.05Ce^{3+} powder phosphor taken at ×5000 magnification is shown in figure 3(a). It is observed that the microstructures of the phosphor are agglomerated with irregular shapes. The surface of the SEM micrograph shows lots of voids and pores due to the large amount of gases such as NO_2 and CO_2 that evolve during combustion method [9]. Figure 3(b) shows the energy dispersive X-ray spectroscopy (EDS) spectrum of BaB_8O_{13}:0.05Ce^{3+} powder phosphor. The spectrum confirms the presence of barium (Ba), Boron (B), oxygen (O) and Cerium (Ce) elements. The concentration of Ba by weight exceeds those of all the other elements and the least concentration (also by weight) was recorded for Ce^{3+} used as a dopant.

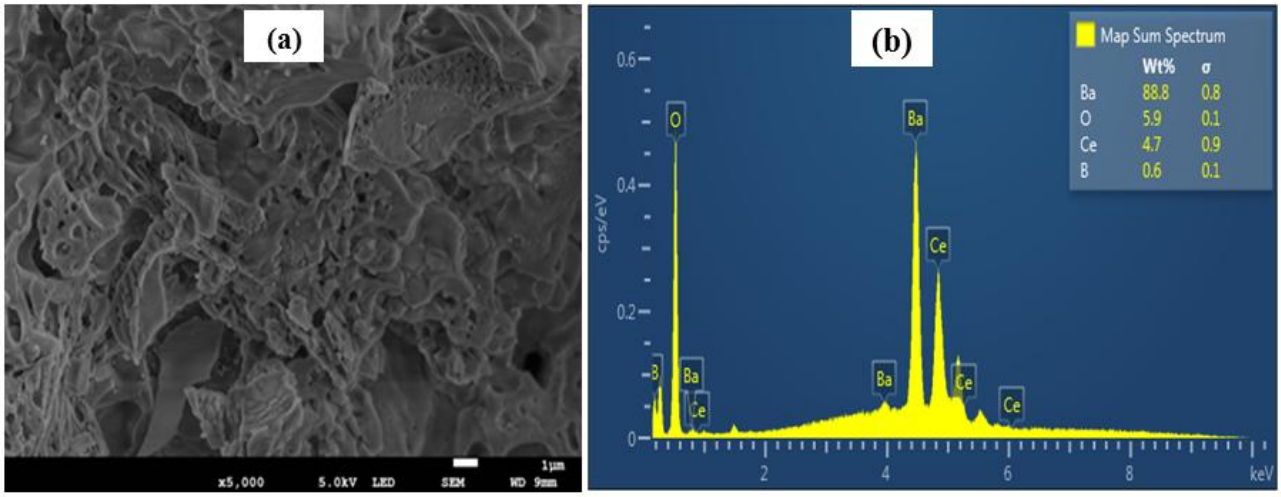

Figure 3. (a) SEM micrograph and (b) EDS spectrum of BaB_8O_{13}:0.05Ce^{3+} phosphor.

Figure 4(a) shows the photoluminescence excitation (PLE) of BaB_8O_{13}:0.05Ce^{3+} phosphor and photoluminescence emission (PL) spectra of BaB_8O_{13}:$x$$Ce^{3+}$ (x = 0.03, 0.05, 0.07, 0.09 and 0.11) powder phosphors. The PLE spectrum consists of a major peak centered at 270 nm and a minor peak at 212 nm due to the $4f^1$ - $5d^1$ excitation transition of Ce^{3+} ions and the excitonic band, respectively

[10]. The feature of the excitation spectrum remains the same when monitored using 515 nm emission peak indicating that the emission obtained is due to same recombination center [11]. When exciting the BaB_8O_{13}:$x$$Ce^{3+}$ (x = 0.03, 0.05, 0.07, 0.09 and 0.11) powder phosphors at 270 nm wavelength, a broad emission peak was observed at 515 nm, which is attributed to the inter-configuration $5d^1 - 4f^1$ allowed transition of Ce^{3+} [9, 12]. The concentration of Ce^{3+} versus relative emission intensity plot of BaB_8O_{13} doped with different concentrations of Ce^{3+} under 270 nm excitation is shown as an inset in figure 4(a). The plot shows PL intensity increased with concentration from 0.03 and maximizes at 0.05 mol beyond which the PL intensity decreased. The decrease in the PL emission intensity beyond the critical concentration could be explained by concentration quenching effect. The probability of energy transfer is greatly dependent on the distance between the activator ions. As the Ce^{3+} doping amount increases the distance between Ce^{3+} ions shortens, which favors the non-radiative pathway by energy transfer among Ce^{3+} ions [13]. Generally, the emission of Ce^{3+} has a doublet character with an energy difference of about 2000 cm^{-1} due to the ground-state splitting ($^2F_{5/2}$ and $^2F_{7/2}$) [14]. To confirm this, the PL spectrum of BaB_8O_{13}:0.05Ce^{3+} (figure 4(b)) was deconvoluted into two Gaussian profiles with peaks centered at 508 nm (19685 cm^{-1}) and 551 nm (18149 cm^{-1}). The energy difference (Δk) between them is about 1536 cm^{-1}, which shows a small difference compared with the theoretical value of 2000 cm^{-1}. This indicates that there is only one type of emission center in the BaB_8O_{13} host lattice [15].

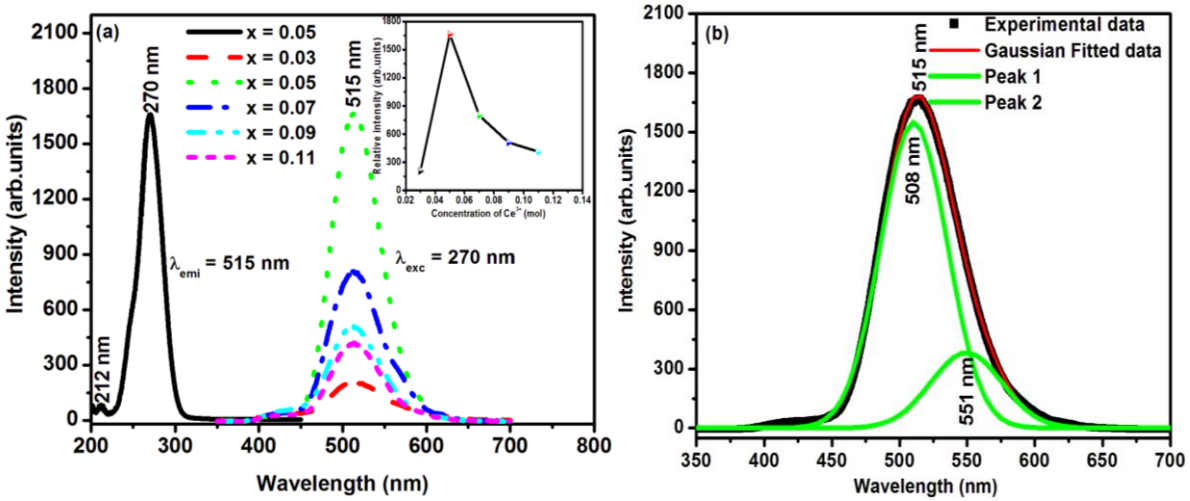

Figure 4. (a) Excitation spectrum of BaB_8O_{13}:0.05Ce^{3+} and emission spectra of BaB_8O_{13}:$x$$Ce^{3+}$ (x = 0.03, 0.05, 0.07, 0.09 and 0.11) powder phosphors, with relative intensity versus concentration of Ce^{3+} as an inset and (b) deconvoluted emission spectrum of BaB_8O_{13}:0.05Ce^{3+} powder phosphor.

The Commission International de I'Eclairage (CIE) 1931 Chromaticity image for BaB_8O_{13}:$x$$Ce^{3+}$ (x = 0.03, 0.05, 0.07, 0.09 and 0.11) phosphor powders excited at 270 nm is shown in figure 5. The CIE coordinate values were found to be (0.243, 0.481), (0.190, 0.572), (0.200, 0.536), (0.192, 0.503) and (0.209, 0.536) for x = 0.03, 0.05, 0.07, 0.09 and 0.1, respectively. The CIE coordinates are in the green region of the spectrum not far from the standard green phosphor with the coordinates (0.31, 0.60), which means this phosphors can be used as a source of green light in many light emitting devices of different types.

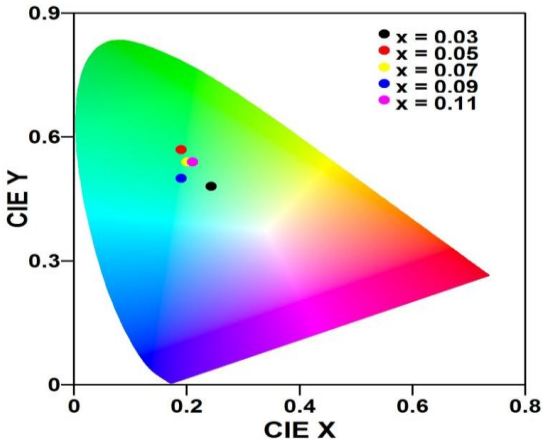

Figure 5: CIE chromaticity diagram of BaB_8O_{13} doped different concentrations of Ce^{3+}.

Conclusion

A detailed synthesis of a series of Ce^{3+} activated BaB_8O_{13} powder phosphors using the combustion method was presented. The phosphors were evaluated for a possible application as a source of green light in light emitting devices. The XRD patterns of the phosphors were found to be consistent with the standard orthorhombic crystal structure of BaB_8O_{13}. The photoluminescence spectroscopy data showed a broad emission centered at 515 nm under the UV excitation of 270 nm. The PL emission intensity was dependent on the concentration of Ce^{3+} with the maximum concentration obtained from the 0.05 mol Ce^{3+} doping. The CIE chromaticity coordinates indicated that the Ce^{3+} doped phosphors exhibit a green color, with coordinates close to those of the standard green phosphor, suggesting that our material is a potential candidate to be used as source of green light in different types of light emitting devices.

Acknowledgements

The authors would like to acknowledge financial assistance from the National Research Foundation (NRF), South Africa: (grants no: AEMD160523165935, SFH13081628745, 93936 and UID. 99378).

References

[1] Zhang J, Han B, Zhang Y and Lv Q 2016 *J. Mater. Sci: Mater Electron*. 27 3906
[2] Lephoto M A, Tshabalala K G, Motloung S J, Ahemen I and Ntwaeaborwa O M 2017 *PhyB*. doi.org/10.1016/j.physb.2017.06.063.
[3] Malchukova E and Boizot B 2014 *J Rare Earth*. **32** 217
[4] Lee S, Huang C, Chan T and Chen T 2014 *Appl. Mater. Interface*. **6** 7260
[5] Devaraja P B, Avadhani D N, Nagabhusana H, Prashantha S C, Sharma S C, Nagabhusana B M, Nagaswarupa H P and Prasad B D 2015 *J. Radiat. Res. Appl. Sci*. **8** 362
[6] Mothudi B M, Ntwaeaborwa O M, Shreyas S Pitale, Swart H C 2010 *J. Alloys. Compd*, **508** 262
[7] Chenari H M, Moafi H F and Rezaee O 2016 *Mater. Res*. **19** 548
[8] Tamrakar R K and Dubey V 2016 *J. Taibah Univ. Sci*. **10** 317
[9] Dhananjaya N, Nagabhushana H, Nagabhushana B M, Rudraswamy B, Shivhakumara C and Chakradhar R 2012 *Bull. Mater. Sci.* **35** 519
[10] Pawade V B, Dhoble N S and Dhoble S J 2015 *Mater. Res. Express.* **2** 095501
[11] Weon G S, Miso P, Jinhyoung K, Sang W J, Insu C, Youngku S 2014 *Thin Solid Films* **565** 293
[12] Sharma S K, Pitale S S, Malik M M, Dubey R N and Qureshi M S 2009 *J. Lumin*. **129** 140
[13] Chen Y, Cheah K W and Gong M 2011 *J. Lumin*. **131** 1589
[14] Zhong J, Zhuang W, Xing X, Liu R, Li Y, Liu Y and Hu Y 2015 *J. Phys. Chem. C* **119** 5562
[15] Zhou J, Xia Z, Yang M and Shen K 2012 *J. Mater. Chem*. **22** 21935

First-principles stability study of olivine $NaMPO_4$ (M: Mn, Fe, Co)

NL Lethole, HR Chauke and PE Ngoepe
Materials Modelling Centre, University of Limpopo, Private Bag X1106, Sovenga, 0727, South Africa
E-mail: Lesley.lethole@ul.ac.za

Abstract. First-principles calculations were carried out to investigate the structural, thermodynamic, electronic and mechanical properties of olivine $NaMPO_4$. All calculations were performed using plane-wave pseudopotential method within the generalised gradient approximation (GGA) functional with Hubbard *U* correction. We note that the calculated lattice parameters are in good agreement to within 6 % with the experimental data. The predicted heats of formation suggest that $NaMnPO_4$ is the most thermodynamic stable structure, with the lowest formation energy (-1292 kJ/mol). The calculated density of states showed that Fe 3*d* states for the $NaFePO_4$ system overlap the Fermi level E_F, suggesting a semi-metallic behaviour leading to good electronic conductivity. On the other hand, $NaCoPO_4$ and $NaMnPO_4$ show insulator behaviour due to the existence of energy band gap around the Fermi Level. Lastly, all the independent elastic constants for all structures satisfy the necessary stability criterion, indicating that all $NaMPO_4$ structures are mechanically stable.

1. Introduction

Sodium transition metal phosphates ($NaMPO_4$), with olivine structure, have recently attracted a lot of interest in battery applications as potential candidates for future cathode battery material. However, very little work has been done on the sodium-based material as many studies have primarily focused on well-developed counterpart, olivine lithium metal phosphates ($LiMPO_4$), due to the significant discoveries and investigations on lithium ion batteries [1, 2, 3, 4, 5]. Concerns regarding the abundance and possibilities of drastically increase in lithium ion batteries prices when demand intensifies may arise. Unlike the olivine $LiMPO_4$, the sodium-based olivine transition metal phosphates are more abundant and inexhaustible in the world [6].

Figure 1 shows the simulation models for olivine $NaMPO_4$ with space group *Pnma*. The M atoms are located in the octahedral sites, while P atoms occupy tetrahedral sites with a distorted hexagonal close-packed framework. The framework is coordinated by oxygen atoms forming layers of edge-sharing MO_6 octahedra, separated by PO_4 tetrahedra. Na ions move within the one-dimensional tunnel formed by the edge sharing LiO_6 octahedrons.

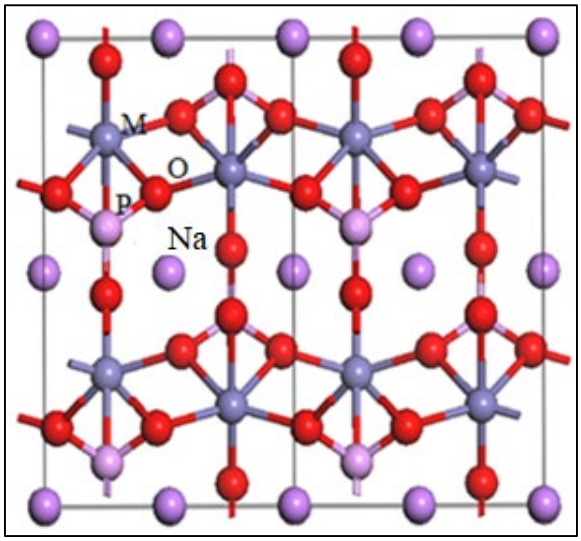

Figure 1 Atomic arrangement of $NaMPO_4$ olivines structures.

The major drawback for the sodium metal phosphates has been their low charge/discharge capacities. Previous studies by Shakoor *et al*. [7] reported that $NaFePO_4$ and $NaCoPO_4$ offer charge/discharge capacities of 12 mAh/g and 2.0 mAh/g, respectively, which is very less compared to the olivine $LiFePO_4$ (170 mAh/g) [8, 9], $LiMnPO_4$ (165 mAh/g) [10] and $LiCoPO_4$ (70 - 86 mAh/g) [9] and other sodium based cathode materials such as $Na_{1.5}VOPO_4F_{0.5}$ (80 mAh/g) and $Na_3V_2(PO_4)F_3$ (90 mAh/g) [11]. Several studies have suggested that the low capacities may be attributed to slow diffusion kinetics of sodium into the structure and the closed packed crystal structure which causes the sodium ion immobility [7, 12]. On the other hand, a study by Sun and Manivannan have shown that the $NaFePO_4$ electrode is capable of maintaining capacity for a large number of cycles, despite low capacity. It was reported that the charge/discharge densities continued to increase for more than 300 cycles [13], making this material a good candidate for large scale energy storage systems for smart grid applications. In addition, studies are required to enhance the $NaMPO_4$ electrochemical activity at room temperature, an important attribute for producing better sodium ion batteries.

Previous studies have reported the maricite $NaFePO_4$ to be seemingly the most thermodynamically stable phase as compared to olivine. It is reported that the maricite phase is 0.016 eV/formula unit more stable than the olivine [6, 14]. However, the edge-sharing FeO_6 octahedrons and lack of cationic channels for Na diffusion make this material an unlikely candidate for sodium ion battery development. In this study, we investigate the structural, thermodynamic, electronic and mechanical properties for the olivine $NaMPO_4$ (M=Fe, Co, Mn) structures to determine their stability and competences as future cathode materials. The heats of formation, electronic densities of states (DOS) and elastic constants will be calculated to mimic the stability trend at 0 K.

2. Methodology

First-principles DFT+*U* calculations were performed using the Vienna *Ab Initio S*imulation Package, VASP [15] to determine stability of olivine $NaMPO_4$. We used the spin-polarised generalised gradient approximation (GGA). A plane-wave cut-off of 500 eV and suitable k-mesh point of 4x6x6 was chosen for geometric optimisation. The Hubbard parameter of U=5.5 eV and J=*1* eV were found to correctly predict the lattice constants of transition metal phosphates [16]. Phonon dispersion curves were calculated with an interaction range of 7.0 Å. The DOS were calculated with the spin taken into account with a smearing width 0.05 eV using a Methfessel–Paxton smearing approach [17].

3. Results and discussion

3.1 Structural and thermodynamic properties

In table 1, we present the calculated lattice constants, heats of formation, elastic constants, moduli and Pugh ratio of $NaMPO_4$ systems. The experimental data are given in parenthesis where available. The structural lattice parameters are obtained by performing full geometry optimisation. The calculated lattice constants have been found to be in good agreement with the experimental to within 6 %, which is expected for a DFT transition metal calculation [18]. Moreover, we note that $NaMnPO_4$ (326.4 $Å^3$) has a larger volume over $NaFePO_4$ (318.2 $Å^3$) and $NaCoPO_4$ (311.7 $Å^3$): this may be due to the large ionic radii of Mn (81 pm) over Fe (75 pm) and Co (71 pm), respectively. The heats of formation of the $NaMPO_4$ olivines have been evaluated to mimic the thermodynamic stability using equation 1:

$$\Delta H_f\left(NaMPO_4\right) = {}^{1}\!/_{N}\left[E_{Total} - \left(E_{Na} + E_M + E_P + 4E_O\right)\right], \qquad 1$$

where E_{Total} is the total energy of $NaMPO_4$, while E_{Na}, E_M, E_P and E_O are the total elemental energies of Na, Fe, P and O in their respective ground-states. We note that $NaMPO_4$ structures show relatively low heats formation, with $NaMnPO_4$ structure showing the lowest value (-1292.6 kJ/mol), suggesting stability over $NaFePO_4$ (-1143.6 kJ/mol) and $NaCoPO_4$ (-1085.5 kJ/mol), respectively. Moreover, we note that our calculated heat formation value for $NaCoPO_4$ (-1086 kJ/mol) overestimates the experimental value (-1547.5 kJ/mol) [19].

Table 1 Calculated lattice constants, heats of formation and elastic properties of olivine $NaMPO_4$ systems. Experimental data is given in parenthesis.

Structure	**a (Å)**	**b (Å)**	**c (Å)**	**V ($Å^3$)**	**ΔH_f (kJ/mol)**
$NaFePO_4$	9.07 (8.99)	6.90 (6.86)	5.08 (5.05)	318.26 (311.35)[a]	-1143.6
$NaCoPO_4$	8.95 (8.88)	6.86 (6.80)	5.07 (5.03)	311.68 (303.28)[b]	-1085.5 (-1547.5)
$NaMnPO_4$	9.17 (9.08)	6.92 (6.90)	5.14 (5.11)	326.38 (320.84)[c]	-1292.6

Elastic Constants (GPa)

C_{ij}	**C_{11}**	**C_{12}**	**C_{13}**	**C_{22}**	**C_{23}**	**C_{33}**	**C_{44}**	**C_{55}**	**C_{66}**
$NaFePO_4$	166.83	59.67	80.58	161.17	65.83	175.17	53.00	61.67	49.33
$NaMnPO_4$	178.17	59.83	70.17	163.67	61.50	163.33	50.33	62.33	51.33
$NaCoPO_4$	184.83	50.00	75.25	178.33	55.58	168.33	47.67	65.67	41.67

Modulus (GPa) and Pugh Ratio

	B_H	**G_H**	**E_H**	**B/G**
$NaFePO_4$	101.37	52.29	133.86	1.94
$NaMnPO_4$	98.55	53.49	135.89	1.84
$NaCoPO_4$	99.10	53.43	135.87	1.86

[a] [20] [b] [19] [c] [6]

3.2 Electronic properties

In order to gain knowledge on the electronic conductivity of $NaMPO_4$ systems as cathode materials, we have calculated their densities of states (DOS). The partial and total DOS of $NaMPO_4$ structures are presented in figure 2. We note that the total and partial DOS are separated, forming a band gap near the Fermi level (E_F). The concepts of Fermi level and band gaps are necessary to understand electronic conductivity of materials. The spin polarised densities of states calculations show that the olivines $NaMnPO_4$, $NaFePO_4$ and $NaCoPO_4$ have energy band gaps of 3.51 eV, 1.17 eV and 1.87 eV, respectively. The energy band gaps for $NaMnPO_4$ and $NaCoPO_4$ are relatively wide, suggesting

insulator behaviour. $NaFePO_4$ show a relatively narrow energy band gap. Moreover, the Fermi level is located on the Fe 3*d* band, suggesting that some valence band states jumps the Fermi level barrier to the conduction band. The energy band gap value and the location of the Fermi level suggest that $NaFePO_4$ is semi-metallic leading to good electric conductivity in Na-ion batteries. The partial density of states shows that the M 3*d* states contribute significantly around the Fermi level, while Na, P and O states contribute minimally. Furthermore, we observe spin-down 3*d* peaks at about 2 eV in all systems and minimum contribution from Na, P and oxidation states. The $NaMnPO_4$ show a single 3*d* peak which may correspond to the Mn^{2+} oxidation state (most stable state), while two degenerate peaks are observed for $NaFePO_4$ suggesting Fe^{2+} and Fe^{3+} oxidation states. Clearly, Na intercalation causes the coexistence of Fe^{2+} and Fe^{3+} in the FeO_6 layers, which may have effect on charge neutrality. This may solved by extracting two electrons from O^{2-} which is reduced and released in the vacuum as O_2 [21]. As a result, the Fermi energy level shifts to higher conductive band, leading to the enhancement of electronic conductivity of $NaFePO_4$ as well as reversible capacity [22], which will be favourable for Na deintercalation. On the other hand, $NaCoPO_4$ shows only Co^{2+} states, since there is no clear distinction between the Co 3*d* peaks.

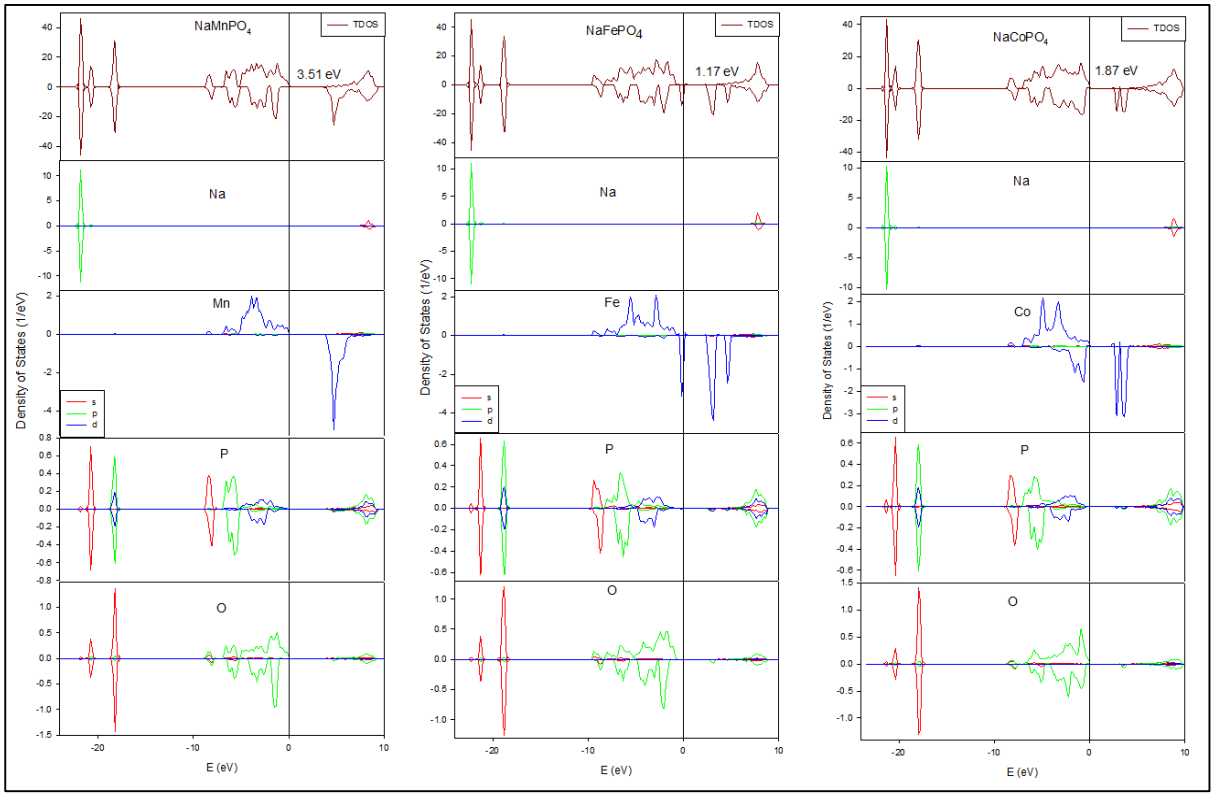

Figure 2 Partial and total density of states plots of olivine $NaMPO_4$ structures.

3.3 Mechanical properties

The elastic constants calculated using a Taylor expansion are presented in table 1 [23].

$$U(v,\varepsilon) = U(V_0,0) + V_0\left[\sum_i \tau_i \varepsilon_i \delta_i + \frac{1}{2}\sum_{ij} C_{ij}\varepsilon_i\delta_i\varepsilon_j\delta_j\right], \qquad 2$$

where $U(V_0,0)$ represents the unstrained system energy, V_0 is the equilibrium volume, τ_i is the element in the stress tensor, and δ_i is a factor of Voigt index. The orthorhombic $NaMPO_4$ structures have nine independent elastic constants (C_{ij}), which are presented in table 1. The Born mechanical stability criteria for orthorhombic systems are [24, 25]:

$(C_{11}-C_{12})>0,\ (C_{11}+C_{33}-2C_{13})>0,\ (2C_{11}+C_{33}+2C_{12}+4C_{13})>0,$

$C_{11}>0,\ C_{33}>0,\ C_{44}>0,\ C_{66}>0$

We note that all stability criteria are satisfied, indicating that $NaMPO_4$ compounds in the olivine structure are mechanically stable. To the best of our knowledge, these are the first recorded elastic constants on $NaMPO_4$ systems.

From the calculated elastic constants, the macroscopic mechanical parameters, namely, Bulk, Shear and Young's modulus are obtained using the Voigt-Reuss-Hill approach [26],

$$B_V=\frac{1}{9}(C_{11}+C_{22}+C_{33})+\frac{2}{9}(C_{12}+C_{13}+C_{23}),\ B_R=\left[(S_{11}+S_{22}+S_{33})+2(S_{12}+S_{13}+S_{23})^{-1}\right],$$

$$G_V=\frac{1}{15}(C_{11}+C_{22}+C_{33}-C_{12}-C_{13}-C_{23})+\frac{1}{5}(C_{44}+C_{55}+C_{66}),$$

$$G_R=15\left[4(S_{11}+S_{22}+S_{33})-4(S_{12}+S_{13}+S_{23})+3(S_{44}+S_{55}+S_{66})\right]^{-1},\ B_H=\frac{1}{2}(B_R+B_V),$$

$$G_{\mathrm{H}}=\frac{1}{2}(G_R+G_V),\ E_H=\frac{9B_HG_H}{G_H+3B_H},$$

where B, G and E are the bulk, shear and Young's modulus, while V, R and H are the Voigt, Reuss and Hill bounds, respectively and S_{ij} is the inverse matrix of the elastic constants matrix C_{ij}, which is given by [27];

$$S_{11}=\frac{(C_{22}C_{33}-C_{23}^2)}{(C_{11}C_{22}C_{33}+2C_{12}C_{13}+C_{23}-C_{11}C_{23}^2-C_{22}C_{13}^2-C_{33}C_{12}^2)},$$

$$S_{12}=\frac{(C_{13}C_{23}-C_{12}C_{33})}{(C_{11}C_{22}C_{33}+2C_{12}C_{13}C_{23}-C_{11}C_{23}^2-C_{22}C_{13}^2-C_{33}C_{12}^2)},$$

$$S_{13}=\frac{(C_{12}C_{23}-C_{22}C_{13})}{C_{11}C_{22}C_{33}+2C_{12}C_{13}C_{23}-C_{11}C_{23}^2-C_{22}C_{13}^2-C_{33}C_{12}^2},$$

$$S_{22}=\frac{(C_{11}C_{33}-C_{13}^2)}{(C_{11}C_{22}C_{33}+2C_{12}C_{13}C_{23}-C_{11}C_{23}^2-C_{22}C_{13}^2-C_{33}C_{12}^2)},$$

$$S_{23}=\frac{(C_{12}C_{13}-C_{11}C_{23})}{(C_{11}C_{22}C_{33}+2C_{12}C_{13}C_{23}-C_{11}C_{23}^2-C_{22}C_{13}^2-C_{33}C_{12}^2)},$$

$$S_{33}=\frac{(C_{11}C_{22}-C_{12}^2)}{(C_{11}C_{22}C_{33}+2C_{12}C\ C_{23}-C_{11}C_{23}^2-C_{22}C_{13}^2-C_{33}C_{12}^2)},$$

$$S_{44}=\frac{1}{C_{44}},\ S_{55}=\frac{1}{C_{55}},\ S_{66}=\frac{1}{C_{66}}.$$

The resultant bulk, shear and Young's modulus are listed in table 1. The bulk and Young's moduli determines hardness and stiffness of the material, respectively, while the shear determines the resistance to deformation under shear stress. The bulk modulus also measure resistance to volume change under pressure [28, 29]. We note that $NaMPO_4$ structures show relatively large positive bulk, shear and Young's moduli, suggesting hardness, high resistance to volume change and deformation and stiffness, respectively. Moreover, we note that $B_H>G_H$, which implies that the parameter limiting the mechanical stability of $NaMPO_4$ structures is the shear modulus (G_H) [30]. Moreover, the Pugh criterion of ductility and brittleness was calculated. Pugh proposed that if B_H/G_H is more than the critical value (1.75), the material is ductile and if less than (1.75), the material is brittle [31]. We note all $NaMPO_4$ structures are

ductile, since B_H/G_H is greater than 1.75, suggest that these materials are able to band without deformation, leading to minimal cracks during battery operation [32].

4. Conclusions

First-principles calculations on $NaMPO_4$ structures have been performed, particularly, structural parameters, heats of formation electronic density of states and elastic constants. It has been shown that the structural parameters obtained by full optimisation are in good agreement with the experimental data to within 6 %, suggesting validity of the approach employed. The heats of formation suggested thermodynamic stability of $NaMnPO_4$ structure (-1292.6 kJ/mol) over $NaFePO_4$ (-1143.6 kJ/mol) and $NaCoPO_4$ (-1085.5 kJ/mol), respectively. The electronic density of states has shown that the $NaFePO_4$ structure is semi-metallic, while $NaMnPO_4$ and $NaCoPO_4$ show insulator behaviour characteristics. The semi-metallic behaviour of $NaFePO_4$ strongly suggest that this system has better electronic conductivity, hence preferred. Lastly, the elastic properties show that the olivine $NaMPO_4$ structures are all mechanically stable and behave in a ductile manner, suggesting lack of cracks during battery operation.

Acknowledgement

This work has been performed at the Materials Modelling Centre, University of Limpopo, supported by the National Research Foundation.

References

[1] Padhi A K, Nanjundaswamy K S and Goodenough J B 1996 *Electrochem. Soc.* **96** 73

[2] Amatucci G G and Pereira N, 2007 *J. Flourine Chem.* **128** 243

[3] Ellis B L, Makahnouk W R M, Weetaluktuk W N R, Ryan D H and Nazar L F 2010 *J. Chem. Mater.* 22 1059

[4] Barker J, Saidi M Y and Swoyer J 2003 *J. Electrochem. Solid-State Lett.* **6** A1

[5] Zhou H, Wang X, Tang A, Liu Z, Gamboab S and Sebastian P J 2006 *J. Power Sources* **160** 698

[6] Lee K T, Ramesh T N, Nan F, Botton G and Nazar L F 2011 *Chem. Mater.* **23** 3593

[7] Shakoor R A, Park Y U, Kim J, Kim S W, Seo D H, Gwon H and Kang K 2010 *J. Korean Battery Soc.* **3** 00

[8] Mizushima K, Jones P C, Wiseman P J and Goodenough J B 1980 *Mater. Res. Bull.* **15** 799

[9] Amine K, Yashuda H and Yamachi M 2000 *Electrochem. Solid-State Lett.* **31** 179

[10] Pivko M, Bele M, Tchernychova E, Logar N Z, Dominko R and Gaberscek M 2012 *Chem. Mater.* **24** 1041

[11] Sauvage S, Quarez E, Trascon J M and Baudrin E 2006 *J. Electrochem. Soc.* **8** 1215

[12] Moreau P, Guyomard D, Gaubicher J and Boucher F 2010 *Chem. Mater.* **22** 4126

[13] Sun A and Manivannam A 2011 *ASC Transactions* **35** 3

[14] Moreau P, Guyomard D, Gaubicher F and Boucher F 2010 *Chem. Mater.* **22** 4126

[15] Kresse G and Furthmüller J 1996 *Phys. Rev. B* **54** 11169

[16] Kresse G and Joubert D 1999 *Phys. Rev.* **59** 1758

[17] Methfessel M and Paxton A 1989 *Phys. Rev. B* **40**, p. 3616

[18] Li G, Azuma H and Tohda M 2002 *Electrochem. Solid-State Lett.* **5** A135

[19] Le S N, Eng W and Navrotsky A 2006 *Solid State Chem.* **179** 3731

[20] Bridson J N, Quinlan S E and Tremaine P R 1998 *J. Chem. Mater.* **10** 763

[21] Wu Y 2015 Lithium-ion batteries, fundamentals and Applications *Tayor and Francis Group* Boca Raton

[22] Kinyanjui M K 2010 Electronic and Structural Properties of Li(1-x)FePO4 (X=0, 0.5,1) Ph.D. Thesis ULM University

[23] Fast L, Wills J M, Johansson B and Eriksson O 1995 *Phys. Rev. B* **51** 17431

[24] Sinko G V and Smirnov N A 2002 *J. Phys. Condens. Matter* **14** 6989

[25] Grimsditch M, Polian A, Brazhkin V and Balitskii D 1998 *J. Appl. Phys.* **83** 3018

[26] Patil S K R, Khare S V, Tuttle B R, Bording J K and Kodambaka S 2006 *Phys. Rev. B* **73** 104118

[27] Ravindran P, Fast L, Korzhavyi P A, Johansson B, Wills J and Eriksson O 1998 *J. App. Phys.* **84** 4904

[28] Chung H Y, Weinberger M B, Yang J M, Tolbert S H and Kaner R B 2008 *Appl. Phys. Lett.* **92** 261904

[29] McHargue C, Darby Jr J B, Yacaman M J and Gasga J R 1997 Norwell, Massachusetts, USA: Kluwer Academic Publishers

[30] Shein I R and Ivanovskii A L 2008 *J. Phys. Condens. Mater* **20** 415218

[31] Pugh S F 1954 *Philos. Mag.* **45** 833

[32] Wang D, Wu X, Wang Z and Chen L 2005 *J. Power Sources* **140** 125

Optimisation of inorganic-organic photoactive hybrid thin films

S.S. Magubane[1], T.F.G. Muller[1], C.J. Oliphant[2] and C.J. Arendse[1].

[1] Department of Physics and Astronomy, University of the Western Cape, Private Bag X17, Bellville 7535, South Africa.

[2]National Metrology Institute of South Africa, Private Bag X34, Lynnwood Ridge, Pretoria 0040, South Africa.

3578636@myuwc.ac.za, siphesihles6@gmail.com

Abstract. Photoactive hybrid films based on inorganic/organic nanocomposites have been widely employed for fabrication of low cost and environmental friendly photovoltaic devices [1-2]. However, silicon nanowires (SiNWs) and poly (3-hexylthiophene-2,5-diyl) also known as P3HT, are promising candidates that still require exploration due to high optical absorption and excellent charge carrier mobility associated with them, respectively [3-4]. An objective of the study was to establish optimised spin coating conditions for P3HT film deposition with high film uniformity and electrical conductivity in order to incorporate SiNWs for enhancement of optical and electrical properties of the film. Uniform hybrid films with satisfactory electric conductivities were obtained.

1. Introduction

In response to the global concern over issues of global warming and unsustainability of the current commercial source of energy based on fossil fuels, research towards the development of low cost renewable sources of energy has gained tremendous interest over the last two decades. Inorganic photovoltaics (PVs) based on crystalline silicon (c-Si) are ubiquitous and exhibit reasonable power conversion efficiency (PCE). However, high temperature and vacuum required for the processing of Si and fabrication of this type of PV leads to high production cost, which needs to be reduced. In this context, other PV technologies such as those based on organic semiconductors (OPVs) have emerged as promising candidates for fabrication of PV technologies at low cost [5, 6], on flexible substrates. In OPVs, the PCE is affected by the morphology of the active layer, the structure and the choice of electron donor (D) and acceptor (A) materials, the ratio of these materials and the interaction in the D-A interface within an active layer [7]. The major setback for OPVs involves the low PCE, which is due to limited charge carrier mobility, as a result of a rapid recombination rate within the active layer [8]. In dealing with shortcomings associated with OPVs, methods such as incorporating inorganic material into polymer matrices have been developed and employed [9-11].

Hybrid solar cells combine advantages of both organic and inorganic materials, where the conjugated polymer absorbs light and acts as the donor, whereas the inorganic material can act as acceptor and electron transporter in the structure. In our films the conjugated polymer and inorganic nanowires (NWs) are mixed together in specific weight ratios. The polymer poly (3-hexylthiophene-2,5-diyl) (P3HT) is

employed for its good hole transporting ability arising from the crystalline ordering of the polymer. As inorganic material, silicon nanowires (SiNWs) offer high surface area per volume ratio providing a large interface for exciton dissociation, therefore leading to high mobility of electrons [12]. This study is about optimizing the composition of P3HT: SiNWs photoactive hybrid layers in order to enhance its electric properties. Other factors contributing toward the improvement of the photoactive layer's conductivity are also taken into account.

2. Experimental details

2.1. Material Synthesis

The conjugated polymer P3HT (Sigma Aldrich) with a molecular weight average between 54000-75000 $gmol^{-1}$, was used as purchased without any further purification or modification. SiNWs were synthesized in the laboratory via metal assisted chemical etching (MACE) process as discussed in literature [4]. However, in this study, Si wafers were immersed into a second etching solution that consisted of a high concentration of hydrofluoric acid (HF) and hydrogen peroxide (H_20_2), in a volume ratio of 10 ml of H_2O_2, 10 ml of HF and 30 ml of H_2O for etching the bases of SiNWs prior to the removal of the silver nanoparticles (Ag NPs) in nitric acid (HNO_3) [4, 13]. In order to detach SiNWs from the bulk Si wafer, the base-etched SiNWs samples were immersed in 5% HF for 3 min to remove the oxide layer from the NWs, and subsequently immersed in a binary solvent of dichlorobenzene (DCB) and chloroform (CF) with (1:1) ratio, and sonicated in an ultrasonic bath for 10 minutes, during which the fragile bases of the SiNWs broke off into the binary solvent. The remaining SiNW-free bulk Si wafer were then removed from the solution containing the NWs.

Using this SiNWs ink, three solutions of different SiNWs concentrations by weight ratio were prepared, P3HT: 1.5 wt% SiNWs, P3HT: 3 wt% SiNWs, and P3HT: 6 wt% SiNWs. The fourth solution of P3HT dissolved in the binary solvent was used as a reference. These solutions were stirred overnight on a digital hot plate stirrer (Lasec) at rotational speed and temperature of 250 rpm and 23° C respectively. Microscope slides with 1-1.2 mm thickness (Lasec), on which hybrid solutions were to be deposited, were ultrasonically cleaned in acetone, ethanol and isopropanol and then rinsed in deionized water. The solutions were then deposited at 1000 rpm for the duration of 80s using a G3P-series spin coater (Specialty Coating Systems) to form photoactive bulk heterojunction hybrid layers.

2.2 Characterization

SiNWs morphology and microstructure were characterized by High Resolution Scanning Electron Microscopy (HRSEM: Zeiss Auriga) and Optical Microscopy (Olympus U-CMAD3, Japan). Optical properties were investigated using UV-Vis absorbance and photoluminescence (PL), (Maya 2000PRO with Deuterium-Tungsten Halogen sources, and HORIBA Jobin Yvon Fluorolog-3 model FL322), respectively. A FEI Tecnai F20 field emission high resolution transmission electron microscope (HR-TEM) was used to examine the crystallinity of the hybrid material.

3. Results and Discussion

It can be seen that base-etched SiNWs before the detachment are vertically aligned on a Si wafer (fig 1 (a)). The diameters of the wires are between 0.17-0.27 μm, while the length is approximately 4.8 μm. Fig 1 (b) depicts that after detachment SiNWs are not of uniform length. This suggest that during sonication SiNWs break randomly due to two possibilities: (1) base-etching not occurring at the same level, and (2) as-synthesised SiNWs varied in length. A thoroughly discussion of SiNWs formation can be found in references 13, and 14&15.

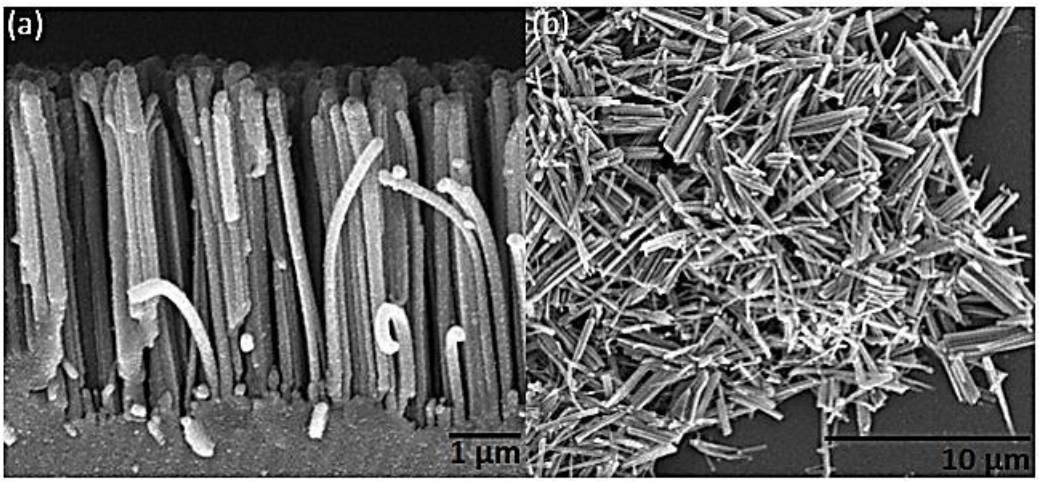

Figure 1: SEM micrographs of SiNWs, (a) cross sectional view of base-etched SiNWs and (b) SiNWs deposited onto a glass substrate by drop casting.

Prior to mixing the SiNWs with the polymer, spin-coating deposition parameters for pristine P3HT were optimised. Different solution concentrations (5, 7.5, 10 and 20 mg/ml of P3HT/DCB/CF), spinning speeds (500, 750, 1000 and 2000 rpm), and spinning durations (20, 40, 60 and 80 s) were investigated. The thickness and the uniformity of the films depended on the entire four distinct stages of the spin-coating process, i.e. dispense stage, substrate acceleration, spin-off and solvent evaporation. All spin coating parameters investigated in this study revealed to have a direct impact on the thickness and the uniformity of the film obtained. The film obtained from a solution concentration of 10 mg/ml spin coated at 750 rmp for the duration 80 s exhibited the highest conductivity and this was considered the optimal condition for pure P3HT.

Optical microscope images of P3HT matrix incorporated with different SiNWs concentrations are depicted in fig 2. It has been reported that film uniformity depend strongly on the choice of organic solvent used [16]. In this study, the binary solvent of dichlorobenzene and chloroform was used due to the high solubility of P3HT in the former and quick evaporation of the latter, which together constructively influence the film produced. It is evident from fig 2 (a-d) that films investigated shows small particles associated with P3HT. This is an indication of the possibility of reorganisation of the polymer during thermal treatment of the film. From fig 2 (b-d) it is observed that SiNWs incorporated in the P3HT matrix are randomly distributed, and are of different sizes. As shown in fig 2 (d), a high concentration of SiNWs enlarges the D-A interface, which could be suitable for effective charge transfer for P3HT: SiNWs. However, this large number of wires could act as recombination sites; perhaps it is for this reason that other complementing techniques are employed to examine the concentration of SiNWs favourable for successful charge separation.

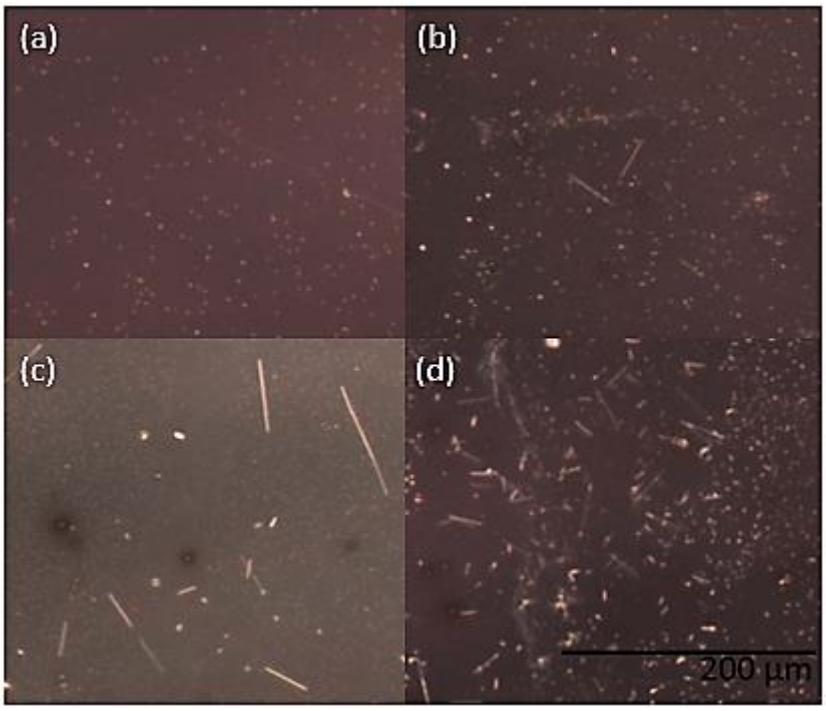

Figure 2: Optical micrographs of hybrid layers, (a) pure P3HT, (b) P3HT: 1.5 wt % SiNWs, (c) P3HT: 3 wt% SiNWs and (d) P3HT: 6 wt% SiNWs.

Fig 3 shows the optical properties of the hybrid layers. The P3HT spectrum in fig 3 depicts two maximum absorption peaks at wavelengths around 520 and 545 nm, which are attributed to the π-π* transition [17]. In addition, a shoulder peak is observed around 600 nm. This shoulder peak is ascribed to the high crystallization and intrachain interaction ordering of the P3HT [1]. It is also noticed from the spectra that upon addition of SiNWs the shape of the P3HT spectrum is retained with a slight broadening of absorption peaks, which suggest better structuring of P3HT in the presence of SiNWs. In the wavelength range between 630-800 nm, it can be observed that addition of SiNWs reduces the absorption of the P3HT matrix. However, further addition of wires recovers the absorption intensity. PL spectra of P3HT and its blend with different concentration of SiNWs is shown in fig 3 (b). The PL peak appears at wavelength around 650 nm, which is characterized by the relaxation of excited π-electrons to its ground state. It is in our interest to observe that blending P3HT with SiNWs quenches the PL peak, this indicates the occurrence of successful charge dissociation at the D-A interface [18]. The maximum quenching is obtained for the blend ratio of P3HT: 3 wt % SiNWs. Further addition of SiNWs into the polymer matrix, i.e. P3HT: 6 wt % SiNWs results in an increased intensity of the PL peak. This increase in the emission intensity may be due to the formation of SiNWs aggregates, which decreases the D-A interface [19].

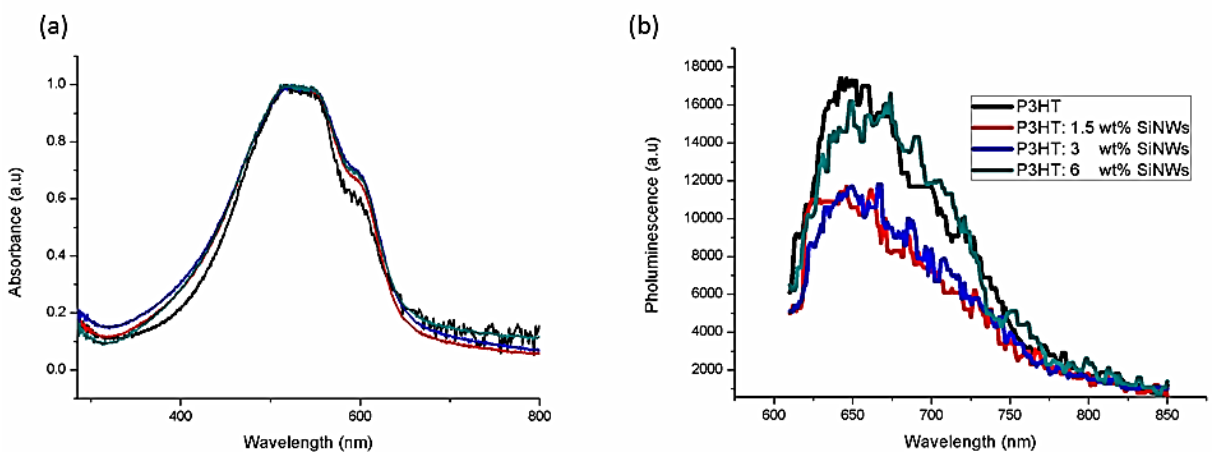

Figure 3: Optical properties of hybrid films, (a) Normalised UV-Vis absorption spectra and (b) photoluminescence spectra.

HRTEM was employed to examine the internal structure and crystallinity of the combination of P3HT and SiNWs. Fig 4 (a) shows that within the matrix, P3HT covers parts of the SiNWs. Fig 4 (b) and the inset indicate that the hybrid film is polycrystalline.

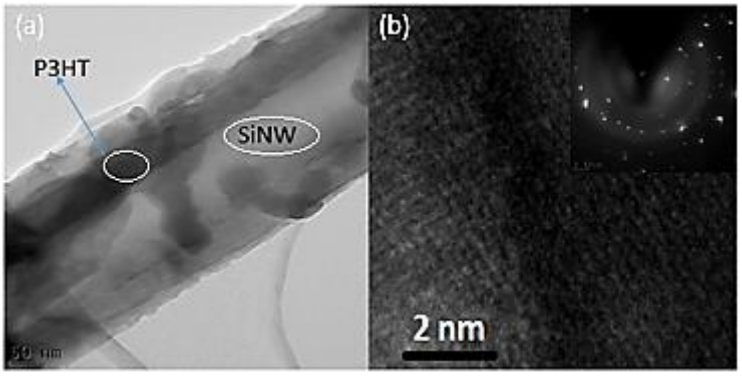

Figure 4: TEM images, (a) SiNWs covered by P3HT and (b) crystallographic information on P3HT: SiNWs, the inset is the SAED pattern for the combination of P3HT: 6 wt % SiNWs.

The thickness and conductivity of the hybrid films measured at room temperature using a Dektak Profilometer and four point probe Hall Effect measurement system are presented in table 1. As expected, the thickness of the hybrid films increase with an increasing content of SiNWs, this could be attributed to the enhanced surface tension of the solutions with an increasing content of SiNWs. Table 1 also reveals that, adding SiNWs into the P3HT matrix increases the electrical conductivity, which is in good agreement with PL results. The decrease in the conductivity of P3HT: 6 wt% SiNWs seems to confirm the suggestion made earlier that an excessive amount of SiNWs encourages formation of recombination sites which degrade the quality of the hybrid film.

Table 1: Thickness and conductivity of spin coated films.

P3HT: SiNWs wt % ratio	Thickness (nm)	Conductivity ($\times 10^{-5}\Omega^{-1}.cm^{-1}$)
P3HT	87	3.39
P3HT: 1.5 wt % SiNWs	89	3.41
P3HT: 3.0 wt % SiNWs	95	3.61
P3HT: 6.0 wt % SiNWs	125	2.52

4. Conclusion

In conclusion, bulk heterojunction photoactive hybrid films composed of P3HT and SiNWs have been prepared by spin coating to establish optimal composition of these materials of interest. Within the photoactive hybrid layer, SiNWs are randomly distributed and the polymer covers SiNWs, thus forming various D-A interfaces essential for charge separation. The maximum conductivity of $3.61\times 10^{-5}\,\Omega^{-1}.cm^{-1}$ was obtained for the blend ratio of P3HT: 3 wt % SiNWs. There is good correspondence between the optical and the electrical properties of the as-prepared hybrid films and these results agree well with literature.

5. Acknoledgements

The authors wish to acknowledge South African National Research Foundation (NRF) Thuthuka program for financial support, and the Electron Microscope Unit (EMU) at UWC for measurements.

References

[1] Braik M, Dridi C, Rybak A, Davenas J and Cornu D 2014 *Phys. Status Solidi* A **211** 670
[2] Davenas J, Dkhil S B, Cornu D and Rybak A 2012 *Energy Procedia* **31** 136
[3] Wright M and Uddin A 2012 *Sol. Energy Mater. Sol. Cells* **107** 87
[4] Liu K, Qu S, Zhang X, Tan F and Wang Z 2013 *Nanoscale Res. Lett.* **8** 88
[5] Krebs F C 2009 *Sol. Energy Mater Sol. Cells* **93** 394
[6] Yue D, Khatau P , You F and Darling S B 2012 *Energy Environ. Sci.* **5** 9163
[7] Muller T, Ramashia T A, Motaung D E, Cummings F, Malgas G, Oliphant C and Arendse C 2016 *Phys. Status Solidi* A **213** 1915
[8] Hoppe H and Sariciftci S N 2004 *J. Mater. Res.* **19** 1924
[9] Azizi S, Braik M, Dridi C, Ouada H B, Ryback A and Davenas J 2012 *Appl. Phys.* A **108** 99
[10] Chehata N, Ltaief A, Beyou E, Ilahi B, Salem B, Baron T, Gentile P, Maaref H and Bouazizi A 2015 *J. Lumin.* **168** 315
[11] He L, Jiang C, Wang H, Lai D, Tan Y H, Tan CS and Rusli 2012 *Appl. Phys. Lett.* **100** 103104
[12] Charrier J, Najar A and Pirasteh P 2013 *Appl. Surf. Sci* **283** 828
[13] Liu Y, Ji G, Wang J, Liang X, Zuo Z and Shi Y 2012 *Nanoscale Res. Lett* **7** 663
[14] Chartier C, Bastide S and Levy-Clement C 2008 *Electrochim. Acta* **53** 5509
[15] Smith Z R, Smith R L and Collins S D 2013 *Electrochim.* Acta **92** 139
[16] Luo S C, Cranium V and Douglas E P 2005 *Langmuir* **21** 2881
[17] Chen T A, Wu X and Rieke R D 1995 *J. Am. Chem. Soc.* **117** 233
[18] Saidi H, Walid A, Bouaziz A, Herrero B R and Saidi F 2017 *Mater. Res. Express* **4** 035007
[19] Dkhil S B, Elbdelli R, Dachraoui W, Faltakh H, Bourguiga R and Davenas J 2014 *Synth. Met.* **192** 74

Structural and thermodynamic properties of Zr-Nb-Co compound.

[1]M M Malebati, [1]P E Ngoepe and [1]H R Chauke

[1]Materials Modelling Centre, School of Physical and Mineral Sciences, University of Limpopo, Private Bag X1106, Sovenga, 0727, South Africa.

Email: magoja.malebati@ul.ac.za

Abstract. More advanced Zr-based alloys are being developed for the more severe operating conditions such as higher burn-up and increased operation temperature, this is due to their good resistance to corrosion and high melting point. In this work, density functional theory have been used to investigate the structural and thermodynamic properties of Zr-Nb-Co system at various concentrations. We used the virtual crystal approximation to introduce small content Co on different $Zr_{97}Nb_3$ composition. We found that the increase in Co concentration enhances the stability of the compound with the $Zr_{97}Nb_3$ being the most preferred composition, and the alloy is stable only at a small Co concentration of about 3 atomic percent (3 at. %). We also found that both binary $Zr_{97}Nb_3$ and ternary $Zr_{97}Nb_{2.5}Co_{0.5}$ structures converges at 1000K, confirming stability at high temperature.

1. Introduction

Zirconium is a very promising material for the nuclear industry and power engineering due to its excellent properties for nuclear environment that will alleviate the radiation effects [1, 2]. It is used as the structural material in a prototype core for nuclear submarines [3]. Zirconium exhibit excellent resistance to radiation in both mechanical behaviour and dimensional stability, low neutron cross-section, good corrosion resistance, high yield strength, fabricability and ductility.

Zirconium and its alloys has attracted significant attention due to its distinctive properties for extensive applications in nuclear and chemical industry [4]. The mixture of zirconium through niobium has shown to have desirable physical and thermodynamic applications [5]. Zr-Nb alloys are being developed to improve the properties of nuclear reactor plants. Most of the developing alloys are found to have higher Nb and lower Sn contents (in Zr-Sn alloys) in order to improve corrosion resistance [6]. Recently, the Nb-based binary solutions have been of much technological and academic interest as the alloys of this kind have good mechanical properties [7]. Alloys with a high percentage of Nb *(x>5)* have high capacity for hydrogenation which mainly causes poor corrosion resistance. As a consequence, alloys with small amount of Nb *(x<5)* are preferred for optimising its application in reactor metallurgy [1].

The effect of alloying elements to Zr-Nb is very important it serves as an effective strengthening element for Zr with low cytotoxicity and low magnetic susceptibility (2.2×10 cm^3 g ^{1}) which depends mostly on the composition and phase constitution [8]. In this paper, we report the effect of cobalt addition on the $Zr_{97}Nb_3$ system and deduce their elastic, electronic and thermodynamic properties at different

concentrations. Furthermore, we investigate the temperature dependence to evaluate the strength and stability of the system at higher temperature conditions.

2. Methodology

The calculations were carried out using first-principles density functional theory (DFT) [9] within the plane-wave pseudopotential method, as implemented in CASTEP code [10]. The electronic exchange-correlation potential was described within generalized gradient approximation (GGA) parameterized by Perdew, Burke, and Enzerhof (PBE) [11]. Interactions in the Brillouin zone were performed with special *k points* of 18 × 18 × 10 mesh parameter in accordance with the Monkhorst and Pack scheme [12]. The ultrasoft pseudopotentials method with a cutoff of 400 eV was used to describe the interaction between electrons and ions, and was sufficient to converge the total energy of the system [13]. The virtual crystal approximation (VCA) [14] was used to introduce a small amount of Co concentration.

3. Results and discussion

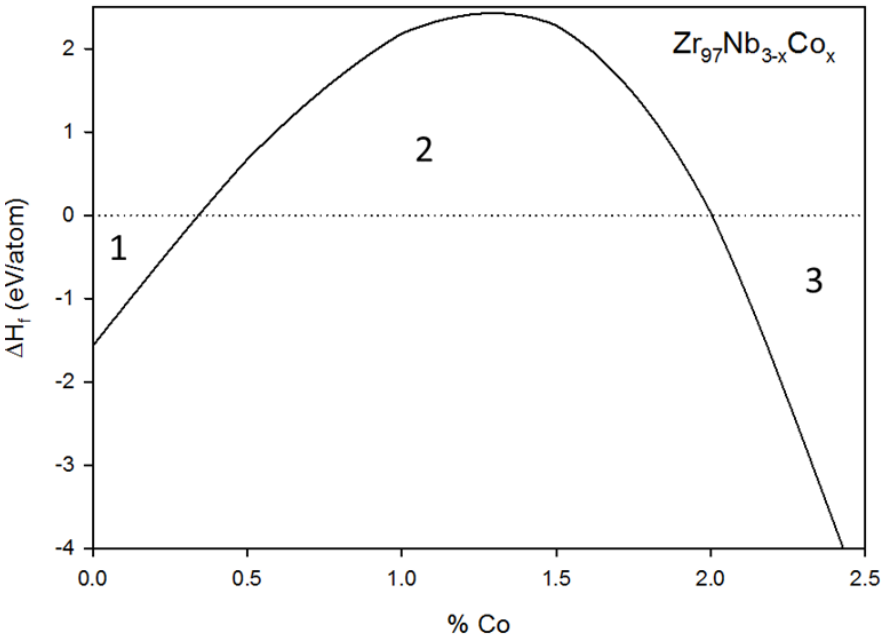

Figure 1. Calculated heats of formation against percentage Co for various $Zr_{97}Nb_3$ structures.

The DFT calculations were performed using VCA to investigate the effect of cobalt addition for various $Zr_{97}Nb_3$ structures. ote that the structures ere obtaine by alloying the –Zr *(a = 3.231 Å, c = 5.171 Å)* with Nb. t has been ascertain that the –phase is in its equilibrium state, the lattice parameters were in good agreement to within 1% of the experimental values. The $Zr_{97}Nb_{3-x}Co_x$ structure was geometrically optimized by allowing both atomic positions and volume to relax until a ground state energy was achieved. However, when Co is added to the system, the lattice parameter increases slightly; the volume increases as the Co content is increased. The thermodynamic stability was evaluated for small Co concentration deduced from the heats of formation:

$$\Delta H_f = E_{Zr_{97}Nb_{3-x}Co_x} - 0.97E_{Zr} - (0.03 - x)E_{Nb} - xE_{Co} \qquad (1)$$

Where, E_{Zr}, E_{Nb}, and E_{Co} are the individual elemental energies in the hcp, bcc, and hcp ground state structures, respectively. At lower Co content we found that the structures yielded lower energies (H_f), suggesting thermodynamic stability. However, as Co was increased, the structure reaches maximum above zero at region 2 in Figure 1 (becomes positive thermodynamically unstable) and drops back to negative. The structure is thermodynamically stable to within 0.4 at. % Co content (region 1) and 2 x 3 (region 3; the structure show transition in region 2 (unstable alloy). This observation support previous report that Zr_xNb alloys with a high percentage of niobium *(x > 5)* causes the deterioration of corrosion properties.

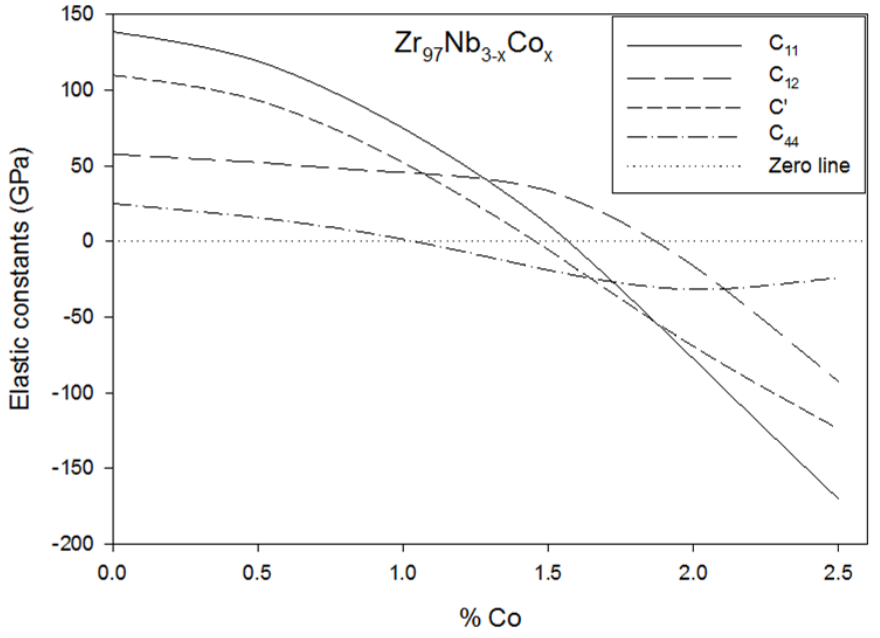

Figure 2. Displaying elastic constants against percentage Co for various $Zr_{97}Nb_3$ structures.

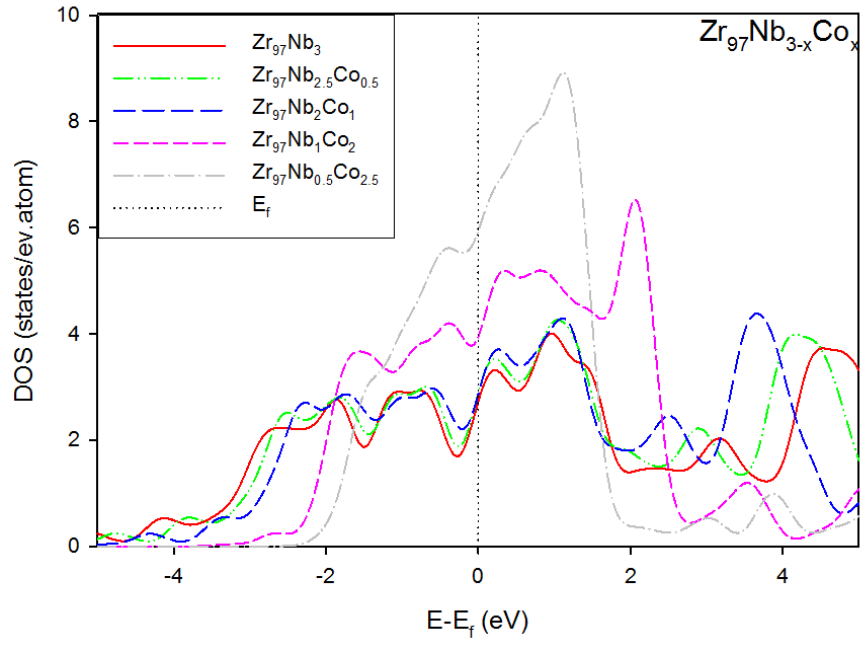

Figure 3. Comparison of the total density of states (tDOS) for the $Zr_{97}Nb_3$ structure at various at. % Co content. The Fermi energy is taken as the energy zero (E-Ef = 0).

The effect of small Co addition on the elastic constants (Cij) were also evaluated. The results are shown in Figure 2. At lower concentrations it is shown that all elastic moduli are positive, the increase in Co content indicates there is softening of elastic moduli above 1.5 at. % Co (C <0, elastically unstable). This findings suggest that the system is mechanically stable at lower concentrations. We also performed the density of states (DOS) calculations to verify the electronic stability of the $Zr_{97}Nb_{3-x}Co_x$ as shown in Figure 3, it is noted that structures without Co content have the lowest peaks at the Fermi energy (electronically stable), the stability trend is observed from the peaks at Fermi energy with respect to the pseudogap. The small amount of Co content show significance effect. We note that the structures with lowest DOS at Fermi correspond to those with low Co content. It was also observed that 0.5 at. % Co content is electronically stable.

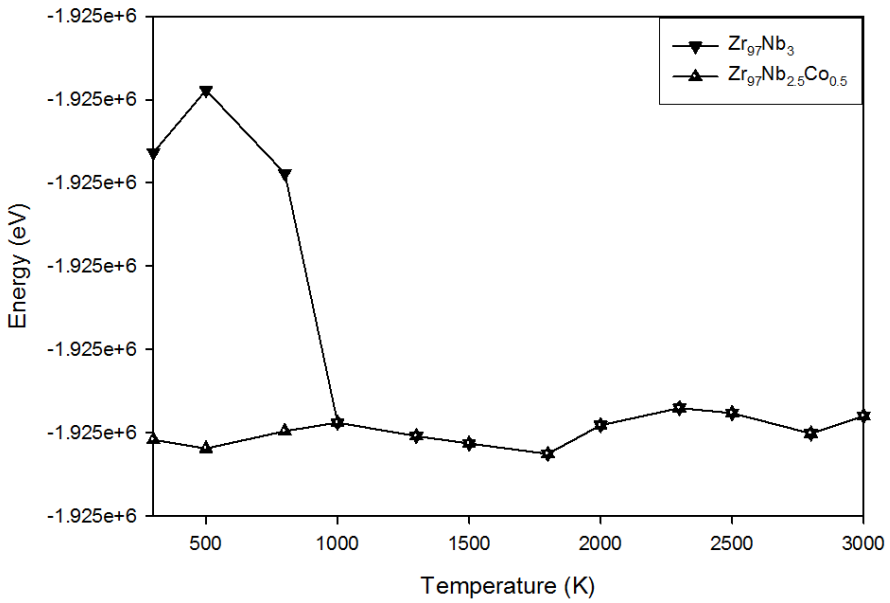

Figure 4. Indicating the temperature dependence of $Zr_{97}Nb_3$ structures at 0.5 at. % Co content.

In Figure 4, we observe that the system is stable at temperatures above 1 000K up to 1 800K since the system energy is minimal at that temperature. This findings suggest that the small addition amount of Co may be crucial in the development of better fuel cladding material, as this may enhance the stability of the system.

4. Conclusion

The equilibrium lattice parameter, heats of formation, elastic properties and electronic structures of the $Zr_{97}Nb_{3-x}Co_x$ alloy were determined using ab initio calculations. It was shown graphically in Figure 2 that the shear modulus is positive (C > 0) for alloys with less amount of Co and becomes unfavourable above 1.5 at. % Co. The DFT results are in agreement with the experimental findings. It was found that the $Zr_{97}Nb_{2.5}Co_{0.5}$ structure is more stable (lowest heats of formation); whereby the VCA showed preference of doping on Co on Nb sublattices at small concentrations. Finally the DOS show that structures with high Co are high in energy while those with small concentration are lowered at Fermi level which confirms condition of stability.

Acknowledgements

The work was carried at the Materials Modelling Centre, University of Limpopo and the Centre for High performance computing (CHPC) in South Africa. The support of the South African Research Chair

Initiative of the Department of Science and Technology and the National Research Foundation is highly recognised.

References

[1] Kharchenko V.O and Kharchenko D.O, 2013, Ab-initio calculations for structural properties of Zr-Nb alloys, *Con. Matt. Phys.*, **16**, 1-8.

[2] Yang Z.N, Zhang F.C, Qu L, Yan Z.G, Xiao Y.Y, Liu R.P and Zhang X.Y, 2014, Formation of duplex microstructure in Zr-2.3Nb alloy and its plastic behaviour at various strain rates, *Int. J. Plast*., **54**, 163-177.

[3] Adamson R.B and Rudling P, 2013, *Materials ageing and degradation in light water reactors* (New Delhi) pp. 151-248.

[4] Zhang S, Zhang X, Zhu Y, Zhang S, Qi L and Liu R, 2012, First principle investigation on elastic and thermodynamic properties of zirconium under pressure, *Comp. mater. Sci,* **61**, 42-49.

[5] Joeng Y.H, Lee K.O and Kim H.G, 2008, Correlation between the tensile strength and corrosion behaviour of heat treated Zr-1.0Nb, *J. Nucl. Mater*, **40**, 505-508.

[6] Zielinski A and Sobieszczk S, 2011, Hydrogen-enhanced degradation and oxide effects in zirconium alloys for nuclear applications, *International journal of hydrogen energy*, **36**, 8619-8629.

[7] Wang Z.W, Li Y, Wang Z, Ma C, Yang H.X, Tian H.F, Shi H.L, Jia L, Zhang F and Li J. Q, 2012, Effects of ordered structure on superconductivity*, EPL*, **97**, 1-2.

[8] Nomora N, Tanaka Y, Suyalatu, Kondo R, Doi H, Tsutsumi Y and Hanawa T, 2009, Effects of phase constitution of Zr-Nb alloys on their magnetic susceptibilities, *Mater. trans,* **50**, 2466-2472.

[9] Kohn W and Sham L.J, 1965, Self-consistent equations including exchange and correlation effects *Phys. Rev. A*, **140**, 1133-1138.

[10] Milman V, Refson K, Clark S.J, Pickard C.J, Yates J.R, Gao S.P, Hasnip P.J, Probert M.I.J, Perlov A and Segall M.D, 2010, Electron and vibrational spectroscopies using DFT, plane waves and pseudopotentials: CASTEP implementation, *J. Mol. Struc*, **954**, 22-35.

[11] Perdew J.P, Burke K and Enzerhof M, 1996, Generalized gradient approximation made simple, *Phys. Rev. Lett,* **13**, 5188-5192.

[12] Monkhorst H.J and Pack J.D, 1976, Special points for Brillouin zone interactions, *Phys. Rev B*, **13**, 5188-5192.

[13] Vanderbilt D, 1990, Self–consistent pseudopotentials in a generalized eigen value formalism, *Phys. Rev B*, **41**, pp.7892-7895.

[14] Bellaiche L and Vanderbilt D, 2000, Virtual crystal approximation revisited: application to dielectric and piezoelectric properties of perovskites, *Phys. Rev. B*, vol. **16**, 7877-7882.

The structural and sensing properties of cobalt and indium doped zinc oxide nanopowders synthesised through high energy ball milling technique

MF Manamela[1*], TE Mosuang[1] and BW Mwakikunga[2]

[1]Department of Physics, University of Limpopo, Private Bag x1106, Sovenga, 0727, South Africa

[2]DST/CSIR National Centre for Nano-Structured Materials, P O Box 395, Pretoria 0001, South Africa

Email: manamela.mf@gmail.com, thuto.mosuang@ul.ac.za

Abstract. High energy ball milling technique was employed to synthesise the undoped ZnO, 5% Co and In single doped and Co-In double doped ZnO nanoparticles. Thereafter, the kenosistec station equipment was used to scrutinise and monitor the mechano-chemically prepared samples for gas sensing application. Ammonia (NH_3) gas is being probed at various temperatures and concentrations in the present work. In all the current against time plots observed, the undoped and double doped ZnO nanoparticles are being favoured at a temperature range 200 – 350 ^oC. Further on, the sensitivity of the undoped and double doped ZnO increase with increasing NH_3 gas concentration. Co doped ZnO nanoparticles were noted to possess a fast recovery while the Co-In doped ZnO nanoparticles possessed fast response time at 10 ppm.

1. Introduction

Over centuries various types of gas sensors such as the optical, electrochemical, catalytic acoustic and semiconductor have being developed [1]. Semiconducting metal oxide gas detectors such as SnO_2-ZnO [2], ZnO-CuO [3], Fe_2O_3-ZnO [4] have been investigated over a range of temperatures to detect most common gases [5], such as H_2S, CO, NH_3, CH_4 and to monitor the environment. Report by Feng et al.[6] indicated that enthanol (C_2H_5OH) gas is highly sensible and reflects fast response for ZnO-based sensors. The gas sensing properties of SnO_2 based sensors are found to be greately influenced by the size and the Debye length of the polycrystalline SnO_2 particles [7]. Mean while, Wang et al. [8] investigations revealed that the gas sensing process depends mainly on the surface reaction where the chemical components, temperature, micro/nano-structure of the sensing layer and humidity play an important role. H_2S is an acidic gas with the density slightly higher than that of air. It is known to have bad odour and is mostly present in industral areas, dumps and sewers. However, the monitoring of the H_2S gas is very important because it is dangerous to humans lives even at low concentrations [9]. It has been mentioned in several papers that the selectivity and sensitivity of gas sensors to H_2S can be improved through additives of hydrophobic silica [10], ceria or basic oxides to the sensing element and even doping with nobel metals like Ag to SnO_2 [11]. Tamaki et al. [7] reported on the extreme sensitivity of 5wt.% SnO_2-CuO to H_2S gas at 200 ^oC. The one dimensional metal oxide (nanobelt or nanowire base sensors) have proved to possess numerous advantages, like higher sensitivity at parts-per-billion (ppb) and above, lower operating temperature and better compatibility compared to the traditional metal oxide sensors [12]. Wang et al. [13] reported on the ZnO nanorods arrays prepared using a hydrothermal route for gas sensing application. In the report ZnO nanorods showed excellent response to NH_3 and CO

exposure. Further on the H_2 gas sensitivity with detection limit of 20 ppm from room temperature (25 ^oC) to 250 ^oC was also observed. ZnO is known to be transparent to visible light and more electrically conductive through doping [14]. The n-type ZnO semiconductor occurs naturally, while the p-type ZnO semiconductor can be produced through co-doping techniques (N and Ga dopants) as indicated by Joseph et al. [15]. Amongst the high-performance gas sensing devices, ZnO nanorods have being found to be sensitive to gases such as H_2, NH_3 and C_2H_5OH at room temperature [16]. In the present work ZnO nanoparticles are prepared using high energy ball milling method; the method which has been found to be adaptable and followed easily. Undoped and doped ZnO nanoparticles are subjected to ammonia (NH_3) gas to check their sensitivity and selectivity.

2. Procedure

The high energy ball milling technique was utilised in preparing the undoped ZnO nanoparticles, 5wt. % of Co-ZnO, In-ZnO and (Co-In)-ZnO nanoparticles samples. These samples were in a powder form; hence they were sonicated in ethanol for 5 minutes before being placed on the micro-hotplate sensor. The x-ray diffraction (XRD) and the scanning electron microscopy (SEM) characterisations as discussed in Manamela et al. [17] were utilised to investigate the structural properties of all the ZnO nanoparticles considered in this paper. The average crystallite size of the doped and undoped ZnO nanoparticles ranged from 13 to 18 nm as calculated using Williamson-Hall equation [17]. The KENOSISTEC station equipment was used to characterise the prepared samples for NH_3 gas sensing at various temperatures (200-350 ^oC) and concentrations (5 -100 ppm). For gas sensing, the ZnO nanoparticles were mixed with ethanol before being coated on the surface of the aluminium substrate. The latter was placed between two Pt electrodes and a heater. The substrates coated with undoped, Co an In doped and Co-In double doped ZnO nanoparticles were then inserted in a chamber within the KENOSISTEC station machine. All the samples were subjected to concentrations of 5, 10, 20, 40, 60, 80, 100 ppm of NH_3 gas. The station was maintained at constant voltage of 5 V. The gas flow in and out was maintained at 5 minutes. Detailed procedures on how a KENOSISTEC sensing station operates can be found on the station website: www.kenosistec.com [18].

3. Gas sensing applications

The gas sensing applications were performed for the undoped, Co and In single doped and Co and In (Co-In) double doped ZnO nanoparticles in NH_3 gas environment. This NH_3 gas detection was performed at four distinct temperatures: 200, 250, 300 and 350 ^oC. It must be mentioned that there is no need to test sensing properties below 200 ^oC as the metal oxides like ZnO do not react with NH_3 gas at low temperatures [19]. The response curves in NH_3 gas environment are plotted for the said temperatures as shown in figure 3.1. The undoped and the double doped (Co-In)-ZnO nanoparticles respond much greater to the NH_3 gas with higher current as compared to the In-ZnO and Co-ZnO nanoparticles. This may be ascribed to the grain sizes of the undoped and (Co-In)-ZnO nanoparticles being smaller compared to those of In-ZnO and Co-ZnO nanoparticles [17]. This suggest that the Co and In combined doping induce more inward strains in the ZnO nanoparticle matrix resulting in decreased volume. All the samples seem to show uneven pattern from 300 ^oC [20]. This indicates that the NH_3 gas sensors performs badly at higher temperatures. In figure 3.1 (a) it has been noted that at 200 ^oC the current increases continuously without returning to the reference baseline as the exposure time is increased. The significance of this is that at 200 ^oC the undoped and double doped ZnO nanopowder samples response instantaneously with recovery time.

In order to investigate the behaviour of sensitivity against concentration the equation: $S = \frac{R_{air}}{R_{NH_3}}$, was used. $R_{gas(NH3)}$ is the resistance in the presence of NH_3 gas and R_{air} is the resistance in the air environment. Now $R_{gas(NH3)}$ contributes 90 % of the response time, while R_{air} holds 10 % of the recovery time. Figure 3.2 shows the graphs of sensitivity against concentration. The sensitivity of the undoped ZnO and (Co-In)-ZnO nanoparticles are constantly increasing with the increasing gas concentration. In addition, it is

observed that the double doped ZnO exceeds the sensitivity of the undoped ZnO at 300 ^{o}C [21] and 350 ^{o}C. This is in good agreement with what Maswanganye et al. [21] obtained when testing NH_3 gas at 300 ^{o}C for (Co-In)-ZnO nanoparticles prepared by sol-gel method. Sensitivity of the undoped ZnO nanoparticles drops at 10 ppm but increases rapidly at 20 ppm to 100 ppm in figure 3.2 (a) and (b). The Co-ZnO nanoparticles show a decrease in sensitivity as the gas concentration is increased in the temperature range 200-300 ^{o}C, thereafter experiences an increasing trend at 350 ^{o}C. The results suggest that the sensitivity of Co-ZnO nanoparticles is very poor at temperatures below 350 ^{o}C. Furthermore, response and recovery are highly compromised as depicted in figure 3.1 (c) and (d). The behavior is evident on the double doped and undoped ZnO nanopowder samples. In general, all this suggest only Co-In doped and the undoped ZnO nanopowder samples have reliable sensitivity at 200 – 250 ^{o}C temperature range. Non-sensitivity of In-ZnO and (Co-In)-ZnO nanoparticles could still be attributed to less reactivity of metal oxide complexes with NH_3 gas at low temperatures. Possibly, In^{3+} ions in theses complexes contribute more in retarding the reaction of ZnO and the NH_3 gas [19]. In the case of Co-In double doped ZnO sample, the grain size effect could come into play, as when the size of the nanoparticles are decreased greatly, the melting point also get reduced [22].
The response and recovery time for NH_3 gas was also investigated at 250 ^{o}C for concentrations of 5, 10, 20, 40, 60, 80, 100 ppm. In table 1, a 10 ppm concentration has been singled out to depict as reasonably low amount of NH_3 gas in the atmosphere at elevated temperatures. The single doped Co-ZnO sample demonstrates a substantially fast recovery time in all the ZnO nanoparticles tested. On the other hand, the double doped (Co-In)-ZnO sample demonstrates the fast response time of the four ZnO nanoparticle samples tested. Of course it can also be seen that both the undoped and the double doped ZnO nanoparticle samples have the same longest recovery time of all the samples investigated.

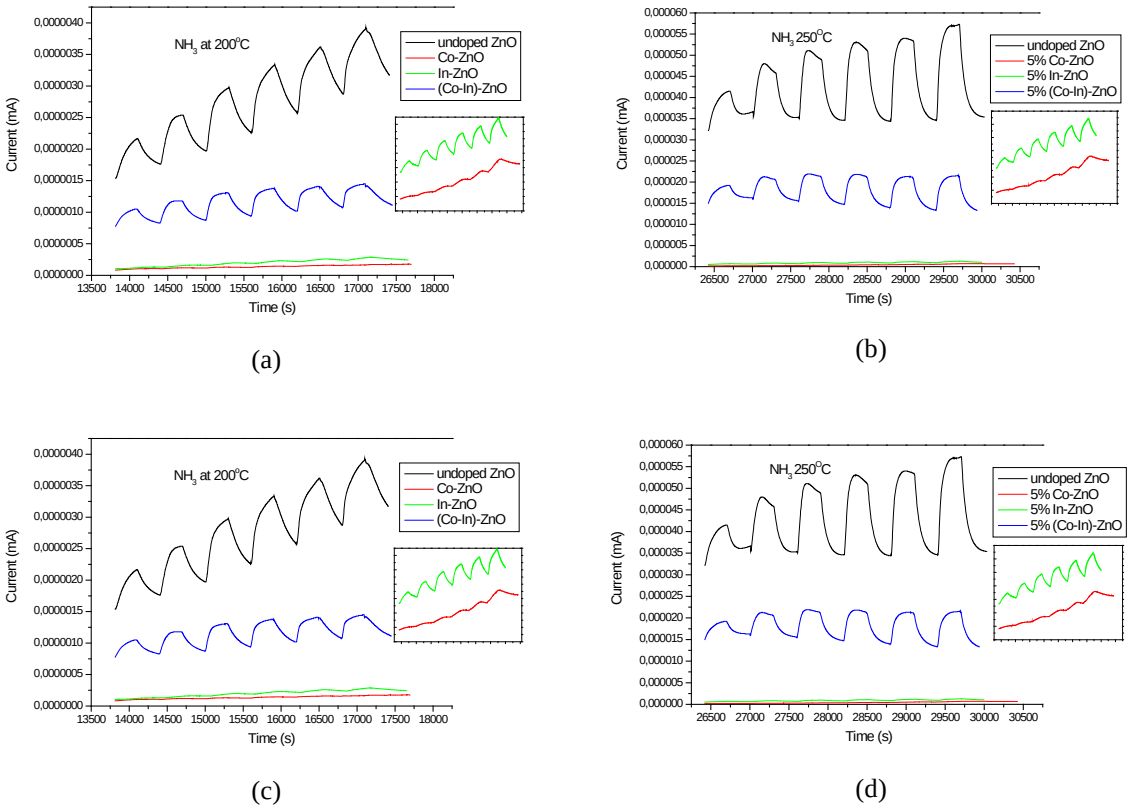

Figure 3.1: The graphs of current against time for the doped and undoped ZnO nanoparticles at various temperatures for the concentrations of 10 and 40 ppm respectively.

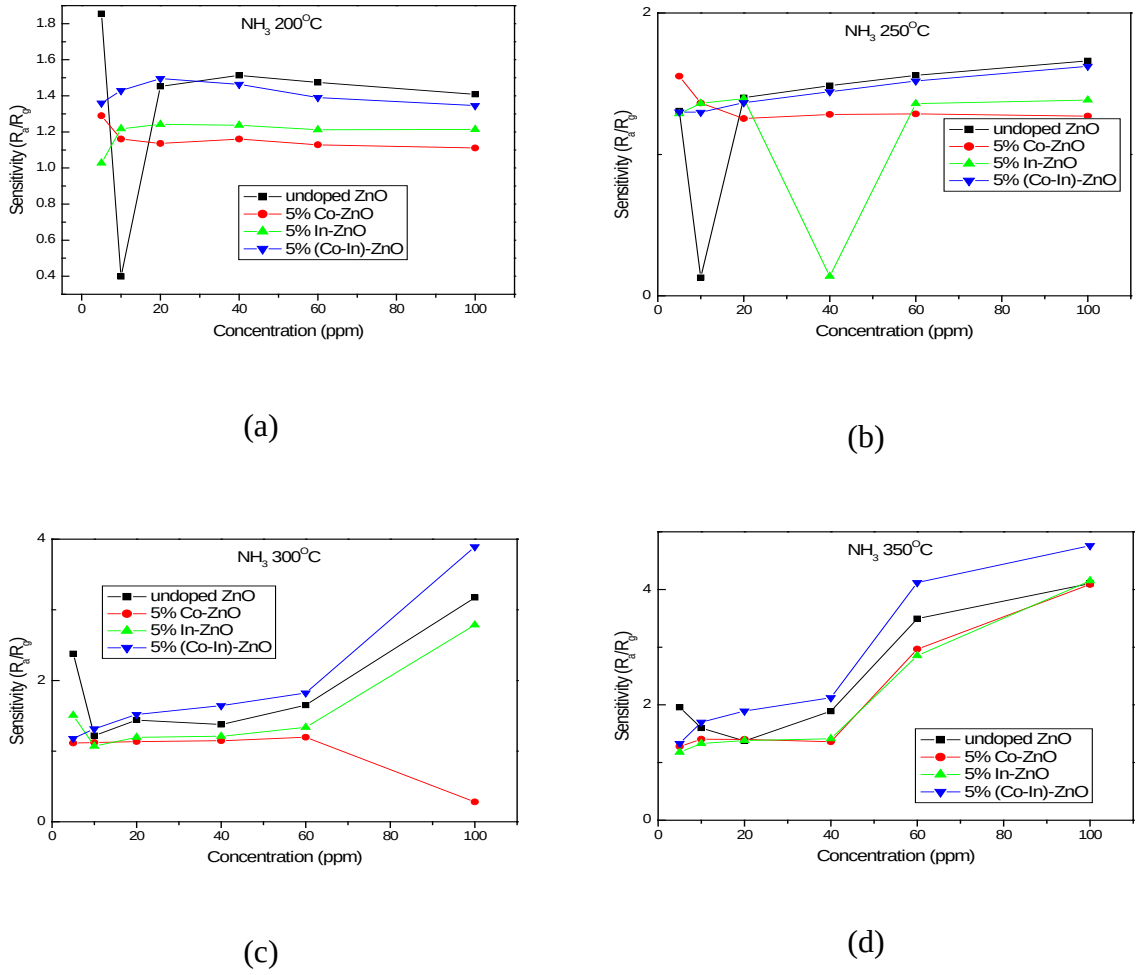

Figure 3.2: The sensitivity versus NH_3 concentration plot for the doped and undoped ZnO nanoparticles at various temperatures.

Table 1. NH_3 gas response and recovery time for the doped and undoped ZnO nanoparticles at 10 ppm.

Sample	Response time (s)	Recovery time (s)
Undoped ZnO	294	304
Co-ZnO	572	23.0
In-ZnO	302	302
(Co-In)-ZnO	289	304

4. Conclusion

ZnO nanoparticles were successfully synthesised by the high energy ball milling technique. The current versus time curves show good response and recovery to the NH_3 gas at lower temperatures, than at higher temperatures. In addition, the undoped and (Co-In)-ZnO nanoparticles are more favoured compared to the Co and In single doped ZnO nanoparticles samples. It has also been observed that the sensitivity of

all the ZnO nanoparticles are much higher at 350 ^{o}C. The Co-ZnO nanoparticles reflect a descending response magnitude with increasing concentration of NH_3 gas at lower temperatures. The Co doped ZnO nanoparticles possess the fast recovery, whereas the (Co-In) double doped ZnO nanoparticles possess the fast response time at 250 ^{o}C.

Acknowledgements
The authors are grateful for the financial support from UL, NRF and IBSA. National Centre for Nano-Structures Materials (NCNSM) at CSIR is thanked for characterisation facilities.

References

[1] Z. Yunusa, M. N. Hamidon, A. Kaiser and Z. Awang, "Gas sensors: A review," *Sensors and transducers*, vol. 168, pp. 61-75, 2014.

[2] J. H. Yu and G. M. Choi, "Electrical and CO Gas Sensing Properties of ZnO-SnO2 Composites," *Sens. Actuat. B.*, vol. 52, p. 251–256, 1998.

[3] D. H. Yoon, J. H. Yu and G. M. Choi, "CO Gas Sensing Properties of ZnO-CuO," *Composite. Sens. Actuat. B*, vol. 46, pp. 15-23, 1998.

[4] C. L. Zhu, Y. J. Chen, R. X. Wang, L. J. Wang, M. S. Cao, X. L. Shi, "Synthesis and Enhanced Ethanol Sensing Properties of α-Fe2O3/ZnO Heteronanostructures.," *Sens. Actuat. B.*, vol. 140, p. 185–189, 2009.

[5] W. Göpel and K. D. Schierbaum, "SnO2 Sensors-Current Status and Future Prospects," *Sens. Actuat. B*, vol. 26, pp. 1-12, 1995.

[6] P. Feng,Q. Wan and T. H. Wang, "Contact-controlled sensing properties of flowerlike ZnO nanostructures," *Appl. Phys. Lett.*, vol. 87, p. 213111, 2005.

[7] Jun Tamaki, Tomoki Maekawa, Norio Miura and Noboru Yamazoe, "CuO-SnO 2 element for highly sensitive and selective detection of H2S," *Sensors and Actuators B, ,* vol. 9, pp. 197-203, 1992.

[8] C. Wang, L. Yin, L. Zhang, D. Xiang and R. Gao, "Metal Oxide Gas Sensors: Sensitivity and Influencing Factors," *Sensors*, vol. 10, pp. 2088-2106, 2010.

[9] T. Maekawa, J. Tamaki, N. Miura and N. Yamazoe, , "Sensing behaviour of CuO loaded SnO2 element for H2S detection," *Chem. Left.*, vol. 1991, pp. 575-578, 1991.

[10] V. Lantto and P. Romppainen, "Response of some SnO2 gas sensors to H2S after quick cooling," *J. Electrochem.Soc.*, vol. 135, pp. 2550-2556, 1988.

[11] J. Lui, X. Huang, G. Ye, W. Lui, Z. Jiao, W. Chao, Z. Zhou and Z. Yu, "H2O detection sensing characteristic of CuO/SnO2 sensor," *Sensor*, vol. 3, pp. 110-118, 2003.

[12] K. Qin, L. Chang-Shi, L. Zhou, L. Yu-Zi, X. Zhao-Xiong, Z. Lan-Sun and L. W. Zhong, "Enhancing the Photon- and Gas-Sensing Properties of a Single SnO2 Nanowire Based Nanodevice by Nanoparticle Surface Functionalization," *J. Phys. Chem. C* , vol. 112, p. 11539–11544, 2008.

[13] J. X. Wang, X. W. Sun, Y. Yang, H. Huang, Y. C. Lee, O. K. Tan and L. Vayssieres, "Hydrothermally grown oriented ZnO nanorod arrays for gas sensing applications," *Nanotechnology*, vol. 17, p. 4995–4998, 2006.

[14] A. Karthigeyan, R.P. Gupta, M. Burgmair , S.K. Sharma, "Influence of oxidation temperature, film thickness and substrate on NO2 sensing of SnO2 ultra thin films," *Sensors and Actuators B*, vol. 87, p. 321–330, 2002.

[15] M. Joseph, H. Tabata and T. Kawai, "n-type electrical conduction in ZnO thin films by Ga and N Codoping," *Japan. J. Appl. Phys.*, vol. 38, pp. L 1205-L 1207, 1999.

[16] Y. J. Chen, X. Y. Xue, Y. G. Wang and T. H. Wang, "Synthesis and ethanol sensing characteristics of single cryystalline SnO2 nanorods," *Appl. Phys. Lett.*, vol. 87, pp. 233503-233505, 2005.

[17] M. F. Manamela, T. E. Mosuang and B. W. Mwakikunga, "Structural and optical property changes of zinc oxide nanopowders doped with cobalt and indium metals mechano-chemically," *Advanced Materials Proceedings*, vol. 3, pp. 213-217, 2018.

[18] M. F. Manamela, "Structural, optical and sensing properties of cobalt and indium doped zinc oxide prepared mechano-chemically," MSc Dissertation, UL, Polokwane, 2017.

[19] L. Chmielarz, A. Wegrzyn, M. Wojciechowska, S. Witkowski and M. Michalik, "Selective catalytic oxidation (SCO) of ammonia to nitrogen over hydrotalcite originated Mg-Cu-Fe mixed metal oxides," *Catalysis Letters*, vol. 141, pp. 1345-1354, 2011.

[20] M. Acuautla, S. Bernardini, M. Bendahan and L. Gallais, "Ammonia sensing properties of ZnO nanoparticles on flexible substrate," in *Proceedings of the 8th International Conference on Sensing Technology, Sep. 2-4*, Liverpool, UK, 2014.

[21] M. W. Maswanganye, K. E. Rammutla, T. E. Mosuang and B. W Mwakinkunga, "The effect of Co and In combinational or individual doping on the structural, optical and selective properties of ZnO nanoparticles," *Sensors and Actuators B*, vol. 247, pp. 228-237, 2017.

[22] C-Y. Chen, M-W Chen and J. R. D Retamal, "Surface effects on optical and electrical properties of ZnO nanostructures," *Pure and Applied Chemistry*, vol. 82, pp. 2055 - 2073, 2010.

Mechanical properties and temperature dependence of B19 $Ti_{50-x}Zr_xPt_{50}$ shape memory alloys

M P Mashamaite[1], H R Chauke[1] and P E. Ngoepe[1]

[1]Materials Modelling Centre, School of Physical and Mineral Sciences, University of Limpopo, Private Bag X1106, Sovenga 0727, South Africa

Email: mordecai.mashamaite@ul.ac.za, mordecai.mashamaite@gmail.com

Abstract. A molecular dynamic study of $Ti_{50-x}Zr_xPt_{50}$ as potential high temperature shape memory alloy has been performed using the LAMMPS code. The lattice dynamics, elastic properties and temperature dependence were deduced to determine the effect of ternary addition with Zr on the Ti sub-lattice at varied temperature range. It was found that the lattice parameter increases with Zr addition, the thermodynamic stability was observed at 5 at. % Zr. Furthermore, the elastic properties showed positive shear modulus for concentrations range 5 - 25 at. % Zr, indicating stability of the structures and instability above 25 at. % Zr concentrations. More importantly, we observed a martensitic transformation behaviour for $Ti_{50-x}Zr_xPt_{50}$ (x= 5.56) at around 1200 K.

1. Introduction

Shape memory alloys (SMAs) design & applications has found commercial use in a broad range of industries including automotive, aerospace, robotics and biomedical [1]. These alloys are able to remember their shape after being deformed when heated above certain temperatures. The practical uses for SMAs are limited to temperature below 373 K [2]. Various alloys such as NiTi, NiAl, TiPd and TiAu have been investigated, amongst them NiTi-based SMAs have been used extensively in industries because of its resistance to corrosion and the fact that the martensitic transformation temperature (Ms) is near room temperature. TiPd undergoes a B2-to-martensite phase transformation with a Ms between 780 and 836 K [2, 3]. However, studies reveal that TiPd exhibits extremely poor shape-memory behavior with little recoverable strain during transformation, even under no-load conditions, which is attributed to a low critical stress for slip in the alloy [4].

A limited number of alloys have potential as high-temperature shape memory alloys (HTSMAs). Hence, HTSMAs are being developed in order to increase the application areas of shape memory alloys [5]. Interest in HTSMA has been growing in the aerospace, automotive, process control and energy industries. One way to increase the transformation temperature is to add significant levels of particular ternary additions [6] which were found to be effective for increasing the transformation temperature [7]. Hence, NiTi-X (X=Pt, Pd, Hf and Zr) shape memory alloys have been studied for high temperature above 373 K applications [8, 9]. However, TiPt has a higher Ms of above 1273 K rendering it suitable for the development of HTSMAs [2]. According to Yamabe-Mitarai et al. [10], $Ti_{50}Pt_{50}$ alloy exhibit very low shape memory effect with a recovery ratio of ~11%, however, the ratio increases between ~40% and ~60% for $Ti_{45}Zr_5Pt_{50}$ [11].

In this work Zr is partially substituted on the Ti sub-lattice of the B19 TiPt to investigate the stability of the structures in terms of their formation energies, and the elastic properties. Furthermore, the temperature dependence was investigated by studying the lattice expansion and mechanical properties of the 5.56 at % Zr structure.

2. Methodology

The first principle density functional theory (DFT) was used to study the TiPt−Zr as a potential HTSMAs, The CASTEP code [12] was employed along with the Ultrasoft pseudopotentials with a plane-wave basis set, to achieve a good convergence with respect to the total energy [13]. We have used the generalized gradient approximation (GGA) of the Perdew-Burke-Ernzerhof (PBE) exchange correlation functional [14]. The Brillouin zone integrations were performed for suitably large sets of *k*-points according to Monkhorst and Pack [15]. The energy cutoff of 500 eV and k-points mesh 8×13×8 for B19 TiPt were used in order to determine the quality of the calculations. A 2x2x1 supercell was used to generate $Zr_xTi_{50-x}Pt_{50}$ compounds by substituting Zr atoms on the Ti site. The temperature dependence calculations were evaluated utilizing molecular dynamics code based Large-scale Atomic Molecular Massively Parallel Simulator (LAMMPS) with an Embedded Atom Method (EAM) module [16] as implemented by Materials Design.

3. Results and Discussion

The equilibrium lattice parameter of the optimized structures and heats of formation are listed in Table 1. We note that our DFT predicted lattice parameters are in good agreement with available experimental and theoretical results for the binary phase. Upon doping, the lattice parameter increases with the increase in Zr content. Furthermore, the heats of formation (ΔH_f), of the intermetallic phases is calculated according to the relation [17, 18]

$$\Delta H_f = E^{TiPt} - [(1-x)E^{Ti}_{solid} + xE^{Pt}_{solid}], \quad (1)$$

where E^{TiPt}, E^{Ti}_{solid} and E^{Pt}_{solid} are the total energies of an intermetallic alloy, and elemental Ti and Pt in their respective ground-state crystal structures, while *x* and *1-x* refers to the fractional concentrations of the constituent elements. The binary B19 $Ti_{50}Pt_{50}$ heats of formation is in good agreement with the previous report. Furthermore, we see that the $Zr_5Ti_{45}Pt_{50}$ structure displayed the lowest heats of formation and is considered the most stable phase, while the $Zr_{45}Ti_5Pt_{50}$ is the least stable with values -4.858 eV/atom and 3.326 eV/atom, respectively.

Table 1 The equilibrium lattice parameters and heats of formation (ΔH_f) of B19 TiPt and B19 $Ti_{50-x}Zr_x$ Pt_{50} ternaries alloys.

B19 Composition	Lattice Parameter						(ΔH_f)
	a	Exp	*b*	Exp	*c*	Exp	
$Ti_{50}Pt_{50}$	4.633	4.550 [2]	2.791	2.730 [2]	4.876	4.790 [2]	-0.827 [19]
$Zr_5Ti_{45}Pt_{50}$	4.655		2.808		4.895		-4.858
$Zr_{10}Ti_{40}Pt_{50}$	4.677		2.825		4.917		-3.944
$Zr_{15}Ti_{35}Pt_{50}$	4.700		2.841		4.937		-2.951
$Zr_{20}Ti_{30}Pt_{50}$	4.722		2.858		4.961		-1.902
$Zr_{25}Ti_{25}Pt_{50}$	4.745		2.876		4.968		-0.831
$Zr_{30}Ti_{20}Pt_{50}$	4.766		2.893		5.013		0.220
$Zr_{35}Ti_{15}Pt_{50}$	4.787		2.912		5.043		1.225
$Zr_{40}Ti_{10}Pt_{50}$	4.807		2.926		5.08		2.205

$Zr_{45}Ti_5Pt_{50}$	4.829	3.146	5.067	3.326

Now, we consider the elastic properties to examine the mechanical stability of these alloys, for pure and doped systems. We calculated the elastic constants for B19 $Ti_{50-x}Zr_xPt_{50}$ structures, as presented in Table 2. Note that the mechanical stability in an orthorhombic crystal leads to the following restrictions:

$$(C_{11} + C_{22} - 2C_{12}) > 0;\ (C_{11} + C_{33} - 2C_{13}) > 0;\ (C_{22} + C_{33} - 2C_{23}) > 0;$$
$$C_{11} > 0;\ C_{22} > 0;\ C_{33} > 0;\ C_{44} > 0;\ C_{55} > 0;\ C_{66} > 0;\ (C_{11} + C_{22} + C_{33} + 2C_{12} + 2C_{13} + 2C_{23}) > 0 \quad (2)$$

We observe that the calculated shear moduli are positive for all structures ($Zr_5Ti_{45}Pt_{50}$, $Zr_{10}Ti_{40}$ Pt_{50}**,** $Zr_{15}Ti_{35}$ Pt_{50}, to $Zr_{25}Ti_{25}$ Pt_{50}) with less Zr concentration satisfying. The structures satisfy mechanical stability. This observation is consistent with the formation energies in table 1. The structures $Zr_{30}Ti_{20}Pt_{50}$, $Zr_{35}Ti_{15}Pt_{50}$, $Zr_{40}Ti_{10}Pt_{50}$ and $Zr_{45}Ti_5Pt_{50}$ are observed to be unstable since the C_{44} is negative. For a completely isotropic material A=1, while values smaller or greater than unity measure the degree of elastic anisotropy. The elastic anisotropy for non-cubic phases is represented by A_1, A_2 and A_3. We note that the calculated A_1 approaches unity with an increase in Zr content. On the contrary, the A_2 and A_3 calculated values are observed to decrease with increase in Zr. The bulk modulus (B) for the $Zr_{10}Ti_{40}$ Pt_{50}**,** $Zr_{15}Ti_{35}$ Pt_{50}, to $Zr_{25}Ti_{25}$ Pt_{50} structures become less in hardness with increasing Zr,

Table 2 The elastic constants (Cij) for B19 $Ti_{50-x}Zr_xPt_{50}$ structures at various concentration, 0K.

Structures	Elasticity (GPa)													
	C_{11}	C_{12}	C_{13}	C_{22}	C_{23}	C_{33}	C_{44}	C_{55}	C_{66}	C'	B	A_1	A_2	A_3
$Zr_5Ti_{45}Pt_{50}$	314	112	145	364	91	319	6	60	69	101	179	0.683	0.035	0.087
$Zr_{10}Ti_{40}$ Pt_{50}	324	117	147	368	89	321	7	62	70	103	186	0.683	0.040	0.099
$Zr_{15}Ti_{35}$ Pt_{50}	317	118	145	367	95	329	8	62	71	99	184	0.716	0.045	0.112
$Zr_{20}Ti_{30}$ Pt_{50}	310	117	148	344	94	325	6	62	71	97	182	0.739	0.035	0.084
$Zr_{25}Ti_{25}$ Pt_{50}	301	119	139	317	89	305	14	62	71	91	179	0.778	0.088	0.203
$Zr_{30}Ti_{20}Pt_{50}$	301	135	148	294	96	304	-70	62	70	83	190	0.851	0.457	1.002
$Zr_{35}Ti_{15}Pt_{50}$	287	136	141	279	94	287	-110	60	69	76	186	0.918	0.756	1.583
$Zr_{40}Ti_{10}Pt_{50}$	272	134	147	303	92	280	-25	58	69	69	180	0.996	0.193	0.364
$Zr_{45}Ti_5Pt_{50}$	267	157	143	192	101	238	-456	48	65	55	194	1.180	4.171	7.023

The effect of temperature on the lattice parameter of the B19 $Ti_{50-x}Zr_xPt_{50}$ (x=5.56) was investigated and is shown in Figure 1. We observe that the lattice parameters a and c increase linearly with temperature, while b decreases. The martensitic transformation is observed around 1200 K, this also correspond to the austenite start at around 1270 K. Above this temperature, we observed expansion of the lattice parameters, mostly the separation of a and c. The lattice ratio a/b and c/b also increases with temperature with values within 1.4 and 1.61, respectively.

Furthermore, we calculated the elastic constant at varied temperature only for the B19 $Zr_{5.56}Ti_{44.44}Pt_{50}$ (Figure 2). Most of the independent Cij satisfy the conditions of stability for the orthorhombic system, with a slight decrease as temperature is increased. The shear moduli $(C_{11} + C_{22} - 2C_{12})$ and $(C_{11} + C_{33} - 2C_{13})$ are positive from (173 K – 2073 K) temperature range, while $(C_{22} + C_{33} - 2C_{23})$ is negative above 1400 K. However, the shear moduli substantially decrease as temperature is increased. This may suggest that the structure could be stable at high temperature condition and likely to enhance the Ms.

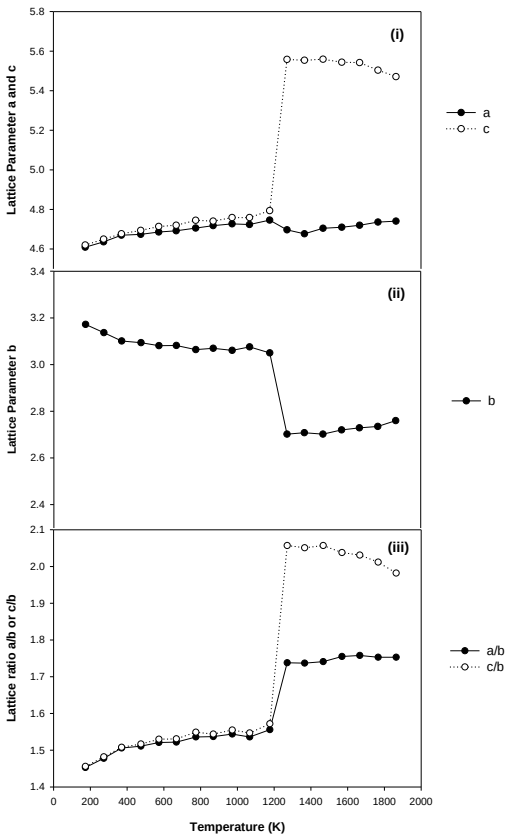

Figure 1 The effect of temperature on lattice parameter (i) a and c, (ii) b and (iii) lattice ratio a/b or c/b of B19 $Zr_{5.56}Ti_{44.44}Pt_{50}$.

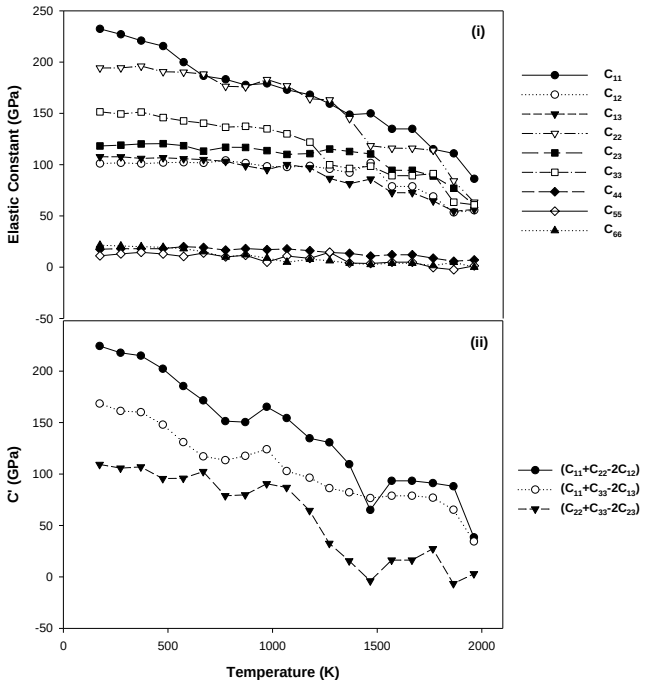

Figure 2 The graph of the (i) elastic constants and (ii) shear moduli C′ against temperature for the B19 $Zr_{5.56}Ti_{44.44}Pt_{50}$ structure.

4. Conclusion

The effect of Zr substitution was investigated on Ti sub-lattice using DFT within the generalised gradient approximations. The $Ti_{50-x}Zr_xPt_{50}$ alloys were determined by varying the concentration of Zr. We found that $Zr_5Ti_{45}Pt_{50}$ is more stable, while $Zr_{25}Ti_{25}Pt_{50}$ is the least stable. We observed that 5 – 25 at. % Zr are more stable as compared to 30 - 45 at. % Zr for elastic constant at 0 K. The temperature dependence of the lattice parameters and elastic properties was investigated within the LAMMPS-EAM code, to deduce the Ms for B19 $Zr_{5.56}Ti_{44.44}Pt_{50}$ ternaries. The B19 $Zr_{5.56}Ti_{44.44}Pt_{50}$ showed martensitic transformation above 1200 K. Interestingly, the lattice ratio c/b and a/b were calculated and found to be 1.56 and 1.57, respectively. Furthermore, it was observed that as the temperature is increased, the shear moduli decreases suggesting stability at elevated temperatures. It can be deduced that the thermodynamic and elastic stability is maintained and this may have good effect on the corrosion resistance over temperature range from 900 to 1400 K.

5. Acknowledgement

The calculations were performed at Materials Modelling Centre, University of Limpopo, South Africa. The support of the South African Research Chair Initiative of the Department of Science and Technology and the National Research Foundation is highly recognised.

References

[1] Biggs T, Cortie M B, Witcomb M J and Cornish L A 2001 Martensitic transformation, microstructure, and mechanical workability of TiPt *Metall. Mater.Trans.* **32A** 1881

[2] Donkersloot H C and van Vucht J H N 1970 Martensitic transformations in gold-titanium, palladium-titanium and platinum-titanium alloys near the equiatomic composition *J. Less-Common Metals*. **20** 83

[3] Cai W, Tanaka S and Otsuka K 2000 *Mater. Sci. Forum*. **327** 279

[4] Otsuka K, Oda K, Ueno Y, Piao M, Ueki T and Horikawa H 1993 The shape memory effect in a $Ti_{50}Pd_{50}$ alloy *Scripta Metall. Mater.* **29** 1355

[5] Ye Y Y, Chan C T and Ho K M 1997 Structural and electronic properties of the martensitic alloys TiNi, TiPd and TiPt *Phys. Rev.B* **56** 3678

[6] Sasaki T T, Hornbuckle B C, Noebe R D, Bigelow G S, Weaver M L, and Thompson G B 2013 Effect of aging on microstructure and shape memory properties of a Ni-48Ti-25Pd (At. Pct) alloy *Metall. and Mater. Trans.* **44**A 1388

[7] Ma J, Karaman I and Noebe R D 2010 High temperature shape memory alloy. *Int. Mater. Rev.* ***55*** 257

[8] Bozzolo G, Noebe R D and Mosca H O 2005 Site preference of ternary alloying additions to NiTi: Fe, Pt, Pd, Au, Al, Cu, Zr and Hf *J. Alloys. Comp.* **389** 80

[9] Firstov G S, Van Humbeeck J and Koval Y N 2004 High-temperature shape memory allloys some recent developements *Mater. Sci. Eng.* A **378** 2

[10] Yamabe-Mitarai Y, Hara T, Miura S and Hosoda H 2010 Shape memory effect and pseudoelasticity of TiPt *Intermetallics* **18** 2275

[11] Wadood A, Takahashi M, Takahashi S, Hosoda H and Yamabe-Mitarai Y 2013 High-temperature mechanical and shape memory properties of TiPt-Zr and TiPt-Ru alloys *Mater. Sci. Eng*. A**564** 34

[12] Clark S J, Segall M D, Pickard C J, Hasnip P J, Probert M J, Refson K and Payne M C 2005 Zeitschrift für Kristallographie *First-principles methods using CASTEP* **220** 567

[13] Payne M C, Teter M P, Allan D C, Arias T A, and Joannopoulos J D 1992 Iterative minimization techniques for ab initio total-energy calculations: molecular dynamic and conjugate gradients *Rev. Mod. Phys.* **64** 1045

[14] Perdew J P, Burke K and Ernzerhof M 1996 *Phys. Rev. Lett.* **77** 3865

[15] Monkhorst H J and Pack J D 1976 Special points for brillouin-zone intergrations *Phys. Rev. B* **13**

5188
[16] Nørskov J K 1979 Electron structure of single and interacting hydrogen impurities in free-electron-like metals *Phys. Rev. B* **20** 446
[17] Phasha M J, Ngoepe P E, Chauke H R, Pettifor D G and Nguyen-Mann D 2010 Link between structural and mechanical stability of fcc- and bcc-based ordered Mg-Li alloys *Intermetallics* **18** 2083
[18] Mahlangu R, Phasha M J, Chauke H R, Ngoepe P E 2013 Structural, Elastic and Electronic Properties of Equiatomic PtTi as Potential High-Temperature Shape Memory Alloy *Intermetallics* **33** 27
[19] Fernando G W, Watson R E and Weinert M 1992 Heats of formation of transition-metal alloys: Full-potential approach and the Pt-Ti system *Phys. Rev. B* **45** 15 8233

Bias enhanced nucleation and growth for improving the opto-mechanical properties of diamond-like carbon films

WM Mbiombi[1,2], **B A Mathe**[12], **D Wamwangi** [1,2], **R Erasmus**[1,2]and **D G Billing**[3]

[1] *DST/NRF Centre of Excellence in Strong Materials, University of the Witwatersrand, Private Bag 3, Wits 2050, Johannesburg, South Africa*
[2] *Materials Physics Research Institute, School of Physics, University of the Witwatersrand, WITS 2050, Johannesburg, South Africa*
[3] *Molecular Sciences Institute, School of Chemistry, University of the Witwatersrand, WITS 2050, Johannesburg, South Africa*

E-mail:wilfred.mbiombi@students.wits.ac.za

Abstract. Diamond-like carbon (DLC) thin film is an amorphous carbon with high amount of sp^3 bonds and it is extensively investigated due to its excellent potential for application as an antireflection coating. Besides it has tunable opto-electronic and mechanical properties that depend on the sp^3/sp^2 fraction. This work seeks to investigate the enhancement of the opto - mechanical properties of DLC thin films by *in situ* control of the nucleation and growth of DLC thin films. Thus DLC thin films have been deposited on SiO_2 substrates using unbalanced RF magnetron sputtering at a constant power density of 4.4 W/cm^2 and various substrate bias voltages in the range -25 to -100 V. Raman spectroscopy has been used to determine the sp^3 fractions from the area ratios of the D-peak and G-peak (I_D/I_G). The results show that ratio vary between (0.55-0.63) corresponding to sp^3/sp^2 ratio in the range (1.07-1.33). Optical spectroscopy measurements in the visible range show a transmittance at 81% for a bias substrate of voltage of -75V, which correlates not only with the largest Tauc – gap of 1.56 eV but also with lowest sp^2 cluster of 15.25 Å. The thicknesses of the films have been determined to be (94-147 nm) using X-ray reflectivity, and decoupled from the optical density in the transmittance data.

1. Introduction

Diamond-like carbon (DLC) thin films continue to inspire a lot of research interest due to their diverse applications and extreme properties such as high hardness, low friction coefficient, chemical inertness, high resistivity and optical transparency. For opto-mechanical applications its wide band gap and low surface roughness have made it a promising candidate for nano-mechanical resonators [1-10].

All the unique combinations of properties have extended the applications of DLC films as protective coatings for optical windows, magnetic storage disks and biomedical coatings and anti-reflection coatings [11]. The ability to tune the sp^3/sp^2 ratio and hydrogen fraction opens the way to improve the optical, electrical and mechanical properties of these materials. This further enhances their application in non-volatile memory as active layers with high scalability and low power

consumption devices [12]. In all the above cases DLC thin films are incorporated as active layer in multilayer devices, thus strain control and stress relaxation play a dominant role in the performance and life span of devices. Despite the wide range of applications. DLC thin films exhibit high compressive internal residual stress, which leads to poor adhesion, and thus limit their commercial use. Using RF magnetron sputtering under diverse substrate bias voltages provides a step towards the establishment of the correlation between microstructure and film – substrate adhesion.

2. Experimental

DLC thin films were prepared by RF magnetron sputtering system employing a 13.56 MHz radio frequency at room temperature with substrate bias voltages between (-25V and -100V). The deposition of the films was done in argon and methane gas ambient on a glass substrate (SiO_2). The RF input power density was set at 4.4W/cm^2 for an Ar/CH_4 ratio of 1:1 using a graphite target. The base pressure of the vacuum chamber was 3.7×10^{-5} mbar while the working gas pressure was set at 2.8×10^{-2} mbar. The thickness and the density of the DLC films for the optical transmission were varied between 94 – 147 nm and 2.10-2.59 g/cm^3, respectively, as measured by X-ray reflectivity. The microstructure of DLC thin films was studied by determining the area and intensity ratios of the D and G peaks using Raman spectroscopy after excitation with a 514.5 nm laser light source. The optical properties of the films were established using UV-vis Cary 500 spectrophotometer in the range 350-1400 nm. This technique enables the measurement of the optical transmittance of the DLC films after subtraction of the contributions of the glass substrate in the calibration.

3. Results and discussion

3.1.Raman Spectroscopy Characterization

Raman spectra of DLC thin films deposited under various substrate bias voltages are presented in figure1. In general, the Raman spectra of the DLC thin films resembles that of disordered graphite and it constitutes of two vibrational modes, namely; the G-peak around 1580-1600 cm^{-1} and the D-peak around 1350 cm^{-1}. These modes are assigned to the zone centre phonons of E_{2g} symmetry and the K-point phonons of symmetry, respectively [13]. The measured spectra of the DLC films were de-convoluted into distinct D- and G peaks using two Gaussian functions as shown in figure1.

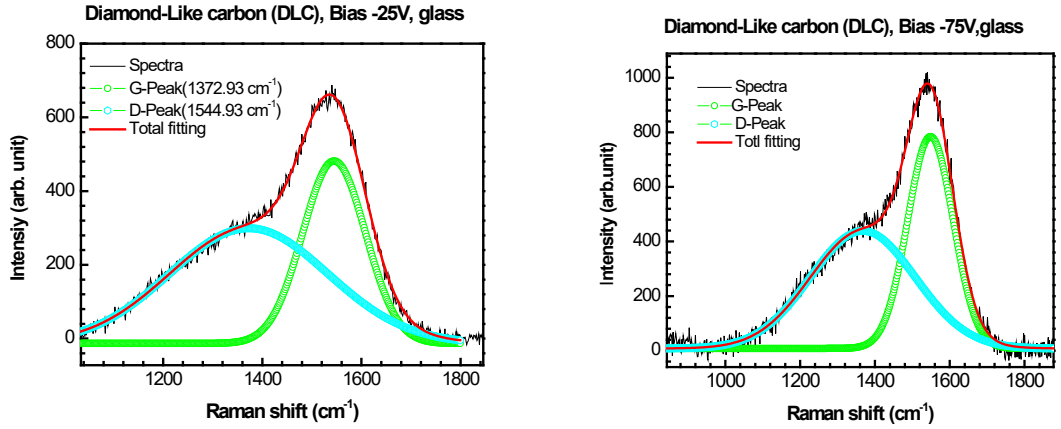

Figure 1. De-convolution of Raman spectra into distinct D- and G- peaks using two Gaussian functions for films deposited at substrate bias voltages of -25 V and -75 V.

Our results indicate that the centroid of the D-peak occurs in the vicinity of (1369.32-1373.49 cm^{-1}) and this corresponds to intensity I_D/I_G and area ratios in the range (0.55-0.63) and (1.28-1.59), respectively. The results further show a decrease in the D-peak position and I_D/I_G ratios with increasing substrate bias voltage. This is attributed to the increase in sp^3 fractions in the films which represent the bonding configuration responsible for the formation of more diamond-like carbon films.

The relationship between I_D/I_G and cluster size defined by equation (1) is an appropriate indication on the formation of DLC thin films;

$$I_D/I_G = C(\lambda)L_a^2 \qquad (1)$$

where C is the constant epen ent on wavelength and L_a is cluster diameter or in-plane correlation length. It is therefore evident that the I_D/I_G ratio decreases with decreasing cluster (L_a) size of the sp^2 bonds. Applying a DC bias voltage to the silicon substrate in ambient CH_4/Ar was observed to optimize DLC nucleation resulting in the highest fraction of sp^3 bonds at -100 V, however nucleation can also be determined by the space charge effects which can lead to a higher sp^3 fraction at lower bias voltage as was observed at (-75 V)[14]. In the CH_4, the H/C ratio is significant, since the hydrogen fraction changes the properties of the films. A typical signature of hydrogenated samples is the increasing photoluminescence background with increasing H content shown in figure 2. This background generally overshadows the Raman signal of a-C:H around 40- 45 at.% of H. The ratio between the slope *m* of the fitted linear background and the intensity of the G-peak, m/I(G), is used as a measure of the bonded H content as shown in figure 2. The bonded hydrogen in DLC was thus estimated using equation (2) and the results included in Table 1. Note that this expression is valid for H>20 at. % [15].

$$H[at.\%] = 21.7 + 16.6\ log\left\{\frac{m}{I(G)}[\mu m]\right\} \qquad (2)$$

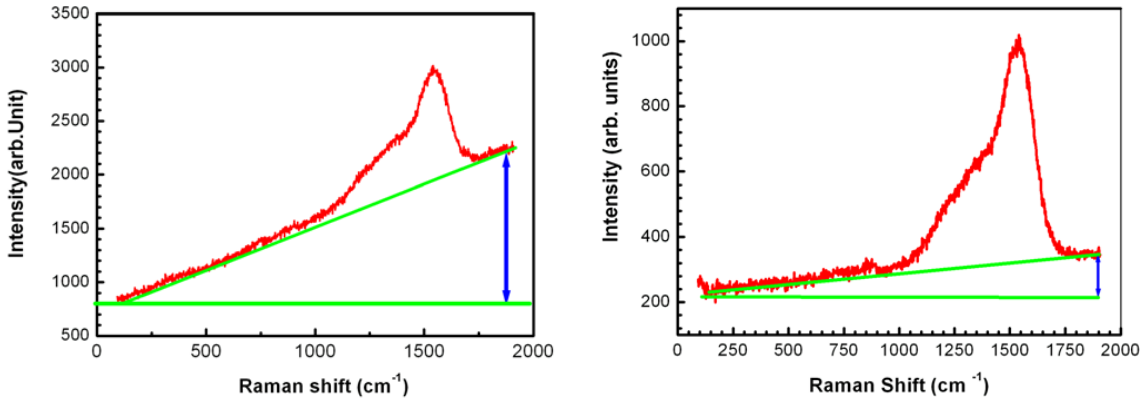

.

Figure 2. The ratio between the slope m of the fitted linear background and the intensity of the G-peak, for -25 V and -75 V.

A summary of the Raman spectroscopy results is presented in Table1. It is observed that the substrate bias voltage increases the hydrogen content in the DLC films up to -75 V, beyond which (at -100 V) a decrease in the amount of hydrogen occurs. This decrease could be attributed to re-sputtering effects arising from plasma etching. Indeed the thickness of the DLC thin films deposited at -100 V is 99 nm compared to 147 nm, that of films deposited at -75 V.This implies that the films deposited on the glass can be classified as diamond-like carbon which has the value between 20 - 40% of hydrogen [16].

Table 1. Different parameters of DLC thin films obtained from the Raman spectra at 514 nm.

Substrate bias voltage (V)	D-peak (cm^{-1})	Area ratio (I_D/I_G)	Height ratio (I_D/I_G)	Sp^3/sp^2 (±0.05)	Hydrogen (at.%)
-25V	1372.93	1.59	0.63	1.07	22.15
-50 V	1369.32	1.45	0.59	1.21	31.27
-75 V	1367.76	1.28	0.55	1.33	38.19
-100V	1373.49	1.51	0.61	1.13	32.52

3.2. Optical spectroscopy

The UV-vis transmission spectra of DLC thin films at various substrate bias voltages (from -25 V to -100 V) are shown in figure 3(a). The dependence of transmission on the optical constants and the film thickness is decoupled from the measurement. Thus the values presented represent the percentage transmission from the intrinsic properties of the DLC film deposited at various substrate bias voltages. The highest transmittance is observed for films deposited with a bias voltage of -75 V, which corroborates with the presence of more sp^3 fractions in the films. Using Beer's law, Tauc's relation and the Fermi-golden rules for interband transitions, the dispersion of absorption coefficient is extracted as shown in figure 3(b). he plot of $h\nu)^{1/2}$ versus ($h\nu$) of DLC films prepared at different bias voltages on the substrate is based on a direct allowed transition to estimate the Tauc gap, and the results are shown in Table 2, where the largest Tauc gap occurs for the films prepared at -75 V bias, owing to the higher sp^3 fraction.

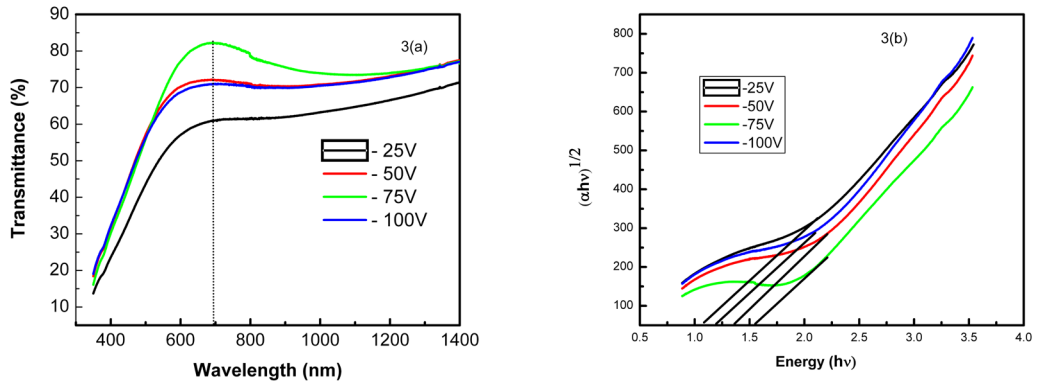

Figure 3 (a) ransmittance ersus a elength an b the plot of $h\nu)^{1/2}$ versus $h\nu$.

Table 2. The mixture of optical property and Raman spectroscopy results for the biased DLC films.

DLC films	Transmission (%)	Tauc gap PL (eV)	Cluster size Height (A)
-25V	58	1.10	17.00
-50 V	69	1.37	16.24
-75V	80	1.56	15.25
-100 V	66	1.20	16.57

The linear extrapolation in fig 3(b) from the straight line to the energy axis gives the Tauc gap of the films under diverse substrate bias. The optical band gap (Eg) of the films has been determined to be: 1.10, 1.37, 1.56 and 1.20 eV, corresponding to the substrate bias voltages of -25 V, -50 V, -75 V and -100 V, respectively. The results in Table 2 show that the Tauc-gap increases with increasing sp^3 fractions, corresponding to more diamond like films tending to be optically transparent, for which the cluster size of DLC thin film is less than 2 nm. The values of Tauc gap determined in this work are in agreement with those reported for a-C:H (1- 2 eV) [15]. The Tauc- gap is mainly determined by the C sp^2 hybridization clusters embedded in the amorphous carbon medium [16] and thus the increase in the Tauc- gap is expected for decreased fraction of sp^2 cluster sizes as shown in Table 2.

4. Conclusion

The present work has shown that DLC films had been successfully deposited onto a glass substrate at room temperature using graphite target and ambient Ar/CH_4 using a radio frequency (RF) magnetron sputtering. The dependence of structural evolution of DLC films as a function of the substrate bias voltage has been demonstrated by a combination of Raman spectroscopy and X-ray reflectivity, where an amorphous matrix evolves into a predominantly sp^3 bonded system with sp^2 chains. Raman and UV-visible spectra further corroborate this evidence indicating that increasing substrate bias voltage leads to the reduction of the cluster size of sp^2 rings, creating more sp^2 chains and the sp^3 bonds. It is thus expected that as fraction of sp^3 bonds increases, the films will also exhibit stronger mechanical characteristics, thus this project will be extended to employ Brillouin scattering technique to measure the Young's modulus of these DLC films.

5. References

[1] Robertson J 1991 *Prog. Solid State Chem*. **21** 199
[2] Robertson J 1992 *Surf. Coatings Technol*. **50** 185
[3] Robertson J 1986 *Adv. Phys*. **35** 317
[4] Koidl P, Wild C, Dischler B, Wagner J and Ramsteine M 1990 *Mater. Sci. Forum* 52 41
[5] Tsai H and Bogy D B 1987 *J. Vac. Sci.* Technol. **A5** 3287
[6] Mckenzie D R 1996 *Rep. Prog*. Phys.**59** 1611
[7] Lifshitz Y1996. *Diamond Rel. Mater.* **5** 388
[8] Lifshitz Y1999 *Diamond Rel. Mater.* **8**1659
[9] Voevodin A A and Donley M S 1996 *Surf. Coatings Technol*.**82** 199
[10] Silva S R P, Carey J D, Khan R U A, Gertner E G, Anguta J V and Nalwa H S 2002 *Handbook of thin film Materials*. (Newyork: Academic Press).
[11] Ray S C, Mbiombi W and Papakonstantinon P 2014 *Applied Mechanics and Materials* 575 pp 292-295
[12] Lin C R et al 2011 *Physics Procedia* **18** 46-50

[13] Ferrari A C and Robertson J 2000. *Phys. Rev.* B.**61** 14095
[14] Zhang X Y, Lai C W and Zhou X 2009 *Journal of Applied* physics **105** 056105
[15] Lubwama M, Corcoran B, Rajani K V , C.S. Wong C S , Kirabira J B, Sebbit A, McDonnell K A, Dowling D and Sayers K 2013 *Surface Coatings Technology* **232** 521-527
[16] Casiraghi C, Ferrari A C and Robertson J 2005- *Phys. Rev. B* **72** 085401

Atomistic simulation of the structure and elastic properties of pentlandite structure (Ir_9S_8)

M A Mehlape, **D Tanzwani and P E Ngoepe**
Materials Modelling Centre, School of Physical and Mineral Sciences, University of Limpopo, South Africa, Private Bag, X1106, SOVENGA, 0727

Email:mofuti.mehlape@ul.ac.za

Abstract. Atomistic simulation was carried out to study the effect of pressure on the structureand elastic properties of pentlandite structure (Ir_9S_8) sulphides. The lattice parameters, bond lengths and elastic constants as a function of pressure are calculated. Pentlandite is a major precious metals-bearing mineral and plays a very important role in mining. Precious metal ores co-exists with base metals either as solid-solution and intergrowths, hence rendering its detailed understanding important for efficient extraction of these precious metals. This work relates to problems in applied areas such as mineralogy, geophysics and geochemistry, whereby phase transition is modified by impurities, so there is the additional concern of the effect of high pressures. We want to see how pressure changes the lattice parameters, elastic constants and bond lengths. We used computational techniques to investigate the effect of high pressure on the pentlandite structure. It was noted that as the pressure increases, the volume decreases. The elastic properties were found to be positive, which satisfies the conditions for a mechanically stable cubic structure.

1. Introduction

The Bushveld Complex has the largest concentration of platinum group elements (PGEs) and these are ruthenium (Ru), rhodium (Rh), palladium (Pd), osmium (Os), iridium (Ir), and platinum (Pt) [1]. Pentlandite minerals are known to host such precious metals, either as solid solutions or as intergrowths [2] and in order to achieve high recoveries of such metals it is necessary to float pentlandites efficiently, particularly in reefs that are less explored, such as the platreef. These PGEs exist in different structures and they could form pentlandite structure (Ir_9S_8), which makes them significant sulphide minerals. Owing to their high concentration in the Bushveld Complex, it draws much attention in investigating their structure and elastic properties. In one of the studies of sulphide minerals within the Merensky Reef deposit of the Bushveld Complex, it was found that Ir, Os and Ru reside in solid solution in pentlandite and pyrrhotite, Rh and some Pd in pentlandite [3]. Our focus is on the atomistic simulation of structural and elastic properties of iridium-bearing mineral within pentlandite (Ir_9S_8). Ir has properties that are resistant to corrosion, and together with its alloys is used in chemical industry, medical devices and jewellery manufacture [4]. The study on the elastic properties of minerals play key role in the studies of earth's deep interior [5]. Furthermore, theory and computation play an increasingly important role in the field of mineral physics by allowing the scientist to probe environments, such as the deep Earth, that are challenging or impossible to access extensively by experiment [6]. Determination of high-pressure mineral structure is crucial for understanding all other pressure-induced property changes in the deep Earth [7]. Elastic properties describe the volume and shape changes that occur when stresses are applied to a material [8].

Pentlandite, Ir_9S_8 structure

The conventional unit cell of the pentlandite has the formula $Ir_{36}S_{32}$ and contains a cubic close-packed arrangement of sulphide ions containing 64 tetrahedral holes and 32 octahedral holes. Of the 64 tetrahedral holes, 32 are occupied by Ir^{2+} ions, these being distributed through the lattice in groups of eight which lie at the corners of sub-cubes of edge length 0.250 nm. Of the 32 octahedral holes, 28 are pseudo-octahedral, distorted, and empty, whereas four are truly octahedral and each contains an Ir atom in a formally zero oxidation state. Thus the solid attains the overall stoichiometry Ir_9S_8 [9]. Figure 1 shows the conventional unit cell of Ir_9S_8. The Ir_9S_8 has a space group *Fm3m*.

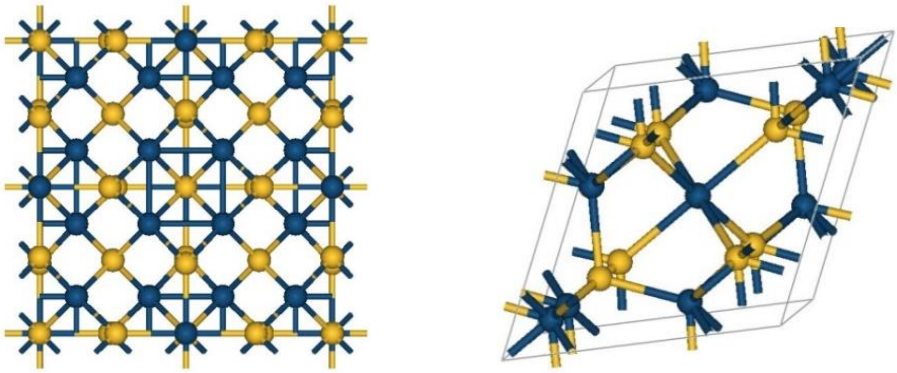

Figure 1: Conventional ($Ir_{36}S_{32}$) and primitive (Ir_9S_8) unit cell of pentlandite structure. Blue and yellow spheres represent metal (Ir) and sulphur (S) atoms respectively.

2. Computational Method

The atomistic simulation method uses interatomic potential functions to describe the total energy of a system in terms of atomic coordinates [10]. The atomistic simulation method in this study was conducted using General Utility Lattice Program (GULP) code [11], which requires the use of interatomic potential functions. GULP code allows the use of two-body, three-body, four-body, six-body, and many body potentials depending on demands of research [12]. The cell geometry of Ir_9S_8 was assigned as a = b = c = 9.928 Å, and α = β = γ = 90 with space group *Fm3m*. Geometry optimization calculations were performed on the structure and elastic constants at pressures ranging between 0 and 40 GPa in the steps of 5 GPa. In this work, we consider the approximation for describing the pentlandite structure, which is the rigid ion model potential. This is an empirical approach and relies on a set of parameters, which were modified using cobalt pentlandite potentials (Co_9S_8) [13]. The potential models can accurately describe the bulk and surface structure properties, lattice constants, and elastic properties of sulphides [14], oxides [15], and other pentlandite structures [16]. The calculations are based on the Born ionic model [17] of a solid and parameters were derived for short range interactions represented by the Buckingham potential, Morse potential and three body terms:

Buckingham Potential

In the Buckingham potential, the repulsive term is replaced by an exponential term and potential takes the form

$$U(r_{ij}) = A_{ij}exp(-r_{ij}/\rho_{ij}) - C_{ij}r_{ij}^{-6} \quad (1)$$

where $A_{ij}$and ρ_{ij} are parameters that represent the ion size and hardness, respectively, while C_{ij} describe the attractive interaction and r_{ij} is the distance between ion i and ion j. The first term is known as the Born-Mayer potential and the attraction term (second term) was later added to form the Buckingham potential. Very often, for the cation-anion interactions, the attractive term is ignored due to the very small contribution of this term to the short-range potential, or, alternatively, the interaction is subsumed into the A and ρ parameters.

Morse Potential

The Morse potential is used to model the interactions between covalently bonded atoms and has the form

$$U(r_{ij}) = D_{ij}\left(\left(1 - exp\left(-\beta_{ij}(r_{ij} - r_0)\right)\right)^2 - 1\right) \quad (2)$$

where D_{ij} is the bond dissociation energy, r_0 is the equilibrium bond distance, and β_{ij} is a function of the slope of the potential energy well. The Coulombic interactions between covalently bonded atoms are often partially or totally ignored as the Morse potential already contains the attractive component of the interaction between neighbours.

Three-Body Potential

A further component of the interactions of covalent species is the bond-bending term, which is added to take into account the energy penalty for deviations from the equilibrium value. Hence, this potential describes the directionality of the bonds and has a simple harmonic form:

$$U(\theta_{ijk}) = \frac{1}{2}k_{ijk}(\theta_{ijk} - \theta_0)^2 \quad (3)$$

where k_{ijk} is the three-body force constant, θ_0 is equilibrium angle and θ_{ijk} is the angle between two interatomic vectors $i - j$ and $j - k$. Table 1 gives the potential parameters used in this study.

Table 1: The modified potential parameters for pentlandite structure (Ir_9S_8) used in this study.

Potential			
Buckingham potential	$A_{ij}\,(eV)$	$\rho_{ij}\,(\text{Å})$	$C_{ij}\,(eV\text{Å}^6)$
S-S	1130.533064	0.184528	0.00
Morse potential	$D_{ij}\,(eV)$	$B_{ij}\,(eV)$	$r_0\,(\text{Å})$
Ir-S	3.0	1.633754	2.20
Three body potential	$k_{ijk}\,(eV.rad^{-2})$	$\theta_0\,(^\circ)$	
S-Ir-Ir	0.82	109.503	
Ir-S-S	2.89	109.503	
Ion charges		Charge (e)	
Metal (Ir) core		0.40	
Sulphur (S) core		-0.45	

3. Results and Discussions

The effect of pressure on the structural and elastic properties of pentlandite is discussed in this section. First we discuss the structure and elastic properties under zero pressure. Table 2 shows that optimized structural parameters are in good agreement with the experimental and other theoretical results. A pentlandite cubic structure M_9S_8 has three independent elastic constants (C_{11}, C_{12} and C_{44}). The elastic constants of a typical cubic structure obey the criteria $C_{11} - C_{12} > 0$, $C_{44} > 0$, $C_{11} + 2C_{12} > 0$. As a result calculated values of elastic constants satisfy both the structural and cubic stability conditions, meaning that the crystal structure is stable under zero pressure.

Table 2 Comparing our results with previous experimental and theoretical data for pentlandite under zero pressure. [a] [18], [b] [19], [c] [20], [d] [21], [e] [22].

Parameter	Present Study	Other Theoretical	Experimental
Lattice parameters			
$a(\text{Å})$	9.809	9.948[a], 9.918[b], 9.927[c], 9.977[d]	9.928[e]
$V(\text{Å}^3)$	943.86	974.44[b]	978.56[c]
Bond lengths (Å)			
Ir-S	2.111	2.122[c]	2.127[d]
Ir-Ir	2.468	2.514[c]	2.505[d]
Elastic Constants (GPa)			
C_{11}	209.5	212.0	
C_{12}	121.1	123.8	
C_{44}	49.9	49.4	
Bulk Modulus (GPa)	150.5	153.2	

Pressure effect

We determine the structure and elastic constants of pentlandite structure up to the pressure of 40 GPa. The effect of high pressure on the structure and elastic properties of pentlandite are reported to further validate the modified potential model. It was reported that, the effect of pressure on the elastic properties in materials is important for predicting and understanding some physical properties like, the interatomic forces, mechanical stability, phase transition mechanisms, dynamic fracture, earthquakes and the internal structures of earth [12]. Again the behavior of earth materials at high pressure is central to our understanding of the structure, dynamics, and origin of the earth [23]

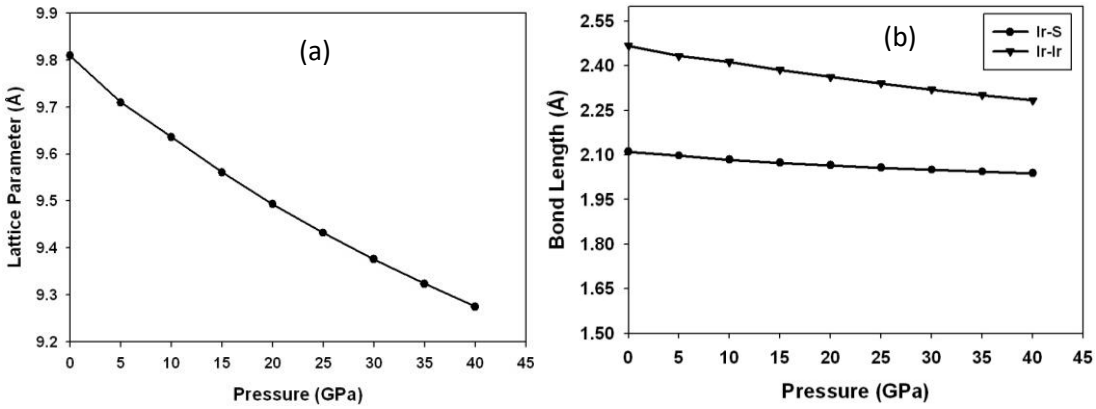

Figure 2: The (a) lattice parameter and the (b) bond lengths as a function of increasing pressure.

.

Figure 2 (a) shows the graph of lattice parameter as a function of increasing pressure. As expected the lattice parameter decreases with the increasing pressure ranging between 0 and 40 GPa. Figure 2(b) shows the graph of bond lengths as a function of pressure. In both cases the actual change is linear with increasing pressure; however bond lengths for Ir-Ir are predicted to shorten much more slowly than those of Ir-S pair, due to the metallic behaviour of pentlandite structure.

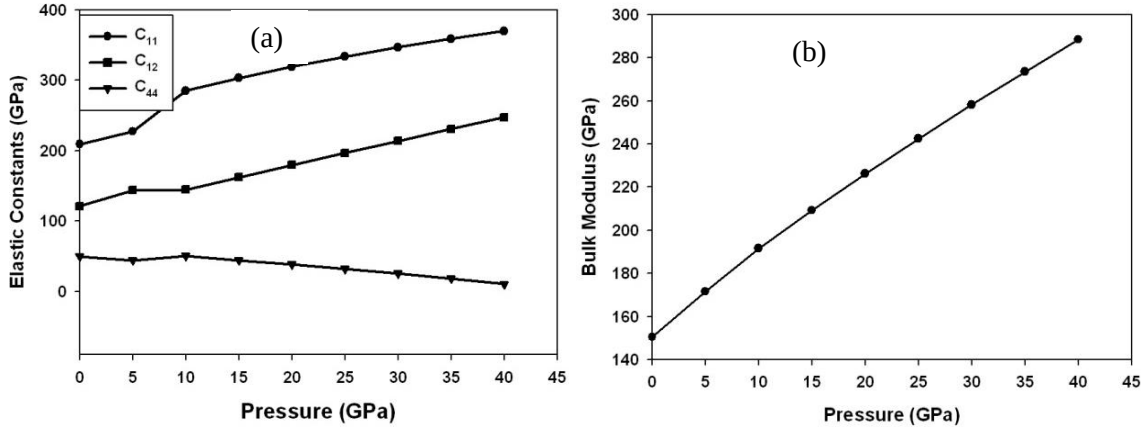

Figure 3: The variation of the (a) elastic constants and (b) Bulk modulus as a function of increasing pressure.

Figure 3(a) represents the elastic constants (C_{11}, C_{12} and C_{44}) of M_9S_8 at the pressure interval between 0 GPa and 40 GPa. The elastic constants C_{11} and C_{12} show a positive and smooth increase as a function of increasing pressure; however C_{44} show a decrement as a function of increasing pressure. Similar observations of the decrement of C_{44} with the increasing pressure have earlier been reported by Varshney et al [23] for the strontium chalcogenides. This implies that $C_{11}$and C_{12} are more sensitive to the change of pressure than the C_{44}. It has been reported by Karki and coworkers [24] that elastic constants increase monotonically with increasing pressure; and that in few cases whereby elastic constants decrease with increasing pressure which implies an elastic instability. There are no available experimental and theoretical data to cross-check the present results, however these results can provide a useful reference for future studies. The variations in bulk modulus with increasing pressure are shown in Figure 3(b). It can be seen from the graph that bulk modulus increase as pressure increases, which shows that the hardness of these material increases with increasing pressure. The increment is expected due to its direct proportionality to applied pressure ranging between 0 GPa and 40 GPa.

4. Conclusion

Atomistic simulation has been carried out to study the effect of pressure on structure and elastic properties of pentlandite structure, Ir_9S_8. The structural properties suggest good agreement when compared with experimental and other theoretical data. The elastic constants were found to be positive, which satisfies the conditions for a mechanically stable cubic structure. Thus the refitted potentials gave reasonable results and may further be helpful to future studies regarding the structural and elastic properties, and other related properties of pentlandite structure.

Acknowledgements

The work was done at the Materials Modelling Centre (MMC), University of Limpopo. The authors acknowledge the National Research Foundation (NRF) for their financial support.

References

[1] O'Connor T C and Shacklenton N J 2013 *Platin. Met. Rev.* **57** 302
[2] Wang Q and Heiskanen K 1990 *Int. J. Miner. Process.* **29** 99
[3] Ballahaus C and Sylvester P 2000 *J. Petrol.* **41** 545
[4] Vidhate K 2015 *Adv. Appl. Sci. Res.* **6** 180
[5] Bass J 2008 *Phys. Earth Planet. Inter*. **170** 207
[6] Gale J D and Wright K 2010 *Rev. Mineral. Geochem.* **71** 391
[7] Yuan H and Zhang L 2017 *Matter. Radiat. Extreme*. **2** 117
[8] Bass J D, Sinogeikin S V and Li B 2008 *Elements* **4** 165
[9] Hoodless R C, Moyes R B and Wells P B 2006 *Catal. Today* **114** 377

[10] Liu Z-J, Sun X-W, Song T, Guo Y, Zhang C-R and Zhang Z-R 2016 *Bull. Mater. Sci*. **39** 1319
[11] Gale J D 1997 *J. Chem. Soc.:Faraday Trans*. **93** 629
[12] Güler E and Güler M 2013 *Adv. Mater. Sci. Eng.* Article ID 525673, 5 pages.
[13] Mehlape M A 2013 *PhD Thesis*. University of Limpopo
[14] Sithole H M, Ngoepe P E and Wright K 2003 *Phys. Chem. Miner*. **30** 615
[15] Maphanga R R, Ngoepe P E and Parker S C 2009 *Surf. Sci*. **603** 3184
[16] Mehlape MA, Ngoepe P E and Parker S C 2013 Proceedings of SAIP 98-103 Available online at http://events.saip.org.za
[17] Born M and Huang K. 1954 *Dynamical Theory of Crystal Lattices 1st edition*. Oxford: University Press
[18] Sidik R A and Anderson A B 2006 *J. Phys. Chem. B* **110** 936
[19] Chauke H R, Nguyen-Manh D, Ngoepe P E, Pettifor D G and Fries S G 2002 *Phys. Rev. B* **66** 155105
[20] Burdett J K and Miller G J 1987 *J. Am. Chem. Soc*. **109** 4081
[21] Rajamani V and Prewitt C J 1975 *Can. Mineral.* **13**, 75
[22] Lindqvist M, Lundqvist D and Westergren A 1936 *Svensk Kem. Tidskr*. **48** 156
[23] Varshney D, Jain S, Shriya S and Khenata R 2016 *J. Theor. Appl. Phys.* **10** 163
[24] Karki B B, Stixrude L and Wentzcovitch R M 2001 *Rev. Geophys.* **39** 507

Computational modelling study of the $Ti_{50}Pt_{50-x}Cu_x$ shape memory alloys

R Modiba[1,2], H Chikwanda[1] and P E Ngoepe[2]

[1] Materials Science and Manufacturing, CSIR, PO Box 395, Pretoria, 0001, South Africa

[2] Materials Modelling Centre, University of Limpopo, Private Bag X1106, Sovenga, South Africa

Abstract. Recently, there is a high demand of shape memory alloys that can be used at high temperatures. TiPt is found to be one of the promising alloys with the martensitic transformation temperature of 1300 K. Previous studies showed that the alloy is mechanically unstable with the negati e C mo ulus at 0 . n or er to enhance the mechanical properties of the alloy a thir element Cu was substituted in the TiPt. The stability of the structures with respect to their equilibrium lattice parameters and heats of formation were determined using the density functional theory method embedded in VASP code. It was found that increasing Cu content stabilizes the TiPt ith a positi e C obser ed for 18.25 at.% Cu. Furthermore, we investigated the temperature dependence of the lattice parameters and copper is found to be lowering the martensitic transformation temperature of the TiPt shape memory alloy.

1. Introduction

Shape memory alloys (SMAs), are metallic systems that remembers their original shape when exposed to a certain pressure or temperature. The shape memory effect and pseudo-elasticity of these materials which accounts for the specific way the phase transformation occurs, makes them remarkably different from other materials. Although they have been used commercially, new applications continue to be developed for SMAs [1]. Some of the applications include actuators and medical stents [2, 3, 4, 5]. There is a growing need SMAs that can be used at high temperatures and only a limited number of such alloys have the potential to be high temperature shape memory alloys (HTSMAs). There has been studies reported on the Ti (Ni,Pt) [6, 7, 8] and Ti (Ni,Pd) [9, 10, 11] where the third element addition effect was investigated . However the martensitic transformation temperature (T_m) of these alloys remained below 830 K. The T_m of TiPt is much higher, at approximately 1273 K [12] and this is considered to be of potential technological interest for elevated temperature SMAs applications. It also undergoes a B2-B19 martensitic phase transformation with a transition temperature above 1300 K [12]. However it has been reported that Ti-Pt based alloys exhibit very low shape memory effect due to low critical stress for slip deformation compared to the stress required for martensitic transformation [13, 14] hence it is necessary to enhance the mechanical properties of the equi-atomic alloy for it to be used at higher temperatures. Previous studies suggested that additions of Co, Ni, and Pd on the TiPt lowered the Tm of the TiPt at 6.25 at.% whereas Ir addition increased the martensitic transformation temperature [15, 16]. In this work we investigate the effect of partial substitution of Pt with Cu on the cubic TiPt potential shape memory alloy system using the supercell approach. The equilibrium lattice parameters and elastic constants are studied using density functional theory (DFT) in this paper for the $Ti_{50}Pt_{50-x}Cu_x$ (x=6.25, 18.75 and 25).

In addition; the temperature effect on the B19 orthorhombic phase is investigated using LAMMPS code [15] which is embedded in Materials Design and the results are compared with the available experimental findings.

2. Methodology

The study employed the density functional theory (DFT) method as implemented in the Vienna *ab initio* simulation package VASP [16, 17, 18, 19] with the projector augmented wave (PAW) [20]. An energy cutoff of 500 eV was used as it was sufficient to converge the total energy of the TiPt alloys. For the exchange-correlation functional, the generalized gradient approximation of Perdew and Wang (GGA-PBE) [15] was chosen. The Brillouin zone integrations were performed for suitably large sets of *k*-points according to Monkhorst and Pack [21]. A 2x2x2 supercell of TiPt with 16 atoms was used to substitute some of the Pt with Cu. Semi-empirical embedded atom method (EAM) interatomic potentials of Zhou_2004 [22] incorporated in LAMMPS code [23] were employed to study the temperature effect on the lattice parameters of B19 orthorhombic phase. A 5x5x5 supercell of B19 $Ti_{50}Pt_{50-x}Cu_x$ (x=6.25, 18.75 and 25) having 1024 atoms was used. The minimum and maximum temperatures were set to 100 and 1800 K; respectively. The NPT ensemble integration for 100 ps with timestep of 2 fs was used.

3. Results and discussion

3.1 Elastic properties

In Table1 we show the calculated lattice parameters and elastic properties of the $Ti_{50}Pt_{50-x}Cu_x$ (x=6.25, 18.75, 25). The lattice parameters of the TiPt cubic phase decrease minimally with the addition of Cu content as can be observed in Table 1. Previously, the work on the pure structures of TiPt showed that B structure as unstable ith the C of -32 GPa at 0 K. In this work, when 6.25 at.% of Cu is added, the C_{11} becomes less than C_{12} resulting in a negati e C hich is unstable accor ing to the criterion of the elastic constants [24]. Interestingly, the 18.75 at.% Cu a ition increases the C of TiPt which suggest that at this concentration, the transformation temperature is reduced. It is argued that higher anisotropy *A* is a sufficient condition for B2-B19 martensitic transformation. However, smaller *A* indicates that there is a stronger correlation between C_{44} an C . he origin of B phase is a result of the coupling between C_{44} an C ust as propose by Ren an Otsuka [25].

Table 1. Elastic properties (GPa) of $Ti_{50}Pt_{50-x}Cu_x$ ternaries and their anisotropy *A* using the supercell approach.

Structures	**Lattice parameters**	**C_{11}**	**C_{12}**	**C_{44}**	**C'**	***A***
TiPt [3]	3.18	145	210	45	-32	
$Ti_{50}Pt_{43.75}Cu_{6.25}$	3.16	180	190	54	-10	
$Ti_{50}Pt_{31.25}Cu_{18.75}$	3.13	181	166	49	7.5	7
$Ti_{50}Pt_{25}Cu_{25}$	3.11	179	158	57	10.5	5

The C_{44} can be understood that is related to resistance to {001}[100] shear for cubic crystals which is just the non-basal monoclinic shear re uire by B martensite. herefore C_{44} is crucial for the formation of B martensite an controls the transformation temperature of B to B transformation [28]. The calculated elastic constants at 25 at.% Cu are all positive indicating the mechanical stability of the structure. The anisotropy *A* of both 18.75 and 25 at.% of Cu is larger but positive suggesting the B2 to B19 martensitic transformation.

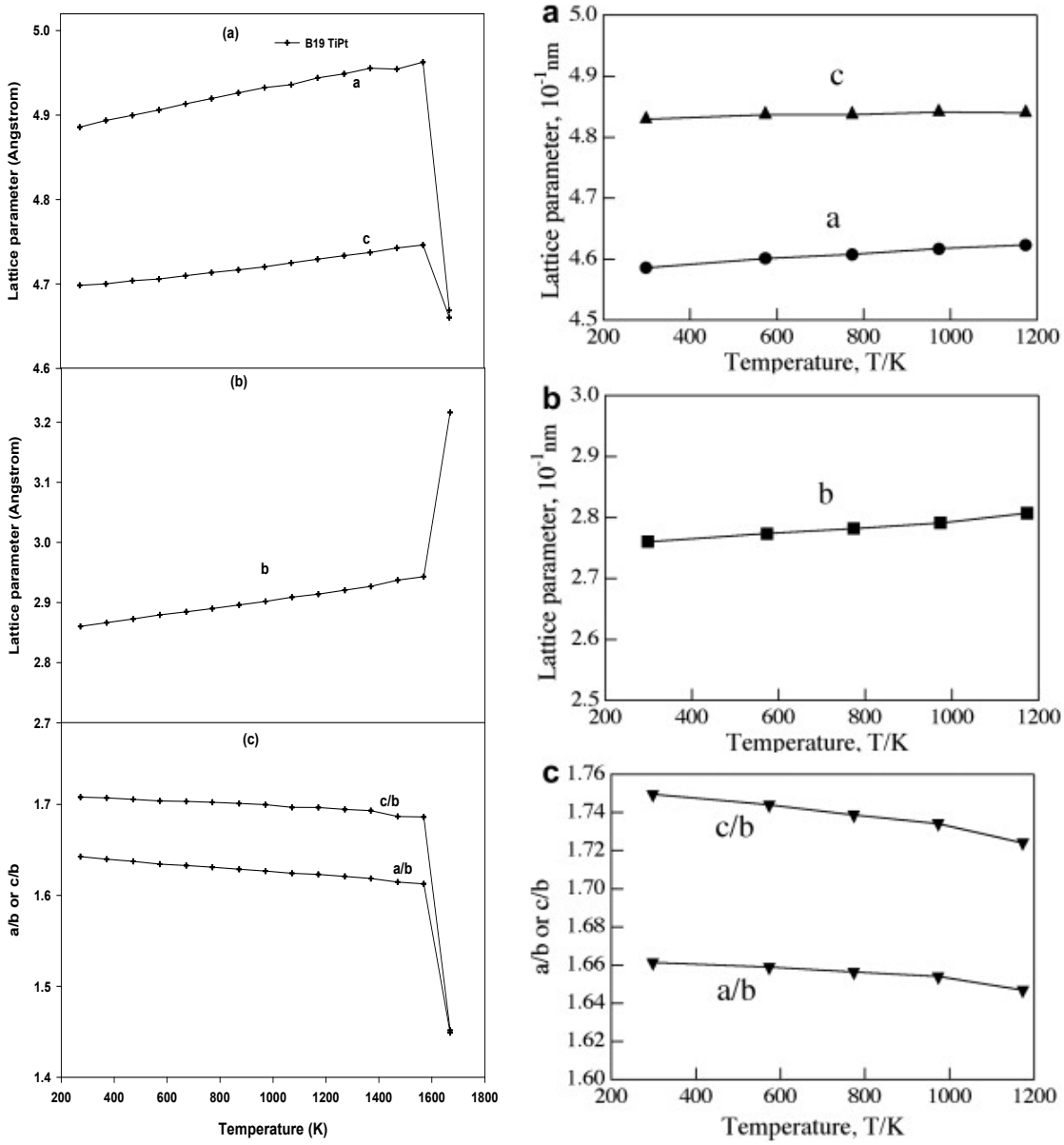

Figure 1: The effect of temperature on the a, c, b, c/b and a/b lattice parameters of the B19 TiPt on the left hand side compared with the experimental results [14] on the right hand side

3.2 Lattice expansion

In Figure 1, the lattice expansion of the B19 orthorhombic phase with temperature for this work is compared with the experimental findings. The lattice parameters of *a* and *c* increase linearly with an increase in temperature. Interestingly, the lattice parameters collapses at approximately 1570 K for both *a* and *c*. The *b* lattice parameter increases linearly with an increase in temperature where a drastic increase is observed at approximately 1570. Yamabe-Mitarai *et al.* investigated the temperature dependence of the lattice parameters for the B19 TiPt experimentally [14] and their results trends are comparable with our findings as shown in Figure 1. The plots of *c/a* and *a/b* ratios are also shown in Figure 1 and decrease linearly with an increase in temperature. Lattice correspondence between the B2 and B19 phase are $[101]_{B2}//a[100]_{B19}$, $[-101]_{B2}//c[001]_{B19}$ and $b[010]_{B2}//b[010]_{B19}$.

The ratios *a/b* and *c/b* should be closer to 1.414, with an increase in temperature, for the B19 to cubic B2 transformation to occur. In Figure 1 (c), *a/b* and *c/b* ratio of the B19 TiPt is 1.451 at approximately 1670 K for this study. The percentage error of the estimated ratio is within 3 % which may suggest that at approximately 1670 K the B19 phase has transformed into cubic B2 phase.

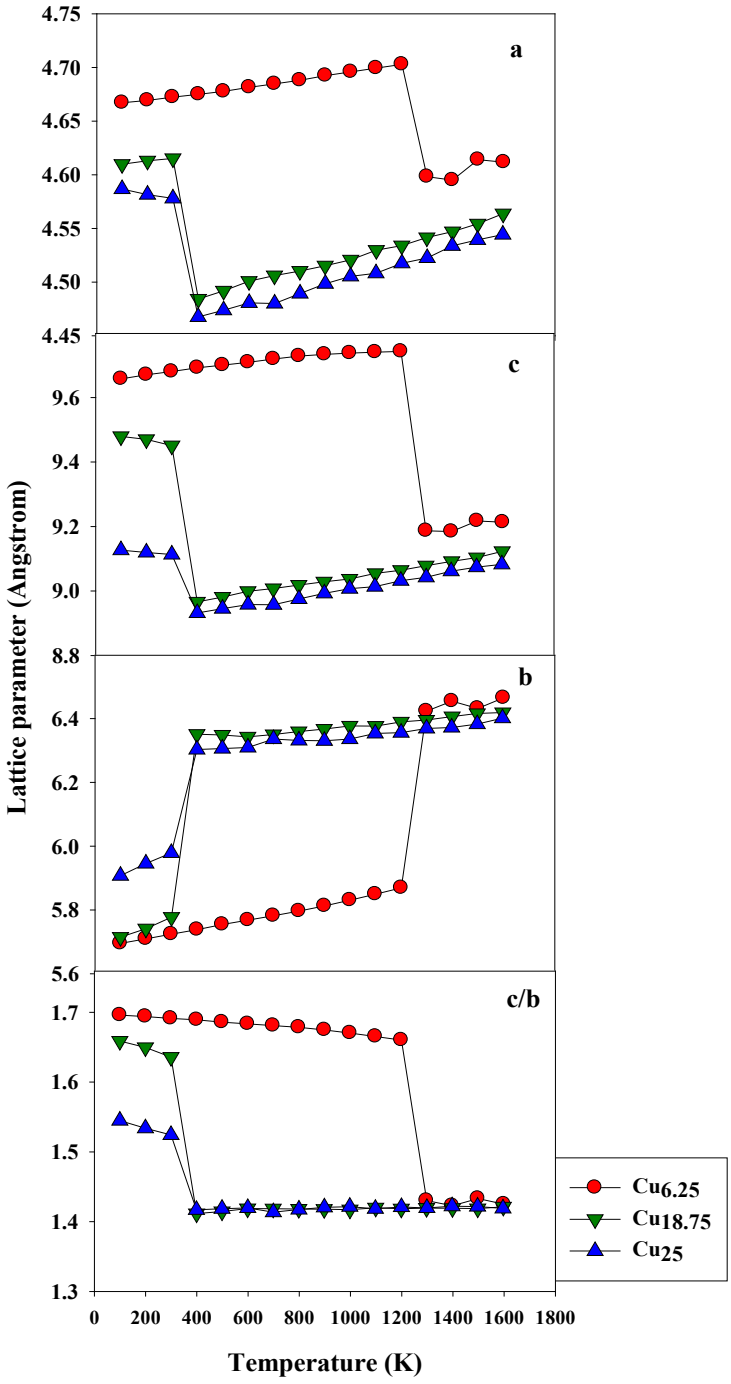

Figure 2. The effect of temperature on the a, c, b and c/b lattice parameters of the B19 TiPt and $Ti_{50}Pt_{50-x}Cu_x$ (x= 6.25, 18.75 and 25)

In Figure 2, we show the plots of lattice constants of $Ti_{50}Pt_{50-x}Cu_x$ with temperature. It is observed that when 6.25 at. % content of Cu is added to the system, the lattice parameter expands linearly and collapses at temperatures of approximately 1200 K which is lower than that observed in Figure 1 for a pure B19 TiPt structure. The c/b ratio is found to be 1.43 at this concentration which can imply that at this point, a transformation to B2 cubic phase is reached. Addition of more content of Cu in the TiPt reduces the transformation temperature drastically as can be observed on the plots of both 18.25 and 25 at.% of Cu. Their lattice parameters collapses at temperatures of about 300 K respectively whereas the 1.41 ratio of c/b is observed at 400 K this suggests that more content of Cu in the TiPt system decreases the transformation temperature of the system.

4. Summary and conclusion

Computational modelling study on the elastic properties and temperature variation in the $Ti_{50}Pt_{50-x}Cu_x$ were performed. The addition of Cu content in TiPt cubic phase was found to be increasing the C mo uli of the phase leading to a positive anisotropy. The elastic constant of both 18.25 and 25 at.% of Cu were found to be stable with all the moduli obeying the elastic stability criterion. Temperature dependence of the lattice parameters were also studied wherein the pure B19 results are comparable with the experimental findings. Smaller amount of Cu addition lowers B19 to B2 phase at temperatures of approximately 1200 K whereas 18.25 and 25 at.% of Cu content reduces the transformation temperature drastically.

Acknowledgements

The authors acknowledge the CSIR and NRF for their financial support. The support of the South African Research Chair Initiative of the Department of Science and Technology and the National Research Foundation is highly recognised. The calculations were carried out using computer resources at the Materials Modelling Centre (MMC) at the University of Limpopo and the Centre for High Performance Computing (CHPC) in Cape Town.

References

[1] Duerig T, Melton K, Stockel D, 1990 *Engineering Aspects of Shape Memory Alloys* Eds Wayman C (London: Butterworth-Heinemann) 89-95
[2] Wu M H and Schetky L M, California: Pacific Grove, 2000 *SMST* 171-182
[3] Otsuka K and Kakeshita T 2002 *MRS Bull*. **27** 91-100
[4] Van Humbeeck J 1999 *Mater. Sci. Eng*. A **273–275** 134-148
[5] Duerig T, Pelton A and Stockel D 1999 *Mater. Sci. Eng*. A **273–275** 149-160
[6] Hosoda H, Tsuji M, Mimura M, Takahashi Y, Wakashima K and Yamabe-Mitarai Y 2003 *MRS Bull*. **753** BB5-51-1–BB5-51-6
[7] Takahashi Y, Inamura T, Sakurai J, Hosoda H, Wakashima K and Miyazaki S 2004, *Trans*. *MRS-J*. **29** 3005-3008
[8] Inamura T, Takahashi Y, Hosoda H, Wakashima K, Nagase T, Nakano T, Umakoshi Y and Miyazaki S 2004 *MRS Bull*. **842** 347-352
[9] Xu Y, Shimizu S, Suzuki Y, Otsuka K, Ueki T and Mitose K 1997 *Acta Mater*. **45** 1503-1511
[10] Suzuki Y, Xu Y, Morito S, Otsuka K and Mitose K 1998 *Mater. Lett*. **36** 85-94
[11] Shimizu S, Xu Y, Okunishi E, Tanaka S, Otsuka K and Mitose K 1998 *Mater. Lett*. **34** 23-29
[12] Donkersloot H C and Van Vucht J H N 1970 *J. Less-Common Met*. **20** 83-91
[13] Yamabe-Mitarai Y, Hara T, Miura S, Hosoda H 2006, *Maters.Trans.* **47** 650-657
[14] Yamabe-Mitarai Y, Hara T, Miura S, Hosoda H 2010, *Intermetallics* **18** 2275-2280
[15] Mahlangu R, Chauke H R and Ngoepe P E 2014 *Advanced Material Science* **1019** 385-390
[16] Chauke H R, Mashamaite M P, Modiba R and Ngoepe P E 2018 *Key Eng. Mater.* **770** 230-238

[17] Plimpton S 1995, *J Comp Phys* **117** 1-19
[18] Kresse G and Hafner J 1993 *Phys. Rev.* B **47** 558-561
[19] Kresse G and Hafner J 1994 *Phys. Rev. B* **49** 14251-14269
[20] Kresse G and Furthmüller J 1996 *Comput. Mat. Sci.* **6** 15-50
[21] Kresse G and Furthmüller J 1996 *Phys. Rev. B* **54** 11169-11186
[22] Blöchl P E 1994 *Phys. Rev.* B **50** 17953-17979
[23] Monkhorst H J and Pack J D 1976 *Phys. Rev.* B **13** 5188-5192
[24] Zhou X W, Johnson R A and Wadley H N G 2004 *Phys. Rev. B* **69** 144113(1)-144113(10)
[25] Plimpton S 1995 *J. Comp. Phys* **117** 1-19
[26] Mahlangu R, Phasha M J, Chauke H R, Ngoepe P E 2013 *Intermetallics* **33** 27-32
[27] Ren X, Miura N, Taniwaki L, Otsuka K, Suzuki T, Tanaka K, Chumlyakov Y I and Asai M 1999 *Mater. Sci. Eng*. A **273-275** 190-194
[28] Zener C 1947 *Phys. Rev.* **71** 846-851

The effect of thiol collectors on nickel-rich (110) pentlandite surface using density functional theory

P P Mkhonto[1], H R Chauke[1] and P E Ngoepe[1]

[1] Materials Modelling Centre, University of Limpopo, Private Bag x1106, Sovenga, 0727, South Africa

E-mail: peace.mkhonto@ul.ac.za, peace.mkhonto@gmail.com

Abstract. *Ab-initio* density functional theory was employed to investigate the interaction of thiol collectors on the nickel-rich pentlandite ($Fe_4Ni_5S_8$) (110) surface, in order to establish an insight into the collecting performances of SEX, SIBX and DEDTP collectors during flotation. The HOMO and LUMO energies of the three collectors were computed from DMol^3 and revealed that SIBX had the strongest ability to donate electrons, while di-Et-DTP accept electrons. Furthermore, the collecting strength of di-Et-DTP on the nickel-rich pentlandite mineral (110) surface is mostly preferred amongst the three collectors. In addition, we observed that the Fe atoms had the strongest adsorption than Ni atoms.

1. Introduction

Nickel mining is popular in over 20 countries including South Africa, contributing in various industrial applications such as stainless steel, coins and rechargeable batteries; as such the demand for nickel is ever growing [1]. Pentlandite, in particular $(Fe, Ni)_9S_8$ is a principal source of nickel [2], however the mineral occurs as intergrowth or in solid solution with pyrrhotite [3] and this makes extraction of mineral difficult. The separation of minerals can be achieved by stage-adding of organic collectors which form important role in rendering the mineral hydrophobic. The collector attach through its polar sulphur atoms to only valuable mineral particles so that water is repelled thus creating a favourable condition for the desired mineral particles to adhere to air bubbles upon collision [4]. As such the air bubbles carry the hydrophobic material (concentrates) to the pulp surface.

Although performing flotation using xanthate collectors is still a challenge, the xanthate collectors are known as low-cost, easy-to-produce collectors which usually give good flotation efficiency. The dithiophosphate are also used but were found not suitable to replace the xanthate on the flotation of pentlandite containing ore [5]. However, the dithiophosphate was found to increase the selectivity during the floatation of pentlandite when it is used as a co-collector with xanthate during flotation [6–8]. Interestingly, the mixture of SIBX and DTP collectors was shown previously to increase the recovery of nickel grades. The increase in cumulative recoveries of nickel indicated the recovery of the pentlandite [8].

In this paper, we employ first principles method to investigate the surface properties of nickel-rich pentlandite mineral, starting from the surface orientation and termination to better understand the surface reaction with SEX, SIBX and di-Et-DTP collectors. Importantly, the interaction of collectors with pentlandite during floatation is an important process to understand extraction of

mineral ore. This investigation will provides information on the collector interaction with pentlandite (110) surfaces that may be applicable to the separation of pentlandite mineral.

2. Computational methodology

In order to investigate the interaction of collectors on (110) surface of nickel-rich pentlandite mineral, we perform *ab initio* quantum-mechanical density functional theory calculations [9, 10], and analyze the density of states and Bader analysis. We use the plane-wave (PW) pseudopotential method with Perdew-Burke-Ernzerhof (PBE) exchange-correlation functional [9], using VASP code [12]. A (110) surface slab composed of four layers before relaxation and six layers after relaxation separated by a vacuum slab of 20 Å was used to mimic the interaction of the adsorbate with the repeating upper slab. The ultrasoft pseudopotential is used with a plane-wave basis set, truncated at cut-off energy of 400 eV since this was found to be sufficient to converge the total energy of the system. Brillouin zone integrations are performed on a grid of 5x5x1 k-points. This is chosen according to the scheme proposed by Monkhorst and Pack [13]. Different termination were sampled and only the less reactive (low surface energy) for (110) surfaces were considered. The surface stabilities for different termination are determined by their surface energy, calculated using equation 1:

$$E_{surface} = \left(\frac{1}{2A}\right)[E_{slab} - (n_{slab})(E_{bulk})] \quad (1)$$

where E_{slab} is the total energy of the cell containing the surface slab, n_{slab} is the number of atoms in the slab, E_{bulk} is the total energy per atom of the bulk and *A* is the surface area. A low positive value of $E_{surface}$ indicates stability of the surface termination. During adsorption the bottom two layers are kept frozen and the top four layers are allowed to interact with the oxygen molecule. The interaction strength of the surface with the adsorbate is shown by the adsorption energy, calculated by equation 2:

$$E_{adsorption} = [E_{system} - (E_{slab} + E_{collector})] \quad (2)$$

where E_{system} is the energy of the surface slab with collector, E_{slab} is the energy of the surface slab and $E_{collector}$ is the energy of the isolated collector molecule. A negative value shows a strong interaction between the adsorbate and the surface, whereas a positive value reveals the opposite.

Now, in order to calculate reaction energies, the optimization of SEX, SIBX and di-Et-DTP were calculated in a cubic cell of a = 25 Å using the same organic collectors, PAW potential, cut-off energy and other precision parameters as in the surface calculations. Further geometry optimizations of the collectors were performed with DMol^3 [14] to calculate the highest occupied molecular orbital (HOMO) and lowest un-occupied molecular orbital (LUMO) energies. These were performed using GGA-PBE functional. The double numerical plus polarisation (DNP) basis set with 4.4 Basis file was set using the DFT Semi-core Pseudopotentials, with other parameters at medium settings. The charge states of the ions at the surface were discussed on the basis of a Bader analysis, which consists of integrating the electron density in a region defined for each atom in such a way that the density gradient flux through the dividing surfaces is zero [15]. An algorithm and a program developed for this purpose by Henkelman *et al.* have been employed [16, 17].

3. Results and discussion

The nickel-rich pentlandite ($Fe_4Ni_5S_8$) (110) surface is shown in figure 1, and the designated atoms as indicated. The surface was cleaved from the optimised bulk pentlandite structure in figure 1a with space group of *Fm-3m* (225) [18]. Their calculated surface and adsorption energies are given in table 1.

Table 1. Calculated surface energy (eV/Å^2) and adsorption energies (eV) of organic collectors adsorbed on (110) nickel-rich pentlandite mineral surface metals.

Surface energy		Adsorption energies					
Surface	$E_{(surface)}$	SEX		SIBX		di-Et-DTP	
		Ni	Fe	Ni	Fe	Ni	Fe
(110)	0.122	–0.884	–1.984	–0.999	–2.126	–1.266	–2.916

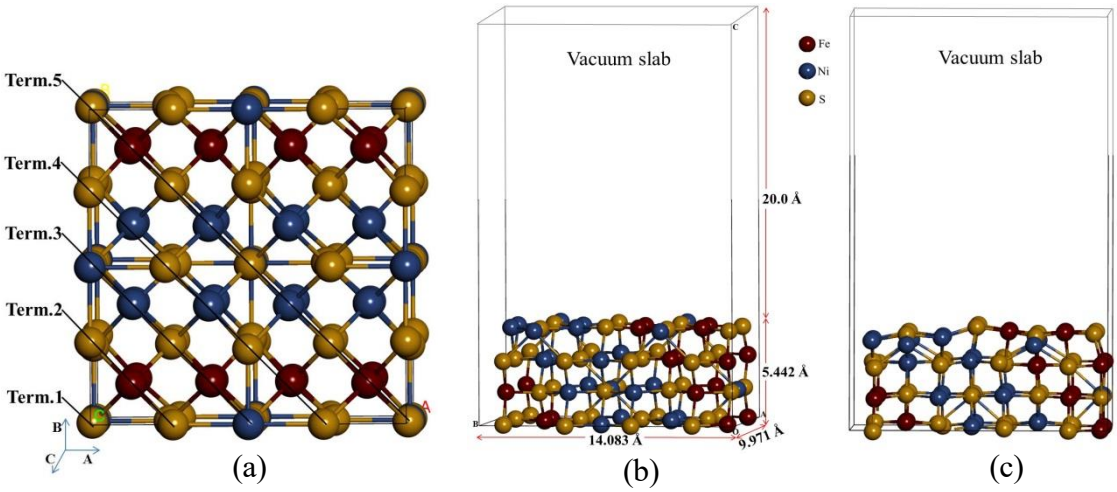

Figure 1: The $Fe_4Ni_5S_8$ pentlandite structures: (a) Convectional bulk structure showing different terminations, (b) (110) surface un-relaxed Term.3 and (c) relaxed stable term.3 surface.

Note that the bonding behavior and charge state of the clean pentlandite surface was discussed from the density of states (DOS) and Bader analysis in our previous work [19], where the DOS showed a metallic characteristic behavior since there was no energy band gap (E_g) observed at the Fermi energy (E_F).

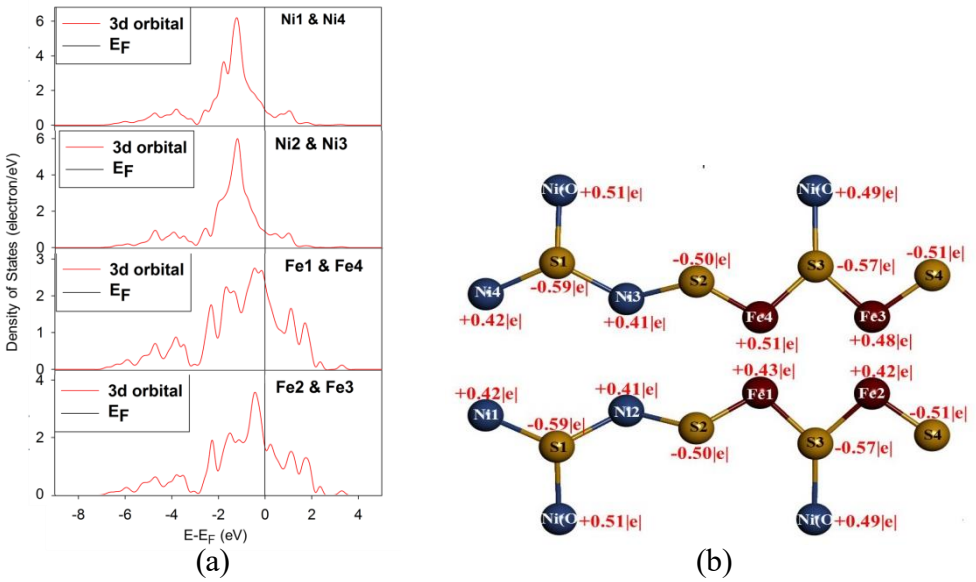

Figure 2: The $Fe_4Ni_5S_8$ pentlandite (110) surface: (a) Top Fe and Ni atoms partial density of states and (b) Bader charges for the top layer atoms.

The PDOS of Ni atoms showed only one sharp peak at the VB and less contribution at E_F, while the PDOS of Fe had broader peaks around E_F. More importantly, we noted that the E_F cuts the top of Fe 3d-orbital (high states at E_F) as shown in figure 2a. The surface relaxation had been discussed previously and we observed that the clean iron atoms were observed to have different charges. This suggested that the iron atoms are not charge ordered and there is alternation of the charges on the irons atoms (figure 2b) [19]. Now, the HOMO-LUMO energies could be significant to describe the electronic behaviour of thiol collectors prior to adsorption on the surface.

Table 2. Calculated HOMO and LUMO Energies (eV) for SEX, SIBX and di-Et-DTP, DMol^3.

	SEX	SIBX	di-Et-DTP
HOMO	–4.677	–4.674	–5.690
LUMO	–1.423	–1.420	–4.834
H–L gap	3.254	3.254	0.856

From the HOMO and LUMO energies calculated using DMol^3 we determined the gap between the HOMO-LUMO (H-L gap) shown in table 2. It has been reported that the molecule with the highest HOMO energy has the strongest ability to donate its electrons to the mineral surface and a molecule with the lowest LUMO energy has the strongest ability to accept electrons from the mineral surface [20]. Based on this report our calculated HOMO and LUMO energies indicates the order of electron donating as: SIBX > SEX > di-Et-DTP and the order of accepting electrons as: di-Et-DTP > SEX > SIBX. Thus the SIBX has the strongest electron donating while the di-Et-DTP has the strongest accepting ability. This is in accordance with the H-L gap, the smaller gap is observed for di-Et-DTP which indicates stronger interaction amongst the collectors and the order or reactivity followed as Et-DTP > SIBX = SEX.

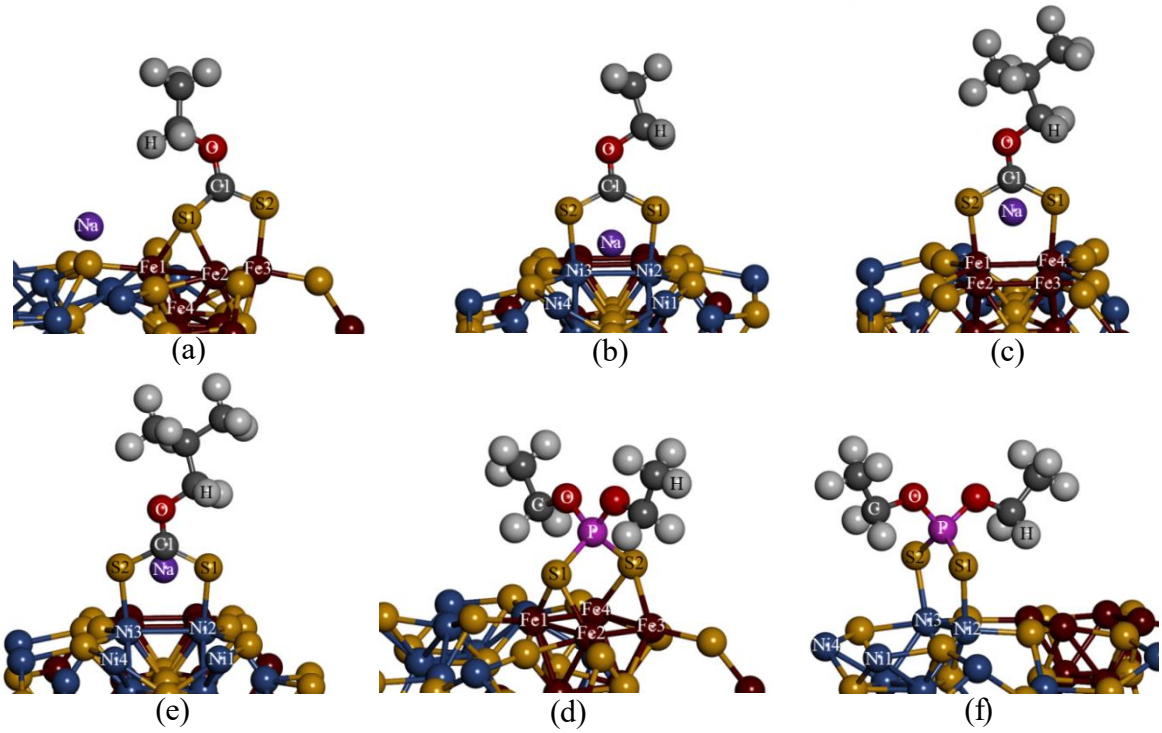

Figure 3: The geometries of xanthate and DTP adsorption on $Fe_4Ni_5S_8$ (110) surface: (a) SEX on Fe-top, (b) SEX on Ni-top, (c) SIBX on Fe-top, (d) SIBX on Ni-top, (e) di-Et-DTP on Fe-top and (f) di-Et-DTP on Ni-top.

In order to ascertain the adsorption of SEX, SIBX and di-Et-DTP on the surface, we considered the most active sites, the Ni-top and Fe-top adsorption sites. Now, when adsorbing on the nickel, we observed that the collectors adsorb and move the nickel atoms back to the upper most layer. Interestingly, we observed that SEX and di-Et-DTP ligand prefer to bridge bond on the iron atoms with the collector sulphur atoms, forming a tripodal and tetrapodal geometry, respectively (figure 3). We also observed that the di-Et-DTP is more favourable and the adsorption energies followed the order as: di-Et-DTP > SIBX > SEX for both Ni-top and Fe-top sites as shown in table 1. A clear increasing trend in adsorption energy from SEX to di-Et-DTP for both Ni-top and Fe-top was observed, which is in agreement with the H-L gap prediction. It is evident that the adsorption energy on Fe is more spontaneous than on Ni site.

4. Conclusions

The adsorption and bonding nature of SEX, SIBX and di-Et-DTP on the (110) surface were described from adsorption energies and electronic structures DFT calculations. An insight on the effect and how flotation process could be enhanced through use of thiol collectors was established. We observed that the di-Et-DTP had the strongest adsorption and more spontaneous on Fe atoms than Ni atoms. Furthermore, we observed that SEX and di-Et-DTP prefer to form a tripodal and tetrapodal geometry on the surface, respectively. These findings suggest that the use of SIBX as collector and di-Et-DTP as co-colletor may improve the floatability of the pentlandite. This investigation provides information on the adsorption mechanism strength of xanthates on pentlandite (110) surfaces that may be applicable to the separation of pentlandite mineral.

Acknowledgements

The calculations were performed at the Materials Modelling Centre (MMC), University of Limpopo. We acknowledge the Centre for High Performance Computing (CHPC) for computing resources, the Department of Science and Technology (DST) and South African Mineral to Metals Research Institute (SAMMRI) for financial support.

References

[1] Ngobeni W A and Hangone G 2013 The effect of using sodium di-methyl-dithiocarbamate as a co-collector with xanthates in the froth flotation of pentlandite containing ore from Nkomati mine in South Africa. *Miner. Eng.* **54** 94–99

[2] Borodaev Yu, Bryzgalov S I A, Mozgova N N and Uspenskaya T 2007 Pentlandite and Co-Enriched Pentlandite as Characteristic Minerals of Modern Hydrothermal Sulfide Mounds Hosted by Serpentinized Ultramafic Rocks (Mid-Atlantic Ridge). *Vestnik Moskovsk Universiteta. Geologiya* **62** 85–97

[3] Rajamani V and Prewitt C T 1973 Crystal chemistry of natural pentlandites. *Can. Mineral.* **12** 178–187

[4] www.jmeech.mining.ubc.ca/MINE290/Froth%20Flotation.pdf. (2012, october 20)

[5] Ngobeni W and Hangone G 2013 The effect of using pure thiol collectors on the froth flotation of pentlandite containing ore. *South Africa. J. Chem. Eng.* **18** 41–50

[6] Bradshaw D J, Buswell A M, Harris P J and Ekmekci Z 2005a Interactive effect of the type of milling media and copper sulphide addition on the flotation performance of sulphide minerals from Meresky ore part 1: pulp chemistry. *Int. J. Miner. Process.* **78** 164–174

[7] Nashwa V M 2007 *The flotation of high talc-containing ore from the great Dyke of Zimbabwe.* Pretoria, South Africa: University of Pretoria

[8] Nyambayo C K 2014 *The use of mixed thiol collectors in the flotation of Nkomati sulphide ore.* Cape Town, South Africa: University of Cape Town

[9] Hohenberg P and Kohn W 1965 Inhomogeneous electron gas. *Phys. Rev. B* **136** 864–871

[10] Kohn W and Sham L J 1965 Self-consistent equations including exchange and correlation effects. *Phys. Rev.* **140** 1133–38

[11] Perdew J P, Burke K and Ernzerhof M 1996 Hybrid functionals based on a screened coulomb potential. *J. Chem. Phy.* **118** 8207–15
[12] Kresse G and FurthermÜller J 1996 Efficient iterative schemes for ab-initio total-energy calculations using a plane-wave basis set. *Phys. Rev. B* **54** 11169–186
[13] Monkhorst H F and Park J D 1976 Special points for Brillouin-Zone integrations. *Phys. Rev. B* **13** 5188–92
[14] Delley B 2000 Density Functional Theory Electronic Structure Program. *J. Chem. Phys. 113*, 7756
[15] Bader R F W Atoms in Molecules: A Quantum Theory, Oxford University Press: London, UK, 1994
[16] Sanville E, Kenny S D, Smith R and Henkelman G 2007 An improved grid-based algorithm for Bader charge allocation. *J. Comput. Chem.* **28** 899–908
[17] Henkelman G, Arnaldsson A and Jonsson H 2006 A fast and robust algorithm for Bader decomposition of charge density. *Comput. Mater. Sci.* **36** 354–360
[18] Geller S 1962 Refinement of the crystal structure of Co9S8. *Acta Crystallogra.* **15** 1195–98
[19] Mkhonto P P, Chauke H R and Ngoepe P E 2015 Ab initio studies of O2 adsorption on (110) nickel-rich pentlandite (Fe4Ni5S8) mineral surface. *Miner.* **5** 665–678
[20] Liu G, Wang Y, Yuan L, Xu Z, Lu Y, Zeng H and Zhong H 2012 A DFT study on the flotation performance of thiol collectors for coper sulphide flotation. *xxvi International Minerals Processing Congress (IMPC)* 02947–02958 New Delhi India

Gas-Sensing Properties of TiO_2 Nanoparticles Double Doped with Ag and Cu

OO Nubi[1] **and TE Mosuang**
Department of Physics, University of Limpopo, South Africa

E-mail: olatunbosun.nubi@ul.ac.za

Abstract. Nanometric powders of titanium dioxide TiO_2 were prepared by the sol-gel synthesis of titanium isopropoxide. With Ag and Cu as dopants, single and double-doped samples, at doping levels of 5% molar weight, were achieved. In addition, undoped samples were also prepared. The samples were dried in air at 100°C and post annealing was done at 300°C and 900°C, in order to obtain the anatase and rutile polymorphs respectively. The changes in the electrical conductivities of representative anatase and rutile TiO_2 nanopowders upon exposure to water-vapour, ammonia (NH_3) and hydrogen (H_2) were then investigated. Sensing measurements for water-vapour was done at room temperature for various humidity levels ranging from 5.4% RH to 88.4% RH. The detection of NH_3 and H_2 gases were carried out at temperatures extending from room temperature to 350°C and over concentration ranges of 25 sccm to 500 sccm and 15 sccm to 200 sccm respectively. The gas-sensing results show that the sol-gel fabricated TiO_2 nanoparticles (particularly in anatase form), has excellent fast and stable dynamic responses to humidity, NH_3 and H_2. They feature good sensitivities, even at low operating temperatures. However, acceptor behaviour, for which there was a conductivity switch from n-type to p-type, was recorded for the Ag-doped rutile powders at operating temperatures of 300°C and 350°C. Overall, the double-doped sample annealed at 300°C was deemed the most promising candidate for gas-sensing.

1. Introduction

The design and fabrication of gas sensors has become one of the most active research fields. Several crystallographic structures, including TiO_2, have been found to be useful as gas sensing materials. Extensive studies of the electric, magnetic, catalytic and electrochemical properties of Titanium dioxide (TiO_2 or Titania) have been conducted by various researchers [1-7].

Humidity and other gases present in a working environment can be highly variable in accordance with several factors. The ability to monitor and control these environments is therefore highly desirable – whether it is for human comfort, storage of various goods or industrial process control. [8]

The usual polymorphs of TiO_2 differ in crystallographic structure – tetragonal anatase and rutile, and orthorhombic brookite – and this difference can exert influences on the sensing properties of TiO_2 based devices [9].

This work attempts to demonstrate the advantage of single or double doping of TiO_2 nanoparticles with Ag and Cu, in gas sensing applications. The response of the TiO_2 species to NH_3 and H_2 presented here serves as a case study for reducing gases.

2. Experimental

2.1. *Synthesis*

Aldrich's reagent-grade precursors, namely $Ti\{OCH(CH_3)_2\}_4$ (Titanium (IV) Isopropoxide), $AgNO_3$ and $CuCl_2$, were used, via the sol–gel route, to prepare the anatase and rutile TiO_2 nanocrystalline samples. Dopant salts were first dissolved in water. This was followed by adding ethanol to the required amount of each dissolved precursor. The dopant solution was then added, in drops, to the Titanium Isopropoxide, while vigorously stirring for 1 hour. The precipitate (xerogel) formed was further diluted with 30 ml water, filtered and left to dry at room temperature for 16 hours. Further drying of the samples was done at 100ºC for 1 hour before being ground to powders. At 5 wt% impurity levels, the undoped (–/TiO_2), single-doped (Ag/TiO_2, Cu/TiO_2) and double-doped (Ag+Cu/TiO_2) species were annealed at temperatures of 300ºC (anatase) and 900ºC (rutile) for one hour [10].

2.2. *Characterisation*

A dynamic computer-automated gas sensing system, KSGAS6S by Kenosistec, Italy, was used. The system is equipped with a 500 ml sensing chamber that accepts a total gas flow rate of 500 sccm. The gas sensing performances of the prepared TiO_2 nanoparticles were tested at various operating temperatures, namely Room (20.8ºC ~ 28.0ºC), 250ºC, 300ºC and 350ºC, and toward ammonia (NH_3) and hydrogen (H_2) gases, as well as ten humidity levels (between 5.4% RH and 88.4% RH).

Calculations for the performance indices (Sensitivity, Response Time and Recovery Time) of each powder, when exposed to various concentrations of the intervening gas, were carried out. The response and recovery times are respectively defined as the times the impedance takes to decline to 10% of its saturation value from the baseline, when the gas is introduced, and to recover 90% of its final value when the flux of air is restored. The sensor sensitivity S (%), was measured by comparing the impedance of the sensor in air R_{air} to that in the target gas R_{gas} using the equation $S\ (\%) = \frac{R_{air}-R_{gas}}{R_{gas}} \times 100$. The calculations also include estimates of baseline drifts, which were calculated as the percentage increase or decrease of the resistance before the gas was introduced for the last time, as compared to the first "gas-out" resistance. Thus the Fractional Baseline Drift, D is given by $D = \frac{R_f - R_i}{R_i} \times 100\%$. This parameter serves as a rough indication of the ability of the sensor material to restore its initial properties (particularly the resistance) after being repeatedly exposed to pulses of increasing gas concentration. Positive values indicate resistances higher at the last "gas-out" than at the first.

3. Results and discussion

3.1. Sensor Response to Humidity (H_2O)

The dynamic response of the prepared undoped anatase –\$TiO_2$ sensor to humidity levels ranging from 5% RH to 88% RH, and measured at room temperature, is presented in Figure 1. The corresponding performance indices are shown in Table 1. The profiles for the doped samples (Ag\$TiO_2$, Cu\$TiO_2$ and Ag+Cu\$TiO_2$) are very similar but with much higher impedances than the undoped –\$TiO_2$ (Figure 2). Consistent with other findings, the doping of TiO_2 improves its gas sensing capabilities [11]. In particular, faster responses were recorded for Ag and Cu doped materials [12].

All powders show reversible and reproducible response to all humidity levels with some short-term stability over several minutes of measurement. Generally, there is a systematic decrease in the measured resistances of sensor material as the intervening "gas" (humidity) is introduced ("gas-in"). Upon withdrawing the gas ("gas-out") 5 minutes later, an increase in the resistance is observed. However, it is apparent that more than 5 minutes is needed to obtain stabilised responses (constant resistance) in gas flow of constant humidity level. Adsorption or desorption processes on the surface of the sensor material can therefore not be fully accounted for with the available data.

Figure 3 displays TiO_2 nanopowder sensor characteristics, featuring the performance indices of Sensitivity, Response Times and Recovery Times. The sensitivity S is found to increase exponentially ($S = 0.62e^{0.06c}$ in the case of the undoped –\TiO_2 powder) as the humidity level/concentration c increases (Figure 3 (a)). This implies that at low concentrations a change in concentration leads to a small response, whereas at higher concentrations, the same change yields a relatively larger response.

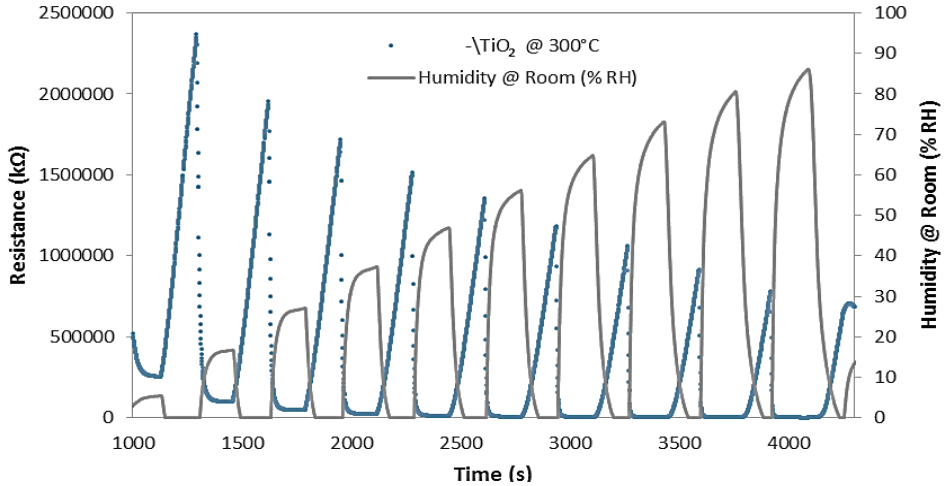

Figure 1. Dynamic response of the undoped anatase –\TiO_2 nanopowders annealed at 300°C, when exposed to various room-temperature humidity levels (5.4% RH – 86.1% RH).

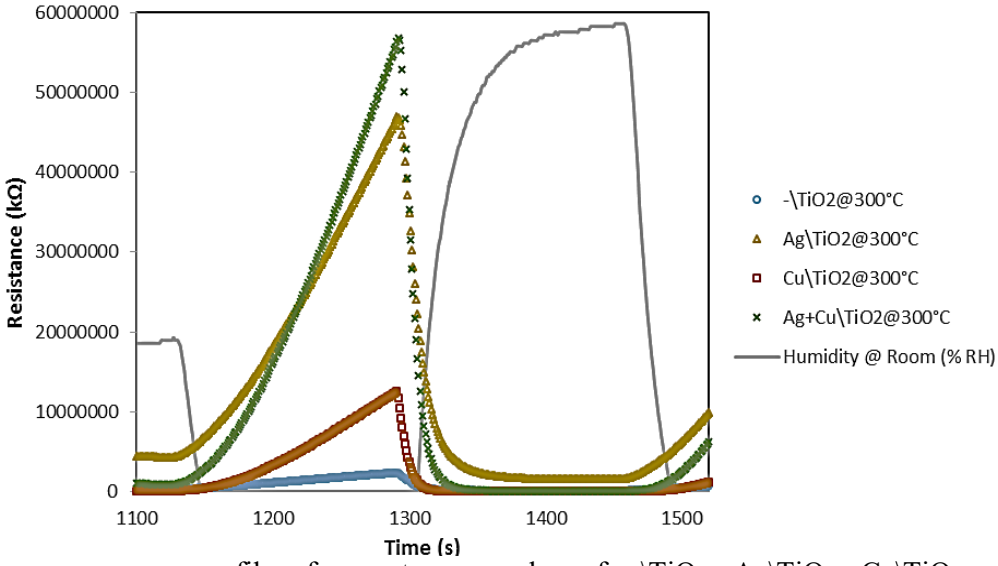

Figure 2. Response-recovery profiles for anatase samples of –\$TiO_2$, Ag\$TiO_2$, Cu\$TiO_2$ and Ag+Cu\$TiO_2$, annealed at 300°C and exposed to room-temperature humidity of 16.7% RH.

Table 1. Performance indices of the undoped anatase –\TiO_2 sample (annealed at 300ºC) that was exposed to various levels of humidity at room temperature.

Humidity (% RH)	Sensitivity	Response Time (s)	Recovery Time (s)	Baseline Drift (%)
5.5	8.38	440.22	530.21	
16.7	18.62	74.71	526.61	
27.1	35.74	62.12	540.09	
37.3	68.39	52.23	548.22	
46.9	129.09	47.73	553.61	
56.2	227.35	44.10	555.43	-66.91
64.8	371.60	40.51	562.62	
73.1	560.25	35.11	566.25	
80.6	795.81	32.41	570.73	
86.1	1105.21	28.81	592.33	

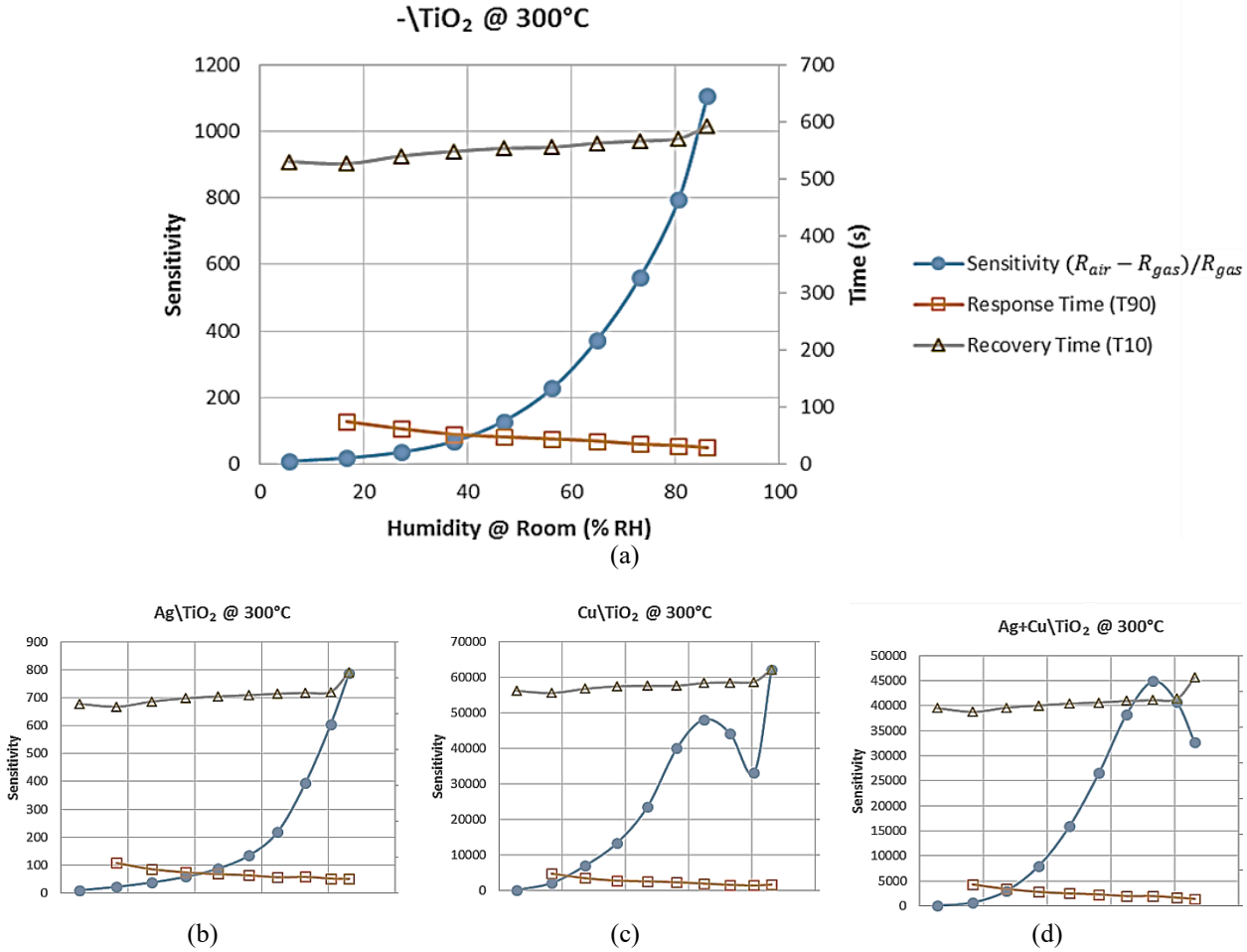

Figure 3. Sensor characteristics of the prepared gas sensors based on (a) the undoped –\$TiO_2$, (b) Ag\$TiO_2$, (c) Cu\$TiO_2$ and (d) Ag+Cu\$TiO_2$. The anatase nanopowders (annealed at 300°C) were exposed to various humidity levels (5.4% RH – 86.1% RH) and measured at room temperature.

In spite of the inflexion in the trend, the Cu-doped sample shows the highest sensitivity levels. Ag\$TiO_2$, on the other hand, was not as sensitive as –\$TiO_2$. The combined influence of Ag and Cu impurities can be observed for the double-doped Ag+Cu\$TiO_2$. Here, the sensitivity levels are above those of Ag\$TiO_2$, but not as high as those of Cu\$TiO_2$. Where the response time is following a decreasing trend in the concentration evolution, the recovery tends to increase, and vice versa.

The dynamic responses of the rutile powders (Figure 4) are not as well-defined as those of the anatase samples, particularly in cases where Cu impurities are present. The impedances, as well as the sensitivities, of the rutile samples are also higher by several orders of magnitude. However, the sensitivities of the undoped and Ag-doped (whether anatase or rutile) still remained fairly exponential. Further, the Ag impurities appear to reduce the sensitivity to humidity, in the case of anatase TiO_2, but improved the parameter in the rutile counterpart. It turns out that the anatase samples are generally better suited for detecting humidity, in terms of reliability, repeatability and stability, but the undoped and Ag-doped rutile TiO_2 have superior performance indices (higher sensitivities, shorter response and recovery times).

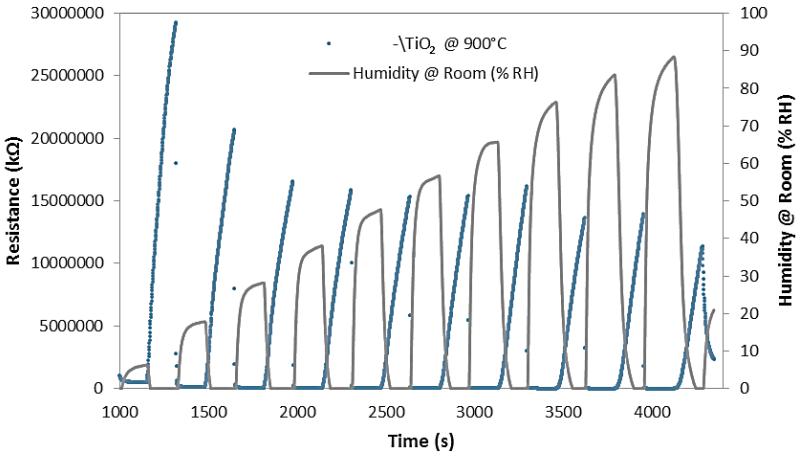

Figure 4: Dynamic response of prepared gas sensors based on undoped rutile –\TiO_2 (annealed at 900°C), when exposed to various room-temperature humidity levels (5.4% RH – 86.1% RH).

3.2. Sensor Response to Ammonia Gas (NH_3)

As it was in the case of humidity, the rutile samples registered higher impedances (over the anatase counterpart) but failed to exhibit discernible dynamic response profiles at certain operating temperatures. Notable are, Ag\$TiO_2$ and Cu\$TiO_2$ at room temperature and at 250ºC, as well as Ag+Cu\$TiO_2$ at 350ºC. In operating environments where temperatures may range between room temperature and 300ºC, the anatase powders will be suitable as sensor material for detecting NH_3, the optimal being the Cu\$TiO_2$. For higher temperatures (at least up to 350ºC) the undoped –\$TiO_2$, in its rutile form, will suffice. The rutile samples not only feature higher impedances over the anatase counterparts, but also higher sensitivities.

3.3. Sensor Response to Hydrogen Gas (H_2)

In mixed phase TiO_2 nanomaterials, the predominance of rutile in anatase-rutile mixture has been found to result in increased sensitivity towards hydrogen [13]. In this investigation however, the rutile samples continue to display responses that, collectively, are below par when compared with those of their anatase counterpart. If the temperature limitation of 300ºC is not an inhibiting factor, then the undoped –\$TiO_2$ rutile powder will be suitable as a sensor material for H_2. The next best performance is observed for the single-doped Cu-impregnated sample (Cu\$TiO_2$). (It has been shown elsewhere [14] that Cu promoted rutile formation.) To cover the entire range from "Room" to 350ºC, the only sample that can be utilised for sensing hydrogen gas is the undoped –\$TiO_2$.

Ag-doped TiO_2 sensors have shown good sensitivities at different concentration hydrogen atmospheres. [15]. The nanomaterial however falls short, when compared with the Cu counterparts in this study.

3.4. *Discussion*

Over three-quarters of the gas-sensing cases investigated here (particularly the anatase species) show excellent fast and stable dynamic responses to humidity, NH_3 and H_2. They feature good sensitivities, even at a low operating temperatures. To deduce the best overall performance for each intervening gas, and at the four operating temperatures, the performance indices of samples were combined. The anatase TiO_2 display more pronounced gas sensing abilities over the rutile. This can be ascribed to the morphological characteristics of the two material categories. Anatase TiO_2 is characterised by a smaller crystallite sizes relative to the rutile powders [10]. This implies higher surface area to volume ratio for anatase and consequently, a greater surface activity over rutile [16].

For the majority of samples tested, the measured resistances decrease upon interacting with the reducing gases – a typical behaviour for *n*-type semiconductors. This is because, the gases act as a reducing agent for the metal-oxide. The process involves the extraction of electrons from its conduction

band by the adsorbed oxygen species at the surface of the semiconductor. In other words, the chemisorbed oxygen species trap free electrons on the surface of the grains which results in a build-up of a negative surface charge. This in turn creates an energetic barrier in the conduction band which electrons must overcome in order to cross to the next grain. When the desired concentration of the target gas is introduced, the gas then reacts with the adsorbed oxygen. This leads to the freeing of previously trapped electrons (i.e. a reduction in the amount of bound surface charge), thereby decreasing the *n*-type carrier content and lowering the barrier potential. Thus, the resistivity decreases in the presence of a reducing gas, owing to electron transfer into the conduction band [17].

However, acceptor behaviour, for which there was a conductivity switch from *n*-type to *p*-type [10], was recorded for the Ag-doped rutile samples (Ag\TiO_2) at operating temperatures of 300ºC and 350ºC. In these cases, it is believed that the Ag dopant impurities modify the electronic structure of TiO_2 and form localised acceptor levels in the forbidden band gap. This leads to the increase in the electron concentration and the decrease in the electrical resistance over a low-to-medium temperature range [16]. The discussion here is only qualitative since generally, the energetic barrier is not constant but changes with varying temperature [17], thereby rendering the temperature dependencies more complicated.

4. Conclusions

According to the estimates provided, to sense water vapour (at room temperature) the anatase Cu\$TiO_2$ comes out on top. NH_3 and H_2 are best detected using undoped rutile –\$TiO_2$, for temperatures ranging from "Room" to 350ºC and probably beyond. Where specific operating temperatures (except at temperatures exceeding 300ºC) are required in applications, the anatase powders remains generally preferred. Otherwise, the rutile samples may come into play. It is also important to note that the double-doped Ag+Cu\$TiO_2$ sample that was annealed at 300ºC, showed better promise in detecting water-vapour, NH_3 and H_2 at various temperatures, over other powders.

Acknowledgements

Gratitude is hereby extended to NRF, IBSA and the University of Limpopo for financial support, and CSIR's Centre for Nanostructured Materials for experimental resources.

References

[1] Mo S-D and Ching W Y 1995 *Phys. Rev.* B **51** 19
[2] Yu J-G, Yu J C, Cheng B, Hark S K and Iu K 2003 *J Solid State Chem.* **174**, 372–380
[3] Shimizu Y 2002 *Chem. Sens.* **18**, no. 2, 42–54
[4] Carney C M, Yoo S and Akbar S A 2005 *Sens. Act. B* **108**, no. 1 29–33
[5] Benkstein K D and Semancik S 2006 *Sens. Act. B,* **113**, no. 1, 445–453
[6] Yadav B C, Shukla R K and Bali L M 2005 *Indian J. Pure Appl. Phys.* **43**, 51
[7] Barsan N, Koziej D and Weimar U 2007 *Sens. Act. B* **121**, 18–35
[8] Fine G F, Cavanagh L M, Afonja and Binions R 2010 *Sensors* **10**, 5469–5502
[9] Alivisatos A P 1996 *J. Phys. Chem.* **100**, no. 31, 13226–13239
[10] Nubi O O, Rammutla K E, Mosuang T E 2016 *Adv. Sci. Lett.* **22**, no. 4, 889–895
[11] Su P G, and Huang L N 2007 *Sens. Act B,* **123**, 501–507
[12] Zare A H and Mohammadi S 2011 *Mater. Sci. Eng.* **17**, 012015
[13] Zakrzewska K and Radecka M 2017 *Nanoscale Res. Lett.* **12**, no. 1, 89
[14] Teleki A, Bjelobrk N and Pratsinis S E 2008 *Sens. Act. B* **130**, 449–457
[15] Hamdan H H, Mohammed G H 2016 *Int. J. Sci. Res.* **5** no. 2, 2224–2233
[16] Garzella C, Comini E, Tempesti E, Frigeri C and Sberveglieri G 2000 *Sens. Act. B* **68**, 189–196
[17] Haidry A A, Schlosser P, Durina P, Mikula M, Tomasek M, Plecenik T, Roch T, Pidik A, Stefecka M, Noskovic J, Zahoran M, Kus P and Plecenik A 2011 *Cent. Eur. J. Phys.* **9**, 1351–1356

Investigation of the magnetic ground state of $PrRu_2Ga_8$ compound

Michael O. Ogunbunmi and André M. Strydom*

Highly Correlated Matter Research Group, Physics Department, University of Johannesburg, P. O. Box 524, Auckland Park 2006, South Africa.

E-mail: amstrydom@uj.ac.za

Abstract. We have investigated the ground state properties of the orthorhombic structure compound $PrRu_2Ga_8$ through electronic and magnetic properties studies. The compound crystallizes in the $CaCo_2Al_8$-type structure, belonging to space group *Pbam* (No. 55). The temperature dependence specific heat shows a λ-type anomaly at $T_N = 3.3$ K, indicating a bulk phase transition probably of antiferromagnetic origin. At the Néel temperature T_N, the entropy approaches the value of 4.66 J/mol.K which is about 0.8Rln(2), where R is the universal gas constant. The analysis of the low temperature specific heat gives $\gamma = 46$ mJ/mol.K^2. The temperature dependence DC magnetic susceptibility $\chi(T)$ confirms the anomaly at 3.3 K and follows the Curie-Weiss law for temperatures above 50 K, with the calculated effective magnetic moment, $\mu_{\text{eff}} = 3.47(2)\ \mu_B$/Pr and Weiss temperature $\theta_p = -7.80(1)$ K. This effective magnetic moment value is in good agreement with the Hund′s rule theoretical free-ion value of 3.58 μ_B for Pr^{3+}. The electrical resistivity data also shows an anomaly at T_N and a broad curvature at intermediate temperatures probably due to crystalline electric field (CEF) effects. The Pr^{3+} in this structure type has a site symmetry of C_s which predicts a CEF splitting of the $J = 4$ multiplet into 9 singlets and thus rule out in principle the occurrence of spontaneous magnetic order. In this article we discuss the magnetic order in $PrRu_2Ga_8$ in line with an induced type of magnetism resulting from the admixture of the lowest CEF level with the first excited state.

1. Introduction

The PrT_2X_8 [T = Fe, Co, Ru, Rh; X=Al, Ga, In] family of compounds are quasi-skutterudites which crystallize in the orthorhombic $CaCo_2Al_8$-type structure with *Pbam* space group (No. 55) [1]. The structure of this family of compounds consists of caged network of atoms and belongs to a class of largely unexplored rare-earth intermetallic compounds. The Pr and T atoms in this structure form a chain parallel to the c-axis and are both separated by the Ga atoms. The Pr^{3+} ion has a site symmetry of monoclinic C_s in the crystal structure and as a consequence, the CEF splitting of the J= 4 multiplet results in 9 singlets [2, 3]. In such systems, the ground state is expected to be a Γ_1 singlet as dictated by Pr^{3+} site symmetry. Hence, the occurrence of spontaneous magnetic order in this family especially where the rare-earth site symmetry predicts a singlet ground state is unexpected. However, recent experimental studies have revealed that in exceptional cases, systems predicted to have a Γ_1 singlet ground state eventually show a magnetic ordering at low temperatures [3–10]. Magnetism in these systems are largely attributed to induced moment magnetism due to the overcritical exchange interactions between the ground state singlet and the first excited state. In this article, we

Table 1. Crystallographic parameters of $PrRu_2Ga_8$ and $LaRu_2Ga_8$ obtained from the Rietveld refinements.

Compound	$PrRu_2Ga_8$	$LaRu_2Ga_8$
Space group	*Pbam* (No. 55)	*Pbam* (No. 55)
a (Å)	12.607(3)	12.65(3)5
b (Å)	14.713(3)	14.715(5)
c (Å)	4.1010(2)	4.112(2)
V (Å^3)	760.68 (4)	766.90 (1)
R_p(%)	6.443	5.610
R_{wp}(%)	8.392	8.237

present results of our investigation on the nature of the ground state in $PrRu_2Ga_8$ compound, the crystal structure of which was first announced by Schlüter and Jeitschko [1].

2. Experimental methods and crystal structure

Polycrystalline samples of $PrRu_2Ga_8$ and $LaRu_2Ga_8$ were prepared by arc melting stoichiometric amounts of Pr, La, Ru and Ga (4N) in an Edmund Bühler arc furnace by a method described in ref. [3]. Room temperature powder X-ray diffraction (XRD) was recorded using a Rigaku Smartlab diffractometer with Cu-K_α radiation. The observed pattern for both samples correctly match that of the *Pbam* space group and no impurity phases were observed within the resolution limit of the instrument. A Rietveld refinement [11] using Fullprof prgram [12] was carried out on the patterns collected and the lattice parameters obtained are presented in Table 1 which are consistent with earlier reports [1, 3, 13]. The Rietveld refinement of the XRD pattern of $PrRu_2Ga_8$ is shown in Fig. 1. In this structure, the shortest Pr-Pr separation is 4.080 Å (about 26% greater than the sum of two Pr ionic radii), Pr-Ga is 3.123 Å (about 7% greater than the sum of their ionic radii) and Pr-Ru is 3.101 Å (about 7% greater than the sum of their ionic radii). In view of this, the structure of $PrRu_2Ga_8$ therefore resembles those of other caged compounds where the Pr atom is enclosed in an oversized cage network formed by Ru-Ga atoms. As stated above, the shortest Pr-Pr separation in the structure which is $\sim$ 26% is greater than the separation between the sum of two Pr ionic radii suggests that the Pr atoms are weakly bonding or may be out of reach of direct magnetic exchange due to no direct orbital overlap. A possible consequence of this will be the suppression of the magnetic transition temperature in systems with a magnetic order parameter in the ground state.

Magnetic properties have been measured using the Magnetic Property Measurement System (Quantum Design Inc. San Diego) between 1.9 K and 300 K with an external magnetic field up to 7 T. The electrical resistivity measurement from 300 K down to 1.9 K was taken using the conventional four probe DC method with contacts made using a spot welding equipment. Specific heat was measured using the quasi-adiabatic thermal relaxation method down to 0.4 K. Both the electrical resistivity and specific heat were measured using the Physical Property Measurement System also from Quantum Design.

3. Magnetic properties

The temperature dependence of magnetic susceptibility $\chi(T)$ of $PrRu_2Ga_8$ measured between 1.9 and 300 K is presented in Fig. 2. For temperatures above 50 K, $\chi(T)$ could be fitted to the Curie-Weiss expression given by; $\chi = N_A\mu_{\rm eff}^2/(3k_B(T-\theta_p))$, where $\mu_{\rm eff}$ and θ_p are the effective magnetic moment and Weiss temperature respectively, N_A is the Avogadro's number and k_B is the Boltzmann's constant. Values of $\mu_{\rm eff} = 3.47(2)\ \mu_B$ and $\theta_p = -7.80(1)$ K are

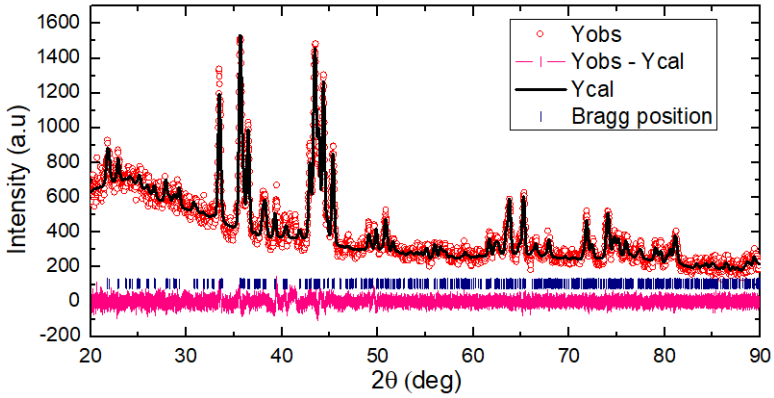

Figure 1. Experimentally observed X-ray diffraction pattern of $PrRu_2Ga_8$ (red circle) along with a Rietveld refinement profile (black line) based on the *Pbam* space group. The Bragg peaks are shown as blue vertical bars.

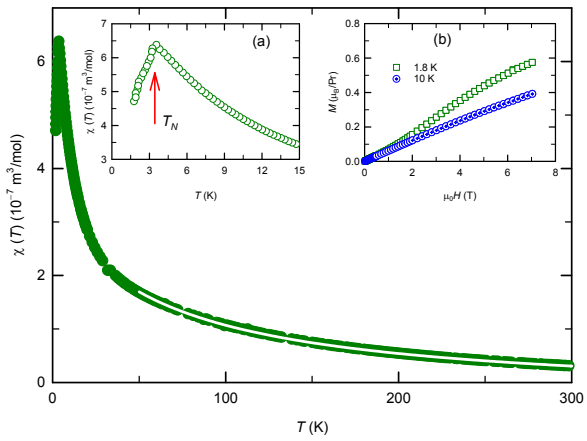

Figure 2. Temperature dependence of magnetic susceptibility $\chi(T)$ of $PrRu_2Ga_8$ together with a Curie-Weiss fit (white-solid line). Inset (a): Low-T of $\chi(T)$ showing an antiferromagnetic ordering at $T_N = 3.3$ K. (b): Isothermal magnetization of $PrRu_2Ga_8$ at 1.8 K and 10 K.

obtained from the least-squares fit. The value of μ_{eff} obtained is fairly reconcilable to the value of $g_J\sqrt{J(J+1)}\mu_B = 3.58\ \mu_B$ expected for a free Pr^{3+} ion. At ~ 3.3 K, $\chi(T)$ develops an anomaly signalling a phase transition possibly of antiferromagnetic origin. The low temperature region of $\chi(T)$ is expanded in inset (a) with the magnetic transition at T_N indicated by the arrow. In inset (b), the isothermal magnetization $M(B)$ of $PrRu_2Ga_8$ is presented in fields up to 7 T. At 1.8 K, an upward curvature in $M(B)$ is seen near 2 T, while closer to 7 T the curvature turns slightly downward again mimicking saturation. The origin of these features are not immediately clear but appears to be matamagnetic in nature. The behaviour of $M(B)$ in 10 K however follows a quasi-linear dependence with fields.

4. Specific heat

The temperature dependence of specific heat $C_p(T)$ of $PrRu_2Ga_8$ and that of the nonmagnetic reference compound $LaRu_2Ga_8$ is presented in Fig. 3. In inset (a), the low temperature $C_p(T)$ of $PrRu_2Ga_8$ and $LaRu_2Ga_8$ together with the electronic contribution to specific heat

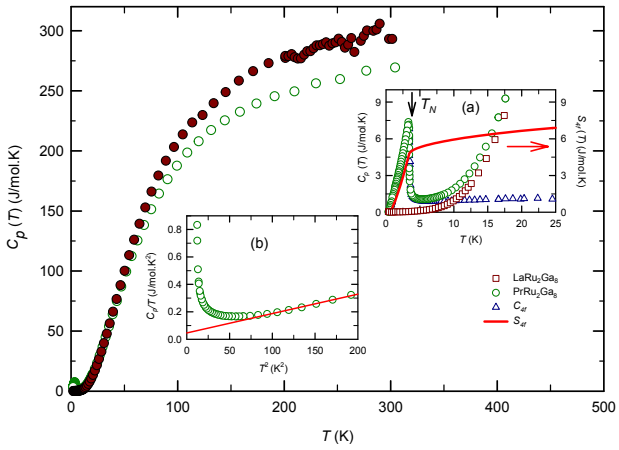

Figure 3. Temperature dependence of specific heat $C_p(T)$ of $PrRu_2Ga_8$ and $LaRu_2Ga_8$. Inset (a): Low-T $C_p(T)$ of $PrRu_2Ga_8$ and $LaRu_2Ga_8$, electronic contribution to specific heat $C_{4f}(T)$ and the magnetic entropy $S_{4f}(T)$. (b): Plot of C_p/T against T^2 together with a Debye fit (red-solid line).

$C_{4f}(T)$ obtained by subtracting the specific heat of $LaRu_2Ga_8$ from that of the main compound $PrRu_2Ga_8$ and the calculated entropy $S_{4f}(T)$ are shown. A λ-type anomaly at $T_N \approx 3.3$ K is clearly indicated by the arrow in the figure for both $PrRu_2Ga_8$ and $C_{4f}(T)$ data indicating a bulk phase transition. $S_{4f}(T)$ is calculated using the expression; $S_{4f}(T') = \int_0^{T'} C_{4f}(T)/TdT$. The value of the entropy around T_N is 4.66 J/mol.K which is $\simeq$ 80% of Rln(2) expected for a doublet ground state. We note however that the full doublet entropy is only released at about 8 K. The estimation of $C_{4f}(T)$ was only carried out up to about 24 K, above which the phonon specific heat dominates. Within this temperature range, a plot of $C_{4f}(T)/T$ against T^2 based on the expression $C_{4f}(T)/T(T \longrightarrow 0) \equiv \gamma$, was found not to be an increasing function of T which consequently renders the extraction of the electronic Sommerfeld coefficient, γ from $C_{4f}(T)$ difficult in the present case. We have therefore used the total specific heat in the estimation of γ as presented in inset (b) of Fig. 3 based on the expression $C_p/T = \gamma + \beta T^2$ and $\beta = 12\pi^4 nR/(5\theta_D^3)$, where n and R are the number of atoms and Universal gas constant respectively. From the least-squares fit, a value of $\gamma = 46.04(3)$ mJ/mol.K^2 and Debye temperature $\theta_D = 248.1(2)$ K are obtained. The γ value obtained here is slightly enhanced compared to that found for ordinary metals which could be due to moderate heavy-electron-like behaviour in the system. The Sommerfeld coefficient γ has a direct relationship with the mass of the quasiparticles in a metal at low temperatures and it gives an idea about their degree of mass enhancement. We note that in a similar iso-structural compound $PrCo_2Ga_8$ [14], an enhanced quasi-particle mass behaviour has been observed while on the other hand, iso-structural aluminides compounds like $PrFe_2Al_8$ and $PrCo_2Al_8$ [3, 13] have been reported to have γ values in the range of ordinary metals ($\approx$ 10 mJ/mol.K^2).

5. Electrical Resistivity

The temperature dependence of electrical resistivity $\rho(T)$ of $PrRu_2Ga_8$ and $LaRu_2Ga_8$ measured between 1.9 and 300 K is presented in Fig. 4. $LaRu_2Ga_8$ shows a typical metallic behaviour from room temperature down to low temperatures with residual resistivity ratio (RRR) of 15.47. $\rho(T)$ of $PrRu_2Ga_8$ shows a broad curvature at intermediate temperatures and an anomaly indicating a phase transition at $T_N \approx 3.3$ K. The RRR of ≈ 6 is observed which is lower compared to that of $LaRu_2Ga_8$. However, the RRR of both compounds suggest a reasonable good crystalline

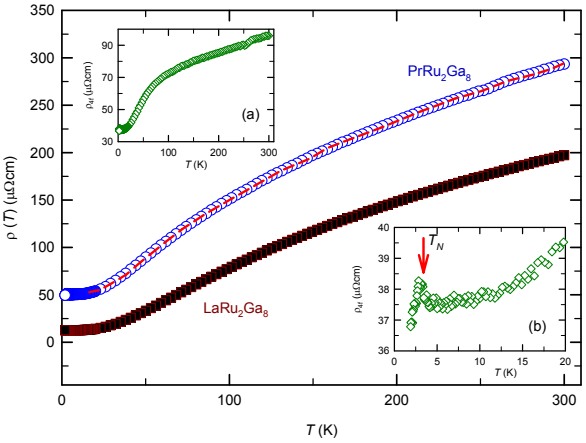

Figure 4. Temperature dependence of electrical resistivity $\rho(T)$ of $PrRu_2Ga_8$ and $LaRu_2Ga_8$. The red-dashed line is a BGM fit described in the text. Inset (a): Electronic contribution to resistivity $\rho_{4f}(T)$. (b): Low-T of $\rho_{4f}(T)$ with an arrow indicating $T_N = 3.3$ K.

quality. Furthermore, for temperatures above 10 K, $\rho(T)$ of $PrRu_2Ga_8$ was fitted to the Bloch-Grüneissen-Mott (BGM) model [15] as indicated by the red-dashed line. The BGM expression is given by;

$$\rho(T) = \rho_0 + \frac{4K}{\Theta_D}\left(\frac{T}{\Theta_D}\right)^5 \int_0^{\Theta_D/T} \frac{x^5 dx}{(e^x - 1)(1 - e^{-x})} + \alpha T^3, \tag{1}$$

where ρ_0 is the residual resistivity due to defect scattering in the crystal lattice, K is the electron-phonon coupling constant, Θ_D is the Debye temperature and also contains a contribution from the electron-electron correlations [16, 17] while αT^3 is the Mott term which describes the s-d interband scattering. Values of $\rho_0 = 49.522$ $\mu\Omega$ cm, $K = 67.588$ $\mu\Omega$ cm K, $\Theta_D = 41.162$ K and $\alpha = -2.607 \times 10^{-6}$ $\mu\Omega$ cm K^{-3} are obtained from the fit. The electronic contribution to resistivity ρ_{4f} obtained by subtracting the phonon contribution from $PrRu_2Ga_8$ is presented in inset (a) while (b) is the low temperature plot of ρ_{4f}. ρ_{4f} shows a strong temperature dependence from room temperature down to ≈ 30 K with a shallow curvature around 100 K. This feature likely originates from possible CEF effect on the resistivity. Below about 30 K, the resistivity is weakly temperature dependent down to ≈ 5 K, below which it rises into a peak centred at 3.3 K which is associated with the magnetic ordering at T_N.

6. Discussion and conclusion

From the electronic and magnetic properties of $PrRu_2Ga_8$, a phase transition at $T_N = 3.3$ K is observed. The magnetic ordering in $PrRu_2Ga_8$ is at variance to the singlet ground state expected based on the C_s site symmetry of the Pr^{3+} in the $CaCo_2Al_8$ structure type. Among other factors, induced magnetism is thought to have been responsible for such observation arising due to the admixture of the first excited CEF level with the ground state singlet when the exchange interaction exceeds a critical value based on the expression for self-induced moment ordering [4, 5];

$$T_c = \Delta\left[\ln\frac{J_{ex}\alpha^2 + n\Delta}{J_{ex}\alpha^2 + n\Delta}\right]^{-1}, \tag{2}$$

where Δ is the energy splitting between the ground state singlet and the first excited state, α is the matrix element between the ground state singlet and the first excited state, n is

the degeneracy of the first excited state, J_{ex} is the exchange interaction and T_c is the mean-field critical temperature. From inelastic neutron scattering (INS) experiment, the exchange interaction can therefore be estimated based on the above expression. In the present analysis, the exchange interaction can be predicted according to the expression; $\theta_p = -J_{ex}J(J+1)/3k_B$, where $\theta_p = -7.8$ K as obtained from magnetic susceptibility analysis, and $J = 4$. The value of $J_{ex} = 0.094$ meV is obtained which is of the same order magnitude with the ordering temperature found in $PrRu_2Ga_8$. An induced magnetic ordering is thus believed to be favoured when the value of 0.094 meV is comparable or greater than that estimated from the INS experiment. A γ value of 46 mJ/mol.K^2 indicates a possible moderate heavy-electron like behaviour in the material. The magnetic susceptibility follows the Curie-Weiss law for temperatures above 50 K and gives $\mu_{\text{eff}} = 3.47\ \mu_B$/Pr which is close to that expected for a free Pr^{3+} ion. Magnetic phenomena in this system may therefore be expected to be governed by a stable and well-defined Pr local magnetic moment. Further measurements in fields and inelastic neutron scattering are required to further explore microscopic aspects and crystal field effects discussed in this article.

Acknowledgement
MOO acknowledges the UJ-URC bursary for doctoral studies in the Faculty of Science. AMS thanks the SA-NRF (93549) and UJ-URC for financial support.

References

[1] Schlüter M and Jeitschko W 2001 *Inorg. Chem.* **40** 6362

[2] Henderson B and Bartram R H 2005 *Crystal-field engineering of solid-state laser materials* (Cambridge University Press)

[3] Nair H S, Ghosh S K, Kumar R and Strydom A M 2016 *J. Phys. Chem. Solids* **91** 69

[4] Adroja D T and Anand V K 2012 *Phys. Rev. B* **86** 104404

[5] Anand V K, Adroja D T, Bhattacharyya A, Hillier A D, Taylor J W and Strydom A M 2014 *J. Phys.: Condens. Matter* **26** 306001

[6] Schobinger-Papamantellos P, André G, Rodriguez-Carvajal J, Moze O, Kockelmann W, Tung L D and Buschow K H J 2001 *J. Magn. Magn. Mater.* **231** 162

[7] Blanco J A, Schmitt D and Sal J C J 1992 *J. Magn. Magn. Mater.* **116** 128

[8] Andres K, Bucher E, S Darack J P and Maita 1972 *Phys. Rev. B* **6** 2716

[9] Nair H S, Ogunbunmi M O, Kumar C M N, Adroja D T, Manuel P, Fortes D, Taylor J and Strydom A M 2017 *J. Phys.: Condens. Matter* **29** 345801

[10] Vejpravová J, J Prokleška V and Sechovskỳ V 2007 *J. Magn. Magn. Mater.* **316** 374

[11] Thompson P, Cox D E and Hastings J B 1987 *J. Appl. Crystallogr.* **20** 79

[12] Rodriguez-Carvajal J 1990 *satellite meeting on powder diffraction of the XV congress of the IUCr* vol 127 (Toulouse, France:[sn])

[13] Tougait O, Kaczorowski D and Noël H 2005 *J. Solid State Chem.* **178** 3639

[14] Ogunbunmi M O, Sondezi B M, Nair H S and Strydom A M 2018 *Physica B* **336** 128

[15] Mott N F and Jones H 1958 *The Theory of the Properties of Metals and Alloys* (Dover publications, inc., Oxford England)

[16] Falkowski M and Strydom A M 2017 *J. Phys.: Condens. Matter* **29** 395601

[17] Pikul A P, Kaczorowski D, Plackowski T, Czopnik A, Michor H, Bauer E, Hilscher G, Rogl P and Grin Y 2003 *Phys. Rev. B* **67** 224417

Numerical simulation of structural, electronic and optical properties of vanadium diselenide (VSe_2)

Elkana Rugut[1], Daniel Joubert[1] and Glenn Jones[2]

1. The National Institute for Theoretical Physics, School of Physics and Mandelstam Institute for Theoretical Physics, University of the Witwatersrand, Johannesburg, Wits 2050, South Africa, Tel: +27117176804; Fax: +27117176879
2. Johnson Matthey Research (PTY) Limited, Scientia, CSIR Campus, Meiring Naude Road, Brummeria, Pretoria, South Africa.

E-mail: elkanatawich@gmail.com

Abstract. VSe_2 belongs to a group of compounds called transition metal dichalcogenides. This group of compounds have been exploited by several researchers both computationally and experimentally because of their intriguing properties such as low resistance, high chemical and mechanical stability and ease of synthesis. These properties make them candidates for various applications ranging from catalysis, electronics, aerospace engineering to plasmonics, just to mention a few. In this study we numerically simulated some of the properties of VSe_2. In this regard, a structural study of VSe_2 was undertaken using Density Functional Theory (DFT) with the Perdew-Burke-Ernzerhof (PBE) exchange correlation functional with two flavours of van der Waal's interaction corrections namely Grimme (D2) and Tkatchenko-Scheffler (TS) to describe the inter-layer interactions of VSe_2 accurately. From the structural data obtained, PBE+D2 describe the structural parameters of VSe_2, when compared to experimental data, best. Vibrational properties via phonon calculations, mechanical properties through elastic constant calculations and energetic properties using the formation and the cohesive energies confirmed that VSe_2 is mechanically, dynamically and energetically stable in its trigonal phase. Furthermore, from electronic band structure and density of states, VSe_2 exhibits metallic character. Optical properties computed using many-body perturbation theory at the BSE level of approximation show that the compound is optically anisotropic with different absorption behaviour in-plane and out-of-plane. From the obtained values of the screened plasma frequency, VSe_2 is a promising plasmonic material.

1. Introduction

After the discovery of the notable electrical, physical, mechanical and optical properties of graphene [1], investigations of the physical properties of layered transition metal dichalcogenides [2] have been a continous source of interesting research. This family of compounds has a general formula MX_2 where M is a transition metal and X is chalcogen. This study is based on VSe_2. Levy and Froidevaux [3] studied VSe_2 experimentally when they were investigating $V_xTi_{1-x}Se_2$ and $Ta_xTi_{1-x}Se_2$ at various concentration levels and environmental conditions. From their analysis, VSe_2 is easy to alloy and crystallyzes in a stable octahedral co-ordination of cations. Close packed sheets of metal atoms (V) are sandwiched between sheets of chalcogen atoms (Se) with stacking sequence Se-V-Se and an inter-layer spacing of about 7 Å. The anisotropy can be attributed to strong intra-layer and weak inter-layer bonding. Wiegers [4] noticed that VSe_2

shows anomalous properties at around 110 K attributed to charge density waves. Due to its application in various fields such as lithium batteries [5] where powdered VSe_2 is one of the cathode components [6], an improved understanding of VSe_2 is valuable. Thus, this study is intended to advance the understanding of the properties of VSe_2. Although bulk VSe_2 has been studied before [7, 8], little has been reported on optical properties [9].
This paper is organized as follows; section 2 is devoted to methodology, section 3 is composed of a presentation of results obtained and a brief discussion whereas a summary and major conclusions of this study are presented in section 4 and lastly acknowledgements are noted in section 5.

2. Methodology

This study is based on a Density Functional Theory (DFT) implementation which solves Kohn-Sham equations using a projector augmented wave method. The generalized gradient approximation in the scheme of Perdew-Burke-Ernzerhof (PBE) [10] was used for the exchange-correlation energy functional as implemented in the Vienna *ab initio* Simulation Package (VASP) code [11, 12, 13]. It is noteworthy that the standard PBE does not describe the long range van der Waal's interaction between the individual layers of VSe_2. In this regard, we used the PBE+D2 method of Grimme [14] and the PBE+TS method proposed by Tkatchenko and Scheffler [15] to account for inter-layer interaction. The two approximations include long range van der Waal's interactions in an empirical manner. Ionic relaxation was done using a conjugate gradient minimization method [16] to minimize the Hellman-Feynman forces among the constituent atoms to less than 1 meV/Å. The cut-off energy for the plane wave basis and self-consistent threshold were set at 700 eV and 10^{-8} eV respectively, in order to achieve good convergence. For the structural study, a gamma centered grid of size $12 \times 12 \times 4$ was used to sample the Brillouin-zone. Phonon calculations were done by applying a finite displacement method using a $3 \times 3 \times 3$ supercell with 81 atoms. By varying the size of the cell from unit cell to supercell, one needs to re-adjust the number of k-points in the irreducible part of the Brillouin-zone. In this regard, the k-mesh was changed from $12 \times 12 \times 4$ to $4\times 4 \times 1$. We applied a stress-strain approach for calculating elastic constants whereby, after extracting our stiffness matrix, it was analyzed to obtain average properties such as bulk (B), Young's (E) and shear (G) modulus as well as Poisson's ratio (ν) among other mechanical properties. In order to calculate optical properties of the material, we had to go beyond the ground state calculation by considering excited state properties of the system. A DFT calculation was performed to obtain the ground state structure of the material of interest by solving the Kohn-Sham equations. DFT [17] output was then used as ingredients for self consistent GW_0 [18] calculations in which only the quasi-particle eigen-energies of the Green's function were updated while keeping the screened coulomb interaction fixed at its initial DFT value. Lastly, a Bethe Salpeter Equation (BSE) [19] calculation based on the GW_0 data was performed to determine optical absorption spectra which include excitonic effects.

3. Results and discussion

3.1. Structural and energetic properties

Table 1. Structural and energetic parameters

Functional	a (Å)	c (Å)	V_0 (Å^3)	α (°)	γ (°)	E_{coh} (eV/atom)	E_{form} (eV/atom)
PBE	3.3520	6.9970	68.10	90	120	-4.314	-0.694
PBE+TS	3.3350	5.9490	57.30	90	120	-4.582	-0.962
PBE+D2	3.2240	6.7300	60.58	90	120	-4.578	-0.958
Exp[3]	3.3480	6.1220	59.43	90	120	-	-
Exp[4]	3.3587	6.1075	59.67	90	120	-	-
Exp[20]	3.3400	6.1200	59.13	90	120	-	-

Table 1 shows structural data of VSe_2. Although PBE described the lattice parameter a well, it overestimated the value of lattice parameter c. On the other hand, PBE+TS underestimated both a and c lattice constants which automatically translates to the volume being underestimated as compared to the given experimental values. PBE+D2 underestimated the a lattice parameter but overestimated the c lattice parameter hence compensating each other resulting in ground state volume that is closer to experimental. Therefore, PBE+D2 gives a better overall description of the structural parameters of VSe_2. The calculated cohesive and formation energies obtained were negative for all the approximations of the exchange-correlation energy used, suggesting that trigonal VSe_2 is energetically stable against decomposition into its constituent atoms and elemental solids. Thus, further studies of VSe_2 were done using PBE+D2 since it reproduces the structural properties better.

3.2. Mechanical properties

Table 2. Calculated independent elastic coefficients (GPa)

C_{11}	C_{12}	C_{13}	C_{14}	C_{33}	C_{44}
133.62	22.30	21.79	-6.76	58.39	18.60

Table 3. Calculated eigenvalues (GPa)

λ_1	λ_2	λ_3	λ_4	λ_5	λ_6
17.410	17.629	49.472	56.856	112.290	164.830

From the calculated elastic coefficients tabulated in Table 2, the elastic constants for VSe_2 fulfilled all the Born stability criterion for trigonal structures [21]. All eigenvalues of the stiffness matrix given in Table 3 were positive which validates its mechanical stability. Three averaging schemes were used in computing B, G, E, ν and B/G, namely, Voight, Reuss and Hill methods [22]. The different schemes help to make comparisons and to check the accuracy of the computed values. From the literature [23], the Voight method gives an upper limit to numerical data since it assumes a uniform strain whereas the Reuss method gives a lower limit to numerical data since it assumes a uniform stress. The Hill method on the other hand gives an average of the two. This trend is consistent with the results of this current study.

Table 4. Calculated B, E, G, ν and B/G

Scheme	B	E	G	ν	B/G
Voight	50.819	87.152	35.890	0.2142	1.42
Reuss	43.950	66.557	26.674	0.2476	1.65
Hill	47.384	76.919	31.282	0.2295	1.51

Pugh proposed that if the B/G value is less than the critical value (1.75), the material is considered brittle [24], otherwise it is ductile. The B/G values obtained using the three averaging schemes were less than 1.75 as shown in Table 4 implying that VSe_2 is brittle.

3.3. Dynamical and electronic properties

VSe_2 is metallic since the valence band maxima and conduction band minima coincide as shown in Figure 1 and 2 which is consistent with existing literature [25]. Moreover, it is dynamically stable in its trigonal phase as backed by phonon dispersion curves in Figure 3 and 4 in which only positive frequencies are noticeable.

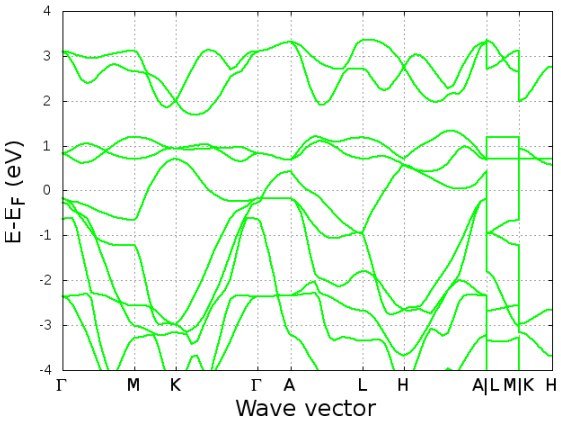

Figure 1. Electronic bands

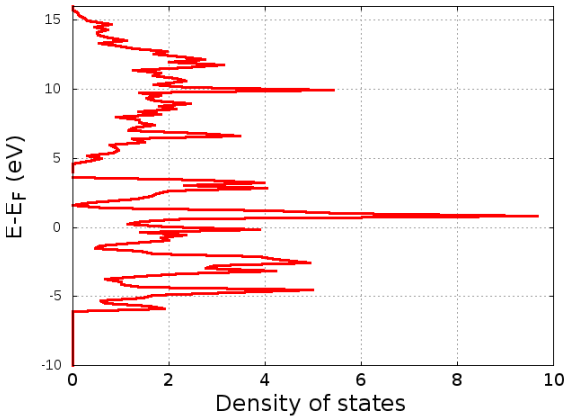

Figure 2. Electronic DOS

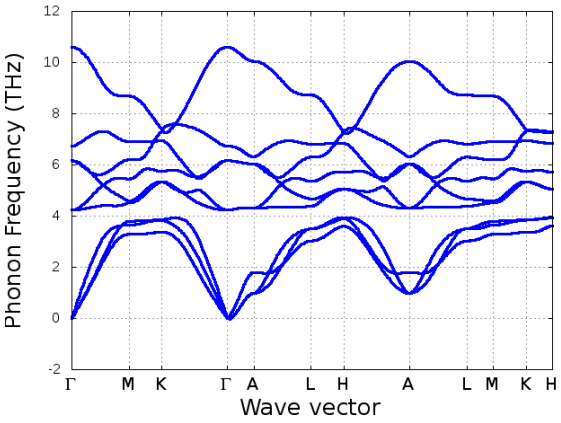

Figure 3. Phonon bands

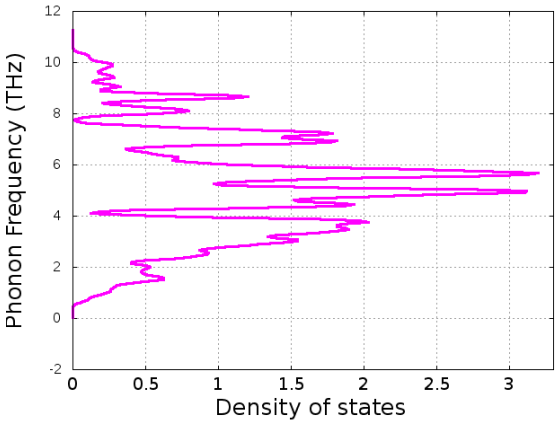

Figure 4. Phonon DOS

3.4. Optical properties

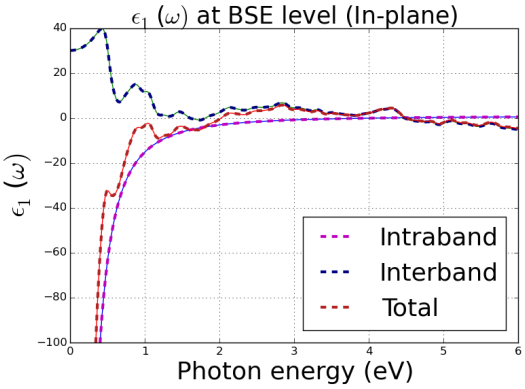

Figure 5. Real part of dielectric function at BSE

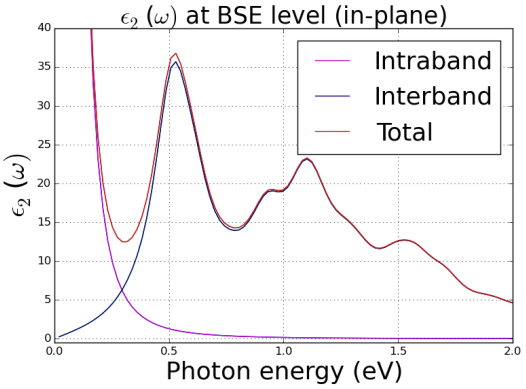

Figure 6. Imaginary part of dielectric function at BSE

At very low photon energies ($0 < \omega \leq 1$ eV) for the imaginary part and ($0 < \omega \leq 3$ eV) for the real part of dielectric function at the BSE level shown in Figure 5 and 6 respectively, it is evident that the intraband contribution is important for a good description of the optical behaviour of metallic systems [26]. In higher energy ranges, its contribution is negligible. Hence, the dielectric constant used in optical analysis should include both intraband and interband contributions.

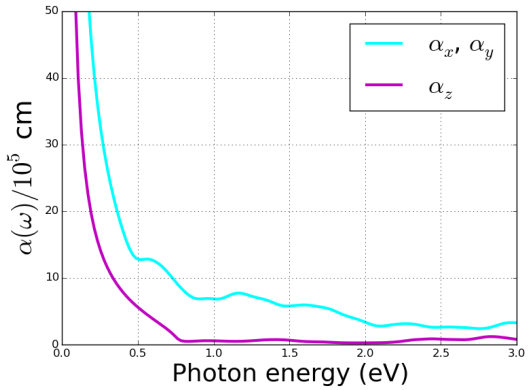

Figure 7. Absorption coefficient

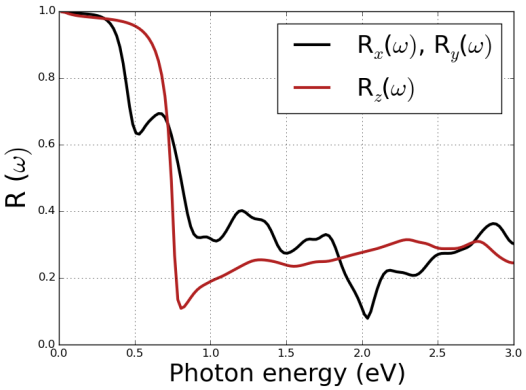

Figure 8. Reflectivity

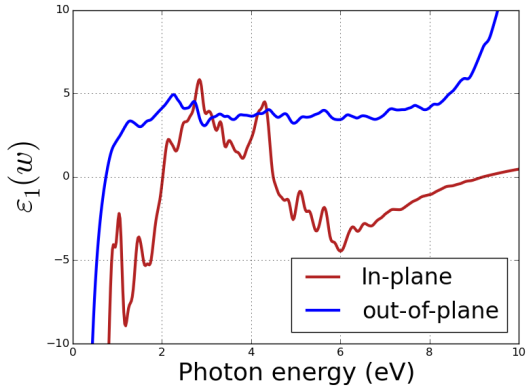

Figure 9. Real part of dielectric

The behaviour of the dielectric function is similar in the two in-plane (x- and y-) directions and we show only in-plane and out-of-plane (z-) values for the optical properties. Within a photon energy range of 0 eV to 3 eV, absorption in-plane is larger that absorption out-of-plane as shown in Figure 7. There is no distinguishing pattern for reflectivity. Within the visible range, maximum absorption peaks occur at the edge of the visible range both in-plane and out-of-plane. The out-of-plane plasma frequency is in infrared region at around 0.7 eV, whereas for in-plane, it is found at around 2 eV, 4.25 eV and 9 eV as shown in Figure 9. From the obtained values of screened plasma frequency, VSe_2 is a promising plasmonic material for radiation polarized for in-plane absorption because its in-plane screened plasma frequencies lie within the visible and ultraviolet region. This is in agreement with a DFT study done by Cudazzo *et al.* [9]. For plasmonic applications, high plasmonic quality in the UV-visible frequency regime is desired [27]. Recall that the screened plasma frequency is located at the point where the total contribution from the intraband and interband contributions to the real part of the dielectric matrix is zero.

4. Summary and conclusion

In this study, we have performed first principles computations on trigonal VSe_2 including structural, elastic, electronic, vibrational and optical properties using DFT and post-DFT many-body perturbation theory. We have established that the lattice parameters obtained after relaxation are in good agreement with existing experimental and theoretical data. From the mechanical properties, VSe_2 is brittle material hence can easily be used to craft components for optical communication, computers and other technological devices. Bulk VSe_2 is metallic and its plasma frequency is located within the visible range, hence it can be applied in plasmonic field which incorporates optics onto nanotechnology.

5. Acknowledgement
This study was financially supported by the Johnson Matthey Technology Centre (Pretoria) under contract number JM6473. We acknowledge Centre for High Computing, Cape Town for computational resources.

References

[1] Neto A C, Guinea F, Peres N M, Novoselov K S and Geim A K 2009 *Reviews of modern physics* **81** 109.
[2] Wang Q H, Kalantar-Zadeh K, Kis A, Coleman J N and Strano M S 2012 *Nature nanotechnology* **7** 699-712.
[3] Levy F and Froidevaux Y 1979 *Journal of Physics* C: *Solid State Physics* **12** 473.
[4] Wiegers G A 1980 *Physica* B+C **99** 151-165.
[5] Whittingham M S 2004 *Chemical reviews.* **104** 4271-4302.
[6] Ōnuki Y, Inada R, Yamanaka S and Kamimura H 1981 *Japanese Journal of Applied Physics* **20** 1583.
[7] Reshak A H and Auluck S 2004 *Physica* B: *Condensed Matter* **349** 310-315.
[8] Zunger A and Freeman A J 1979 *Physical Review* B **19** 6001.
[9] Cudazzo P, Gatti M and Rubio A 2014 *Physical Review* B **90** 205128.
[10] Perdew J P, Burke K and Ernzerhof M 1996 *Physical review letters* **77** 3865.
[11] Kresse G and Hafner J 1993 *Physical Review* B **47** 558.
[12] Kresse G and Hafner J 1994 *Physical Review* B **49** 14251.
[13] Kresse G and Furthmüller J 1996 *Physical Review* B **54** 11169.
[14] Grimme S 2006 *Journal of computational chemistry* **27** 1787-1799.
[15] Bučko T, Lebègue S, Hafner J and Ángyán 2013 *Physical Review* B **87** 064110.
[16] Stich I, Car R, Parrinello M and Baroni S 1989 *Physical Review* B **39** 4997.
[17] Hohenberg P and Kohn W 1964 *Physical review.* **136** B864.
[18] Aryasetiawan F and Gunnarsson O 1998 *Reports on Progress in Physics* **61** 237.
[19] Liegener C M 1981 *Physics Letters* A **85** 324-326.
[20] Hayashi K and Nakahira M 1978 *Journal of Solid State Chemistry* **24** 153-161.
[21] Mouhat F and Coudert F X 2014 *Physical Review* B **90** 224104.
[22] Shein I R and Ivanovskii A L 2008 *Journal of Physics: Condensed Matter* **20** 415218.
[23] Ching W Y, Rulis P and Misra A 2009 *Acta Biomaterialia* **5** 3067-3075.
[24] Pugh S F 1954 *The London, Edinburgh and Dublin Philosophical Magazine* **45** 823-843.
[25] Ruitao L, Robinson J, Sun D, Mallouk T and Terrones M 2014 *Accounts of chemical research* **48** 56-64.
[26] Kim J, Jhi S H and Ryeol K 2011 *Journal of Applied Physics* **110** 083501.
[27] Blaber M G, Arnold M D and Ford M J 2009 *arXiv preprint arXiv* 0908.3707.

Elastic properties of chalcogenide based phase change memories by surface Brillouin scattering

D Wamwangi[1,2], B Mathe [1,2], M Baloi [1], DG Billing[3], C Persch[4], M Salinga[4] and M Wuttig[4]

[1] DST/NRF Centre of Excellence in Strong Materials, University of the Witwatersrand, Private Bag 3, Wits 2050, Johannesburg, South Africa
[2] Materials Physics Research Institute, School of Physics, University of the Witwatersrand, Private Bag 3,WITS 2050, Johannesburg, South Africa
[3] School of Chemistry, University of the Witwatersrand, Private Bag 3, Wits 2050, Johannesburg, Republic of South Africa
[4] I. Physikalisches Institut 1A, RWTH Aachen University, 52056, Aachen, Germany

E-mail:daniel.wamwangi@wits.ac.za

Abstract. Chalcogenide based alloys continue to be intensively investigated as suitable candidates for universal non-volatile memory applications. This is driven by their fast and reversible phase transitions (ns) and their scalability potential. In this work the acoustic hardening of chalcogenide thin films on (100) Si is investigated to establish the bulk and shear modulus in the amorphous phase by surface Brillouin scattering. X-ray Reflectometry has been used to extract film thickness and density requisite parameters for simulation of velocity dispersion curves. Using surface Brillouin studies, phase change samples have shown the Rayleigh surface acoustic wave and higher order guided modes thus indicating a case of a slow on fast film-substrate configuration. The low surface roughness has been determined by X-ray Reflectometry to be less than 0.2 nm for all the films. Applying the elastodynamic surface Green function approach, c_{11} and c_{44} in the range 40-30 GPa and 15-10 GPa respectively were obtained.

1. Introduction

Phase change materials are chalcogenide compounds that have been used as the active medium in non-magnetic data storage [1]. Indeed their applications have varied between write once only memory (WORM), re-writable DVDs and the blue ray discs [2-3]. The concept of storage involves rapid and reversible change in optical and electronic properties using laser or current pulses. The ability to possess numerous storage (changes in resistance) states within a single cell has made them to be considered as potential candidates for highly scalable non-volatile memory devices. Their development as storage devices has been driven by their unique combination of properties such as rapid transformation (ns) between two structural states mediated by an electronic process, also known as threshold switching and stability against spontaneous recrystallization [4-5]. More recently these materials are being investigated for implementation as active medium in nanoelectromechanical systems (NEMS) and microelectromechanical (MEMS) systems due to their high potential for high

speed tunability of the mechanical properties and resonance frequency of the mechanical resonator [6]. This enables the development of lighter, scalable and low power mechanical resonators.

The phase change alloys that have been applied in optical storage comprise mainly of GeSbTe ternary alloys formed from the pseudo-binary tie line of GeTe and Sb_2Te_3 [2]. These alloys are also classified as nucleation dominated since their recrystallization occurs through the formation of critical nuclei through-out the volume of the bit. However there is also another class of phase materials in which phase transformation is dependent on the incubated nuclei at the amorphous and crystalline interface and the crystal growth speed towards the center of the bit. This latter class of materials is also called growth dominated phase change materials and can be easily scaled due to the linearity of the bit size with the laser or current pulse width. Despite the established research on these materials, their disordered state is not unique as the ensemble samples the potential energy landscape to minimize its internal energy with the driving force towards the metastable NaCl - like phase. These structural relaxations in the amorphous state have been attributed to the resistance drift in the phase change random access memories [7]. Thus, besides threshold switching, the thermal properties of phase change materials are crucial for not only the rapid and reversible switch but also for scalability purposes during resistive (joule) heating. Compared to the III –V counterparts, these materials have exceptionally low thermal conductivity even after the structural transition. Thermal conductivity of any material is determined by electronic and phonon transport in the medium and in this work we present the dynamics of the surface phonons in AgIn-Sb_2Te measured by surface Brillouin scattering to determine their elastic constants. The nature of the film - substrate configuration enables the investigation of near surface excitations which include Rayleigh surface acoustic wave (RSAWs), Sezawa waves (SW), pseudo–SAW and interface waves [8-9]. Using a Green's functions approach we determined the elastic properties of isotropic AgIn-Sb_2Te thin films from inverse problem of fitting the dispersion curves where the quality of fit was evaluated by overlaying the power spectrum to the measured surface Brillouin scattering spectrum.

2. Experimental

Thin films of AgIn-Sb_2Te have been grown on (001) Si using RF magnetron sputtering and evaluated for film thickness by X-ray Reflectometry (XRR). The XRR measurements have been performed using the Bruker AXS D8 Discover High resolution diffractometer. A highly collimated monochromatic Cu Kα X-ray beam operating at 1.6 kW in the symmetric geometry condition was used. The film thickness was determined to be 98 nm. Surface Brillouin scattering (SBS) measurements have been performed using a 335mW single mode laser light from a Torus Quantum 532 diode pumped solid state laser. The incident light was focused onto the surface of the film and the backscattered light was collected by a 120 mm focal length lens for frequency analysis using a high contrast Sandercock (3+3) pass Tandem Fabry-Pèrot interferometer [10]. The backscattered geometry was selected for maximum momentum transfer. Thus the incidence angle or film thickness can be varied to generate the surface phonon dispersion spectrum which is dependent on the ratio of the phonon wavelength relative to the film thickness [11]. The backscattering geometry is illustrated in Figure. 1, in which the wave vector of the surface phonons involved in the scattering process is obtained from momentum conservation of components parallel to the surface by the expression:

$$q_{II} = 2k_i sin\ \theta \tag{1}$$

Where $\boldsymbol{k_i} \approx \boldsymbol{k_s}$ is the incident wave vector and θ is the angle of incidence.

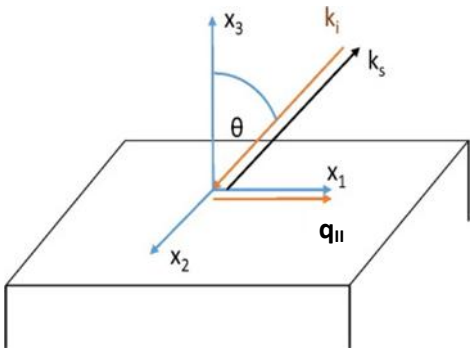

Figure 1. Backscattering geometry showing the propagation of the surface phonon due surface ripple mechanism.

The velocity v of the surface phonon modes for a ripple scattering mechanism is obtained from the frequency shift f as:

$$v = \frac{\pi f}{k_i \sin(\theta)} \tag{2}$$

In this project the film thickness of AgIn-Sb_2Te thin films was measured to be 98 nm while the incidence angle was varied between 51° and 70° to probe the dispersion of surface phonons in the range $1.8 \leq q_{II} d \leq 2.4$.

3. Results and Discussion

3.1. X-ray reflectivity of AgIn-Sb_2Te thin films

X-ray reflectometry was carried out on a 98 nm thin film of AgIn-Sb_2Te deposited on (001) Si, to determine the density and thickness of the film. Figure 2 shows the simulated and raw spectra overlaid on each other from which the density was obtained to be 6.45 ± 0.15 g cm^{-3} after fitting the critical angle ($2\theta = 0.63°$) for total external reflection. The film thickness of the layer was determined to be 98.00 ± 0.18 nm from the Kiessig oscillations using the layer stack, TeO_2/$AgInSb_2Te$/SiO_2/Si, while the exponential decay in the oscillations yielded an interfacial roughness of 0.20 ± 0.01 nm of the main layer.

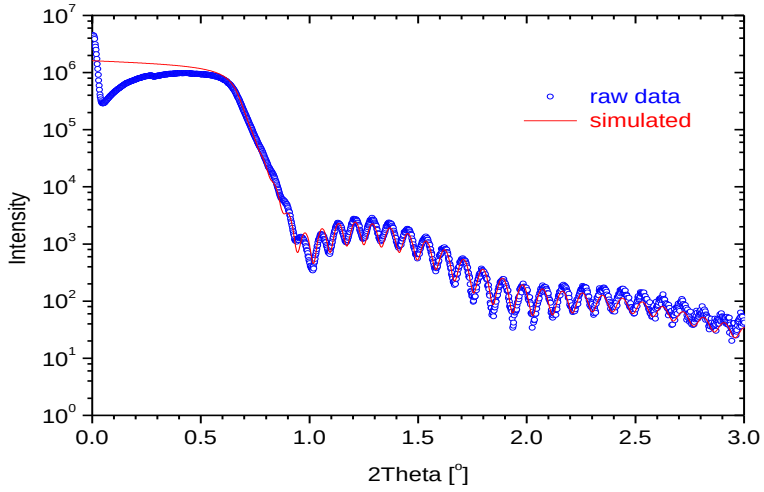

Figure 2. X-ray reflectivity spectra of the raw (blue circles) and simulated curves (red line) used to determine the mass density and thickness of the film.

An amorphous phase (not shown here) has been established in the layer using the Seemann-Bohlin geometry at a glancing incidence angle of 1.0° in omega. This confirms the presence of an isotropic film for which two effective elastic constants can be determined from the surface acoustic wave excitations.

3.2. Surface Brillouin scattering of phase change thin films on (001) Si.

Figure 3 shows a typical surface Brillouin scattering spectra collected for a 98 nm AgIn-Sb_2Te thin film on (001) Si substrate at various incidence angles. The spectra show 5 peaks in the frequency shift between 5 and 20 GHz. These peaks comprise of the most intense peak at 5 GHz corresponding to the true surface wave, known as the Rayleigh surface acoustic wave (RSAW). Notably, additional peaks at higher frequency shifts have been observed and they represent the high frequency guided modes (Sezawa Waves) which emerge from the reflections at the boundary. The presence of guided modes in the film is indicative of a case of slow on fast film - substrate configuration and these modes enable full determination of elastic constants of the phase change films.

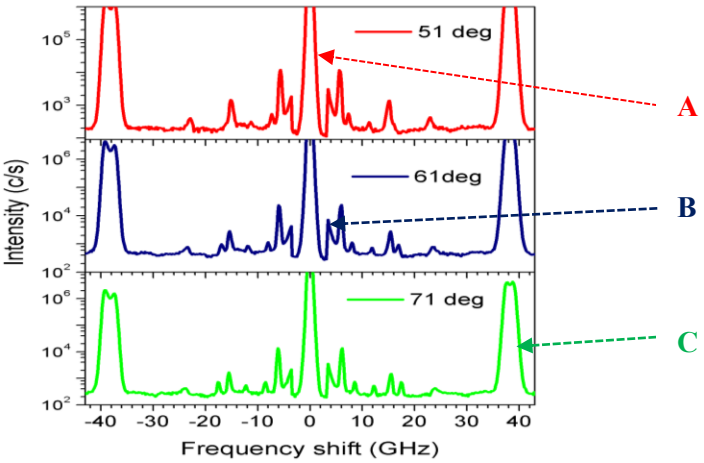

Figure 3. Surface Brillouin scattering spectra of AgIn-Sb_2Te thin film measured in backscattering geometry at 51°, 61° and 71° angle of incidence. The central peak A is an instrumental artefact related to the elastic light whilst B and C are instrumental effects related to alignment of the interferometer.

To determine the dispersive nature of the acoustic excitations, the velocity dispersion curve was plotted as shown (symbols) in figure 4[a] and fitted for the elastic constants using the surface elastodynamic Green's function approach (continuous function in the plot). As shown in figure 4(a), the velocity of the Rayleigh mode is asymptotic to 1500 m/s for large $k_{//}d$ values. For this range of $k_{//}d$, the Rayleigh mode is not influenced by the properties of the substrate and the elastic constant determined is that of the film. On the other hand, as the film thickness approaches zero, the Rayleigh mode will approach to that of Si substrate at 4900m/s along [001] direction. Below this transverse threshold velocity, v_s^T, the dispersive nature of the Rayleigh and Sezawa waves (SW1,SW2 and SW3) is observed as shown in figure 4(a). The cross-sectional plot of figure 4 (b) shows a reasonably good agreement between the power and the experimental spectrum deviations in the spectrum intensity can arise due to reflections of the waves at the boundary.

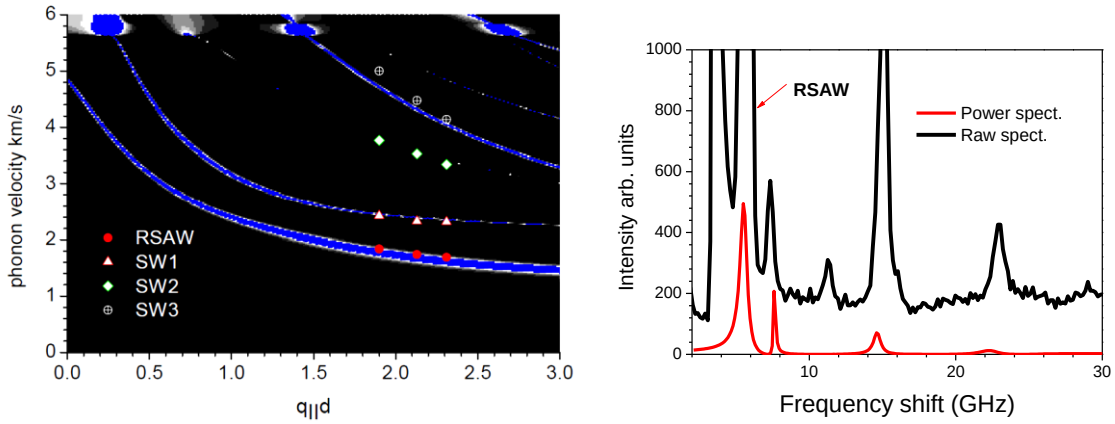

Figure 4. [a] Shows the computed Green's function velocity dispersion curve superimposed onto the discrete plot of the experimental data extracted from the spectra in Figure 3. [b] Cross-sectional plot ($k_{//}d$ = 2.3) showing good agreement between the power spectrum derived from the Green's function and the experimental spectrum of the 98 nm film.

Included in figure 4[a] are the calculated dispersion curves of the discrete spectrum obtained from the least squares fitting to the experimental data using a combination of numerical solution of the wave equation and the surface elastodynamic Green's function approach [12-13]. This least-square fitting procedure allows for the inverse extraction of the thin film elastic constants. Since the phase change thin films are amorphous, hence elastically isotropic, two sets of effective elastic constants fully describe the system, and these have been determined from the best fit to be C_{11} = 34.4 ± 0.4 GPa and C_{44} = 14.3 ± 0.3 GPa respectively.

Using these values and the relation, $E = c_{11} - \frac{2c_{12}^2}{c_{11}+c_{12}}$ [12-14] yields the Young's modulus E = 30.1 GPa and a Poisson ratio, υ = 0.11. The shear modulus of AgIn-Sb_2Te is equal to the C_{44} component of the elastic constant tensor. The values of the Young's Modulus are in the same range as those measured by Kalb (E = 22.6 GPa) and Blachowicz *et al* (E = 24.5 GPa, $\nu = 0.27$) [15 -16] using two independent techniques. The variation in the Poisson ratio could be attributed to the non-uniqueness of the disordered state of these materials.

4. Conclusion

In this work, surface Brillouin scattering technique has demonstrated the presence of and dispersive nature of high order resonances in the chalcogenide compounds, in addition to the Rayleigh surface acoustic wave (RSAW). The Rayleigh velocity has been determined to 1837 m/s which is much lower than that of Si (4800m/s), thus representing the case of a slow on fast film-substrate configuration. Using two effective elastic constants for an isotropic AgIn-Sb_2Te thin film, we successfully determined the room temperature Young's modulus (30.1 GPa), shear modulus (14.3 GPa), as well as the Poisson's ratio (0.11). The values are within range of reported literature values obtained using independent methods, thus demonstrating the versatility of the surface Brillouin scattering technique.

5. Acknowledgements

The authors wish to thank NRF for financial support to the project and National Laser Centre for provision of laser infrastructure and financial support for the Surface Brillouin scattering project.

6. References

Feinleib J, deNeufville J, Moss S C and Ovshinsky S R 1971 *Appl. Phys. Lett.* **18** 254
Yamada N, Ohno E, Akahira N, Nishiuchi K, Nagata K and Takao M 1987 *Jpn. J.Appl. Phys.*
26 66
[3] Wuttig M and Namada Y 2007 *Nat. Mat*. **6** 824
[4] Raoux S, Welnic W and Lelmini D 2010 *Chem. Rev.***110** 240
[5] Boniardi M, Redaelli A, Pirovano A, Tortorelli I and Pellizzer F 2009 *J. Appl. Phys*. **105** 084506
[6] Nazeer H, Bhaskaran H, Woldering L A and Abelmann L 2015 *Thin Solid Films* **592** 69
[7] Sebastian A Papandreou N, Pantazi A, Pozidis H and Eleftheriou E 2011 *J. Appl. Phys*. **110** 084505
[8] Wittkowski T, Distler G, Jung K, Hillebrands B and Comins J D 2004 *Phys. Rev. B*. **69** 205401
[9] Comins J D, Every A G, Stoddart P, Zhang X, Crowhurst J C and Hearne G 2000 *Ultrasonics* **38** 450.
[10] Sandercock J R 1982 *Light Scattering in Solids III (*Berlin:Springer-Verlag)
[11] Fioretto D, Carlotti G, Palmieri L, Socino G and Verdini L 1993 *et al., Phys. Rev. B.***47** 15286
[12] Every A G 2001 *Elastic properties of solids: static and dynamic principles. Handbook of Elastic properties of Solids, Liquids and Gases* vol 1, ed M Levy, H Bass and R Stern (New York: Academic Press)
[13] Farnell G W 1970 *Physical Acoustics* ed W P Mason and R N Thurston (New York: Academic Press)
[14] Nye J F 1972 *Physical Properties of Crystals* (Oxford: Oxford University Press)
[15] Kalb J 2002 PhD thesis Aachen.
[16] Blachowicz T, Beghi M G, Güntherodt G, Beschoten B, Dieker D and Wuttig M 2007 *J.Appl. Phys.* **102** 093519

Thermoelectic properties of $Sm_3Rh_4Ge_{13}$

S P Xhakaza[1], B M Sondezi[1] and A M Strydom[1]

[1] Highly Correlated Matter Research Group, Physics Department, University of Johannesburg, P. O. Box 524, Auckland Park 2006, South Africa

E-mail: psindisiwe@gmail.com

Abstract. We report the first results on thermoelectric properties of the cubic intermetallic compound $Sm_3Rh_4Ge_{13}$. The compound displays semiconductor-like behaviour with high resistivity $\rho(T)$ values and a negative temperature coefficient in $\rho(T)$ throughout the entire temperature range investigated. The thermal conductivity, $\kappa_T(T)$ observed in $Sm_3Rh_4Ge_{13}$ is extremely low and only weakly temperature dependent. A high thermopower amounting to 34 μV.K^{-1} is observed at room temperature. We discuss the origins of a low charge carrier density and anharmonic lattice vibration modes in this cage-type system.

1. Introduction

Thermoelectricity is a general phenomenon that can be seen in electrically conductive materials due to heat transport by charge carriers and scattering processes between charge carriers. Materials of high thermoelectric merit are capable of converting waste heat to useful electricity and *vice versa*. Therefore, applications in clean energy is a key reason for studying thermoelectricity [1]. This has motivated researchers to search for new and more efficient thermoelectric materials. The efficiency of the material is determined by the dimensionless thermoelectric figure of merit $zT = S^2T/(\rho\kappa)$, in terms of the Seebeck coefficient (thermopower) S, electrical resistivity ρ and thermal conductivity κ. Samarium is one of the elements that has received comparably less attention in the family of ternary intermetallic compounds of composition $R_3X_4Ge_{13}$ (R = rare-earth element and X = d-electron element), especially in thermal transport properties. Sm-based compounds occasionally exhibit heavy-fermion or strongly correlated electron features which is an aspect that will make this study of particular interest in the correlated electron and quantum matter communities.

The $CoSb_3$ skutterudite structure in particular has been of much interest and it contains two large empty cages per unit cell, filling the empty cages with rare-earth atoms resulting in an enhanced thermoelectric figure of merit [2]. Upon substitution of the rare-earth element, $Sm_{0.6}Co_4Sb_{12}$ for example achieved a maximum value zT = 0.8 at 716 °C [3]. The existence of $Sm_3Rh_4Ge_{13}$ has been reported by Venturini *et al*. [4], among thirty-four new ternary germanide compounds of composition $R_3T_4Ge_{13}$. Among these germanides interesting physics have been studied. Kong *et al*. [5] reported thermoelectric properties of $R_3Ru_4Ge_{13}$ (R = Y, Dy, Ho and Lu) in which high thermopower values were observed at room temperature with very low thermal conductivity, however these materials did not display very high figure of merit values $R_3X_4A_{13}$ (R = rare-earth, X = d-electron element, A = p-electron element) crystallizes in a cubic space group $Pm\bar{3}n$, involving two formula units per unit cell. The development of $R_3X_4A_{13}$ phases is credited to Remeika *et al*. [6]. In this paper, we explore thermoelectric properties of $Sm_3Rh_4Ge_{13}$.

2. Experimental method

A polycrystalline sample of $Sm_3Rh_4Ge_{13}$ was prepared by arc-melting high-purity elemental constituents of Sm (4N), Rh (4N) and Ge (5N). The stoichiometric ratio of the elements was melted using an Edmund Buehler arc-furnace under an atmosphere of purified Argon gas. The melted sample was overturned and melted five times to ensure good homogeneity. The sample was then wrapped in tantalum foil and set for annealing in an evacuated quartz tube for 5 days at 700 °C followed by further annealing for 7 days at 900 °C. Powder x-ray diffraction (XRD) patterns were obtained in a Rigaku SmartLab diffractometer using Cu-Kα1 radiation. The phase analysis was carried out by simulating the obtained experimental powder pattern with theoretical calculated patterns using Powder-Cell [7]. The powder diffractogram showed good agreement with the expected $Pm\bar{3}n$ space group. A structural survey of a piece of the sample was performed using GSAS software. The Rietveld fit (red line) and experimental data (cycle symbol) with expected Bragg positions as vertical lines are shown in figure 1. The value of the lattice parameter estimated from the fit was a = 0.8978(5) nm in close agreement with the previously reported value [4] of a = 0.8984(7) nm.

The sample was cut into geometries appropriate for various measurements. Physical properties comprising electrical resistivity, thermal conductivity and thermopower were studied on a Physical Properties Measurement System (PPMS) from Quantum Design (San Diego), using the thermal transport platform. All measurements were conducted from room temperature down to 2 K.

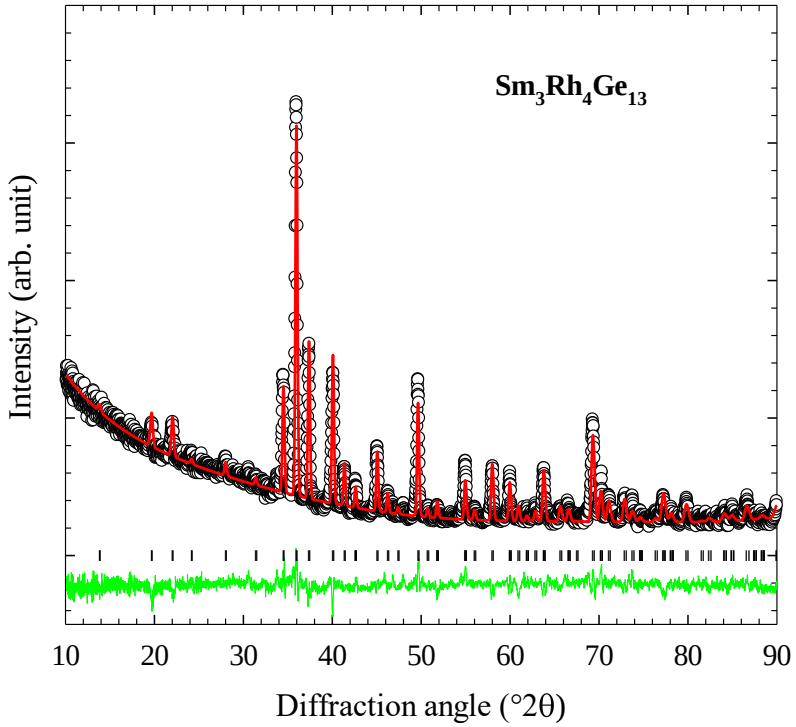

Figure 1: Experimental powder X-ray pattern of $Sm_3Rh_4Ge_{13}$ (circle symbol), Rietveld refinement fit (red line), difference curve (green line) and expected Bragg positions (vertical marks).

3. Results and discussion

3.1. Electrical transport

The temperature dependence of resistivity, $\rho(T)$ of $Sm_3Rh_4Ge_{13}$ is presented in the main panel of figure 2. In general, a semiconductor-like behavior is observed. The overall $\rho(T)$ values are ~ 100 times greater than in ordinary metals, and moreover $\rho(T)$ increases with decrease in temperature through the entire range. Similar behavior was observed in superconducting non-magnetic compounds $Y_3X_4Ge_{13}$ (X = Rh, Ir, Os) and $Lu_3X_4Ge_{13}$ (X = Rh, Co, Os) [8, 9, 10]. This trend of semiconducting behavior is also observed in a range of similar magnetic $R_3Ru_4Ge_{13}$ compounds having R = Sm, Nd, Dy, Ho and Er [5, 11, 13] as well as $Yb_3Ir_4Ge_{13}$ [12]. No phase transition is observed in $\rho(T)$ anywhere in $Sm_3Rh_4Ge_{13}$ in figure 2 and we furthermore note that $\rho(T)$ increases unabatedly towards $T \rightarrow 0$. As a first observation we note that the presence of a magnetic ion R in $R_3X_4Ge_{13}$ is not directly connected to semiconducting behavior as $Y_3Rh_4Ge_{13}$ [8] displays similar behavior. Further, germanium may at first sight be attributed to the prevalence of semiconducting behavior in these compounds on account of the presence of 65 % atomic percentage of Ge in the formula, but semiconductivity is not ubiquitous among the germanides. We note for instance the case of $Yb_3Co_4Ge_{13}$ with weak metallic behavior and $Yb_3Rh_4Ge_{13}$ which shows a well-defined metallic electrical resistivity [8, 12]. An activated type of resistivity has been observed in many of $R_3X_4A_{13}$ systems [13]. In order to analyze the electrical resistivity the high temperature region was described (see fit in inset of figure 2) in terms of simple energy gap by the expression $\rho(T) = C \exp(-T/\Delta)$ with C = 5400 $\mu\Omega$.cm and the energy gap value Δ = 158.7 K.

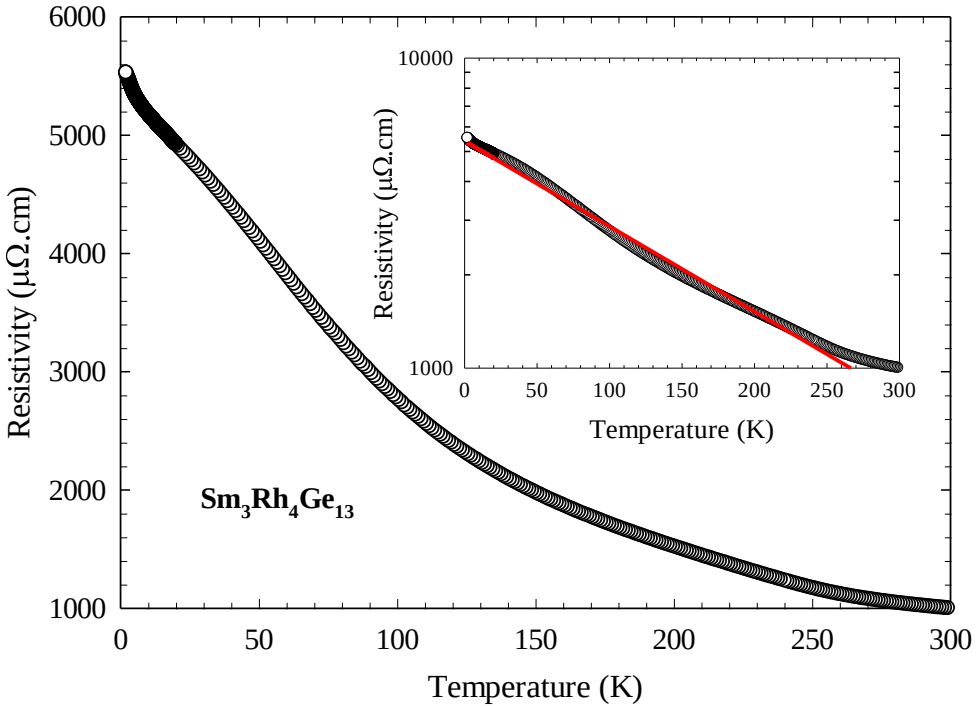

Figure 2: The electrical resistivity as a function of temperature plotted in the main panel. Inset: $\rho(T)$ on a semi-log axis where the solid line is an exponential fit in terms of a single energy gap.

3.2. Thermal transport

The thermal transport in $Sm_3Rh_4Ge_{13}$, including total thermal conductivity $\kappa_T(T)$, electrical resistivity $\rho(T)$ and thermopower $S(T)$ were all measured concurrently using a thermal transport measurement platform in the PPMS cryogenic facility. The temperature dependence of $\kappa_T(T)$ was measured upon cooling down very slowly under quasi-adiabatic conditions from room temperature

to 2 K with results as shown in figure 3a using open circles. We note that $\kappa_T(T)$ is overall extremely low, by more than an order of magnitude as compared to thermal conductivity in ordinary metals. The thermal conductivity bears a resemblance to that of $Sm_3Ru_4Ge_{13}$ [11] and to many skutterudites, a structure type that is recognized as a promising materials class for developing novel thermoelectric materials [14, 15].

The electronic contribution $\kappa_e(T)$ to total thermal conductivity $\kappa_T(T)$ was extracted by means of the Wiedemann-Franz relation;

$$\kappa_e(T) = \frac{L_0 T}{\rho(T)} \quad (1)$$

where the Lorenz number is $L_0 = 2.44 \times 10^{-8}$ WΩ.K^{-2}. The lattice (phononic) thermal conductivity $\kappa_L(T)$ contribution to total thermal conductivity was extracted by using the expression:

$$\kappa_T(T) = \kappa_L(T) + \kappa_e(T). \quad (2)$$

This expression assumes that possible contributions to κ_T from magnon heat transport are ignored. The estimated $\kappa_e(T)$ contribution is smaller than that of the lattice conductivity by more than two orders of magnitude compared to the total thermal conductivity contribution as shown in figure 3a using red closed circle symbols. Such conductivity behaviour suggests that heat is carried by phonons much more efficiently than by electrons. From figure 3a, we can thus approximate the lattice to $\kappa_L(T) \simeq \kappa_T(T)$. A weak plateau above $T \sim 50$ K is evident in $\kappa_T(T)$ between 10 K and 200 K which signifies glassy behaviour in the thermal conductivity and is likely the result of optical (anharmonic phonon) modes produced by the cage-like structure of $Sm_3Rh_4Ge_{13}$ [9]. Below 10 K the electronic contribution produces a $\kappa_e(T) \sim T$ dependence which is typical for metallic behaviour and above 100 K electronic contribution produces a $\kappa_e(T) \sim T^2$ dependence.

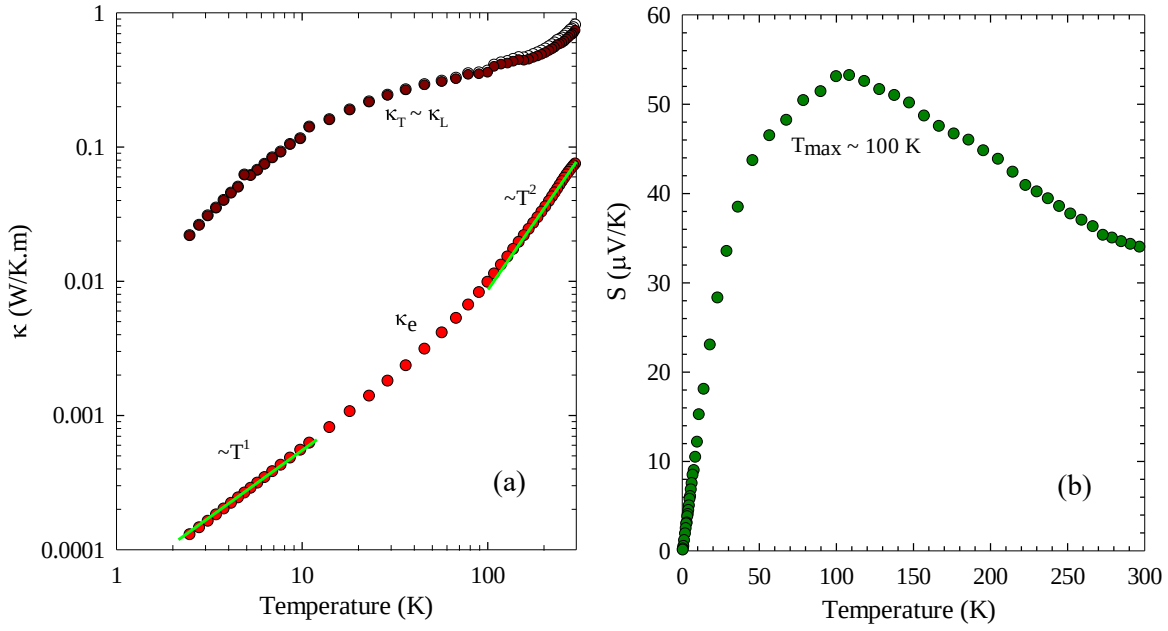

Figure 3: (a) Temperature dependence of the total thermal conductivity $\kappa_T(T)$ of $Sm_3Rh_4Ge_{13}$ plotted in log-log scale along with the electronic contribution, $\kappa_e(T)$ and lattice contribution $\kappa_L(T)$. The Seebeck coefficient, S is plotted in (b) and displays a maximum at T_{max} =100 K.

The thermopower shown in figure 3b reaches the value of 34 μV.K^{-1} at room temperature. This value is in between that of metals (~ 1 – 10 μV.K^{-1}) and semiconductors (~ 10^2 – 10^3 μV.K^{-1}). The value of thermopower is related to that of $Y_3Ir_4Ge_{13}$ and $R_3Ru_4Ge_{13}$ (R = Sm, Y, Dy, Ho and Lu) [5, 9, 11]. A positive thermopower $S(T)$, peak in $S(T)$ at T_{max} ~ 100 K, quasi-exponential $\rho(T)$ and $\rho(T)$ energy gap of ~ 158 K all support consistently that this is a narrow-gap activated semiconducting system, with gapping at the Fermi energy responsible for all the anomalous thermal and electronic transport behaviours.

4. Conclusions

We have reported on findings of a thermoelectric study on $Sm_3Rh_4Ge_{13}$. Structural analysis of the x-ray diffraction confirms the compound to adopt the cubic space group $Pm\bar{3}n$. The thermal transport exhibits only weak temperature dependence in thermal conductivity below room temperature and 2 K. The thermopower reaches fairly high and positive values which resembles a hole-dominated character near the Fermi surface as is also supported by the activated type behavior found in the electrical resistivity.

Acknowledgements

SPX acknowledges the Faculty of Science at UJ and the SA-NRF Scarce Skills Development Funds master's degree scholarship and research group of Highly Correlated Matter Physics for their endless support. BMS acknowledges NRF-Thuthuka grant (99231) and AMS thanks the SA-NRF and the FRC/URC of UJ for financial assistance.

References

[1] Zlatic V and Hewson A 2011 *New Material for Thermoelectric Applications* (Springer)
[2] Meinser G P, Morelli D T, Hu S, Yang J and Uher C 1998 *Phys. Rev. Lett.* **80** 3551
[3] Zhang Q, Chen C, Kang Y, Li X, Zhang L, Yu D, Tian Y and Xu B 2015 *Mater. Lett*. **143** 41-3
[4] Venturini G, Méot-Mayer M, Malaman B and Roques B 1985 *J. Less-Common Met*. **113** 197
[5] Kong H, Shi X, Uher C and Morelli D T 2007 *J. Appl. Phys*. **102** 023702
[6] Remeika J P *et al* 1980 *Solid State Commun*. **34** 923-26
[7] Krauss W and Nolze G 1996 *J. Appl. Cryst.* **29** 301
[8] Strydom A M 2014 *Acta. Phys. Polon. A.* 1**26** 319-20
[9] Strydom A M 2007 *J. Phys.: Condens. Matter*. **19** 386205
[10] Rai B K, Oswald I H W, Wang J K, McCandless G T, Chan J Y and Marosan E 2015 *Chem. Mater*. **27** 2488
[11] Nair H S, Kumar R, Britz D, Ghosh S K, Reinke C and Strydom A M 2016 *J. Alloys. Comp*. **669** 254-61
[12] Rai B K, Oswald I H W, Chan J Y and Morosan E 2016 *Phys. Rev. B.* **93** 035101
[13] Ghosh K, Ramakrishnan and Chandra G 1993 *Phys. Rev. B.* **48** 10435
[14] Rogl G, Grytsiv A, Failamani F, Hochenhofer M, Bauer E and Rogl P 2017 *J. Alloys. Comp.* **695** 682-696
[15] Shi X, Yang J, Salvador J R, Chi M, Cho Y Y, Wang H, Bai S, Yang J, Zhang W and Chen L 2011 *J. Am. Chem. Soc.* **133** 7837-46

DIVISION B – NUCLEAR, PARTICLE AND RADIATION PHYSICS

Measurements of natural radioactivity in soil using an array of cerium doped lanthanum bromide scintillator detectors

M Bashir[1,2,3], R T Newman[2]and P Jones[3]

[1]Department of Physics, Ibrahim Badamasi Babangida University Lapai, Nigeria
[3]Department of Physics, Stellenbosch University, South Africa
[2]Department of Subatomic Physics, iThemba Laboratory for Accelerator Based Sciences, South Africa

E-mail: 20791089@sun.ac.za

Abstract. An array of eight 2" $\times$ 2" $LaBr_3$:Ce scintillator detectors linked to a XIA PIXIE-16 Digital Signal Processing data-acquisition system was used to measure KCl, U ore, Th ore, and soil reference samples placed in the centre (17.5 cm from each detector) of the array (with all detectors lying in the horizontal plane) for 12 hours per sample. The absolute full-energy peak gamma-ray detection efficiencies of each detector was determined. The weighted average absolute full-energy peak detection efficiencies were found to be $3.21 \times 10^{-2} \pm 8.96 \times 10^{-4}$ %, $2.57 \times 10^{-2} \pm 8.79 \times 10^{-4}$ %, $1.87 \times 10^{-2} \pm 6.34 \times 10^{-4}$ % at 1461 keV (^{40}K), 1764 keV (^{238}U) and 2615 keV (^{232}Th) respectively. For the soil reference sample, the weighted average activity concentrations for ^{40}K and ^{232}Th series radionuclides were consistent with zero to within measurement uncertainties. For the same sample the activity concentration of ^{238}U series radionuclides was consistent with zero when an interval of $\pm 2\sigma$ about the mean value is considered.

1. Introduction

The efficiency of $LaBr_3$:Ce detectors is 1.2 - 1.7 times better at detecting gamma-rays than NaI:Tl detectors above 350 keV and have an energy resolution of 2.5 - 3.0 % at the 662 keV gamma-line of Cs-137, compared to 6 - 7 % for NaI:Tl detectors for 3.8 cm by 3.8 cm (1.5" $\times$ 1.5") detectors [1, 2]. The detector crystal has other advantages such as a high scintillation light output with a fast decay time [3] which make it to be an excellent detector choice for high count rate scenarios, and is capable of performing well with count rates up to 500 kHz[5]. The light output of $LaBr_3$:Ce crystals displays improved temperature stability compared to traditional NaI:Tl scintillators, varying by less than 1% between 0°C and +55°C [1, 6].

There are challenges associated with using $LaBr_3$:Ce detectors. First, $LaBr_3$:Ce is itself radioactive, due to the presence of radioactive ^{138}La [1, 2]. La-138 accounts for 0.09% of naturally occurring lanthanum and produces two gamma-rays: a 788.7 keV from beta decay to ^{138}Ce, and a 1435.8 keV from electron capture to ^{138}Ba, and X-rays: 32.2 keV ($K_{\alpha 1}$), 31.8 keV ($K_{\alpha 2}$), 36.4-37.3 keV (K_{β}), 3.9-5.9 keV (L) from β^+ decay and 95.7 keV from β^- decay. The activity concentration of ^{138}La in the scintillator material determined from the sum peak at 1468 keV is 12.9 Bq/kg [1]. As of now, it is still unclear whether this internal radioactivity acts

as a fundamental limitation for low-level activity measurements of natural occuring radioactive materials (NORM).

2. Materials and methods

An array of eight 2" × 2" in. $LaBr_3$:Ce scintillator detectors linked to a XIA PIXIE-16 Digital Signal Processing data-acquisition system was used as shown in Fig. 1. ^{137}Cs and ^{22}Na were used for energy calibration. The KCl, U and Th ore, soil reference and background samples were counted for 12 hours each. Each of these samples was placed in 1.0 L Marinelli beaker and placed 17.5 cm from each detector for measurements. The background measurement was done using an empty Marinelli beaker. Further information about the reference sample is given in Table 1. The absolute full-energy peak (FEP) detection efficiencies of the detectors were evaluated using Eqn 1 and the activity concentration determined using Eqn. 2 [7]:

$$\varepsilon = \frac{N_c}{A \times m \times t \times P_\gamma} \tag{1}$$

$$A = \frac{N_c}{\varepsilon \times m \times t \times P_\gamma} \tag{2}$$

where N_c is the full-energy peak count, t is the counting time in seconds, A is the activity concentration in Bq/kg, m is mass of the sample in kg and P_γ is the probability of emission of the particular gamma-ray being measured.

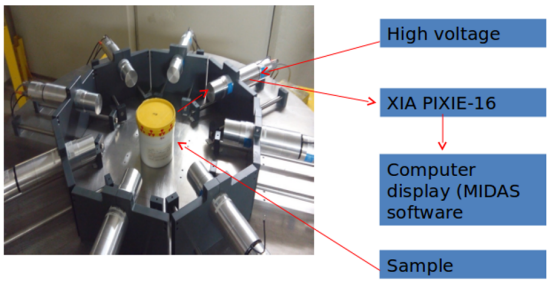

Figure 1. Experimental setup showing an array of 2" × 2" $LaBr_3$:Ce detectors and reference sample placed in the centre.

Table 1. Reference sample information

Sample	Mass (kg)	Activity (Bq/kg)	Supplier	IAEA code
`Potassium Chloride`	1.29080	16259 ± 172	IAEA	RGK-1
`Uranium Ore`	1.40912	4940 ± 99	IAEA	RGTh-1
`Thorium Ore`	1.36494	3248 ± 17	IAEA	RGU-1
`Soil`	1.50263	Vary for each radionuclide (see Table 2)	IAEA	IAEA-375

3. Results and discussion

The absolute full-energy peak (FEP) detection efficiency determined at 1461 keV (^{40}K), 1764 keV (^{238}U) and 2615 keV (^{232}Th) are shown in Fig. 2. This efficiencies were measured using the potassium chloride; uranium ore and thorium ore samples respectively (see Table1). The variation in the efficiency values between detectors could be due to slight shifts in the sample

position toward a certain detector and/or scattering. The weighted average absolute full-energy peak (FEP) detection efficiency as a function of gamma-ray energy is shown in Fig. 3. The experimental points exhibit a power-law behaviour which was fitted by the following equation:

$$\varepsilon = a\left(\frac{E}{E_0}\right)^b$$

where ε is the full-energy peak efficiency; E is gamma-ray energy in keV; E_0 is an arbitrary energy to make the argument dimensionless [here, $E_0 = 1$ keV]; and a, b are the coefficients extracted by a least-squares fit to the experimental data.

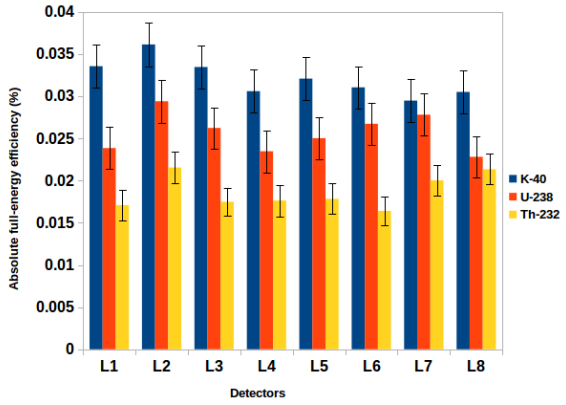

Figure 2. The absolute full-energy peak (FEP) detection efficiency for the eight detectors.

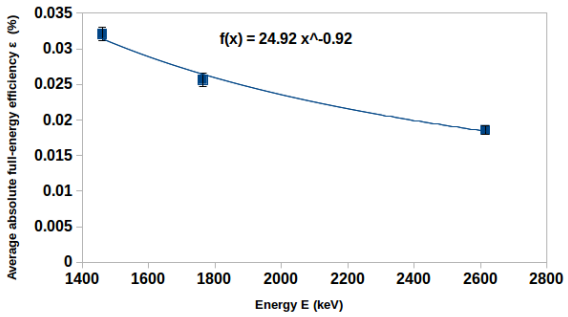

Figure 3. Average absolute full-energy peak (FEP) detection efficiency as a function of energy.

Table 2 gives the activity concentration of ^{40}K, ^{238}U and ^{232}Th series radionuclides measured in the soil reference sample using the detection efficiencies discussed above. For the soil reference sample, the weighted average activity concentrations for ^{40}K and ^{232}Th series radionuclides were consistent with zero to within measurement uncertainties. For the same sample the activity concentration of ^{238}U series radionuclides was consistent with zero when an interval of $\pm 2\sigma$ about the mean value is considered. For the measurement setup and conditions described here the minimum detectable activty (MDA) of ^{40}K; ^{238}U and ^{232}Th series radionuclides are 2391 Bq/kg; 524 Bq/kg and 369 Bq/kg, respectively. This explains the activity concentration results for the soil reference sample found in this study.

4. Conclusion

This paper presented the absolute (FEP) detection efficiencies of $LaBr_3$:Ce scintillators placed at a distance 17.5 cm away for volume samples (Marinelli geometry); for 1461 keV (^{40}K), 1764 keV (^{238}U) and 2615 keV (^{232}Th). These efficiencies were used to calculate the activity concentration of ^{40}K, ^{238}U and ^{232}Th series radionuclides in the soil reference sample. The soil activity concentration were found to be below the MDA for the setup used in this study.
In order to address this problem we are now investigating ways to reduce the influence of room background on our measurements by making use of passive shielding.

Table 2. Activity concentration of ^{40}K, ^{238}U, ^{232}Th in soil reference sample

Detector	K-40 (Bq/kg)	U-238 (Bq/kg)	Th-232 (Bq/kg)
L1	1079 ± 1681	257 ± 703	623 ± 474
L2	1248 ± 1594	570 ± 583	-34 ± 400
L3	-195 ± 1670	-230 ± 625	-4 ± 443
L4	-2458 ± 1866	134 ± 707	-168 ± 485
L5	-912 ± 1753	200 ± 658	141 ± 456
L6	-3366 ± 1851	912 ± 632	-1299 ± -536
L7	1035 ± 1892	244 ± 597	171 ± 407
L8	-2546 ± 1854	528 ± 715	234 ± 386
Average	-633 ± 623	332 ± 289	14 ± 156
Expected range	$417.0 - 432.0$*	$19.0 - 29.8$*	$19.2 - 21.9$*
Expected mean	424.0*	24.4*	20.5*

* IAEA/AL/075 report on the intercomparison run (IAEA-375)

This work is based on the research supported wholly by IBB University/TETFUND, National Research Foundation of South Africa (99037) and iThemba LABS (Laboratory for Accelerator Based Science).

References

[1] Rozsa *et al.,* 2009 http://www.crystals.saint-gobain.com/sites/imdf.crystals.com/files/documents/brillance_performance_summary.pdf
[2] Ciupek K *et al.,* 2014 *J. Radioanal. Nucl. Chem.* **299** 1345-1350
[3] Favalli A, Mehner H C, and Simonelli F 2008 *Radiat. Meas.*, **43** 506-509
[4] Milbrath, B D *et al.,* 2006 http://www.pnl.gov/main/publications/external/technical_reports/PNNL-15831.pdf
[5] Loher B *et al.,* 2012 *Nucl. Instrum. Methods Phys. Res. Sect. A Accel. Spectrometers, Detect. Assoc. Equip.*, **686** 1-6 http://dx.doi.org/10.1016/j.nima.2012.05.051
[6] Moszynski M *et al.,* 2006 *Nuclear Instruments and Methods in Physics Research* A, **568** 739-751
[7] Gilmore G R 2008 John Wiley and Sons, Ltd p.151

Investigating the diffusion of Xe implanted into glassy carbon

MYA Ismail[1,2*], JB Malherbe[1], OS Odutemowo[1], TT Hlatshwayo[1], EG Njoroge[1], E Wendler[3]
[1]*Department of Physics, University of Pretoria, Pretoria, 0002 South Africa*
[2]*Department of Physics, University of Zalingei, Zalingei, Central Darfur State, Sudan*
[3]*Institut fürFestkörperphysik, Friedrich-Schiller Universität, 07743 Jena, Germany*

E-mail: u16306873@tuks.co.za

Abstract. Recently, there has been a renewed interest in employing glassy carbon to contain radioactive fission products. One of the fission products, Xe is significant by itself due to its high neutron absorption cross section and high production as a fission product. 200 keV Xenon (Xe) ions were implanted in the glassy carbon samples to a fluence of 1×10^{16} Xe^{+} cm^{-2} at room temperature. The diffusion of the implanted Xenon in the glassy carbon was measured using Rutherford backscattering (RBS) after vacuum annealing.

1. Introduction

Glassy carbon (GC) is an apparently isotropic, continuous and non-porous material, showing conchoidal surface fracture. It is a non-graphitizing carbon which combines glassy and ceramic properties with those of graphite [1]. Unlike graphite, glassy carbon has a fullerene-related microstructure This leads to a great variety of unique materials properties. Its high strength, high hardness and also high impermeability to gases, suggest that glassy carbon must have a unique structure different from those of regular carbons [2]. These properties allow glassy carbon to be used in a wide range of applications such as in nuclear waste storage containment material.

Waste storage facilities should be designed and operated to minimize the probability and consequences of incidents and accidents. Factors that should be considered include the following: impermeability to the fission products, chemical stability against corrosion caused by processes within the waste and/or external conditions, protection against radiation damage and/or thermal damage, especially stability against the degradation of materials and resistance to impacts from operational loads or due to incidents and accidents [3].

[*]Corresponding author.
Email: u16306873@tuks.co.za

Xenon (Xe) is a noble gas mainly produced in nuclear fission reactions. It consist of various radioactive isotopes including Xenon-135, which is of considerable significance in the operation of nuclear power reactors. The reason being that it acts as a neutron absorber or poison that can slow down or stop the chain reaction after a period of operation [4]. A major contribution to the sequence of events leading to the Chernobyl nuclear disaster was the failure to anticipate the effect of xenon poisoning on the rate of the nuclear fission reaction [5]. Xenon-135 is a product of U-235 fission and has a very large neutron-capture cross section. It also decays radioactively with a half-life of 9.1 hours. Little of the Xe-135 results directly from fission; most comes from the decay chain, Te-135 to I-135 to Xe- 135 [6].

In this study, the diffusion behavior of implanted Xe in glassy carbon was investigated. As has been mentioned above, this information is necessary to determine the effectiveness of glassy carbon as a good material for constructing the casks used in nuclear waste storage.

2. Experimental procedure

The glassy carbon (Sigradur®G) samples were polished with 1 μm and 0.5 μm respectively with diamond solutions. The samples were implanted with 200 keV xenon ions to a fluence of 1×10^{16} ions/cm^2 at room temperature. The implanted sample was annealed in vacuum at temperatures increasing in steps of 100 °C from 300 °C to 1000 °C for 5h at each temperature. The depth distribution of the implanted xenon before and after each annealing step was analyzed using Rutherford backscattering spectroscopy (RBS).The RBS spectra were acquired using 1.6 MeV He^+ ion beam at beam current of 15nA. The RBS spectra were converted into the respective depth profiles of the implanted xenon. The resulting RBS depth profiles were fitted with a MATLAB program that was written by Malherbe et al [7] to extract diffusion coefficients from an initial Gaussian profile.

3. Results and discussion

Fig. 1 shows the RBS depth profile of 200 keV xenon implanted in glassy carbon at room temperature. The profile was compared with the spectra obtained from the TRIM ion distribution simulation. Fig. 1 also contains the vacancy distribution obtained from TRIM [8]. The experimental projected range, R_p, was estimated by fitting the Xe depth profile with a Gaussian equation. The value obtained is 120 nm. This value obtained for the room temperature implanted Xe depth profile is comparable to the 119 nm obtained from TRIM. The experimental straggling, ΔR_p value obtained is about 34 nm which is higher than the 21 nm obtained from TRIM. The higher ΔR_p obtained from the as-implanted Xe profile suggests a broader ion distribution to that suggested by TRIM.

Some of the implanted samples were annealed in vacuum at 300 °C -1000 °C in steps of 100 °C for 5 hours – see Fig. 2 (a) and (b). Two diffusion mechanisms can be clearly observed from the spectra shown. The first diffusion regime is between 300 °C - 800 °C. The RBS profiles obtained after annealing the samples at these temperatures showed no noticeable diffusion of the implanted Xe.

The lack of diffusion at these temperatures can be attributed to the presence of defects in the near surface region of the GC substrate. This statement is supported by the TRIM vacancy distribution shown in Fig. 1. The $R_{p(vac)}$ is about 79 nm which is significantly lower than the R_p value of the as-implanted Xe depth profile (120 nm). This discrepancy implies that the defects introduced into the GC substrate are concentrated towards the surface.

In the second diffusion regime (900 °C - 1000 °C), movement of Xe into the bulk of the GC was observed with the formation of a bimodal distribution. The migration of Xe into the GC was accelerated at 1000 °C with a new Xe peak formed within the bulk of the GC. The diffusion coefficients at temperatures 900 °C - 1000 °C were calculated to be $D = 4.3 \times 10^{-21}$ m^2/s and $D = 6.7 \times 10^{-21}$ m^2/s respectively. The lack of diffusion at these temperatures might be due to the presence of defects in the implanted region of the glassy carbon substrate acting as traps for the implanted xenon.

The diameter of Xe atom of 216 pm is much larger that the C atom of 77 pm. Thus, it effectively represents the boundary between the radiation damaged glassy carbon and the pristine bulk. This penetration of xenon into pristine glassy carbon together with the segrational kind of diffusion of the

implanted xenon atoms towards the bulk at the higher annealing temperatures.

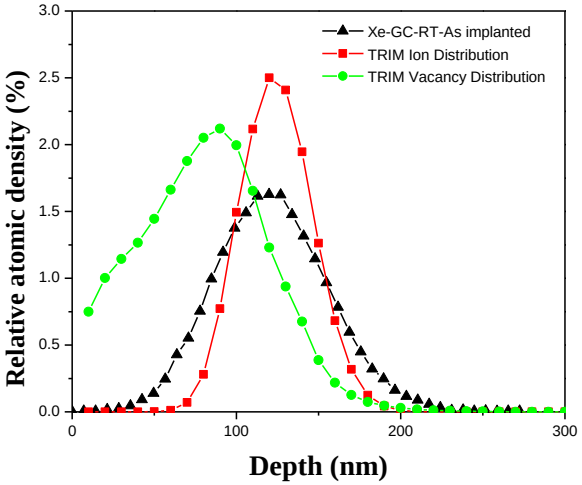

Figure 1. Depth profile of 200 keV Xe^{+} ions implanted in glassy carbon at room temperature and vacancy distribution from TRIM [8].

The movement of Xe deeper inside the GC substrate indicated that the implanted Xe will be diffused towards the bulk of GC after annealing at temperatures above 900 °C. This suggests that a Fickian type of diffusion is not responsible for the diffusion observed in this regime. Odutemowo et al [9] studied the diffusion of strontium in glassy carbon and observed a similar phenomenon when they annealed their Sr implanted GC samples at high temperatures. However, the segregation of Sr was observed towards the surface of GC instead of towards the bulk as observed in our results. They suggested that a prime factor to be considered in this segregational kind of diffusion is the Gibb's free energy of the system.

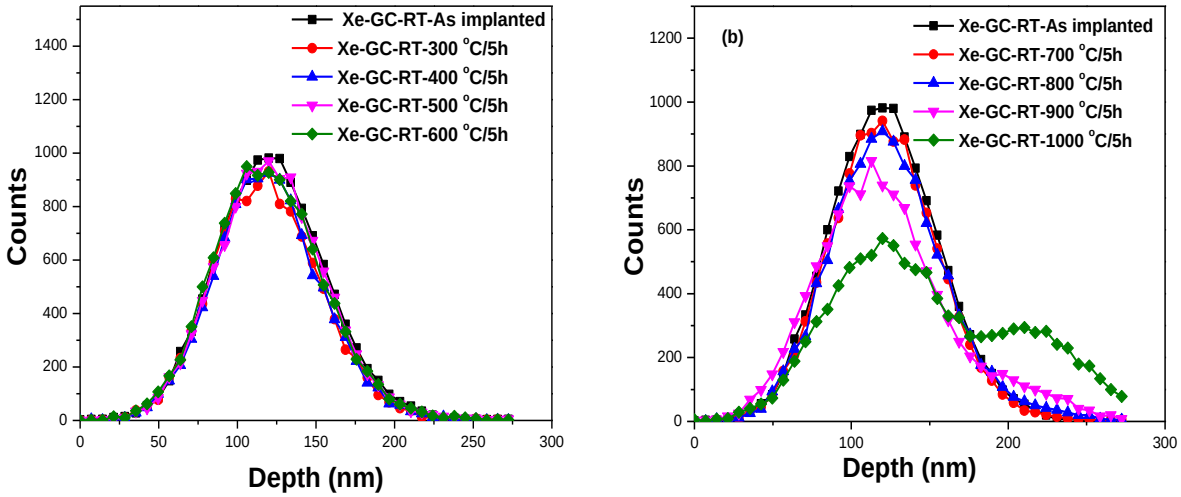

Figure 2. RBS Depth profiles of Xe implanted at room temperature after isochronal annealing at (a) 300 °C - 600 °C for 5 h and (b) 700 °C - 1000 °C for 5 h.

In order to estimate the diffusion coefficient of Xe in glassy carbon, the RBS depth profiles obtained at 300 – 1000 °C were fitted with an in-house MATLAB program. The MATLAB program fits experimental depth profiles to the solution of the Fick diffusion equation with originally a Gaussian profile and with a perfect sink at the surface. Examples of such fit are shown in Fig. 3. The fitting of the RBS spectra show that the diffusion coefficient of Xe in GC could not be estimated. This is in agreement with the results discussed earlier (no noticeable diffusion of Xe was observed).

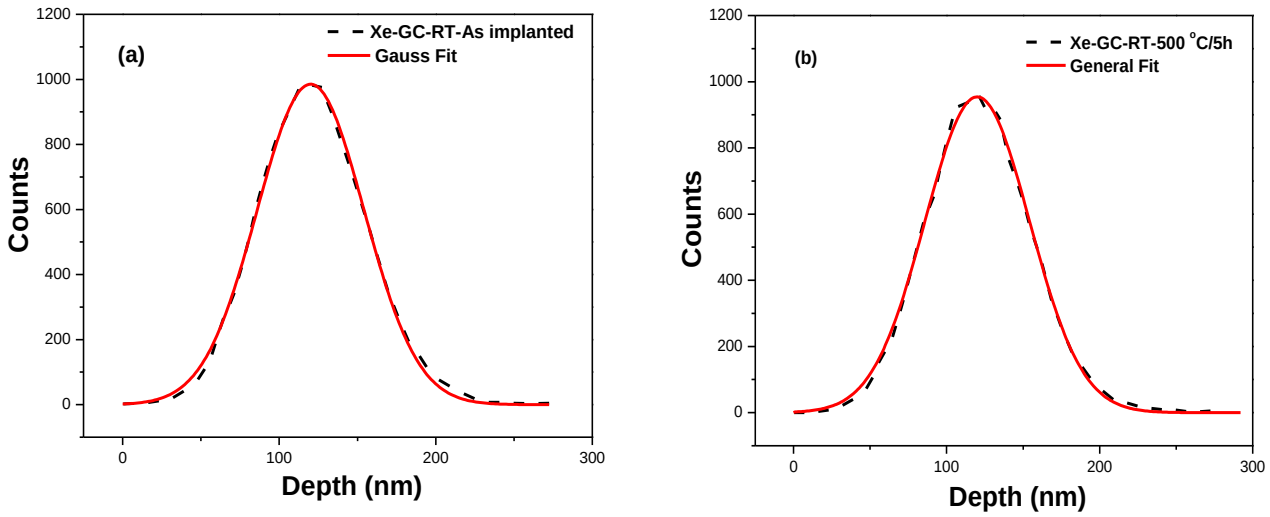

Figure 3. The MATLAB program fitted to the sample (a) implanted at RT, (b) annealed at 500 °C.

4. Conclusion

The diffusion behavior of Xe in GC was investigated using Rutherford backscattering spectrometry (RBS). RBS depth profiles obtained after annealing the sample at 300 °C – 800 °C showed that there was no diffusion of the implanted Xe into the bulk or towards the surface of GC. This non-diffusion was attributed to the presence of defect traps acting as a diffusion barrier towards the surface of GC. At the highest annealing temperatures (900 °C – 1000 °C), there was a movement of Xe into the bulk of the GC with a new peak (indicating segregation) formed within the GC bulk. The lack of diffusion of Xe in GC shows that glassy carbon is a good containment material for xenon.

Acknowledgement

The financial supports of the UP postgraduate bursary the University of Pretoria (South Africa) and the Ministry of Higher Education, the University of Zalingei (Sudan) are highly acknowledged.

References

[1] Noda T, Inagaki M, and Yamada S 1968 A Comment on the Structure of Glassy Carbon *Bulletin of the Chemical Society of Japan*. vol. 41, no. 12. pp. 3023-3024
[2] SPI Supplies 2009 *Glassy Carbon Product Information* pp. 1–5. www.2SPI.com accessed Nov. 10, 2016
[3] Krause H 1972 *Storage of radioactive waste,* vol. 59, no. 9, pp. 412-417
[4] Wiley J & Sons Ltd 2010 *Radionuclides in the Environment* ISBN 978-0-470-71434-8
[5] Garland WJ 2003 *Xenon Effects on Nuclear Reactor Reactivity 4D03 course notes*, pp. 1-6
[6] Roggenkamp PL 2000 *The Influence of Xenon-135 on Reactor Operation* pp. 49-56
[7] Malherbe JB, Selyshchev PA, Odutemowo OS, Theron CC, Njoroge EG, Langa DF,

Hlatshwayo TT 2017 Diffusion of a mono-energetic implanted species with a Gaussian profile *Nucl. Instrum. Methods Rel. Phys*. **406** 708-713

[8] Ziegler J 2012 SRIM computer code-2012 www.srim.org. accessed May 24, 2017.

[9] Odutemowo O S, Malherbe J B, Theron CC, Njoroge EG, Wendler E 2016 *"In-situ RBS studies of tium implanted glassy carbon,"* Vacuum, vol. 126, no. March, pp. 101–105

Calculation of the energy produced from radiative capture in SAFARI-1

L. Jurbandam[1], O. M. Zamonsky[2]

[1] School of Physics, University of Witwatersrand, Johannesburg, 2050, South Africa
[2] The South African Nuclear Energy Corporation SOC Ltd (Necsa), P1900, P. O. Box 852, Pretoria, 0001, South Africa

E-mail: Linina.jurbandam@necsa.co.za

Abstract. The knowledge of the fission Q-value is important for the safety analysis of a nuclear reactor. This value is around 200 MeV/fission in all nuclear reactors, where the energy released from radiative capture (Qγc) is the main source of differences between reactors. In this work, we present a detailed calculation of (Qγc) produced in SAFARI-1 using the MCNP-5 (Monte Carlo N-Particle) code. MCNP is a probabilistic transport code that has the capability of solving general geometries with continuous energy data. In particular, we calculate the reaction rate of the nuclides that contributes majorly to the heating in the SAFARI-1 core. From the nuclear reaction rate and the energy released per radiative capture reaction (binding energy), the total energy produced from radiative capture was calculated. In previous work, the radiative capture energy was calculated as an energy deposition using MCNP-5. From the energy deposition calculation, (Qγc) was calculated as 5.42 MeV/fission. Using the energy production method, (Qγc) was calculated as 5.31 MeV/fission. Typical values for (Qγc) ranges between 3 - 12 MeV/fission. This work takes a closer look at how to arrive at these values using the two methods in MCNP-5.

1. Introduction

The knowledge of the recoverable fission Q-value is important for the safety analysis of a nuclear reactor. Physicists and engineers require the reactor specific Q-value to normalize calculated quantities to the total power of the reactor. The fission Q-value of a nuclear reactor is the sum of all the radiation energy components such as energy released from fission products, neutrons, prompt and delayed photons, beta decay and neutrinos. Radiative capture photons also forms part of the components that make up the Q-value, however, (Qγc) is not released in the fission process but recovered after fission in the core. It is important to note that the Q-value is calculated per fission event in the reactor core. Another important fact to note is that the mass of the neutrino is extremely small, consequently, there is no interaction with matter, and all the energy released from neutrinos is lost in the reactor. Although the energy released from neutrinos cannot be recovered from the fission process itself, part of the energy can be recovered from radiative capture. Almost all the components that make up the fission Q-value can be approximated from nuclear data libraries, with the exception of the energy deposited from radiative capture (Qγc). This component is reactor specific due to the fact that it is dependent on the materials present in the core. The process of radiative capture involves the capture of a neutron by the medium with the formation of an unstable compound nucleus. The subsequent

release of nuclear binding energy in the process of de-excitation of the compound nucleus is done through the emission of gamma radiation. The deposition of the energy of these gamma rays in the system is the so called (Qγc). The Q-value contribution from radiative capture may range from 3 - 12MeV/fission [1]. As a result of this energy range, it can be seen that the radiative capture component may add a significant difference to the estimated Q-values which most scientists generally accept as 200 MeV/fission.

The goal of the paper is to present a method of calculating the reactor specific energy deposition from radiative capture released in SAFARI-1 per fission event. We followed the methodology used in [2] for the Advanced Test Reactor. We use MCNP-5 to calculate the total number of radiative capture reactions produced per fission in the core and then multiply it by the energy released per reaction (binding energy). In a previous work [3], MCNP was used to calculate the energy deposition in SAFARI-1 applying a different approach. Previously, MCNP was used to calculate the heat deposited in the reactor from radiative capture by tracking the gammas produced in the de-excitation of the compound nucleus from birth to death. In this work, we also aim to verify the value that was previously calculated. A description of the MCNP model of SAFARI-1, as well as the procedure to calculate the energy deposited from radiative capture is presented in the following sections. In the last section of the paper, the results for the calculations are documented and discussed.

2. Description of SAFARI-1

SAFARI-1 is a 20 MW tank in pool type material testing reactor (MTR), located at Necsa, Pelindaba, South Africa. The reactor core is contained inside the reactor vessel, which is inside the reactor pool. The reactor vessel is immersed in light water which serves as coolant, moderator and shielding. The reactor core consists of 26 fuel assemblies and 6 control rod assemblies. The control rod assembly consists of two regions namely the absorbing region and the followers that contain fuel. Apart from the molybdenum production assemblies, it contains several positions for neutron irradiation of samples. For this work, the sample positions were filled with water. SAFARI-1 uses 19.7 % enriched uranium as fuel. Surrounding the core is a beryllium reflector and the aluminium core box.

3. SAFARI-1 Analysis Codes

The two main codes used in support of the operation of SAFARI-1, are the OSCAR-4 code system and MCNP. The OSCAR-4 (OSCAR) code system, which is developed and maintained in the Radiation and Reactor Theory (RRT) Section at Necsa, is used for reactor reload design and core-follow analysis. It contains a three-dimensional, multigroup, nodal diffusion code which performs the calculations in a six energy group structure for homogeneous nodes. During core depletion analysis, OSCAR tracks the depletion history of each fuel element in the reactor core [4].

For detailed transport calculations, the Monte Carlo code MCNP, version 5.1.51 [5], is used. MCNP is a general-purpose Monte Carlo N-Particle transport code that is used in RRT for neutron, photon and coupled neutron/photon transport. MCNP's general geometry modelling capability and the use of pointwise cross-sections are amongst its main features that makes it so applicable for the analysis of complex problems. In general OSCAR and MCNP are used in conjunction, i.e. OSCAR provides MCNP with the appropriate core depletion state for the detailed transport analysis.

4. MCNP Model of SAFARI-1

The MCNP model for SAFARI-1 that was developed at RRT is shown in Figure 1. It includes the reactor core, the core box, the reactor tank and the beam tubes. Inside the reactor tank is a grid plate with a rectangular arrangement of 89 positions where different assembly types can be loaded. The core is surrounded by a beryllium reflector and some aluminium and lead assemblies. Positions D6 and F6 contain the Isotope Production Rigs (IPRs) for irradiation of samples but for this work they are filled with water.

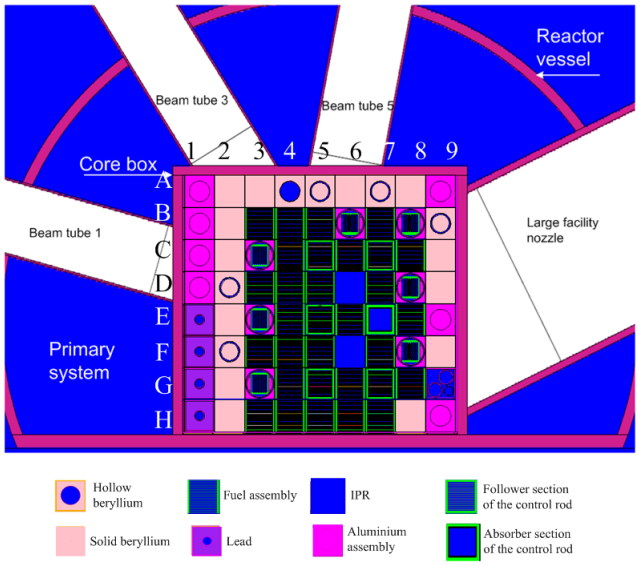

Figure 1: MCNP model of SAFARI-1

Figure 1 shows a planar view of the model with the fuel, control rod elements and control rod fuel follower, at the active regions of these components. The fuel elements are MTR type fuel with 19 plates each. The fuel plates consist of a Uranium-Silicide-Aluminium (U3Si2-Al) powder dispersed core, enclosed in an aluminium-alloy cladding. The control rod assemblies consist of an upper absorber section and a lower fuel section connected through a rigid aluminium coupling mechanism. The absorbing section consists of an aluminium box that contains a cadmium layer as an absorber. The fuel section, also called the control rod follower, is similar to the fuel elements but is constructed inside an aluminium box and contains only 15 plates.

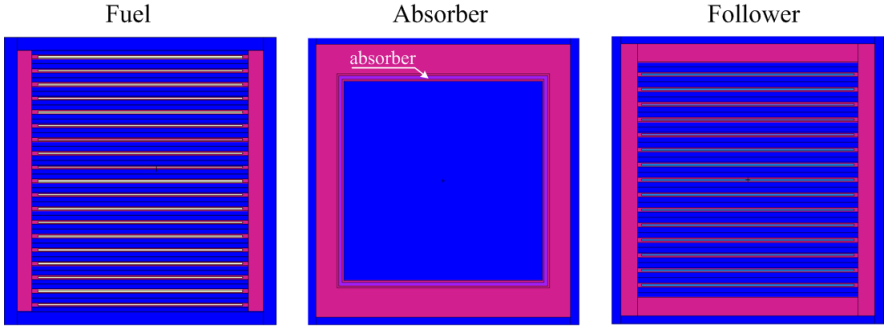

Figure 2: View of the fuel element, absorber and fuel follower

5. Methodology

MCNP is a probabilistic transport code that has the capability of solving generalized geometries using continuous energy data. For this work, MCNP-5 was used to calculate the total number of capture reactions produced from every isotope that contributes majorly to the heating in SAFARI-1. The ENDF-VII library was utilized. The MCNP radiative capture nuclear reaction rate is given by Equation (1). Note that the reaction rate is calculated for isotopes present in every cell of SAFARI-1. The MCNP model of SAFARI-1 consists of more than 3 000 cells.

$$\text{Radiative capture reaction rate} = N_i \int \varphi(\vec{r}, E)\sigma_{ci}(\vec{r}, E)dEdV \tag{1}$$

where:

- N_i = number density of isotope (atoms/barn/cm)
- $\varphi(\vec{r}, E)$ = energy dependent neutron flux (n/cm^2/neutron born in the system)
- $\sigma_{ci}(\vec{r}, E)$ = radiative capture cross section for isotope (barns).

The i^{th} isotopes in Equation (1) are from the elements that contribute majorly to radiative capture heating in the core. Table 1 shows a list of elements present in the different components of the core. From Figure 1 and Table 1 it can be seen that the majority of the core consists of hydrogen and aluminium. Impurities may be present in the material compositions and were not taken into account for this calculation.

Table 1: List of elements present in the reactor core

Hydrogen	**Aluminium**	**Cadmium**	**Silicon**	**Beryllium**	**Uranium**
Water coolant Primary system	Fuel plates Follower Structural assembies	Control rod Irradiation devices	Fuel meat Follower	Fuel meat Follower	Reflector

In order to calculate the number of capture reactions produced per fission in the core, the MCNP capture reaction rate obtained with Equation (1) is multiplied by $\frac{\nu}{k_{eff}}$ (number of neutrons produced per fission). Binding energy is released during radiative capture. By multiplying the total number of capture reactions produced per fission, by the binding energy released per radiative capture, the total amount of radiative capture energy released in the core per fission event can be calculated. Table 2 lists the various nuclides with their associated binding energies that were used for the final calculations.

Table 2: Binding energies of the nuclides present in SAFARI-1

Target element	Target isotope	Compound nucleus	Binding energy (MeV)
Aluminium	Al-27	Al-28	7.7307
Silicon	Si-28	Si-29	8.4751
	Si-29	Si-30	10.617
	Si-30	Si-31	6.5940
Hydrogen	H-1	H-2	2.2245
Cadmium	Cd-106	Cd-107	7.9243
	Cd-108	Cd-109	7.3197
	Cd-110	Cd-111	6.9741
	Cd-111	Cd-112	9.3979
	Cd-112	Cd-113	6.5401
	Cd-113	Cd-114	9.0421
	Cd-114	Cd-115	6.1386
	Cd-116	Cd-117	5.7669
Uranium	U-235	U-236	6.1386
	U-238	U-239	5.7669
Beryllium	Be-9	Be-10	6.8149

6. Results

Calculations were performed using MCNP-5 for 100 active cycles with a well converged fission source. 200 000 histories were simulated for each cycle. Individual calculations were performed for nuclides contributing to radiative capture in the SAFARI-1 core. Table 3 shows the results that were obtained using the above methodology.

Table 3: Calculated energies from radiative capture in SAFARI-1

Target element	Energy due to radiative capture	% Contribution
Uranium	1.77	33.24 %
Hydrogen	1.62	30.46 %
Aluminium	1.18	22.22 %
Cadmium	6.04×10^{-1}	11.38 %
Beryllium	1.30×10^{-1}	2.46 %
Silicon	1.27×10^{-2}	0.24 %
Total	5.31	100 %

From Table 3, it can be seen that the total energy recovered from radiative capture was calculated as 5.31 MeV/fission. As expected, the highest contributor is uranium due to it having a high capture cross-section. Hydrogen and aluminium are also high contributors which could be because the majority of the core is made up of it.

7. Conclusion

By calculating the radiative capture reaction rate in MCNP-5, we calculated the total energy produced from radiative capture in SAFARI-1. This was calculated to be 5.31 MeV/fission. Previously [3], (Qγc) calculated as 5.42 MeV/fission by tracking all the gammas produced in the de-excitation of every compound product. The reason for the difference could be due to the fact that we did not consider impurities in the recent radiative capture calculation. The difference is small, around 2 %; therefore we can have confidence in our results. Future work will focus on the inclusion of the heat deposited from the decay products of radiative capture, since some of the product nuclei undergo radioactive decay.

8. References

[1] Brown FB et al 2008 *Int Conf on Reactor Physics, Monte Carlo: Advances and Challenges* (Interlaken, Switzerland)
[2] Sterbentz JW *Q-value (MeV/fission) Determination for the Advanced Test Reactor*. Idaho National Laboratory VHTR Program; Idaho Falls, Idaho
[3] Jurbandam L 2015 *Evaluation of the fission energy deposition in the SAFARI-1 nuclear reactor* Hons Johannesburg: University of Witwatersrand
[4] Prinsloo RH et al 2012 *OSCAR-4 System Overview*, RRT-OSCAR-REP-12002, Necsa Internal Report
[5] X-5 Monte Carlo Team MCNP - A General N-Particle Transport Code, Version 5 Volume I: Overview and Theory, LA-UR-03-1987 (2003, updated 2005), *Los Alamos National Laboratory.*

The impact of an extended Inner Detector tracker on the $W^{\pm}W^{\pm}jj$ measurement in pp collisions at the High-Luminosity LHC with the upgraded ATLAS detector

Dr. Claire Lee[1], Raynette van Tonder[2], Dr. Sahal Yacoob[2]

[1]Brookhaven National Lab, PO Box 5000, Upton, NY 11973-5000, United States of America
[2]Department of Physics, University of Cape Town, Private Bag X3, Rondebosch 7701, South Africa

E-mail: VTNRAY001@myuct.ac.za

Abstract. Vector Boson Scattering has been identified as a promising process to study the nature of electroweak symmetry breaking. The best channel for VBS measurements is same-electric-charge W boson scattering: a rare Standard Model process that has a distinctive experimental signature of a same-electric-charge lepton pair and two high energy forward jets. The study of the electroweak production mechanism of $W^{\pm}W^{\pm}jj$ scattering will continue through to the High-Luminosity LHC (HL-LHC) physics program. During this program, the HL-LHC will not only operate at an increased centre of mass energy of 14 TeV, but also produce an instantaneous luminosity of $L = 7 \times 10^{34}\,\mathrm{cm}^{-2}\mathrm{s}^{-1}$. Several upgrades of various sub-detectors of the ATLAS detector are scheduled to cope with the intense radiation and the high pileup environment. The prospects for a $W^{\pm}W^{\pm}$ measurement after the LHC and ATLAS detector upgrades will be discussed, with a focus on the impact of an extended tracking detector. The effect of the upgraded Inner Detector on the measurement for the same-electric-charge $W^{\pm}W^{\pm}$ scattering process is evaluated by analysing simulated events with two leptons of the same electric charge, at least two jets and missing transverse energy.

1. Introduction

Vector Boson Scattering (VBS) is a process of great interest. In the absence of a Standard Model (SM) Higgs boson, the longitudinally polarised WW scattering amplitude grows as a function of centre of mass energy squared and violates unitarity at approximately $\sqrt{s} \approx 1\,\mathrm{TeV}$ [1]. A Higgs scalar regulates the scattering amplitude of this process at high energies, restoring unitarity [2]; however, it is still unclear whether the recently discovered Higgs boson [3] [4] fully unitarizes the longitudinally polarised WW scattering amplitude over all energies or whether alternative mechanisms are also involved [5–7]. Representative Feynman diagrams of the contributing processes are shown in Figure 1. The best channel for VBS measurements is same-electric-charge W boson scattering [8], which provides a window to investigate the mechanism of electroweak symmetry breaking. An incredibly rare process, same-electric-charge W boson scattering, can occur at hadron colliders like the Large Hadron Collider (LHC) as an interaction of W bosons that are radiated off incoming proton beams. These W bosons scatter and subsequently decay, we select events where W bosons decay leptonically i.e. $W^{\pm} \to l^{\pm}\nu,\ l = e, \mu$ giving the distinctive

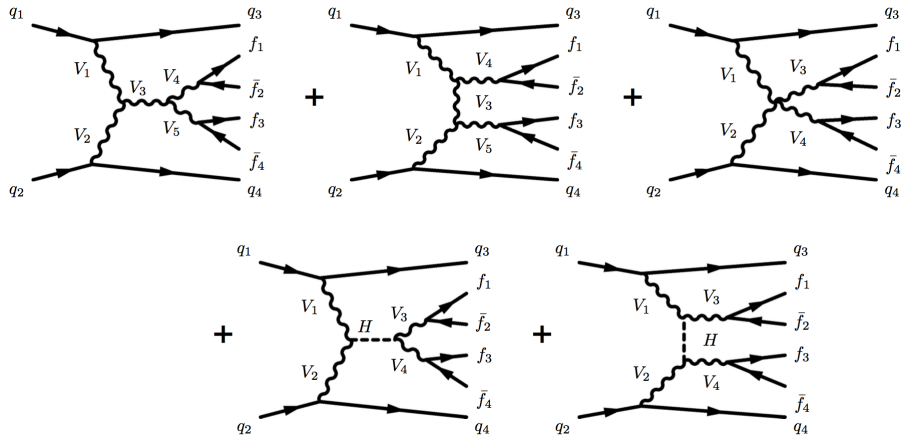

Figure 1. Representative Feynman diagrams of $VVjj$-EW production. The VBS scattering topology includes either a triple gauge coupling vertex, the t-channel exchange, a quartic boson coupling vertex or a Higgs boson exchange in the s- or t-channels. The lines are labelled by quarks (q), vector bosons (V) and fermions (f).

experimental signature of a lepton pair with the same electric charge and two high energy forward jets. The study of the electroweak production of $W^{\pm}W^{\pm}jj$ is an important task that will be continued through to the High-Luminosity LHC (HL-LHC) physics program.

2. Upgrades of ATLAS sub-detectors

Over the coming decade the LHC instantaneous luminosity is expected to increase to $2-5\times 10^{34}\,\mathrm{cm}^{-2}\mathrm{s}^{-1}$ with respect to the design luminosity, ultimately leading up to the HL-LHC physics program and the associated upgraded ATLAS detector [9]. Besides operating at an increased centre of mass energy of $\sqrt{s}=14\,\mathrm{TeV}$, the HL-LHC will also produce a total integrated luminosity of $L=3000\,\mathrm{fb}^{-1}$ corresponding to an average of $\mu=200$ inelastic pp collisions per bunch crossing. To cope with the intense radiation and the increased pileup environment the ATLAS sub-detectors will require several significant upgrades or replacements. In particular, the current ATLAS Inner Detector will be completely replaced with all-new Inner Trackers (ITk). Candidate designs for the inner tracking system has been updated to cover a wider range in pseudorapidity from $|\eta|\leq 2.7$ up to $|\eta|\leq 4.0$ [10]. In addition, a proposed very forward muon-tagger, attached to the Muon Spectrometer's new small wheels will enable the reconstruction of forward muons within a pseudorapidity of $|\eta|\leq 4.0$. The prospects of a $W^{\pm}W^{\pm}jj$-EW measurement at the upgraded LHC and ATLAS detector is investigated in the following sections, with a focus on the extension of the inner tracking system and the addition of a forward muon-tagger.

3. Simulating $W^{\pm}W^{\pm}$jj-EW scattering at 14 TeV

Signal and background processes are simulated with the use of Monte Carlo samples at a centre of mass energy of 14 TeV with the number of events scaled to a total integrated luminosity of $L=3000\,\mathrm{fb}^{-1}$. The $W^{\pm}W^{\pm}jj$-EW and $W^{\pm}W^{\pm}jj$-QCD production processes are simulated with Madgraph aMC@NLO [11] interfaced with Pythia 8 [12] for parton showering, hadronisation and the underlying event modelling. The dominant background process, WZ + jets production, is simulated using Sherpa v2.2.0 [13] [14], with next-to-leading-order accuracy. Included in the WZ + jets background estimate is both the strong and electroweak production mechanisms of this process. Additional pp pileup interactions, with an average of 200 interactions per bunch

Table 1. Selection criteria for $W^{\pm}W^{\pm}jj$-EW events.

Description	Selection requirement
Lepton selection	Exactly 2 leptons with $p_T > 25\,\text{GeV}$
Dilepton charge and separation	$\Delta R_{l,l} \geq 0.3$, $q_1 \times q_2 > 0$
Dilepton mass	$m_{ll} > 20\,\text{GeV}$
Z_{ee} veto	$\lvert m_{ll} - m_Z \rvert > 10\,\text{GeV}$
E_T^{miss}	$E_T^{miss} > 40\,\text{GeV}$
Jet selection and separation	At least two jets with $\Delta R_{l,j} > 0.3$
Di-jet rapidity separation	$\lvert \Delta y_{ij} \rvert > 2.4$
Third-lepton veto	0 additional preselected leptons
Di-jet mass	$m_{jj} > 500\,\text{GeV}$
Lepton centrality	$\zeta > 0$

crossing, are generated with Pythia 8 and are added event-by-event to recreate the high pileup environment associated with the HL-LHC. Other background processes that could mimic the final state of $W^{\pm}W^{\pm}jj$ are not simulated. Rather, the contributions from these processes are estimated by making use of the background contributions observed in the Run I $W^{\pm}W^{\pm}jj$ analysis at $\sqrt{s} = 8\,\text{TeV}$ [15] [16].

The total background contribution is estimated by summing the final event yields from the $W^{\pm}W^{\pm}jj$-QCD and WZ + jets processes and scaling the result to account for the non-simulated background contributions. Scale factors were derived from the relative background composition observed in the 8 TeV analysis and calculated for individual channels. The calculated scale factors are 2.2, 1.2 and 1.8 for the ee, $\mu\mu$ and $e\mu/\mu e$ channels, respectively, while the scale factor for the combined channels is 1.7 [17].

4. Object and event selection

Events are preselected by either a single-muon or single-electron trigger and require a transverse momentum of 25 GeV for leptons. Additionally, muons and electrons with transverse momenta $p_T > 6$ and 7 GeV are also preselected and are defined as loose leptons. Several forward tracking scenarios are considered: in the case where no forward tracking is available, the leptons are restricted to $|\eta| \leq 2.7$, while in the case where forward tracking is available a scenario is considered where only electron reconstruction is available to $|\eta| \leq 4.0$. The possibility of a forward muon-tagger is also considered, which would allow for both electron and muon reconstruction up to $|\eta| \leq 4.0$.

Furthermore, jets with $p_T > 30\,\text{GeV}$ and $|\eta| < 4.5$ are considered. A selection requirement is applied to all jets with transverse momenta below 100 GeV in order to distinguish between jets resulting from a hard scatter interaction and pileup jets, which result from the accompanying soft scatter interactions. This requirement is based on track confirmation, which makes use of the fraction of the p_T of the tracks from the associated hard scattering vertex to the jets. Selection criteria based on this requirement are applied over an η region which is related to two different tracking scenarios. In the case where forward tracking is not available, the selection criteria are applied for jets up to $|\eta| \leq 2.5$ and for jets up to $|\eta| \leq 3.8$ with forward tracking.

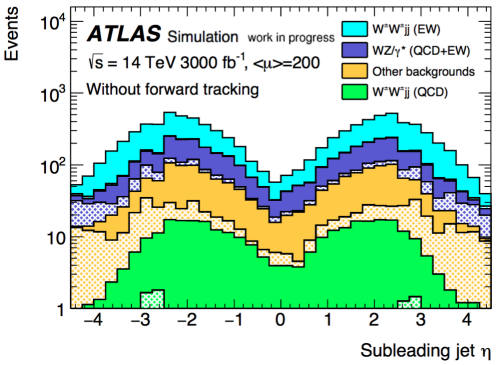

Figure 2. Pseudorapidity (η) distribution of the sub-leading jets after all analysis criteria have been applied, for the case where tracking covers up to $|\eta| \leq 2.7$.

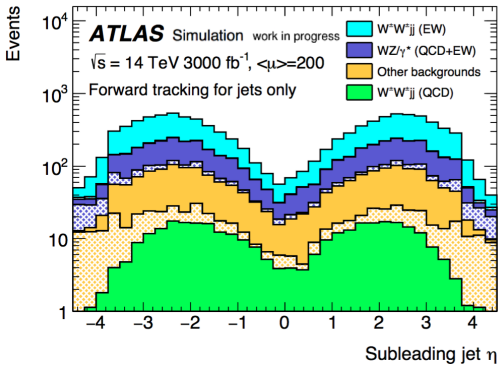

Figure 3. Pseudorapidity (η) distribution of the sub-leading jets after all analysis criteria have been applied, for the case where tracking covers up to $|\eta| \leq 4.0$.

Significant contamination from pileup jets must be reduced by increasing the p_T threshold for jets outside the tracking region from 30 to 70 GeV. After the jets and leptons have been selected, selection criteria are applied based on the unique experimental signature of $W^{\pm}W^{\pm}jj$-EW scattering, shown in Table 1. The final requirement, lepton centrality, is based on the kinematic signature of the leptons and jets and is given by:

$$\zeta = \min[\min(\eta_{l1}, \eta_{l2}) - \min(\eta_{j1}, \eta_{j2}), \max(\eta_{j1}, \eta_{j2}) - \max(\eta_{l1}, \eta_{l2})]. \quad (1)$$

5. Impact of an extended Inner Detector tracker and forward muon-tagger

The extension of the Inner Detector's tracking capabilities to cover a pseudorapidity range up to $|\eta| \leq 4.0$ enables the ability to differentiate pileup jets from jets originating from the hard scatter events in the forward regions, thus reducing contributions from background processes containing jets while also increasing the overall signal yield. The pseudorapidity distributions for the sub-leading jets after all selection criteria have been applied, are shown in Figure 2 and 3, for the $W^{\pm}W^{\pm}jj$-EW signal sample together with the other contributing backgrounds with or without the availability of forward tracking, respectively. Solid colours indicate jets originating from hard scatter events, while the hashed fills indicate jets originating from pileup events. A distinctive step in the signal sample is visible between $|\eta| = 2.5$ and $|\eta| = 3.8$. These ranges correspond to the availability of forward tracking for jets, which indicates the raised acceptance p_T for jets over a larger region.

Increasing the pseudorapidity coverage for electrons and muons is advantageous since it provides the ability to reconstruct leptons within a larger range of the detector. Additionally, there is an increased acceptance of additional forward leptons, which consequently leads to a stronger third-lepton veto for events. For this reason, the third-lepton veto suppresses a significant amount of background contributions with three leptons in the final state, especially the dominant WZ + jets process. This is due to the increased likelihood of reconstructing and detecting the third lepton from the WZ decay, which can be seen in the pseudorapidity distributions for the loose leptons before the third-lepton veto has been applied (Figure 4 and 5). The strongest suppression of the WZ background is therefore provided by the more efficient third-lepton veto.

The effect of a very forward muon-tagger is investigated by varying the acceptance p_T threshold for the loose muons, for each of the four considered tracking scenarios. Three cases are

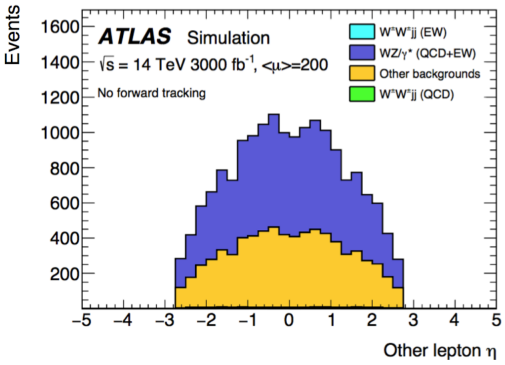

Figure 4. Pseudorapidity (η) distribution of the loose leptons before the third-lepton veto, for the case where tracking covers up to $|\eta| \leq 2.7$.

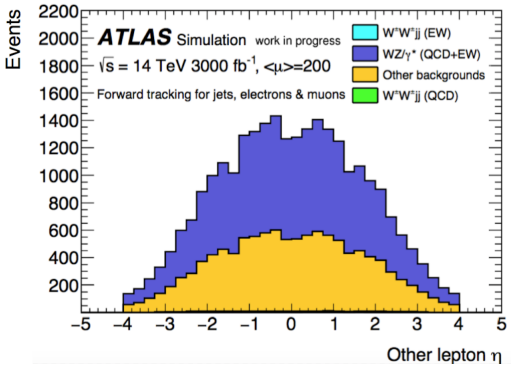

Figure 5. Pseudorapidity (η) distribution of the loose leptons before the third-lepton veto, for the case where tracking covers up to $|\eta| \leq 4.0$.

considered namely, $p_T = 6$, 10 and 15 GeV, where $p_T > 6$ GeV is the nominal acceptance for loose muons. Figure 6 shows the changes in the significance of the $W^{\pm}W^{\pm}jj$-EW measurement with respect to the increased p_T threshold for each of the four tracking scenarios. From this plot it can be seen that the largest gain in signal significance is provided by the case where forward tracking is available for both electrons and muons, since muons can be detected with greater efficiencies. In addition, the background contributions in the $\mu\mu$ channel is smaller as opposed to the background contributions with electrons. Furthermore, the significance of the $W^{\pm}W^{\pm}jj$-EW measurement decreases rapidly when the p_T threshold is raised, which is due to the fact that an increased amount of background events pass the third-lepton veto.

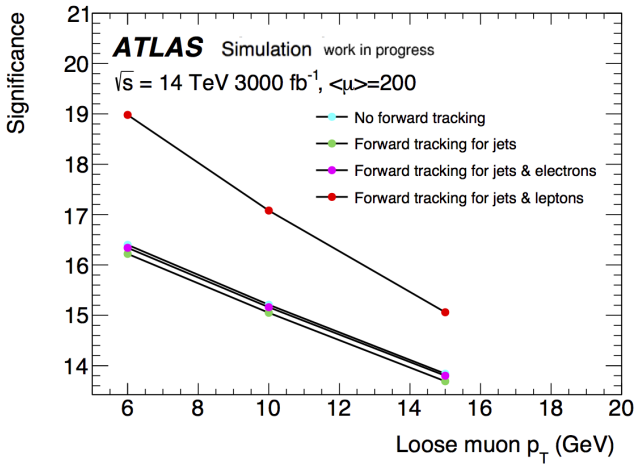

Figure 6. Effect of varying the loose muon transverse momentum on the significance of the $W^{\pm}W^{\pm}jj$-EW measurement for each of the four considered tracking scenarios.

6. Conclusion

The prospects of a $W^{\pm}W^{\pm}jj$-EW measurement at the HL-LHC looks promising with an extended inner tracking system and a forward muon-tagger. The forward tracker provides an

increased background rejection, due to excellent pileup rejection in the forward regions. In addition, the extended coverage for leptons enables the reconstruction and identification of leptons in the forward region, hence providing a more effective third-lepton veto. By extending the inner tracking system the $W^{\pm}W^{\pm}jj$-EW scattering signal yield can be increased by 12% with the increased pseudorapidity coverage for jets. The signal yield can be further increased by 14% in combination with the third-lepton veto. Consequently, the expected significance of the $W^{\pm}W^{\pm}jj$-EW measurement is improved by 16%, which makes the scenario where forward tracking is available for jets, electrons and muons the optimal case.

The effect of a forward muon-tagger was further investigated by varying the p_T acceptance threshold for loose muons. It was found that fewer muons were accepted leading to an increased amount of background events passing the third-lepton veto. Consequently, the significance of the measurement decreased rapidly from a significance of 19 for $p_T = 6\,\text{GeV}$ to 15 for $p_T = 15\,\text{GeV}$ in the case where forward tracking is available for jets and both electrons and muons.

Studies of the effect of an extended-η ATLAS detector on the $W^{\pm}W^{\pm}jj$-EW measurement will continue in the future.

Acknowledgments
I wish to express my sincere gratitude for the guidance of my supervisor, Dr. Sahal Yacoob, as well as Dr. Claire Lee. In addition, I would also like to thank the UCT Postgraduate Funding Centre for funding this research.

References

[1] Rindani S D 2009 *Physics at the Large Hadron Collider* (Springer) p 45
[2] Alboteanu A, Kilian W and Reuter J 2008 *J. High Energy Phys.* 010
[3] ATLAS Collaboration 2012 *Phys. Lett. B* **716** 1–29
[4] CMS Collaboration 2012 *Phys. Lett. B* **716** 30–61
[5] Veltman M J G 1977 *Acta Phys. Polon. B* **8** 475–492
[6] Lee B W, Quigg C and Thacker H B 1977 *Phys. Rev. Lett.* **38** 883
[7] Lee B W, Quigg C and Thacker H B 1977 *Phys. Rev. D* **16** 1519
[8] Zhu B *et al.* 2011 *Eur. Phys. J. C* **71** 1
[9] ATLAS Collaboration 2015 CERN-LHCC-2015-020, LHCC-G-166 URL `http://cds.cern.ch/record/2055248`
[10] ATLAS Collaboration 2016 ATL-PHYS-PUB-2016-025 URL `https://cds.cern.ch/record/2223839`
[11] Alwall J *et al.* 2014 *J. of High Energy Phys.* **2014** 1–157
[12] Sjöstrand T *et al.* 2015 *Comput. Phys. Commun.* **191** 159–177
[13] Gleisberg T *et al.* 2009 *J. of High Energy Phys.* **2009** 007
[14] Höche S *et al.* 2009 *J. of High Energy Phys.* **2009** 053
[15] ATLAS Collaboration 2014 *Phys. Rev. Lett.* **113** 141803
[16] ATLAS Collaboration 2016 *arXiv preprint arXiv:1611.02428*
[17] ATLAS Collaboration 2017 ATL-PHYS-PUB-2017-023 URL `https://cds.cern.ch/record/2298958`

High-fidelity modelling of the ETRR-2 research reactor

M. Mashau[1], S.A. Groenewald[1] and F.A. van Heerden[1]

[1] The South African Nuclear Energy Corporation SOC Ltd (Necsa), P1900, P. O. Box 852, Pretoria, 0001, South Africa

E-mail: maurice.mashau@necsa.co.za

Abstract. This study forms part of the on-going International Atomic Energy Agency (IAEA) Coordinated Research Project (CRP) which primarily focuses on benchmarking computational tools against experimental data for research reactors. It is important to benchmark these tools against experimental data as part of evaluating their capabilities in simulating physical phenomena which take place during reactor operation. Necsa has recently developed a framework for performing nuclear reactor core calculations, which integrates both stochastic and deterministic modelling methods in a consistent way. In this work, this calculational system is applied to the ETRR-2 benchmark problem in aid of code validation. In particular, a series of control rod calibration experiments are modelled as initial qualification of the model, whereafter a series of cycle depletion analysis is conducted to validate the burn-up capability of the package.

1. Background and motivation

This work forms part of the on-going IAEA CRP which primarily focuses on benchmarking computational tools against experimental data for research reactors. In the general run of the IAEA CRP projects for research reactors, a platform is made available for interested institutions to submit their reactor specifications, experiment descriptions and experimental data for benchmark studies. A previous IAEA CRP 1496 [1] mainly focused on benchmarking neutronics and thermal-hydraulics computational methods and tools against experimental data for operation and safety analysis of research reactors, whereas the current IAEA CRP [2] focuses on burn-up and activation calculations. Research reactors are widely used for material/fuel testing, neutron activation studies, silicon doping, medical and industrial isotope production and other applications. For safe and efficient reactor operation, reactor core planning and core-follow calculations are to be performed for every operational cycle. It is therefore important to benchmark computational tools against experimental data as part of evaluating their capabilities in simulating physical phenomena which take place during reactor operation. With the ever increasing computing power, the capabilities of computational tools have been considerably improved over the years. However, before any computational tool can be licensed to perform routine reactor calculations, it must have been extensively verified and validated against experimental data. The nuclear industry is strictly regulated and for this reason the CRP project was primarily initiated to promote/ensure safe and efficient operation of research reactors through the use of computational tools which are validated against experimental data. Necsa has recently developed a tool which integrates both Monte-Carlo and deterministic based codes in a

consistent way. For instance, it allows the creation of detailed unified heterogeneous 3D models, which can then be deployed to generate input for various underlying codes such as MCNP [3], Serpent [4] and also the OSCAR-4 [5] nodal diffusion solver. In this particular work, the tool was used to prepare detailed models for the Egyptian 2nd Testing Research Reactor (ETRR-2) benchmark, which is part of the current CRP on multi-cycle core depletion and material activation analysis. The models were then employed in the Monte-Carlo criticality and burn-up code, Serpent II, to simulate ETRR-2 benchmark experiments.

2. Facility overview

ETRR-2 is a 22 MW open pool tank type, multi-purpose research reactor in Egypt. The facility has been successfully utilized for material testing, silicon transmutation, medical radioisotope production, neutron activation analysis and neutron radiography. It is fuelled with low-enriched (19.7%) fuel elements, cooled and moderated with light water and reflected by beryllium blocks. The core configuration consists of a 6 $\times$ 5 array of 29 fuel elements, six neutron absorbing control blades, two control guide boxes and a central position for cobalt irradiation. The core is surrounded by four chambers that can be filled with gadolinium solution which is used as a secondary shutdown mechanism. The ex-core region consists of a configurable aluminium grid with beryllium blocks, hollow aluminium boxes and aluminium blocks which make up the last row of the grid positions.

3. Experimental description

3.1. Control rod experiment

The facility was commisioned in the early 90s and its first criticality was achieved in 1997 [6]. During the commisioning stage, a series of control rod calibration experiments were performed for which the results and experimental descriptions were made available in a previous IAEA CRP [7]. Typically, these experiments are perfromed at low reactor power to avoid feedback effects. The reactor core is adjusted to be at a super-critical state by withdrawing control rod to be calibrated by a certain distance and reactivity is measured. The reactor is then brought back into a critical state by inserting a rod which is not being calibrated. This procedure is repeated over and over again until the calibrated rod is fully extracted from the core. From such experiments, differential and integral rod worth curves can be derived. These curves are often used to charaterize the absorbing capability of control rods as a function of extraction position. Since the commisioning cores and corresponding experiments consist of fresh fuel elements, such experiments provide a good platform to verify and validate calculational models without having to deal with extra uncertainties associated with burn-up and cycle modelling. Core SU-29-2SO was choosen from the previous CRP as a basic core configuration to test the models before doing the multi-cycle core depletion analysis for four burn-up cycles. In particular, control rod 5 calibration was simulated using control rods 3 and 6 to compensate for change in reactivity.

3.2. Fuel burn-up experiment

From the four operating cycles, three irradiated fuel elements were removed at different operational cycles from the core for experimental burn-up measurements. Burn-up is usually determined by measuring the content/concentration of a particular fission product of interest which results from prompt fission. Burn-up measurement techniques which yield high quality results are usually costly and time consuming [8]. A low-cost technique which is still relatively efficient is the gamma spectrometry method. This technique is widely used to calculate burn up by measuring the activity of the particular fission product of interest. In this study, Cs-137 was also used as a fission monitor/counter to calculate % burn-up for the three spent fuel elements using the following Equations 1 and 2, respectively.

$$\%\,\text{Burn up} = \frac{\text{number of fissioned atoms}}{\text{intial number of U} - 235\,\text{atoms}} \tag{1}$$

where,

$$\text{Number of fissioned atoms} = \frac{\text{number of Cs} - 137\,\text{atoms}}{\%\,\text{yield of Cs} - 137\,\text{from fission}}. \tag{2}$$

Cs-137 fission % yield was determined from the mass distribution curve of fission products for all actinides (the yield is very similar for U-235 and Pu-239). In addition, calculated burn-up results for the three irradiated/spent fuel elements were also provided for comparison by the benchmark suppliers.

4. Calculational approach adopted and model description

Using the code independent pre-processor, detailed heterogeneous models are created in preparation of the ETRR-2 benchmark problem. The models are created based on the ETRR-2 facility specifications document [9] which include material specifications and geometric description of the reactor components. A library of in-core and ex-core reactor components is built which is later on used to create a complete core layout. With this new modelling approach, an attempt is made to model the reactor as accurate as possible. In this work, the models are then deployed to generate Serpent input for Monte-Carlo based calculations. Figure 1 illustrates a 3D model of the ETRR-2 reactor with fuel elements, control rods, cobalt irradiation device and the second shutdown system surrounding the core.

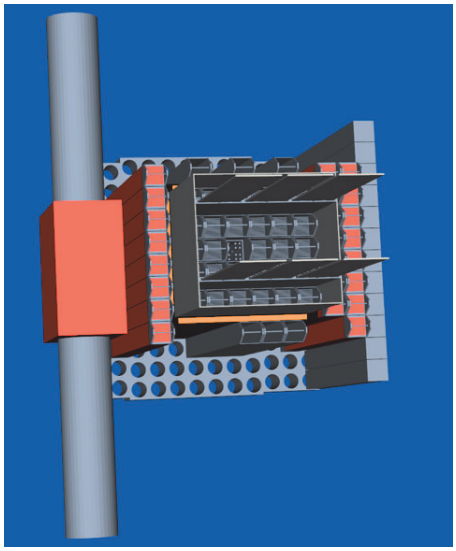

Figure 1: 3D model of the ETRR-2 reactor

However, it must be pointed out that some assumptions had to be made in the modelling process, especially where certain material, structural and operational descriptions were not given. For instance, in the case of cobalt irradiation device no description was given for the spacer element, cobalt pellets, material specifications for the top and bottom structure and cobalt has negative reactivity effects. No plant operational history with control rod positions was given and as a result a rod search method was implemented and used, assuming two rods are fully extracted from the core throughout the operational cycles. No indication of reactor power delivered and as result a constant power per cycle was assumed.

5. Results and discussion

5.1. Control rod calibration

Figure 2 shows the calculated and measured control rod 5 differential rod worth curves from the selected core SU-2SO. It must be noted that for the first 13 steps, control rod 5 was calibrated using rod 3 to compensate for the change in reactivity and rod 6 was used to compensate for the remaining cases untill rod 5 was fully extracted from the reactor core. It is clearly seen from Figure 2 that our model over-estimated the measured values in most cases and under-estimated in few. Some of the calculated points are way off and this could be attributed to the model convergence, fission source term not fully converged for those cases. Our model was also overly sensitive to reactivity changes hence in some cases it over-estimated the measured valules. Conceptually, the differential rod worth curve is expected to peak towards the center of the core where there is high neutron flux but in this case the flux profile is suppresed and this could be due to the presence of Co-59 pellets in the irradiation device. Since no description was provided for the cobalt loading pattern and the spacer element, this could have also contributed to the offset observed towards the center of the core. However, moving from the center towards the top of the core, our model agrees with the measured values except for the last value.

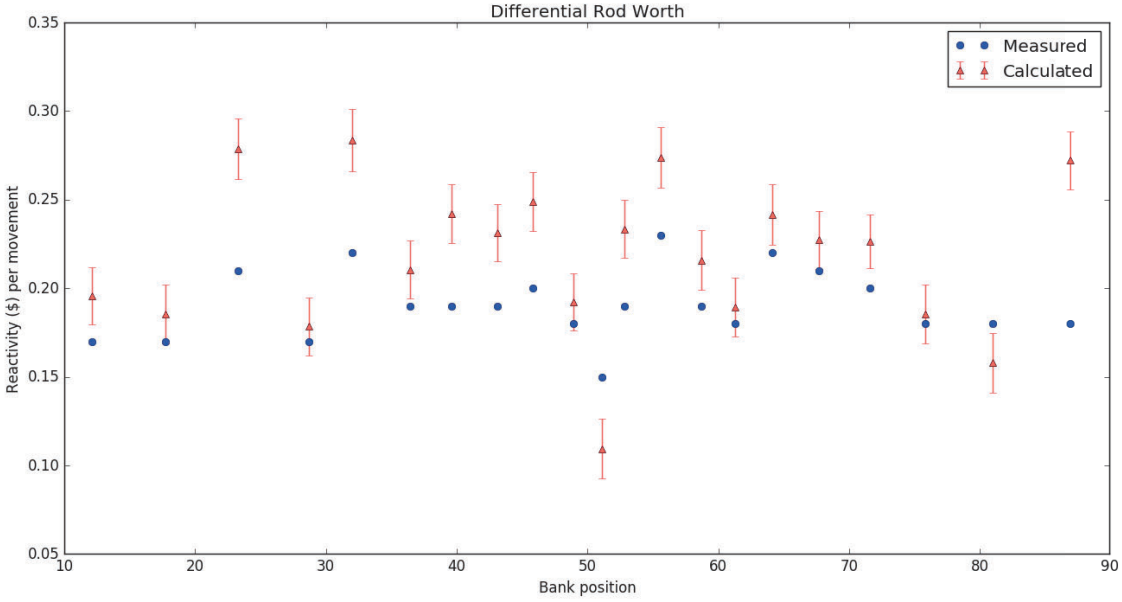

Figure 2: A comparison between the calculated and measured differential rod worth curves for control rod 5 calibration

From the differential rod worth curves in Figure 2, corresponding integral rod worth curves were derived as shown in Figure 3. Once again it can be clearly observed from Figure 3 that our model deviated from the measured values, more especially moving towards the center of the core all the way the top of the core.

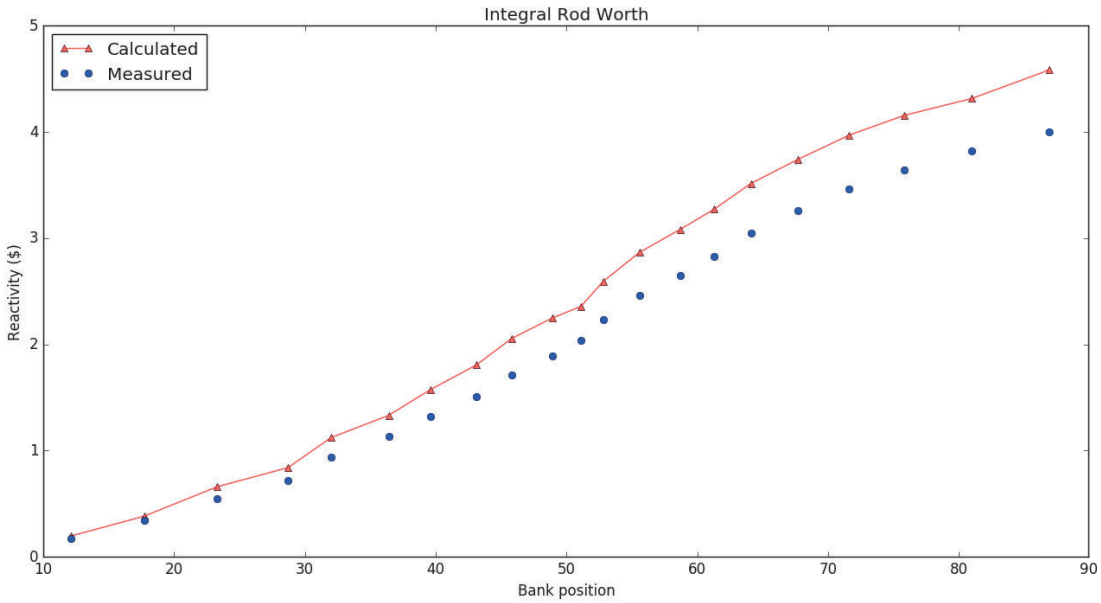

Figure 3: A comparison between the calculated and measured integral rod worth curves for control rod 5 calibration

5.2. Fuel burn-up calculations

Table 1 shows the results of the calculated and experimentally measured % burn up for the three selected spent fuel elements. In our case, Equations 1 and 2 were used to calculate % burn up for the three spent fuel elements using Cs-137 as fission monitor. For elements 1FE001 and 2FE001, our model was relatively closed to the measured % burn up as compared to what the benchmark supplier predicted/calculated. The low burn-up values are more sensitive to rod positions. However, it turned out that for element 1FE007 prediction by the benchmark supplier was closer to the measured value as compared to what our model predicted. It must be noted that the benchmark supplier calculated their % burn up with all rods out, whereas in our model a rod search method was utilized with two rods fully extracted and the remaining four rods moving as a bank. It is more accurate to use a rod search method to perform reactor calculations than to do them with all rods out.

Table 1: Comparison between measured and calculated % burn-up for the three irradiated fuel elements

Fuel element ID	**Mass of U-235** (gram)	**Measured burn-up**	**Calculated burn-up** (benchmark providers)	**Calculated burn-up** (Necsa)
1FE001	148.2	3.26 %	4.23 %	3.60 %
1FE007	148.2	10.70 %	11.10 %	11.70 %
2FE001	209	20.92 %	22.61 %	20.11 %

6. Conclusion

As far as control rod calibration are concerned, our model mostly over-predicted the measured values and under-predicted them in few cases. However, the model at least followed the trend of the experimental data even though there was an offset between the calculated and measured values. On the other hand, the calculated % burn up results were in good agreement with the measured values and therefore the burn up capability of the Serpent code was successfully validated for this ETRR-2 benchmark exercise. For future work, further studies are to be conducted more specifically in the case of control rod calibration experiments. This work forms part of our submission to the current IAEA CRP on benchmarking computational tools against experimental data for research reactors.

7. References

[1] IAEA Research Reactor Innovative Methods Group CRP 2013, RR Benchmarking Database: Facility Specification & Experimental Data, *Technical Report Series 480*, Vienna, Austria.
[2] IAEA CRP (T12029) 2015 Benchmarks of Computational Tools against Experimental Data on Fuel Burnup and Material Activation for Utilization, Operation and Safety Analysis of Research Reactors (Status: on-going)
[3] X-5 Monte Carlo Team MCNP - A General N-Particle Transport Code, Version 5 Volume I: Overview and Theory, LA-UR-03-1987 (2003, updated 2005), *Los Alamos National Laboratory*.
[4] Leppänen J et al 2015 *Ann. Nucl. Energy*, **82** (2015) 142-150.
[5] Stander G, Prinsloo RH, Müller EZ, Tomaševiċ DI 2008 *Int Conf on Reactor Physics, Nuclear Power: A sustainable Resource* (Interlaken, Switzerland)
[6] Bissani M 2006 Joint Assessment of ETRR-2 Research Reactor Operations Program, Capabilities, and Facilities, Technical Report UCRL-TR-221284, *Lawrence Livermore National Laboratory*, USA.
[7] IAEA 2013 Proceedings Series on (CRP 1496) *RR Benchmarking Database: facility description and experiments* ETRR-2 Nuclear Reactor Experimental Data.
[8] Devida et al 2004 "Hotlab" Plenary Meeting, Halden, Norway
[9] Abdelrazek ID, Villarino EA 2015 ETRR-2 Nuclear Reactor: Facility Specification

Assessing the impact of rock phosphate storage on uranium and thorium concentration in soil samples from Richards Bay using neutron activation analysis

F B Masok[1], P L Masiteng[1], R D Mavunda[1,2], P P Maleka[3] and Hartmut Winkler[4]

[1] University of Johannesburg, Applied Physics and Engineering Mathematics Department, P.O Box 17011, Doornfontein 2028, South Africa
[2] Radiation Protection Training Centre, South African Nuclear Energy Corporation (Necsa), PO Box 582, 0001 South Africa
[3] Department of Subatomic Physics, iThemba LABS, National Research Foundation, P.O.Box 722, 7129 Somerset West, South Africa
[4] Department of Physics University of Johannesburg, Auckland Park 2006, South Africa

E-mail: masokfelix@gmail.com

Abstract. Determination of radionuclides in soil samples is important to estimate the radiation level to which persons are directly or indirectly exposed especially from a health physics point of view. In this study, the concentration of parent radionuclides ^{238}U, ^{232}Th and ^{40}K were measured in soil samples around a rock phosphate storage facility at Richards Bay. Ninety soil samples were collected from 30 sampling positions. Gross alpha and beta activity concentration measurements were first performed using a gas flow proportionality counter to estimate the total activity of each sample without regards to specific radionuclides. The samples were further analyzed for ^{238}U and ^{232}Th concentrations using neutron activation analysis (NAA) by irradiating with thermal neutrons flux of about 1×10^{14} n cm^{-2}.s^{-1} in a nuclear research reactor (SAFARI 1) at NECSA. The total mean values (mean±S.D) of elemental concentrations for ^{238}U, ^{232}Th and ^{40}K in all the samples studied were 2.29 ± 0.95 ppm, 7.77 ± 3.98 ppm and 0.44 ± 0.32 at % for uranium, thorium and potassium respectively. The elemental concentrations of ^{238}U, ^{232}Th and ^{40}K are lower than the corresponding values reported worldwide for natural sources by a factor of 0.15, 0.30 and 0.68 respectively.

1. Introduction

Despite their positive values and uses for the production of fertilizer, animal feed supplements and industrial chemicals [1], research [2, 3, 4, 5] has shown that phosphate rocks contain a substantial concentration of uranium, thorium and their decay products. When phosphate rocks are applied to soil, they elevate the radioactivity levels in the soils [2, 6, 7]. The radionuclides in soil can be incorporated into human bodies through inhalation of contaminated soil dust by workers, other site users or a member of the general public. Leaching of these radioactive nuclides is another source of dissemination and possible transfer to waters and finally to human beings and animals [4]. Gamma radiation from natural radionuclides and cosmic rays constitute external exposure while those derived from inhalation and ingestion through foods and drinking water constitute internal exposure to humans [8]. About 80% of radiological dose contributed from

the environment are derived from the natural radionuclides while the remaining 20% are from cosmic rays and nuclear processes [9]. The natural radionuclides of concern in the terrestrial environment are mainly Uranium-238, Thorium-232, Potassium-40 and the radioactive radon gas produced as a result of decay of the first two aforementioned parent nuclides [9].

Richards Bay is an industrial area located on latitude 28° 48' S and longitude 32° 02' E in KwaZulu Natal Province, South Africa. The area is well known for its harbour facility and industrial activities. Rock Phosphate mined in Phalaborwa in Limpopo is transported by rail about 750 km to Richards Bay where it is stored prior to export or used by Foskor Richards Bay as raw material. Environmental problems associated with naturally occurring radioactive materials (NORMs) in solid mineral mining and processing occurs during drilling, processing, transportation and storage. These usually lead to the spread of NORMs contaminating the environment and subsequently result in potential radiation exposure of workers and members of the general public. Although research has reported a low concentration of radionuclide in rock phosphate stored in this study area [10], and a good water quality of the area, no available literature is published about the distribution of radionuclides in soil. This study is aimed at surveying the concentration of NORMs in soil samples around the rock phosphates storage facility at Richards Bay with an intention to map out hot spots in terms of radioactivity concentration level.

Figure 1. Map of study area showing sampling positions

2. Material and methods

2.1. Sampling and sample preparations

Ninety soil samples were collected from 30 sampling positions (Figure 1) divided into the coal area (Area 1, four sampling positions), the rock phosphate storage area (Area 2, 17 sampling position) and the control area (Area 3, nine sampling position). It is worth mentioning that more samples were collected from Area 2 because it is the area of interest for this study. Collected samples were dried in an oven at a temperature of 105 °C for 24 hrs and then milled to powder. About 1.00 g of each powder soil sample was sealed in polythene ampoules and further encapsulated in polythene foil to avoid superficial contamination during irradiation and handling. Prepared samples were irradiated with thermal neutrons at NECSA (SAFARI 1) producing a neutron flux of about 1×10^{14} n.cm^{-2}.s^{-1} at the core of the reactor. During neutron activation in a reactor,^{238}U and ^{232}Th undergo the following nuclear process.

$$^{238}U(n,\gamma) \longrightarrow ^{239}U \longrightarrow ^{239}Np \tag{1}$$

$$^{232}Th(n,\gamma) \longrightarrow ^{233}Th \longrightarrow ^{232}Pa \tag{2}$$

The gamma rays emitted were measured using a closed end coaxial high-purity germanium (HPGe) detector with a relative efficiency of 25.1%, peak to Compton ratio of 40.2:1 and a resolution of 2.3 keV at 1332 keV of ^{60}Co. The detector was calibrated for energy and efficiency using ^{152}Eu with an activity of (18.6 ± 0.5) kBq at reference date of 2006 February 09 at 12.00 GMT. The activity concentration of ^{40}K was determined directly from the gamma energy line of 1460.8 keV without sample irradiation. Gamma energy peaks of 277.6 keV and 312.2 keV from the decay of ^{239}Np and ^{233}Pa were used for the identifications of ^{238}U and ^{232}Th respectively. Elemental content was determined relative to certified reference materials which were irradiated and counted under the same conditions as the samples. Reference materials were supplied by the South African National Bureau of Standards. The experiment was carried out in the Radio-analysis laboratory at the South African Nuclear Energy Corporation (NECSA), Pretoria, South Africa. The background was determined by treating an empty capsule as the sample. The uncertainty value reported is calculated mainly from counting statistics and it is not the standard deviation obtained from replicate measurements.

2.2. Activity calculations and determination of elemental concentration

Following the spectrum analysis, the specific activity of ^{233}U and ^{232}Th were determined in units of Bq.kg^{-1} and then converted into total elemental concentrations (F_E) in units of part per million (ppm) of ^{238}U, ^{232}Th and % of ^{40}K using equation (3) [11].

$$F_E = \frac{M_E C}{\lambda_E N_A f_{(A,E)}} \times A_E \tag{3}$$

Where, M_E,λ_E,$f_{(A,E)}$ and A_E are the atomic mass (kg.mol^{-1}), the decay constant (s^{-1}), the fractional atomic abundance in nature and the measured specific activity concentration (Bq.kg^{-1}) respectively of the corresponding element E. N_A is the Avogadro number 6.023 × 10^{23} atoms mol^{-1}, C is a constant with values of 10^6 for ^{238}U and ^{232}Th as well as 10^2 for ^{40}K that converts the ratio of the elements to soil mass into part per million of ^{238}U, ^{232}Th or a percentage of ^{40}K. Using equation (3), this yields the same results as the conversion factors of

$$\begin{gathered} 1\text{ppm} = 12.25\ \text{Bq.kg}^{-1}\ \text{of}\ ^{238}\text{U} \\ 1\text{ppm} = 4.06\ \text{Bq.kg}^{-1}\ \text{of}\ ^{232}\text{Th and} \\ 1\ \% = 131\ \text{Bq.kg}^{-1}\ \text{of}\ ^{40}\text{K} \end{gathered}$$

given in IAEA technical document 390 as utilized by [12].

3. Results and discussion.

3.1. Gross alpha and gross beta activities

The gross alpha and beta activity is a first order estimate performed to obtain the total activity concentration of radionuclides in a sample without considering specific nuclides. Figure 2 shows the total activity concentration of each sampling position.

3.2. Elemental concentrations in soil samples

The elemental concentrations of uranium, thorium and potassium obtained from the three areas where soil samples were collected are summarized in Table 1. The measured arithmetic mean and standard deviation of elemental concentrations for ^{238}U, ^{232}Th and ^{40}K in all the samples studied are 2.29 ± 0.95 ppm, 7.77 ± 3.98 ppm and 0.44 ± 0.32 at % respectively, while the revised median values obtained worldwide are 2.67 ppm, 11.08 ppm and 1.34 at % respectively. The above-mentioned worldwide mean values were derived by transforming the corresponding worldwide average concentrations of 33, 45 and 420 Bq.kg^{-1} for ^{238}U, ^{232}Th and ^{40}K radionuclides [9] into

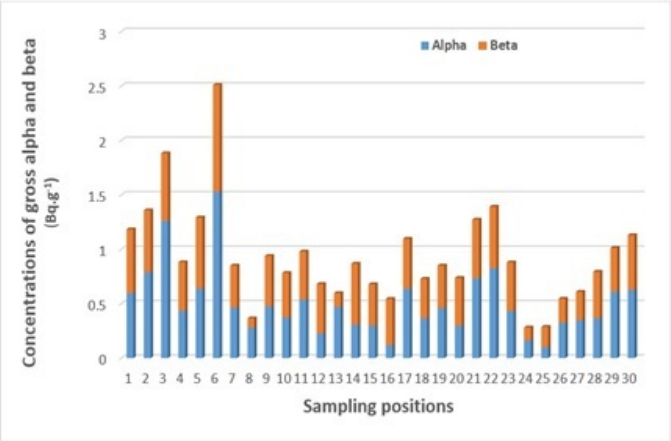

Figure 2. Gross alpha and gross beta activity concentrations of each sampling position from where soil samples were collected.

Table 1. Elemental concentrations of ^{238}U, ^{232}Th and ^{40}K in soil samples studied.

Sampling Area	Number of samples	Parameters	Elemental concentrations (ppm) ^{238}U (ppm)	^{232}Th (ppm)	^{40}K at (%)
Area 1	12	Min	2.48 ± 0.12	8.86 ± 0.34	0.36 ± 0.14
		Max	4.19 ± 0.17	18.58 ± 0.38	0.60 ± 0.15
		Ave ± S.D	3.39 ± 0.8	14.47 ± 4.58	0.47 ± 0.13
Area 2	51	Min	1.04 ± 0.07	1.44 ± 0.22	0.01 ± 0.001
		Max	3.76 ± 0.15	13.09 ± 0.33	0.88 ± 0.21
		Ave ± S.D	2.29 ± 0.92	7.30 ± 2.82	0.47 ± 0.20
Area 3	27	Min	0.84 ± 0.05	2.25 ± 0.09	MDA
		Max	2.81 ± 0.18	8.45 ± 0.25	0.99 ± 0.22
		Ave ± S.D	1.81 ± 0.69	5.69 ± 2.41	0.38 ± 0.32
Total	90	Min	0.84 ± 0.05	1.44 ± 0.22	MDA
		Max	4.19 ± 0.17	18.58 ± 0.38	0.99 ± 0.22
		Ave ± S.D	2.29 ± 0.95	7.77 ± 3.98	0.44 ± 0.32
World average			2.67	11.08	1.34

^{238}U, ^{232}Th and ^{40}K elemental concentrations respectively using Equation (3). This study reveals that the total mean concentration of ^{238}U, ^{232}Th and ^{40}K measured in soil samples from Richards Bay (this study area) are 85%, 70% and 32 at % of corresponding values reported worldwide. Hence they are all lower by a factor of 0.15, 0.30 and 0.68 compared to the corresponding worldwide average values for soil samples from non-mining areas.

From Table 1, area 1 exhibited the highest concentrations in uranium and thorium with an arithmetic mean value (mean ± S.D) of 3.39 ± 0.8 ppm and 14.47 ± 4.58 ppm respectively. As can be seen from Figure 3, columns 2 and 3, the highest concentration of ^{238}U, ^{232}Th and ^{40}K were measured in soil samples collected from area 1 and 2. This can be attributed to industrial activities and mined minerals handled within these area. Although comparable and within the range of some areas globally (see Table 2), the total mean elemental concentrations of ^{238}U,

Table 2. Concentrations of ^{238}U, ^{232}Th and ^{40}K in soil samples from different countries [11]

Countries	^{238}U (ppm)	^{232}Th (ppm)	^{40}K at (%)
Spain	1.1 - 13.8	1.7 - 50.3	0.2 - 5.2
Rajasthan, India	2.4 - 6.3	10.6 - 26.1	0.2 - 0.5
Italy	4.6 - 5.7	18.0 - 21.0	1.9 - 2.5
Russaifa, Jordan	3.9 - 42.4	2.1 - 6.7	0.1 - 1.0
Alps-Apennines, Italy	0.3 - 5.6	0.3 - 16.7	0.1 - 5.1
Cyprus	0.0004 - 3.2	0.003 - 9.8	0.0001 - 1.9
South Africa (Present study)	0.8 - 4.2	1.4 - 18.6	0.0 - 0.44

^{232}Th and ^{40}K observed in soil from the rock phosphate storage area (Table 1, Area 2) are still below the world mean elemental concentrations values of the same radionuclide reported in the UNCSCEAR 2000 report [9] for soil from non-mining areas. Furthermore, from Table 2 it is clear that the corresponding elemental concentration values of ^{238}U, ^{232}Th and ^{40}K obtained from this study fall within the lower range of most reported values from other areas globally. Since natural radioactivity is directly related to the content of radioactive elements in the soil, Richards Bay can be considered as one of the world areas that exhibit low level of natural radioactivity.

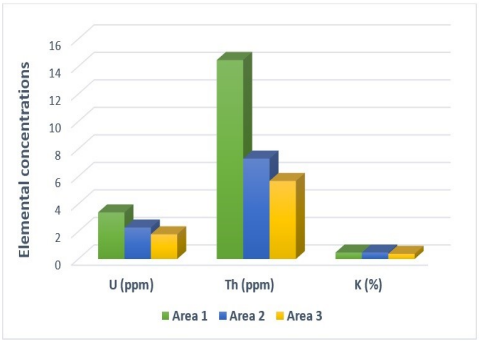

Figure 3. Mean values of ^{238}U, ^{232}Th, ^{40}K

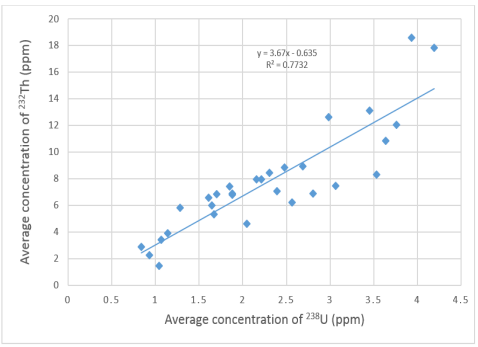

Figure 4. Correlation of ^{238}U and ^{232}Th

3.3. Correlation between ^{238}U and ^{232}Th

The relationship between uranium and thorium can be considered in terms of the thorium and uranium ratio [11]. Figure 4 show the correlation of Th/U with a fitting relation of a linear type yielding a correlation coefficient of 0.88. The theoretical expected ratio of Th/U is approximately 3.00 for normal continental crust [11]. Corresponding values obtained for this ratio in this study vary from 1.38 to 4.53 with an arithmetic mean and standard deviation of 3.30 ± 0.73 which is consistent with the continental crust. The high values of Th/ U ratio in some samples is an indication that the soil samples analyzed are thorium enriched or uranium depleted due to natural processes [9, 12] such as weathering and leaching in this area. However, thorium enrichment indicates the presence of a significant amount of monazites and zircon [13], and this is evident in the quantity of zircon mined by Richards Bay minerals company (RBM) in Richards Bay [14]. Hence, it is observed that Richards Bay is rich in Thorium concentration.

4. Conclusion

The concentration of ^{238}U and ^{232}Th in 90 soil samples collected around a rock phosphate storage facility were analyzed by means of neutron activation analysis and found to be of continental crust level. There were no hot spot identified with regards to radioactivity concentration level within this study area, however the concentrations of ^{238}U and ^{232}Th was found to be slightly enhance by anthropogenic activities within this area. The elemental concentration of ^{238}U, ^{232}Th and ^{40}K were found to be lower than their corresponding values reported worldwide for soil samples from non-mining areas by a factor of 0.15, 0.30 and 0.68 respectively. Therefore, the influence of rock phosphate storage in Richards Bay on the concentration of ^{238}U and ^{232}Th in soil of this area is at present negligible. Since the radioactivity level depends directly on the content of radionuclides within a given sample, Richards Bay in KwaZulu Natal, South Africa can be considered as one of the areas around the world that exhibit low level of radioactivity in soil. Furthermore, a strong correlation 0.88 was found between the concentrations of thorium and uranium, suggesting thorium enrichment in soil of this area.

Acknowledgments

The authors wish to acknowledge management of port of Richards Bay for granting permission for this studies to be conducted on their precinct. We also appreciate the assistance offered by laboratory technicians of the radioanalysis laboratory at NECSA during sample analysis.

References

[1] Tufail M, Akhtar N and Waqas M 2006 Radioactive rock phosphate: the feed stock of phosphate fertilizers used in Pakistan. *Health physics.* IV; **90** 361-70

[2] Wassila B and Ahmed B 2011 The radioactivity measurements in soils and fertilizers using gamma spectrometry technique. *J. Environ. Radioact.* **102** 336-39

[3] Banzi F P, Kifanga L D and Bundala F M 2000 Natural radioactivity and radiation exposure at the Minjingu phosphate mine in Tanzania *J. Radiol Prot.* **20** 41-51

[4] Azouazi M, Ouahidi Y, Fakhi S, Andres Y, Abbe J C and Benmansour M 2001 Natural radioactivity in phosphates, phosphogypsum and natural waters in Morocco. *J. Environ. Radioact.* II; **54** 231-42

[5] Makweba M M and Holm E 1993 The natural radioactivity of the rock phosphates, phosphatic products and their environmental implications. *Sci. Total Environ.* I; **133** 99 -110

[6] Tufail M Akhtar N and Waqas M 2006 Measurement of terrestrial radiation for assessment of gamma dose from cultivated and barren saline soils of Faisalabad in Pakistan.*Radiat. Meas.* IV; **41** 443-51

[7] Mlwilo N A Mohammed N K and Spyrou N M 2007 Radioactivity levels of staple foodstuffs and dose estimates for most of the Tanzanian population. *J. Radiol Prot* IV; **27** 471

[8] FAO I ILO N and PAHO W 1996 International basic safety standards for protection against ionizing radiation and for the safety of radiation sources (IBSS). *IAEA Safety series* 115

[9] UNSCEAR 2000 *Sources and Effects of Ionizing Radiation: United Nations Scientific Committee on the Effects of Atomic Radiation. UNSCEAR 2000 Report to the General Assembly, with Scientific Annexes, Vol. I* (United Nations, New York) pp 115 - 16

[10] Masok F B, Masiteng P L, Mavunda R D and Maleka P P 2016 Health effects due to radionuclides content of solid minerals within Port of Richards Bay, South Africa. *Int. J. Environ. Res. Public Health* XII; **13** 1180

[11] Tzortzis M and Tsertos H 2004 Determination of thorium, uranium and potassium elemental concentrations in surface soils in Cyprus. *J. Environ. Radioact.* III; **77** 325-38

[12] Al-Hamarneh I F and Awadallah M I 2009 Soil radioactivity levels and radiation hazard assessment in the highlands of northern Jordan. *Radiat. Meas.* **44** 102-10

[13] Mohanty A K, Sengupta D, Das S K, Vijayan V and Saha S K 2004 Natural radioactivity in the newly discovered high background radiation area on the eastern coast of Orissa, India. *Radiat. Meas.* II **38** 153-65

[14] Williams G E and Steenkamp J D 2006 Heavy mineral processing at Richards Bay minerals *Southern African Pyrometallurgy.* Edited by R.T. Jones, South African Institute of Mining and Metallurgy, Johannesburg, 5-8 March 2006.

Composite Scintillators - A new type of radiation hard scintillator

J.E Mdhluli[1,a], Yu I Davydov[2], V Baranov[2], S Mthembu[1], R Erasmus[1], H Jivan[1], B Mellado[1], E Sideras-Haddad[1], A Boyarintsev[3], T Nepokupnaya[3], Y Onufriyev[3], I Vasiliev[3]

[1]School of Physics, University of the Witwatersrand, Johannesburg, Wits 2050, South Africa.
[2]Joint Institute for Nuclear Research, Dubna, Russia.
[3]Institute for Scintillation Materials of NAS of Ukraine.

E-mail: [a]joyemmie@gmail.com

Abstract. Composite scintillators are new promising detectors for use in severe radiation environments. They consist of crystal granules embedded into an optical transparent medium. This ensures a high radiation hardness within the scintillator with comparison to normal plastic scintillators. However, composite scintillators are low opacity materials as a result of the light scattered by the small crystal granules.
We report on optical and structural properties of these composite scintillators after irradiation using a neutron beam of above $1 \times 10^{14} n/cm^2$ generated by the IBR-2 reactor at the Frank Laboratory of Neutron Physics in Dubna, Russia. The irradiation effects were characterized using Raman spectroscopy, Light yield and Light Transmission measurements. We further report on the advantages and disadvantages of these composite scintillators; and problems that need to be addressed. Preliminary results indicate a small change in the light yield after neutron irradiation.

1. Introduction

The scintillation market already consists of many scintillation material such as liquid scintillators, scintillation plastics, crystals and ceramics. In high energy physics detectors, we require materials that will combine the advantages of scintillations crystals and the cost efficiency of plastic scintiallators into one material. The search for this materials has led to composite scintillators.

Composite scintillators are materials that consist of two or more components with a clear boundary between the matrix and the filler. They consists of an optical transparent medium with dispersed granules of scintillator. However, the challenge faced with this material is the fact that it is a low-transparent medium. This problem was solved by introducing an optical guide material over the scintillation layer. The composite scintillator material therefore consists of optical medium material made of either epoxy, poly-vinyltoulene and silicone. The light guide material is made of quartz glass and silicone or sapphire and molding silicone. The scintillation crystal is made of either silicates, garnets and diamond. This material will have applications in neutron detection, x-ray detection, gamma-ray detection and high energy physics detectors.

Multiple studies have been conducted to test the response of the different components of the materials under proton irradiation[1]-[4]. This study focuses on how the composite scintillators will behave under high neutron irradiation.

2. Theory

Neutrons are highly penetrating particles with zero charge and indirectly ionizing radiation. They can induce large radioactive doses through activation in the body of a material. Neutrons can be produced through various techniques with the most common being nuclear reactors, nuclear fission sources like DT-generators, accelerator-based sources which involve the spallation mechanism and radioactive decay of elements like Cf-252 [6]. Nuclear fission can either be a radioactive decay process or a nuclear reaction where a nucleus of an atom will split into smaller parts of lighter nuclei. Spallation is a process where fragments of a material are ejected from a body due to stress or impact. A spallation source produces pulsed or quasi-continuous neutron beams through the acceleration of protons hitting a target material of a heavy nuclei and releasing neutrons, where one spallation reaction can release up to 30 neutrons per incident proton particle [7]. Neutrons are widely used in the nuclear industry for material research, imaging and medical physics.

As compared to electrons, photos and heavy charged particles, neutrons undergo extremely weak electromagnetic interactions. Neutrons pass through matter largely impeded and only interact with the atomic nuclei. The nuclear reactions that occur between the neutrons and the atomic nuclei have a very low probability associated with them and hence Monte Carlo Techniques (MCNP) are used to perform neutron transport calculations. The probability for a reaction between two particles to occur can be measured through the cross section. The probability of a neutron between a neutron and an individual particle or nucleus is defined as the microscopic cross section whilst the probability of the interaction between neutron and bulk material is defined as macroscopic cross section[6].

When high energy neutrons interact with materials or materials are bombarded with neutrons, the material will degrade and be damaged through the process of collision cascades created within the material. The created collision in turn will produce point defects and dislocations within the material, these dislocations and defects are responsible for the microstructural changes that occur over time to materials that are exposed to radiation. The damage occurring in the material is a result of the interaction of an energetic particle with a lattice atom within a material. The collision causes a significantly large amount of kinetic energy transfer to the lattice atom from the neutron, the atom is then displaced from its lattice site and becomes what is known as a primary knock-on atom (PKA). As the PKAs collide with each other, they lose energy with each collision and terminate as interstitials; and effectively creating a series of Frenkel defects within the lattice. Another consequence of the collisions is heat, this is created from the electronic energy loss. The magnitude of the damage caused by a single 1 MeV of a neutron creating a PKA in an ion lattice is such that it will produce approximately 1100 Frenkel pairs. This is the cause of the damage within the material and the degrading of the material over time with exposure to radiation[8].

The IBR-2 reactor of the Frank Laboratory of Neutron Physics (FLNP) that belongs to the Joint Institute for Nuclear Research (JINR) in Dubna, Russia will be used to expose the materials to neutrons. A beam of neutrons will be extracted from the rector core, the core is of an irregular hexahedron shape that is composed of fuel element sub-assemblies. There is a three circuit and two loops cooling system where the first and the second circuits consist of liquid sodium coolants and the third is air. The IBR-2 produces one of the most intense pulse neutron

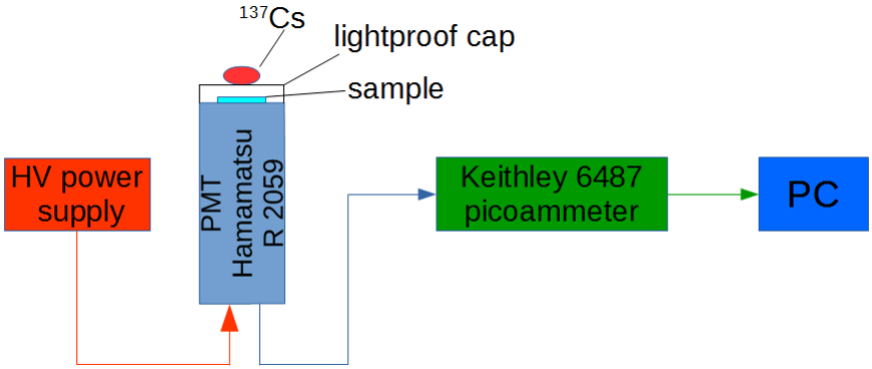

Figure 1. Schematic diagram of the pico-ammeter used for light yield measurements.

fluxes in the world at the moderator surface with a neutron flux of $\approx 10^{16} n/cm^2/s$ and a power of 1850 MW per pulse [9][10]. Fast neutrons in the energy range of $1-10MeV$ were used in this study, fast neutrons create the most damage on materials due to the high energy. Fast neutrons were chosen specifically since these are the same energies found in high energy experiments like the ATLAS detector of the LHC [11] .

3. Experimental Procedure

The materials under study are the YSO:Ce crystals that consists of Slygard-184 optical silicone as a light guide and the YSO single crystal with YSO based granules, these crystals have dimensions $2cm \times 2cm$. The YSO single crystal scintillators with YSO based granules were irradiated with a beam of fast neutrons generated by the IBR-2 reactor core. Channel number three of the reactor was used for the study [9]. Three samples were irradiated with various neutron fluxes to measure the effect of neutron flux to the samples. The total flux exposed to the samples ranged between $3.8 \times 10^{12} n/cm^2$ and $1.8 \times 10^{14} n/cm^2$ and one sample was left un-irradiated for comparison measurements. Irradiation took place during the Autumn Run (17 October 2016 to 3 November 2016) of the IBR-2 reactor.

Light yield measurements were performed at the Dzhelepov Laboratory for Nuclear Problems (DLNP), the set up is illustrated in the figure above. The samples was placed above a photomultiplier tube (PMT) purchased from Hamamatsu. The PMT type used was the R2059 which is a head-on type PMT that has a bialkali photocathode material and a quartz window material. A lightproof cap covered the sample to avoid electromagnetic radiation. The signal detected by the PMT is measured using a pico-ammeter and recorded onto the PC system. THis setup is illustrated in Fig. 1. Measurements were performed in the absence of a radioactive source and thereafter, a cobalt-60 source was used to excite the samples. Measurements were performed soon after irradiation in November 2016, three more measurements were done thereafter with the last one performed in June 2017.

4. Results and Discussion

Sample 1 in the figures below represents the un-irradiated sample. Sample 2 represents the sample irradiated with $3.8 \times 10^{12} n/cm^2$, sample 3 represents the irradiated sample of $1.7 \times 10^{13} n/cm^2$ and sample 4 was exposed to the highest neutron flux of $1.8 \times 10^{14} n/cm^2$. Figure 2 shows the measurements done with residual current by testing the response of the composite scintillators when they are not excited by any radiation. We observe in Fig. 2 that the sample produces a

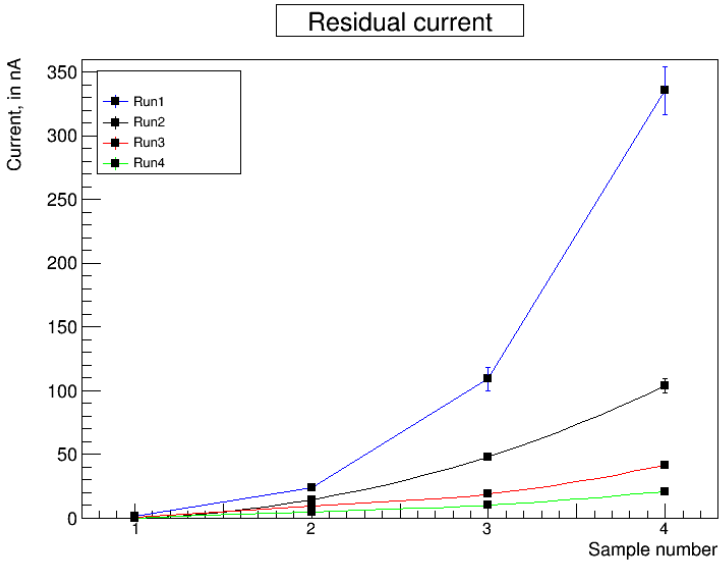

Figure 2. Residual current measurements for the composite scintillator.

greater current at samples irradiated with the higher neutron flux. We observe that the scintillators recover over time, especially sample number 4. Run 1, 2, 3 and 4 in Fig. 2 and 3 represent the different measurements done on the samples after irradiation. The first measurement referred to as Run 1 was performed immediately after irradiation in November 2016, the second in February 2017, the third in April 2017 and the last and forth run was performed in June 2017.

Figure 3 shows the response of the composite scintillators when they are exposed to a radioactive source, cobalt-60 that emits gamma radiation. The gamma rays emitted from the cobalt source excited the composite scintillators and luminescences as a result. From this figure, we observe that the sample does not show the same behaviour as in Fig. 2. As observed in the graph, the light yield of the composite scintillators is significantly lower with response to a source as compared to when no gamma radiation is exposed to the samples. From Fig. 3, there is no significant change between the irradiated and un-irradiated samples.

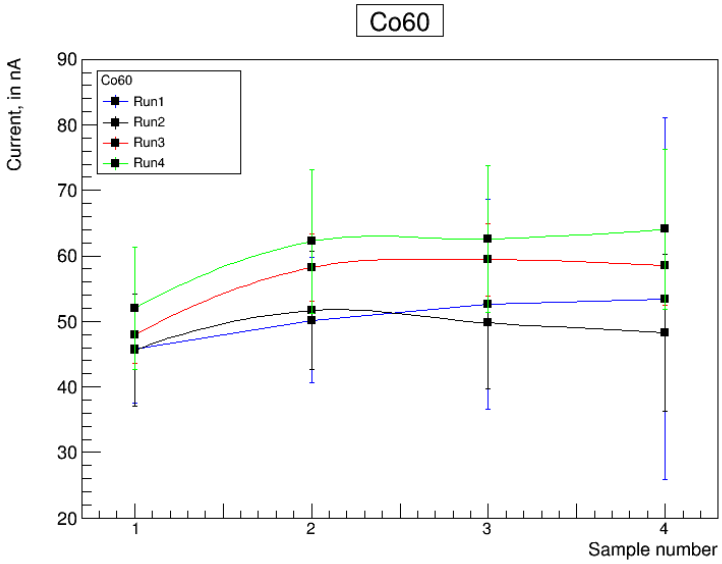

Figure 3. Co-60 current measurement for the composite scintillators.

5. Closing Remarks

From the results shown above, we observe how the composite scintillators are able to recover over time. The irradiated samples have a higher light yield as compared to that of un-irradiated sample when irradiated with gamma source (current due to induced activity is subtracted). We can conclude from the results shown in Fig. 2 and 3 that the composite scintillators do degrade under neutron radiation however further studies will need to be conducted with higher neutron fluxes since we only start to observe a significant change between the un-irradiated sample and sample number four that was exposed to a neutron flux of $1.8 \times 10^{14} n/cm^2$. The total neutron fluence the tile calorimeter of the ATLAS detector is exposed to in a year is $10^{12} n/cm^2$ [11], we are using this as a standard for the study and therefore we will need to go to higher neutron fluxes to study how the composite scintillators will be affected over time. Light transmission, Raman spectroscopy and photoluminescence measurements will be conducted to observe if the there is any change in other properties of the scintillators.

5.1. Acknowledgments

We would like to acknowledgement our collaborators from the Institute for Scintillation Materials of NAS of Ukraine for providing us with the composite scintillator materials. We would also like to acknowledge the Frank Laboratory for Nuclear Physics for the use of the IBR-2 reactor. Lastly, we acknowledge the SA-consortium and SA-JINR collaboration for the financial support.

References

[1] Ren-Yuan Zhu, 2015 *J. of Phys: Conference series* **587** 012055.
[2] Feygelman V M, Walker J K, Harmon J P, 1990 *Nucl. Instr. Meth. A* **290** 131.
[3] Feygelman V M, Walker J K, Harmon J P, 1990 *Nucl. Instr. Meth. A* **295** 94.
[4] Feygelman V M, Walker J K, Harmon J P, 1991 *Nucl. Instr. Meth. B* **53** 309.
[5] Holbert H E, Radiation effects and damage [Online] Available: *http://holbert.faculty.asu.edu/eee560/RadiationEffectsDamage.pdf/* [Accessed 24 06 2017]
[6] Hamilton D, Neutron Interactions with Matter [Online] Available: *https://pdfs.semanticscholar.org/presentation/2eb5/e6ac53e9e60e6a33c919e3e2a1fb3dbc3dae.pdf* [Accessed 04 10 2018]
[7] Bisanti P, 1986 *Magnetic properties of matter* (Turin:World Scientific) ed Borsa F, Tognetti V p 385-408

[8] Carpenter J M, 2004 *Neutron production, moderation and characterization of sources.*
[9] Bulavin M, 2015 Irradiation facility at the IBR-2 reactor for investigation of material radiation hardness *NIM* **B343** p26 - 29.
[10] FLNP, Frank Laboratory of Neutron Physics [Online] Available: *http://nph.jinr.ru/en/facilities/ibr-2* [Accessed 28 08 2018]
[11] Vasilescu A, 1997 Overview on the radiation environment in ATLAS and CMS SCT and the irradiation facilities used for damage tests. [Online] *preprint available as: ROSE/TN/97-3* Available: *http://cern.ch/rd48.*

Geometrical validation of New Small Wheel simulation software

Chilufya Mwewa[2], Valentina Cairo[1], Andrea Dell'Acqua[1], Andrew Hamilton[4], Verena Martinez[3], Sahal Yacoob[2]

CERN[1], University of Cape Town[2], University of Illinois[3], Quest University[4]

E-mail: chilufya.mwewa@cern.ch[2]

Abstract. The Large Hadron Collider (LHC), the largest hadron accelerator ever built, began operations in 2009 at centre-of-mass energies of 0.9 TeV and had reached 8 TeV by the end of 2012. This era was called Run I. After a long shutdown (LS1) of two years (2013-2014), the LHC resumed operations in 2015 (Run II) and has reached a record luminosity of 1.74×10^{34} $\mathrm{cm}^{-2}\mathrm{s}^{-1}$, exceeding its design luminosity of 10^{34} $\mathrm{cm}^{-2}\mathrm{s}^{-1}$. At the end of Run II (2018), the LHC will undergo another shutdown (LS2) in preparation for even higher luminosity scenarios during Run III. Such high luminosities are anticipated to affect, among other things, the tracking and triggering of muons in the ATLAS detector's muon spectrometer due to high counting rates (mostly from increased cavern background) and fake high transverse momentum tracks. To address this issue, the ATLAS collaboration will replace the innermost stations in the muon spectrometer end caps (Small Wheels) with a set of precision tracking and trigger detectors capable of handling high rates - the New Small Wheels (NSW). The NSW design is proposed to have two types of detector technologies: Small Strip Thin Gap Chambers for triggering and Micro Mesh Gas Structures for precision tracking. The performance of the NSW at these high rates is currently being studied in simulations. A validation study to check how well the simulation software depicts the geometry of the NSW detector planes is presented here.

1. Introduction

The Large Hadron Collider (LHC) is the world's largest particle accelerator with a circumference of about 27 km [1]. It accelerates two like-charge particle beams (either protons or heavy ions such as lead ions) in opposite directions and collides them at four different points once they have reached the desired energies. The interaction points each have a particle detector which captures the outcome of the collisions. These detectors include; ATLAS, A Large Ion Collider Experiment (ALICE), the Compact Muon Solenoid (CMS) and LHC Beauty (LHCb).

The LHC began operations in 2009 and by 2012, it achieved centre-of-mass energies of 8 TeV leading to the discovery of the Higgs boson [2]. During this period, also called Run I, the LHC operated at luminosities of about 0.6×10^{34} $\mathrm{cm}^{-2}\mathrm{s}^{-1}$ [3]. It is currently in Run II and operating at center-of-mass energies of 13 TeV and luminosities of about 1.74×10^{34} $\mathrm{cm}^{-2}\mathrm{s}^{-1}$ [4]. By 2021 (Run III), it is expected to operate at centre-of-mass energies of 14 TeV and luminosities $> 2 \times 10^{34}$ $\mathrm{cm}^{-2}\mathrm{s}^{-1}$ which implies that high particle rates would be encountered by the detector. To prepare for these high rates, the LHC will undergo a shutdown for upgrade between 2019 and 2020. In addition, the detectors will also be upgraded in order to be able to cope with these high rates. Details of the LHC timeline can be found on the LHC high luminosity project

website [5].

This paper focuses on the upgrade of the ATLAS detector's innermost Muon stations called the Small Wheels (SWs). These stations will be replaced by New Small Wheels (NSWs) during the next shutdown. In particular, the focus of this paper is the validation of the software used to simulate the performance of the NSWs. In Section 2, the general layout of the ATLAS detector and the NSWs is presented. Section 3 highlights the NSW simulation software with Section 3.1 showing the validation procedures used to test NSW simulation software and also some results of these studies. Finally, a summary is given in Section 4.

2. ATLAS and the New Small Wheel

ATLAS [6], one of the LHC's general purpose detectors, is a 45 m long and 25 m high particle detector as shown in Figure 1. It is designed in a multilayer fashion with each layer having specialized material suitable for the detection of the diverse debri of particles that emerge from the collisions. These layers include; the inner detector, the electromagnetic and hadronic calorimeters and the muon spectrometer respectively from the interaction point outwards. The inner detector mainly measures the momentum of charged particles. The electromagnetic calorimeters measure energies deposited by particles that interact via the electromagnetic and strong forces respectively. The muon spectrometer measures the momentum of muons. In addition, the inner detector and muon spectrometer are surrounded by a magnetic field of 2T and 4T respectively to aid in the bending of particles and hence the momentum measurement. Every second, the ATLAS detector interacts with particles emerging from approximately 10^9 proton-proton collisions. By 2021, the numbers will have doubled and not all components of the ATLAS detector will be able to work effectively at these extreme conditions. Therefore, in order for ATLAS to benefit from the large statistics arising from these rates and better probe for new physics such as supersymmetry [7], it needs to be upgraded. To this effect, ATLAS will mainly improve the level 1 (L1) trigger system by upgrading the L1 Calo trigger in the calorimeters [8], install a Fast TracKing trigger system (FTK) [9] and replace the small wheels in the muon spectrometer with New Small Wheels (NSWs) [3]. The focus here is on NSWs.

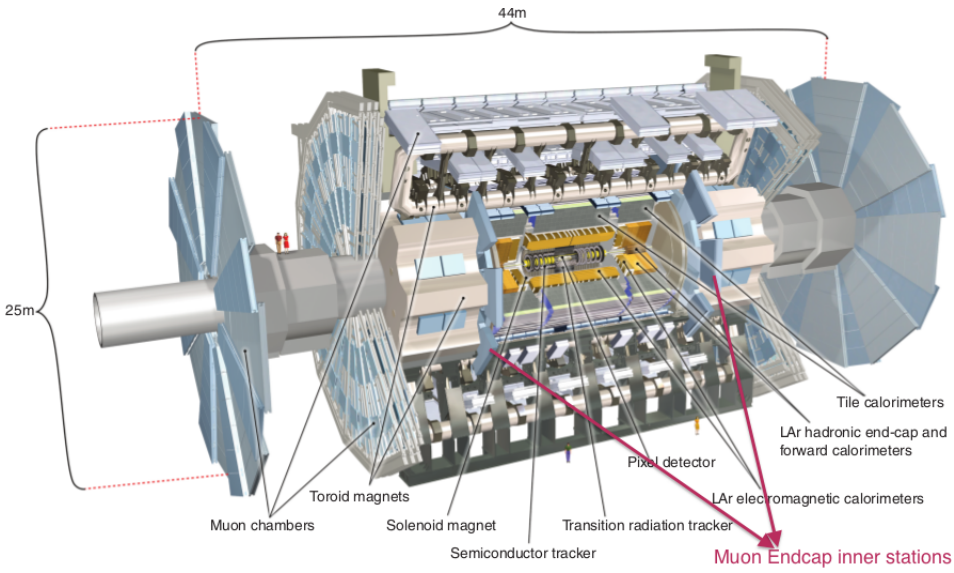

Figure 1. Schematic drawing of the ATLAS detector showing all subdetectors and the positions of the small wheels (Muon endcap inner stations) [6]

At high luminosity, the muon spectrometer is expected to have a reduction in the tracking performance due to a high rate of cavern background. In addition, unacceptable rates of fake high transverse momentum (P_T) L1 muon triggers are also expected [3]. To account for this, the ATLAS collaboration will replace the small wheels in the innermost endcap muon stations with NSWs. The NSWs will be placed at the same location as the small wheels, at Z = ±7 m from the interaction point and cover a pseudorapidity (η) range of 1.3< $|\eta|$ < 2.7. The small

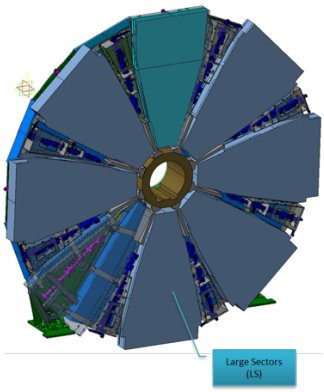

Figure 2. NSW sectors [13]

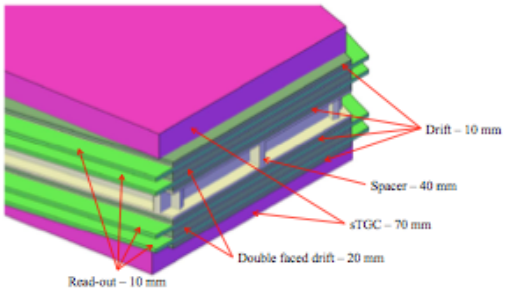

Figure 3. sTGC and micromegas quadruplets [3]

wheels are composed of Thin Gap Chambers (TGCs) for triggering plus Muon Drift Tubes (MDTs) and Cathode Strip Chambers (CSCs) for precision tracking [10]. On the other hand, NSWs will only have two types of detector technologies. These are namely MicroMesh Gaseous detectors (MicroMegas) primarily for precision tracking and small-strip Thin Gap Chambers (sTGCs) primarily for triggering [3]. The NSWs are made up of large and small sectors as shown in Figure 2. Figure 3 shows a zoom-in view on one of these sectors, with two Micromegas quadruplets (in green) sandwiched between two sTGC quadruplets (in pink). Each of these quadruplets is made up of four detection layers and hence there are 16 detection layers per sector. Figures 4 and 5 show schematic drawings of the layout of each of these layers for the sTGCs and micromegas respectively. Figure 4 shows an sTGC layer of two graphite readout electrodes (in form of Printed Circuit Boards (PCBs)) with a gas layer in between them. Each PCB has either pads or strips and inserted in the gas layer is a tungsten wire which is also used for readout. For improved angular resolution, the strips have a much smaller pitch (about 3.2mm) than the TGCs. Pads, on the other hand, aid in the identification of tracks originating from the interaction point and have a much larger pitch of 80mm. In addition, pads also help to define the region of interest to be used when reading out the strips and the wire. The gas is a mixture of CO_2 (55%) and n-pentane (45%) [11]. Figure 5 shows a micromegas layer also with two graphite electrodes (PCBs) and a gas gap. One of the PCBs acts as the cathode (drift electrode) and the other acts as the anode (readout electrode). An amplification mesh is placed at 100 μm from the readout such that the voltage between the drift and the mesh is about 100 V and that between the mesh and the readout is about 45 kV hence providing good tracking resolution at high luminosity conditions.

The production of various parts of the NSWs is currently underway and software has been developed to test their performance in simulation. The next section highlights the features of this software and its validation procedure.

3. NSW simulation software

In general, ATLAS simulation is done in three steps. Firstly, an event generator generates groups of particles or single types of particles. The output of the generator is then passed

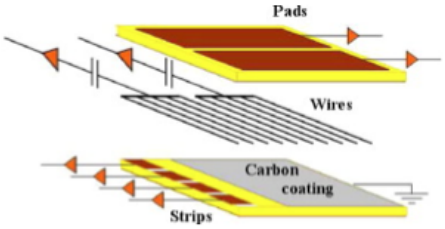

Figure 4. sTGC operation [3]

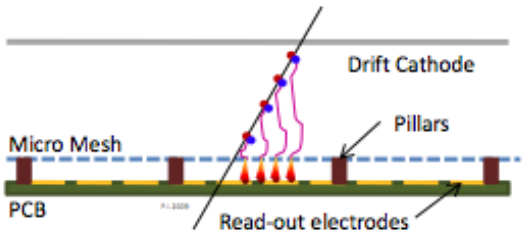

Figure 5. Micromegas operation [3]

to the simulation where the physics interaction of the particles with the detector material is simulated and produces energy deposits called hits. Finally, simulation hits are passed to the digitizer which converts the hits into voltages and current pulses for triggering and reconstruction purposes. The ATLAS simulation software is built in the ATLAS software framework known as Athena and makes use of the GEANT4 simulation packages. More details on the software can be found in reference [12].

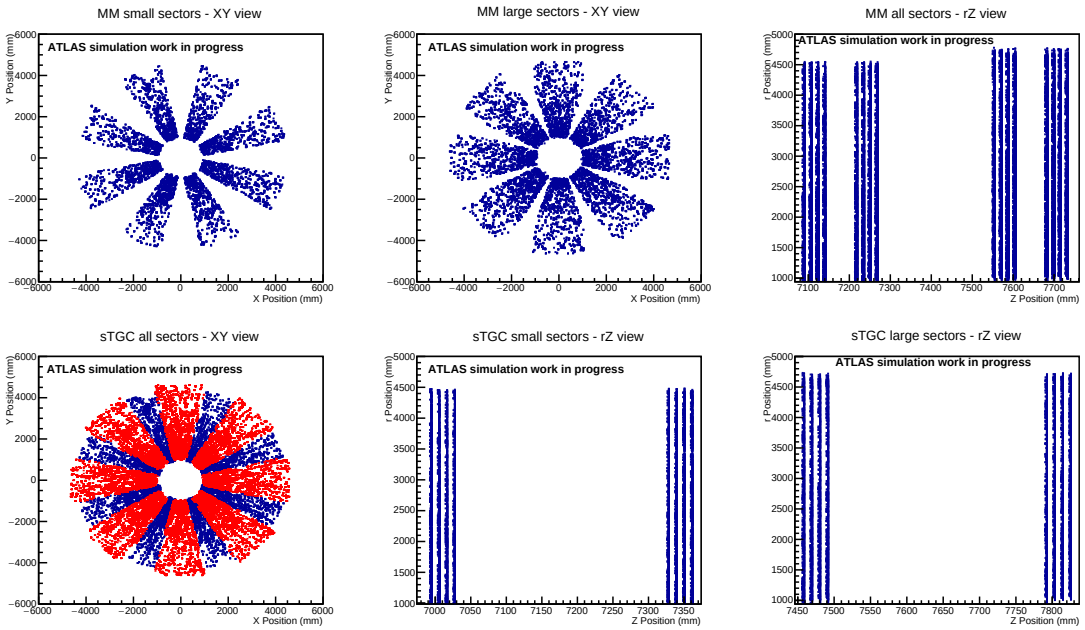

Figure 6. Example of NSW RTT histograms

3.1. Validation

Prior to the assessment of the physics performance in the simulation software, the performance of the software itself has to be validated. ATLAS currently uses two validation procedures which test the software on a nightly basis since the software is constantly evolving. The ATLAS Tests Nightly (ATN) checks for compilation errors and the Run Time Tester (RTT) checks for runtime errors and produces histograms that can be used to check, for example, the geometry of the NSWs. Figure 6 shows an example of the sets of histograms set in the NSW RTT to

validate the software during the simulation step. These are shown for the A-side part of the detector (i.e NSW at positive Z). The top row shows some micromegas plots with the first and second column showing transverse view plots of the small and large sectors respectively. The last column shows the longitudinal view of both the small (first two quadruplets) and large (last two quadruplets) sectors. The second row shows sTGC plots with the first column showing the transverse view of both the small (blue) and large (red) sectors. The second and third columns show the longitudinal view of the small and large sectors respectively. These and many other histograms from both the A-side and C-side are assessed for their geometrical positions and dimensions, their hit coverage and so on. Any defects (bugs) found are then fixed accordingly. Note that only the gas gaps (active areas) are seen during the simulation step since that is the only part of the detector from which the particles' energy deposits are sampled. As an illustration

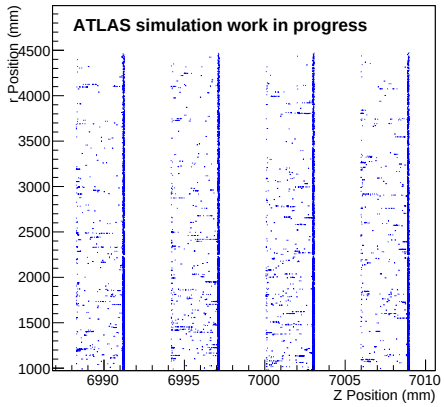

Figure 7. sTGC small confirm quadruplet prior to the fixes

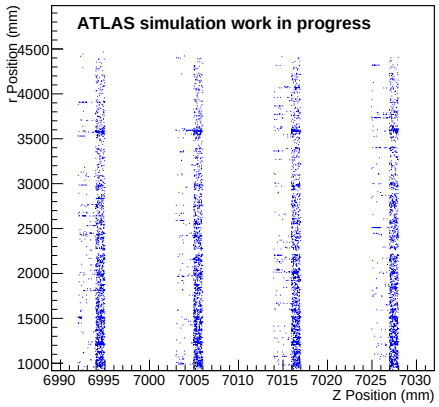

Figure 8. sTGC small confirm quadruplet after the fixes

of the geometry checks and bug fixes done, we zoom into the first quadruplet of the sTGC small sectors as shown in Figure 7. Here, we notice that the center of the quadruplet is at ≈ 6998.5 mm. However, the sTGC parameter book (a detailed book of all sTGC parameters) indicates 7010 mm. This is indicative of some mismodelling in the software responsible for building the detector geometry at the simulation step. This software is called the GeoModel and it is the first place we look at for this kind of defect. GeoModel reads parameters from a configuration file which is created directly from a parameter book. It then builds detector volumes and models them in accordance with the engineering specifications of a particular detector. Looking into this software, we found that an sTGC quadruplet was being modelled as having five PCBs (each 2.85 mm wide) and four gas gaps (each 3 mm wide) and arranged (modelled) as shown in Figure 9. However, the engineering drawing shows 8 PCBs (each 1.5mm wide) and four gas gaps (each 2.8 mm wide) as well as some honeycomb material in which these layers are slotted as shown in Figure 10. Therefore, this geometry was re-modelled in the GeoModel software and the center of this quadruplet corrected to 7010 mm as shown in Figure 8. This was also corrected for all sTGC quadruplets and consequently, positions between sTGCs and micromegas were also corrected. Note that this software is constantly evolving and the engineering specifications at the early stages of manufacturing also evolve. Therefore, it is important to regularly check that the software is modelling the NSWs according to the specified engineering model and hence that was the purpose of this study.

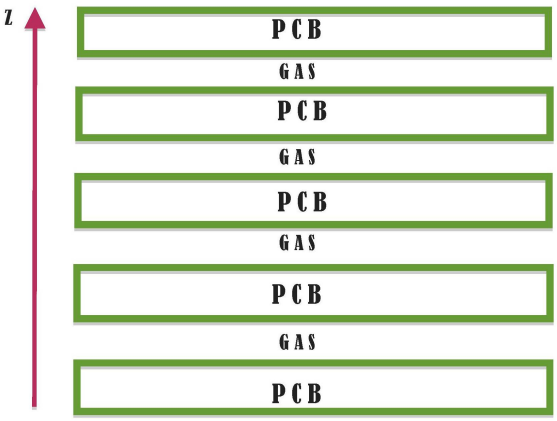

Figure 9. Model of an sTGC in GeoModel prior to the fixes

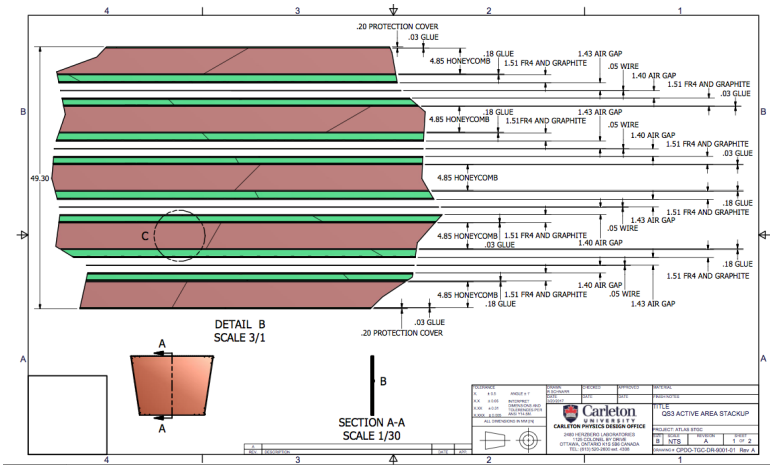

Figure 10. Engineering drawing of an sTGC quadruplet

4. Conclusion

This paper has shown the implementation of validation histograms into the ATLAS RTT for the purpose of validating how well the NSW simulation software depicts the geometry of the NSWs. It has also been illustrated that this type of validation is crucial as both ATLAS software and engineering specifications of the detectors constantly evolve. Therefore, for an efficient validation of the NSW physics performance in the software, the software needs to be validated to ensure that its modelling of the NSWs is accurate. Implementation of digitization validation checks into the RTT is also being done. However, this is beyond the scope of this paper.

References

[1] Evans L and Bryant P 2008 *JINST* **3** S08001
[2] ATLAS Collaboration 2012 *Physics Letters B* **716**
[3] ATLAS Collaboration 2013 *New Small Wheel Technical Design Report* (CERN-LHCC-2013-006)
[4] ATLAS Luminosity Public Results 2017
`https://twiki.cern.ch/twiki/bin/view/AtlasPublic/LuminosityPublicResultsRun2`
[5] LHC high luminosity project website 2017
`project-hl-lhc-industry.web.cern.ch/content/project-schedule`
[6] ATLAS Collaboration 2008 *JINST* **3** S08003
[7] ATLAS Collaboration 2014 *Search for Supersymmetry at the high luminosity LHC with the ATLAS Detector* (ATL-PHYS-PUB-2014-010)
[8] Schwienhorst R 2016 *JINST* **11** C01018
[9] Cavaliere V *et al* 2016 *JINST* **11** C02056
[10] Eldik N 2007 Ph.D. thesis (CERN-THESIS-2007-045)
[11] Perez E 2015 *Small-Strip Thin Gap Chambers for the Muon Spectrometer Upgrade of the ATLAS Experiment* (ATL-MUON-PROC-2015-004)
[12] ATLAS Collaboration 2010 *European Physical Journal C* **70** 3
[13] IRFU website 2017
`http://irfu.cea.fr/en/Phocea/Vie_des_labos/Ast/ast_technique.php?id_ast=2225`

Reconstruction of missing energy in events with two photons at the ATLAS detector in Large Hadron Collider

K G Tomiwa[1*], Xifeng Ruan[1], Shell-may Liao[1], Bruce Mellado[1]

[1] School of Physics, University of the Witwatersrand, Johannesburg 2050, South Africa

E-mail: kehinde.gbenga.tomiwa@cern.ch

Abstract. The missing transverse momentum in the ATLAS experiment is defined as the momentum imbalance in the plane transverse to the beam axis. That is the resultant of the negative sum of all the particles that are detected. A precise estimation of the missing transverse energy is essential for many physics studies at the LHC, such as Higgs boson estimated in the diphoton decay channel, as well as for searches of physics beyond the Standard Model. The reconstruction of missing energy is sensitive to the presence of additional collisions, usually referred to as pile-up. A new method is being proposed to reduce the effect of pileup events in ATLAS experiment. This article describes the performance of missing energy in respect to the improvement of vertex methods in ATLAS experiment.

1. Introduction

Missing transverse energy (E_T^{miss})is very important to many physics analysis in the Large Hadron Collider (LHC). The missing transverse energy is used in the Higgs boson searches and search for physics Beyond the Standard Model (BSM) like the evidence of supersymmetry or hidden sector particles like the dark matter particles. Unlike most Standard Model particles the dark matter particles and neutrinos do not leave traces inside particle physics detectors, because of the non-interacting nature of these particles with detector material we can only infer their presence through missing transverse energy in the detector.

The E_T^{miss} is transverse momentum imbalance created by the detector and well-measured objects in an event [1] . Previous studies have shown that the reconstruction and measurement of the E_T^{miss} are greatly affected by pileup interaction from other proton-proton collision vertices in the same bunch crossing event [2], this in turns leads to what is known as fake E_T^{miss}. The same vertex method is introduced and its performance in suppressing fake E_T^{miss} is studied. This method is used in searches in the decay channel of Higgs to two photons in association with E_T^{miss} [3]. The corresponding phenomenology is described in Ref [4].

2. ATLAS Detector

The ATLAS detector is one of the particle detectors in the LHC, the detector is built around one of the interacting points along the LHC ring. It is a multipurpose system of particle detector used in measuring missing transverse energy, jet energy, hadrons taus, and muons. The detector

Table 1. Samples used for the background processes relevant in this analysis. The $V\gamma$ and $V\gamma\gamma$ are leptonic decay including Z to neutrinos. using full simulation (Full Sim) and Fast simulation (AFII) procedures

Process	Num. Events	Generation	Simulation
ggF, $h \to \gamma\gamma$ 125 GeV	95000	PowhegPythia8EvtGen AZNLOCTEQ6L1	Full Sim
Zh, $h \to \gamma\gamma$ 125 GeV	49800	Pythia8EvtGen A14NNPDF23LO	Full Sim
$h \to \gamma\gamma$ + 3 Jets	106010000	Sherpa CT10	AFII
$V\gamma$ ($V = Z, W^{\pm}$)	4991400	Sherpa CT10	Full Sim
$V\gamma$ ($V = Z, W^{\pm}$)	6982000	Sherpa CT10	Full Sim
$V\gamma\gamma$ ($V = Z, W^{\pm}$)	29800	Sherpa CT10	Full Sim
$V\gamma\gamma$ ($V = Z, W^{\pm}$)	38000	Sherpa CT10	Full Sim
mH275mx60	5000	PowhegPythia8EvtGen AZNLOCTEQ6L1	Full Sim

is composed of three main systems namely the inner detector (ID), the hadronic calorimeter and the muon spectrometer, the three systems are arranged in a barrel-plus-endcaps [5].

The inner detector covers the pseudorapidity range of $\eta < 2.5$, it has three layers (silicon pixel detector, silicon microstrip detector, and transition radiation tracker). The ID is used for precise vertex measurement, extra tracking of particles and particle identification. There are two types calorimeters in the ATLAS detector, the liquid argon (LAr) sampling electromagnetic calorimeter which is situated outside next to the hadronic calorimeter (TileCal), it covers region of $|\eta| < 3.2$ and the steel scintillator tile calorimeter (TileCal) covering the range of $|\eta| < 1.7$. The muon spectrometer (MS) is the outer most part of the ATLAS detector, the MS is used in the reconstruction of the muon. Each subsystem of the ATLAS detector has different functionality, they are combined to in measuring physics processes.

3. Monte Carlo samples used

The samples used for performance checks are listed in table 1. These samples are classified into two categories, based on whether the samples physics processes will lead to real or fake E_T^{miss}. The gluon-gluon fusion (ggF) and $\gamma\gamma$ are Higgs signal and background samples respectively, these samples have no process that leads to E_T^{miss}, hence E_T^{miss} estimated in this samples are regarded as fake E_T^{miss}. The other samples in the list are: Zh, $V\gamma$, $V\gamma\gamma$ and MH275mx260 (BSM sample with decay dark matter particle) are particles with real E_T^{miss}, the E_T^{miss} is as a result of either dark matter particle or decay to neutrinos.

4. Reconstruction of E_T^{miss}

E_T^{miss} is an imbalance in the sum of energy of all particles in the transvers plane of the detector, it is reconstructed using the energy deposited in the calorimeter and muon spectrometer. The E_T^{miss} components are calculated by:

$$E_{x(y)}^{miss} = E_{x(y)}^{miss,calo} + E_{x(y)}^{miss,\mu} \tag{1}$$

The calorimeter term in Equation 1 is calculated based on reconstructed physics objects (electrons, photons, taus, jets and muons) associated with cells, cells which are not associated with physics objects are tagged $E_{x(y)}^{miss,CellOut}$. The $E_{x(y)}^{miss,calo}$ term is given by:

$$E_{x(y)}^{miss,calo} = E_{x(y)}^{miss,calo,e} + E_{x(y)}^{miss,calo,\gamma} + E_{x(y)}^{miss,calo,\tau} + E_{x(y)}^{miss,calo,jets} + E_{x(y)}^{miss,calo,\mu} + E_{x(y)}^{miss,CellOut} \tag{2}$$

each term in Equation 2 is calculated from the negative sum of the calibrated cell energies corresponding to objects as follows:

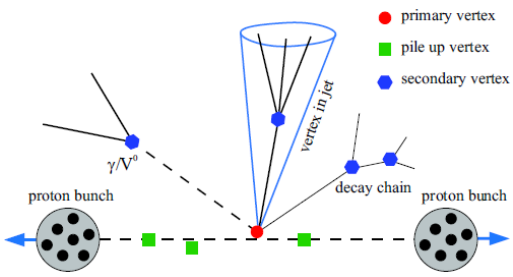

Figure 1. Vertex in the ATLAS detector [6]

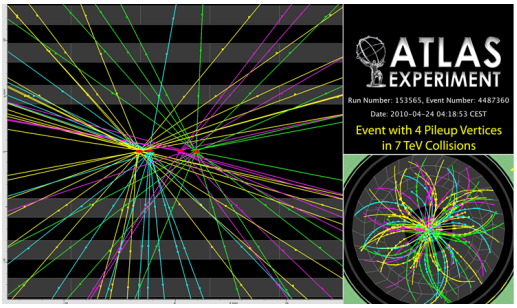

Figure 2. Vertices in the ATLAS detector [6]

$$E_x^{miss,term} = -\sum_{i=1}^{N_{cell}} E_i \sin\theta_i \cos\phi_i, \qquad E_y^{miss,term} = -\sum_{i=1}^{N_{cell}} E_i \sin\theta_i \cos\phi_i \tag{3}$$

The muon term in Equation 1 is calculated from the momenta of muon reconstructed with $|\eta| < 2.7$ as follows:

$$E_{x(y)}^{miss,\mu} = -\sum_{muons} P_{x(y)}^{\mu} \tag{4}$$

E_T^{miss} and its angle ϕ^{miss} are calculated by:

$$E_T^{miss} = \sqrt{(E_x^{miss})^2 + (E_y^{miss})^2}, \qquad \phi^{miss} = \arctan(E_y^{miss}, E_x^{miss}) \tag{5}$$

5. Vertex of interaction in ATLAS detector

Figures 1 and 2 show some typical vertices during proton-proton collision in the ATLAS detector, only one of these vertices is the vertex of interaction for physics process (primary vertex). Most analysis in ATLAS used the method called the hardest scatter (HS) vertex method in reconstructing or identifying the primary vertex, the hardest vertex method identifies the primary vertex as the vertex with the highest scalar sum square of transvers momentum out of all vertex ($\sum(p_T^{track})^2$).

This method is not effective for the analysis with photons like the $H \to \gamma\gamma + E_T^{miss}$, hence another method called photon pointing method was developed [2]. Since photons tracks are seen in the calorimeter (except for converted photons), this method employed a neural network algorithm (K-nearest neighbor algorithm) in pointing two photons tracks from the calorimeter to the inner detector, so the point of interception is identified as the primary vertex.

6. Pile-up in ATLAS detector and pile-up suppression methods

Pile-up vertices are the other vertices due to additional collisions accompanying the HS collision. The jet term of the E_T^{miss} algorithm uses the jet vertex tagger (JVT) index to suppress pile-up [2]. A cut is placed on jet $p_T > 60$ GeV, $|\eta| > 2.4$ and $|JVT| > 0.59$.

From Fig. 3 we see the JVF cut is not 100% efficient in the suppression of pileup, about 40% of events cannot be distinguished as either from PU or HS collision. This introduce fake missing E_T^{miss}. in addition to this Fig. 4 illustrates the scenario which can lead to fake E_T^{miss}, when the JVT cut rejects a jet object in an event due to cut efficiency, the E_T^{miss} algorithm sometimes identified this rejected object as missing energy. This is the motivation behind the development of the same vertex method.

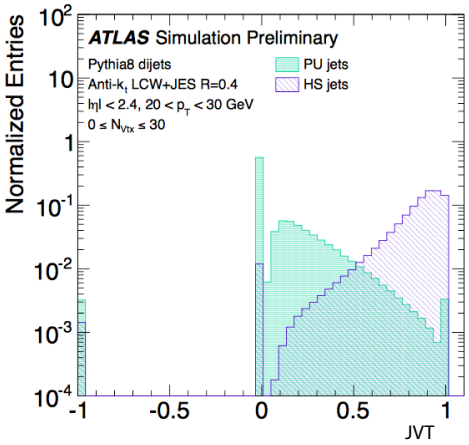

Figure 3. JVT PU and HS jets [6]

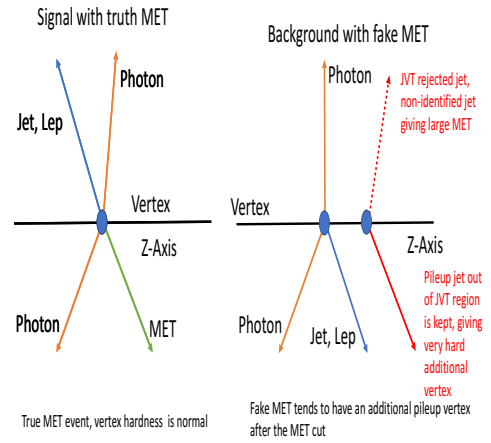

Figure 4. Same vertex method

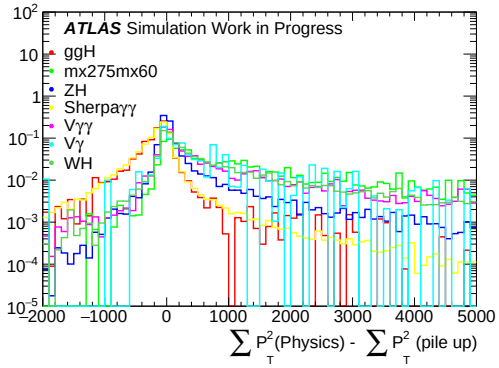

Figure 5. Difference between hardest vertex method and photon pointing methods

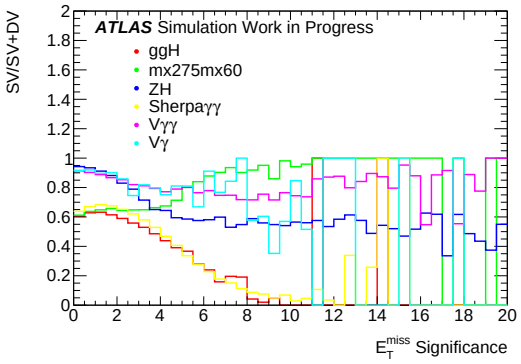

Figure 6. Fraction of event that pass E_T^{miss} significance cut

7. Same vertex method

The same vertex method tries to reduce or distinguish between background and signal events by comparing the consistency between the two vertex reconstruction methods, the same vertex method places an additional requirement on event selection, the vertex selected by the hardest scattered vertex (HS) must be same as the one selected by the photon pointing (PP) vertex selection method. This is implemented by requiring the $\sum(p_T^{track})^2(Physics) - \sum(p_T^{track})^2(Pile-up)$ to be larger than 0. The same vertex method is used in addition to the selection using E_T^{miss} and E_T^{miss} significance (defined as E_T^{miss} / E_T^{miss}resolution).

Figure 5 shows the distribution of $\sum(p_T^{\text{track}})^2(\text{Physics}) - \sum(p_T^{\text{track}})^2(\text{Pile} - \text{up})$ for different samples, the region [-5000,0] is region of fake E_T^{miss}, the samples with fake E_T^{miss} have a higher number of events in this region as compared with the samples with real E_T^{miss}. An opposite observation is seen in the other region of the distribution [0, 5000] as the samples with real E_T^{miss} have a higher number of events. This trend shows that $\sum(p_T^{\text{track}})^2(\text{Physics}) - \sum(p_T^{\text{track}})^2(\text{Pile} - \text{up})$ is effective in identifying an isolated event with fake E_T^{miss}.

Figure 6 shows the fraction of events that passes the same vertex selection against the inclusive selection in E_T^{miss} significance bins. Again we see the same vertex method is able to seperate

samples with fake E_T^{miss} and real E_T^{miss}, a veto on E_T^{miss} significance greater 3.0 will significantly reduce background events.

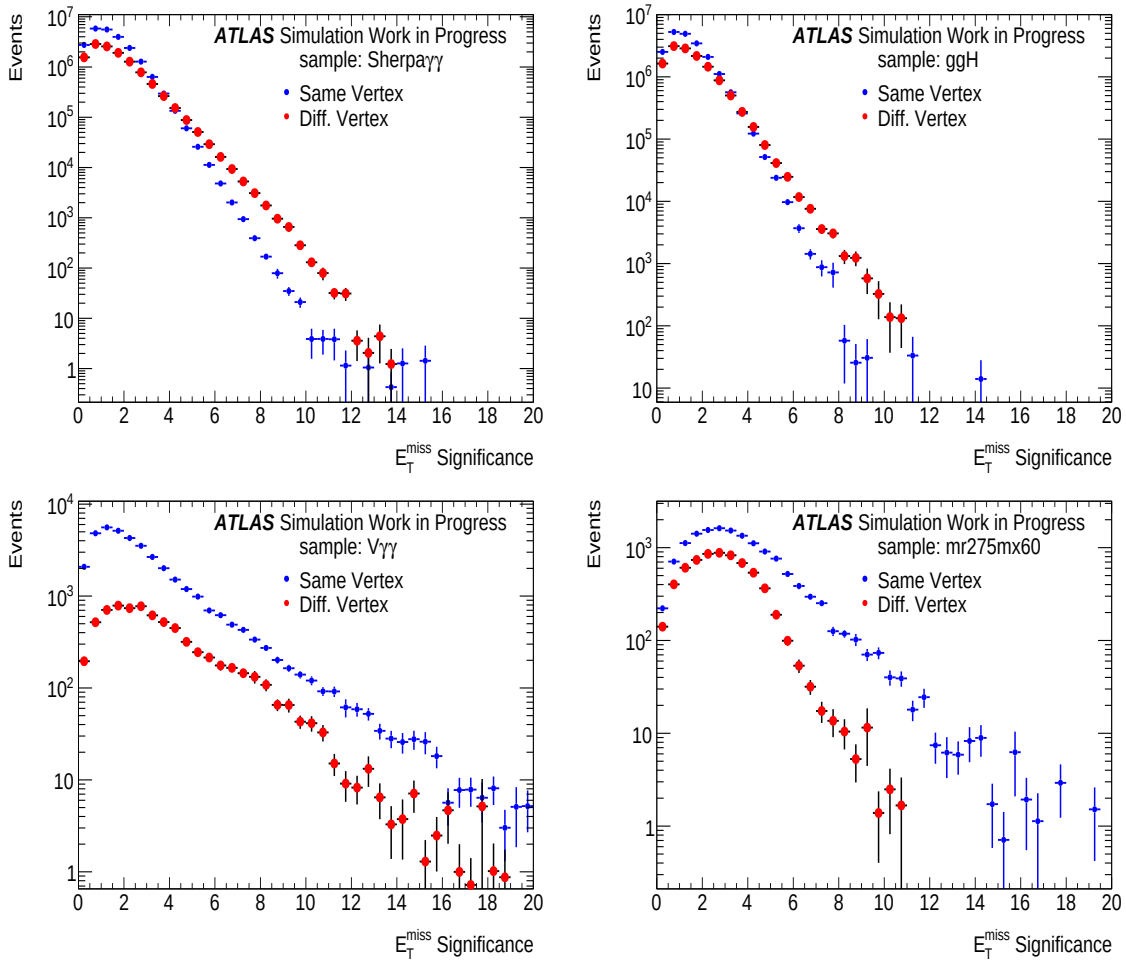

Figure 7. Events in same vertex and different vertex for different sample

7.1. Performance of same vertex method

Figure 7 shows the performance of selecting events with the same vertex method as compared with selecting events without the same vertex method (different vertex) for ggF, $h \to \gamma\gamma$+3jets, $V\gamma$ and $V\gamma\gamma$. ggF and $h \to \gamma\gamma$+3jets are samples with fake E_T^{miss} and they have comparable event distributions in the same vertex and different vertex phase space, this is because of the contribution from fake E_T^{miss} arisng from the JVF cut and Pile-up contribution. This implies events with fake E_T^{miss} can be rejected without lossing much efficiency in the analysis. On the other hand, events wth different vertex selection are much lower than the events with same vertex selection for $V\gamma$ and $V\gamma\gamma$ (samples with real E_T^{miss}) as expected.

Figures 8 and 9 show the mass spectrum of Higgs decay to two photons in the Higgs signal side-band (background). Figures 8 is the side band without any requirement on same vertex method and Figures 9 is the side-band with a requirement on same vertex method after a E_T^{miss} significance > 5.5. A significant reduction (about 60%) in signal side-band events is seen by comparing the two distributions.

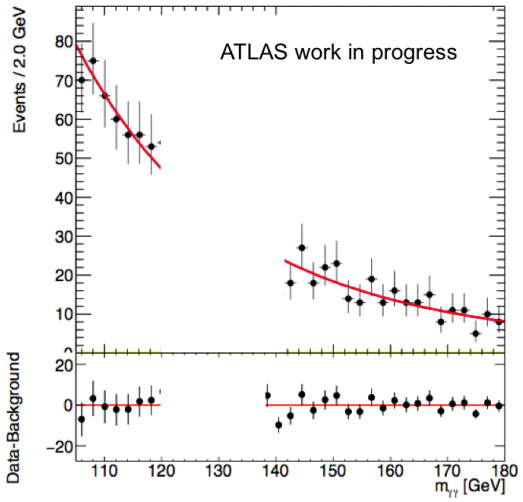

Figure 8. Blinded-data Sideband without same vertex cut

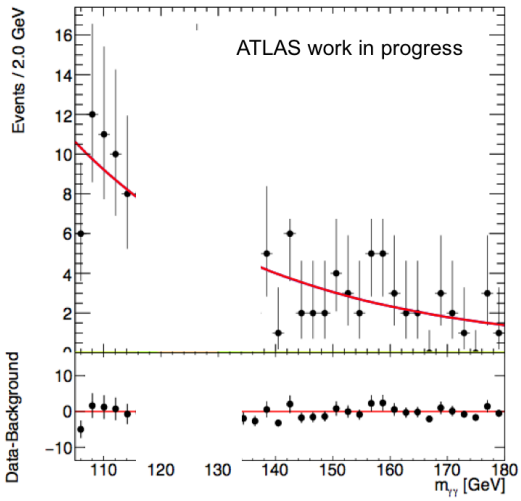

Figure 9. Blinded-data Sideband with same vertex cut

8. Conclusions

This paper has presented a new method of suppressing background events in the search for dark matter particles in ATLAS detector. The missing transverse energy is important to the search for new physics and $H \rightarrow \gamma\gamma + E_T^{miss}$ process in particular. However, the reconstruction missing transverse is sensitive to pile-up event from jets, miss-identification of photons or jets events which may lead to fake E_T^{miss}. To mitigate the effect of this error a study on the vertex selection was done and it was observed that background events and fake E_T^{miss} events can be significantly reduced by requiring same vertex from the Photon pointing and Hardest scattered method of vertex reconstruction. From Figures 8 and 9 about 60% of background events were reduced by using the same vertex method, this method has been validated by the ATLAS performance group. The same vertex method has been used in the search for dark matter in association with a Higgs boson decaying to two photons [3].

References

[1] Hrynevich A (ATLAS Collaboration) 2017 ATLAS jet and missing energy reconstruction, calibration and performance in LHC Run-2 Tech. Rep. ATL-PHYS-PROC-2017-045. 06 CERN Geneva URL `https://cds.cern.ch/record/2263777`

[2] Aaboud M *et al.* (ATLAS Collaboration) 2014 Tagging and suppression of pileup jets with the ATLAS detector Tech. Rep. ATLAS-CONF-2014-018 CERN Geneva URL `https://cds.cern.ch/record/1700870`

[3] Aaboud M *et al.* (ATLAS Collaboration) 2017 (*Preprint* `1706.03948`)

[4] von Buddenbrock S, Chakrabarty N, Cornell A S, Kar D, Kumar M, Mandal T, Mellado B, Mukhopadhyaya B, Reed R G and Ruan X 2016 *Eur. Phys. J.* **C76** 580 (*Preprint* `1606.01674`)

[5] Aaboud M *et al.* (ATLAS Collaboration) 2009 (*Preprint* `0901.0512`)

[6] Aaboud M *et al.* (ATLAS Collaboration) 2016 *Eur. Phys. J. C* **77** 332. 52 p

Performance of various event generators in describing multijet final states at the LHC

Stefan von Buddenbrock

School of Physics, University of the Witwatersrand, Johannesburg 2050, South Africa.

E-mail: `stef.von.b@cern.ch`

Abstract. At the Large Hadron Collider (LHC), the most abundant processes which take place in proton-proton collisions are the generation of multijet events. These final states rely heavily on phenomenological models and perturbative corrections which are not fully understood, and yet for many physics searches at the LHC, multijet processes are an important background to deal with. It is therefore imperative that the modelling of multijet processes is better understood and improved. For this reason, a study has been done with several state-of-the-art Monte Carlo event generators, and their predictions are tested against ATLAS data using the Rivet framework. The results display a mix of agreement and disagreement between the predictions and data, depending on which variables are studied. Several points for improvement on the modelling of multijet processes are stated and discussed.

Introduction

The biggest challenges to deal with in proton-proton (pp) collisions arise from multijet processes, as far as Standard Model (SM) backgrounds are considered. Due to the nature of quantum chromodynamics (QCD), multijet production processes have the largest cross sections at the Large Hadron Collider (LHC). In addition to this, their partial reliance on non-perturbative QCD makes them difficult to deal with from a theoretical perspective. This is because simulation of fragmentation and hadronisation depend on a non-perturbative calculations, these often being done using phenomenological models. It is therefore of importance to study the performance of event generators in describing multijet final states, since certain combinations of matrix element (ME) calculations, parton shower (PS) and hadronisation models do not always provide an accurate description of the data.

In ATLAS, a number of generators are used to model multijet processes. These are discussed in detail in the next section. The predictions of these generators can be compared both to each other and to data corrected for detector effects (unfolded datasets). The simplest way of doing this is by using the Rivet analysis system [1], which has a large set of built in analyses and distributions of unfolded data from various experiments. This short paper will present a subset of distributions relating to multijet processes, and compare the current set of ATLAS Monte Carlo (MC) multijet samples to unfolded data. From these results, information can be extracted about how to improve the modelling of the generators for future generation of samples in ATLAS.

Multijet event generators in ATLAS

A variety of MC event generators are used for studying multijet topologies in ATLAS. These involve different combinations of ME and PS programs. For a general review of event generators currently used in LHC physics, the reader is encouraged to look at Ref. [2]. Below is a list of the event generators considered in this study, as well as a few notes about their set up:

- Pythia 8 [3]: The prediction by Pythia 8 is sliced up by jet p_{T} using filters. The lowest p_{T} filtered samples use the Pythia 8 built in diffractive scattering processes (`SoftQCD`) to generate events. The rest of the slices use the elastic scattering processes (`HardQCD`). The chosen tune for the Pythia 8 samples is the A14 tune [4], which assumes the `NNPDF23LO` parton density function (PDF).
- Sherpa [5]: The official Sherpa samples make use of a $2 \to 3$ ME calculation,[1] matched with a CKKW scheme to a default Sherpa PS that use the CT10 tune. This sample has known issues with forward jets. The Sherpa prediction is also sliced in jet p_{T}.
- Powheg+Pythia 8 [6]: The Powheg ME is generated using the `Dijet` code that is provided with version 2 of the Powheg-Box. It is passed to the Pythia 8 PS, with the A14 tune. The sample is also sliced in jet p_{T}.
- Herwig++ [7]: Like Pythia 8, the Herwig++ sample makes use of the built-in `MEMinBias` process to simulate diffractive scattering for the lowest two slices in jet p_{T}, and the `MEQCD2to2` for the remaining slices. These samples make use of the UE-EE5 tune, and therefore the `CTEQ6L1` PDF.
- MG5_aMC@NLO+Pythia 8 [8]: The MG5_aMC@NLO+Pythia 8 samples use a $2 \to 4$ ME matched with a Pythia 8 PS using the CKKW-L scheme. The ME makes use of the `NNPDF30NLO` PDF, while the PS uses the A14 tune as described above. These samples are sliced at the ME level in parton H_{T}.

Key comparisons to data

As mentioned above, Rivet is used to compare the predictions of these variables against each other and unfolded data. In this short paper, the predictions are compared in the context of three different aspects of jet physics, namely azimuthal decorrelations, jet fragmentation and jet shapes. Note that all jets considered in the following analyses are constructed using the anti-k_{T} algorithm [9] with a radius parameter of $R = 0.6$.

Azimuthal decorrelations

Purely elastic scattering of QCD partons most often results in a dijet event – that is, exactly two well separated jets in the final state. In such a case, the azimuthal separation between the two jets should be π radians. However, in theory, one expects to see more QCD interactions in the elastic scattering of quarks and gluons. This extra activity can produce more jet activity in multijet events. Depending on how much more activity is found in the event, the azimuthal angle between the two leading jets will deviate from π. This is known as an azimuthal decorrelation.

In order to study azimuthal decorrelations, one typically looks at the azimuthal angle between the two leading jets in multijet events. ATLAS performed a differential cross section measurement of azimuthal decorrelation variables with the Run 1 7 TeV dataset [10]. The corresponding Rivet routine for this analysis is `ATLAS_2014_I1307243`. In Figure 1, some comparison plots are shown from this analysis. The different generators mostly perform well against the data, although discrepancies arise in different regions of the distributions, particularly for Herwig++.

[1] That is, up to three partons can be generated in the final state.

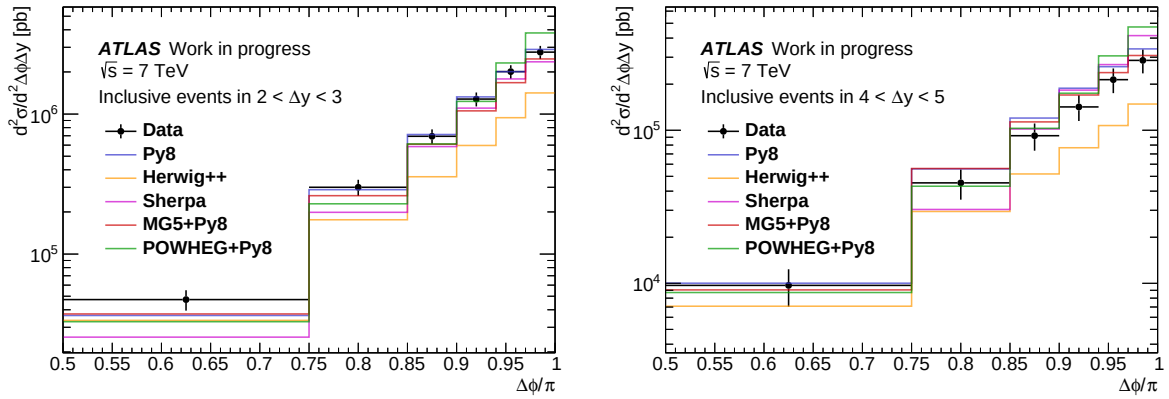

Figure 1. Differential cross section measurements as a function of the azimuthal angle between the two leading jets in multijet events [10]. The plots are made for inclusive multijet events in bins of rapidity separation, with $2 < \Delta y < 3$ on the left and $4 < \Delta y < 5$ on the right.

Jet fragmentation

The behaviour of the fragmentation function used in different PS models is most commonly studied by looking at the densities of jet constituents in selected jets. The simplest RIVET routine to use when studying jet fragmentation is `ATLAS_2011_I929691`, which is a 7 TeV measurement of charged jet constituent densities as a function of three different variables [11]. Firstly, the variable z is scanned, which is the fraction of longitudinal momentum carried by a jet constituent:

$$z = \frac{\vec{p}_{\text{jet}} \cdot \vec{p}_{\text{ch}}}{|\vec{p}_{\text{jet}}|^2}. \tag{1}$$

Here, $\vec{p}_{\text{ch}}$ denotes the 3-momentum of the charged jet constituent, and $\vec{p}_{\text{jet}}$ is the 3-momentum of the jet. Secondly, the distance between the jet axis and the jet constituent in units of ϕ and y is scanned over (denoted by r). And thirdly, the jet constituent's momentum transverse to the jet axis, $p_{\text{T}}^{\text{rel}}$, is scanned over:

$$p_{\text{T}}^{\text{rel}} = \frac{|\vec{p}_{\text{ch}} \times \vec{p}_{\text{jet}}|}{|\vec{p}_{\text{jet}}|}. \tag{2}$$

In Figure 2, plots are shown for jet constituent densities as a function of two of these variables. In this case, HERWIG++ arguably performs the best compared with the data, and SHERPA tends to perform the poorest. This is most probably due to the old version of SHERPA used by ATLAS in the official samples. Recent studies on newer SHERPA samples in ATLAS have seen the problems with jet fragmentation fixed, although these results could not be shown in this short paper.

Jet shapes

Jet algorithms can tell us about the geometry of the constituents of a jet. But to understand how energy is distributed in the average jet, it is more instructive to look at jet shapes. Similarly to jet fragmentation measurements, jet shapes are studied through looking at jet constituent densities. These are distributed as a function of the distance away from the axis of a jet, r. Typically, we look at the jet p_{T} weighted density in bins of annulus areas in the jet cone,

$$\rho(r) = \frac{1}{\Delta r N_{\text{jet}}} \sum_{\text{jets}} \frac{p_{\text{T}}(r - \Delta r/2, r + \Delta r/2)}{p_{\text{T}}(0, R)}, \tag{3}$$

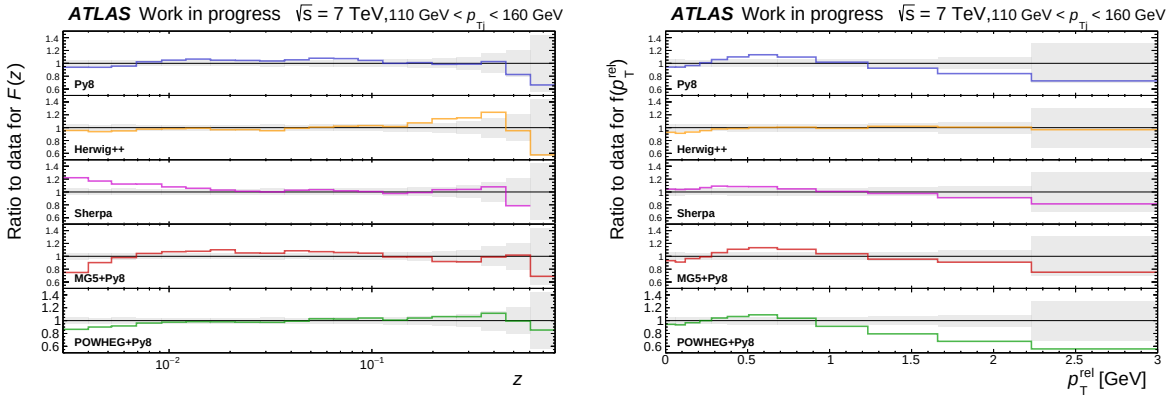

Figure 2. Ratio plots of the different event generators compared to the data in measurements of jet constituent densities as a function of z (left) and $p_{\mathrm{T}}^{\mathrm{rel}}$ (right) [11]. These plots are both shown in the same bin of jet p_{T}.

where $p_{\mathrm{T}}(r_1, r_2)$ is the sum of the jet constituent p_{T} between r_1 and r_2 away from the jet cone axis. In addition to this, we measure the integrated p_{T} weighted density,

$$\Psi(r) = \frac{1}{N_{\mathrm{jet}}} \sum_{\mathrm{jets}} \frac{p_{\mathrm{T}}(0, r)}{p_{\mathrm{T}}(0, R)}. \tag{4}$$

The RIVET routine `ATLAS_2011_S8924791` contains a large set of doubly differential jet shapes corresponding to an ATLAS 7 TeV measurement [12]. In Figure 3, some plots are shown in a single bin of the ATLAS analysis. Here, most of the generators considered agree relatively well with the data. It should be noted that POWHEG+PYTHIA seems to predict a different jet shape than what is seen in the data.

Summary

Using the ATLAS multijet samples, comparisons have been made to unfolded data using RIVET. Three different measurements have been considered in this short paper. In each, it can be seen that the different generators tend to perform better in some regions of the phase space than

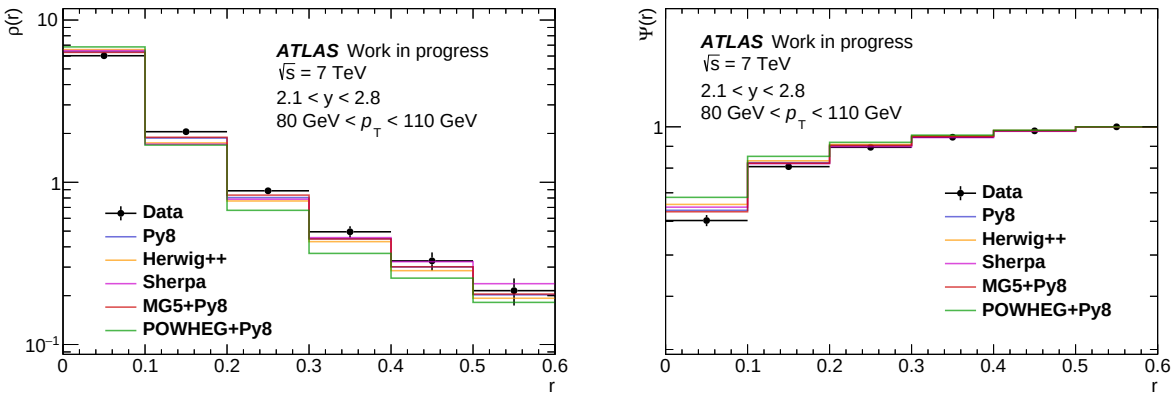

Figure 3. Jet shape measurements in terms of differential p_{T} density (left) and integrated p_{T} density (right) [12].

others, while there is no clear choice for one generator performing systematically better than any of the others.

However, the information from these comparisons is still useful for the ATLAS collaboration to improve the modelling of multijet processes by knowing where the current predictions fail. There are yet many more measurements that can be considered in this study, and in future these studies will be extended to a more comprehensive study.

References

[1] Buckley A, Butterworth J, Lonnblad L, Grellscheid D, Hoeth H, Monk J, Schulz H and Siegert F 2013 *Comput. Phys. Commun.* **184** 2803–2819 (arXiv:1003.0694)

[2] Buckley A *et al.* 2011 *Phys. Rept.* **504** 145–233 (arXiv:1101.2599)

[3] Sjöstrand T, Ask S, Christiansen J R, Corke R, Desai N, Ilten P, Mrenna S, Prestel S, Rasmussen C O and Skands P Z 2015 *Comput. Phys. Commun.* **191** 159–177 (arXiv:1410.3012)

[4] ATLAS Collaboration 2014 ATLAS Pythia 8 tunes to 7 TeV data ATL-PHYS-PUB-2014-021 URL https://cds.cern.ch/record/1966419

[5] Hoeche S, Krauss F, Schonherr M and Siegert F 2013 *JHEP* **04** 027 (arXiv:1207.5030)

[6] Alioli S, Nason P, Oleari C and Re E 2010 *JHEP* **06** 043 (arXiv:1002.2581)

[7] Bahr M *et al.* 2008 *Eur. Phys. J.* **C58** 639–707 (arXiv:0803.0883)

[8] Alwall J, Frederix R, Frixione S, Hirschi V, Maltoni F, Mattelaer O, Shao H S, Stelzer T, Torrielli P and Zaro M 2014 *JHEP* **07** 079 (arXiv:1405.0301)

[9] Cacciari M, Salam G P and Soyez G 2008 *JHEP* **04** 063 (arXiv:0802.1189)

[10] ATLAS Collaboration 2014 *Eur. Phys. J. C* **74** 3117 (arXiv:1407.5756)

[11] ATLAS Collaboration 2011 *Eur. Phys. J. C* **71** 1795 (arXiv:1109.5816)

[12] ATLAS Collaboration 2011 *Phys. Rev. D* **83** 052003 (arXiv:1101.0070)

Production of the Madala boson in association with top quarks

Stefan von Buddenbrock

School of Physics, University of the Witwatersrand, Johannesburg 2050, South Africa.

E-mail: stef.von.b@cern.ch

Abstract. The Madala hypothesis is the prediction of a new heavy scalar, the Madala boson, that has had previous success in explaining several anomalies in LHC Run 1 and 2 data. In the literature, the Madala boson has so far primarily been discussed in the context of its dominant production mode, gluon fusion. However, it can be shown that a study of its production in association with top quarks can provide us with crucial information about the model, as well as explain the enhancement of top associates Higgs production that has been observed in the data – most notably in leptonic channels. For this study, Monte Carlo events have been produced and passed through a detector simulation. These events are then run through an event selection designed by a CMS search for a single top quark in association with a Higgs boson. A fit is made to the CMS data, yielding a parameter constraint on the Madala hypothesis. With the Madala hypothesis prediction, an effective signal strength is calculated and compared with the observed values.

Introduction

The search for physics beyond the Standard Model (BSM) has gained considerable interest since the discovery of the Standard Model (SM) Higgs boson, h [1, 2]. In the years since, a plethora of models extending the SM have been proposed with the potential of being discovered experimentally at the Large Hadron Collider (LHC) – for a recent review, see Ref. [3]. One such model that has previously been discussed in the literature is known as the *Madala hypothesis*. The key postulate of this model is the hypothetical existence of a heavy scalar H – the *Madala boson* – which interacts strongly with the SM Higgs boson and an additional Higgs-like scalar singlet S – which can act as a portal to some arbitrary BSM physics [4]. Applying the hypothesis to several Run 1 experimental results also placed constraints on the mass of H, with a best fit point at $m_H = 272^{+12}_{-9}$ GeV [5]. The mass of S has not yet been constrained at the present time of writing, but it is considered in the range $m_S \in [130, 200]$ GeV. This is due to the fact that a rich combination of the production of multiple leptons can be explored in this mass range [4], due to the fact that the the S will decay dominantly to pairs of massive gauge bosons (as opposed to b-quarks, which are the dominant decays for Higgs-like scalars with lower masses).

So far, the majority of studies done on the Madala hypothesis have looked dominantly at the gluon fusion (ggF) production mechanism of H. While ggF is indeed assumed to have a large production cross section, it should be noted that the same theoretical vertices required for ggF require that H can also be produced in association with top quarks (ttH) with a non-negligible cross section. This is a tantalising prospect, since both Run 1 and Run 2 searches for top associated Higgs production (tth) have shown significant excesses, particularly in leptonic

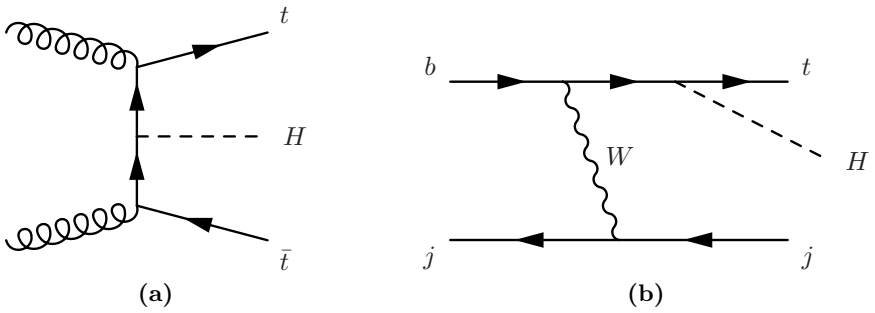

Figure 1: The leading order (LO) Feynman diagrams for (a) ttH and (b) tH production. Note that the diagram on the right assumes a five-flavour (5F) proton – that is, b-quarks are assumed to be a non-negligible component of the partonic structure of the proton.

channels. When measuring the signal strength of tth using $\mu_{tth} = \sigma_{tth}^{\text{obs}}/\sigma_{tth}^{\text{SM}}$, it can be shown that a combination of the experimental search results in leptonic channels yields a value of $\mu_{tth} = 1.92 \pm 0.38$ [6]. This can be quantified as around a 2.4σ deviation from the SM.

It is therefore of interest to apply the Madala hypothesis to tth results, in order to understand whether it can shed light on the excesses seen in the data. The Madala boson, if it is produced in association with top quarks, can decay into a Higgs boson, therefore mimicking the signature searched for in the existing experimental tth search channels.

Modelling top associated Madala production

Typically in tth searches, signal contributions can come both from Higgs production in association with one or two top quarks, labelled as th and tth, respectively. This is no different for top associated H production. The dominant Feynman diagrams for top associated H production can be seen in Figure 1.

In the SM, it is well known that due to the negative interference between the Yukawa couplings and the Higgs couplings to the weak vector bosons, the production cross section of th is far smaller than that of tth. This is not true for tH production, however. Following the logic in Ref. [7] and the fact that H is assumed to couple weakly to the vector bosons [5], it turns out that

$$\sigma_{tH} \simeq \sigma_{ttH}, \tag{1}$$

and so both tH and ttH are non-negligible processes in the Madala hypothesis. The top Yukawa coupling to the H is assumed to be Higgs-like, and further scaled by the free dimensionless parameter β_g. Therefore, one can find the ttH production cross section by first taking the associated value for a heavy Higgs boson from the CERN yellow book [8], and then by multiplying it by β_g^2. In the Run 1 fit result [5], β_g was constrained to be 1.5 ± 0.6.

For this short paper, we assume that H has one dominant decay mode, $H \to Sh$. Furthermore, S is chosen to be Higgs-like, such that all branching ratios (BRs) are already determined; this choice drastically reduces the number of free parameters in the model. This choice also enhances the number of leptons one would find as a result of the decay of S, since for a Higgs-like particle with a mass near $2m_W$, the BR for $S \to WW$ becomes dominant. These W bosons in the final state can then decay leptonically to provide a source of multiple lepton production. In particular, a non-negligible production of two same-sign leptons is possible through the cascade decays, a process that is highly suppressed in the SM.

To simulate tH and ttH production, the hard scatter processes were produced at LO using Monte Carlo (MC) event generation in MadGraph [9]. This was done using a custom-designed model file using the Universal FeynRules Output (UFO) [10]. These MC events were passed

Table 1: Summary of the event selection and categorisation for the CMS Run 2 single top search. These criteria closely mimic the selection done in Ref. [13], since a comparison to data is performed. This selection is used on the output n-tuple created by the DELPHES fast detector simulation.

Event selection	
No lepton pair with $m_{\ell\ell} < 12$ GeV	
$N_{b\text{-jets}} \geq 1$	
$N_{\text{jets}} \geq 1$ (not including b-jets)	
Event categorisation	
Same-sign 2 lepton	*Tri-lepton*
Exactly 2 same-sign leptons	Exactly 3 leptons
$\ell\ell = e\mu$ or $\mu\mu$	Leading lepton $p_{\text{T}} > 25$ GeV
Leading lepton $p_{\text{T}} > 25$ GeV	Second and third lepton $p_{\text{T}} > 15$ GeV
Sub-leading lepton $p_{\text{T}} > 15$ GeV	No lepton pair with $\lvert m_{\ell\ell} - m_Z \rvert < 15$ GeV

to PYTHIA 8.2 [11] for the resonance decays, parton shower (PS), and hadronisation processes. Finally, the PYTHIA output was run through the DELPHES 3 fast detector simulation [12] to account for detector effects. The output from DELPHES was used for the analysis presented in the next section.

Comparisons with CMS data

A relatively recent experimental result (at the time of writing) was chosen for the comparison of the Madala hypothesis with data from the LHC. The chosen experimental result is a search done by the CMS collaboration for a single top quark in association with a Higgs boson [13]. It should be noted upfront that even though it has been labelled as a "single top" search, the event selection (shown in Table 1) is compatible with both single and double top associated production of both the Higgs and Madala bosons.

The analysis done in the CMS Run 2 single top search is performed by a boosted decision tree (BDT), so a direct comparison with their final results is difficult. However, the paper did present distributions of three key variables that were made after an event preselection detailed in Table 1. These variables are: the largest absolute pseudo-rapidity of any jet in the event, the separation in azimuthal angle between the leading same-sign lepton pair, and the jet multiplicity.

To compare the Madala hypothesis with the data presented by the CMS Run 2 single top search, BSM events were generated and run through a CMS detector simulation as detailed in the section above. Only one mass point was considered for the analysis, since the acceptances into the preselection regions of the chosen analysis were determined to be not significantly sensitive to the change in the mass of S. Rather, the ability of the process to produce a final state with two same-sign leptons is what fundamentally determines the preselection acceptance, and in the proposed mass range for S, this does not change significantly since the BRs of S do not change significantly. The mass of H was set to 270 GeV (in line with the Run 1 fit result [5]), while the mass of S was set to 140 GeV, such that the $H \to Sh$ decay could be kept on-shell.

The events were filtered according to the selection and categorisation detailed in Table 1, and then plotted as a function of the three key variables listed above. The SM background and its associated uncertainty was read off of the figures in Ref. [13]. The BSM prediction was scaled to the appropriate cross section from Ref. [8] multiplied by a best fit value of β_g^2 and added to the SM prediction. The results of this can be seen for the $e\mu$ and $\mu\mu$ channels in Figure 2. It should be noted that the best fit value of β_g^2 was negative for the tri-lepton channel, and therefore the plots have not been included in this short paper.

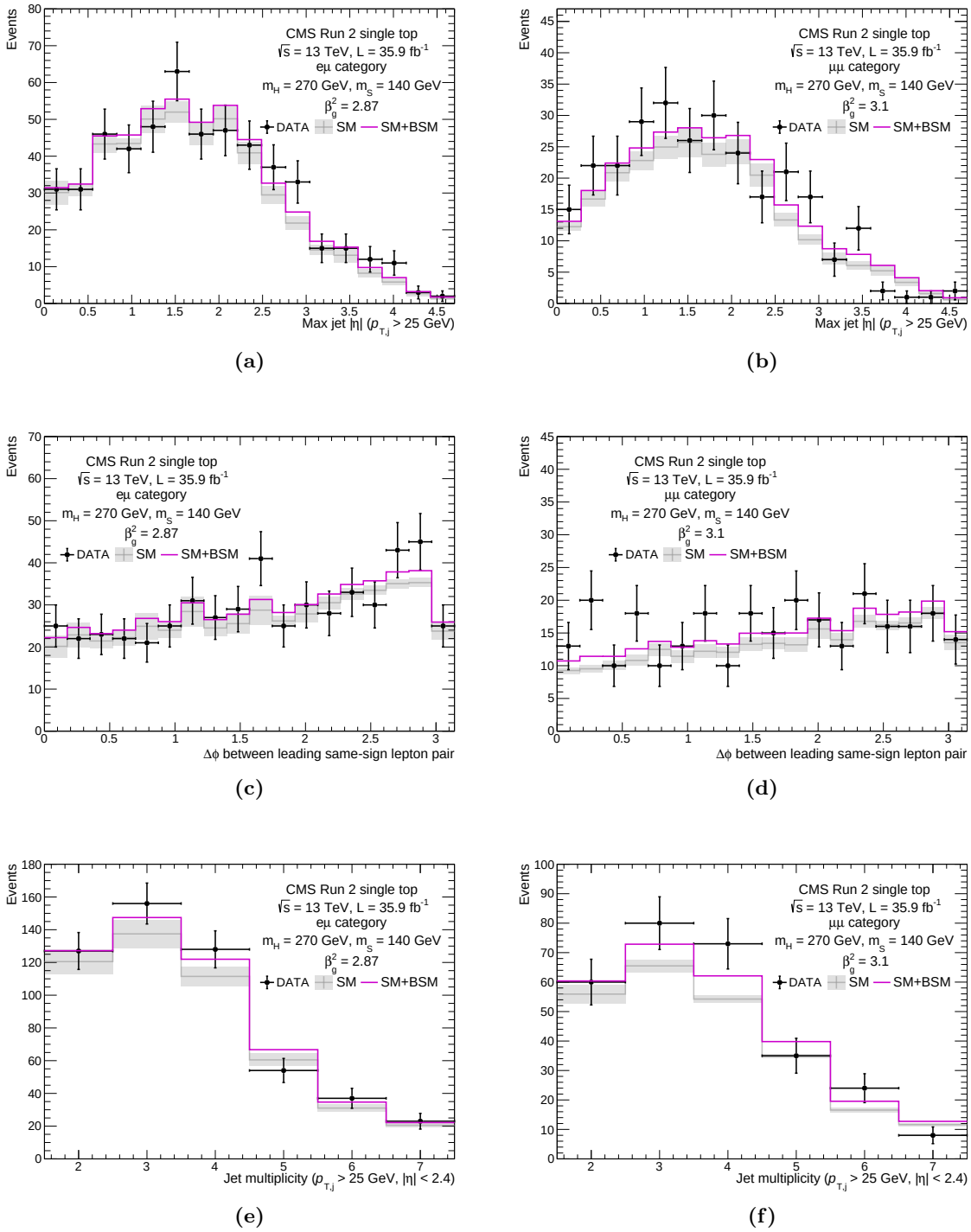

Figure 2: The plots of (a-b) maximum jet pseudo-rapidity, (c-d) azimuthal separation between the leading same-sign lepton pair and (e-f) jet multiplicity from the CMS Run 2 single top search. These have been separated into the $e\mu$ channel (left) and the $\mu\mu$ channel (right). The tri-lepton channel did not yield a positive BSM signal, so the plots have been omitted. The BSM predictions are scaled by the best fit values of β_g^2 as described in the text. The mass points considered for the BSM prediction are $m_H = 270$ GeV and $m_S = 140$ GeV.

Table 2: The best fit values for β_g^2 for each channel in the CMS Run 2 single top search. The combined result was obtained by summing Equation 2 over all channels. The Run 1 fit result from Ref. [5] has been listed to show the compatibility between the new and old results.

Channel	**Best fit** β_g^2
$e\mu$	3.10 ± 1.02
$\mu\mu$	2.87 ± 1.04
Tri-lepton	-0.93 ± 0.92
Combined	1.48 ± 0.57
Run 1 fit result	2.25 ± 1.80

The best fit values of β_g^2 were computed as follows. A global χ^2 was constructed by adding a χ^2 for each bin and in each observable per channel. For each bin i, the global χ^2 therefore took the form of Pearson's test statistic,

$$\chi^2 = \sum_i \frac{\left(N_i^{\text{data}} - N_i^{\text{SM}} - \beta_g^2 N_i^{\text{BSM}}\right)^2}{\left(\Delta N_i^{\text{data}}\right)^2 + \left(\Delta N_i^{\text{SM}}\right)^2}, \tag{2}$$

where the N_i factors are the event yields per bin i, and the ΔN_i factors are their associated uncertainties. The BSM uncertainty is not included since it is dominated by the SM and statistical uncertainty. The best fit value of β_g^2 is obtained by minimising Equation 2 while leaving β_g^2 free. A 1σ uncertainty on this best fit value is taken as the envelope around which Equation 2 can vary by one unit away from the mean fit value of β_g^2. The results of this process can be seen in Table 2.

Discussion

As can be seen in Figure 2, the BSM prediction does a relatively good job of explaining the CMS data in the $e\mu$ and $\mu\mu$ channels – this is possibly best seen in the jet multiplicity distributions. As noted before, the fit to the tri-lepton data did not yield a positive BSM signal. Note that a negative value of β_g^2 is not physical, however the fit value is still included in the results due to the fact that the whole dataset for the CMS search is statistically limited. In addition to this, the further categorisation of the data into the three channels further limits the statistical reach of the analysis. It is therefore far more sensible to treat the combined fit value as a result with statistical power, while the fits to the individual categories behave more like statistical fluctuations around the combined best fit value. Whether or not the poor fit to the tri-lepton channel yields any information about the nature of the model's ability to accurately describe the data in terms of lepton multiplicity is unclear, due to the statistical limitations of the dataset. The combination of all channels shown in Table 2 is still dominated by the di-lepton channels, of which the best fit values of β_g^2 have relative uncertainties of ~ 35 %, whereas for the tri-lepton channel it is ~ 100 %. The combined best fit value of β_g^2 equates to around a 2.6σ deviation from the SM.

As mentioned in the introduction, a combination of leptonic tth searches can be quantified by the signal strength parameter $\mu_{tth} = 1.92 \pm 0.38$ as calculated in Ref. [6]. Using the combined best fit value of β_g^2 in Table 2, the corresponding value of μ_{tth} for the analysis done in this short paper is compatible with this, and is equal to 1.32 ± 0.51. Combining the results of this short paper with the global combination done in Ref. [6], a significance of 3.5σ in excess of the SM can be computed.

The CMS Run 2 single top search has corroborated previous results that have been calculated using the Madala hypothesis. It is still, however, only one analysis that can be analysed from the Run 2 dataset. It is imperative, then, to continue constraining the model with other data in leptonic *tth* searches from both CMS and ATLAS. More importantly, it is prudent to compare the predictions of the Madala hypothesis with differential distributions, rather than single measurements of signal strength, since distributions provide a more statistically rich picture of potential deviations from the SM. It should be noted also that the simplification of assuming a Higgs-like S particle could also be generalised to more complicated and phenomenologically rich models. However, so far the compatibility of the results in this paper with previous results from the Madala hypothesis is an encouraging outcome of the study, which will lead to further work done on constraining the properties of the Madala boson.

References

[1] ATLAS Collaboration 2012 *Phys. Lett.* **B716** 1–29 (arXiv:1207.7214)

[2] CMS Collaboration 2012 *Phys. Lett.* **B716** 30–61 (arXiv:1207.7235)

[3] Csaki C, Lombardo S and Telem O 2018 TASI Lectures on Non-supersymmetric BSM Models Tech. rep.

[4] von Buddenbrock S, Chakrabarty N, Cornell A S, Kar D, Kumar M, Mandal T, Mellado B, Mukhopadhyaya B, Reed R G and Ruan X 2016 *Eur. Phys. J.* **C76** 580 (arXiv:1606.01674)

[5] von Buddenbrock S, Chakrabarty N, Cornell A S, Kar D, Kumar M, Mandal T, Mellado B, Mukhopadhyaya B and Reed R G 2015 (arXiv:1506.00612)

[6] von Buddenbrock S 2017 *Proceedings of KRUGER2016* (arXiv:1706.02477)

[7] Farina M, Grojean C, Maltoni F, Salvioni E and Thamm A 2013 *JHEP* **05** 022 (arXiv:1211.3736)

[8] de Florian D *et al.* (LHC Higgs Cross Section Working Group Collaboration) 2016 (arXiv:1610.07922)

[9] Alwall J, Frederix R, Frixione S, Hirschi V, Maltoni F, Mattelaer O, Shao H S, Stelzer T, Torrielli P and Zaro M 2014 *JHEP* **07** 079 (arXiv:1405.0301)

[10] Alloul A, Christensen N D, Degrande C, Duhr C and Fuks B 2014 *Comput. Phys. Commun.* **185** 2250–2300 (arXiv:1310.1921)

[11] Sjöstrand T, Ask S, Christiansen J R, Corke R, Desai N, Ilten P, Mrenna S, Prestel S, Rasmussen C O and Skands P Z 2015 *Comput. Phys. Commun.* **191** 159–177 (arXiv:1410.3012)

[12] de Favereau J, Delaere C, Demin P, Giammanco A, Lemaître V, Mertens A and Selvaggi M (DELPHES 3 Collaboration) 2014 *JHEP* **02** 057 (arXiv:1307.6346)

[13] CMS Collaboration 2017 Search for production of a Higgs boson and a single top quark in multilepton final states in proton collisions at $\sqrt{s} = 13$ TeV Tech. Rep. CMS-PAS-HIG-17-005 CERN Geneva URL http://cds.cern.ch/record/2264553

DIVISION C – PHOTONICS

Cell death induced by combination of Phthalocyanine photosensitizer and Doxorubicin on MCF-7 breast carcinoma cells.

E.C. Aniogo, B.P. George and H. Abrahamse

Laser Research Centre, Faculty of Health Sciences, University of Johannesburg, P.O. Box 17011, Doornfontein, 2028 South Africa.
Tel: +27 11 559 6833; Fax: +27 11 559-6884

Email: habrahamse@uj.ac.za

Abstract. Cancer is one of the common diseases that affect and threatens our human existence. Breast cancer is an invasive heterogeneous disease and the second most common disease among woman worldwide. For a degenerative disease like cancer to be cured, multiple therapeutic agents that target different pathological processes must be applied. For this reason, combination therapy remains an alternative strategy to combat diseases like cancer. In this study, we evaluated the anticancer effect of sulfonated zinc phthalocyanine (ZnPcS) mediated photodynamic therapy in combination with low dose doxorubicin (0.5 μM) on MCF-7 cancer cells. In addition, we explore the cell death pathway elicited by combination treatment. MCF-7 cells were incubated with low dose doxorubicin for 20 h, afterwards, various concentrations of phthalocyanine were added and further incubated for 4 h. Thereafter, the cells were irradiated with 681.5 nm diode laser at 4.74 wM/cm^2 for 17 min 36 sec (5 J/cm^2), and the cellular responses were measured. Cellular morphology was observed using inverted microscopy while the proliferation of cells was measured with homogenous ATP quantitative assay. The mechanism of cell death was investigated using Annexin V/PI flow cytometric analysis. Findings from this study show that combination of phthalocyanine mediated photodynamic therapy and doxorubicin significantly enhances the anticancer efficacy of phthalocyanine-doxorubicin combination on MCF-7 cells than when used individually. It was observed that this combination treatment led to an apoptotic cell death pathway. Hence, this study suggests a new treatment opportunity for breast cancer to enhance its effectiveness and which warrants further investigation for its potential to reverse multidrug resistance.

1. Introduction

Cancer continues to dominate among the major cause of mortality worldwide despite knowledge of its treatment at the cellular level. Breast cancer is the most frequently diagnosed and the most common cause of cancer death among woman [1]. Global cancer statistics showed that nearly 1.7 million new cases of breast cancer were diagnosed in 2012, which represents about 25% of all cancers in woman [2]. Photodynamic therapy is an emerging attractive treatment regime that has already been used on patients suffering from superficial cancers. It involves the systematic use of a light sensitive chemical called a photosensitizer in the presence of light and oxygen to induce destruction of cancerous cells through the production of superoxide radicals that cause oxidative stress and thus cell death [3]. PDT efficacy greatly depends on the production of reactive oxygen species that attack cellular targets within the cells and leads to cell damage and death [4]. ZnPcS mediated PDT has demonstrated its effectiveness in the treatment of breast cancer cell line [5]. Recently, most therapeutic investigations are now focusing on combining one or two treatment modalities, which can sum the advantages of each individual

treatment, increase treatment efficacy and reduce dose dependent toxicity [6]. Thus, our study aimed to evaluate the anticancer effect of phthalocyanine mediated photodynamic therapy in combination with low dose doxorubicin (0.5 μM) on MCF-7 cancer cells and explore the mode of cell death.

2. Methodology

2.1 Cell culture and Laser Irradiation

MCF-7 breast cancer cell lines (ATCC HTB-22) were used in this study. Appropriately, 5×10^5 cells were seeded in 3.4cm^2 diameter culture dishes and incubated for 4 h to allow the cells to attach and recover homeostatically. Experimental cells were divided into four groups; untreated controls, cells treated with doxorubicin, PDT treated cells and cells treated with a combination of PDT and doxorubicin. Three different concentrations (0.25, 0.5 and 1μM) were used for both doxorubicin and zinc phthalocyanine photosensitizer. For combination treatment, suboptimal concentration of doxorubicin (0.5μM) was used with each of the three concentrations of the zinc phthalocyanine photosensitiser. The choice to use suboptimal concentration was to diminish the possible side effects of chemotherapeutic agent while retaining its efficacy. Laser irradiation was performed using a 681.5 nm diode laser and its parameters are shown in Table 1. Cellular responses were analyzed 24 h after treatment. Cellular morphology was observed using inverted microscopy while the proliferation of cells was measured with homogenous ATP quantitative assay. The mechanism of cell death was investigated using Annexin V/PI flow cytometric analysis. The statistical analysis was performed on four repeats of each sample and significant difference were considered at $p<0.05$ (*), $p<0.01$ (**), and $p<0.001$ (***).

Table 1. Laser parameters.

Parameters	**Laser**
Name and type	Semiconductor (diode)
Wavelength	681.5 nm
Spectrum	Red (visible)
Wave emission	Continuous
Spot size	9.1 cm^2
Power output	43 mW
Power density	4.74 mW/cm^2
Fluence	5 J/cm^2
Irradiation time	17 Minutes 36 Seconds

3. Results

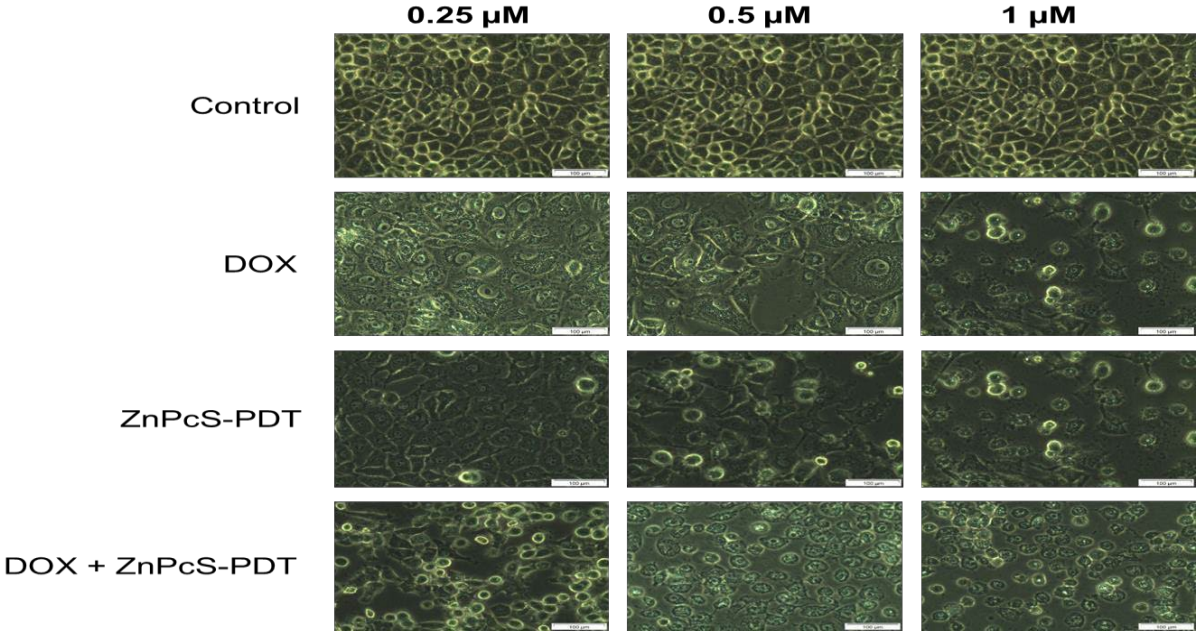

Figure 1. Morphology of MCF-7 cells after treatment investigated using an inverted light microscope with 200X magnification.

The results showed morphological changes like cell membrane damage, rounding up and floating of cells in the culture medium in cell groups treated with either doxorubicin or photodynamic therapy when compared to the untreated control. Combined treated group was observed to have an increased number of rounding and floating cells, indicative of dying cells. Likewise, there was a significant decrease in the cellular viability and proliferation within the combined treated groups. Despite the high antiproliferative efficacy of 1 µM ZnPcS-PDT and 0.5 µM doxorubicin, the percentage of apoptotic cells was approximately 47% which was significant when compared to untreated control. We observed fewer non-apoptotic cells. Altogether, these results showed strong efficacy and enhanced anticancer effects when a low dose doxorubicin chemotherapy is combined with phototherapy mediated by zinc phthalocyanine.

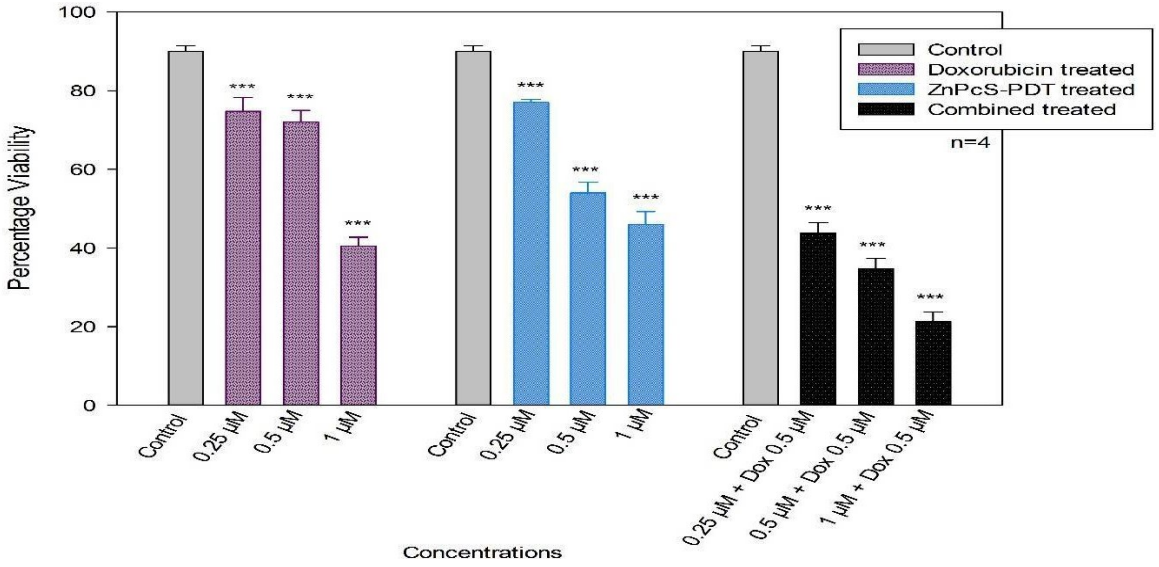

Figure 2 Trypan blue exclusion cell viability assays. There was a significant decrease in the viability of cell across a treated group when compared to the untreated control. Results represents the mean ± standard error of four independent experiments. Significant differences between treated groups and control are shown as ***$P< 0.001$

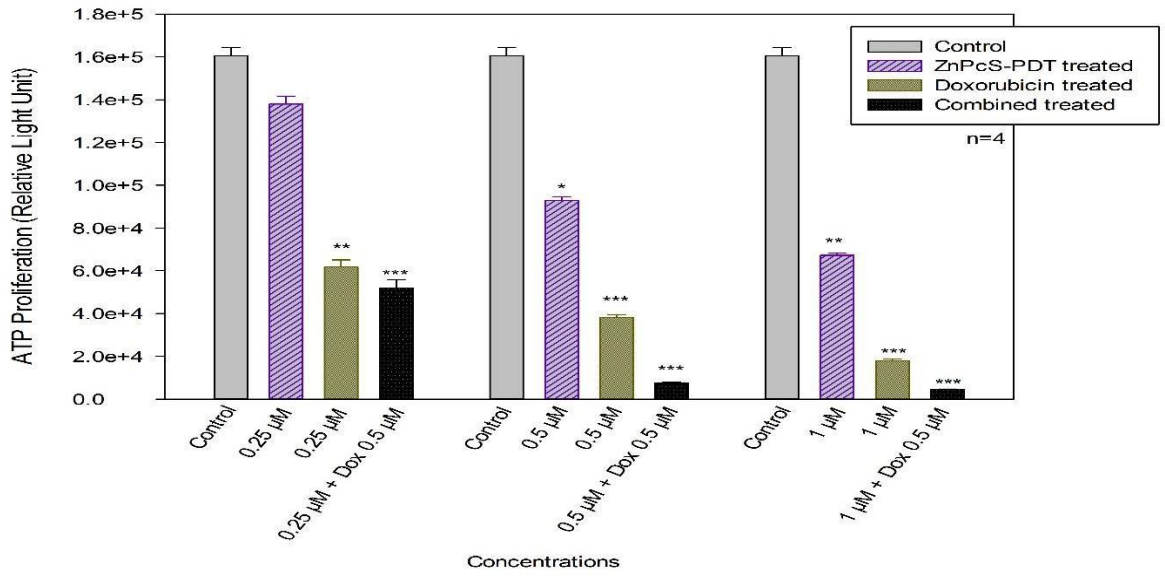

Figure 3 Cell proliferation measured by Adenosine triphosphate luminescent assay. There was a significant reduction in the rate of cellular proliferation within the combination treatement group compared to the untreated control. Results represent the mean ± standard error of four independent experiments. Significant differences between treated groups and control are shown as ***$P < 0.001$; **$P < 0.01$; *$P < 0.05$

Table 2 Flow cytometric assessment of cell death pathway with various concentration of ZnPcS-PDT in combination of 0.5 μM DOX. Cells were stained with Annexin V-FITC/PI and results represent the mean ± SE of three independent duplicate experiment. Significant differences between treated groups and control are shown as ***$P < 0.001$; **$P < 0.01$

Groups	LL-Normal cells (%)	LR- Early apoptotic cells (%)	UR- Late apoptotic dead cells (%)	UL non-apoptotic cells (%)
Control	93.79 ± 0.29	2.11 ± 0.14	3.64 ± 0.20	0.46 ± 0.05
0.25 μM + 0.5μM DOX	70.48 ± 1.70***	17.39 ± 2.33**	12.0 ± 1.17**	0.13 ± 0.03
0.5 μM + 0.5μM DOX	68.61 ± 0.49***	22.48 ± 2.41***	7.89 ± 1.49	1.02 ± 0.54
1 μM + 0.5μM DOX	52.89 ± 2.44***	31.10 ± 2.80***	15.88 ± 1.34**	0.13 ± 0.06

4. Discussion and Conclusion

Degenerative diseases like cancer have shown to involve multiple pathologic processes, which make most mono-therapeutic modalities to be ineffective. Doxorubicin is the most common chemotherapeutic agent used for fighting cancer malignancies but its toxicity and development of drug resistance have been a major problem limiting its use [7]. Photodynamic therapy, directly or indirectly produce an increase reactive oxygen species that kill tumor cells, induces inflammatory and immune response with tumor vasculature shutdown that effectively leads to tumor control [8]. It was hypothesized that the use of another anticancer agent whose mechanism of action also involves the formation of toxic oxygen radicals may also enhance the effectiveness of photodynamic therapy. Hence, we explore the interaction and therapeutic efficacy of combining doxorubicin and photodynamic therapy in cancer treatment. Such combination therapies are currently been investigated as an alternative treatment modality for various cancer types. The sole aim of combination therapy is to reduce the dose of the toxic chemotherapeutic agents and their side effects while still retain its therapeutic value [9]. Recent studies by Ruiz-Gonzalez et al. [10] demonstrated the potentiation in pheiphorbide a mediated photodynamic therapy with the addition of low dose concentration of doxorubicin. Similar studies by De-Freitas et al. [6] showed that photodynamic therapy mediated by either methylene blue or photogem in combination with cisplatin chemotherapy has low mutagenic potential, which elicits the potential of such combined therapy in diminishing the toxicity of antineoplastic drugs. We have demonstrated in MCF-7 cancer cell lines that ZnPcS-PDT tumor killing can be significantly increased with low dose of doxorubicin. Agostinis and colleagues reported that photodynamic therapy could evoke three main cell death pathways with apoptosis being the major mode of cell death [11]. Other evidence suggests that doxorubicin activity can produce reactive oxygen radicals, which trigger the induction of cell death through apoptosis [12,13]. Reactive oxygen species have been known to be a cellular stress factor that can effectively induce an active mode of cell death, apoptosis if produced over a certain level of quantity [14]. Subsequently, we investigated the mode of cell death after the combination treatment and our results showed that majority of cells were undergoing apoptosis. It was observed MCF-7 cancer cells incubated with 1 μM ZnPcS photosensitizer with 0.5 μM doxorubicin have a significant number of cells in the early apoptosis and late apoptotic stage. Morphology alterations induced by this combination therapy were similar to apoptosis as cells gradually loss their morphological characteristic and become rounded. We observed fewer non-apoptotic cells thus suggesting apoptosis as the undergoing mode of cell death. Doxorubicin

and photodynamic therapy have demonstrated the formation of reactive oxygen species hence results obtained in this study are indicative that apoptosis is the mode of cell death which is in consensus with previous studies mentioned particularly the combination of photogem mediated photodynamic therapy with cisplatin [6]. This study has demonstrated that photodynamic therapy may be enhanced by the addition of cytotoxic agents like doxorubicin at lower doses and still provides great efficacy in destroying cancer cell. In an attempt to increase the therapeutic effect of doxorubicin and possibly reduce its side effects and development of resistance, doxorubicin should be combined with photodynamic therapy. Obviously, further studies are needed to compare other cytotoxic agents in combination with photodynamic therapy for possible synergistic, additive or antagonistic effect. Moreover, studies to delineate the mode of action of doxorubicin and photodynamic therapy warrants further studies.

Funding

This research work is supported by the South African Research Chairs Initiative of the Department of Science and Technology and National Research Foundation of South Africa (Grant No 98337).

References

[1] Cancer facts and figures for Africans Americans, 2016-2018. Available at; www.cancer.org
[2] Ferlay J, Steliarova-Foucher E, Lortet-Tieulent J, Rosso S, Coebergh J W, Comber H, Forman D, and Bray F. 2013 *Eur J Cancer.* **49** 1374
[3] Verma S, Watt G M, Mai Z, and Hasan T. 2007 *J Photochem Photobiol.* **83** 1
[4] Tong Z, Miao P, Liu T, Jia Y, and Liu X. 2012 *Acta Pharmacol Sin.* **33** 1319
[5] Tynga I M, Houreld H H, Abrahamse H. 2013 *J Photochem Photobiol.* **120** 171
[6] De-Freitas L M, Serafim R B, De-Sousa J F, Moreira T F, Dos-Santos C T, Baviera A M, Valente V, Soares C P, and Fontana C R. 2017 *BMC Cancer.* **17** 123
[7] Mitry AM, Edwards GJ. 2016 Int J Cardiol Heart Vasc.10 17
[8] Postiglione I, Chiaviello A, and Palumbo G. 2011 *Cancers.* **3** 2597
[9] Paiva M B, Palumbo M, Greggio B, and Sercarz J A. 2011 *Current Cancer Treatment* **9** 176
[10] Ruiz-Gonzalez R, Milan P, Bresoli-Obach R, Stockert J C, Villanueva A, Canete M, and Nonell S. 2017 *Cancers* **9** 18
[11] Agostinis P, Berg K, Cengel k A, Foster T H, Girotti A W, Gollnick S O, Hahn S M, Hamblin M R, Juzeniene A, Kessel D, Korbelik M, Moan J, Mroz P, Nowis D, Piette J, Wilson B C, and Golab J. 2011 *CA Cancer J Clin.* **61** 4
[12] Mizutani H, Tada-Oikawa S, Hiraku Y, Kojima M, and Kawanishi S. 2005 *Life Sci.* **76** 1439 [13] Osman A, Bayoumi H, Al-Harthi S E, Damanhouri Z A, and Elshal M F. 2012 *Cancer Cell Int.* **12** 47
[14] Plaetzer K, Kiesslich T, Oberdanner C B, and Krammer B. 2005 *Curr Pharm Des.* **11** 1151

Photobiomodulation activates the JAK/STAT signalling pathway in diabetic wounded cells *in vitro*

S W Jere, H Abrahamse and N N Houreld

Laser Research Centre, Faculty of Health Sciences, University of Johannesburg, P.O. Box 17011, Doornfontein, 2028 South Africa.
Tel: +27 11 559 6833; Fax: +27 11 559-6884

Email: nhoureld@uj.ac.za

Abstract. The Janus Kinase/Signal Transducer and Activator of Transcription (JAK/STAT) pathway is involved in the transmission of external signals via receptors to the nucleus. Diabetic wounds develop due to various mechanisms, including decreased cell migration. Photobiomodulation (PBM) induces cellular migration and wound healing. However, the mechanism/s involved in the stimulation of migration are not completely understood. This investigation aimed to determine the effect of PBM on migration and the activation of the JAK/STAT signaling pathway in a diabetic wounded cell model. Diabetic wounded human skin fibroblast cells (WS1) were exposed to a diode laser at 660 nm with a fluence of 5 J/cm^2 and incubated for 48 h. Non-irradiated (0 J/cm^2) cells served as controls. Cellular migration was monitored microscopically and the activation (phosphorylation) of JAK2, STAT1 and STAT5 was analyzed by the enzyme linked immunosorbent assay (ELISA). PBM significantly increased p-JAK2, p-STAT1 and p-STAT5, and increased cellular migration. We suggest that PBM stimulates migration of diabetic wounded cells *in vitro* via the JAK/STAT signaling pathway, which enhances wound healing in hyperglycemic conditions.

1. Introduction

Diabetes is a metabolic disease characterized by increased blood glucose that affects several organs and systems of the body. The projected global prevalence of diabetes is 438 million, representing 7.8% of the global populous by 2030. Diabetes mellitus (DM) is involved in the impairment of acute wound healing, posing a threat to diabetic patients who are prone to developing chronic diabetic foot ulcers (DFU). It is estimated that 3% of the 15% of diabetic patients who develop lower limb ulcers end up with an amputation [1]. Literature elucidates that reduced growth factors/receptors due to an imbalance in proteinases and proteinase inhibitors, and the increased presence of senescent cells reduce or stop the healing process in diabetic wounds [2]. Immediately after injury, damaged tissue initiates a dynamic series of interactive and overlapping phases, involving hemostasis, inflammation, proliferation and remodeling. A complex cascade of pathways for cytokines and growth factors regulate the initiation of these processes. The wound repair process may be arrested or delayed in one of the phases, usually inflammation, that leads to chronic wound formation as inflammatory cells persistently deposit pro-inflammatory cytokines and proteases causing cell death and abnormal development of granulation tissue [3]. In wound healing, the JAK/STAT signaling pathway is critical in transducing signals for cytokines and growth factors, and are negatively regulated by phosphatases

and suppressor of cytokine signaling (SOCS) proteins [4]. While this process is true in acute wounds, it is disrupted in chronic wounds due to reduced cell potency, growth factors and growth factor receptors. Proteinases play a crucial role in remodeling of the extracellular matrix (ECM). However, their uncontrolled expression, as observed in chronic wounds, degrade proteins including growth factors and receptors [3].

The JAK/STAT pathway is one of the most critical pleiotropic signaling pathways used by cells to pass external cellular signals for cytokines and growth factors to the nucleus [5]. The binding of cytokines and growth factors to the JAK/STAT associated receptor triggers receptor dimerization, leading to the activation of JAK. This in turn phosphorylates the intracellular receptor tyrosine residues that become docking sites for the latent cytoplasmic transcription factor, STAT. The phosphorylated STATs detach from the receptor tyrosine residues to dimerize and translocate to the nucleus where they bind to specific sequences on the deoxyribonucleic acid (DNA) for signal translation [6]. Deregulation of this pathway may lead to pathological consequences including chronic inflammatory and cancer defects [2]. A variety of cytokines, chemokines, hormones and growth factors use the JAK/STAT pathway to initiate critical events including cell proliferation, migration, cytokine secretion and apoptosis [7]. Specific combinations of JAK/STAT are paired with each receptor resulting in the transduction of specific information culminating into a specific cellular response pattern [8]. The potential of the JAK inhibitor, AZD1480, for the treatment of small cell lung cancer (SCLC) resulted in the attenuated growth of SCLC cells *in vitro* and *in vivo*. AZD1480 was also seen to effectively prevent interleukin (IL)-6-induced JAK2 and STAT3 phosphorylation, exerting anti-tumor function effects by decreasing proliferation and increasing apoptosis of colorectal cancer (CRC) cells. The tumor genesis inhibition was found consistent with the reduced activated JAK2 and activated STAT3, including a reduced expression of the targeted genes c-Myc, cyclin D2 and IL-6 for STAT3 [9].

Photobiomodulation (PBM) is a therapeutic modality that involves the modulation of bio-systems by low-energy light to stimulate cellular biologic activities. It requires the exposure of compromised tissue to low energy light (typically in the form of laser light or light emitting diodes) to induce healing, and is used for various pathological conditions like wound repair and pain control among others. PBM induces wound healing by activating cell proliferation and migration, and strengthening the tensile of the wound matrix. The technique is believed to be effective if used at an appropriate and optimal wavelength, usually in the visible red and near infrared (NIR) region of the spectrum [10]. Cellular responses to PBM are induced by increased cellular chemical energy that is stimulated by the photon energy absorbed by cellular mitochondrial chromophores. Cellular metabolism is then initiated by activating or deactivating enzymes that alter other macromolecules such as DNA and ribonucleic acid (RNA) [11]. PBM at a fluence of 5 J/cm^2 and a wavelength within the visible red and NIR spectrum has positive effects on wound healing and normalizes cellular processes.

2. Methodology

WS1 human skin fibroblast cells purchased from the American Type Culture Collection (ATCC, CRL-1502) were grown using standard culture procedures. For experiments, 6 X 10^5 cells were seeded into 3.4 cm diameter tissue culture plates and incubated at 37°C in 5% CO_2 to allow for attachment. Two models were used in the study, namely diabetic and diabetic wounded. After 24 h, a central scratch was performed 30 min pre-irradiation in the wounded model by creating a cell free zone bordered by cells on both sides of the "wound" in the confluent monolayer [12]. An *in vitro* diabetic model was achieved by continuously growing WS1 cells in supplemented Minimum Essential Medium (MEM) containing an additional 17 mM/L D-glucose, thereby creating a hyperglycemic condition [13]. Cell culture plates with the lids off were exposed to laser light from above in the dark. A 660 nm diode laser at 5 J/cm^2 was used (table 1) and cells incubated for 48 h. Morphology and cell migration was

assessed by light microscopy. The Enzyme Linked Immunosorbent Assay (ELISA), at an absorbance of 450 nm, was used to detect phosphorylated (p-)JAK2, p-STAT1 and p-STAT5. Each experiment was repeated four times (n=4) and each assay done in duplicate, the average of which was used. Statistical analysis was done using SigmaPlot version 13 (Systat Software, Inc.). The Student *t* test was used to determine statistical significance between irradiated experimental groups and non-irradiated control groups. Statistical significance is shown in the graphs as *p<0.05, **p<0.01 and ***p<0.001.

Table 1. Laser parameters.

Light source	Diode laser
Energy density (J/cm^2)	5
Power density (mW/cm^2)	11
Wavelength (nm)	660
Emission	Continuous wave
Spot size (cm^2)	9.1
Power output (mW)	100
Irradiation time	7 min 6 sec

3. Results

In this study, PBM at a wavelength of 660 nm with a fluence of 5 J/cm^2 resulted in a significant increase in cellular migration (figure 1). Cells appeared spindle shaped with two or more polar projections. This is characteristic of fibroblast cells. Following irradiation, diabetic wounded cell models presented with a significant increase in cell migration towards the center of the scratch compared to non-irradiated diabetic wounded cell models. There was complete wound closure in irradiated cells at 48 h, while non-irradiated control cells displayed incomplete closure. These results are consistent with results reported from other studies that were conducted under similar conditions [14]. Irradiation at a wavelength of 660 nm with a fluence of 5 J/cm^2 resulted in the activation and phosphorylation of JAK2, STAT1 and STAT5 (figure 2). There was a significant increase in p-JAK2 in irradiated diabetic and diabetic wounded cells ($p<0.05$), as well as in p-STAT1 in both diabetic and diabetic wounded cells ($p<0.001$ and $p<0.05$, respectively), and p-STAT5 ($p<0.01$).

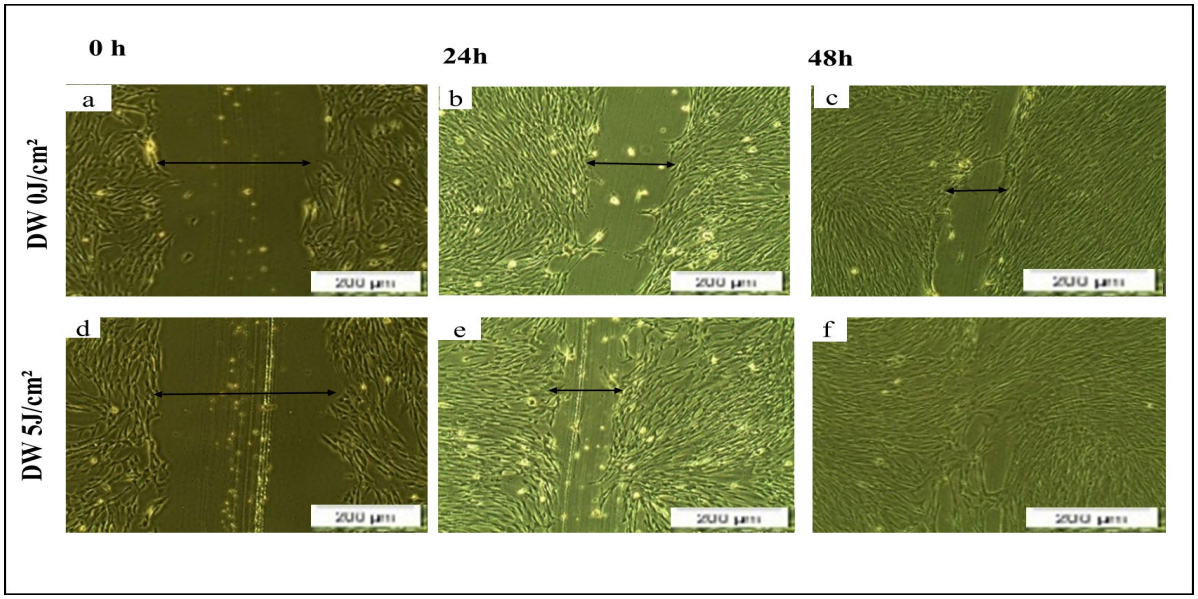

Figure 1. Cell migration was assessed by inverted light microscopy at 0 h, 24 h and 48 h in (a, b, c) diabetic wounded non-irradiated cells (DW 0 J/cm^2) and diabetic wounded (d, e, f) irradiated cells (DW 5 J/cm^2). Irradiation increased cellular migration rate.

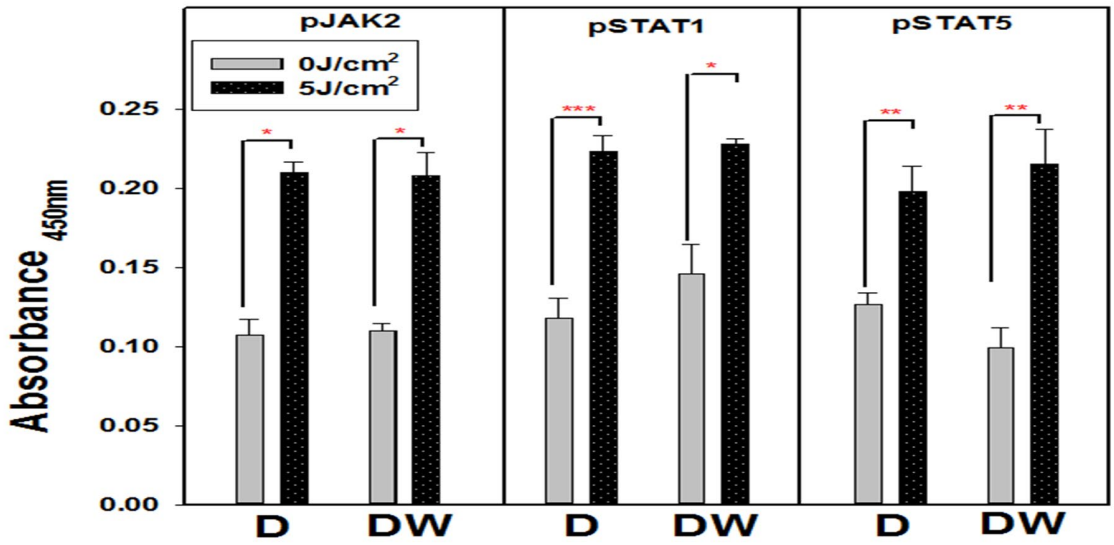

Figure 2. Phosphorylated (p)-JAK2, p-STAT1 and p-STAT5 as determined by ELISA. Irradiated (at 660 nm with 5 J/cm^2) diabetic (D) and diabetic wounded (DW) cells were compared to non-irradiated (0 J/cm^2) cells. Significant probability is shown as *P<0.05 **P<0.01 and ***P<0.001.

4. Discussion and Conclusion

JAK/STAT is one of the signaling pathways that is critical in wound healing [15]. It is involved in the transduction of extracellular cytokine and growth factor signals to the nucleus, resulting in cell migration. In chronic diabetic wounds, there is a reduced presence of growth factors and overall cellular function and migration [16]. Irradiation of diabetic wounded cells at a wavelength of 660 nm with a fluence of 5 J/cm^2 stimulates the JAK/STAT signaling pathway *in vitro* by phosphorylating JAK2, STAT1 and STAT5. Therefore, therapeutic agents that would target this signaling pathway, such as PBM, may reduce the healing time and resources for chronic diabetic wounds. However, further investigations on the molecular response of wounded diabetic cells following PBM may be required for a better understanding of the mechanisms and signaling pathways involved. In conclusion, the present study suggests that PBM at a wavelength of 660 nm with a fluence of 5 J/cm^2 has a therapeutic effect on diabetic wounded cells *in vitro* by increasing cell migration through the JAK/STAT signaling pathway.

Acknowledgements

This work is based on the research supported by the South African Research Chairs Initiative of the Department of Science and Technology and National Research Foundation (NRF) of South Africa (Grant No 98337), as well as grants received from the University of Johannesburg (URC), the African Laser Centre (ALC) (student scholarship), and Council for Scientific and Industrial Research (CSIR) -

National Laser Centre (NLC) Laser Rental Pool Program (grant number LREHA01). All lasers were supplied and set up the NLC.

References

[1] Wukich D K 2015 *World J. Orthop.* **6** 331-9
[2] Feng Y, Sanders A J, Ruge F, Morris C, Harding K G and Jiang W G 2016 *Int. J. Mol. Med*. **38** 1349-58
[3] Dhall S 2014 Retrieved from; http://escholarship.org/uc/item/8q0019n4 .
[4] Sasi W, Sharma A K and Mokbel K 2014 *Mol. Biol. Int.* doi: 10.1155/2014/630797
[5] Groner B and Vafaizadeh V 2014 *Mol. Cell Endocrinol.* **382** 552-9
[6] Villarino A V, Kanno Y, Ferdinand J R and O'Shea J J 2015 *J. Immunol.* **194** 21-7
[7] Zundra S and Neurath M F 2016 *Vaccines* doi:10.3390/vaccines4010005
[8] Murry P J 2007 *J. Immunol*. **178** 2623-9
[9] Lee J H, Park K S, Alberobello A T, Kallakury B, Weng M, Wang Y and Giaccone G 2013 *Clin. Cancer Res*. **19** 6777-86
[10] Ma H, Li Y, Chen H, Kang M and Liu T C 2012 *Int. J. Photoenergy***.** doi:10.1155/2012/838496
[11] Houreld N N 2014 *The Scientific World Journal*. doi: 10.1155/2014/398412
[12] Ayuk S M, Houreld N N and Abrahamse H 2012 *Diabetes Technol. Ther.* **14** 1110-7
[13] Houreld N N 2012 *9th WALT Congress* (QT Gold Coast, Surfers Paradise, Australia, September 28-30, 2012,)
[14] Houreld N N and Abrahamse H 2010 *Diabetes Technol. Ther*. **12** 971-8
[15] Belacortu Y and Paricio N 2011 *Dev. Dyn.*, **240** 2379- 404
[16] Mat Saad A Z, Khoo T L and Halim A S 2013 *ISRN Endocrinol.* doi: 10.1155/2013/608313

Characterization of the spectral irradiance lamps at NMISA

Macdufe Mkabela[1,2*], Pieter Du Toit[1], Rheinhardt Sieberhagen[1], Walter Meyer[2]

[1] National Metrology Institute of South Africa, Private bag X34, Lynnwood Ridge, 0040, South Africa
[2]University of Pretoria, Private Bag X20, Hatfield, 0028, South Africa

E-mail: *mmkabela@nmisa.org

Abstract: This work investigates some of the uncertainty contributions to the spectral irradiance calibration of UV-C lamps. The radiometry concepts and the instrumentation used are addressed first. In ultraviolet (UV) spectroradiometry, spectral irradiance measurements have large uncertainties mainly due to a low signal-to-noise ratio (SNR) in the UV region; however other factors may also contribute to these high uncertainties. Therefore quantifying the sources of uncertainties is important to improve the accuracy of the measured results. We characterized a low pressure mercury lamp when compared to a tungsten halogen lamp when used as standards for spectral irradiance at the National Metrology Institute of South Africa (NMISA), in terms of stability, translation, and orientation. We found that the calibrations of the UV-C low pressure mercury lamps are not suitable as standard lamps for calibration of UV-C due to uncertainties introduced by orientation, translation and, instability effects of this lamp.

1. Introduction

Metrology is concerned with the accurate measurement of physical quantities and requires the determination of uncertainty of measurement. Radiometry is the field concerned with the accurate measurement of radiant energy (Q) across the entire electromagnetic spectrum (EMS), and the determination of how this energy is transferred from a source, through a medium, and to a detector [1]. Traditionally, radiometry assumes that the propagation of light can be modelled using the laws of geometric optics, and in practice radiometric measurements are limited to the optical (ultraviolet (UV), visible (VIS), and infrared (IR)) region. The International Commission on Illumination (CIE) divides the UV region into four regions (VUV, UV-C (200 nm – 280 nm), UV-B, and UV-A) based on the biological effects on microorganisms [2]. In this study we focus on the measurement of UV-C radiation of the EMS. The UV-C radiation is important because of its germicidal effectiveness on microorganisms in air and other media.

The use of radiation in the germicidal region can help combat the spread of mycobacterium tuberculosis (TB) and other microorganisms in South Africa, mainly at hospital in waiting areas and treatment rooms. This technology is referred to as air UV germicidal irradiation (UVGI) [3]. Accurate measurement of the UV-C radiation emitted by UVGI lamps is very important for the safety of staff and patients, and South African citizens in general.

The radiometric quantities of interest are introduced here. Radiometric quantities are usually wavelength dependent; the spectral quantities are radiometric quantities taken as a function of wavelength. The flux Φ emitted by the source incident on a surface per unit area dA of that surface is called irradiance E.

$$E = \frac{d\Phi}{dA}. \quad (1)$$

The measurement of spectral irradiance (measured in W/m^2/nm) of a lamp is performed with a spectroradiometer. The basic spectroradiometer consists of a monochromator, combined with a detector on the exit slit and an integrating sphere (IS) on the entrance slit. The measured result has an uncertainty associated with it, calculated using the uncertainty budget (UB). In this paper, we highlight some of the contributors to the uncertainty budget (UB) including the stability, orientation, and translation of the lamp.

2. Measurement method.

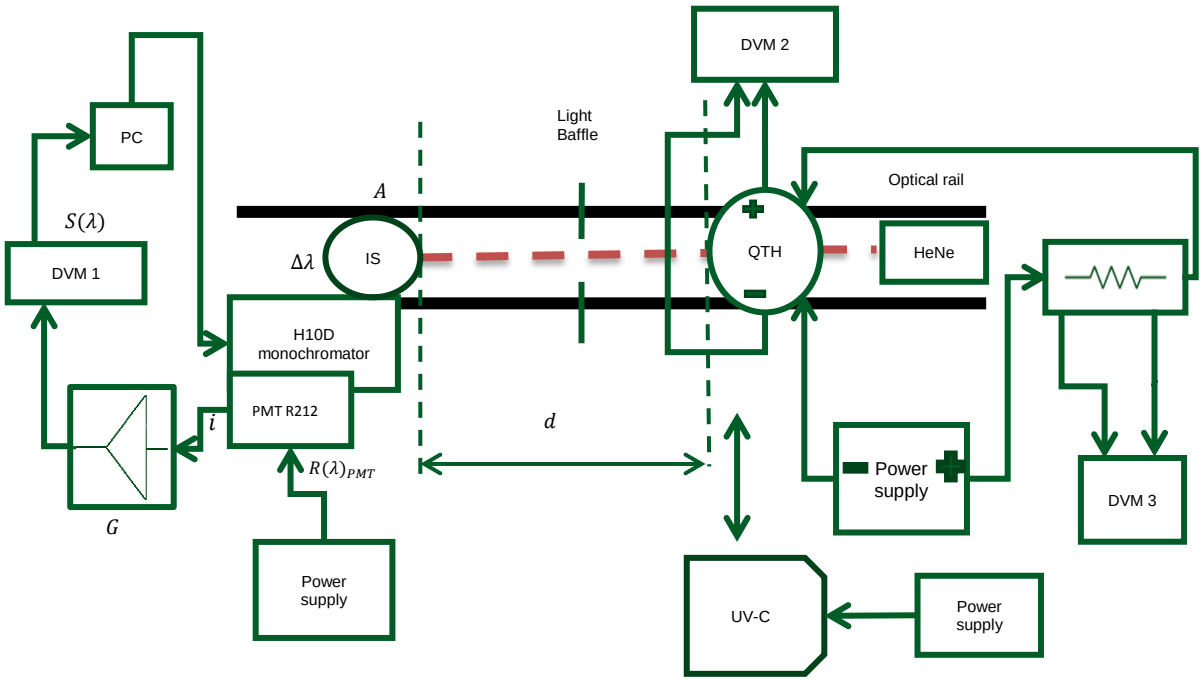

Figure 1: The measurement setup of the spectral irradiance lamp calibrations at NMISA. The setup makes use of a substitution method where one lamp is measured at a time.

The measurement setup in Figure 1 makes use of the substitution measurement method, which is a direct comparison with the value of a reference standard, having similar properties to the unit being measured (UUT) [4]. During an actual calibration, the spectral irradiance of a UUT (UV-C) is determined by a direct comparison with a calibrated spectral irradiance standard (QTH) lamp with known spectral irradiance using a spectroradiometer. During an actual calibration, the QTH standard lamp is measured at its respective position first and substituted with the UV-C lamp which is measured at a displacement position suitable for that calibration. The standard lamp is measured the second time to check repeatability. The measured voltage $S(\lambda)^{STD}$ is the measured spectral output voltage of the standard lamp and is modeled by

$$S(\lambda)^{STD} = E(\lambda)^{STD} R(\lambda) \Delta\lambda A. \quad (2)$$

Equation 2 can be explained as follows: $E(\lambda)^{STD}$ is the spectral irradiance emitted by a spectral irradiance standard lamp incident on the IS with an aperture area A, spectrally dispersed by a monochromator with a spectral bandwith $\Delta\lambda$ falling onto the photomultiplier tube (PMT) detector, and the spectroradiometer has spectral irradiance responsivity $R(\lambda)$ which is a combination of IS throughput $\rho(\lambda)$, diffraction efficiency of monochromator gratings $M(\lambda)$, PMT response $R(\lambda)_{PMT}$, and the gain G of the amplifier (which converts the current signal from the PMT into a voltage signal). Similarly the spectral output voltage of the UUT $S(\lambda)^{UUT}$ is modeled by:

$$S(\lambda)^{UUT} = E(\lambda)^{UUT} R(\lambda)\, \Delta\lambda\, A. \quad (3)$$

where $R(\lambda)$, $\Delta\lambda$, and A remain the same during calibration since $E(\lambda)^{STD}$, $S(\lambda)^{STD}$, and $S(\lambda)^{UUT}$ are known, the spectral irradiance $E(\lambda)^{UUT}$ of the UUT can be determined from equations 2 and 3 as:

$$E(\lambda)^{UUT} = \frac{S(\lambda)^{UUT}}{S(\lambda)^{STD}} E(\lambda)^{STD}. \quad (4)$$

Equation 4 is known as the measurement equation for spectral irradiance calibration.

The spectral irradiance of lamps is influenced by lamp stability, translation, and orientation. Each uncertainty contributor is evaluated using a model associated with it. The stability of lamps was monitored by two temperature controlled silicon (Si) photodiode at time *t*, and the following model was used:

$$E(\lambda) = \frac{\Phi(t)}{A} \quad (5).$$

$\Phi(t)$ is the flux incident on the area A of the Si photodiodes detector surfaces, and $E(\lambda)$ is the spectral irradiance emitted by the lamp. The uncertainties associated with translation of lamps were quantified using the inverse square law of point source model as:

$$E = \frac{I}{d^2}. \quad (6)$$

Where d is the distance from the lamp to the IS, I is the lamp intensity, and E is lamps irradiance. The inverse square law is valid only when the light source approximates a point source. A lamp approximates a point source if the distance to the lamp is at least five times greater than the largest dimension of the source [5]. The uncertainties in orientation of the lamps were quantified using $I = I_\theta cos\,\theta$ for a Lambertian distribution. θ is the angle between the optical axis and the direction of normal incidence for the spectroradiometer aperture. For a non Lambertian distribution, an alignment factor $(1-\gamma)$ is determined individually for each lamp, with γ determined from the small variations of the direction with respect to the burning position and the direction of emittance as the average of repeated alignments [6]

The spectral irradiance unit is derived from the high temperature blackbody (HTBB) radiator which employ's Plank's radiation law [7]. In the UV region, a 1000 W quartz tungsten halogen (QTH) and a 30 W deuterium lamps are generally used as standard lamps [8,9]. The QTH lamp is the most commonly used transfer standard for spectral irradiance in the wavelength region 250 nm to 2500 nm due to their good stability and ease of use [10]. The QTH lamp used here was calibrated at a specified distance (500 mm in our case) while operating at a current of approximately 8.000 A. The current was measured with a standard resistor and DVM 3 in Figure 1 using Ohm's law while the stability of the lamp was monitored by measuring the terminal voltage (normally 120 V) using DVM 2. The QTH lamp distance was realized with a rod cut and calibrated to this specific distance.

The UUT is a UV-C low pressure (LP) mercury (Hg) lamp. Between the lamps and the IS, baffles were used to minimize stray light. The IS in front of the monochromator is used to minimize the polarization of the light source by a complete depolarization of lamps and is coated internally with a reflective material ($BaSO_4$) that has a spatially uniform and uniformly diffuse reflectance [11], with the aim to combine radiant flux. The direct irradiation of the monochromator by lamps is avoided due to resultant variation in the irradiance distribution in the monochromator [2]. A double grating monochromator with a very low stray light level was used to disperse light, with a bandwidth of 4 nm. Before the start of measurements, the wavelength scale of the monochromator was confirmed to be within its calibrated uncertainty using known spectral lines from a mercury (Hg) pencil lamp.

The spectrally dispersed light was detected by the PMT detector with a spectral response from 185 nm – 650 nm, and a maximum response at 340 nm [12]. The PMT was powered by a high voltage of 700 V for all measurements in this paper. A helium neon (HeNe) laser is used to align the optical instruments (lamps, monochromator, and baffles) on the optical rail.

3. Results and discussions

The spectral output voltage stability of the QTH and the LP Hg lamps was measured with a spectroradiometer at 10 minutes interval after the lamps had been warmed-up. The low radiation output of the QTH lamp in the UV-C region, results in a low signal-to-noise ratio (SNR). As a result, the QTH lamp uncertainties were quantified in the visible region (441.5 nm and 450.5 nm) with the assumption that, the effect in orientation and translation on the output signal was the same at UV-C wavelengths. The LP Hg lamp however had a high output resulting in a significant signal around 251 nm to 255 nm as expected because of the Hg peak at 253.66 nm, and the uncertainties were quantified at 255 nm. The output stability of the two lamps was also monitored by two temperature stabilized UV-enhanced Si photodiodes at 10 minute intervals, for an independent indication of lamp stability and the results are tabulated in Table 1.

Table 1: The input electrical voltage (U) of the QTH lamp and the spectral output voltage (S) stability of both lamps.

Time [min]	t_1 (0 min)	t_2 (10 min)	t_3(20 min)	σ	U_{xi} [%]
QTH voltage (U) [V]	113.29	113.27	113.24	2.56E-02	0.02
QTH lamp current (J) [A]	8.00017	8.00022	8.00028	5.15E-05	0.001
Si -QTH (Φ) [A]	1.5174	1.5173	1.5171	8.99E-03	0.01
Si-LP Hg (Φ) [A]	0.0142	0.01419	0.01409	5.37E-01	0.5

The symbols used in Table 1 are defined as follows: t is the time in minutes at which measurements were taken, σ is the standard deviation of the measurements in Table 1, and U_{xi} is the relative uncertainties in percentage calculated by dividing the σ with the average of t_1, t_2 and t_3. U is the QTH lamp voltage measured in volts directly at DVM 2 in Figure 1 simultaneously with the QTH lamp current J measured in amperes as calculated from the voltage across DVM 3 and the standard resistor. Si-(Φ) is the output signal of the lamps monitored with the Si photodiodes detectors.

The input electrical voltage stability of the QTH lamp was measured using a four wire technique directly from DVM 2 (Figure 1) at 10 minute intervals simultaneously with the lamp time stability (measured with the spectroradiometer) and the lamp output monitored with the Si photodiodes. The time stability of the QTH standard lamp had a calculated relative uncertainty of 0.5 % compared to 3 % of the LP Hg UV-C lamp. The measured input electrical voltage of the QTH standard lamp on average was 113.27 V compared to the calibration certificate value of 113.11±0.03 V. The +0.13 V observed drift from the certificate value was speculated to be due to temperature effects of the DVM 2. The monitored lamps output of the QTH standard and LP Hg UV-C lamps with the Si photodiodes on average showed that the QTH standard lamp was more stable with a relative uncertainty of 0.01 % compared to 0.5 % of the LP Hg UV-C lamp. The Si photodiodes detectors results agreed with the time stability results, where the QTH standard lamp was in both cases more stable than the LP Hg UV-C lamp as expected.

A point source approximation was tested for both lamps (Figures 2 and 3). As expected, in both wavelengths (441.5 nm and 450.5 nm), the QTH lamp closely approximated a point source except for positions closer than 500 mm (400 mm and 300 mm). Because of the large dimensions of the LP Hg lamp it deviated from the point source approximation. We used the inverse square law of point sources Equation 6 as our model to calculate the theoretical values in Figures 2 and 3. The effect of orientation (or rotation around vertical axis) was measured at the calibrated positions of the lamps. The QTH lamp is close to symmetric; therefore, theoretically, the orientation of the QTH lamp should not have significant effect on the output signal. The difference in spectral output voltage (expressed as a percentage) produced by the lamps when displaced by 1 mm from their calibrated positions is shown in Table 2.

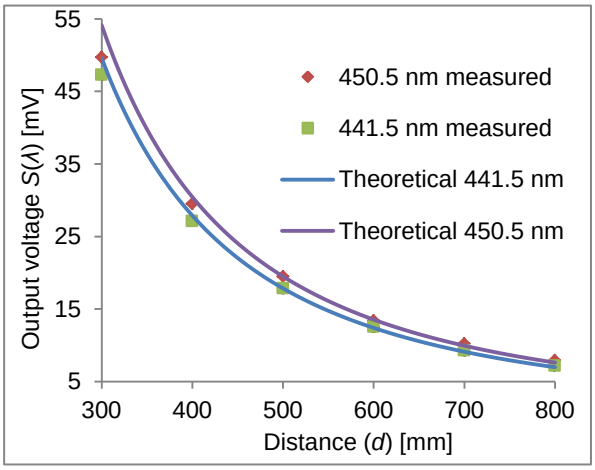

Figure 2: The point source approximation of the QTH lamp at 441.5 nm and 450.5 nm.

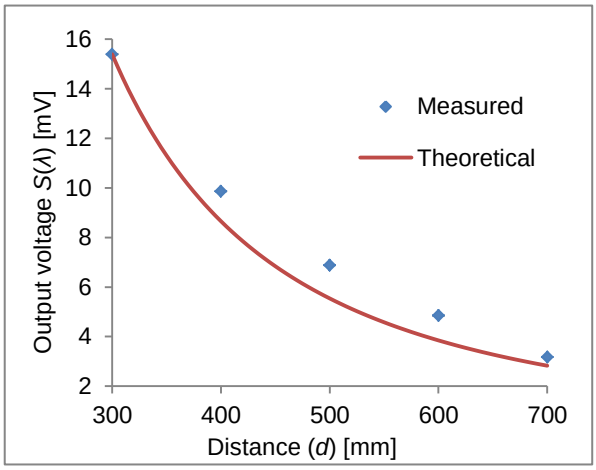

Figure 3: The point source approximation of the LP Hg lamp at 255 nm.

The 1 mm distance was chosen because with the setup at NMISA we are confident that we cannot make an error of more than 1 mm when positioning our lamps. Hence, only the effect in spectral output voltage generated by 1 mm (the worst case for each lamp) will be included in the UB. -1 mm, was when the lamps were moved closer to the spectroradiometer and +1 mm was further away from the spectroradiometer. The lamps were very sensitive to translation. For +1 mm displacement, the QTH lamp showed 0.1 % effect which was higher than 0.01 % for the LP Hg lamp

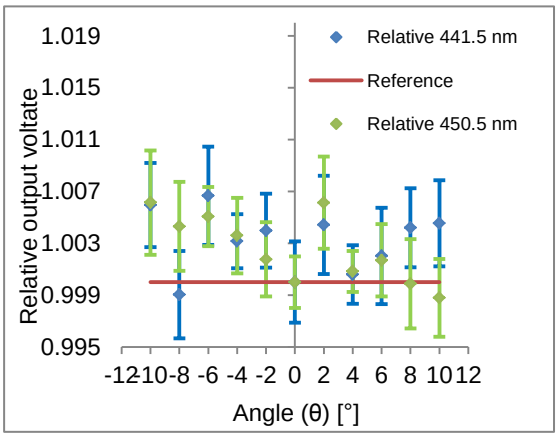

Figure 4: The orientation effect of the QTH lamp at 441.5 nm and 450.5 nm.

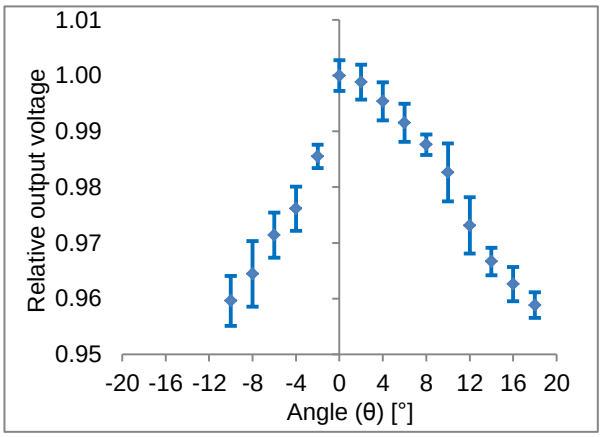

Figure 5: The angular dependence of the LP Hg lamp at 255 nm.

The LP Hg UV-C lamp had two lamp tubes mounted parallel to each other emitting light equally in all directions, but they are mounted in front of a reflector that reflects light towards the front of the lamp. Because of this, the LP Hg UV-C lamp was expected to have higher angular dependence than the QTH standard lamp. The effect of orientation of both lamps is shown graphically in Figures 4 and 5 and the calculated relative uncertainties are summarised in Table 3. As expected the QTH standard lamp had a smaller angular dependence compared to the LP Hg UV-C lamp. Furthermore, the LP Hg UV-C lamp showed an asymmetric distribution, probably due to misaligned lamp tubes or lower output from one of the lamp tubes. With the spectroradiometry setup at NMISA, we are confident that

the lamps orientation cannot be misaligned by more than 2 °, hence, only the relative uncertainties in the spectral output voltage caused by a 2 ° misalignment were included in the UB for both lamps.

Table 2: The translation effect of the QTH and LP Hg lamps.

Distance [mm]	QTH lamp 450.5 nm	LP Hg lamp 255 nm
+1	-0.07 %	-0.01 %
-1	0.9 %	0.8 %

Table 3: The orientation effect of the QTH and LP Hg lamps.

Position [°]	QTH lamp 450.5 nm	LP Hg lamp 255 nm
+2	0.4 %	-1.5 %
-2	0.6 %	-0.8 %

4. Conclusions and future work

The spectral irradiance measurement setup was characterized for translation, orientation and stability. The QTH lamp was more stable compared to the LP Hg UV-C lamp when monitored with Si photodiodes detectors. Also, the QTH lamp showed a long term drift from the lamp voltage with the lamp current very stable at 8.0002 A ± 0.0006 A. The effect of translation had a calculated relative uncertainty of 0.8 % for a 1 mm displacement from the calibrated positions for both lamps. For a 2 degrees misalignment from the optical axis, the QTH measured output signal changed by maximally 0.6 % while the LP Hg lamp changed by 1.5 %, which indicated an expected high angular dependence.

For future work, the deuterium lamp will also be characterized for translation, orientation, and stability. Due to its high spectral irradiance, the deuterium lamp is an ideal lamp to use as standard in the UV-C region. It will be investigated for use as a working standard or a primary standard. We will also test the systems temperature dependence with respect to the laboratory ambient conditions during measurements.

5. References

[1] Zalewski E F 1995 *Radiometry and Photometry Handbook of Optics* Vol **2** (Dunbury: Hughes Dunbury Optical Systems) pp 24-73

[2] CIE 1989 *International Lighting Vocabulary* (Vienna: Central Bureau of the Commission Internationale de l'Eclairage)

[3] Kowalski W 2010 *UVGI handbook: UVGI for air and surface disinfection* (New York: Springer Science & Business Media) pp 1-12

[4] Sauter G and Goodman T 2011 *Determination of measurement uncertainties in Photometry* SP1 1 (Vienna: Commission Internationale De L'Eclairage CIE Central Bureau) p 4

[5] Ryer A 1997 *The light measurement handbook* (Peabody: International Light Technologies) pp 26-7

[6] Schanda J (Ed) 2007 *Colorimetry:Understanding the CIE system* (New Jersey: John Wiley & Sons) pp 376-83

[7] Planck M 1901 On the law of distribution of energy in the normal spectrum *Annals of Physics* **4** p 553

[8] Woolliams E R, Fox N P, Cox M G, Harris P M and Harrison N J 2006 Final report on CCPR K1-a spectral irradiance from 250 nm to 2500 nm *Metrologia* **43** 1A 02003

[9] Sperfeld P 2008 Spectral irradiance 200 nm to 350 nm *Report of the CIPM key comparison CCPR-K1.b*

[10] Sanders C L and Rotter R 1984 *The Spectroradiometric Measurement of Light Sources* (Paris: Bureau central de la CIE) p 47

[11] Kostkowski H J 1997 *Reliable Spectroradiometry* (La Plata: Spectroradiometry Consulting) pp 247-9

[12] Photomultiplier Tube R212 TPMS1041E01 June 1998 Hamamatsu Photonics K K downloaded 11 March 2016 http://pdf.datasheetcatalog.com/datasheet/hamamatsu/R212.pdf

Analysis and Performance of a closed loop external cavity diode laser control system

Victory Opeolu[1], Kessie Govender[2], Adrian Wyngaard[2], Ouassini Nemraoui[3], Gerhard De Jager[4], and Jordan Scarrott[2]

[1,2,3]Department of Electrical, Electronic, Computer and Mechatronics Engineering, Cape Peninsula University of Technology, Symphony Way, Bellville, Cape Town, 7535, South Africa
[4]Department of Electrical Engineering, University of Cape Town, Rondebosch, 7701, South Africa

E-mail: [1]opeolu.victory@gmail.com

Abstract. External cavity diode lasers (ECDL) are commonly used in laser cooling experiments involving rubidium atoms. The laser frequency is finely tuned by adjusting the cavity length and the diode current. This is done by locking the ECDL to an appropriate rubidium transition using a saturation absorption Spectroscopy (SAS) setup together with a proportional-integral-derivative (PID) controller. In this paper, we give an overview of the analysis and performance of the closed loop control system using theoretical and numerical modelling as well as approaches used to create a system model.

1. Introduction

Semiconductor diode lasers, first demonstrated in laboratories more than forty years ago, have become a crucial part of modern technology. They are widely used for telecommunication, precise measurements, medicine, laser absorption spectroscopy and so much more. Automatic control has also come a long way since James Watt's centrifugal governor for the speed control of a steam engine. It has become crucial in science and engineering systems such as missile guidance, aircraft-piloting systems, etc. Automatic control provides a means for attaining optimal performance of dynamic systems [1].

Laser diodes are primarily developed for applications in wavelength division multiplexing (WDM) technology, coherent communication systems and sensing in precise measurements [2]. They are also used in atomic spectroscopy but more recently, they are used in laser cooling of atoms. This involves the cooling of atomic and molecular samples to near absolute zero using one or more laser fields. Doppler cooling is the most common method and is used to cool low density gases (e.g. rubidium) down to the microkelvin range. Lasers needed for cooling need to be precisely controlled to successfully get precise and accurate results. This is achieved by locking the laser frequency to specific atomic transitions of the chosen gas [3].

Although laser diodes have been used in laser cooling experiments, however, very little has been done with regards to analysis of closed loop feedback systems using external cavity laser diodes. There has been some analysis done but there were analytical in nature and focused only on the laser diodes [4, 5], not on the control system. [4] does provide some analysis of laser control using saturated absorption spectroscopy but they are modelled based on laser rate

equations. This paper discusses the performance of a closed-loop control system for locking an external cavity diode laser.

2. System Components

Figure 1 shows a general overview of the system to be modelled. It consists of a PID controller, an external cavity diode laser and a feedback setup in the form of a saturated absorption spectroscopy experiment. The solid lines represent voltages and the dashed lines represents the laser beam.

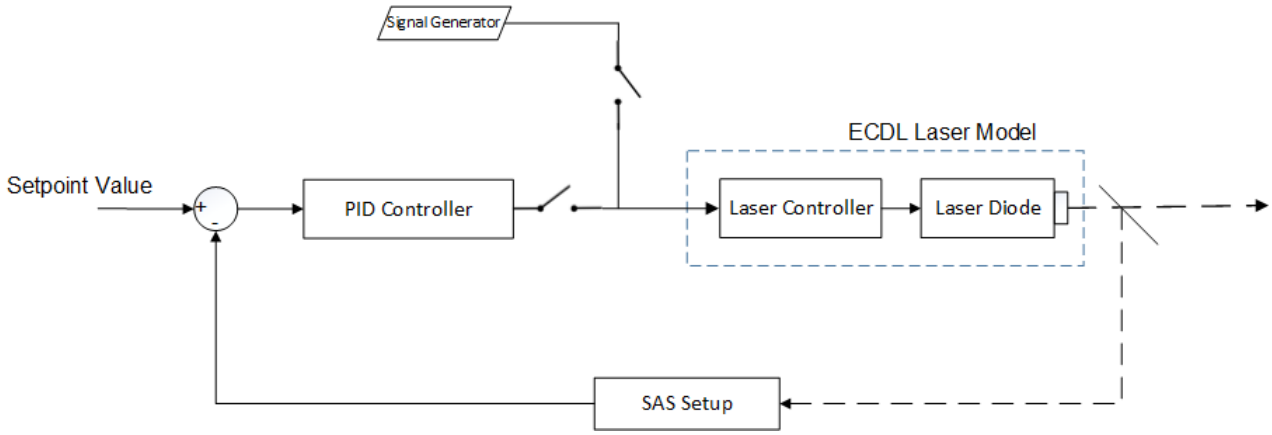

Figure 1. Overall block diagram of the laser control system

2.1. External Cavity Diode Laser (ECDL)

The ECDL primarily consists of a semiconductor diode laser cavity with reflective coatings on one facet, the other facet being the side at which the light emerges, a collimator for coupling the output of the diode laser and an external mode-selection filter [2]. The diode is placed in an external cavity, the length of which is controlled using a piezoelectric device. The resonant frequency of the cavity is given by $F = cn/L$, where c is the speed of light, n is an integer and L is the cavity length.

2.2. Saturated Absorption Spectroscopy (SAS)

The feedback consists of a saturated absorption setup which acts as the sensing element of the system. This setup produces an output signal that is proportional to the laser frequency, depending on where this frequency is compared to a particular hyperfine response. This response function is a Lorentzian curve. The saturated absorption spectroscopy setup is used to counteract the thermal motion of the atoms, thus producing a true Lorentzian output. More details on saturated absorption spectroscopy can be found in [3, 6].

When the laser frequency is scanned across the atomic transition range, we obtain a response similar to that shown in Figure 2 and each of these peaks has a Lorentzian shape such as that shown in Figure 3. In doppler cooling, the aim is to lock onto one of the hyperfine peaks.

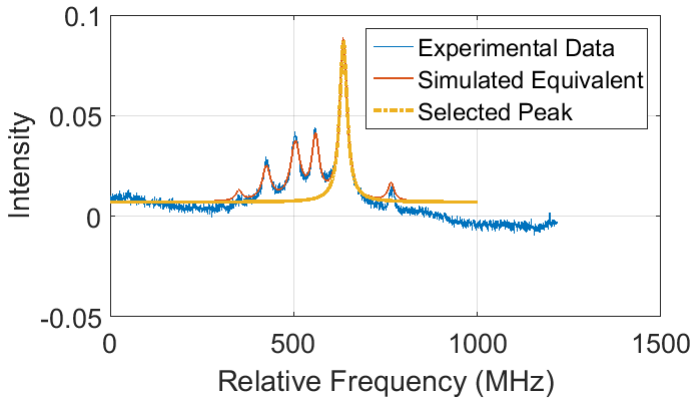

Figure 2. Hyperfine Structure of ^{85}Rb, $F = 3$ to $F' = 1, 2, 3$ [7]

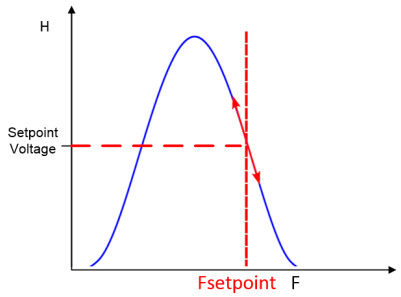

Figure 3. Typical Lorentzian curve

For our simulations, we use a series of Lorentzian curves to represent the feedback characteristic of the closed loop system. We try to lock onto one side of the curve as shown in Figure 3.

2.3. PID Controller

PID control is the most commonly used control algorithm. The coefficients: proportional, integral, and derivative are varied to get the optimal response from a system [1]. The difference between the setpoint value and the output of the saturated absorption spectroscopy setup (the difference/error signal) is determined. The error signal is amplified, integrated (and sometimes differentiated) before being fed back to the piezoelectric device.

3. Simulation Analysis

Figure 4 shows the control model of the system.

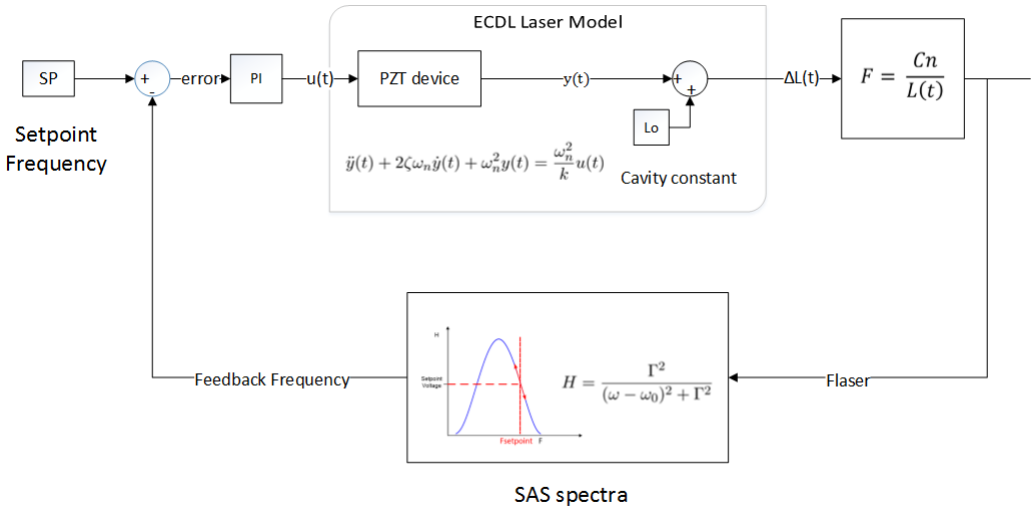

Figure 4. ECDL Frequency Control Model

The external cavity diode laser has a piezoelectric device that behaves as a Mass-Spring-Damper system. When a force (input voltage) $u(t)$ is applied to the piezoelectric crystal, its atoms are slightly displaced from their initial positions, thus creating a change in cavity length [8]. The relationship between the displacement Δy and the input force $u(t)$ can be represented by the differential equation:

$$\ddot{y}(t) + 2\zeta\omega_n\dot{y}(t) + \omega_n^2 y(t) = \frac{\omega_n^2}{k}u(t) \tag{1}$$

where ω_n is the resonant frequency, k is the stiffness of the crystal, ζ is the damping ratio and u is the input voltage.

We rewrite the above as:

$$\ddot{y}(t) + A\dot{y}(t) + By(t) = Cu(t) \tag{2}$$

where $A = 2\zeta\omega_n$, B $= \omega_n^2$ and C $=\omega_n^2/k$.

We calculate the displacement y using two difference equations:

$$\dot{y_1} = y_2; \tag{3}$$

$$\dot{y_2} = Cu(t) - Ay_2 - By_1; \tag{4}$$

where $y_1 = y$ in (2).

To solve this system, we use the Euler method as follows:

$$y_1(n) = \Delta t * y_2(n-1) + y_1(n-1) \tag{5}$$

$$y_2(n) = \Delta t * (Cu(n-1) - Ay_2(n-1) - By_1(n-1)) + y_2(n-1) \tag{6}$$

The rate of change of displacement $\Delta y_1(t)$ in the device influences changes in the cavity length of the laser, ΔL, which in turn controls the laser frequency.

We model the saturated absorption spectroscopy curve using a series of Lorentzian curves with each curve described by:

$$H = \frac{\Gamma^2}{(\omega - \omega_0)^2 + \Gamma^2} \tag{7}$$

where Γ is the width of the absorption curve shape, ω_0 is the resonant atomic transition frequency and ω is the laser frequency. ω is this case is the F_laser as shown in Figure 4

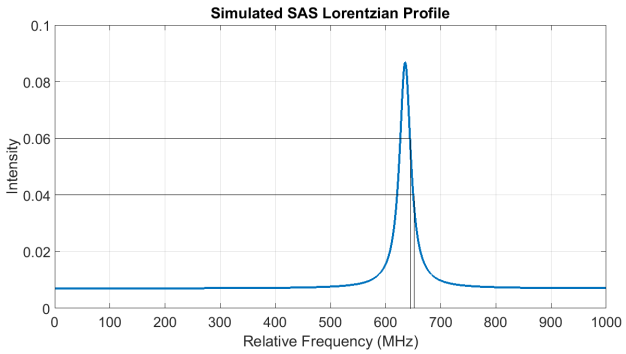

Figure 5. Simulated Lorentzian curve

We define the Lorentzian with results obtained from a saturated absorption spectroscopy (SAS) experiment. The Lorentzian curve, as shown in Figure 5 represents one of the hyperfine peaks shown in Figure 2. We choose a setpoint on the curve that corresponds to a certain laser frequency (on the right side of the curve). We simulated our system choosing two setpoint values 0.04 and 0.06, which corresponds to 645.9 MHz and 641.5 MHz respectively as seen in Figure 5. The feedback signal is subtracted from the setpoint value to get the steady state error. The PID block amplifies the error signal, integrates and implements differentiation, and its output (a summation of all three coefficients) is fed back to the piezoelectric device as a voltage input, making it a closed loop system.

4. Results and Analysis

Assuming the laser's initial undisturbed frequency is 648 MHz, we simulate the system to check its response to a step input from 643.5 to 645.9 MHz and 641.5 MHz respectively. The results are shown in Figure 6.

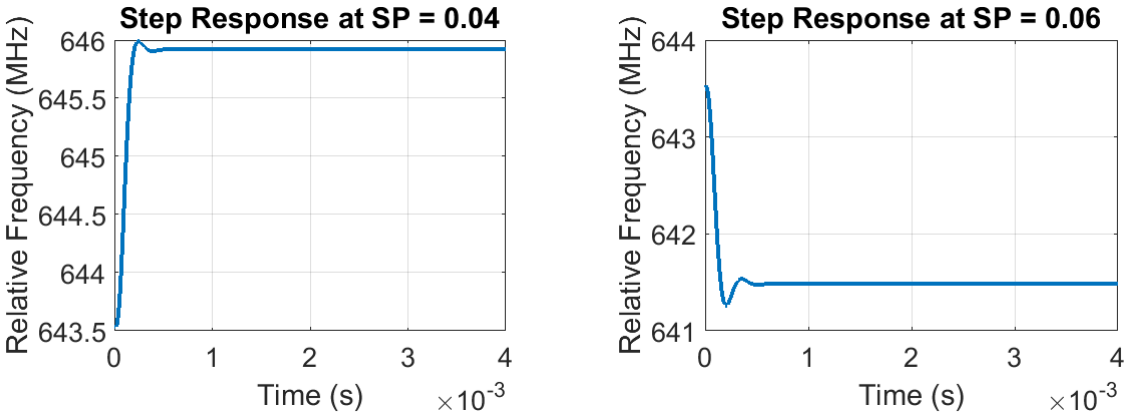

Figure 6. Step response of system

In a spectroscopy experiment various factors may affect the stability of the laser frequency such as the laser current, temperatures of the laser and its mount, air pressure, vibration and so on. We simulate these external factors in the form of disturbances in Figures 7 and 8. We first added a disturbance in the form of an impulse at a certain point in time for each setpoint frequency and the results can be seen in Figure 7.

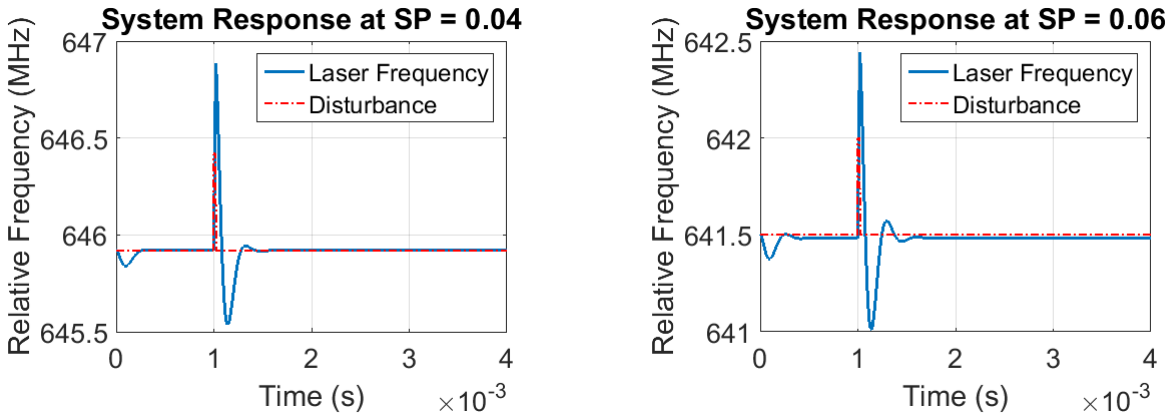

Figure 7. System response to impulse disturbance

The impulse disturbance implies the system had a random external influence at a certain point in time e.g. someone touched the laser head while the experiment was running. After adding a impulse disturbance, we notice the model behaves as an underdamped system. It first overshoots then settles down back to the specified setpoint (645.9 MHz and 641.5 MHz).

We also simulate external factors that may influence the laser frequency over a long period of time (e.g. a sudden rise in temperature of the laser mount) by adding a pulse disturbance over a chosen sample range (1000 $\backsim$ 2500 samples). Our results in Figure 8 show the laser frequency is still controlled to the setpoint values despite the disturbance occurring over a long period of samples.

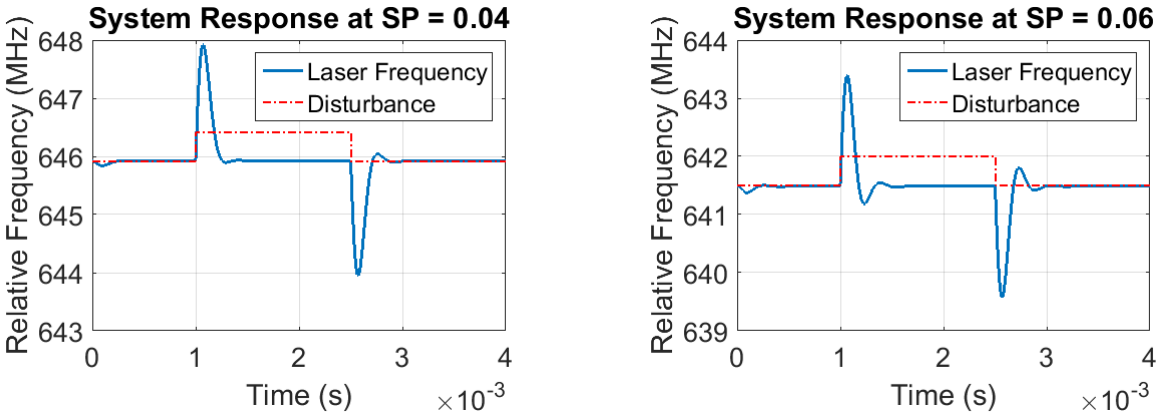

Figure 8. Plots with a pulse disturbance at a specific time sample range

5. Discussion and Conclusions

Numerical analysis of the closed loop system was implemented in Matlab using model parameters closely resembling those of the experiment. However for numerical reasons, the laser frequency was chosen to be a lot lower.

The Simulation showed that the system is slightly underdamped, with oscillation in the output dying within one or two oscillations. The system is capable of responding to slip changes i.e. the output follows the input as the setpoint is varied. In the case of sudden disturbances, the system is able to return to the initial state it was before the disturbance is applied.

More accurate representation of actual experimental parameter will be needed in the model for comparing experimental data.

References

[1] Ogata K 1970 *Modern Control Engineering* (New Jersey: Prentice-Hall, Inc.)
[2] Cunyun Y 2004 *Tunable External Cavity Diode Lasers* (Texas: World Scientific Publishing Co.) p 4
[3] Weel M and Kumarakrishnan A 2002 *Can. J. Phys.* **80** 1449–1458
[4] Genov G, Lellinger T E, Halfmann T and Peters T 2017 *J. Opt. Soc. Am. B* **34** 2018–2030
[5] Debs J E, Robins N P, Lance A, Kruger M B and Close J D 2008 *Appl. Opt.* **47** 5163–5166
[6] Preston D W 1996 *Amer. J. of Phys* **64** 1432–1436
[7] Wyngaard A 2017 Experimental study of the weak field zeeman spectra of ^{85}Rb and ^{87}Rb (*Preprint* `SAIP Conference proceedings`)
[8] Bentley J P 1995 *Principles of Measurement Systems* (New York: Longman Scientific & technical) p 163

Experimental study of the weak field Zeeman spectra of ^{85}Rb and ^{87}Rb

A Wyngaard[1], G De Jager[2], C Steenkamp[3] and K Govender[4]

[1,4] Department of Electrical, Electronic and Computer Engineering, Cape Peninsula University of Technology, Bellville, Cape Town, 7535, South Africa

[2] Department of Electrical Engineering, University of Cape Town, Cape Town, 7701, South Africa

[3] Department of Physics, University of Stellenbosch, Stellenbosch, 7599, South Africa

E-mail: [1] 210176296@mycput.ac.za

Abstract. We report on the measurement and analysis of the magnetic sub-levels of rubidium 85 and 87 that are observed in the presence of a weak magnetic field. Included is the standard hyperfine interaction. The experiment was performed using a saturated absorption spectroscopy setup with a set of Helmholtz coils placed around the rubidium vapour cell in order to generate a magnetic field. An external cavity diode laser was frequency modulated and the output split into three beams, two weak probe beams and a strong pump beam which counter-propagates and overlaps one of the probe beams. These beams were sent through a rubidium vapour cell where a magnetic field was applied. The time axis of each oscilloscope capture was converted to frequency using a calibration factor determined through previously measured values for hyperfine peak separations. The converted spectra were fitted with Lorentzian curves to estimate energy level separations, and the experimental and theoretical magnetic sub-level separation was plotted as a function of the magnetic field.

1. Introduction

It has been shown that there are multiple approaches to analysing the Zeeman shift in the magnetic hyperfine structure of rubidium (Rb) [1, 2]. A possible application of the Zeeman effect has been demonstrated in the investigation of low-field magnetometry [3]. These studies typically depend on comparing experimental results with predictions that are based on the average effects of interactions between electrons, and between electrons and the nucleus; thus, results may vary for multi-electron atoms.

Our study looked at the energy level separation for two magnetic energy levels of ^{85}Rb and ^{87}Rb in the presence of a weak magnetic field. The study was limited to using linearly polarised light, where the transitions between magnetic levels are those for which $\Delta m_F = 0$.

This study forms part of a larger experiment involving the cooling and trapping of Rb atoms using a magneto-optical trap. Since such an experiment requires knowledge of the energy structure of Rb and how the structure is affected by magnetic fields, investigating the Zeeman effect served as an ideal method for gaining such knowledge.

2. Theory

In the presence of an external magnetic field, the degeneracy associated with levels specified by the m quantum number is removed. These magnetic levels have energies that are a function of the magnetic field. At the hyperfine stage each level denoted by the quantum number F is split into $2F+1$ magnetic levels denoted by m_F. This magnetic hyperfine structure is shown in Figures 1 and 2. Also shown in these figures are the transitions between $F = 3$ and $F' = 4$, and $F = 2$ and $F' = 3$; for which $\Delta m_F = 0$, which is the special case we consider in this paper.

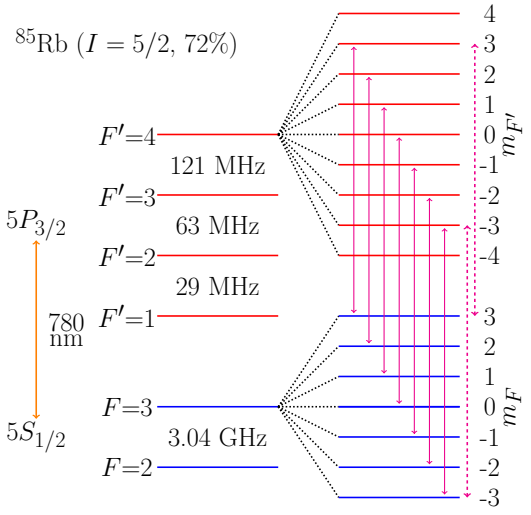

Figure 1. ^{85}Rb $F = 3$ to $F' = 4$ magnetic hyperfine structure. Ground states are denoted by F, excited states are denoted by F', and magnetic states are prefixed with m. Only the transitions for linearly polarised light are shown (solid arrows). The dashed arrows are explained in Section 4.2.

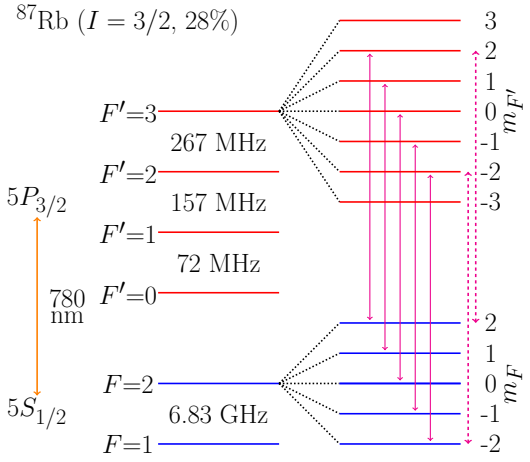

Figure 2. ^{87}Rb $F = 2$ to $F' = 3$ magnetic hyperfine structure. Ground states are denoted by F, excited states are denoted by F', and magnetic states are prefixed with m. Only the transitions for linearly polarised light are shown (solid arrows). The dashed arrows are explained in Section 4.2.

In the weak field regime, where the internal magnetic field is dominant, the orbital and spin angular momenta remain coupled and the Hamiltonian is given by

$$H = \underbrace{\left[H_0' + \zeta(r)\vec{L}\cdot\vec{S}\right]}_{H_0} + \underbrace{A\vec{I}\cdot\vec{J} + \frac{\mu_B}{\hbar}\left(g_J\vec{J} + g_I\vec{I}\right)\cdot\vec{B}}_{H'} \tag{1}$$

where H_0 is the basic atomic Hamiltonian including the spin-orbit coupling (fine structure), H' represents the interaction between the nucleus and electron (hyperfine structure), and the magnetic dipole moments of the atom interacting with an external magnetic field $\vec{B}$, A is a constant, μ_B is the Bohr magneton, and g_J and g_I are the g-factors [4, 5].

Taking a closer look at H' in Equation (1),

$$H' = A\vec{I}\cdot\vec{J} + g_J\frac{\mu_B}{\hbar}\vec{J}\cdot\vec{B} + g_I\frac{\mu_B}{\hbar}\vec{I}\cdot\vec{B}\ , \tag{2}$$

we see the hyperfine structure energy $A\vec{I}\cdot\vec{J}$ which is due to the interaction of the nuclear spin with the magnetic field created by the orbiting electron, and two more terms which are a

function of the external magnetic field. These two terms are the energy contributions from the magnetic levels due to the interaction of the net orbital and spin dipole moment of the electron with an external magnetic field, and the interaction of the nuclear spin dipole moment with an external magnetic field. The quadrupole interaction term has been neglected in our analysis of the magnetic hyperfine energy levels.

3. Experimental Setup

A saturated absorption setup was used to measure the hyperfine energy levels. The setup is shown in Figure 3. It consists of a Rb vapour cell which is illuminated by a strong pump beam that is linearly polarised by the half-wave plate (HWP) and polarising beam splitter (PBS) combination. The pump beam is then reflected by a mirror, attenuated by a neutral density (ND) filter, and the polarisation is rotated 90 degrees by a quarter-wave plate (QWP) before passing back through the Rb cell. This beam now acts as a probe beam which is monitored by a photodetector. We linearly scan the frequency of the laser to cover the range needed and we use a Michelson interferometer to determine the separation between hyperfine levels. This separation is then used to calibrate measurements of the magnetic hyperfine levels.

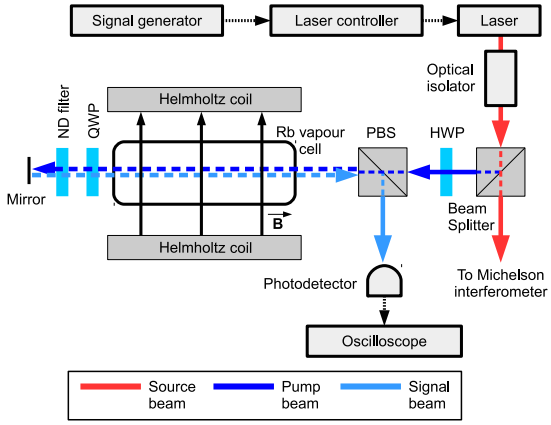

Figure 3. Saturated absorption spectroscopy setup with a set of Helmholtz coils that are used to generate a uniform magnetic field across the Rb vapour cell.

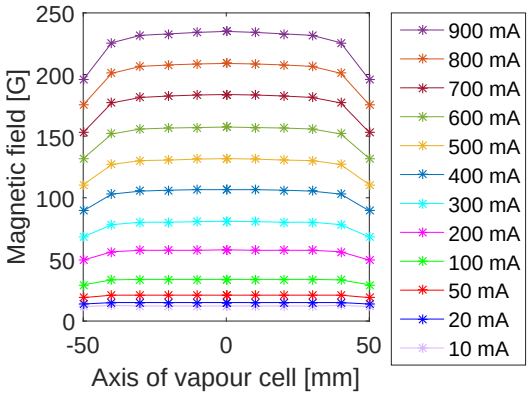

Figure 4. Various magnetic field strengths measured at several positions between the Helmholtz coils. The Rb cell is in the -40 to 40 mm region.

To examine the Zeeman effect we added a set of Helmholtz coils such that the magnetic field is perpendicular to the laser beams. The magnetic field across the Rb cell was measured for various current settings, as shown in Figure 4. In the region of the Rb cell (-40 to 40 mm), the field is approximately constant.

4. Results

4.1. Computational Analysis

Using the uncoupled basis $|J\, m_J\, I\, m_I\rangle$ to diagonalise the Hamiltonian matrix H' described in Section 2, we obtained the energy levels of the hyperfine magnetic sub-levels at various values of $\vec{B}$. Figures 5 and 6 show plots of the $5S_{1/2}$ and $5P_{3/2}$ energy levels of ^{87}Rb for several values of $\vec{B}$, a similar analysis has been done for ^{85}Rb but is not shown. The predictions agree with those given by others [3, 4, 5].

This computational analysis of the energy shift between magnetic levels was then compared to our experimental analysis of Zeeman spectra acquired from a saturated absorption setup.

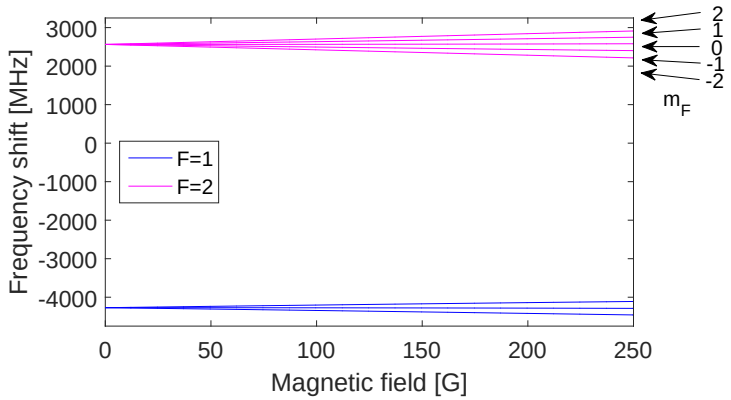

Figure 5. ^{87}Rb $5S_{1/2}$ magnetic hyperfine structure for several values of $\vec{B}$. The arrows indicate the magnetic energy levels, denoted by m_F, for the $F = 2$ ground state.

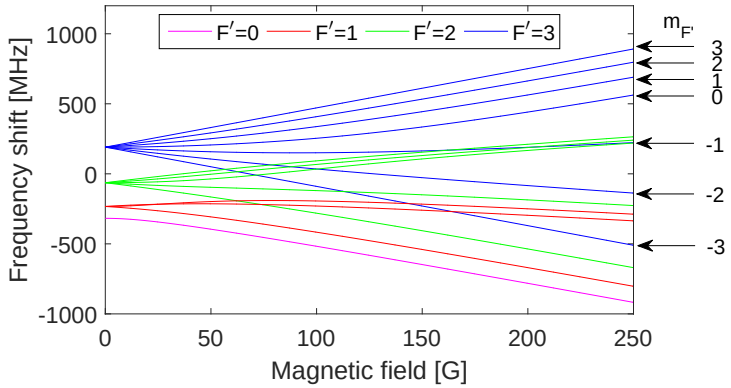

Figure 6. ^{87}Rb $5P_{3/2}$ magnetic hyperfine structure for several values of $\vec{B}$. The arrows indicate the magnetic energy levels, denoted by $m_{F'}$, for the $F' = 3$ excited state.

4.2. Experimental Analysis

In Figure 7 we show the hyperfine spectrum for ^{85}Rb as the laser frequency is varied. This spectrum corresponds to transitions from $F = 3$ to $F' = 2, 3, 4$ in Figure 1. For the Zeeman analysis we focused on the rightmost hyperfine peak corresponding to the $F = 3$ to $F' = 4$ transition. The spectrum in Figure 8 corresponds to ^{87}Rb transitions from $F = 3$ to $F' = 2, 3, 4$, shown in Figure 2. Here we focused on the rightmost hyperfine peak for Zeeman analysis, this peak corresponds to the $F = 3$ to $F' = 4$ transition.

Figures 9 and 10 show sequences of the splitting of the hyperfine peaks as the magnetic field is varied. We measured the separation between these peaks and compared them with those obtained from the computational analysis shown in Figures 5 and 6. This is shown in Figures 11 and 12. For ^{85}Rb the measured values correspond to the difference in transition energy from level $m_F = 3$ to $m_{F'} = 3$ and $m_F = -3$ to $m_{F'} = -3$, indicated by dashed arrows in Figure

1. In the case of ^{87}Rb the measured values correspond to a difference in transition energy from level $m_F = 2$ to $m_{F'} = 2$ and $m_F = -2$ to $m_{F'} = -2$, indicated by dashed arrows in Figure 2.

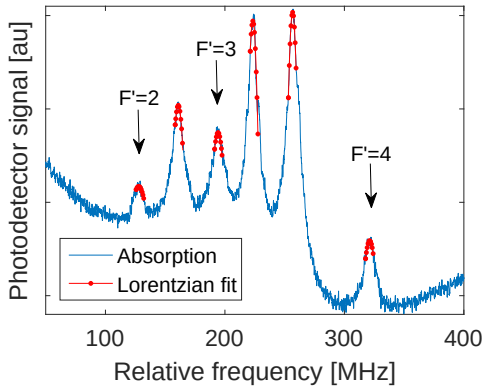

Figure 7. Saturated absorption spectrum of ^{85}Rb showing hyperfine transitions from $5S_{1/2}$ $F = 3$ to $5P_{3/2}$ $F' = 2$, 3, 4.

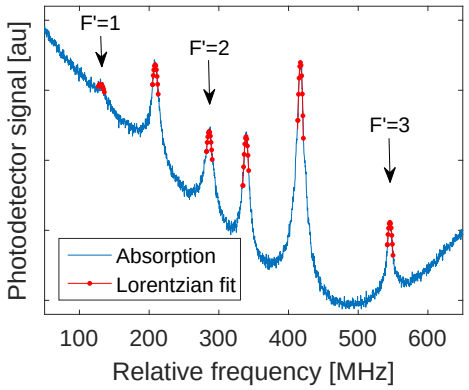

Figure 8. Saturated absorption spectrum of ^{87}Rb showing hyperfine transitions from $5S_{1/2}$ $F = 2$ to $5P_{3/2}$ $F' = 1$, 2, 3.

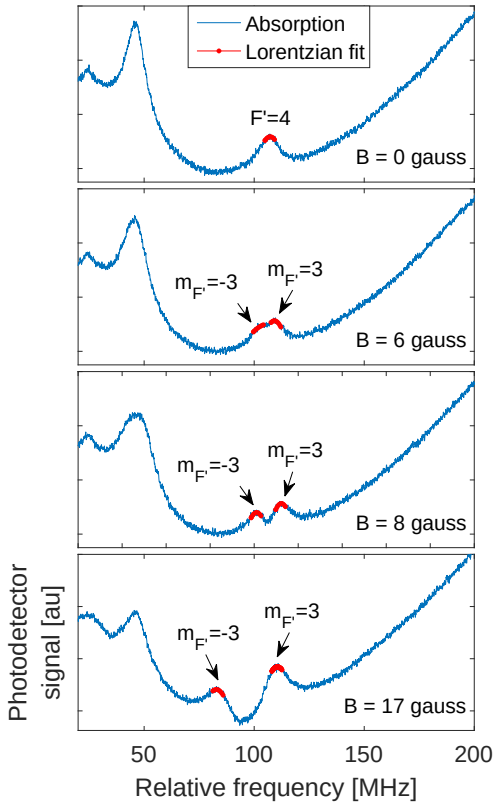

Figure 9. Saturated absorption spectrum of ^{85}Rb showing the transition from $5S_{1/2}$ $F = 3$ to $5P_{3/2}$ $F' = 4$. As the magnetic field is increased, $5P_{3/2}$ $F' = 4$ splits into magnetic sub-levels, $m_{F'} = -3, 3$.

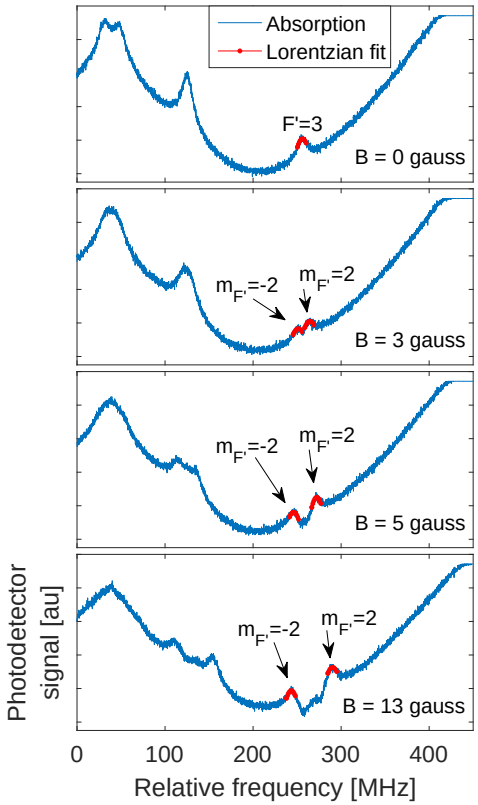

Figure 10. Saturated absorption spectrum of ^{87}Rb showing the transition from $5S_{1/2}$ $F = 2$ to $5P_{3/2}$ $F' = 3$. As the magnetic field is increased, $5P_{3/2}$ $F' = 3$ splits into magnetic sub-levels, $m_{F'} = -2, 2$.

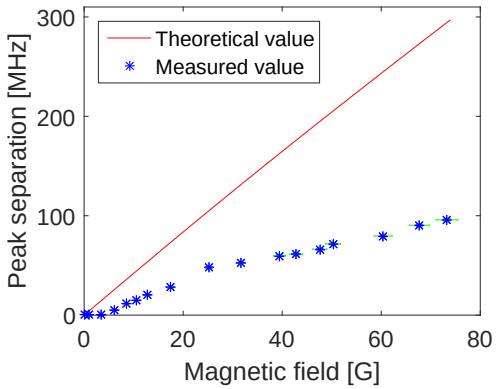

Figure 11. Computational versus experimental shift in frequency for the ^{85}Rb $5S_{1/2}$ $F = 3$, $m_F = -3, 3$ to $5P_{3/2}$ $F' = 4$, $m_{F'} = -3, 3$ magnetic hyperfine transitions. The uncertainty of each measurement is given as green bars.

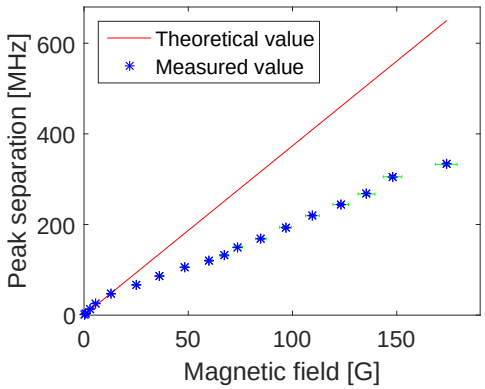

Figure 12. Computational versus experimental shift in frequency for the ^{87}Rb $5S_{1/2}$ $F = 2$, $m_F = -2, 2$ to $5P_{3/2}$ $F' = 3$, $m_{F'} = -2, 2$ magnetic hyperfine transitions. The uncertainty of each measurement is given as green bars.

5. Summary

We have demonstrated an experimental setup for the investigation of the Zeeman effect on the magnetic hyperfine structure of ^{85}Rb and ^{87}Rb. An analysis of the theoretical and experimental data shows large variations for both ^{85}Rb and ^{87}Rb. The difference between theoretical and experimental values is greater for ^{85}Rb. This may be due to the fact that we have neglected the quadrupole interaction in our theoretical analysis of the Zeeman effect; this interaction may need to be considered as it is larger for ^{85}Rb than ^{87}Rb, due to the higher nuclear spin value.

Additionally, the theory is an approximation which considers the average effects of interactions between electrons as well as between electrons and the nucleus, this may lead to inconsistencies between the prediction and experiment for multi-electron atoms such as rubidium.

References

[1] Bowie J, Boyce J and Chiao R 1995 *J. Opt. Soc. Am. B* **12** 1839–1842
[2] Kim J, Kim H, Moon H and Lee H 1997 *J. Opt. Soc. Am. B* **14** 2946–2947
[3] Ram N, Pattabiraman M and Vijayan C 2007 *J. Phys. Conf. Ser.* **80** 1–10
[4] Steck D 2013 Rubidium 85 d line data available online at URL `http://steck.us/alkalidata (revision 2.1.6, 20 September 2013)`
[5] Steck D 2015 Rubidium 87 d line data available online at URL `http://steck.us/alkalidata (revision 2.1.5, 13 January 2015)`

DIVISION D1 – ASTROPHYSICS

Structure formation with causal bulk viscosity

Giovanni Acquaviva[1], Anslyn John[2] and Aurélie Pénin[3]

[1] Institute of Theoretical Physics, Faculty of Mathematics and Physics, Charles University in Prague, 18000 Prague, Czech Republic
[2] Department of Mathematics, Rhodes University, Grahamstown 6139, South Africa
[3] Astrophysics and Cosmology Research Unit, School of Mathematical Sciences, University of KwaZulu-Natal, Durban 4041, South Africa

E-mail: gioacqua@utf.troja.mff.cuni.cz, a.john@ru.ac.za, aurelie.c.penin@gmail.com

Abstract.

Dissipative features of dark matter affect its clustering properties and could lead to observable consequences for the evolution of large–scale structure. We analyse the evolution of cold dark matter density perturbations allowing for the possibility of bulk viscous pressure in a causal dissipative theory. Our analysis employs a Newtonian approximation for cosmological dynamics and the transport properties of bulk viscosity are described by the Israel–Stewart theory. We obtain a third order evolution equation for density perturbations. For some parameter values the density contrast can be suppressed compared to results obtained in the ΛCDM scenario. For other values causal bulk viscous dark matter can exhibit an enhancement of clustering.

1. Introduction

The universe evolved from a hot, dense, homogeneous initial state to its present cool, diffuse and inhomogeneous state during a period of 13.8 billion years [1]. The origin of large scale structure is described by the gravitational instability paradigm [2]. In its simplest form the matter content of the universe is initially in hydrodynamic equilibrium. Density perturbations with wavelengths larger than the Jeans scale are unstable and this mechanism is thought to be responsible for the development of large scale structure and eventually galaxies. A universe consisting only of baryonic matter requires more than 14 billion years to produce the observed distribution of galaxies via the gravitational instability mechanism. Large amounts of cold dark matter (CDM) are required to salvage the structure formation scenario. Further arguments for the existence of dark matter follow from the rotation curves of galaxies [3], lensing by clusters [4] and the power spectrum [1] of the cosmic microwave background (CMB). The ΛCDM model includes a cosmological constant to account for the late time acceleration of the expansion [5].

Despite its great successes the ΛCDM model encounters some problems when addressing the question of structure formation. Persistent discrepancies exist between dark matter N–body simulations and observations. These include the "missing satellites" problem where simulations overproduce the number of satellite galaxies [6] and the "core–cusp" problem where dwarf galaxies have density profiles much flatter at the center than are predicted by simulation [7].

Proposed solutions to these problems involve including baryonic feedback [8, 9], the warm dark matter (WDM) hypothesis [10] or extensions to general relativity i.e. modified gravity [11, 12, 13]. Including dissipative features – such as viscosity – in CDM is another approach

[14]. This can suppress small scale structures in comparison to the ΛCDM scenario and thus help to alleviate the tension between theory and observation.

Several authors have included bulk viscosity in cosmological models [14, 15]. Given that dark matter empirically doesn't interact with normal matter (baryons and radiation), bulk viscosity is used as a phenomenological model of possible self–interaction and consequent dissipation within the dark fluid itself [15]. Most of the literature in this context invokes the Eckart theory [16], where systems relax to equilibrium instantaneously. Here bulk viscous pressure perturbations travel infinitely fast and violate causality. Even though the Israel–Stewart theory [17] represents a physically more robust way of of modelling dissipation (it is generically stable and causal), it is however more difficult to treat analytically.

In this paper we allow dark matter to have a bulk viscous pressure with a finite relaxation time, τ, by using the causal Israel–Stewart transport equation. We determine the growth of dark matter density perturbations in this model and compare our results to the ΛCDM and Eckart models.

2. Viscous cosmology

To tackle the problem of structure formation with viscous dark matter we adopt a minimal model where the universe is comprised solely of spatially homogeneous and isotropic dark matter. The matter obeys Hubble's law i.e. $\mathbf{u} = H(t)\mathbf{r}$ and cosmic dynamics is governed by the Navier–Stokes equations viz.

$$\frac{\partial \rho}{\partial t} + \nabla \cdot (\rho \mathbf{u}) = 0 \tag{1}$$

$$\rho \left(\frac{\partial}{\partial t} + \mathbf{u} \cdot \nabla \right) \mathbf{u} = -\nabla p - \nabla \Pi + \rho \nabla \Phi \tag{2}$$

$$\nabla^2 \Phi = 4\pi G \rho. \tag{3}$$

Dark matter is thus modelled as a self–gravitating fluid with mass density, ρ, velocity $\mathbf{u}$, pressure, p, and bulk viscous pressure, Π. The gravitational potential, Φ, is determined by Poisson's equation. This Newtonian treatment is a good approximation for non–relativistic matter on sub–horizon scales and at late times.

In the Eckart theory the bulk viscous pressure obeys the constitutive relation

$$\Pi = -\zeta \nabla \cdot \mathbf{u} \tag{4}$$

where ζ is the coefficient of bulk viscosity [18] viz.

$$\zeta = \zeta_0 \left(\frac{\rho}{\rho_0} \right)^s. \tag{5}$$

and quantities evaluated at the present time are indicated with the subscript 0. The exponent s encapsulates our ignorance about how the dissipation due to bulk viscosity arises from possible microscopic considerations. One only knows that, in the context of irreversible thermodynamics, the transport coefficients for a dissipative fluid depend on a certain power of the temperature, which in turn (due to Gibbs' fundamental relation) depends on a power of the energy density ρ. Hence, the most generic choice for the bulk viscosity coefficient is $\zeta \propto \rho^s$. In the absence of a microscopic connection, the exponent s is effectively a free parameter to be fixed by observations.

In the Israel–Stewart theory the bulk viscosity obeys the more complicated transport equation

$$\tau \dot{\Pi} + \Pi = -\zeta \nabla \cdot \mathbf{u} - \frac{\epsilon}{2} \Pi \tau \left[\nabla \cdot \mathbf{u} + \frac{\dot{\tau}}{\tau} - \frac{\dot{\zeta}}{\zeta} - \frac{\dot{T}}{T} \right] \tag{6}$$

where τ is the relaxation time, T the temperature and the overdot represents time derivatives in comoving coordinates. In the Newtonian limit this operator reduces to the convective derivative i.e. $\frac{D}{Dt} = \frac{\partial}{\partial t} + \mathbf{u}\cdot\nabla$.

The dimensionless bookkeeping parameter, ϵ, only assumes the values 0 or 1. It was artificially introduced into Eqn. (6) as a way to later distinguish between terms arising from the full Israel–Stewart theory (where $\epsilon = 1$) and the truncated Israel–Stewart (TIS) model (where $\epsilon = 0$). The TIS model is a commonly used approximation of Eqn. (6) because, while keeping the causal character of the full theory, it is analytically simpler. However, it has been shown [19, 20] that the truncated version agrees with the full theory only in very specific cases. Physically speaking, the condition for the validity of the truncation translates to a condition on the relative magnitude between the bulk pressure and the energy density of the fluid. In a cosmological setting, and specifically in a background (non–perturbative) analysis, the problem is that this condition might hold in some cosmic epoch but not necessarily at all times. In general, however, it is expected that the truncated and full theories agree in near–equilibrium situations.

A crucial difference between these two theories of dissipative phenomena is that in Israel–Stewart theory, systems have a finite relaxation time, τ. By contrast, in Eckart theory, systems relax instantaneously, i.e. $\tau = 0$. This implies that bulk viscous pressure perturbations travel infinitely fast as $c_b^2 = \frac{\zeta}{(\rho+p)\tau}$. where c_b is the sound speed of bulk viscous pressure perturbations. Causality is restored in Israel–Stewart theory.

Perturbing and linearising the system (1) - (3) leads to an evolution equation for the density contrast, $\delta \equiv \delta\rho/\rho$, which is *valid for any pressure source* viz.

$$\ddot{\delta} + 2H\dot{\delta} + \left(\frac{c_s^2 k^2}{a^2} - 4\pi G\rho\right)\delta = -\frac{k^2}{a^2\rho}\delta\Pi. \tag{7}$$

We recover the standard cosmology for inviscid pressure when $\delta\Pi = 0$. For non–expanding fluids ($a = 1, H = 0$) we recover the original Jeans instability criterion viz. $k^2 < \frac{4\pi G\rho}{c_s^2}$, where $c_s^2 = \frac{dp}{d\rho}$ represents the adiabatic sound speed. Including the causal, Israel–Stewart transport equation we obtain a third order evolution equation:

$$\begin{aligned} H\tau\, a^3\delta''' &+ \left\{\Big[3(\epsilon - q) + 1\Big]H\tau + 1\right\} a^2\,\delta'' \\ &+ \left\{\left[(3\epsilon(2-q) + j - 3q - 4) - \frac{4\pi G\rho}{H^2} + \epsilon\frac{k^2\,\Pi}{a^2H^2\rho}\right]H\tau + (2-q) + \frac{k^2\zeta}{a^2H\rho}\right\} a\,\delta' \\ &+ \left\{\left[\frac{4\pi G\rho}{H^2}(4 - 3\epsilon)\right]H\tau + \frac{k^2}{a^2H^2\rho}\Big((s-1)\Pi - 3H\zeta\Big) - \frac{4\pi G\rho}{H^2}\right\}\delta = 0\ , \end{aligned} \tag{8}$$

where primes denote derivatives with respect to the scale factor. In this equation q and j are the deceleration and jerk parameters respectively viz. $q = -\ddot{a}a\dot{a}^{-2}$ and $j = -\dddot{a}a^2\dot{a}^{-3}$. When $\tau \to 0$ (or equivalently $c_b^2 \to \infty$) Eq.(8) reduces to Eckart's form [15]. The non-viscous ΛCDM case is recovered when $\zeta_0 \to 0$.

3. Analysis

There are three characteristic timescales viz. (i) the expansion time $t_e \sim H^{-1}$, (ii) the collapse time $t_c = (4\pi G\,\rho)^{-1/2}$ and (iii) the relaxation time $\tau = (\zeta_0\,\rho^{s-1})/(c_b^2\,\rho_0^s)$. Since we are looking at the matter-dominated era, $t_e = 2/(3H)$ and, using the Friedmann equation, any ratio between t_e and t_c is constant. Ratios involving τ however are time dependent. In Eq.(8) the relaxation time always appears in the form:

$$H\,\tau = \frac{2}{3}\frac{\tau}{t_e} \tag{9}$$

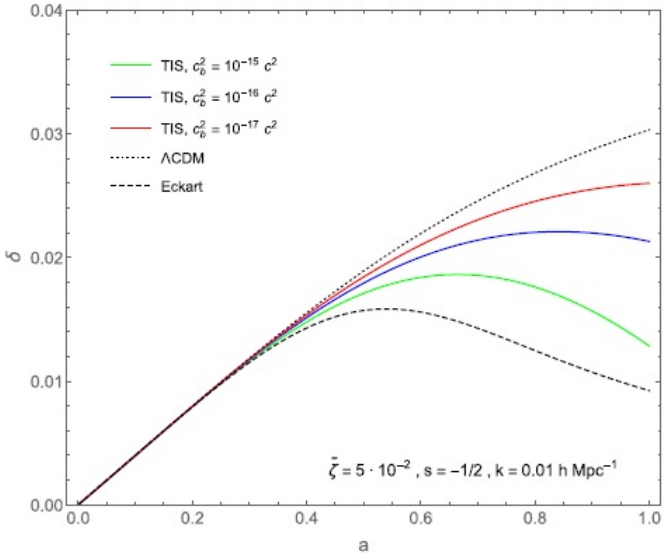

Figure 1. Evolution of the density contrast, $\delta(a)$, for $s = -1/2$, varying c_b^2 in TIS for $k = 0.01h$ Mpc^{-1}.

The deviation between IS and Eckart theories can be characterised by τ/t_e. In general, when the relaxation time is non–negligible the two theories will differ. The two theories converge when $\tau/t_e \to 0$ and the condition for negligible departure from Eckart is given by

$$\frac{\tau}{t_e} \ll 1 \quad \Rightarrow \quad \frac{\zeta_0}{c_b^2}\sqrt{\frac{8\pi G}{3\rho_0}}\, a^{3(\frac{1}{2}-s)} \ll 1. \tag{10}$$

Once the time-independent ratio ζ_0/c_b^2 is fixed, this condition depends strongly on s which appears in the exponent of the scale factor. If $s < 1/2$ then the condition $\tau/t_e \ll 1$ always holds for $a \ll 1$: IS and Eckart coincide at early times and the deviations can show up only at later times. If $s > 1/2$ then $\tau/t_e \gg 1$ holds at early times. Here significant deviation between IS and Eckart already appears for $a \ll 1$. The critical value $s = 1/2$ has been reported in previous studies of the background evolution of cosmological models eg. in [21, 22].

The density contrast evolution equation (8) can be numerically integrated and a typical result is displayed in Figure 1. We characterise the magnitude of clustering by the amplitude of δ at late times. The standard ΛCDM model displays the most clustering, whilst CDM with Eckart viscosity has the most strongly suppressed clustering. CDM models with truncated Israel-Stewart (TIS) viscosity lie between the two extremes. Our results indicate that Israel-Stewart viscosity models could suppress clustering at late times and alleviate the structure evolution problems. More detailed analysis can be found in [23]. For certain parameter ranges an increase in clustering compared to the non–viscous CDM case was predicted. This is surprising as a viscous fluid should be more resistant to clustering than an inviscid fluid. A possible explanation for this could be that the relevant parameter ranges i.e. values of the exponent s are unphysical. The adiabatic condition viz. $\frac{DS}{Dt} = 0$ needs to be modified to account for viscous energy dissipation. This is a topic for future investigation.

4. Conclusion

We examined the effect of bulk viscosity on the growth of dark matter perturbations in the causal Israel–Stewart dissipative theory. A third order evolution equation for the density contrast was

derived and analysed both analytically and numerically.

The numerical solutions were compared to those obtained for both the standard ΛCDM scenario as well as the non–causal Eckart theory. The deviation in behaviour of the density contrast from the ΛCDM and Eckart models depends sensitively on the exponent s appearing in the bulk viscosity coefficient, ζ. If $s < 1/2$ the IS models diverge from ΛCDM only at late times, whilst if $s > 1/2$ this divergence starts to occur at much earlier times. If dark matter admits bulk viscosity with coefficient $s < 1/2$ in the IS theory, the growth of structure is suppressed at late times. This may serve to alleviate the tension between the clustering of dark matter predicted by ΛCDM and that inferred by astronomical observations.

If $s > 1/2$ the IS models can exhibit greater clustering than for ΛCDM. This result is surprising as a viscous fluid should experience greater resistance to clumping than an inviscid fluid. We suspect that the parameter range might be unphysical and that this issue may be addressed by examining the energy equation for the system and establishing that the fluid's entropy is always increasing.

As expected the Eckart models approach ΛCDM in the limit of vanishing viscosity. The IS models however can still mimic ΛCDM even with non–zero viscosity if one chooses appropriate values for sound speed of bulk viscous pressure perturbations, c_s. Our analysis is based on a Newtonian approximation and solving the fully relativistic problem is the subject of future work. Other studies that merit attention are determining observational constraints on the viscosity parameters, as well as investigating the effects of viscosity on non–linear clustering.

Acknowledgments

AJ acknowledges financial support from Rhodes University. AP is funded by a NRF SKA Postdoctoral Fellowship. GA is funded by the grant GACR-14-37086G of the Czech Science Foundation.

References

[1] Ade P A, Aghanim N, Arnaud M, Ashdown M, Aumont J, Baccigalupi C, Banday A, Barreiro R, Bartlett J, Bartolo N *et al.* 2016 *Astron. Astrophys.* **594** A13.
[2] Weinberg S 2008 *Cosmology* (Oxford University Press.)
[3] Persic M, Salucci P and Stel F 1996 *Mon. Not. R. Astron. Soc.* **281** 27
[4] Clowe D, Bradač M, Gonzalez A H, Markevitch M, Randall S W, Jones C and Zaritsky D 2006 *Astrophys. J. Lett.* **648** L109
[5] Peebles P J E and Ratra B 2003 *Rev. Mod. Phys.* **75** 559
[6] Moore B, Ghigna S, Governato F, Lake G, Quinn T, Stadel J and Tozzi P 1999 *Astrophys. J.* **524** L19
[7] Donato F, Gentile G, Salucci P, Martins C F, Wilkinson M I, Gilmore G, Grebel E K, Koch A and Wyse R 2009 *Mon. Not. R. Astron. Soc.* **397** 1169
[8] Brooks A M, Kuhlen M, Zolotov A and Hooper D 2013 *Astrophys. J.* **765** 22
[9] Zolotov A, Brooks A M, Willman B, Governato F, Pontzen A, Christensen C, Dekel A, Quinn T, Shen S and Wadsley J 2012 *Astrophys. J.* **761** 71
[10] Viel M, Becker G D, Bolton J S and Haehnelt M G 2013 *Phys. Rev. D* **88** 043502
[11] Moffat J W 2006 *J. Cosmol. Astropart. P.* **2006** 004
[12] Capozziello S, Cardone V F and Troisi A 2007 *Mon. Not. R. Astron. Soc.* **375** 1423
[13] Bohmer C, Harko T and Lobo F 2008 *Astropart. Phys.* **29** 386
[14] Li B and Barrow J D 2009 *Phys. Rev. D* **79** 103521
[15] Velten H, Schwarz D J, Fabris J C and Zimdahl W 2013 *Phys. Rev. D* **88** 103522
[16] Eckart C 1940 *Phys. Rev.* **58** 919
[17] Israel W and Stewart J 1979 *Ann. Phys.* **118** 341
[18] Belinskii V and Khalatnikov I 1975 *Zh. Eksp. Teor. Fiz* **69** 401
[19] Maartens R *arXiv:astro-ph/9609119*
[20] Zimdahl W 1996 *Physical Review D* **53** 5483
[21] Barrow J D 1988 *Nucl. Phys. B* **310** 743
[22] Acquaviva G and Beesham A 2015 *Classical Quant. Grav.* **32** 215026
[23] Acquaviva G, John A and Pénin A 2016 *Phys. Rev. D* **94** 043517

Exploring the potential of the dark matter candidate from the Madala hypothesis with multi-frequency indirect detection

Geoff Beck and Sergio Colafrancesco

School of Physics, University of the Witwatersrand, Private Bag 3, WITS-2050, Johannesburg, South Africa

E-mail: geoffrey.beck@wits.ac.za

Abstract. The Madala hypothesis was proposed by members of the Wits-ATLAS group to account for several anomalies in both ATLAS and CMS data at the LHC. This hypothesis extends the standard model through the addition of two scalar bosons and a hidden sector that can provide a dark matter candidate. This hidden sector interacts with the standard model only through the mediation of one of these scalars S. The couplings of S are not amenable to investigation in current collider data and so are assumed to be Higgs-like to reduce the parameter space of the model. Our previous work [1] has shown that these couplings can be limited via indirect dark matter detection experiments in gamma-rays (for resonant annihilations into S). Here we will treat the dark matter and S masses independently, and we generalise our previous work [1] and examine what fraction of the cosmological dark matter abundance can be accounted for by particles in the hidden sector of the Madala hypothesis dark matter when these annihilate to standard model products via a Higgs-like S. We will also extend our gamma-ray analysis of Madala hypothesis dark matter to include the constraints of diffuse radio data from the Coma galaxy cluster in addition to the Fermi-LAT gamma-ray data from both this target and the Reticulum II dwarf galaxy.

Our analysis indicates that either the Madala hypothesis cannot provide the bulk of cosmologically relevant dark matter, or the S boson cannot be simply Higgs-like. These apply unless the candidate particle exceeds a mass of ~ 200 GeV. Both these scenarios may reduce the attractiveness of the hypothesis as the second case will imply that many free parameters must be added to describe S, greatly weakening fit significances for the model. To investigate the full consequences of this further work will necessitate using larger astrophysical data sets to strongly constrain details about S.

1. Introduction

The Madala hypothesis has three important constituents: a heavy Higgs-like Madala boson H, a mediator scalar S, and a Dark Matter (DM) candidate χ. This hypothesis was put forward to explain anomalies seen in both ATLAS [2] and CMS [3], particularly in the transverse momentum of the Higgs boson as well as event excesses in multi-lepton final states [4, 5, 6, 7]. The scalar mediator S is introduced to mitigate problems in quartic couplings [5], through it, χ can interact both with H and the Standard Model (SM). Given that the run-1, preliminary run-2 [6] and the latest run-2 releases [8], data from the Large Hadron Collider (LHC) did not remove the excesses attributed to the Madala particles, and that it provides a candidate for the missing content of the universe, it is worthwhile to examine the properties of the model from an astrophysical

standpoint. We note that more recent developments in the Madala hypothesis have focussed upon using a UV-complete extra Higgs doublet model with an additional singlet S scalar [9], rather than the effective field theory used in [4, 5, 6, 7] which may have lead to excess lepton production in certain scenarios [9]. There remains the potential for the S boson to couple to a DM particle, though that is not considered yet [9]. Importantly, the phenomenology of the S boson is not substantially impacted by the more advanced models being employed. Thus, the results presented here will still place limits on the SM couplings of S provided it also couples to a dark sector.

Here we can investigate the χ properties and thus those of S, which cannot be strongly limited by current collider data [5], through methods of indirect DM detection. That is, we can place limits on the properties of pathways from χ to the SM by predicting resulting fluxes of gamma-rays, synchrotron and Inverse Compton (IC) emission within cosmic structures and comparing these to known spectra/upper-limits for these target environments.

In this work we will use diffuse radio data from the Coma galaxy cluster [10] as well as Fermi-LAT [11] gamma-ray limits on both Coma [12] and the Reticulum II dwarf galaxy [13] to examine the consequences of the simplifying assumptions used to describe S. This being that S has Higgs-like couplings to the SM. In order to model this we will use decay branching data for Higgs-like particles from [14]. We will do this by determining 3σ confidence level upper-limits on the $\chi\chi \rightarrow$ SM annihilation cross-section and comparing these to the canonical relic values [15]. If the derived limits rule out the allowed relic values, then it is sufficient to say that χ cannot constitute all cosmologically relevant DM. We then take the ratio of the derived cross-section with lower-limit of the relic band to determine the maximal allowed fraction of the cosmological abundance of DM that can be composed of χ particles from the Madala hypothesis. Unlike our previous work [1], where we study whether astrophysical data allow for Higgs-like S, we do not study only the resonant case $m_S = 2m_\chi$, we allow m_S and m_χ to be independent. We will also extend the work from [1] by determining upper-limits on the branching ratio of S to W bosons if χ is assumed to constitute all of DM by making use this generalised mass scenario and by including radio data. We choose the W boson channel as it was the most promising in previous analysis [1].

We find that, with both Coma radio and Reticulum II gamma-ray data, we can limit χ particle DM with a Higgs-like S mediator to $\mathcal{O}(10\%)$ of the cosmological DM abundance, and can rule out Higgs-like couplings to W bosons for a broad range of χ masses, $\sim$ 10 - 250 GeV, using both radio and gamma-ray data.

This paper is structured as follows: in Section 2 we explain our DM annihilation models with resultant emissions and halo details discussed in 3. The results are shown and discussed in Section 4.

2. Dark Matter Annihilation

The Madala DM χ particles annihilate to S bosons that can decay to SM particles [5]. The annihilation cross-section found by astrophysical probes will be an effective one, from $\chi\chi \rightarrow$ SM.

The source function for particle i (electrons/positrons or photons) with energy E from a $\chi\chi$ annihilation and subsequent S decay is taken to be

$$Q_i(r, E) = \langle \sigma V \rangle \sum_f \frac{dN_i^f}{dE} B_f \left(\frac{\rho_\chi(r)}{m_\chi} \right)^2 , \quad (1)$$

where r is distance from the halo centre, $\langle \sigma V \rangle$ is the non-relativistic velocity-averaged annihilation cross-section, f labels the annihilation channel intermediate state with a branching fraction B_f and differential i-particle yield $\frac{dN_i^f}{dE}$, $\rho_\chi(r)$ is the radial density profile of χ particles

in the halo, and m_χ is the χ mass. The f channels used will be quarks $q\overline{q}$, electron-positron e^+e^-, muons $\mu^+\mu^-$, τ-leptons $\tau^+\tau^-$, W bosons W^+W^-, Z bosons ZZ, and photons $\gamma\gamma$.

The yield functions $\frac{dN_i^f}{dE}$ are taken from the Pythia routines in DarkSUSY [16, 17] as well as [18, 19] and the model independent formulation within the micrOMEGAs package [20, 21].

3. Indirect Detection in Coma and Reticulum II

For the DM-induced γ-ray production, the resulting flux calculation takes the form

$$S_\gamma(\nu, z) = \int_0^r d^3r' \, \frac{Q_\gamma(\nu, z, r)}{4\pi D_L^2} \, , \tag{2}$$

with $Q_\gamma(\nu, z, r)$ being the source function for frequency ν and position r within the given DM halo at redshift z, and D_L is the luminosity distance to the halo. In the case of Reticulum II, we will instead calculate the resulting gamma-ray flux based on the astrophysical J-factor:

$$J(\Delta\Omega, l) = \int_{\Delta\Omega} \int_l \rho^2(\mathbf{r}) dl' d\Omega' \, , \tag{3}$$

with $\rho(r)$ being the halo density profile, the integral being extended over the line of sight l, and $\Delta\Omega$ is the observed solid angle. The flux is then found to be

$$S_\gamma(\nu, z) = \langle \sigma V \rangle \sum_f \frac{dN_i^f}{dE} B_f J(\Delta\Omega, l) \, . \tag{4}$$

The halo of Reticulum II is found to have $J = 2 \times 10^{19}$ GeV^2 cm^{-5} [22].

For the Coma galaxy cluster, the local emissivity for the $i-th$ emission mechanism (synchrotron, ICS, bremsstrahlung) can then be found as a function of the electron and positron equilibrium distributions as well as the associated power (for power functions P_i see [23, 24])

$$j_i(\nu, r, z) = \int_{m_e}^{M_\chi} dE \, \left(\frac{dn_{e^-}}{dE} + \frac{dn_{e^+}}{dE} \right) P_i(\nu, E, r, z) \, , \tag{5}$$

where $\frac{dn_{e^-}}{dE}$ is the equilibrium electron distribution from DM annihilation (see [23, 25] for details) The flux density spectrum within a radius r is then written as

$$S_i(\nu, z) = \int_0^r d^3r' \, \frac{j_i(\nu, r', z)}{4\pi D_L^2} \, . \tag{6}$$

In Coma we will assume the following halo data following [24]: the virial mass is given by $M_{vir} = 1.33 \times 10^{15}$ M$_\odot$, with virial concentration $c_{vir} = 10$, and that the density profile is of the Navarro-Frenk-White (NFW) form [26]. The thermal electron distribution and magnetic field profiles are taken from the best-fit values of [27] and [28] respectively. We also use an annihilation flux boosting factor from dense halo substructure in Coma that is ~ 30 following methods described in [29, 30]. We will show results both with and without this boosting factor.

Taking a spectral function S_i, we can compare it to data from the Coma cluster and Reticulum II and find 3σ confidence level exclusion limits on the value of $\langle \sigma V \rangle$ for the process $\chi\chi \rightarrow$ SM.

4. Results and Discussion

Here we display the fraction of the cosmological DM abundance accounted for by Madala model DM. This is derived by determining the annihilation cross-section limits placed on the decay of Higgs-like coupled S, for a range of χ masses, by the spectra of the Coma galaxy cluster (radio and gamma [10, 12]) and the Reticulum II dwarf galaxy gamma-ray spectrum [13]. If this cross-section falls below the range of the canonical thermal relic value (2 - 4 $\times 10^{-26}$ cm^3 s^{-1}) [15] then the ratio of the derived limit and lower end of the canonical band is taken to be the maximal fraction of DM accounted for. As the candidate model is already limited to annihilating too slowly to constitute all of the observed present epoch abundance.

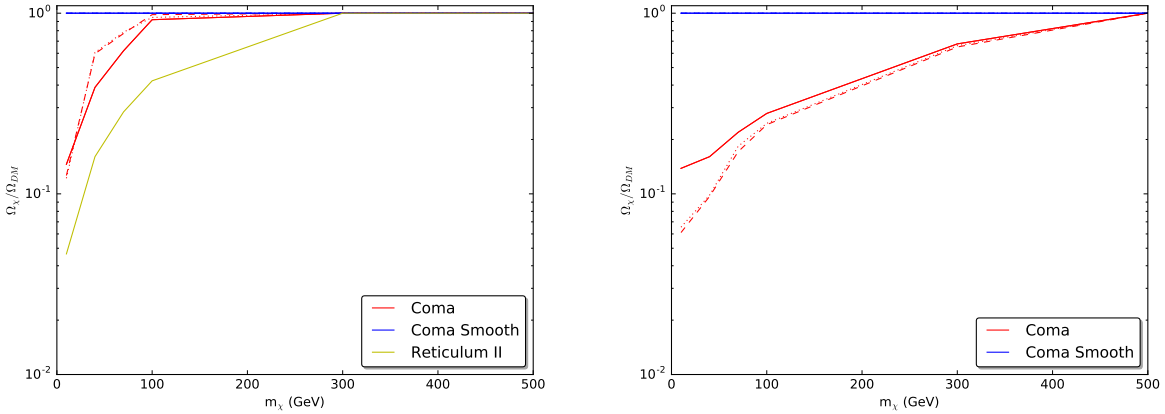

Figure 1. Maximal cosmological DM fraction accounted for by Madala χ particles. The solid, dashed, and dotted lines correspond to S masses 130, 160, and 200 GeV respectively. Coma Smooth shows the case without substructure boosting. Left: gamma-ray limits. Right: limits from Coma radio data.

In the left-hand panel of Figure 1 we show the DM fraction limits imposed on χ by the Fermi-LAT gamma-ray data. These indicate that Coma can only constrain this fraction for $m_\chi < 70$ GeV when the substructure boosting factor is used. However, the Reticulum II spectrum places strong limits that force χ to provide $< 40\%$ of the DM abundance while $m_\chi \leq 100$ GeV. These limits become weaker as the χ mass increases because the upper-limits in Reticulum II rise as a power-law for higher frequencies and the peak of DM-induced spectrum shifts with m_χ.

In the right-hand panel of Fig. 1 we see that the radio limits are significant provided a boost factor of $\mathcal{O}(10)$ from substructure is assumed. Since this is conservative within the literature, and based on robust halo simulations [29], it is not an undue assumption in a structure as large as the Coma cluster. The limits in this case are very similar to those from Reticulum II. However, they become stronger for larger m_S, due to fact that the harder resulting spectra conflict with the spectral profile of diffuse radio emissions in Coma (due to increased W boson production at larger m_S).

For a very general analysis of the Madala hypothesis DM candidate, under the same simplifying assumptions used to limit the space of free-parameters in the model [5] (that S is Higgs-like), we have shown that current data from the Reticulum II dwarf galaxy and the Coma galaxy cluster is sufficient to limit the possible abundance of Madala-associated DM particles to $\mathcal{O}(10\%)$ if $m_\chi \leq 100$ GeV. This expands on previous work [1] showing that it may be possible to use gamma-ray data to place limits on the couplings of S to the standard model, and possibly even rule-out a Higgs-like S if Madala DM is to constitute the entire cosmological abundance. Here we have also removed some of less general assumptions from the prior work

(that only resonant S production was considered).

Using the same modelling techniques as applied here, we will be able to generalise the analysis of [1] to also allow the χ and S masses to be independent, opening a much broader capacity to constrain the couplings of S to the SM. This is in addition to the inclusion of radio data, which is shown to have similar independent constraining power to that of the previously employed gamma-ray data. We demonstrate this generalisation below in Figure 2. This displays the 3σ confidence level limits on the branching ratio of S to W bosons from both gamma-rays (left panel) and radio data (right panel) when thermal relic annihilation cross-sections are assumed [15]. This is displayed as a ratio of the branching ratio to that of b_h the required fraction for a Higgs-like particle of mass m_S [14]. We see that the conclusion of [1] is not substantially weakened by this generalisation, with evidence limiting the possibility of a Higgs-like S boson coming from both Reticulum II gamma-ray data and Coma diffuse radio data while $m_\chi \lesssim 250$ GeV.

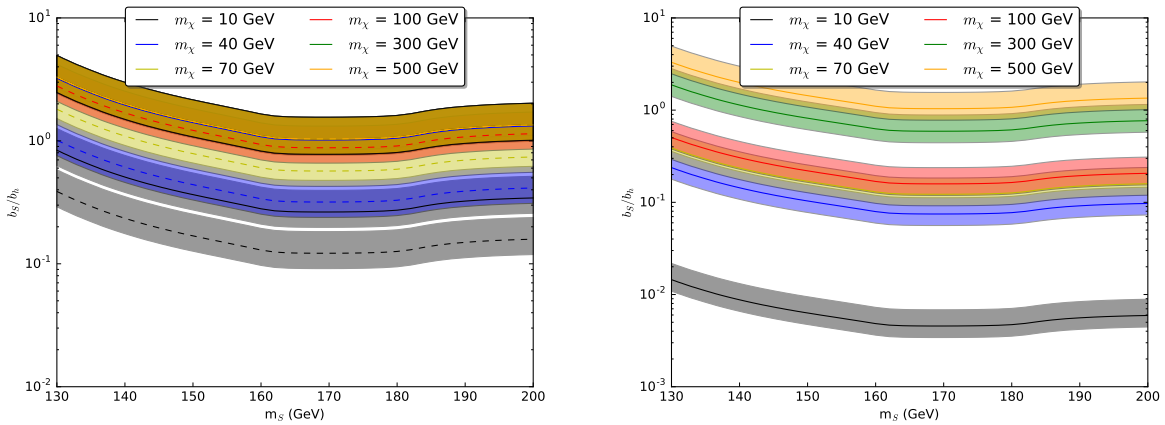

Figure 2. Upper-limits at 95% confidence level for the branching fraction into W^+W^- compared to that required for Higgs-like couplings at a given m_S when χ provides all DM. Shaded areas cover the thermal relic band region $2 - 4 \times 10^{-26}$ cm^3 s^{-1} [15]. Left: gamma-ray limits with Coma in solid and Reticulum II in dashed. Right: limits from Coma radio data.

By bringing the viability of the simplifying Higgs-like assumption into question we can see that either many more free parameters must be added to the Madala model, which will require further astrophysical data to constrain accurately and may lower the significance of existing fits to excesses, or the χ particle of the Madala hypothesis must take a back seat as a candidate to explain all of DM. Both of these scenarios may well serve to weaken the attractiveness of the proposed Madala model. However, a final possibility is that the hidden sector particle χ is of large mass, > 200 GeV, limiting its ability to be put forward as an explanation in scenarios like the galactic centre gamma-ray excess [31] as well as its detectability in collider experiments. This work remains especially relevant due to the persistence of the motivating LHC excesses into run-2 data [8].

Acknowledgments

This work is based on the research supported by the South African Research Chairs Initiative of the Department of Science and Technology and National Research Foundation of South Africa (Grant No 77948). G.B. acknowledges support from a post-doctoral grant through the same initiative and institutions. We acknowledge useful discussions with B. Mellado on the Madala hypothesis proposed by members of the Wits-ATLAS group to account for several anomalies in both ATLAS and CMS data at the LHC.

References

[1] Beck G and Colafrancesco S 2017 to appear in *Proc. of Wits/iThemba labs High Energy Particle Physics Workshop 2017* (arXiv: 1704.08031)
[2] Aad G et al 2008 *JINST* **3** S08003
[3] Della Negra M, Petrilli A, Herve A and Foa L 2008 *CMS Physics Technical Design Report Vol. I: Software and Detector Performance* `http://doc.cern.ch//archive/electronic/cern/preprints/lhcc/public/lhcc-2006-001.pdf`
[4] von Buddenbrock S, Chakrabarty N, Cornell A S, Kar D, Kumar M, Mandal T, Mellado B, Mukhopadhyaya B and Reed R G 2015 *Preprint* arXiv:1506.00612
[5] von Buddenbrock S, Chakrabarty N, Cornell A S, Kar D, Kumar M, Mandal T, Mellado B, Mukhopadhyaya B, Reed R G and Ruan X 2016 *Eur. Phys. J.* C **76** 580 (arXiv:1606.01674)
[6] von Buddenbrock S 2017 *Preprint* arXiv: 1706.02477
[7] Fang Y, Kumar M, Mellado B, Zhang Y and Zhu, M 2017 Submitted to the *White Paper of the Hong Kong University of Science and Technology Institute of Advanced Studies High Energy Physics Conf. 2017* (arXiv: 1706.06659)
[8] ATLAS Collaboration 2017 ATLAS-CONF-2017-058 `https://cds.cern.ch/record/2273874/files/ATLAS-CONF-2017-058.pdf`
[9] von Buddenbrock S, Cornell A S, Iarilala E D R, Kumar M, Mellado B, Ruan X and Shrif E M 2018 *Preprint* arXiv:1809.06344.
[10] Thierbach M, Klein U and Wielebinski R 2003 *A&A* **397** 53
[11] Atwood W B et al for the Fermi-LAT collaboration 2009 *ApJ* **697** 1071 (arXiv:0902.1089)
[12] Ackermann M et al for the Fermi-LAT collaboration and Rephaeli Y 2016 *ApJ* **819**(2) 149 (arXiv: 1507.08995)
[13] Drlica-Wagner A et al for the Fermi-LAT collaboration and Abbott T et al for the DES collaboration 2015 *ApJ* **809** L4 (arXiv: 1503.02632)
[14] Heinemeyer S (ed) et al for the LHC Higgs Cross Section Working Group 2013 *Handbook of LHC Higgs Cross Sections: 3. Higgs Properties : Report of the LHC Higgs Cross Section Working Group* (CERN) (arXiv: 1307.1347)
[15] Steigman G, Dasgupta B and Beacom J F 2012 *Phys. Rev.* D **86** 023506
[16] Sjöstrand T 1994 *Comput. Phys. Commun.* **82** 74
[17] Gondolo P, Edsjo J, Ullio P, Bergstrom L, Schelke M and Baltz E A 2004 *JCAP* **0407** 008
[18] Cirelli M, Corcella G, Hektor A, Htsi G, Kadastik M, Panci P, Raidal M, Sala F and Strumia A 2011 *JCAP* **1103** 051 (arXiv 1012.4515)
[19] Ciafaloni P, Comelli D, Riotto A, Sala F, Strumia A and Urbano A 2011 *JCAP* **1103** 019 (arXiv: 1009.0224)
[20] Belanger G, Boudjema F, Pukhov A and Semenov A 2007 *Comput. Phys. Commun.* **176** 367 (arXiv:hep-ph/0607059)
[21] Belanger G, Boudjema F, Pukhov A and Semenov A 2013 *Preprint* arXiv:1305.0237
[22] Bonnivard V, Combet C, Maurin D, Geringer-Sameth A, Koushiappas S M, Walker M G, Mateo M, Olszewski E, Bailey J I 2015 *ApJ* **808** L36
[23] Beck G and Colafrancesco S 2016 *JCAP* **05** 013
[24] Colafrancesco S, Profumo S and Ullio P 2006 *A&A* **445** 21
[25] Colafrancesco S, Profumo S and Ullio P 2007 *Phys. Rev.* D **75** 023513
[26] Navarro J F, Frenk C S and White S D M 1999 *ApJ* **462** 563
[27] Briel U et al. 1992 *A&A* **25**9 L31
[28] Bonafede A et al 2010 *A&A* **513** A3
[29] Sanchez-Conde M and Prada F 2014 *MNRAS* **442**(3) 2271 (arXiv:1312.1729)
[30] Ng K et al 2014 *Phys. Rev.* D **89** 083001 (arXiv: 1310.1915)
[31] Calore F, Cholis I, McCabe C and Weniger C 2015 *Phys. Rev.* D **91** 063003 (arXiv:1411.464)

Spectral analysis of *Fermi*-LAT gamma-ray bursts with known redshift and their potential use as cosmological standard candles

Feraol F. Dirirsa[1,*], Soebur Razzaque[1] and Frédéric Piron[2] on behalf of the *Fermi*-LAT Collaboration

[1]Department of Physics, University of Johannesburg, P. O. Box 524, Auckland Park 2006, South Africa

[2]Laboratoire Univers et Particules de Montpellier, Université de Montpellier, CNRS/IN2P3, place Eugène Bataillon, 34095 Montpellier cedex 5, France

E-mail: *fdirirsa@uj.ac.za

Abstract. Long duration Gamma-Ray Bursts (GRBs) may serve as new standard candles to constrain cosmological parameters by probing the Hubble diagram well beyond the range of redshift currently accessible using type-Ia supernovae. The standardization of GRBs is based on relations which correlate two or more parameters, found from gamma-ray spectral modelling, of which one is strongly dependent on the cosmological model. Amati relation, in particular, is between the source rest frame energy ($E_{i,p}$) at which the prompt gamma-ray spectral energy distribution peaks and the isotropic-equivalent bolometric energy (E_{iso}). We have selected a sample of 23 long GRBs (LGRBs) and 2 short GRBs (SGRBs) with known redshifts, which have been detected by the *Fermi* GBM and LAT instruments in eight years of operations, from July 2008 to December 2016. We have derived $E_{i,p}$ and E_{iso} for these LGRBs and SGRBs using the GBM and LAT data in joint spectral fits, often requiring multiple components, thus extending the computation of E_{iso} to the GeV range. Our results show that LGRBs detected by the *Fermi*-LAT with significant GeV emission are consistent with the Amati relation. These results further enhance the possibility to use the GRBs as cosmological standard candles.

1. Introduction

Gamma-ray bursts (GRBs) are energetic astronomical events that can be observed from redshift (z) up to ~ 9.4 [1]. High redshift GRBs may be used for gathering information of the cosmological evolution of the universe, which has been difficult to retrieve by other cosmological probes. According to observations, the GRBs can be classified as either long GRBs (LGRBs) lasting for more than 2 seconds or short GRBs (SGRBs) lasting for less than or equal to 2 seconds [2]. The limit between the diverse population of SGRBs and LGRBs are inferred through the observed durations T_{90} (i.e. the time to accumulate between 5% and 95% of the total counts in the burst). The LGRBs are perceived as a highly promising tool to probe the process of cosmological parameters, like the Type Ia Supernova (SNe Ia) [4]. The high-energy emission of LGRBs has been studied with the Energetic Gamma-Ray Experiment Telescope (EGRET) that covers the energy range from 30 MeV to 30 GeV [5]. Since 2008 the *Fermi*-Large Area Telescope (LAT) opened a new era for the study of high energy emission from GRBs [3] that detected more than

135 GRBs until July 2017. The two *Fermi* telescopes, the GRB Monitor (GBM) [6] and LAT [7], span an energy band from 8 keV to above 300 GeV. The GBM comprises of 12 Sodium Iodide (NaI) devices covering energies from 8 keV to 1 MeV and a pair of Bismuth Germanate (BGO) detectors (b0 and b1) covering energies from 200 keV to 40 MeV. Observations of the GRB prompt emission led to several phenomenological correlations among the emission properties. One of the most studied one is the Amati relation [8] that correlates the isotropic radiated energy (E_{iso}) in the 1-10^4 keV energy band and the photon energy of the νF_ν spectrum, both computed in the GRB rest frame. Many studies have been performed to test this correlation using various samples of LGRBs, collected from different gamma-ray telescopes [9, 10, 11, 12]. The results from those studies show that the $E_{i,p} - E_{iso}$ correlation may be used as a redshift estimator for GRBs [13] to constrain the cosmological parameters.

Since the spectra of GRBs detected by the *Fermi*-LAT/GBM extend up to a few tens of GeV in the cosmological rest-frame, the commonly adopted E_{iso} computation in the 1 keV - 10 MeV band is rather narrow, thus biasing the correlation. The samples of LGRBs used to compute the correlation were also collected from the telescopes with narrow energy bands with the peak of the spectrum outside the observed energy window [14]. Therefore, the joint *Fermi* GBM-LAT sample is valued for the correlation study by providing extended energy coverage to characterize a peak energy as well as validate the E_{iso} integrated over the energy range from 1 keV to 100 MeV. In this study, we assess a sample of 23 *Fermi* LGRBs and 2 SGRBs observed up to the LAT energy range until December 2016. For these data, the correlation between $E_{i,p}$ and E_{iso} in the cosmological rest frame have been studied.

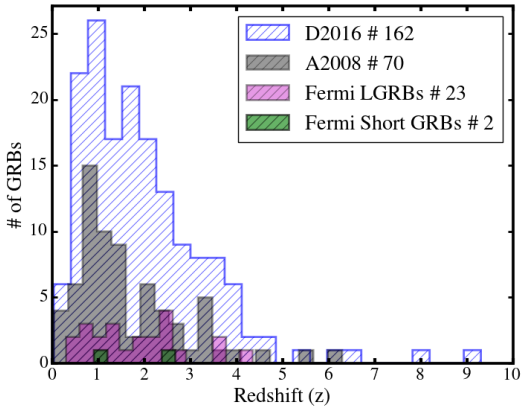

Figure 1. The redshift distributions of GRBs used by Amati et al. 2008 (A2008) [10], Demianski et al. 2016 (D2016) [15], *Fermi* LGRBs (magenta hatch) and *Fermi* SGRBs (green hatch). The list of *Fermi* LGRBs and SGRBs with redshift are given in Table 2.

2. Sample and data analysis

We conduct our analysis on the *Fermi* sample of 23 LGRBs and 2 short GRBs with identified redshift z. Their redshifts are derived from photometric or optical spectroscopy or calculated theoretically (i.e. estimate a redshift of $\sim$1.55 for GRB 131014A [16]) covering the time period until December 2016. For GRB 110721A, the possibility that the object is an early-type galaxy at $z = 3.512$ has been considered (E. Berger GCN 12193, 2011). We use data from the GBM NaI detectors that have source angles less than 50 degrees, the data of BGO detector closer to the source and the LAT data. In order to subtract the GBM background spectrum for the spectral analysis, we have defined two background intervals before and after the prompt emission for each

energy channel. For each emission episode, we fit the spectrum with a second-order polynomial function to a user-defined background and interpolate this fit across the source interval. We have used the standard 128 energy bins of the CSPEC data-type, for NaI using the channels from ∼8 keV to ∼900 keV cutting out the over-flow high energy channels (corresponding to the Iodine K-edge from ∼30 ∼40 keV, see [6]). For BGO, we have used data from ∼220 keV to ∼40 MeV and ∼210 keV to ∼40 MeV for b1 and b0, respectively. For the LAT analysis, we have used the pass-8 data with Transient class events (`Transient20E`) by selecting them from within a 10-degrees radius of interest. The data is binned in 30 logarithmically spaced energy steps between 30 MeV and 300 GeV. Since, we consider energies below 100 MeV, the `gtlike` tool was used for the binned maximum-likelihood analysis of the data which offers the possibility to account for correcting the energy dispersion effect. We derive the observed spectrum and the detector response matrix using the *Fermi* Science Tools `gtbin` and `gtrspgen`. To produce a background spectrum file, the background estimation tool `gtbkg` was used.

For the spectral analysis, we have considered different functions because of the variety of spectral models that constrain the emission for the T_{90} duration as reported in Table 1. The fits are composed of three main components: (a) Band model (Band) [17], which smoothly connects two power laws joined by an exponential cutoff, (b) the low energy power law with an exponential high energy cutoff, so called Comptonized (Comp), and (c) the smoothly broken power-law (SBPL) [18]. We have also considered additional components in our spectral fits [19]: (I) the power law (PL) $dN/dE(E|A,\alpha_1) = A(E/100\ keV)^{\alpha_1}$, where α_1 is the photon index, and (II) the Black Body model (BB) $dN/dE(E|A,kT) = AE^2/(\exp(E/kT)-1)$, where kT is the thermal temperature.

Table 1. The GRB names, triggers and the spectral fit parameters for 25 *Fermi* GRBs

GRB name	Triggers	Model	$T_{05}-T_{95}$	α or γ	β	E_p or E_0	kT	α_1	C-Stat/dof$^{(*)}$
GRB 160625B	n7+n9+b1+LAT	Band+BB+PL	188.45-650.54	-0.40 ± 0.06	-2.70 ± 0.02	642.92 ± 15.48	27.94 ± 1.09	-2.16 ± 0.04	1462.9/354
GRB 160521B	n6+n7+n8+b1+LAT	Band	0.32-3.14	-0.48 ± 0.03	-2.62 ± 0.06	161.62 ± 4.16			547.15/468
GRB 160509A	n0+n1+n3+b0+LAT	Band+	7.68-379.4	-0.87 ± 0.08	-5.16 ± 0.49	8591.48 ± 68.27			
		Comp+PL		-0.79 ± 0.04		317.14 ± 16.60		-1.76 ± 0.10	1741.9/474
GRB 150514A	n3+n6+n7+b0+LAT	Band	0.00-10.8	-1.45 ± 0.08	-2.33 ± 0.05	76.28 ± 8.26			590.57/472
GRB 150403A	n3+n4+b0+LLE	Band+BB	3.33-25.60	-1.02 ± 0.02	-2.95 ± 0.10	793.63 ± 52.55	33.30 ± 1.58		524.75/358
GRB 150314A	n0+na+n1+n9+b1+LAT	Band	0.6-11.29	-0.63 ± 0.01	-3.02 ± 0.10	357.38 ± 4.78			1333.0/588
GRB 141028A	n6+n7+n9+b1+LAT	Band	6.66-38.16	-0.91 ± 0.02	-2.37 ± 0.02	396.45 ± 15.29			691.79/473
GRB 140619B	n1+n9+b1+LAT	SBPL	0.00-1.41	-0.46 ± 0.21	-2.28 ± 0.07	1428.7 ± 306.7			416.86/362
GRB 131231A	n0+n3+n7+b0+LAT	Band	13.31-44.31	-1.23 ± 0.01	-2.65 ± 0.03	225.17 ± 3.02			1665.0/476
GRB 131108A	n0+n3+n6+n7+b0+b1+LAT	SBPL	0.32 - 19.32	-0.99 ± 0.02	-2.23 ± 0.01	205.32 ± 6.91			950.58/716
GRB 131014A	n9+na+nb+b1+LAT	Band+BB	0.96-4.16	-0.40 ± 0.01	-2.85 ± 0.03	418.39 ± 6.99	33.53 ± 0.85		791.75/469
GRB 130518A	n3+n6+n7+b0+b1+LAT	Band	9.9-57.9	-0.89 ± 0.01	-2.71 ± 0.03	458.85 ± 9.22			1357.1/592
GRB 130427A	n6+n9+na+b1+LAT	Band+PL	11.23-142.34	-1.41 ± 0.01	-2.27 ± 0.01	219.61 ± 4.38		-1.22 ±0.21	2105.1/488
GRB 120624B	n1+n2+na+b0+b1+LAT	SBPL	-258.05-13.31	-1.04 ± 0.01	-2.78 ± 0.04	379.49 ± 8.15			2015.7/588
GRB 110731A	n0+n1+n6+n7+n9+b0+b1+LAT	Band+PL	0 - 7.3	-0.24 ± 0.10	-2.43 ± 0.08	260.70 ± 11.12		-1.95 ± 0.04	1277.9/826
GRB 110721A	n6+n7+n9+b1+LAT	Band	0.45 - 24.9	-1.12 ± 0.01	-2.60 ± 0.03	780.87 ± 43.32			666.74/473
GRB 100414A	n7+n9+n11+b1+LAT	Band	2.0 - 28.4	-0.50 ± 0.02	-2.91 ± 0.06	578.89 ± 11.69			750.82/469
GRB 091208B	n10+n9+b1+LAT	Band	0.26 - 15.26	-1.29 ± 0.07	-2.53 ± 0.12	98.22 ± 9.74			422.09/351
GRB 091003A	n0+n3+n6+b0+b1+LAT	Band	1.09 - 22.19	-1.08 ± 0.01	-2.79 ± 0.05	452.21 ± 17.44			674.54/600
GRB 090926A	n6+n7+n8+b1+LAT	SBPL	2.05-22.05	-0.90 ± 0.01	-2.27 ± 0.01	171.50 ± 2.36			945.02/478
GRB 090902B	n0+n2+n9+b0+b1+LAT	Band+PL	0-22	-0.53 ± 0.01	-4.14 ± 0.28	760.66 ± 7.69		-1.92 ± 0.01	1320.6/601
GRB 090510	n3+n6+n7+n9+b0+b1+LAT	SPBL	0.002: 1.744	-0.86 ± 0.03	-2.26 ± 0.03	1873.00 ± 212.70			788.82/720
GRB 090328	n7+n8+b1+LAT	Band	4.67-61.67	-1.04 ± 0.02	-2.37 ± 0.04	703.75 ± 47.16			769.08/360
GRB 090323	n6+n7+n9+n11+b1+LAT	SBPL	-1.0 - 173	-1.29 ± 0.01	-2.50 ± 0.02	399.44 ± 17.17			1558.6/597
GRB 080916C	n3+n4+b0+LAT	SBPL	0 - 66	-1.11 ± 0.01	-2.20 ± 0.01	270.46 ± 12.20			579.20/364

Notes. α and β are the lower and higher photon indices for Band and SBPL functions, respectively. E_0 is the SBPL e-folding energy in keV. γ is the photon index of Comp. E_p is the Band or Comp peak energy in keV. C-Stat/dof$^{(*)}$ is the ratio of the value of the C-stat resulting from the fit and the associated degrees of freedom (dof)−This results cannot be used to estimate goodness of fit nevertheless compare to C-stat for models.

3. Testing the $E_{i,p} - E_{iso}$ correlation for the bright *Fermi* GRBs

To measure the fitting parameters generated by the `rmfit` package and uncertainty on those parameters, we use Monte Carlo simulations by assuming the parameters follow a multivariate Gaussian function. Using the covariance matrix obtained from the spectral fit, 10,000 sets of random values were generated for the parameters and the most probable value of the final

distribution with 68.27% confidence interval was selected. These results are reported in Tables 1 and 2. The E_{iso} and $E_{i,p}$ are also chosen as the most probable values of the final distributions, and errors derived from the 1σ confidence interval around these values are reported in Table 2.

Table 2. Analysis of $E_{i,p}$ and E_{iso} in the GRB rest-frame

GRB name	z	$E_{i,p}$ (keV)	E^{+}_{iso} (erg)	E^{++}_{iso} (erg)
GRB 160625B	1.406^{a}	1546.86 ± 37.25	$(4.35 \pm 0.06)\times10^{54}$	$(4.94 \pm 0.07)\times10^{54}$
GRB 160521B	$z > 2.5^{b}$	565.67 ± 14.55	$(1.71 \pm 0.03)\times10^{53}$	$(1.85 \pm 0.06)\times10^{53}$
GRB 160509A	1.17^{c}	19334.10 ± 652.25	$(1.83 \pm 0.05)\times10^{54}$	$(3.65 \pm 0.14)\times10^{54}$
GRB 150514A	0.807^{d}	137.84 ± 14.93	$(1.26 \pm 0.05)\times10^{52}$	$(1.37 \pm 0.07)\times10^{52}$
GRB 150403A	2.06^{e}	2428.51 ± 160.80	$(8.52 \pm 0.18)\times10^{53}$	$(9.53 \pm 0.27)\times10^{53}$
GRB 150314A	1.758^{f}	985.66 ± 13.20	$(7.27 \pm 0.10)\times10^{53}$	$(7.60 \pm 0.17)\times10^{53}$
GRB 141028A	2.33^{g}	1320.18 ± 50.90	$(6.40 \pm 0.07)\times10^{53}$	$(7.98 \pm 0.12)\times10^{53}$
GRB 140619B	2.67 ± 0.37^{h}	5192.46 ± 1210.86	$(4.38 \pm 1.12)\times10^{52}$	$(8.03 \pm 2.37)\times10^{52}$
GRB 131231A	0.6439^{i}	370.15 ± 4.97	$(1.92 \pm 0.01)\times10^{53}$	$(2.01 \pm 0.02)\times10^{53}$
GRB 131108A	2.40^{j}	1163.20 ± 28.54	$(1.14 \pm 0.04)\times10^{54}$	$(1.53 \pm 0.05)\times10^{54}$
GRB 131014A	$\sim1.55^{k}$	1066.90 ± 17.83	$(1.14 \pm 0.01)\times10^{54}$	$(1.22 \pm 0.01)\times10^{54}$
GRB 130518A	2.49^{l}	1601.40 ± 32.19	$(1.67 \pm 0.02)\times10^{54}$	$(1.89 \pm 0.02)\times10^{54}$
GRB 130427A	0.3399^{m}	294.25 ± 5.86	$(9.29 \pm 0.06)\times10^{52}$	$(1.06 \pm 0.01)\times10^{53}$
GRB 120624B	0.57 ± 0.07^{n}	595.02 ± 20.37	$(1.85 \pm 2.74)\times10^{53}$	$(1.96 \pm 2.94)\times10^{53}$
GRB 110731A	2.83^{o}	998.47 ± 42.59	$(4.86 \pm 0.11)\times10^{53}$	$(5.98 \pm 0.23)\times10^{53}$
GRB 110721A	3.512^{p}	3523.30 ± 195.47	$(1.39 \pm 0.03)\times10^{54}$	$(1.79 \pm 0.04)\times10^{54}$
GRB 100414A	1.368^{q}	1370.82 ± 27.68	$(5.87 \pm 0.08)\times10^{53}$	$(6.35 \pm 0.12)\times10^{53}$
GRB 091208B	1.063^{r}	202.63 ± 20.10	$(2.26 \pm 0.12)\times10^{52}$	$(2.37 \pm 0.17)\times10^{52}$
GRB 091003A	0.8969^{s}	857.81 ± 33.08	$(9.58 \pm 0.16)\times10^{52}$	$(1.02 \pm 0.02)\times10^{53}$
GRB 090926A	2.1062^{t}	861.41 ± 8.52	$(1.95 \pm 0.01)\times10^{54}$	$(2.50 \pm 0.02)\times10^{54}$
GRB 090902B	1.822^{u}	2146.57 ± 21.71	$(3.29 \pm 0.02)\times10^{54}$	$(3.49 \pm 0.03)\times10^{54}$
GRB 090510	0.903^{v}	5927.47 ± 459.00	$(3.69 \pm 1.45)\times10^{51}$	$(6.75 \pm 3.23)\times10^{51}$
GRB 090328	0.736^{w}	1221.71 ± 81.87	$(1.16 \pm 0.03)\times10^{53}$	$(1.42 \pm 0.05)\times10^{53}$
GRB 090323	3.57^{x}	2060.23 ± 138.07	$(4.30 \pm 0.10)\times10^{54}$	$(5.35 \pm 0.17)\times10^{54}$
GRB 080916C	4.35 ± 0.15^{y}	2434.39 ± 108.43	$(3.57 \pm 0.14)\times10^{54}$	$(5.33 \pm 0.19)\times10^{54}$

Notes. E^{+}_{iso} and E^{++}_{iso} are computed in the $1 - 10^4$ keV and $1 - 10^5$ keV energy range of cosmological rest frame by assuming a standard ΛCDM cosmology with $H_0 = 69.6$ km s^{-1} Mpc^{-1} , $\Omega_m = 0.286$ and $\Omega_\Lambda = 0.714$, respectively.
References for the redshift: (*a*) Xu et al. GCN 19600 (2016); D'Elia et al. GCN 19601 (2016), (*b*) Ruffini et al. GCN 19456 (2016), (*c*) Tanvir et al. GCN 19419 (2016), (*d*) de Ugarte Postigo et al. GCN 17822 (2015), (*e*) Pugliese et al. GCN 17672 (2015); Golenetskii et al. GCN 17677 (2015), (*f*) de Ugarte Postigo et al. GCN 17583 (2015); Golenetskii et al. GCN 17587 (2015), (*g*) Xu et al. GCN 16983 (2014), (*h*) Ruffini et al. *ApJ* 808 190 (2015), (*i*) Xu et al. GCN 15645 (2013); Cucchiaras GCN 15652 (2013), (*j*) de Ugarte Postigo et al. GCN 15470 (2013); Golenetskii et al. GCN 15480 (2013), (*k*) Guiriec et al. (2015), (*l*) Snchez-Ramrez et al. GCN 14685 (2013); Cucchiara et al. GCN 14687 (2013), (*m*) Xu et al. 776 98 (2013), (*n*) de Ugarte Postigo et al. GCN 13395 (2012), (*o*) Tanvir et al. GCN 12225 (2011), (*p*) Berger GCN 12193 (2011); Grupe et al. GCN 12212 (2011), (*q*) Cucchiara and Fox GCN 10606 (2010), (*r*) Wiersema et al. GCN 10263 (2009), (*s*) Cucchiara et al. GCN 10031 (2009), (*t*) Malesani et al. GCN 9942 (2009); Cenko et al. GCN 10049 (2009), (*u*) Cucchiara et al. GCN 9873 (2009), (*v*) Rau et al. GCN 9353 (2009); Ackermann et al. (2010), (*w*) Cenko et al. GCN 9053 (2009), (*x*) Chornock et al. GCN 9028 (2009), and (*y*) Greiner et al. *A&A* 498 89 (2009).

The Amati relation between E_{iso} and $E_{i,p}$ can be parametrized as follows:

$$\log \frac{E_{i,p}}{\mathrm{erg}} = k + m \log \frac{E_{iso}}{\mathrm{keV}}, \tag{1}$$

where k and m are the intercept and slope of this linear equation. For notation, we define $x = \log \frac{E_{iso}}{\mathrm{erg}}$ and $y = \log \frac{E_{i,p}}{\mathrm{keV}}$, and fit the correlated data $\{x_i, y_i\}$ with uncertainties $\{\sigma_{xi}, \sigma_{yj}\}$, to the linear relation $y = k + mx$. Following the description of Wang et al. (2015) [20], the parameter y should not only depend on x, but also depend on an extrinsic variance (σ_{ext}) to quantify the hidden cosmological parameters in E_{iso} through the luminosity distance (d_L). The optimal parameters (k, m and σ_{ext}) can be obtained by minimizing the chi-square function $\chi^2 = \sum_{i=0}^{N-1}(y_i - k - mx_i)^2/(\sigma_{yi}^2 + m^2\sigma_{xi}^2 + \sigma_{ext}^2)$, where N is the number of GRBs, such that the reduced $\chi^2 = 1$ [20]. This method gives a value for the parameter σ_{ext} to quantify the extrinsic error. The correlations coefficient for both energy range 1 - 10^4 keV and 1 - 10^5 keV corresponding to the 22 *Fermi* LGRBs are $\rho_{sp} = 0.79$ and $\rho_{sp} = 0.80$, respectively, which are very significant (see Table 3, column 4).

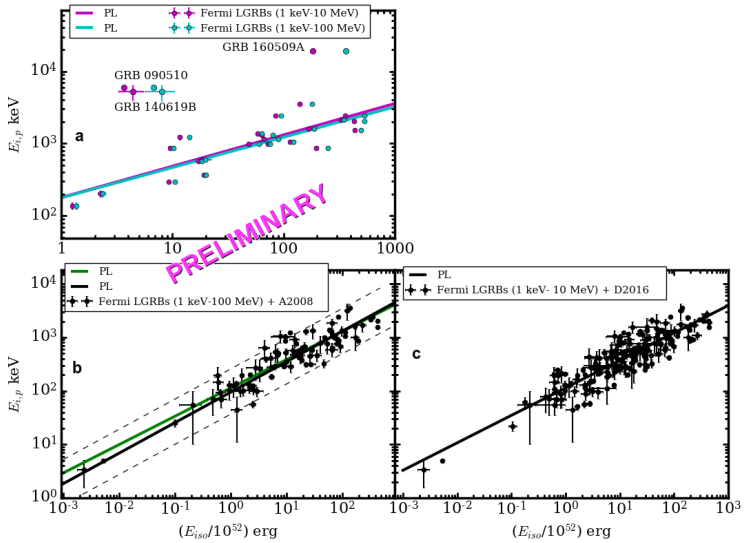

Figure 2. The Amati relation in the $E_{i,p}$ - E_{iso} plane. All the fitting lines are plotted over the data points when the reduced χ^2 is unity. In panel a) the magenta and cyan lines represent the fits to the *Fermi* LGRBs data with E_{iso} computed for (1 keV -10 MeV) and (1 keV - 100 MeV), respectively. In panel b) the green line depict the fit to the joint A2008 and *Fermi* LGRBs data, the black line show the A2008 fit and black dashed lines are the 2σ scatter limits of $E_{i,p}$ - E_{iso} correlation [10]. In panel c) the black line shows the fit to the joint D2016 and *Fermi* LGRBs (1 keV - 10 MeV) data. The fit parameters are reported in Table 3.

Table 3. The results of the $E_{i,p}$ - E_{iso} correlation fitting data when the reduced χ^2 is unity.

Figure	Reference	N	ρ_{sp}	m	k	σ_{ext}
a	*Fermi* LGRBs (1 keV - 10 MeV)	22	0.79	0.434 ± 0.071	178.858 ± 54.18	0.197 ± 0.022
	Fermi LGRBs (1 keV - 100 MeV)	22	0.80	0.420 ± 0.066	176.932 ± 53.105	0.194 ± 0.021
b	*Fermi* LGRBs + A2008	92	0.88	0.529 ± 0.027	112.790 ± 10.305	0.194 ± 0.027
c	*Fermi* LGRBs + D2016	184	0.87	0.513 ± 0.023	113.800 ± 8.125	0.205 ± 0.016

We have also estimated the free parameters (k, m and σ_{ext}) by using the combined *Fermi* LGRBs, A2008 and D2016 data sets. As an example, by using the reduced χ^2 for 22 *Fermi* LGRB data (E_{iso} computed in 1 keV - 10 MeV), the estimated value of k, m and σ_{ext} are ∼181.628, ∼0.430 and ∼0.26, respectively. When the reduced χ^2 is ∼ 1, the parameters k and σ_{ext} are reduced to 178.858 and 0.197, respectively. In Fig. 2a), we find SGRBs 140619B and 090510 as clear outliers of the correlations in the $E_{i,p} - E_{iso}$ plane. Long GRB 160509A is also considered as outlier due to the effect of joint spectral fitting by the Band and Comp functions. The peak energy obtained from this model [21] is higher in the $E_{i,p}$ - E_{iso} plane, but the effect on E_{iso} is insignificant. If we fit the data in Fig. 2b with a simple power law, we find an index ∼0.53 and a normalization ∼112, consistent with the results of previous analysis (e.g. Amati 2002). The best power law fit of the joint *Fermi* LGRBs (1 keV - 10 MeV) and D2016 data shown in Fig. 2c gives the index ∼0.51 and normalization ∼ 114 with the very significant Spearman's correlation coefficient $\rho_{sp} = 0.87$.

4. Conclusion

We have reported the correlation of $E_{i,p}$ and E_{iso} in the source rest frame for the GRBs with very high energy emission detected by the *Fermi*/LAT-GBM with known redshift. The spectral analysis has been performed using uniform time duration T_{90} and homogenous energy range selection. Using the parameters found from gamma-ray spectral modelling, $E_{i,p}$ and E_{iso} are computed which are strongly dependent on the cosmological model. The linear case with errors on both $E_{i,p}$ and E_{iso} axis, and extrinsic variance of the data has been shown, giving the χ^2 formula. The best-fit value of the parameter m is in the range 0.425-0.529, which can be compared to $m = 0.434$-0.513 obtained in all samples when the reduced χ^2 approaches to unity. Our results show that the *Fermi* LGRB emission, detected by LAT up to 10 MeV and 100 MeV, further provide a significant contribution to the study on the reliability of the Amati relation. In addition, we also found that LGRBs in the $E_{i,p} - E_{iso}$ plane follow similar correlation as measured using other instruments and short GRBs do not follow this correlation. Finally, the extremely energetic long GRB 080916C and GRB 090323 with significant GeV emission detected by the *Fermi*-LAT further confirm and extend the Amati relation with very high isotropic radiated energy $(5.33 \pm 0.19)\times10^{54}$ erg and $(5.35 \pm 0.17)\times10^{54}$ erg in the energy range 1 - 10^5 keV. We deduce that the *Fermi*-LAT/GBM GRBs with high energy emission are consistent with the Amati relation and could be used as effective cosmological standard candles.

Acknowledgments

The *Fermi*-LAT Collaboration acknowledges support for LAT development, operation and data analysis from NASA and DOE (United States), CEA/Irfuand IN2P3/CNRS (France), ASI and INFN (Italy), MEXT, KEK, and JAXA (Japan), and the K.A. Wallenberg Foundation, the Swedish Research Counciland the National Space Board (Sweden). Science analysis support in the operations phase from INAF (Italy) and CNES (France) is also gratefully acknowledged. The work presented in this paper was supported in part by an MWGR 2015 grant from the National Research Foundation with Grant No. 93273 and ORCID.

References

[1] Cucchiara A *et al.* 2011 *The Astrophysical Journal* **736** 7
[2] Bissaldi E *et al.* 2011 *The Astrophysical Journal* **733** 97
[3] Gehrels N and Razzaque S 2013 *Frontiers of Physics* **8** 661–678
[4] Riess A G *et al.* 1998 *The Astronomical Journal* **116** 1009
[5] Fichtel C *et al.* 1994 *The Astrophysical Journal Supplement Series* **94** 551–581
[6] Meegan C *et al.* 2009 *The Astrophysical Journal* **702** 791
[7] Atwood W *et al.* 2009 *The Astrophysical Journal* **697** 1071
[8] Amati L *et al.* 2002 *Astronomy & Astrophysics* **390** 81–89
[9] Amati L 2006 *Monthly Notices of the Royal Astronomical Society* **372** 233–245
[10] Amati L *et al.* 2008 *Monthly Notices of the Royal Astronomical Society* **391** 577–584
[11] Ghirlanda G *et al.* 2005 *Monthly Notices of the Royal Astronomical Society: Letters* **361** L10–L14
[12] Heussaff V, Atteia J L and Zolnierowski Y 2013 *Astronomy & Astrophysics* **557** A100
[13] Atteia J L 2003 *Astronomy & Astrophysics* **407** L1–L4
[14] Sakamoto T *et al.* 2009 *The Astrophysical Journal* **693** 922
[15] Demianski M, Piedipalumbo E, Sawant D and Amati L 2017 *Astronomy & Astrophysics* **598** A112
[16] Guiriec S *et al.* 2015 *The Astrophysical Journal* **814** 10
[17] Band D *et al.* 1993 *The Astrophysical Journal* **413** 281–292
[18] Ryde F 1999 *Astrophysical Letters and Communications* **39** 281 (*Preprint* `astro-ph/9811462`)
[19] Guiriec S *et al.* 2015 *The Astrophysical Journal* **807** 148
[20] Wang J, Wang F, Cheng K and Dai Z 2016 *Astronomy & Astrophysics* **585** A68
[21] Guiriec S *et al.* 2011 *The Astrophysical Journal Letters* **727** L33

Optimization of galaxy identification algorithms in large HI surveys

T Gqaza[1], R C Kraan-Korteweg[1], B Frank[1], M Ramatsoku[1,3], T H Jarrett[1], E Elson[1] and A C Schroeder[2]

[1] Department of Astronomy, University of Cape Town, Private Bag X3, Rondebosch, 7700, Cape Town, South Africa

[2] South African Astronomical Observatory, PO Box 9, Observatory, 7935, Cape Town, South Africa

[3] Kapteyn Astronomical Institute, University of Groningen, Landleven 12, 9747 AV Groningen, The Netherlands

E-mail: gqztem001@myuct.ac.za

Abstract. The upcoming neutral hydrogen (HI) blind SKA-precursor surveys like Fornax and LADUMA, will produce extremely large volumes of spectral data cubes. Fully automated source-finding and parametrization algorithms will prove more efficient than visual examination methods. Such algorithms have been developed and rigorously tested on simulated HI data cubes. Their performance is not fully known when it comes to spectral cubes with true HI line emission. In this paper, we present preliminary results on the comparison of three galaxy identification methods (i.e. visual, semi-automated and fully automated). For these tests, the Westerbork Synthesis Radio Telescope (WSRT) Perseus-Pisces (PP) HI data cube is used. Visually, we detected 194 galaxy candidates, of which 90.2% have semi-automated cross-matches. We also present preliminary results from the initial run of SoFiA applied on 44.4% of the data cube. The final outcome, after the full comprehensive analysis is finalised, will be fed back to pipeline developers for possible optimization.

1. Introduction

An in-depth study of the neutral hydrogen content of the universe is of paramount importance for understanding star-formation, gas and galaxy evolution. As a result various HI surveys are planned for the Square Kilometre Array (SKA) precursors MeerKAT, APERTIF and ASKAP (e.g. LADUMA [1], Fornax HI survey [2], Northern sky HI shallow survey [3] and WALLABY [4]). These surveys will produce large quantities of HI data cubes containing up to hundreds of thousands galaxies. Hence the traditional method of galaxy identification through visual inspection will prove cumbersome. An HI data cube is a three-dimensional representation of HI-line emission where two of the axes are spatial positions (e.g. RA and Dec) and the third one is frequency (i.e. the velocity of the HI emission).

In preparation for this big data epoch, a handful of fully-automated source-finding and parametrization software have been developed. These software are based on advanced source-finding algorithms like the Characterised Noise HI (CNHI) source-finder [5]; 2D-1D Wavelet Reconstruction source-finder [6]; the Smooth Plus Clip (S + C) source-finder [7] and the standard source-finder for the Australian SKA pathfinder (ASKAP), DUCHAMP [8].

In 2012, Popping et al. [9] tested three of the aforementioned source-finding algorithms. Their focus was on testing the reliability and completeness of each algorithm. The tests were conducted on two different 3D spectral data cubes, which contained simulated HI sources and continuum sources, respectively. In

parallel the same group tested DUCHAMP on a data cube containing real sources [10]. These studies partially led to the development of a more advanced and flexible fully-automated software known as the Source-Finding Application (SoFiA) [11]. SoFiA's primary objective is to search a spectral cube and identify sources, then extract HI parameters. It is the first software that combines three different source-finding algorithms (i.e. CNHI, S + C and the basic threshold source-finder). SoFiA uses negative detections to quantify source reliability [7]. It also uses busy functions [**?**] to describe HI global profiles of the detected sources [12].

In this paper, we present preliminary results of a comparison of three different source-finding methods, namely visual inspection, semi-automated and fully automated. Fully automated software like SoFiA and its predecessors are ideal for bigger surveys. They can process large amounts of data in relatively short time frames. They also utilize recent statistical methods to quantify reliability. Knowing how these fully automated software tools compare to visual inspection on large spectral data cubes is critical. For smaller surveys (hundreds of sources) a combination of automated and Visual identification methods might produce complete and reliable results. Hence we also explore semi-automated source identification methods.

2. HI data cube

The data cube used in this paper is the Perseus-Pisces Supercluster (PP) hexagonal mosaic covering 9.6 sq.deg. It was observed in 2012 with the Westerbork Synthesis Radio Telescope (WSRT) in the Netherlands. The data cube is composed of 35 pointings and each is separated by 0.5 deg. Each pointing has a total integration time of 2×6 hours. The total effective bandwidth of the volume surveyed is 67 MHz. It covers a Doppler-shifted velocity range of $cz = 2400 - 16600$ km s^{-1}. The data cube has rms noise of 0.4 mJy.

3. Methodology

3.1. Visual inspection: Galaxy identification and parametrization

We intended to produce a reliable WSRT ZoA[1] PP source catalogue by visual search. We achieved this by having three authors search 4 out of 9 subcubes spanning the entire velocity range of $2400-16600$ km s^{-1}, using a visualisation tool (KVIS) from KARMA [13] . Each searcher compiled a candidate list. All three lists were handed to one author who acts as an adjudicator, to produce a final candidate list. In addition the adjudicator searched the rest of the subcubes. The HI parametrization was carried out using a specialized python script and MBSPECT module from MIRIAD [14]. For each candidate a corresponding sub-volume was extracted, from which the weighted emission sum along the spectral line was calculated. Each resulting one-dimensional spectrum was visualised and a lower-order polynomial was fit to the channels without HI emission and subtracted. The integrated flux density ($S_{\rm int}$) and the peak flux ($S_{\rm peak}$) were calculated across the channels with line emission. The systemic velocity ($V_{\rm sys} = cz$) was taken as the average of velocities corresponding to 50% of the peak flux from the line profile. Linewidths at 20% and 50% level of the peak flux density (ω_{20} and ω_{50}) were calculated using a width-maximiser method from MBSPECT. For each detection a zeroth moment (M_0) map was produced by collapsing the subcube along the spectral axis. Another miriad module (i.e. IMSAD) was used to fit a Gaussian to the histogram of the M_0 in order to get a flux-weighted centroid of the detected candidate.

3.2. Semi-automated source identification

In 2016, Ramatsoko et al. [15] published a source catalogue of the WSRT ZoA PP data cube. Here, we present the summary of the galaxy identification procedure they used (for details, see [15]). They first corrected for spatial noise variation by multiplying the cube by an inverse square weighted noise (σ^{-2}) in each of the 35 pointings. The original cube of spatial resolution (2300×1600) was smoothed up to (3000×3000). The resulting cube was then smoothed in velocity to four different resolutions, namely: Hanning smoothing (16.5 km s^{-1}) and a Gaussian smoothing kernel corresponding to four, six and eight channels (i.e. 33, 49.5 and 66 km s^{-1}). They ran the Groningen Image Processing System (GIPS) software on all eight different angular and spectral resolution combinations. A detection was accepted if it met

[1] Zone of Avoidance (ZoA) is the region of the sky which appears devoid of extragalactic objects when viewed on optical wavelengths.

the galaxy criteria explained in Ramatsoko et al. [5]. This method led to the detection of 683 galaxy candidates. After post visual inspection of all candidates, 235 out of 683 were identified as imaging artefacts or RFIs[2] and were rejected. Further analysis led to a rejection of another 237 candidates as they had features consistent with noise peaks. This resulted in a semi-automated catalogue with 211 galaxies.

4. Early results

4.1. Visual and semi-automated

A total number of 194 detections is achieved through visual inspection of the entire spectral cube. Figure 1 shows the distribution of total HI mass as a function of radial velocity (also known as a sensitivity curve). The black and the red curves show predicted HI mass limits of this survey assuming a 3σ flux detection for 100 and 250 $\mathrm{km\,s^{-1}}$ linewidth galaxies, respectively. Green dots indicate detections with ω_{50} less than 100 $\mathrm{km\,s^{-1}}$, red dots are detections with ω_{50} in-between 100 and 250 $\mathrm{km\,s^{-1}}$ and blue dots have ω_{50} greater than 250 $\mathrm{km\,s^{-1}}$. The detected candidates have a total HI mass ($\log(\mathrm{M_{HI}/M_{\odot}})$ ranging from 7.81 to 10.24 (see the right panel of Figure 2). The visual method finds low HI mass detections across the entire velocity range as well as narrow-linewidth galaxy candidates.

4.2. Semi-automated counterpart

We use a position-velocity-based algorithm to search for cross-matches. Each galaxy has a unique flux weighted centroid, but it can slightly differ to that of its counterpart due to the manner in which it was derived. To counterpoise this bias, we allow a spatial (Δs) and spectral deviation (Δv) of 3000 and 100 $\mathrm{km\,s^{-1}}$, respectively from the centroid. Let us suppose galaxy X with coordinates (ℓ, b, v) has a counterpart X', then X' coordinates (ℓ', b', v') must conform to Eq. 1, where s is either the Galactic longitude (ℓ) or latitude (b).

$$s - \Delta s \leq s' \leq s + \Delta s \quad v - \Delta v \leq v' \leq v + \Delta v \tag{1}$$

Table 1. Summary of cross match galaxies between visual and semi-automated output catalogue.

Measurements	**Visual**	**Semi-automated**
`No.`of galaxies	194	211
`No.`of galaxies with counterparts	175 (90.2%)	175 (82.9%)
`No.`of galaxies without counterparts	19 (9.8%)	36 (17.1%)
`Narrow-linewidths:`$\omega_{20} \leq 100$ $\mathrm{km\,s^{-1}}$	47.4%	19.4%
`Intermediate-linewidths:`$100 \leq \omega_{20}\,[\mathrm{km\,s^{-1}}] \leq 250$	42.1%	77.8%
`Massive-linewidths:`$\omega_{20} > 250$ $\mathrm{km\,s^{-1}}$	10.5%	2.8%

[2] RFIs are man made Radio Frequency Inference signals (e.g. Global Positioning Satellites) that could be orders of magnitudes stronger than the observed celestial signal.

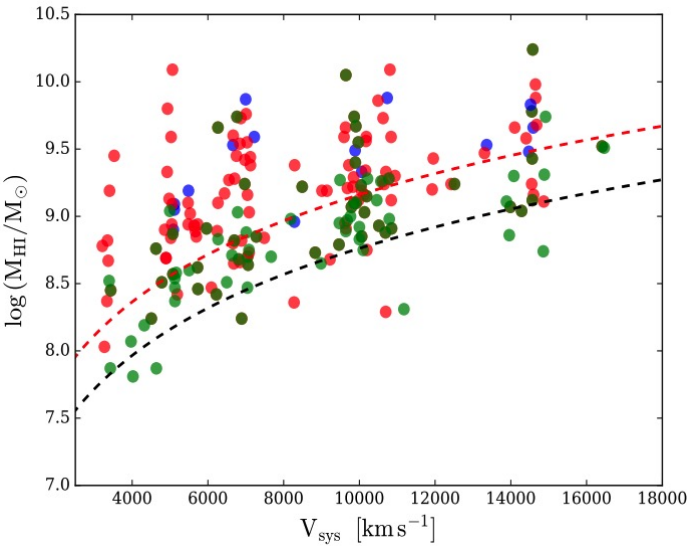

Figure 1. The logarithm of total HI mass of all detected galaxies (through Visual inspection) as a function of radial velocity. The red and the black dashed lines show the HI mass limit of the WSRT dataset assuming a 3σ detection with 100 and 250 $\mathrm{km\,s^{-1}}$ linewidths, respectively. The green dots indicate detected galaxies with measured linewidths less than 100 $\mathrm{km\,s^{-1}}$. The red dots indicate galaxies of linewidths between 100 & 250 $\mathrm{km\,s^{-1}}$ whereas the blue dots show galaxies with linewidths greater than 250 $\mathrm{km\,s^{-1}}$.

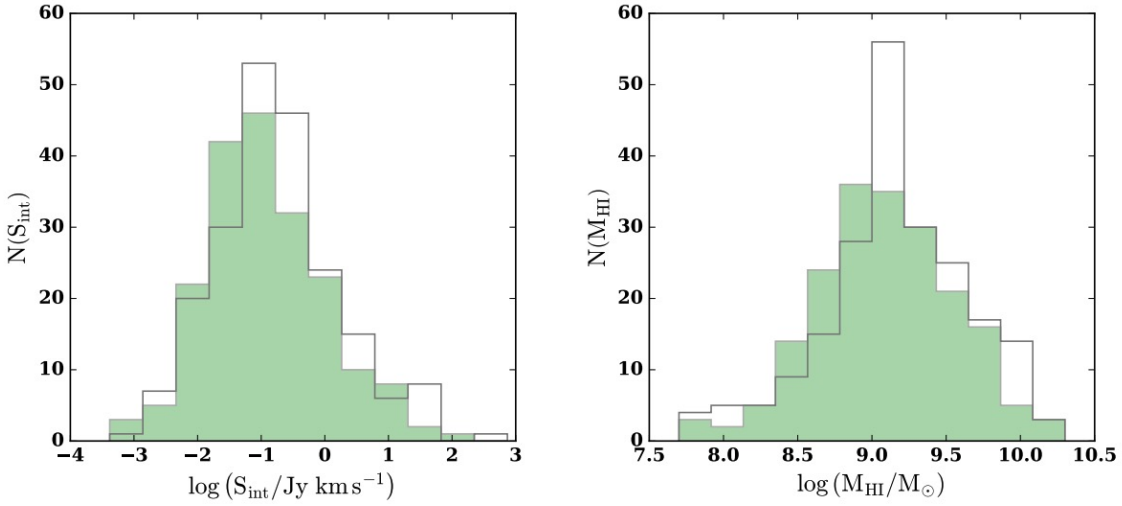

Figure 2. HI parameter comparison between visual and semi-automated galaxy detection in the WSRT PP HI data cube. Green indicates the HI distribution based on the visual catalogue, whereas the open grey histogram is based on semi-automated results. Left panel: logarithm distribution of integrated flux $\log(\mathrm{S_{int}/Jy\ km\,s^{-1}})$, right panel: the logarithmic distribution of HI mass $\log(\mathrm{M_{HI}/M_\odot})$.

Of the 194 visual detections, 175 (90.2%) semi-automated cross-matches were found. Table 1 presents a cross match summary between the two methods. In Figure 2 we compare the distribution of the HI parameters of identified galaxies from visual versus semi-automated catalogues (see Sect. 3.2). The right panel shows the logarithmic distribution of total HI mass. The green histogram represents visual detections, and the non-filled grey histogram represents the semi-automated distribution. The semi-automated HI mass distribution ranges from $\log(\mathrm{M_{HI}/M_\odot}) = 7.70$ to 10.30 with a mean HI mass of $\log(\mathrm{M_{HI}/M_\odot}) = 9.15$. On the other hand, the visual HI distribution ranges from $\log(\mathrm{M_{HI}/M_\odot}) = 7.81$ to 10.24, with a mean of $\log(\mathrm{M_{HI}/M_\odot}) = 9.08$. The left panel shows the logarithm of the integrated line flux, with the visual integrated mean line flux being 0.67 $\mathrm{Jy\,km\,s^{-1}}$ and the minimum detected flux

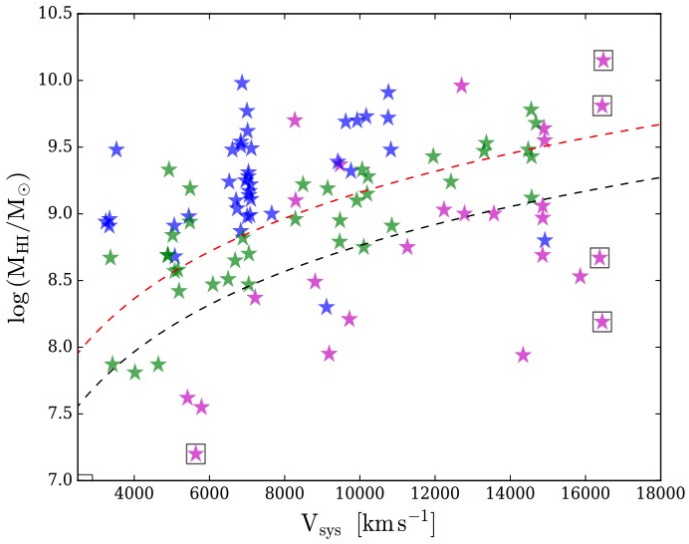

Figure 3. The logarithm of total HI mass of all detected galaxies (through visual inspection) as a function of radial velocity. The red and the black dashed lines show the HI mass limit of our survey assuming a 3σ detection with 100 and 250 km s^{-1} linewidths. Blue stars indicate galaxies identified by both visual inspection and SoFiA, green stars: galaxies identified by the visual method only. Magenta stars: galaxy candidates identified by SoFiA only. Stars enclosed by black open squares: SoFiA's false detections.

is 34 Jy km s^{-1}, while semi-automated method returns a minimum integrated flux of 40 Jy km s^{-1} and $S_{\rm int} = 0.84$ Jy km s^{-1}.

The two galaxy identification methods have a good overlap between. A large fraction of the sources that don't overlap are fainter detections below the sensitivity limit. A broader discussion is given in section 5.

4.3. SoFiA *preliminary result*

SoFiA has over 50 parameters that have to be set before it can be run successfully. For a quick look at the data, the default settings can yield reasonable results, but aiming for a more reliable and complete search fine tuning is required. There are at least 15 unique parameters for which their combinations lead to immediate differences in the total number of identified galaxy candidates. To get the most optimal results in terms of reliability and completeness, we extracted two subcubes containing a bright and a faint galaxy from the cube. Where reliability is defined as the ratio of True Positives (TP) over total number of detections (false positives + true positives), and completeness as the total number of TP over total number of all sources in the cube (both detected and undetected). One parameter file was tuned to identify the faint sources, a second one tuned SoFiA to detect the bright sources. The two parameter files were then merged into one file which in principle should then detect from faint narrow-linewidths sources to bright and wider-linewidths ones. We used the S+C source-finder with a flux threshold of 3σ (i.e. 1.20 mJy). All detections with reliability greater than 95% were accepted as positive candidates. The merged parameter file was run in four of the subcubes making up the WSRT PP HI data cube. Figure 3 presents the galaxy candidates obtained by running SoFiA. To get an idea of the performance of SoFiA, we plot the preliminary results alongside the visual results (see Figure 1). With SoFiA we identified 67 galaxy candidates, 56.7% have visual cross-matches (blue stars). But there are 43.3% without counterparts (magenta stars). The magenta stars enclosed by open black squares indicate galaxies that are consistent with noise or are found on the edges of the cube (i.e. $V_{\rm sys} \geq 16\,000$ km s^{-1}) where the noise is relatively high and a detection's reliability are compromised. Green stars show candidates within the searched fields that are not yet identified with SoFiA.

5. Discussion and conclusion

We have shown that both the visual and semi-automated galaxy identification methods extract a similar number of galaxies (194 and 211, respectively). Unlike the visual method, the semi-automated method was applied on smoothed cubes. Out of 194 visually identified galaxies, only 9.3% have no semi-automated cross-matches, compared to 17.6% of semi-automated. This means that the semi-automated has found

more sources than the Visual method. All the sources without cross-matches will be further assessed for their likelihood of being genuine and if so, why the respective methods were unsuccessful in uncovering them.

We compiled a parameter file (for running SoFiA) that in principle should return more than 80% of the galaxies identified through the visual method but so far we have managed 56.7%. In order to achieve higher completeness, further fine-tuning of the parameter file are currently underway. To quantify reliability of each detection, careful visual examination of all sources without counterparts is necessary. This will allow us to do a comprehensive analysis of all three methods; give feedback to the SoFiA developers on where possible optimization can be made to result to a more complete and reliable source catalogue and advise SoFiA uses on which combination of parameters to fine tune and under which conditions.

Acknowledgements

This work is based upon a research supported by the South African National Research Foundation (NRF), the Department of Science and Technology (DST) and National Astrophysics and Space Science Program (NASSP). We thank Prof. Patricia A. Henning for her contribution to this work. TG is immensely grateful to Dr. Paolo Serra, Dr. Gyula Jozsa and Dr. Khaled Said for useful discussions. We also thank the developers of SoFiA for having an open ear and showing interest on the outcome of this project.

References

[1] Holwerda B W, Blyth S L, and Baker A J 2011 *Proceedings of the International Astronomical Union* **7** 496499
[2] Serra P 2011, *The MeerKAT Fornax Survey Fornax, Virgo, Coma et al., Stellar Systems in High Density Environments* page 49
[3] Verheijen M, Oosterloo T, Heald G and Van Cappellen W 2009 *Panoramic radio astronomy: wide-field 1-2*
[4] Duffy, A R Meyer, M J Staveley-Smith, L Bernyk, M Croton, D J Koribalski, B S Gerstmann, D and Westerlund, S , 2012 , *Monthly Notices of the Royal Astronomical Society* , **426** , 3385-02
[5] Jurek R 2012 *Publications of the Astronomical Society of Australia* **29** 251-61
[6] Flöer L and Winkel B 2012 *Publications of the Astronomical Society of Australia* **29** 244-50
[7] Serra P, Jurek R and Flöer L 2012 *Publications of the Astronomical Society of Australia* **29** 296-00
[8] Whiting M T 2012 Monthly Notices of the Royal Astronomical Society **421** 3242-56
[9] Popping A, Jurek R, Westmeier T, Serra P, Flöer L, Meyer M and Koribalski B 2012 *Publications of the Astronomical Society of Australia* **29** 318-339
[10] Westmeier T, Popping A and Serra P 2012 *Publications of the Astronomical Society of Australia* **29** 276-95
[11] Serra P et. al 2015 *Monthly Notices of the Royal Astronomical Society* **448** 1922-29
Westmeier T Jurek R Obreschkow D Koribalski B S and Staveley-Smith L 2013 *Monthly Notices of the Royal Astronomical Society* **438** 1176-90
[12] Gooch R 2006 *KARMA Users Manual, ATNF* reference link
[13] Sault R and Killeen N 1996 *Multichannel image reconstruction image analysis and display (miriad) users guide, ATNF* reference-link
[14] Ramatsoku M Verheijen M Kraan-Korteweg R JÂťozsa G Schröder A Jarrett T Elson E van Driel W de Blok W and Henning P 2016 *Monthly Notices of the Royal Astronomical Society* **460** 923-41
[15] Westmeier T and Jurek R and Obreschkow D and Koribalski B S and Staveley-Smith L 2014 *The busy function: a new analytic function for describing the integrated 21-cm spectral profile of galaxies, mnras* **438** 1176-90

Reverberation mapping of a $z \sim 0.375$ active galactic nucleus

M.S Hlabathe[1,2], E. Romero-Colmenero[1,3], S. M. Crawford[1] and LCO AGN Key collaboration

[1]South African Astronomical Observatory, PO Box 9, Observatory, Cape Town, South Africa
[2]Astronomy Department, University of Cape Town, Private Bag X3, Rondebosch 7701, South Africa
[3]Southern African Large Telescope, PO Box 9, Observatory, Cape Town, South Africa

E-mail: mh@saao.ac.za

Abstract. Reverberation mapping is a technique that measures the time lag between the variable optical continuum from the accretion disk and the spectral line emission from the photo-ionized gas surrounding a super-massive black hole. The time lag is used to estimate the size of the emitting region, which is then assumed to be related to the mass of the super-massive black hole in the core of the active galactic nucleus. Using observations from the Southern African Large Telescope and Las Cumbres Observatory, we measure a time lag of $28.1^{+10.4}_{-27.7}$ days between the continuum and the broad Hβ feature in SDSS J143832.40+024804.1, an active galactic nucleus at $z = 0.375$. When combined with the velocity dispersion of the Hβ feature, we get a 1-sigma upper limit on the black hole mass to be 3.1×10^8 M$_\odot$. These are preliminary results, extensive checks will be made to further refine the mass of the central black hole of SDSS J143832.40+024804.1.

1. Introduction

Broad emission lines are one of the prominent characteristics of type 1 Active Galactic Nuclei (AGN) [1]. Owing to the limitations of the resolution of present and even foreseeable future astronomical instruments, we have no way to resolve the broad emission line regions (BLRs) in AGN by direct observations. However, the structure of AGN on the smallest possible scales can still be probed through a process known as reverberation mapping [2, 3].

In AGN, stochastic continuum emission is produced from matter falling onto the accretion disk causing thermal instabilities within the disk. This continuum emission induces emission lines from gas clouds in the nearby (very few parsecs) BLR and more distant (tens of parsecs) narrow line region (NLR). Observationally, the emission lines in the BLR are broadened due to the high velocities and large Doppler shifts of the emitting clouds orbiting the central super-massive black hole (SMBH). Any variability in the continuum is 'echoed' by the gas clouds in the BLR after some time, with a time delay (τ) that depends on the light-travel time from the accretion disk to the BLR ($r = c\tau$). Combining τ and the velocity dispersion (σ_{line}) of the broad emission line, we can estimate the SMBH mass as $\mathrm{M_{SMBH}} = f r \sigma^2_{line}/G$, where f is a dimensionless factor to take into account geometric and orientation effects. Blandford & Mckee [2] were the first to establish reverberation mapping in trying to measure the black hole mass of an AGN.

Given the successful application of dynamical methods and reverberation mapping, there is strong evidence (both observational and theoretical) that there is a close connection between SMBH growth and galaxy evolution. Empirical relationships have been derived between the SMBH mass and the luminosity of the host galaxy bulge ($M_{BH} - L_{bulge}$), and between the SMBH mass and the spheroid velocity dispersion of the host galaxy bulge ($M_{BH} - \sigma_*$) for both nearby quiescent galaxies [4, 5] and distant AGN. To further understand the SMBH-galaxy connection, we need to compare and calibrate these correlations between local and distant samples. Unfortunately, due to observational difficulties associated with the reverberation mapping technique, there have been only $\sim$ 50 SMBH mass estimates to date [6–10, e.g.]. The main difficulty lies in obtaining long monitoring campaigns with good signal-to-noise and cadence to ensure an accurate measurement of SMBH masses - poor reverberation mapping sampling leads to SMBH mass estimates with larger uncertainties [11].

In this paper, we estimate the SMBH mass in SDSS J143832.40+024804.1, an AGN at a redshift of $z \sim 0.375$, based on our Hβ observations. It is at this redshift that both Hβ and MgII(2800Å) can be observed at optical wavelengths, providing the unique opportunity to calibrate the SMBH mass estimates between these two samples (Hβ and MgII(2800Å)). This paper is the first step in a campaign that will also include MgII(2800Å) observations. We describe the observations and data analysis in Sect. 2, the measurement of the time lag in Sect. 3 and the estimate of the mass of the SMBH in Sect. 4.

2. Observations and Data analysis

We have obtained spectra from Southern African Large Telescope (SALT)[1] and continuum images for three AGN from several reverberation mapping campaigns as part of the Las Cumbres Observatory (LCO)[2] Key Project on Reverberation Mapping of AGN Accretion Flows [12]. In this paper we undertake the analysis of one of these AGN, SDSS J143832.40+024804.1, using only spectroscopic data from SALT. To carry out this analysis, continuum and emission line light curves are both derived from spectroscopy to estimate the lag and to measure the width of the emission line.

2.1. Spectroscopy

The spectra of SDSS J143832.40+024804.1 (ra = 14:38:32.40, dec = +02:48:04.20, J2000), were collected using SALT over 20 nights, from March 2015 to July 2016. In this work, we focus on the 16 spectra from 2015. The RSS spectrograph covers a wavelength range from $5200 - 8220$Å with a spectral resolution of $R \sim 1170$. Data reduction was handled using PySALT[3] [13]. The zSALT[4] pipeline currently incorporates PySALT and IRAF to fully automate the reduction steps which include bias subtraction, gain correction, cross-talk correction, amplifier mosaicing, and cosmic ray removal. The wavelength solution was calculated interactively using PySALT *specidentify*, a task to identify arc lines. The multiple spectral images taken on the same night were then median combined to produce one spectral image. The spatial center and the FWHM of SDSS J143832.40+024804.1 were used to extract the 1-D spectra. Flux calibration using spectrophotometric standard stars was done using *specsens*, a task defined in PySALT. The standard star calibration was then applied to spectra with the same observing configuration. Finally, telluric absorption was corrected for in our spectra.

Next, we flux calibrated our spectra based on the flux of the narrow emission line [O III] λ5008Å, so that there is constant flux of [O III] λ5008Å from one spectrum to the next.

[1] https://www.salt.ac.za
[2] https://lco.global
[3] http://pysalt.salt.ac.za/
[4] https://github.com/crawfordsm/zSALT

This is because we assumed the [O III] λ5008Å line not to be variable in the timescale of our monitoring campaign: the light travel time across the NLR is large (of the order of years) and the recombination time is also large (order of years), so for any short-term variability (few weeks to months), [O III] λ5008Å flux is essentially constant [14]. This process was accomplished by first, selecting the high signal-to-noise spectrum from 2015-03-03 as our reference spectrum. We then fitted the [O III] λ5008Å line in each individual spectrum, measuring its flux and rescaling the entire spectrum based on the flux of our chosen reference spectrum. We then aligned our spectra using the centre of the [O III] λ5008Å line in the reference spectrum. From the [O III] λ5008Å line recalibrated spectra, we construct the mean spectrum for Year 1 (2015), which can be seen in Fig 1.

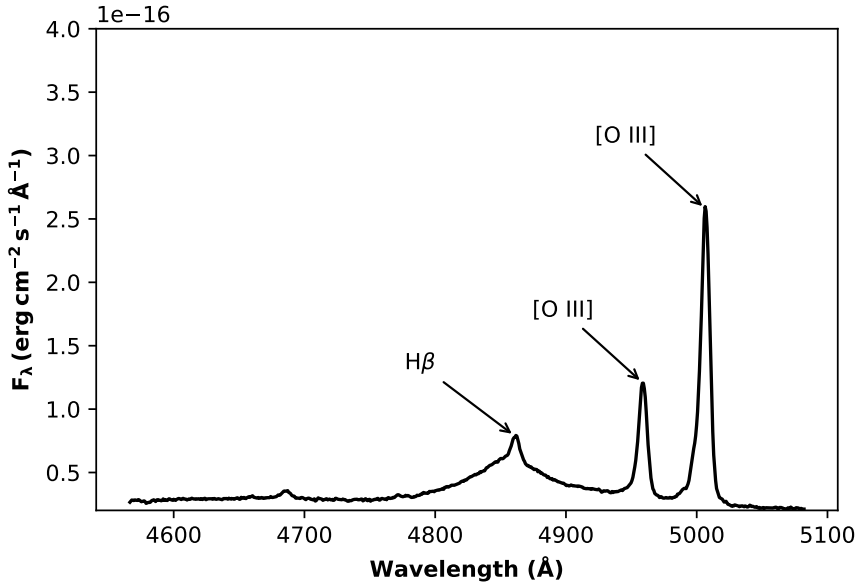

Figure 1. The mean spectrum of SDSS J143832.40+024804.1 for Year 1.

3. Time Lag Measurement

The spectroscopic continuum light curve at 5080Å and spectroscopic Hβ light curve are shown in Fig. 2. Both the Hβ light curve and continuum light curve at 5080Å were obtained through the use of *PREPSPEC* [15].*PREPSPEC* again re-calibrated our [O III] λ5008Å pre-normalized spectra using the method described in [16]. After PREPSPEC is done with the flux calibration, it combines all individual spectra to produce mean and rms spectra. *PREPSPEC* then decomposes the spectra into various components, allowing for the measurements of the continuum and Hβ light curves. The Hβ light curve was obtained by integrating the flux after subtracting the best-fitting model components except for the broad Hβ model. The continuum light curve is generated by measuring flux at 5080Å in the rest frame. We then quantify the amplitude variability of the Hβ and continuum light curves as 0.061 ± 0.003 and 0.264 ± 0.004 respectively. The relatively small Hβ amplitude variability will limit the reliability of the time lag measurement [17].

3.1. Cross correlation

We employ the interpolation cross correlation function (ICCF, [18]) as implemented by [19] to cross correlate the Hβ and continuum light curve at 5080Å. The cross correlation function

(CCF) is measured twice. First by cross correlating the continuum with interpolated Hβ light curve, second by cross correlating the interpolated continuum with Hβ light curve. The final cross correlation is taken as the average of the two cross correlation results[5]. We define our cross correlation lag by the centroid τ_{cent} and the peak τ_{peak}. We report the lag of $\tau_{cent} = 28.1$ days and $\tau_{peak} = 29.0$ days (e.g., Fig 3).

To estimate the lag uncertainties, we employed the flux randomization and random subset selection method (FR/RSS, [20]). For each realization, N (same size as the original set) pairs of randomly selected measurements are drawn from the original dataset regardless of whether or not they have been previously selected. This results in some of the pairs being excluded and others being selected more than once. In the resulting set, redundant measurements are ignored which effectively reduces the set to typically 37% of the original set. Each measurement A_i from the drawn subset is modified by adding random Gaussian deviates based on the associated error α_i. Each drawn subset gives a cross-correlation series from which τ_{cent} and τ_{peak} are derived. Many realizations, in this case 3000, are used to build up a cross-correlation distribution which yields the median lag (τ_{cent} and τ_{peak}) and the 68.27% confidence interval. From the distribution, we obtained the uncertainties as $\tau_{cent} = 28.1^{+10.4}_{-27.7}$ days and $\tau_{peak} = 29.0^{+10.2}_{-32.0}$ days.

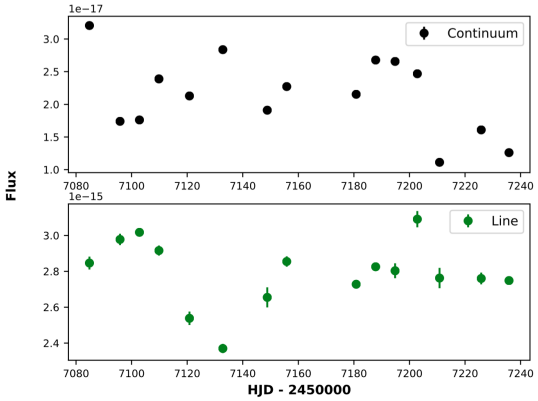

Figure 2. Continuum at 5080Å (top panel) and broad Hβ light curve (lower panel).

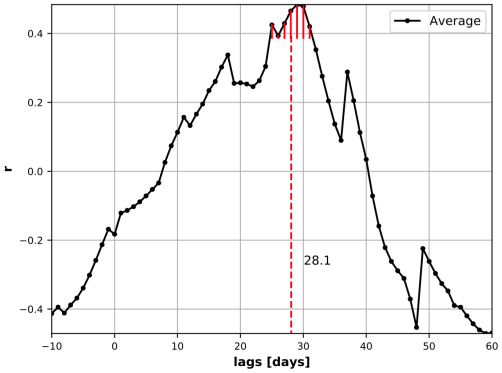

Figure 3. The CCF of Hβ and continuum light curves of SDSS J143832.40+024804.1 using only Year 1. The red dotted lines indicate all values above 80% threshold used to calculate τ_{cent}, yielding 28.1 days. We also record a τ_{peak} of 29.0 days. The lags are from -10 to 60 with the spacing of 1 day.

4. Black Hole Mass

To estimate the mass of the super-massive black hole, we need two parameters, the lag τ and the velocity dispersion of the emission line σ_{line}. σ_{line} is usually obtained from the rms spectra, the variable part of the emission line. Given that our rms spectra has a very weak Hβ variability and is dominated by residuals, we use the mean spectra instead. We construct the mean spectra by subtracting contributions from the narrow lines from each of the individual spectrum used to create the mean spectra. We used the fact that the ratio between [O III] λ5008/[O III] λ4959 is fixed at a value of 3, whereas the ratio Hβ_{narrow}/[O III] λ5008 varied from spectrum to spectrum. Since we measured our Hβ line width from the mean spectra, we adopt the [21]

[5] https://github.com/hlabathems/iccf

calibration of the dimensionless factor for the line dispersion derived from the mean spectra, $f = 3.85$. Combining τ and σ_{line}, the black hole mass of $2.2^{+0.9}_{-2.2}\,(10^8\,\mathrm{M}_\odot)$ was calculated. Due to under-sampling of our data, our measured time lag (and also the black hole mass) is consistent with zero. We also state that our light curves do not have enough data points and do not show significant variability to deduce beyond conviction that Hβ light curve does indeed lag the continuum light curve. Therefore the black hole mass we quote here of $3.1 \times 10^8\,\mathrm{M}_\odot$ is just an upper limit (1-sigma upper limit), and is based on the assumption that the two light curves are correlated.

Table 1. Reverberation mapping measurements of SDSS J143832.40+024804.1

AGN	Line	Amplitude variability	τ_{cent}	τ_{peak}	σ_{line}	FWHM	Mass
			(Days)	(Days)	(km s^{-1})	(km s^{-1})	(10^8 M$_\odot$)
1438	Hβ	0.061 ± 0.003	$28.1^{+10.4}_{-27.7}$	$29.0^{+10.2}_{-32.0}$	3235 ± 30	4974 ± 220	$2.2^{+0.9}_{-2.2}$

5. Summary

We used the spectra taken with SALT during 2015 campaign to measure the mass of the central black hole in SDSS J143832.40+024804.1. We then constructed Hβ and continuum light curves from the individual spectra using iraf, pysalt and prepspec, and we measure the Hβ lag to be $28.1^{+10.4}_{-27.7}$ days and $29.0^{+10.2}_{-32.0}$ days for τ_{cent} and τ_{peak}, respectively. We measure the velocity dispersion of the broad Hβ line to be $3235 \pm 30\,(\mathrm{km\ s^{-1}})$ from the mean spectra. Combining the Hβ lag (τ_{cent}) estimates with the velocity dispersion measurement obtained from the width of the Hβ emission line, we measure a mass for the central black hole of $2.2^{+0.9}_{-2.2}\,(10^8\,\mathrm{M}_\odot)$. Our large uncertainty is primarily due to under-sampling of the light curve, and it will improve with the analysis of the full set of observations for SDSS J143832.40+024804.1. Future analysis and observations will allow calibrating our black hole mass by placing it in context to the most recent $M_{BH} - L_{bulge}$ and $M_{BH} - \sigma_*$ measurements.

Acknowledgements

MH acknowledges the NRF PDP and SAAO for support. All of the observations reported in this paper were obtained with SALT. We thank the observers and staff at SALT and LCO.

References

[1] Seyfert C K 1943 *ApJ* **97** 28

[2] Blandford R D and McKee C F 1982 *ApJ* **255** 419–439

[3] Peterson B M 1993 *PASP* **105** 247–268

[4] Ferrarese L and Ford H 2005 *Space Sci. Rev.* **116** 523–624 (*Preprint* `astro-ph/0411247`)

[5] Kormendy J and Gebhardt K 2001 Supermassive black holes in galactic nuclei *20th Texas Symposium on relativistic astrophysics* (*American Institute of Physics Conference Series* vol 586) ed Wheeler J C and Martel H pp 363–381 (*Preprint* `astro-ph/0105230`)

[6] Wandel A, Peterson B M and Malkan M A 1999 *Astronomische Nachrichten* **320** 319

[7] Kaspi S, Smith P S, Netzer H, Maoz D, Jannuzi B T and Giveon U 2000 *ApJ* **533** 631–649 (*Preprint* `astro-ph/9911476`)

[8] Peterson B M, Ferrarese L, Gilbert K M, Kaspi S, Malkan M A, Maoz D, Merritt D, Netzer H, Onken C A, Pogge R W, Vestergaard M and Wandel A 2004 *ApJ* **613** 682–699 (*Preprint* astro-ph/0407299)

[9] Bentz M C, Walsh J L, Barth A J, Baliber N, Bennert V N, Canalizo G, Filippenko A V, Ganeshalingam M, Gates E L, Greene J E, Hidas M G, Hiner K D, Lee N, Li W, Malkan M A, Minezaki T, Sakata Y, Serduke F J D, Silverman J M, Steele T N, Stern D, Street R A, Thornton C E, Treu T, Wang X, Woo J H and Yoshii Y 2009 *ApJ* **705** 199–217 (*Preprint* 0908.0003)

[10] Denney K D, Peterson B M, Dietrich M, Vestergaard M and Bentz M C 2009 *ApJ* **692** 246–264 (*Preprint* 0810.3234)

[11] Park D, Woo J H, Treu T, Barth A J, Bentz M C, Bennert V N, Canalizo G, Filippenko A V, Gates E, Greene J E, Malkan M A and Walsh J 2012 *ApJ* **747** 30 (*Preprint* 1111.6604)

[12] Valenti S, Sand D J, Barth A J, Horne K, Treu T, Raganit L, Boroson T, Crawford S, Pancoast A, Pei L, Romero-Colmenero E, Villforth C and Winkler H 2015 *ApJ* **813** L36 (*Preprint* 1510.07329)

[13] Crawford S M, Still M, Schellart P, Balona L, Buckley D A H, Dugmore G, Gulbis A A S, Kniazev A, Kotze M, Loaring N, Nordsieck K H, Pickering T E, Potter S, Romero Colmenero E, Vaisanen P, Williams T and Zietsman E 2010 PySALT: the SALT science pipeline *Observatory Operations: Strategies, Processes, and Systems III* (*Proc. SPIE* vol 7737) p 773725

[14] Peterson B M 2009 *Active galactic nuclei* p 138

[15] Shen Y, Horne K, Grier C J, Peterson B M, Denney K D, Trump J R, Sun M, Brandt W N, Kochanek C S, Dawson K S, Green P J, Greene J E, Hall P B, Ho L C, Jiang L, Kinemuchi K, McGreer I D, Petitjean P, Richards G T, Schneider D P, Strauss M A, Tao C, Wood-Vasey W M, Zu Y, Pan K, Bizyaev D, Ge J, Oravetz D and Simmons A 2016 *ApJ* **818** 30 (*Preprint* 1510.02802)

[16] van Groningen E and Wanders I 1992 *PASP* **104** 700–703

[17] Peterson B M 2014 *Space Sci. Rev.* **183** 253–275

[18] Gaskell C M and Sparke L S 1986 *ApJ* **305** 175–186

[19] White R J and Peterson B M 1994 *PASP* **106** 879–889

[20] Peterson B M, Wanders I, Horne K, Collier S, Alexander T, Kaspi S and Maoz D 1998 *PASP* **110** 660–670 (*Preprint* astro-ph/9802103)

[21] Collin S, Kawaguchi T, Peterson B M and Vestergaard M 2006 *A&A* **456** 75–90 (*Preprint* astro-ph/0603460)

Modelling the hardening of gamma-ray spectra by extragalactic background light

Ayman M. Kudoda[*1], **A. Faltenbacher**[*]

[*]School of Physics, University of the Witwatersrand, Johannesburg 2050, South Africa.

E-mail: [1]ayman.kudoda@students.wits.ac.za

Abstract. The interactions of Extragalactic Background Light (EBL) photons and γ-rays from distant quasars result in the steepening of the γ-ray spectrum at very high energies. The underlying process is the γ-ray absorption induced by pair production ($\gamma + \gamma' \rightarrow e^+ + e^-$) which is dependent on γ-ray energy and EBL energy density. We present a realistic model of the EBL based on the semi-analytical galaxy catalogues from the Millennium data base plus a homogeneous component assumed to be the accumulated light from distant galaxies. This approach reflects the fluctuations in the EBL due to the inhomogeneous galaxy distribution in a realistic manner. Our model predicts well the steepening of the spectral index of distant γ-ray sources as a function of redshift. In agreement with our previous purely analytical results the differences in the opacity due to individual γ-ray paths experiencing different EBL fluctuations are negligible.

1. Introduction

The extragalactic background light (EBL) is the light integrated from all extragalactic sources since the recombination era. Consequently, it comprises a wealth of information on star formation and the evolution history of the Universe. Its spectrum lies between $0.1 - 1000\,\mu m$, with two distinct humps: a first hump between 0.1 and 10 μm due to direct stellar emission; a second hump between 10 and 1000 μm, which is caused by the dust. Measurements of the EBL can be used to provide constraints on star formation models and the baryonic matter content of the Universe [1].

Direct measurement of the EBL is difficult because of strong foreground contamination by galactic and zodiacal light. Indirect measurements have been obtained by studying the attenuation of the spectra of distance γ-ray sources. This is possible because the γ-rays emitted from distance sources (quasars) get absorbed along the way by the EBL photons through pair production ($\gamma + \gamma' \rightarrow e^+ + e^-$). This process causes a steepening of the spectral index of the quasars in the VHE regime [2]. While the attenuation depends on the γ-ray energy and the EBL density along the line of sight. Clustering of galaxies on a scale of up to 100 Mpc causes fluctuations in the EBL density. Here we present a semi-analytical model to determine the EBL and its fluctuations based on a realistic dark matter density distribution.

Although it should be possible to constrain the EBL density and its fluctuations from observations of distant quasars, our understanding of the intrinsic source spectrum is incomplete. In fact, it is difficult to differentiate between the source-inherent effects and the signature of the EBL on the observed spectrum [3]. Figure 1 shows observed VHE spectral indices (Γs) of selected high-synchrotron-peaked BL Lac (HBL) objects as a function of redshift (data obtained from

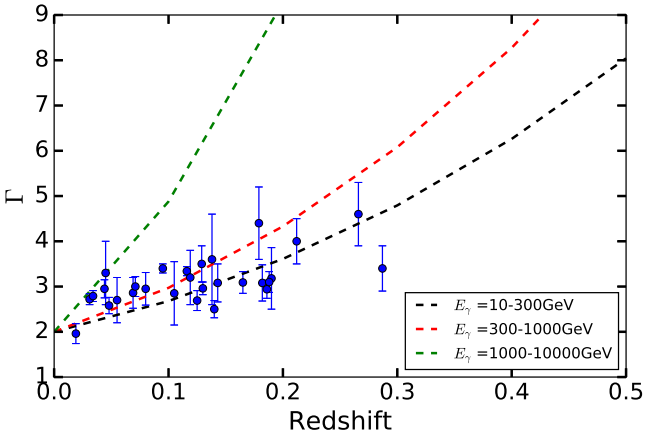

Figure 1: Observed spectral indices Γ of the hard γ-ray for HBL objects as a function of redshift (data obtained from table 1 in [4] excluding extreme HBLs and those with uncertain redshifts. The dashed lines represent the predictions of our EBL model for the observed (absorbed) Γ if the intrinsic spectrum is $\Gamma_{\rm Interact} = 2.0$. Different lines correspond to different γ-ray energy ranges used to determine the spectral index.

table 1 in [4] excluding extreme HBLs and those with uncertain redshifts). As can be seen in the Figure, there is a clear correlation between the Γs and redshift [4]. Gamma-rays of more distant sources have a higher probability to interact with the EBL along the path and this steepen the VHE spectra.

It is interesting to find out whether the scatter in the spectral indices is an intrinsic feature of different sources or the effect of the variation in the optical depth along the path from the source to the observer. In our previous work [5, 6] (here after KF17), we developed a purely analytical framework for computing the EBL fluctuation by calculating upper and lower limits in the star formation rate (SFR) and implementing them in the EBL model by [8, 9]. Our model predicted maximum changes of $\pm 10\%$ in the γ-ray transmissivity. This is also in agreement with the result reported by [10, 11]. However, this translates into only marginal differences in the power-law slopes of the deabsorbed γ-ray spectra ($\lesssim \pm 1\%$). This variation is not enough to describe the observed scatter.

In this work we use semi-analytical galaxy catalogues from the Millennium data base [12, 13] which enable us to trace the path of the γ-ray through a more realistic EBL photon field. By generating a statistical ensemble of different γ-ray paths the stochastic distribution of γ-ray opacities can be investigated.

2. The EBL Model

In order to evaluate the EBL energy density along the γ-ray path we used the simulated MR7 galaxy catalog [12, 13] and constructed cylinders with comoving radius of 50 Mpc from $z = 0$ up to $z = 0.5$. We avoided repetition of structures along the line of sight by randomly rotating and shifting the snap-shots to match the comoving distance at a specific redshift. Figure 2 shows an example of the resulting cylinders up to $z = 0.5$. We assigned a spectrum to each galaxy in the cylinder based on its age, metallicity and mass (all properties readily extracted from MR7 catalogue) using the simple stellar populations synthesis library: bc03 [14], assuming each galaxy has single stellar populations. To get the number of photons in the stellar component we used an empirical function for the escape fraction formula [8]. Then by integrating the energy trapped by the escape fraction formula and assuming quasistatic equilibrium, the total energy trapped is

then re-radiated in the IR, distributed among three black body with temperatures (40, 70 and 450 K). We then added the stellar and the dust components to get the galaxy spectrum from ultraviolet (UV) to infrared (IR) regimes.

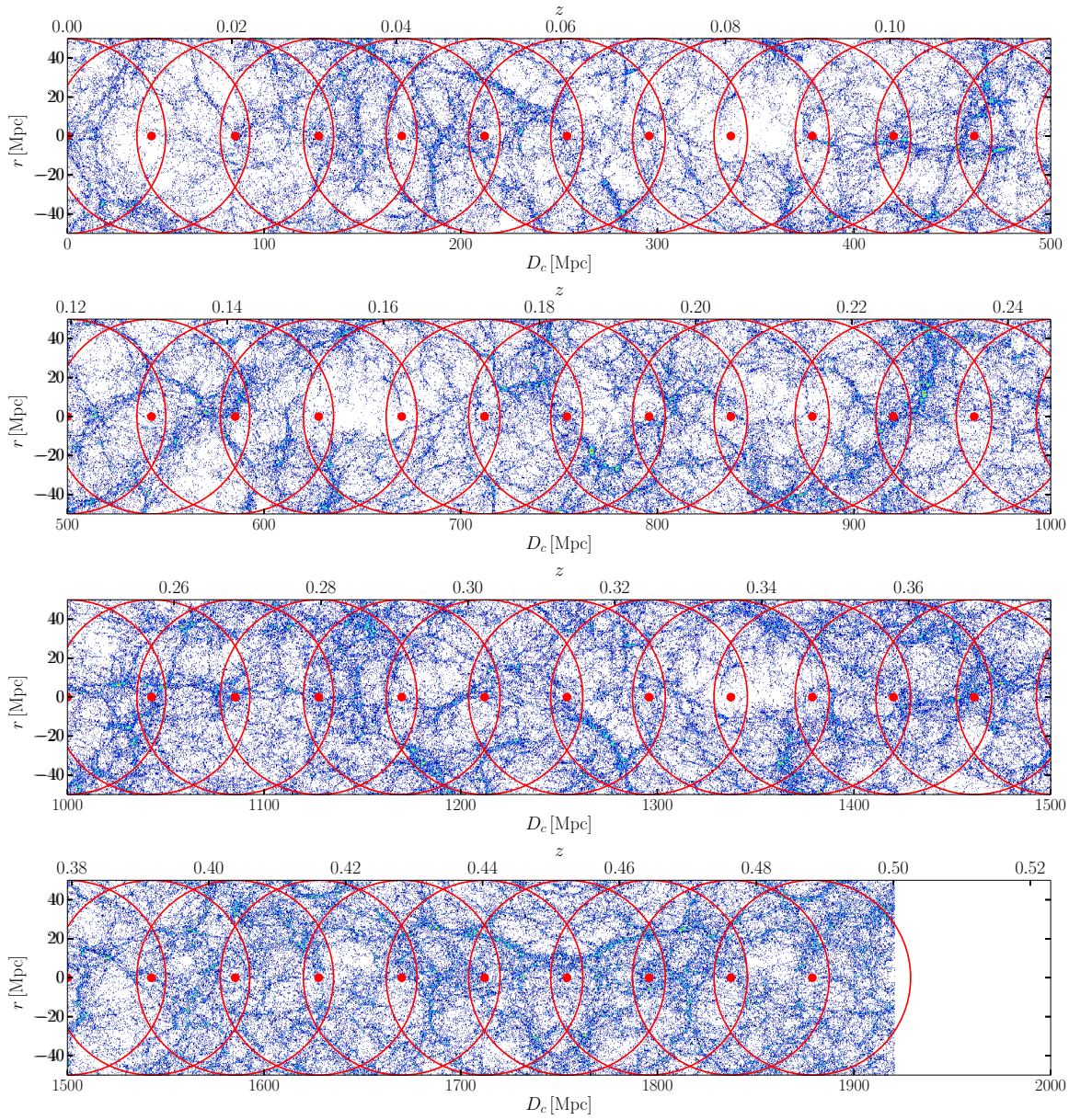

Figure 2: Light cone (cylinder) with comoving radius of 50 h^{-1}Mpc from $z = 0$ up to $z = 0.5$. The red points in the middle of the cylinder represent the locations where the local EBL density from a sphere of radius 50 Mpc (red circles) was computed.

By choosing points along the γ-ray path (central line of the cylinder) with $dz = 0.01$ separation (shown as red dots in figure 2), we computed the light contribution of the galaxies in a sphere of radius 50 h^{-1}Mpc around these points applying $1/r^2$ luminosity profile. To evaluate the total EBL energy at each z we added a homogeneous background to the local EBL density computed following [6]. Figure 3 shows the EBL spectrum at different redshifts in yellow lines with the KF17 model in blue lines. The complete model is presented in [7].

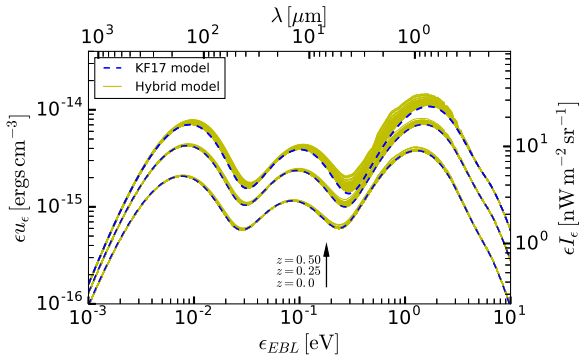

Figure 3: The EBL intensity at different redshifts in yellow lines, the blue dashed lines are the corresponding EBL intensity obtained using KF17.

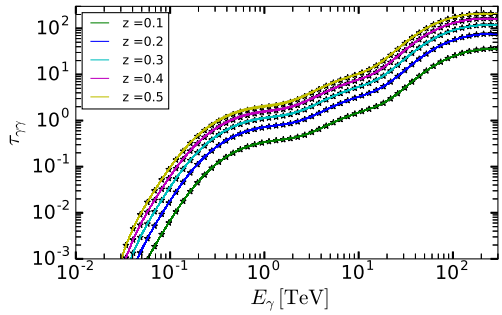

Figure 4: The γ-ray opacity ($\tau_{\gamma\gamma}$) in the cylinders at different redshifts ($z = 0.1$ to $z = 0.5$) with E_γ energy range of 10^{-2} to 300 TeV in solid line, where the stars show the opacity calculated using the KF17 model.

3. Results and Discussion

With the model described above we produced a realistic EBL spectra which allow us to determine the EBL intensity along the individual γ-ray paths. Following equation No.17 in [8], we calculate the γ-ray opacity for various γ-ray paths as shown in figure 4. The figure displays the opacity at different redshifts from $z = 0.1$ up to $z = 0.5$ and γ-ray energy between $10 - 10^4$ GeV. The opacity increases rapidly above 300 GeV. This suggests different EBL attenuation effects for different γ-ray energy ranges. The opacities for the ensemble of γ-ray paths are very similar and would lie on top of each other as shown in solid lines in figure 4, and for comparison we show opacities for KF17 model in stars-lines.

Assuming $\Gamma = 2.0$ as the source's intrinsic spectral index at different redshifts, we use the opacity discussed above to compute the observed spectral index at three different energy ranges: $10 - 300$, $300 - 10^3$ and $10^3 - 10^4$ GeV, as shown in figure 1 in black, red and green dashed lines, respectively. The model spectral index retains the observed correlation with redshift. As expected, the observed spectral index steepen more rapidly if measured within increasing energy ranges.

4. Conclusion

In this paper we investigated the γ-ray opacity based on a realistic EBL model. The EBL was computed based on the simulated inhomogeneous galaxy distribution plus a homogeneous EBL component assumed to originate from galaxies at larger distances. The opacities were computed for an ensemble of γ-rays distributed throughout the simulation box. Based on the γ-ray opacity we determined the steepening of the observed spectral index of the γ-ray source with redshift. The simulated behaviour agrees with the observed steepening of the hard γ-ray spectra. The differences in the opacity due to fluctuations in the EBL (integrated EBL along various γ-ray paths) are marginal. Thus, our EBL model which, by construction, includes the contribution of individual galaxies very close to the γ-ray path cannot account for the scatter in the spectral indices seen in figure 1.

Acknowledgments

This research was supported by the German Academic Exchange Service (DAAD). The Millennium Simulation (MR7) databases used in this paper and the web application providing

online access to them were constructed as part of the activities of the German Astrophysical Virtual Observatory (GAVO).

References

[1] Dwek E and Krennrich F 2013 *Astroparticle Physics* **43** 112
[2] H.E.S.S. Collaboration, Abramowski A, Acero F, et al. 2013 *Astronomy & Astrophysics* **5** 550 A4
[3] Mazin D and Raue M 2007 *A&A* **471** 439
[4] Sinha A, Sahayanathan S, Misra R, Godambe S and Acharya B S 2014 *ApJ* **795** 91
[5] Kudoda A M and Faltenbacher A 2015 3rd Annual Conference on High Energy Astrophysics in Southern Africa (HEASA2015) 20
[6] Kudoda A M and Faltenbacher A 2017 *MNRAS* **467** 2896
[7] Kudoda A M and Faltenbacher A 2018 *MNRAS* **481** 405
[8] Razzaque S, Dermer C D and Finke J D 2009 *ApJ* **697** 483
[9] Finke J D, Razzaque S and Dermer C D 2010 *ApJ* **712** 238
[10] Furniss A, Sutter P M, Primack J R and Domínguez A 2015 *MNRAS* **446** 2267
[11] Abdalla H and Böttcher M 2017 *ApJ* **835** 237
[12] Lemson G and the Virgo Consortium 2006 *arXiv:astro-ph/0608019*
[13] Guo Q, White S, Angulo R E, et al. 2013 *MNRAS* **428** 1351
[14] Bruzual G and Charlot S 2003 *MNRAS* **344** 1000

Probing quantum gravity through strong gravitational lensing

S Marongwe[1]**, M. Mafu**
Department of Physics and Astronomy
Botswana International University of Science and Technology, P. Bag 16, Palapye, Botswana
E-mail: stuartmarongwe@gmail.com

Abstract. We report the use of Einstein rings to reveal the quantized and dynamical states of spacetime in a region of impressed gravitational field as predicted by the Nexus Paradigm of quantum gravity. This in turn reveals the orbital speeds of objects found therein and the radius of curvature of the quantized spacetime. Similarities between the nexus graviton and the singular isothermal sphere (SIS) in the cold dark matter (CDM) paradigm are highlighted. However unlike the singular isothermal sphere, the nexus graviton does not contain singularities or divergent integrals. This provides a viable solution to the core cusp problem. In this work, data from a sample of fifteen Einstein rings published on the CfA-Arizona Space Telescope Lens Survey (CASTLES) website is used to probe the quantized properties of spacetime.

Keywords: (Quantum Gravity; Gravitational Lensing; Dark Matter; Quantum Vacuum; Graviton)

1. Introduction

In 1937, Zwicky [1] provided the first reproducible evidence of the presence of unseen matter in the Coma Cluster group of galaxies by applying the classic virial theorem. In the same paper he also suggested that the gravitational field of galaxy clusters is expected to deflect the light observed from background galaxies. Today, numerous observations [2,3,4,5,6] have confirmed the presence of Zwicky's dark matter and most studies [7,8,9,10] have used gravitational lensing to explore its distribution in cluster groups. Strong lensing allows the determination of important physical parameters such as the total mass of the lensing object without any assumptions on the dynamics. Einstein rings (ER) are particularly important in constraining the mass within the Einstein radius with great accuracy. Currently, it is thought that dark matter is the source of much of the lensing potential. Here we report the use of ERs to calculate the quantum state of spacetime in the presence of the baryonic mass. A remarkable feature of the Nexus Paradigm of quantum gravity is that under certain critical conditions, the intrinsic curvature of spacetime in the n-th quantum state is the source of deflection and not the curvature due to the presence of baryonic mass. This feature is clearly illustrated in the Bullet Cluster [11].

2. Theoretical Background

The nature of dark matter along with that of dark energy is one of the most perplexing unsolved problems in astrophysics and has largely divided the astrophysical community into some suggesting a modification of the law of gravity [12,13,14,15] and others suggesting the presence of unseen baryonic or non-baryonic matter [16,17,18,19]. The Nexus Paradigm of quantum gravity [20, 21] is a part of a third approach that seeks to explain dark matter and dark energy as an effect from quantum gravity. In this paradigm, spacetime is a nexus graviton field with 10^{60} eigenstates.

A nexus graviton in the *n*-th quantum state as described in Ref:[20-21] is a spherically symmetric pulse or wave packet of four-space with the following components

$$\Delta x_n^{\mu} = \frac{2r_{HS}}{n\pi}\gamma^{\mu}\int_{-\infty}^{\infty} sinc(k^{\mu}x_{\mu})e^{ikx}dk^{\mu}$$

$$= \gamma^{\mu}\int_{-\infty}^{\infty} a_{nk}\varphi_{(nk\mu)}dk^{\mu} \quad (1)$$

Here γ^{μ} are the Dirac matrices, r_{HS} is the Hubble radius, $\varphi_{(nk\mu)} = sinc(k^{\mu}x_{\mu})e^{ikx}$ are Bloch energy eigenstate functions $kx = k^{\mu}x_{\mu}$, $k^{\mu} = \frac{n\pi}{r_{HS}^{\mu}}$, $n = \pm 1, \pm 2 \ldots 10^{60}$ and the metric $ds^2 = g_{(n)\mu\nu}dx^{\mu}x^{\nu}$ is the intensity of the pulse computed from the the inner product of Eqn(1). Percieving the metric equation as the intensity of a four- pulse forms the basis of the nexus graviton formulation of space-time.

The norm squared of the four- momentum of the *n*-th state graviton is

$$(\hbar)^2 k^{\mu}k_{\mu} = \frac{E_n^2}{c^2} - \frac{3(nhH_0)^2}{c^2} = 0 \quad (2)$$

where H_0 is the Hubble constant (2.2 x 10^{-18} s^{-1}) and can be expressed in terms of the cosmological constant, Λ as

$$\Lambda_n = \frac{E_n^2}{(hc)^2} = \frac{k_n^2}{(2\pi)^2} = n^2\Lambda \quad (3)$$

The curvature of spacetime in the *n*-th quantum state is then expressed as

$$G_{(n)\mu\upsilon} = n^2\Lambda g_{\mu\upsilon} \quad (4)$$

where $G_{(n)\mu\nu}$ is the Einstein tensor of spacetime in the *n*-th state. The dark energy arises from the emission of a ground state graviton such that Eqn. (4) becomes

$$G_{(n)\mu\upsilon} = (n^2 - 1)\Lambda g_{\mu\upsilon} \quad (5)$$

If the graviton field is perturbed by the presence of baryonic matter then Eqn.(5) becomes

$$G_{(n)\mu\upsilon} = kT_{\mu\nu} + (n^2 - 1)\Lambda g_{\mu\upsilon} \quad (6)$$

From Ref.[20] the solution to Eqn. (4) is computed as

$$ds^2 = -\left(1 - \left(\frac{2}{n^2}\right)\right)dt^2 + \left(1 - \left(\frac{2}{n^2}\right)\right)^{-1} dr^2 + r^2(d\theta^2 + sin^2\theta d\varphi^2) \quad (7)$$

In the above equation n = 1 state refers to the ground state of spacetime and is the quantum state of space inside a black hole event horizon. The state in close proximity to this event horizon is the *n*=2 state. There are no singularities in Eqn. (7).

For weak gravitational fields that characterize distances ranging from solar system to cosmic scales, the solution to Eqn.(6) for an aggregation of baryonic matter *M(r)* within a radius *r*, as provided in Ref.[20] is expressed as

$$\frac{d^2r}{dt^2} = \frac{GM(r)}{r^2} + H_0 v_n - H_0 c \quad (8)$$

Here *c* is the speed of light.

The first term on the right is the Newtonian gravitational acceleration, the second term is a radial acceleration induced by spacetime in the *n*-th quantum state and the final term is acceleration due to dark energy. The dynamics becomes strongly non-Newtonian when

$$\frac{GM(r)}{r^2} = H_0 c = \frac{v_n^2}{r} \quad (9)$$

These are conditions in which the spacetime curvature due to baryonic matter is annulled by that due to the presence of dark energy. Under such conditions

$$r = \frac{v_n^2}{H_0 c} \tag{10}$$

Substituting for *r* in Eqn.(9) yields

$$v_n^4 = GM(r)H_0 c \tag{11}$$

This is the baryonic Tully – Fisher relation. The conditions permitting the dark energy to cancel out the curvature due to baryonic matter leave quantum gravity as the unique source of curvature. Thus condition (9) reduces Eqn.(8) to

$$\frac{d^2 r}{dt^2} = \frac{dv_n}{dt} = H_0 v_n \tag{12}$$

From which we obtain the following equations of galactic and cosmic evolution

$$r_n = \frac{1}{H_0} e^{(H_0 t)} (GM(r)H_0 c)^{\frac{1}{4}} \tag{13}$$

$$v_n = e^{(H_0 t)} (GM(r)H_0 c)^{\frac{1}{4}} \tag{14}$$

$$a_n = H_0 e^{(H_0 t)} (GM(r)H_0 c)^{\frac{1}{4}} \tag{15}$$

Here r_n is the radius of curvature of spacetime in the *n*-th quantum state (which is also the radius of the *n*-th state nexus graviton), v_n the radial velocity of objects embedded in that spacetime, and a_n, their radial acceleration within it. The amplification of the radius of curvature with time explains the existence of ultra-diffuse galaxies and the spiral shapes of most galaxies (see Refs: [20-21]). The increase in radial velocity with time explains why early type galaxies composed of population II stars are fast rotators. Eqn.(15) explains late time cosmic acceleration which began once condition (9) was satisfied or equivalently from Eqn.(6), when the density of baryonic matter was at the same value as that of dark energy. Thus condition (9) also explains the Coincidence Problem.

3. Gravitational lensing and quantum gravity

In the context of the Nexus Paradigm, a gravitational field is a region of spacetime in a low quantum state or a zone with a low vacuum expectation value

$$\langle \psi_n(r_i) | T_{00} | \psi_n(r_j) \rangle = n^2 \rho_{DE} \tag{16}$$

where ψ_n is the wave function of the quantum vacuum in the *n*-th quantum state and ρ_{DE} is the density of dark energy. From Ref.[20], the flow of spacetime in each quantum state of curvature r_n, induces a constant radial speed onto any test particle embedded within it of

$$v_n = H_0 r_n = c/n \tag{17}$$

The deflection of light through gravitational lensing by spacetime in the *n*-th quantum state is

$$\alpha = (\theta - \beta) D_{ls}/D_s = 4/n^2 \tag{18}$$

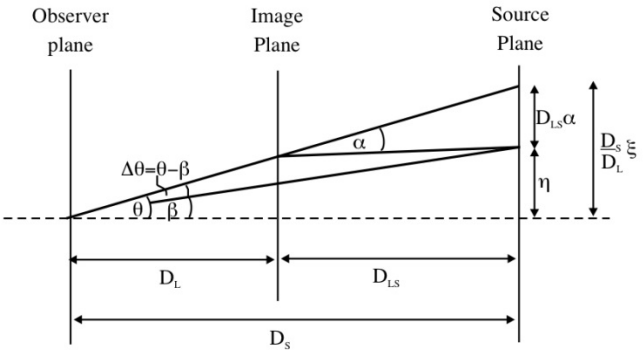

Fig.1

From which we obtain

$$n = 2\sqrt{\frac{D_S}{D_{ls}(\theta - \beta)}} \tag{19}$$

Thus the orbital speed of a particle embedded in the *n*-th quantum state is

$$v_n = c\sqrt{\frac{D_{ls}(\theta-\beta)}{4D_s}} = e^{(Ht)}(GM(r)H_0c)^{\frac{1}{4}} \quad (20)$$

In the case where 0 an Einstein ring forms and Eqn.(20) becomes

$$v_n = c\sqrt{\frac{D_{ls}\theta_E}{4D_s}} = e^{(Ht)}(GM(r)H_0c)^{\frac{1}{4}} \quad (21)$$

Here we observe similarities with the cold dark matter (CDM) model where the dispersion velocities for a SIS are calculated from

$$\sigma = c\sqrt{\frac{D_{ls}\theta_E}{4\pi D_s}} \quad (22)$$

Hence Eqn.(21) is the link between the CDM paradigm and the baryonic Tully-Fisher relation. In such a scenario r_n, would denote the radius of the CDM halo. However, in the Nexus Paradigm, the CDM is vacuum energy as described by Eqn.(16).Moreover Eqn.(7) describing the nexus graviton has no singularity nor divergences found in the SIS model.

If the radial velocity and baryonic mass content in the lensing system are known then one can calculate the time *t*, which has elapsed since the lensing system became a system in dynamical equilibrium as stipulated by condition (9).

4. Results

We apply Eqn.(17) and Eqn.(21) to determine the value of *n*, r_n, v_n and a_n for a spherically symmetric lensing system from a sample of fifteen ERs lenses published on the CASTLES website (www.cfa.havard.edu/castles/) . The calculations assume a flat universe in which H_0=69.6 km/s/Mpc 0. $_M$= 0.286 .The results are displayed in Table 1.

Table 1

Lens	D_{ls}/D_s	θ_E/asc	n	r_n/Mpc	v_n/kms^{-1}	$a_n/10^{-10}$m/s^{-2}
JVA B1938+666	0.50	0.44	1948	2.27	154.0	0.0034
B0218+357	0.17	0.16	5508	0.80	54.5	0.0012
PG1115+080	0.64	1.16	1054	4.19	284.6	0.0063
B1608+656	0.35	1.14	1268	3.49	236.6	0.0052
RXJ1131-1231	0.45	1.90	982	4.50	305.5	0.0067
Q0047-2808	0.58	1.35	1027	4.30	292.1	0.0064
PMNJ0134-0931	0.37	0.37	2456	1.80	122.1	0.0027
HE0230-2130	0.49	1.03	1231	3.62	243.7	0.0054
CFR503.1077	0.34	1.05	1581	2.80	189.8	0.0042
HST15433+5352	0.52	0.59	1640	2.69	182.9	0.0040
MG1549+3047	0.83	0.85	1081	4.09	277.5	0.0061
PKS1830-211	0.34	0.50	2214	2.00	135.5	0.0030
MG2016+112	0.33	1.76	1192	3.71	251.7	0.0055

Q2237+030	0.94	0.89	993	4.45	302.1	0.0066
HE0435-1223	0.51	1.21	1156	3.82	259.5	0.0057

5. Discussion

The results indicate that the orbital velocity of the constituents of a lensing system can be attributed to a globule of quantized vacuum energy called the nexus graviton of density $n^2\rho_{DE}$ with a radius of dimensions in the order of a few megaparsecs. When in close proximity to other gravitons, tidal forces arise which transform the nexus graviton from a spherical shape to an ellipsoid. The profile of the ellipsoid is an ellipse and the graviton radius becomes

$$r_n = \frac{R_n}{1-ecos\varphi} \tag{23}$$

Where e is the eccentricity.

Hence the orbital velocity becomes

$$v_n = H_0 r_n = \frac{H_0 R_n}{1-ecos\varphi} \tag{24}$$

From which we calculate density as

$$\rho = \frac{c^2}{v_n^2}\rho_{DE} = \frac{R_H^2(1-ecos\varphi)^2\rho_{DE}}{R_n^2} = n^2(1-ecos\varphi)^2\rho_{DE} \tag{25}$$

where R_H is the Hubble radius. The deflection of light under these conditions becomes

$$\alpha = (\theta-\beta)D_{ls}/D_s = 4/n^2(1-ecos\varphi)^2 \tag{26}$$

Here we notice an increase in vacuum energy density with a decrease in curvature radius. The density profile is thus stratified in quantized concentric radii $r_n=R_H/n$ with a maximum radius at $R_N<R_H$ and the minimum at $R_{min}=R_H/10^{60}$. Spacetime in the inner core of the nexus graviton is therefore flat as described by Eqn.(7) and curved at large radii. In the CDM paradigm, the gravitational lensing at galactic and cosmic scales is an effect arising largely due to the presence of the hypothetical dark matter in the lensing system and so it can be used to constrain the dark matter mass model of lenses as in Fig.2. In the Nexus Paradigm, the gravitational lensing can be used to constrain the value of the quantum state n of spacetime within the lensing system also as in Fig.2. The relationship between the quantum state of space-time and the hypothetical dark matter is expressed in Eqn.(28) if $M(r)$ is considered as the dark matter distribution.

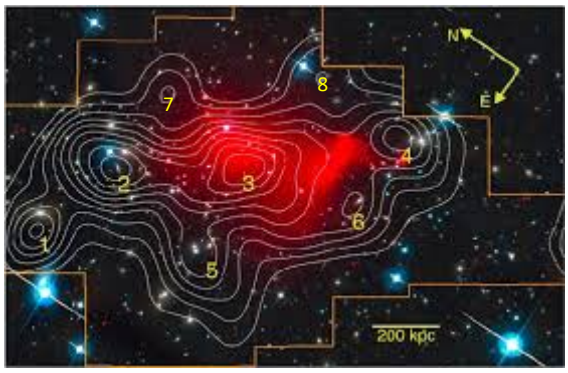

Fig.2 The Abell 520 Cluster

The Abell 520 cluster in Fig.2 shows eight interacting nexus gravitons. The interaction deforms each graviton into an ellipsoid of cross section described by Eqn. (25).

By comparing the quantized metric of Eqn.(7) with Schwarzschild metric we notice that the quantum state of spacetime around baryonic matter increases with distance from the mass

$$\frac{2}{n^2} = \frac{2GM(r)}{c^2 r} \tag{27}$$

Such that

$$n^2 = \frac{c^2 r}{GM(r)} \tag{28}$$

Thus the curvature of spacetime in the inner core of the nexus graviton is only curved by the presence of baryonic matter and not by the increased vacuum energy density. This provides a viable solution to the so called core-cusp problem [22] of astrophysics. If the nexus graviton is surrounded by multiple gravitons tugging on it gravitationally, then the eccentricity becomes a function of the azimuthal angle ψ. Two gravitons of radii $r_n=f(\psi)$ and $r_s=g(\psi)$will intersect when $f(\psi) =g(\psi)$.

6. Conclusion

In this work we have used Einstein rings to reveal the quantized and dynamical states of spacetime in a region of impressed gravitational field as predicted by the Nexus Paradigm of quantum gravity. This endeavour has enabled us to constrain orbital speeds of objects found therein and the radius of curvature of the quantized spacetime, a technique similar to the singular isothermal sphere in the cold dark matter paradigm. The benefit of the nexus graviton formulation is that unlike the singular isothermal sphere, it does not contain singularities or divergent integrals. This provides a viable solution to the core cusp problem.

Acknowledgments

We gratefully appreciate the funding and support from the Department of Physics and Astronomy at the Botswana International University of Science and Technology (BIUST).

References

1. Zwicky F 1937 *ApJ86*,**217**
2. Sarazin C L 1988 CUP, Cambridge
3. Jauzac M *et al* 2015 *MNRAS* **446**,4132-4147
4. Leauthaud A *et al* 2015 *MNRAS* **446** 1874-1888
5. Clowe D *et al*, 2012 *Astrophys.J.* **758**,128
6. Israel M *et.al*, 2014 *A&A* **564**,129
7. Massey R *et al* , 2013 *MNRAS* **429**, 661-678
8. Ellis R S 2010 *Phil. Trans. R. Soc. A* 2010 **368** 967-987
9. Zhandov V I, Alexandrov A N, Fedrova EVK and Sliusar V M 2012 *Astronomy and Astrophysics* **2012**, Article ID 906951
10. Kitching T *et al*, 2015 *Astronomy and Computing* **10** 9-21
11. Clowe D *et al* 2006 *Astrophys.J.* **648**(2) (2006) 109–113.
12. Milgrom M 1983 *Astrophys. J.* **270** 371–389.
13. Olmo G J 2005 *Phys. Rev. D* **72** 083505.
14. Li B, Sotiriou T P and Barrow J D 2011 *Phys. Rev. D* **83** 104017.
15. Capozziello S 2002 *Int. J. Mod. Phys. D* **11** 483–491.
16. Goodman M and Witten E 1985 *Phys.Rev. D* **31**(2) 3059.
17. Cushman P *et al* 2013, *Preprint* hep-ex.1310.8327v2
18. Archambault S *et al*. 2009 [PICASS0 Collaboration] *Phys. Lett. B* **682**(2) 185–192.
19. The CDMS II Collaboration 2010 *Science* **327**(5973) 1619–1621.
20. Marongwe S 2015 *Int. J. Geom. Methods Mod. Phys.* **12**(4) 1550042,
21. Marongwe S 2017 *Int. J. Mod. Phys. D* **26** 1750020
22. De Blok WJG 2009 *preprint [astro-ph.CO]* 0910.3538v1

Quasi-Newtonian scalar-tensor cosmologies

Heba Sami and Amare Abebe
Center for Space Research, North-West University, Mafikeng 2735, South Africa
E-mail: hebasami.abdulrahman@gmail.com

Abstract. In this contribution, classes of shear-free cosmological dust models with irrotational fluid flows will be investigated in the context of scalar-tensor theories. In particular, the integrability conditions describing a consistent evolution of the linearised field equations of quasi-Newtonian universes are presented.

1. Introduction

Although general relativity theory (GR) is a generalization of Newtonian gravity in the presence of strong gravitational fields, it has no properly defined Newtonian limit in cosmological scales. Newtonian cosmologies are an extension of the Newtonian theory of gravity and are usually referred to as *quasi-Newtonian*, rather than strictly Newtonian formulations [1, 2, 3]. The importance of investigating the Newtonian limit for general relativity in cosmological contexts is that, there is a viewpoint that cosmological studies can be done using Newtonian physics, with the relativistic theory only needed for examination of some observational relations [1]. General relativistic quasi-Newtonian cosmologies have been studied in the context of large-scale structure formation and non-linear gravitational collapse in the late-time universe. This despite the general covariant inconsistency of these cosmological models except in some special cases such as the spatially homogeneous and isotropic, spherically symmetric, expanding (FLRW) spacetimes. Higher-order or modified gravitational theories of gravity such as $f(R)$ theories of gravity have been shown to exhibit more shared properties with Newtonian gravitation than does general relativity.

In [1], a covariant approach to cold matter universes in quasi-Newtonian cosmologies has been developed and it has been applied and extended in [2] in order to derive and solve the equations governing density and velocity perturbations. This approach revealed the existence of integrability conditions in GR. The purpose of the current study is two-fold: to apply the lineaized covariant consistency analysis and study the existence of quasi-Newtonian cosmological space-times in scalar-tensor theories of gravitation. A direct result of our analysis will be presented in the form of the integrability conditions we derive.

1.1. $f(R)$ and scalar-tensor models of gravitation

The so-called $f(R)$ theories of gravity are among the simplest modification of Einstein's GR. These theories come about by a straightforward generalisation of the Lagrangian in the Einstein-Hilbert action [4, 5] as

$$S_{f(R)} = \frac{1}{2}\int d^4x\sqrt{-g}\Big(f(R) + 2\mathcal{L}_m\Big)\,, \tag{1}$$

where $\mathcal{L}_m$ is the matter Lagrangian and g is the determinant of the metric tensor $g_{\mu\nu}$. Another modified theory of gravity is the scalar-tensor theory of gravitation. This is a broad class of gravitational models that tries to explain the gravitational interaction through both a scalar field and a tensor field. A sub-class of this theory, known as Brans-Dicke (BD) theory, has an action of the form

$$S_{BD} = \frac{1}{2}\int d^4x\sqrt{-g}\left[\phi R - \frac{\omega}{\phi}\nabla_\mu\phi\nabla^\mu\phi + 2\mathcal{L}_m\right] , \tag{2}$$

where ϕ is the scalar field and ω is a coupling constant considered to be independent of the scalar field ϕ. An interesting aspect of $f(R)$ theories of gravity is their proven equivalence with the BD theory of gravity [5, 6] with $\omega = 0$. If we define the $f(R)$ extra degree of freedom [1] as

$$\phi \equiv f' - 1 , \tag{3}$$

then the actions (1) and (2) become dynamically equivalent.
In a FLRW background universe, the resulting non-trivial field equations lead to the following Raychaudhuri and Friedmann equations that govern the expansion history of the Universe [7]:

$$\dot{\Theta} + \frac{1}{3}\Theta^2 = -\frac{1}{2(\phi+1)}\Big[\mu_m + 3p_m + f - R(\phi+1) + \Theta\dot{\phi} + 3\phi''\Big(\frac{\dot{\phi}^2}{\phi'^2}\Big) + 3\ddot{\phi} - 3\frac{\dot{\phi}\dot{\phi}'}{\phi'}\Big] , \tag{4}$$

$$\Theta^2 = \frac{3}{(\phi+1)}\Big[\mu_m + \frac{R(\phi+1)-f}{2} + \Theta\dot{\phi}\Big] , \tag{5}$$

where $\Theta \equiv 3H = 3\dfrac{\dot{a}}{a}$, H being the Hubble parameter, $a(t)$ is the scale factor, and μ_m and p_m are the energy density and isotropic pressure of standard matter, respectively.
The linearised thermodynamic quantities for the scalar field are the energy density μ_ϕ, the pressure p_ϕ, the energy flux q_a^ϕ and the anisotropic pressure π_{ab}^ϕ, respectively given by

$$\mu_\phi = \frac{1}{(\phi+1)}\Big[\frac{1}{2}\Big(R(\phi+1) - f\Big) - \Theta\dot{\phi} + \tilde{\nabla}^2\phi\Big] , \tag{6}$$

$$p_\phi = \frac{1}{(\phi+1)}\Big[\frac{1}{2}\Big(f - R(\phi+1)\Big) + \ddot{\phi} - \frac{\dot{\phi}\dot{\phi}'}{\phi'} + \frac{\phi''\dot{\phi}^2}{\phi'^2} + \frac{2}{3}(\Theta\dot{\phi} - \tilde{\nabla}^2\phi)\Big] , \tag{7}$$

$$q_a^\phi = -\frac{1}{(\phi+1)}\Big[\frac{\dot{\phi}'}{\phi'} - \frac{1}{3}\Theta\Big]\tilde{\nabla}_a\phi , \tag{8}$$

$$\pi_{ab}^\phi = \frac{\phi'}{(\phi+1)}\Big[\tilde{\nabla}_{\langle a}\tilde{\nabla}_{b\rangle}R - \sigma_{ab}\Big(\frac{\dot{\phi}}{\phi'}\Big)\Big] . \tag{9}$$

The total (*effective*) energy density, isotropic pressure, anisotropic pressure and heat flux of standard matter and scalar field combination are given by

$$\mu \equiv \frac{\mu_m}{(\phi+1)} + \mu_\phi, \quad p \equiv \frac{p_m}{(\phi+1)} + p_\phi, \quad \pi_{ab} \equiv \frac{\pi_{ab}^m}{(\phi+1)} + \pi_{ab}^\phi, \quad q_a \equiv \frac{q_a^m}{(\phi+1)} + q_a^\phi . \tag{10}$$

1.2. Covariant equations
Given a choice of 4-velocity field u^a in the Ehlers-Ellis covariant approach [8, 9], the FLRW background is characterised by the equations [2, 3]

$$\begin{aligned} &\tilde{\nabla}_a\mu_m = 0 = \tilde{\nabla}_a p_m = \tilde{\nabla}_a\Theta , \quad q_a^m = 0 = A_a = \omega_a , \\ &\pi_{ab}^m = \sigma_{ab} = E_{ab} = 0 = H_{ab} , \end{aligned} \tag{11}$$

[1] f' , f'', etc. are the first, second, etc. derivatives of f w.r.t. the Ricci scalar R.

where Θ, A_a, ω^a, and σ_{ab} are the expansion, acceleration, vorticity and the shear terms. E_{ab} and H_{ab} are the "gravito-electric" and "gravito-magnetic" components of the Weyl tensor C_{abcd} defined from the Riemann tensor R^a_{bcd} as

$$C^{ab}{}_{cd} = R^{ab}{}_{cd} - 2g^{[a}{}_{[c}R^{b]}{}_{d]} + \frac{R}{3}g^{[a}{}_{[c}g^{b]}{}_{d]} \ , \tag{12}$$

$$E_{ab} \equiv C_{agbh}u^g u^h, \qquad H_{ab} \equiv \tfrac{1}{2}\eta_{ae}{}^{gh}C_{ghbd}u^e u^d \ . \tag{13}$$

The covariant linearised evolution equations in the general case are given by [2, 3, 10]

$$\dot{\Theta} = -\frac{1}{3}\Theta^2 - \frac{1}{2}(\mu + 3p) + \tilde{\nabla}_a A^a \ , \tag{14}$$

$$\dot{\mu}_m = -\mu_m\Theta - \tilde{\nabla}^a q^m_a \ , \tag{15}$$

$$\dot{q}^m_a = -\frac{4}{3}\Theta q^m_a - \mu_m A_a \ , \tag{16}$$

$$\dot{\omega}^{\langle a\rangle} = -\frac{2}{3}\Theta\omega^a - \frac{1}{2}\eta^{abc}\tilde{\nabla}_b A_c \ , \tag{17}$$

$$\dot{\sigma}_{ab} = -\frac{2}{3}\Theta\sigma_{ab} - E_{ab} + \frac{1}{2}\pi_{ab} + \tilde{\nabla}_{\langle a}A_{b\rangle} \ , \tag{18}$$

$$\dot{E}^{\langle ab\rangle} = \eta^{cd\langle a}\tilde{\nabla}_c H^{\rangle b}_d - \Theta E^{ab} - \frac{1}{2}\dot{\pi}^{ab} - \frac{1}{2}\tilde{\nabla}^{\langle a}q^{b\rangle} - \frac{1}{6}\Theta\pi^{ab} \ , \tag{19}$$

$$\dot{H}^{\langle ab\rangle} = -\Theta H^{ab} - \eta^{cd\langle a}\tilde{\nabla}_c E^{\rangle b}_d + \frac{1}{2}\eta^{cd\langle a}\tilde{\nabla}_c \pi^{\rangle b}_d \ , \tag{20}$$

and the linearised constraint equations are given by

$$C^{ab}_0 \equiv E^{ab} - \tilde{\nabla}^{\langle a}A^{b\rangle} - \frac{1}{2}\pi^{ab} = 0 \ , \tag{21}$$

$$C^a_1 \equiv \tilde{\nabla}_b\sigma^{ab} - \eta^{abc}\tilde{\nabla}_b\omega_c - \frac{2}{3}\tilde{\nabla}^a\Theta + q^a = 0 \ , \tag{22}$$

$$C_2 \equiv \tilde{\nabla}^a\omega_a = 0 \ , \tag{23}$$

$$C^{ab}_3 \equiv \eta_{cd(}\tilde{\nabla}^c\sigma^d_{b)} + \tilde{\nabla}^{\langle a}\omega^{b\rangle} - H^{ab} = 0 \ , \tag{24}$$

$$C^a_5 \equiv \tilde{\nabla}_b E^{ab} + \frac{1}{2}\tilde{\nabla}_b\pi^{ab} - \frac{1}{3}\tilde{\nabla}^a\eta + \frac{1}{3}\Theta q^a = 0 \ , \tag{25}$$

$$C^a_b \equiv \tilde{\nabla}_b H^{ab} + (\mu + p)\omega^a + \frac{1}{2}\eta^{abc}\tilde{\nabla}_b q_a = 0 \ . \tag{26}$$

2. Quasi-Newtonian spacetimes

If a comoving 4-velocity $\tilde{u}^a$ is chosen such that, in the linearised form

$$\tilde{u}^a = u^a + v^a, \quad v_a u^a = 0, \quad v_a v^a << 1 \ , \tag{27}$$

the dynamics, kinematics and gravito-electromagnetics quantities (11) undergo transformation. Here v^a is the relative velocity of the comoving frame with respect to the observers in the quasi-Newtonian frame, defined such that it vanishes in the background. In other words, it is a non-relativistic peculiar velocity. Quasi-Newtonian cosmological models are irrotational, shear-free dust spacetimes characterised by [2, 3]:

$$p_m = 0 \ , \quad q^m_a = \mu_m v_a \ , \quad \pi^m_{ab} = 0 \ , \omega_a = 0 \ , \quad \sigma_{ab} = 0 \ . \tag{28}$$

The gravito-magnetic constraint equation (24) and the shear-free and irrotational condition (28) show that the gravito-magnetic component of the Weyl tensor automatically vanishes:

$$H^{ab} = 0 \ . \tag{29}$$

The vanishing of this quantity implies no gravitational radiation in quasi-Newtonian cosmologies, and equation (26) together with equation (28) show that q_a^m is irrotational and thus so is v_a:

$$\eta^{abc}\tilde{\nabla}_b q_a = 0 = \eta^{abc}\tilde{\nabla}_b v_a \ . \tag{30}$$

Since the vorticity vanishes, there exists a velocity potential such that

$$v_a = \tilde{\nabla}_a \Phi \ . \tag{31}$$

3. Integrability conditions

It has been shown that the non-linear models are generally inconsistent if the silent constraint (29) is imposed, but that the linear models are consistent [2, 3]. Thus, a simple approach to the integrability conditions for quasi-Newtonian cosmologies follows from showing that these models are in fact a sub-class of the linearised silent models. This can happen by using the transformation between the quasi-Newtonian and comoving frames. The transformed linearised kinematics, dynamics and gravito-electromagnetic quantities from the quasi-Newtonian frame to the comoving frame are given as follows:

$$\tilde{\Theta} = \Theta + \tilde{\nabla}^a v_a \ , \tag{32}$$

$$\tilde{A}_a = A_a + \dot{v}_a + \frac{1}{3}\Theta v_a \ , \tag{33}$$

$$\tilde{\omega}_a = \omega_a - \frac{1}{2}\eta_{abc}\tilde{\nabla}^b v^c \ , \tag{34}$$

$$\tilde{\sigma}_{ab} = \sigma_{ab} + \tilde{\nabla}_{\langle a} v_{b\rangle} \ , \tag{35}$$

$$\tilde{\mu} = \mu, \quad \tilde{p} = p, \quad \tilde{\pi}_{ab} = \pi_{ab}, \quad \tilde{q}_a^{\phi} = q_a^{\phi} \tag{36}$$

$$\tilde{q}_a^m = q_a^m - (\mu_m + p_m)v_a \ , \tag{37}$$

$$\tilde{E}_{ab} = E_{ab}, \quad \tilde{H}_{ab} = H_{ab} \ . \tag{38}$$

It follows from the above transformation equations that

$$\tilde{p}_m = 0 \ , \quad \tilde{q}_a^m = 0 = \tilde{A}_a = \tilde{\omega}_a \ , \quad \tilde{\pi}_{ab}^m = 0 = \tilde{H}_{ab} \ , \quad \tilde{\sigma}_{ab} = \tilde{\nabla}_{\langle a} v_{b\rangle} \ , \quad \tilde{E}_{ab} = E_{ab} \ . \tag{39}$$

These equations describe the linearised silent universe except that the restriction on the shear in equation (39) results in the integrability conditions for the quasi-Newtonian models. Due to the vanishing of the shear in the quasi-Newtonian frame, equation (18) is turned into a new constraint

$$E_{ab} - \frac{1}{2}\pi_{ab}^{\phi} - \tilde{\nabla}_{\langle a} A_{b\rangle} = 0 \ . \tag{40}$$

This can be simplified by using equation (17) and the identity for any scalar φ:

$$\eta^{abc}\tilde{\nabla}_a A_c = 0 \Rightarrow A_a = \tilde{\nabla}_a \varphi \ . \tag{41}$$

In this case φ is the covariant relativistic generalisation of the Newtonian potential.

3.1. First integrability condition

Since equation (40) is a new constraint, we need to ensure its consistent propagation at all epochs and in all spatial hypersurfaces. Differentiating it with respect to cosmic time t and by using equations (9), (19) and (22), one obtains

$$\tilde{\nabla}_{\langle a}\tilde{\nabla}_{b\rangle}\Big[\dot{\varphi} + \frac{1}{3}\Theta + \frac{\dot{\phi}}{(\phi+1)}\Big] + \Big[\dot{\varphi} + \frac{1}{3}\Theta + \frac{\dot{\phi}}{(\phi+1)}\Big]\tilde{\nabla}_a\tilde{\nabla}_b\varphi = 0 \ , \tag{42}$$

which is the first integrability condition for quasi-Newtonian cosmologies in scalar-tensor theory of gravitation and it is a generalisation of the one obtained in [2], *i.e.*, (42) reduces to an identity for the generalized van Elst-Ellis condition [1, 2, 3]

$$\dot{\varphi} + \frac{1}{3}\Theta = -\frac{\dot{\phi}}{(\phi+1)} \ . \tag{43}$$

Using equation (14) with the time evolution of the modified van Elst-Ellis condition, we obtain the covariant modified Poisson equation in scalar-tensor gravity as follows:

$$\tilde{\nabla}^2\varphi = \frac{\mu_m}{2(\phi+1)} - (3\ddot{\varphi} + \Theta\dot{\varphi}) + \frac{1}{2(\phi+1)}\Big[f - R(\phi+1) + \Big(\frac{3\dot{\phi}'}{\phi'} - \Theta\Big)\dot{\phi} - 3\ddot{\phi} + 3\Big(\frac{2}{(\phi+1)} - \frac{\phi''}{\phi'^2}\Big)\dot{\phi}^2 - \tilde{\nabla}^2\phi\Big] \ . \tag{44}$$

The evolution equation of the 4-acceleration A_a can be shown, using equations (43) and (22), to be

$$\dot{A}_a + \Big[\frac{2}{3}\Theta + \frac{\dot{\phi}}{(1+\phi)}\Big]A_a = -\frac{1}{2(1+\phi)}\Big[\mu_m v_a + \Big(\frac{1}{3}\Theta + \frac{\dot{\phi}'}{\phi'} - \frac{2\dot{\phi}}{(1+\phi)}\Big)\tilde{\nabla}_a\phi\Big] \ . \tag{45}$$

3.2. Second integrability condition

There is a second integrability condition arising by checking for the consistency of the constraint (40) on any spatial hyper-surface of constant time t. By taking the divergence of (40) and by using the following identity:

$$\tilde{\nabla}^b\tilde{\nabla}_{\langle a}A_{b\rangle} = \frac{1}{2}\tilde{\nabla}^2 A_a + \frac{1}{6}\tilde{\nabla}_a(\tilde{\nabla}^c A_c) + \frac{1}{3}(\mu - \frac{1}{3}\Theta^2)A_a \ , \tag{46}$$

which holds for any projected vector A_a, and by using equation (41) it follows that:

$$\tilde{\nabla}^b\tilde{\nabla}_{\langle a}\tilde{\nabla}_{b\rangle}\varphi = \frac{2}{3}\tilde{\nabla}_a(\tilde{\nabla}^2\varphi) + \frac{2}{3}(\mu - \frac{1}{3}\Theta^2)\tilde{\nabla}_a\varphi \ . \tag{47}$$

By using equations (47), (22) and (25), one obtains:

$$\begin{aligned}
&\tilde{\nabla}_a\mu_m - \Big[\dot{\phi} + \frac{2}{3}(\phi+1)\Theta\Big]\tilde{\nabla}_a\Theta + \frac{1}{(\phi+1)}\Big[\frac{f}{2} - \mu_m + \Theta\dot{\phi} - \frac{\Theta\dot{\phi}'(\phi+1)}{\phi'}\Big]\tilde{\nabla}_a\phi \\
&-2(\phi+1)\tilde{\nabla}^2(\tilde{\nabla}_a\varphi) - 2\Big[\mu_m + \frac{R(\phi+1)}{2} - \frac{f}{2} - \Theta\dot{\phi} - \frac{\Theta^2(\phi+1)}{3}\Big]\tilde{\nabla}_a\varphi \\
&-\tilde{\nabla}^2(\tilde{\nabla}_a\phi) = 0 \ ,
\end{aligned} \tag{48}$$

which is the second integrability condition and in general it appears to be independent of the first integrability condition (42). By taking the gradient of equation (43) and using equation (22), one can obtain the peculiar velocity:

$$v_a = -\frac{1}{\mu_m}\Big[2(\phi+1)\tilde{\nabla}_a\dot{\varphi} + \Big(\frac{\dot{\phi}'}{\phi'} - \dot{\varphi} - \frac{3\dot{\phi}}{(\phi+1)}\Big)\tilde{\nabla}_a\phi\Big] \ . \tag{49}$$

By virtue of equations (15) and (16), v_a evolves according to

$$\dot{v_a} + \frac{1}{3}\Theta v_a = -A_a \ . \tag{50}$$

The coupled evolution equations (45) and (50) decouple to produce the second-order propagation equation of the peculiar velocity v_a. By using equations (4) and (5) in equation (50) one obtains:

$$\ddot{v}_a + \Big[\Theta + \frac{\dot{\phi}}{(\phi+1)}\Big]\dot{v}_a + \Big[\frac{1}{9}\Theta^2 - \frac{1}{6(\phi+1)}(5\mu_m - f - 4\Theta\dot{\phi})\Big]v_a + \frac{1}{(\phi+1)}\Big[\frac{\dot{\phi}}{(\phi+1)} - \frac{\phi''}{2\phi'} - \frac{\Theta}{6} - \frac{\dot{\phi}'}{2\phi'} + \frac{\phi''\dot{\phi}}{2\phi'^2}\Big]\tilde{\nabla}_a\phi = 0\,. \tag{51}$$

By substituting equation (49) into equation (50) one obtains

$$2(\phi+1)\tilde{\nabla}_a\ddot{\varphi} + 2\Big[\dot{\phi} + \Theta(\phi+1)\Big]\tilde{\nabla}_a\dot{\varphi} - \Big[\mu_m - 2(\phi+1)\ddot{\varphi} + \ddot{\phi} - \frac{\dot{\phi}\dot{\phi}'}{\phi'} - \frac{\dot{\phi}^2\phi''}{\phi'^2} + \dot{\varphi}\phi' + \frac{3\dot{\phi}^2}{(\phi+1)}\Big]\tilde{\nabla}_a\varphi + \Big[\frac{3\phi''\dot{\phi}\dot{\phi}'}{\phi'^3} + \frac{\ddot{\phi}'}{\phi'} - \frac{\dot{\phi}'^2}{\phi'^2} - \frac{\dot{\phi}\dot{\phi}''}{\phi'^2} + \frac{\Theta\dot{\phi}'}{\phi'} - \frac{\dot{\varphi}\dot{\phi}'}{\phi'} - \frac{2\phi''\dot{\phi}^2}{\phi'^4} - \frac{3\dot{\phi}^2\phi''}{\phi'^2(\phi+1)} - \Theta\dot{\varphi} - \ddot{\varphi} + \frac{3\dot{\phi}}{(\phi+1)^2} + \frac{\phi'''\dot{\phi}^2}{\phi'^3} - \frac{3\ddot{\phi}}{(\phi+1)} - \frac{3\Theta\dot{\phi}}{(\phi+1)}\Big]\tilde{\nabla}_a\phi = 0\,. \tag{52}$$

By using equation (15) together with equation (43), one can show that the acceleration potential φ satisfies

$$\ddot{\varphi} = \frac{1}{9}\Theta^2 + \frac{1}{6(\phi+1)}\Big[\mu_m + f - R(\phi+1) - 3\ddot{\phi} + \Theta\dot{\phi} + \frac{3\dot{\phi}\dot{\phi}'}{\phi'} - \frac{3\dot{\phi}^2\phi''}{\phi'^2} + \frac{6\dot{\phi}^2}{(\phi+1)} - \tilde{\nabla}^2\phi\Big] - \frac{1}{3}\tilde{\nabla}^2\varphi\,. \tag{53}$$

4. Conclusion

In this work, we have demonstrated how imposing special restrictions to the linearized perturbations of FLRW universes in the quasi-Newtonian setting result in the integrability conditions that give us consistency relations for the evolution and constraint field equations in the scalar-tensor theories of gravity. In addition, we have derived the velocity and acceleration propagation equations in scalar-tensor theories.

Acknowledgments

HS acknowledges that this work is based on the research supported in part by the National Research Foundation of South Africa (Grant Numbers: 112544) and the financial support of the Center for Space Research, NWU, to attend the *62nd Annual Conference of the South African Institute of Physics*. AA acknowledges that this work is based on the research supported in part by the National Research Foundation of South Africa (Grant Number 109257) and the Faculty Research Committee of the Faculty of Natural and Agricultural Sciences of NWU.

References

[1] Van Elst H and Ellis G F R 1998 *Classical and Quantum Gravity* **15** 3545
[2] Maartens R 1998 *Physical Review D* **58** 124006
[3] Abebe A, Dunsby P K S and Solomons D 2016 *International Journal of Modern Physics D* **26** 1750054
[4] Sotiriou T P and Faraoni V 2010 *Reviews of Modern Physics* **82** 451
[5] Sotiriou T P 2006 *Classical and Quantum Gravity* **23** 5117
[6] Frolov A V 2008 *Physical Review Letters* **101** 061103
[7] Carloni S, Dunsby P and Troisi A 2008 *Physical Review D* **77** 024024
[8] Ehlers J 1993 *General Relativity and Gravitation* **25** 1225–1266
[9] Ellis G F and Bruni M 1989 *Physical Review D* **40** 1804
[10] Maartens R and Triginer J 1997 *Physical Review D* **56** 4640

DIVISION D2 – SPACE SCIENCE

Ensemble Estimation of Network Parameters: A Tool to Improve the Real-time Estimation of GICs in the South African Power Network

M.J. Heyns[1,2], S.I. Lotz[1], P.J. Cilliers[1], C.T. Gaunt[2]

[1]South African National Space Agency, Space Science Directorate, Hermanus, South Africa
[2]Department of Electrical Engineering, University of Cape Town, Cape Town, South Africa

E-mail: mheyns@sansa.org.za

Abstract. It has long been known that large grounded conducting networks on the surface of Earth, such as power lines or pipelines, are affected by solar activity and subsequent geomagnetic storms. With the increased use of electrical technologies, society has become more and more dependent on electrical power and power networks. These power networks form extensive grounded conductors which are susceptible to geomagnetically induced currents (GICs). GICs at any specific node in a power network are assumed to be linearly related to the horizontal vector components of an induced plane-wave geoelectric field by a pair of network parameters. These network parameters are not easily measured in the network, but may be estimated empirically. In this work, we present a new approach of using an ensemble of network parameters estimates. The ensembles include a huge number of parameter pair estimates calculated from simultaneously solving pairs of time instances of the governing GIC equation. Each individual estimate is not the true state of the system, but a possible state. Taking the ensemble as a whole though gives the most probable parameter estimate. The most probable parameter estimate for both network parameters, as defined by their respective ensembles, is used directly in the modelling of GICs. The ensembles themselves however allow for further analysis into the nature of GICs. An improvement is seen when comparing the out-of-sample performance of the ensemble estimates with previous GIC modelling in the South African power network during the Halloween Storm of 2003. For the first time, it is shown that errors in the GIC modelling chain are absorbed into the network parameter estimates. Using a range of estimates from the ensemble, a GIC prediction band is produced. This band corresponds to an error estimate for predicted GIC. Furthermore, it has been explicitly shown for the first time that estimated network parameters vary with GIC magnitude during an event. This behaviour is then used to refine the parameter estimation further and allow for real time dynamic network parameter estimation.

1. Introduction

Modelling geomagnetically induced currents (GICs) entails not just modelling a single system, but rather a chain of coupled systems. The general driver of a geomagnetic storm disrupts current systems in the near-Earth environment and hence the geomagnetic field. Fluctuations in the geomagnetic field through a closed path including the power network induces a geoelectric field and an electromotive force (EMF), which ultimately drives the GIC. The effects of the resulting GICs in these networks can be particularly damaging and costly [1], especially in high-latitude regions. Lesser, but still significant effects have also been observed at mid-latitudes [2–4].

There are a few governing assumptions made in GIC modelling. It is assumed that the induced geoelectric field is driven by a spatially constant plane-wave geomagnetic field over the system

[5]. Such an induced geoelectric field would be uniform if the conductivity of Earth is dependent only on depth (laterally constant). Typical causes of such a geomagnetic field would be a very long (relative to the system) uniform sheet or line current. These assumptions are idealised cases which can be thought of as first order approximations [6]. In reality, the ionospheric current systems are exceptionally complex, non-uniform and highly variable. At mid-latitudes the useful plane-wave geomagnetic field assumption is more accurate than in auroral regions where the auroral electrojet is the dominant current system. This current system is more variable and closer compared to the mid-latitude drivers, making the interactions more complicated [3, 7, 8].

1.1. Network Parameters

Due to the conductivity and extent of the Earth, the main component of the driving EMF comes from the induced geoelectric field at the surface of the Earth. This results in a linear relation between the geoelectric field and the resulting GIC through Ohm's law, defined by the projection of the effective geoelectric field onto the network and the sum of all resistances in the induction loop (which is dominated by network resistances). This results in the governing GIC equation in Cartesian coordinates,

$$GIC(t) = aE_x(t) + bE_y(t), \tag{1}$$

where E_x and E_y are the horizontal geoelectric field components in the Northerly and Easterly directions respectively. Since the network parameters are scaling factors that also penalise non-alignment of the geoelectric field vector with the network, the preferred direction for the geoelectric field to produce large GICs can be found. The ratio of network parameters b/a as used in previous work [9] is encoded in this direction (in this case effectively the angle from North). Any deviation or non-alignment of the geoelectric field from the preferred direction would result in a fraction of the total geoelectric field magnitude contributing to the measured GIC. These traditional network parameters, with units of Akm/V, are usually determined analytically using available information about the network, which is often inaccurate.

2. Model Development

From simultaneous GIC and $E_{x,y}$ data, a single estimate of the network parameters can be derived empirically [8, 10]. It is assumed that these parameters are constant over the time scale of a geomagnetic event, only changing with major alterations of power network related hardware or operations [11]. Due to associated errors at each point in the GIC modelling chain, it has been observed that different empirical values of a and b may be derived for different data subsets defined by magnitude or conductivity [8, 10]. This suggests that a number of errors from different drivers are absorbed into these parameters. To acknowledge these errors and borrowing notation from Wik et al. [8], where α and β represent the empirically derived network parameters, we can redefine the governing equation to,

$$\Gamma(t) \approx \alpha E_x(t) + \beta E_y(t), \text{ where} \tag{2}$$

$$\Gamma(t) \equiv GIC(t) + GIC(t)_{err} \text{ (or the GIC as measured)}, \tag{2a}$$

$$\alpha \equiv a\big(1 + E_x(t)_{err}/E_x(t)\big) \text{ and} \tag{2b}$$

$$\beta \equiv b\big(1 + E_y(t)_{err}/E_y(t)\big). \tag{2c}$$

Given a time-series of n time instances, each a measured state of the system, taking any two relevant and comparable time instances would allow for α and β to be solved for simultaneously. Using all possible combinations of time instance pairs would result in $n(n-1)/2 \approx n^2/2$ (for large n) sets of empirical network parameter estimates. These estimates are collected into the ensembles $\boldsymbol{\alpha}$ and $\boldsymbol{\beta}$. Using a similar approach of statistical mechanical ensembles, each estimate in the ensemble represents a possible state of the real system. When all states are considered together and the result normalised appropriately, an ensemble becomes a probability distribution of system states.

Previous empirical estimation has generally included a fit of sorts that results in a single estimate. One approach is to use a least squares routine and fit equation (1) to the data [8]. Another approach is to select near-zero crossings of the geoelectric field for a single geoelectric field component and solve equation (1). This generates a number of single parameter estimates and a linear fit is then applied (excluding outliers) to find the final estimate [10]. It has also been shown that the ratio of network parameters can be found empirically from data [12]. If a single parameter is known, this ratio can be used to find the other parameter in the parameter pair [9]. All these methods estimate the network parameters and absorb effects analytical methods don't, but do not give an indication of any variation in the parameters (in which errors are propagated), whereas the spread of the resulting ensembles do.

2.1. Data Sources and Selection

This work analyses the Grassridge (GRS) substation in the South African power network, where previous GIC modelling has been done. Measured 2-sec transformer neutral GIC data for 31 March 2001 and 29-31 October 2003 is used. This data range spans geomagnetic storms and no network changes were made during this time (comparable time instances). The geoelectric field data used in this work is derived from 1-min magnetometer data measured at Hermanus (which has been shown to be 'local' enough for GIC modelling [13]). This process makes use of the magnetotelluric method with a layered Earth conductivity model [12]. The conductivity profiles used in this work include the local empirically derived 10-layer profile for Grassridge [9] and the non-local 5-layer for Québec (QUE) [14]. To make use of relevant data, a process of data selection was implemented. In previous work this entailed using only GIC data which satisfies $|GIC| > 0.1 \times RMS(GIC)$, where $RMS = \sqrt{\Sigma_{i=1}^{n} GIC(t_i)^2/n}$ (root mean square), and further selection of significant geoelectric field time instances (which can lead to biasing). Since ensemble estimation is robust and makes use of all possible combinations of time instances, this selection can be relaxed and varied, with the only criterion being that there need to be enough time instances to create a large representative ensemble.

3. Ensemble Estimation Results

In order to compare ensemble estimation to previous work the same GIC data selection criterion is used initially. The data from the Halloween Storm of 29 October 2003 is kept out of the ensemble training as a validation set (not done in previous work). Figure 1 shows the resulting normalised $\boldsymbol{\alpha}$ ensemble histogram (with a similar result applicable for $\boldsymbol{\beta}$). It should be noted that although the probability distribution has the expected bell-shape as predicted from equation (2b), it also has significantly heavy tails (variance and higher order moments are undefined). In this case, the median and not the mean is the best measure of central tendency and hence the most probable network parameter estimate. Also shown is the effect of using different conductivity profiles, with the local empirically derived profile having less spread but no shifting of the peak. This shows that errors made in the derivation of the geoelectric field are absorbed into the empirical network parameters.

3.1. Comparison with Previous Work

A comparison is made with the empirical network parameter estimates of two previous studies, namely Ngwira et al. [9] and Matandirotya et al. [10]. Both these studies used the first day of the Halloween Storm, 29 October 2003, for GIC modelling. During this day, the period between 06:00 and 12:00 is highly disturbed according to SYM-H and the period between 19:00 and 24:00 is relatively disturbed (see Figure 3). The periods 06:00-12:00 and 19:00-24:00, will be referred to as the Primary and Secondary Storm Phases respectively. In addition to this, Matandirotya et al. [10] used the finite element method (FEM) to further improve the derived geoelectric field results (not done in this work).

To measure the performance of the modelling a number of error metrics are used, namely the $RMSE$ (root mean square error), RE (relative error) and Pearson's correlation coefficient

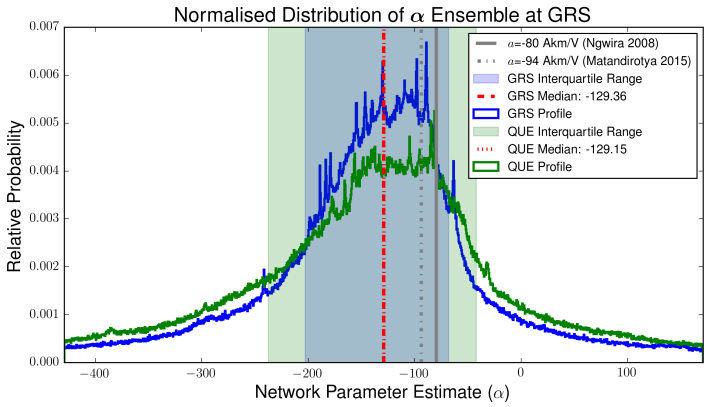

Figure 1. Comparison of the $\boldsymbol{\alpha}$ distributions derived from the local (GRS) and Québec (QUE) conductivity profiles. This behaviour also holds for the $\boldsymbol{\beta}$ distributions. The interquartile range shown is used to model a prediction band (Figure 3). Also shown are the network parameter estimates from previous work.

ρ. The first two metrics quantify the error in absolute amplitude and are defined by,

$$RMSE = \sqrt{\frac{\sum_{i=1}^{n}(GIC_{obs}(t_i) - GIC_{mod}(t_i))^2}{n}} \quad \text{and} \quad RE = \frac{GIC_{obs} - GIC_{mod}}{GIC_{obs}}. \quad (3)$$

Using the previous work's definition, only the median RE for $|GIC| > 1$ A is considered and the result is shown as a percentage [10]. Pearson's correlation coefficient on the other hand is defined in the normal way and quantifies the correlation. The results summarised in Table 1 below show that ensemble estimation does significantly better in general (an overall improvement of more than 10% using the locally based conductivity profile and more than 5% using the non-local profile).

Table 1. Ensemble estimation results compared to previous work.

Data	RMSE [A] (ρ) 06:00-12:00	19:00-24:00	00:00-24:00	RE%
Ngwira Set (a=-80, b=1 A km/V)				
FEM	0.96	1.07	1.35	51
Matandirotya Set (a=-94, b=24 A km/V)				
FEM	1.38	1.11	0.98	41
Grassridge Profile (α=-129.36, β=7.90 A km/V)				
GRS	**1.42 (0.88)**	**0.54 (0.97)**	**0.86 (0.88)**	**30**
Québec Profile (α=-129.15, β=5.61 A km/V)				
QUE	1.78 (0.78)	0.81 (0.93)	1.12 (0.79)	35

3.2. Network Parameter Dependence on GIC Magnitude

Relaxing the criterion for using significant GIC data (considering that already only data corresponding to geomagnetic storms is used), we can use different percentile windows relating to GIC magnitude to quantify the previously observed behaviour that different empirical network parameters are obtained for different data subsets. Taking a 25% percentile window for GRS results in more than 1 million parameters pairs per window, satisfying the condition that a representative ensemble is produced. Arranging the percentile range estimates along increasing values of measured GIC in Figure 2 shows that α and β are apparently not constant and vary with GIC intensity as the storm evolves (since GIC magnitude varies with time). At small magnitude GICs, the network parameters are negligible. This suggests that the preferred direction is indeterminate and that these cases are often a result of miss-alignment and/or a small geoelectric field. As the GIC strength grows, the network parameters become more and more relevant. This is not the case with the β parameter at GRS which stays close to zero. This is a

function of the directionality weighting from the network. GRS is located at a stable endpoint in the network with only a single, approximately North-South directed line. Therefore the β parameter, which scales the Eastward geoelectric field component E_y, is small. This suggests that GICs at GRS are practically independent of the Eastward component of the geoelectric field, which has been seen in previous analysis [2, 9, 10]. Even with this variation, the preferred direction as defined by the ratio of network parameters remains constant.

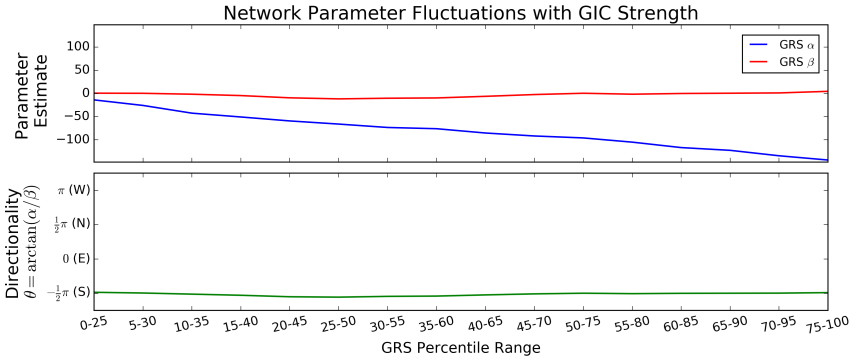

Figure 2. Plot of empirical network parameter estimates at GRS for different magnitude defined GIC percentile ranges. Also shown is the constant ratio of network parameters (network defined directionality).

3.3. GIC Prediction Band

The spread in the distributions of estimated network parameters suggests that using single values of α and β to relate GIC to induced geoelectric field is not correct. Instead of using this approach, we can use the interquartile range of $\boldsymbol{\alpha}$ and $\boldsymbol{\beta}$ (see Figure 1) to predict an associated range of GICs. This network parameter range would span the typical error propagated in the GIC modelling chain, without straying into the heavy tails. Since we are most concerned about the largest GICs, we then use the values of α and β in this interquartile range that will maximise the range of resulting GIC. This approach results in a GIC band, as shown in Figure 3, instead of a single estimate. This gives a handle on the uncertainty in the prediction at any time.

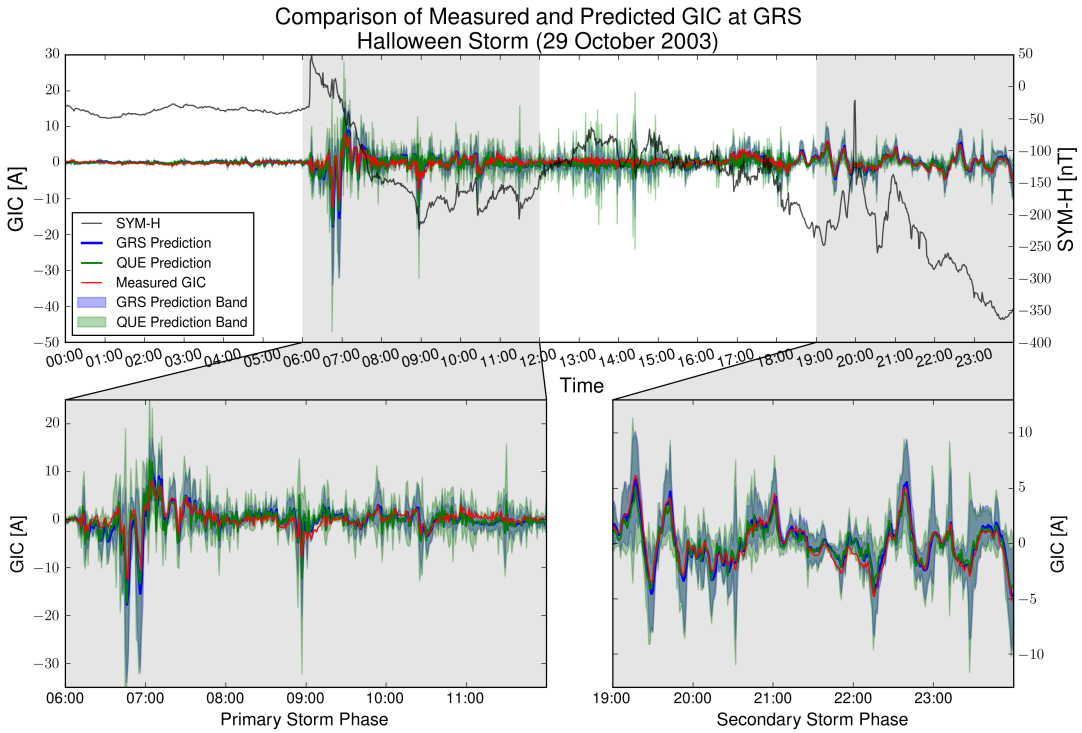

Figure 3. A GIC prediction band produced using a range of estimates.

3.4. Dynamic Network Parameters

Using the observed correlation of the network parameters with GIC magnitude, dynamic network parameters can be created to further improve modelling. The percentile window shifted through all the percentiles results in an overlap of estimates for a given GIC magnitude. Using a weighted mean of these overlapping estimates would result in a single representative estimate for a corresponding GIC magnitude. Calculating an arbitrary GIC magnitude's relevant percentile in the ensemble would then allow the representative network parameter estimate to be mapped to it. Using the GRS data with its low resolution and the non-local QUE profile (that should do a lot worse than a locally derived profile) we see an improvement nonetheless (see Table 2). Also shown are the highest percentile range parameters, appropriate for extreme value modelling.

Table 2. Dynamic network parameter estimation using GIC magnitude.

Québec Profile	RMSE [A] (ρ) 06:00-12:00	19:00-24:00	00:00-24:00	RE%
Static Parameters	1.78 (0.78)	0.81 (0.93)	1.12 (0.79)	35
Dynamic Parameters	1.75 (0.82)	0.72 (0.94)	1.05 (0.82)	36
Extreme Parameters	1.97 (0.79)	0.78 (0.93)	1.21 (0.79)	36

4. Discussion and Conclusion

Not only does ensemble estimation give a much better prediction compared to previous analytical and empirical methods, but the uncertainty in GIC modelling is also quantified. It has been shown how errors made in the derivation of the geoelectric field components are reflected in the network parameters. Taking this into account and a range of values for each of the network parameters, a band of GIC may be calculated instead of a single estimate. Further analysis has also explicitly shown for the first time that the network parameters are not constant and are correlated with GIC strength and hence storm phase. Using this to define dynamic or extreme parameter estimates further improves GIC modelling accuracy and usefulness. These approaches can be incorporated into a real-time probabilistic prediction scheme, with direct application to mitigation schemes for power utilities and other relevant parties.

References

[1] Oughton E J, Skelton A, Horne R B, Thomson A W P and Gaunt C T 2017 *Space Weather* **15** 65–83

[2] Koen J 2002 *Geomagnetically Induced Currents in the Southern African Electricity Transmission Network* PhD Thesis University of Cape Town

[3] Kappenman J G 2003 *Space Weather* **1**

[4] Gaunt C T and Coetzee G 2007 *2007 IEEE Lausanne Power Tech* 807–812

[5] Pirjola R 1982 *Geophysica* **18** 1–161

[6] Boteler D H and Pirjola R J 2017 *Space Weather* **15** 258–276

[7] Boteler D H and Pirjola R J 1998 *Geophysical Journal International* **132** 31–40

[8] Wik M, Viljanen A, Pirjola R, Pulkkinen A, Wintoft P and Lundstedt H 2008 *Space Weather* **6**

[9] Ngwira C M, Pulkkinen A, McKinnell L A and Cilliers P J 2008 *Space Weather* **6**

[10] Matandirotya E, Cilliers P J and Van Zyl R R 2015 *Space Weather* **13** 185–195

[11] Viljanen A, Pirjola R, Prácser E, Ahmadzai S and Singh V 2013 *Space Weather* **11** 575–584

[12] Pulkkinen A A, Pirjola R and Viljanen A 2007 *Earth, Planets and Space* **59** 999–1006

[13] Ngwira C M, McKinnell L A, Cilliers P J, Viljanen A and Pirjola R 2009 *Space Weather* **7**

[14] Boteler D and Pirjola R 1998 *IEEE Transactions on Power Delivery* **13** 1303–1308

DIVISION E – EDUCATION

Influence of guided inquiry on first-year students' attitudes to laboratory activities and performance in physics

V M Baloyi[1], W E Meyer[1], E Gaigher[2] & M A Graham[2]

[1]Department of Physics, University of Pretoria, Private bag X20, Hatfield, Pretoria, South Africa, 0028.
[2]Department of Science, Mathematics and Technology Education, University of Pretoria, Private bag X20, Hatfield, Pretoria, South Africa, 0028.

vonani.baloyi@up.ac.za, walter.meyer@up.ac.za

Abstract. This paper reports on the effect of Socratic questioning integrated with guided-inquiry (GI) on students' attitudes to physics laboratory activities and academic performance. Ninety seven first-year Bachelor of Science physics students participated in this study at a well-established South African university. The students were assigned systematically to control (C) and experimental (E) groups. The C group did recipe-based practical activities, while the E group did GI practical activities. At the end of the semester, data were collected using the written practical and hands-on examinations, follow-up focus group interviews as well as the theory examinations. Results indicated that the E group outperformed the C group in certain questions, but also performed worse in most of the questions. Overall, there were differences between the C and E groups, however the differences were not statistically significant. We conclude that GI laboratory activities did not enhance first-year physics students' academic performance. It was also found that, the E group students developed a positive attitude towards the GI practical activities, while the C group students appreciated the procedural approach followed in their recipe-based practical activities. The results of this study however, contribute to the understanding of current science laboratory practices, learning processes and the potential effects of inquiry-based instruction at university level.

1. Introduction

Inquiry-Based Science Education (IBSE) is encouraged by science education reform documents [1, 2, 3]. IBSE is believed to enhance the deep understanding of scientific inquiry (SI) process skills and science literacy [4]. It is believed that engaging students in SI can assist them in applying their critical and creative skills when performing scientific investigations, using observations and inferences to formulate empirically based explanations [1]. Integrating guiding questions in inquiry-based activities may direct students' thinking and help teachers to understand students' thinking [5]. The teaching approach was based on Socrates' use of questioning to assist a student to think, analyze and seek for new information [6]. Learning Physics is considered to be about constructing knowledge on the basis of experimentation and reasoning, rather than memorizing facts [7, 8]. The current study posits that the GI physics laboratory activities may bring about changes in students' thinking and problem-solving skills [9].

The current paper reports on part of a study that was undertaken at a South African university to investigate whether changing some of the first year university physics traditional laboratory activities into GI format may influence students' attitudes towards laboratory work and performance in physics

[7]. The rationale behind this transformation was that the previous practice of doing the traditional practical laboratory activities was procedural [10] which, according to research, does not enhance students' thinking skills [11]. The aim of this paper is to examine if the combination of guiding questions and GI physics laboratory activities would help students develop positive attitudes towards laboratory work as well as developing a better academic performance. This paper addresses the following research question: *To what extent does GI based instruction in laboratory practical activities as compared to traditional recipe based laboratory practical activities influence first-year university students' attitudes towards laboratory work and performance in physics?* The results of this study may enhance the understanding of current science laboratory practices, learning processes and the potential effects of inquiry-based instruction at university level.

2. Literature review

2.1. Inquiry

Inquiry has a plethora of meanings, however it is broadly described as scientific investigations that encourage classroom practices like posing questions which focus at knowledge attainment and development [12]. The design of the GI laboratory practical activities was informed by McDermott and the Physics Education Group's [13] Physics by Inquiry (PbI) model. The critical component of PbI curriculum is the use of guiding questions where students are encouraged to work in small groups and guided through step-by-step questions when performing activities. According to social constructivist learning theory, effective learning occurs when teachers and students collaboratively work together to co-generate knowledge through investigations, posing questions and finding solutions [14, 15].

2.2. Inquiry-based Instruction versus Traditional Instruction

Inquiry-based teaching approaches use a range of teaching strategies that involve a student as an active agent in the knowledge construction rather than passive recipient of information [16]. Inquiry encourages student-centred approaches and uses instructional practices such as observations, formulating questions, realising gaps in one's knowledge base and conducting investigations to close the gaps. Traditional teaching approaches promote transmission of researched knowledge to students, while student centred approaches like inquiry inspire students to construct knowledge by engaging in investigative activities. Additionally, it is believed that learning by conducting investigations is conducive to students understanding of how knowledge is generated [17]. Inquiry-based teaching helps students to use a deep approach to learning whereas the traditional teaching method encourages students to use a superficial approach [18].

2.3. Role of guiding questions in academic performance in physics

Arons [7] argued that the use of Socratic questioning may assist students to shift from declarative to operational knowledge. Declarative knowledge is knowledge that can be stated and operational knowledge is knowledge that can be applied (through a series of operations) [7]. Utilization of Socratic questioning and students' experiences may guide students to a superior understanding of scientific knowledge, reasoning abilities and logical thinking skills [19]. Syh-Jong's [20] study on the effectiveness of talking and writing in a collaborative environment showed that students do not only defend their science conceptions but also incorporate other students' ideas in clarifying their understanding. In another study, Crouch, Watkins, Fagen and Mazur [21] employed Peer Instruction (PI) which is a teaching approach of guiding all students in the learning process using structured questions for more than ten years in the introductory Physics at Harvard University. It was found in this study that PI promoted students' conceptual reasoning and quantitative problem solving skills.

3. Methodology

The current study followed an experimental design using a mixed methods approach [22], located within the post-positivist paradigm. Post-positivism allowed the researcher to explore the cause and effect of GI laboratory activities on students' academic performance [23] as well as to understand how multiple realities are created and maintained by participants in their personal views of physics knowledge [22]. All 220 Bachelor of Science students (132 males and 88 females) registered for the calculus-based introductory physics course were invited to participate, but only 97 students gave written consent and were systematically assigned to either the C or the E groups. Participation was voluntary and students could withdraw at any time. The C group performed the traditional recipe-based laboratory activities, while the E group performed GI laboratory activities. The physics practical laboratory activities conducted during the session served as a background context for the physics content [24] and the intervention programme lasted for eight weeks.

All groups of students performed the same recipe-based practical activities during the first semester. However, during the second semester, the C group performed the recipe-based laboratory activities following recipe-based instructions while the E group did GI laboratory activities following GI instructions. The GI and the recipe-based practical activities covered essentially the same physics content and used identical equipment. Care was taken to ensure that any questions asked had been sufficiently covered by both C and E groups.

The combined practical examination (i.e. the written and hands-on practical examination) was administered at the end of the term. The marking of combined practical examination and theory examination was done by laboratory assistants and lecturers respectively as in previous years. The quantitative results were analyzed statistically by the researcher to compare the performance of students doing either recipe-based or GI practical activities

Following the practical examination, focus group interviews were conducted to validate the data found through the combined practical examination. All students were invited by e-mail, only sixteen students (9 females and 7 males) responded and were interviewed by the researcher. No incentives were offered. Nine were from the C group while the other seven students were from the E group. There were three unstructured focus group interviews comprised of two groups of five students and one group of six students, where each interview lasted for an hour. In this paper, we will focus specifically on the questions probing the attitudes students had towards the laboratory work (questions 1, 2 and 5). The interviews were transcribed in full in a text file and transcriptions were analyzed following the guidelines by Lesh and Lehrer [25], that is, transcriptions were read several times, refined as meaning became clear, coded and analyzed for differences in students' experiences of C and E groups.

4. Results and discussions

4.1. Focus group interviews

Examples of students' answers during the interviews conducted at the end of the term are shown in Table 1. As can be seen from the responses to question 1, students in the E group (students C and D) could see the advantage of GI laboratory practical activities over recipe based activities. They felt that the practical activities were not difficult and that the practical activities aided their understanding and gave them more confidence in applying physics principles and they enjoyed the more interactive nature of the experiments.

Interestingly, the students in the C group (students A and B) who performed recipe-based practical activities felt that clear guiding instructions were essential, which suggests that these students enjoyed the step-by-step procedures when conducting practical activities. From the answers to question 2 it was clear that students in the E group (students G and H) enjoyed the challenge of GI activities. This

may be an indication that GI gives students an opportunity to grow and overcome the need for recipe-like instructions, while students in the control group appreciated recipe based instructions simply

Table 2 Average scores in percentage point (pp) of the C and E groups in individual questions of the combined practical examination and theory examination

Short summary of question	Average score (%)		
	C	E	E-C (pp)
Combined practical examination (Written and hands-on)	64	62	-2
Written section of practical examination	60	56	-4
Hands-on section of practical examination	74	74	0
Theory examination mark	56	59	3

because they had no other experiences. Interestingly, student F in the C group realized that he would learn better if he were challenged to find a solution instead of just given the answer. In question 5, both groups expressed the view that the practical activities exposed them to new situations and contributed to their understanding of the application of physics to real experiments. It was observed that although students who performed recipe-based practical activities felt the need for guiding instructions, the students in the E group demonstrated a shift in their views about learning, confidence and thinking skills and came to appreciate the GI-based practical activities.

4.2. Practical and theory examination

From Table 2 it can be seen that the C group performed 4 pp better than the E group in the written practical examination, while there was no difference in the hands-on practical examination. In the theory examination mark, the E group performed 3 pp better than the C group. These differences are not statistically significant, and the results suggest that the GI laboratory practical activities had a very small negative effect on students' performance in the combined practical examination and a very small effect on the performance of students in the theory examination. It was also observed that E group students performing the GI practical activities took longer to do the same experiment when compared to C group students, as GI promotes a deeper level of understanding in contrast to the traditional model that promotes surface learning [2].

5. Conclusion

The study was designed to investigate whether GI activities would significantly enhance academic performance and attitudes to practical activities. It was found that the GI laboratory practical activities had only a very small effect on performance in the combined practical examination and the theory examination. We argue that the GI physics laboratory activities in this study did not result in a measureable enhanced performance, because theory examination in the current study did not focus on testing conceptual understanding and scientific process. Similar to the current study there are numerous studies that found that inquiry based activities do not improve academic performance. Research studies conducted by El-Nemr [26] and Lott [27] have shown that inquiry-based approaches had a small positive effect on students' academic achievement in examinations.

The E group students developed a positive attitude towards the GI practical activities, while the C group students appreciated the procedural approach followed in their recipe-based practical activities. This is in agreement with the findings in other studies that have demonstrated that Problem Based Learning provided a thought-provoking, encouraging and enjoyable approach to learning and promoted better attitudes and thinking skills in students [28].

The results of this study should not be generalized to first–year physics students' across South Africa or other countries. It is possible that some physics concepts may have been better addressed than others by the selection of the GI activities, though not by intention. It is therefore recommended that further research be undertaken to shed more light on how students' understanding of certain physics concepts are enhanced by GI activities. In conclusion, we believe that the insight gained in this study may guide transforming undergraduate science courses and may contribute to understanding of

Table 1: Examples of students' views expressed during the focus group interviews.

Interview questions	Group	Response
1. How did you experience the practical activities in general?	C	Student A: "The important thing we have done as you start the practicals you get your information sheet. And then it will describe how you will set up the equipment and that was very important part. Because you give that much preparation about terminology, about the practical you are going to do beforehand. But unless all those instructions for setting up the equipment were clear, all the preparation will mean nothing." Student B: "They were fine for me because we got instructions and we knew basically the outline of practicals. So we knew what to do sort of most of them but then as she said if you don't know the work behind the practicals then you became bit sketchy. There was also a chance to realise how much you know of your work at the time that u can study further for upcoming examinations."
	E	Student C: "Okay, basically the practical activities were fine not difficult but they actually exposed us to variety of physics things that we did not know about before. Like, the apparatus we were using during the practicals and some other physics concepts that we actually learnt in class. But we didn't know how to apply; we were actually given chance to actually see the application of those physics concepts during the practicals. Like for example, connecting those circuits. We only knew how to draw the circuit but didn't actually know how to connect what materials until we do the physics practicals." Student D: "I enjoyed the practical sessions this semester (second semester). They were much easier than last semester's practicals (first semester's practicals). Although the format wasn't very much different, the practicals were just easier. And also when we covered the work in the lectures, we had already done some of the practicals that were related to the classroom's theory content."
2. Would you prefer more guidance in the practical activity or more opportunity to investigate in your own way?	C	Student E: "I think that, the thing is, it really made it easier to relate to the theory and the fact that practical did not take that much preparation. I think that was nice because the thing is like we do not have time to spend hours and hours to prepare for something. And then the fact that usually we were preparing for an hour may be for the practicals and it was not that hard. You can actually like see how everything is coming together. You can see the full picture when doing the practicals, because they made it easier to understand the topic and they made it easier to write test because like if you forgot something, you can think ohh what did we do in a practical and you could actually make a comeback from that." Student F: "I agree with that because there is a thing like if you actually have to struggle to get something right you are going to remember like what you got wrong and what you got right on your own. Whereas if you get guidelines you are going to forget because it is just like a routine, just listen and repeat. You won't like make some conclusions on your own it will be somebody's work on your paper. I think that is repeating the same thing over and over again."
	E	Student G: "I would prefer to investigate on my own, so that I figure out things on my own. Because when you are guided you just follow the procedure but then at the end of the day you acquire less knowledge than when you do things on your own and see what is going on, like individually." Student H: "It is also nice (the one where you are given more opportunity to investigate on your own) because it actually make you think of what you are doing and giving the thing of like challenging yourself, like okay maybe if I do this and then maybe it will work. If I do this let us just see what happens on my own. And if you felt like then you just can't, you can ask the demonstrator to come and help."
5. Do you think the practical activities influenced your views in this regard?	C	Student J: I do not think like my view changed about science but I think it really got enhanced. And I felt more certain about what I felt about science because the thing is like now being able to prove staff and being able to see the law in front you like you see it actually hands on. You actually experience like that is happening, that is the truth and that makes you comfortable with science. And interacting with it because I think some people might escape because it so much info that you do not know where to like take a word or what to leave because you are so scared that there is so much laws such that you need to memorise. But now after like doing all the practicals, I think it really enhanced the fact that I now believe in laws when I see them on paper. So when something is now given I will actually believe more than I used to.
	E	Student K: Yes, well I think the practicals did demonstrate what we were learning about in theory or what we know in theory. So that when we see things in the real world, we understand how it all fits together, what is actually going on behind the bigger main concept."

the perceptions of science held by undergraduates, assisting university lecturers to improve scientific literacy in future scientists and diverse university graduates.

Acknowledgements
Funding was provided by the Sasol Inzalo Foundation and the National Research Foundation of South Africa Thuthuka Grant number: TTK14061168807.

References

[1] Department of Education 2012 Curriculum and Assessment Policy Statement: Physical Sciences (Grade 10 – 12) (Pretoria: Government Printer)
[2] National Research Council 2012 A Framework for K-12 Science Education *practices, cross-cutting concepts, and core ideas* (Washington, DC: National Academy Press)
[3] Next Generation Science Standards Consortium of Lead States 2013 Next generation science standards: By states, for states (Washington, DC: National Academies Press)
[4] Laugksch R C 2000 *Sci. Educ*. **84** 71
[5] Clough M P 2007 *Iowa. Sci. Teach. J.* **34** 2
[6] Crockett C 2004 *Educ. Leadership.* **61** 34
[7] Arons A 1993 *Phys. Teach.* **31** 278
[8] Clough M P and Olson J K 2008 *Sci. Educ.***17** 143
[9] McDermott L C, Heron P R L, Shaffer P S and Stetzer M R 2006 *Am. J. Phys.* **74** 763
[10] Banchi H and Bell R 2008 *Sci. Child.* **2** 26
[11] McDermott L C 1993 *Am. J. Phys.* **61** 295
[12] Blanchard M R, Southerland S A and Granger E M 2008 *Sci. Teach. Educ.* **93** 322
[13] McDermott L C and the Physics Education Group at the University of Washington 1996 *Physics by Inquiry, Vols. I and II* (New York, NY: John Wiley & Sons Inc)
[14] Vygotsky L S 1978 *Mind in society The development of higher psychological processes* (Cambridge, MA: Harvard University Press)
[15] Kruckeberg R 2006 *Sci. & Educ.* **15** 1
[16] Loyens S M M, Rikers M J P and Schmidt H G 2007 *Eur. J. Psychol. Educ.***22** 179
[17] Gibbs G 1988 Learning by Doing: A Guide to Teaching and Learning Methods (London, UK: Further Education Unit)
[18] Brew A and Boud D 1995 *High Educ.***29** 261
[19] Hake R R 2004 *The Arons-Advocated Method* [Electronic Version]. Retrieved on July 8, 2008 from http://physics.indiana.edu/~hake/AronsAdvMeth-8.pdf
[20] Syh-Jong J 2007 *Educ. Res.* **49** 65
[21] Crouch C, Watkins J, Fagen A and Mazur E 2007 *Research -Based Reform of University Physics* **1** 40
[22] Creswell J W 2009 Research Design: Qualitative, Quantitative and Mixed Methods Approaches 3rd Ed (Thousand Oaks, CA: Sage)
[23] Hesse-Biber S N and Leavy P 2011 The Practice of Qualitative Research 2nd Ed (SAGE Publications, Inc)
[24] Khishfe R and Abd-El-Khalick F 2002 *J. Res. Sci. Teach.* **39** 551
[25] Lesh R and Lehrer R 2000 Iterative refinement cycles for videotape analyses of conceptual change In R Lesh (Ed.) *Handbook of research data design in mathematics and science education* (Mahwah, NJ: Lawrence Erblaum Associates) pp. 665–708
[26] El-Nemr M 1980 A Meta-Analysis of the Outcomes of Teaching Biology as Inquiry (Doctoral Dissertation, University of Colorado, 1979), Dissertation Abstracts International, 40, 5812A. (University Microfilms International No 80-11274).
[27] Lott G *J. Res. Sci. Teach.* **20** 437
[28] Bonwell C C and Eison J A 1991 *Active Learning: Creating Excitement in the Classroom* (Washington, DC: ASHE-ERIC)

Students' explanation of motion in real-life context

P Molefe and M N Khwanda

Physics Department, P. O. Box 524, University of Johannesburg, Auckland Park 2006, South Africa.

Email address: pmolefe@uj.ac.za

Abstract. The concepts of force and acceleration are crucial when motion in both one and two dimensions is described. The relationship between the two concepts were explained in terms of Newton's first and second law of motion which is included in both high school and university first year physics curriculum. It is expected that both high school and university first year Physics students can be able to explain motion in real- life context in terms of terminologies used in Newton's first and second law. The paper present students' explanation of motion after viewing PhET simulations. Preliminary results revealed some discrepancy in students understanding of both Newton's first and second law.

1. Introduction and background

Before Galileo and Newton, many people thought objects slowed down or stop because they have the tendency to do so. They thought that, if you want the object to continue moving, the force must be applied on the object. But those people weren't considering the many forces (e.g., friction, gravity, and air resistance) here on Earth that cause objects to change their velocity. A considerable number of studies have been conducted within basic mechanics, and according to [1], conceptions of force constitute the dominant theme in the misconceptions' literature. Among the widely-used instruments for probing the students' conceptions about force is The Force Concept Inventory (FCI), see [2]. This instrument, with carefully constructed multiple-choice questions, has been used in schools and universities worldwide for many years, often to assess the achievements of teaching methods in mechanics. Results show that the Newtonian understanding of force remains a challenge for students across international contexts and levels of study [3-4]. Students' are often found to reason their conceptual understanding as if they were not taught Newtonian mechanics. They associate force with movement, understand force as something an object carries and will be used up during movement, and anticipate that large objects are acting with small force than small objects in an interaction see [5] for an overview of student conceptions.

Many studies of misconceptions in mechanics and other areas suggest that they form part of students' alternative frameworks, which needs to be challenged and replaced by more scientific ways of thinking. However, studies have argued, misconceptions are not necessarily held by students prior to teaching, but might just as well be as a result of the teaching process [6].Therefore, PhET simulations presents the concepts of force and motion that are important to understand how simulation(s) may contribute to students' inconsistent or flawed conceptions. The study was aimed at assessing how students explained real contexts in terms of Newton's first and second law.

2. Methodology

2.1.1. Design

This was a once-off post-test design aimed at comparing the two groups of students taught using different methods. Their background in terms of the symbols or levels they obtained in grade 12 in selected subjects are shown in figure 1 below.

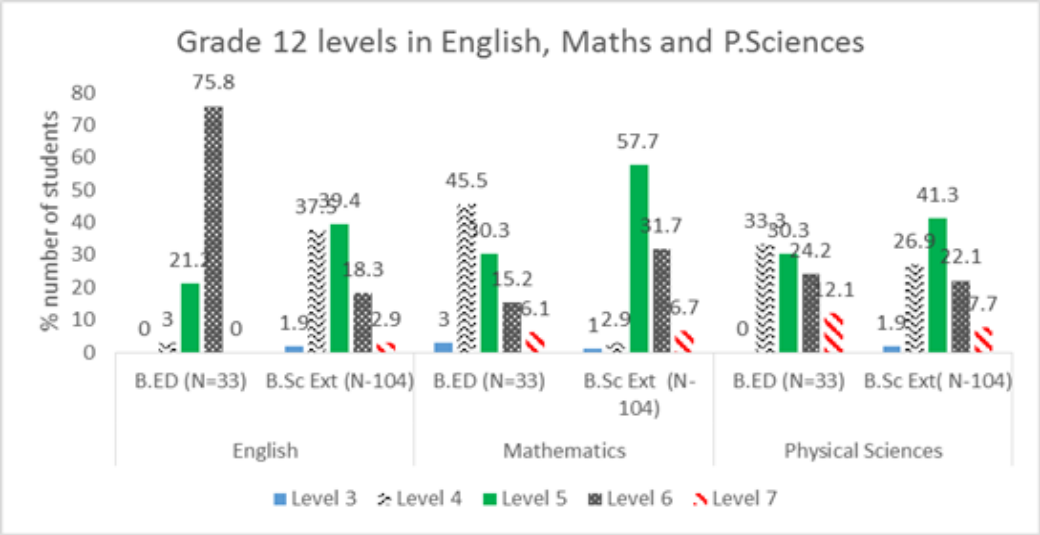

Figure 1: Student's grade 12 results in selected subjects

Based on figure 1, there were no significant difference in terms of the levels obtained by both students in physical sciences, however the majority of B.Ed students scored well in English. We expected B.Ed students to explain better that B.Sc. students based on their English grade 12 results.

2.1.2. The instrument used to collect data

Four questions probing students' understanding of Newton's first and second law of motion were developed by authors with an aim to probe student's understanding of how they apply these two laws in real life context as demonstrated by a simulated picture shown in some of the figures below. To specific questions focused on the assessment of " constant force implies constant speed or velocity misconception", the impact of the equilibrant force on accelerated motion, the impact of adding a mass on motion in two dimensions and the impact of frictional surface on the motion of an object.

2.1.3. Procedure

The two Newton's laws were taught and explained in detail using different examples and exercises in the respective classes that the study is taken. Given that first-year students were taught the concepts of force and acceleration in their high school curriculum, care was taken in the use of the terminologies and formulae, and PhET simulation (which can freely be accessed or downloaded at the following link: https://phet.colorado.edu/en/simulation/forces-and-motion-basics) to explain the concepts of the force and acceleration.

The data was collected from two different first-year classes; first-year teacher's class and four-year first-year students (physics first-year extended students). This data was collected using the google forms in the form of questionnaires. Questions were formulate to be answered as follows correct

choice, stating the law and then use the law to justify their answers. Both classes were given the questionnaires in class to answer in a period of 45 minutes. The first-year teachers class consisted of 33 students and all responded to the questionnaires and the extended students constitute of 111 with 104 students present in the day of the data collection.

3. Results and Discussion

3.1. Constant force implies constant speed or velocity misconception

The second question was aimed at assessing students' if they still hold the misconception that "constant force implies constant speed or velocity". It was framed as follows: *A person pulls a stationery cart on a frictionless surface with a constant force of magnitude 50 N to the left as shown on the diagram. What do you think will happen to the motion of the cart while being pulled with a constant force of 50 N?* The percentage results of students' options are shown in figure 3.

Figure 2: Simulated diagram for question 1

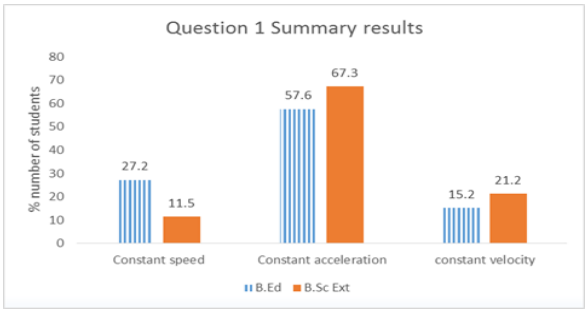

Figure 3: Question 1 results

The results on figure 3 shows that the majority of students both in B.Ed and B.Sc extended chose correctly, but about 100 % was expected since the topic was covered in high school and then revised at tertiary institution, it was expected that students would answer correctly and justify their choices using the relevant physics law. For example we expected their answers to be as follows: correct choice, state the law and then use the law to justify their answers. The correct answer for the question was option B (acceleration is constant), looking at answers students gave as their explanations for their choices, their explanations revealed that they were unable to clearly justify their choices, to apply physics laws correctly while justifying their choices. For example, one of the students' explanations about their choices in question 1 was as follows*: "The object will move at a constant acceleration because the object will move at a constant velocity unless acted upon by an unbalanced force"* The explanation revealed that some students do not see constant force as an unbalanced force which is a misconception. Further analysis of students' incorrect explanations revealed that some still held that constant force implied a constant speed or velocity and others revealed that they think on frictionless surface the speed is constant. Other students were unable to state newton's second law correctly because they stated that the net force is directly proportional to acceleration, which should be the opposite.

3.2. The impact of equilibrant force on moving object.

The question probed student's understanding of the impact of equilibrant force when an object is accelerating as shown in figure 4, which was about newton's first law. The question was as follows: *"The person exerts a force of 50 N and the cart was set in motion to the left, while in motion another*

person exerts a force of 50 N to the right, what do you think will happen to the motion of the cart?" Students' options in percentages are shown in figure 5.

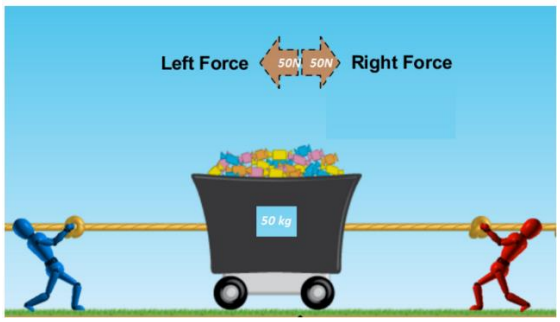

Figure 4: Simulated diagram for question 2

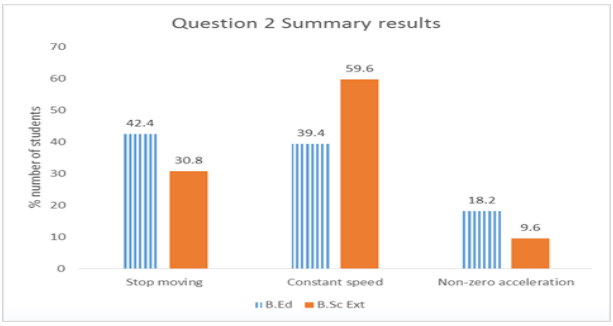

Figure 5: Question 2 results

The results in figure 5 show that the majority of B.Sc Extended (59.6 %) chose the correct answer when compared to 39.4 % of B.Ed students. We expected students to use Newton's first law to justify their choices. However the results revealed that some students associated net-zero force with only objects at rest as indicated by the response written by one of the students: "*We have the resultant force of zero so the cart won't move due to zero acceleration*". Students' incorrect choice and incorrect explanations revealed that they still have misconceptions about the necessity of the net force to sustain motion [7-9]. Others explained that when forces are balanced, an object stops, which shows that they do not know how to apply Newton's first law.

3.3. **The impact of additional mass on horizontal motion.**

When the constant net force was maintained, an additional mass of 50 kg was added as shown in figure 6, students were probed to choose and explain their answers. The question was tricky in such way students were expected to reason based on the overall impact of adding 50 kg on the resulting motion.

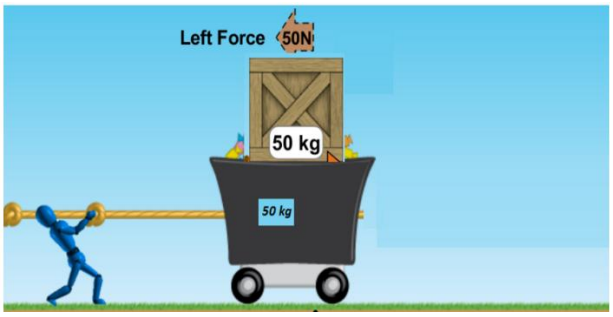

Figure 6: An additional mass of 50 kg added to the trolley

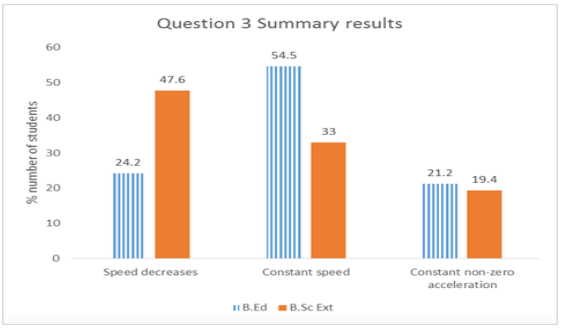

Figure 7: Question 3 results

The most appropriate answer was that the resulting motion would have a constant acceleration because the net force was still constant after the addition of a 50 kg. Figure 7 revealed that few students 21.2 % B.Ed students and 19.4 % B.Sc Ext students answered correctly.

3.4 The impact of friction on the motion of an object.

This was the follow up of the previous questions. It was framed as follows: *If the box of mass 50 kg is added to the chart in question 3. What do you think will happen to the motion of the chart if the surface where tires are moving is rough?* We expected students to explain that the net force would gradually decrease and hence causing the motion to slow down. According to figure 8, all B.Ed. students answered correctly while very few (8.1 %) B.Sc. students did not answered correctly. The results suggest that the impact of friction on a moving object was well understood by students.

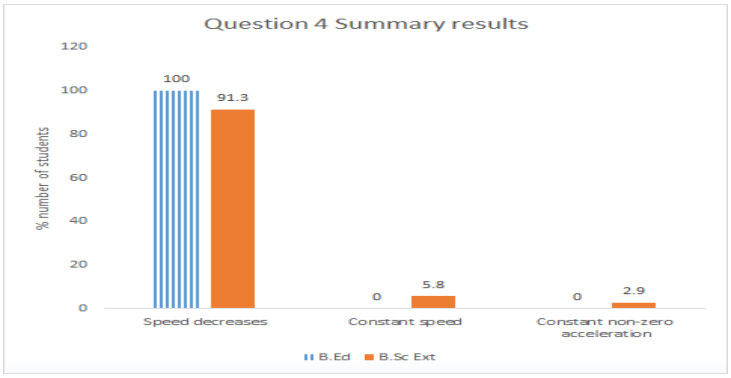

Figure 8: Question 4 results

4. Conclusion

Through the analysis of the students' explanation about a real context simulated from PhET program, some of the challenges students experienced were revealed when many students were unable to justify their options using the correct physics law(s) or principles, it is suggested that in future, instructors use scientific explanations models to develop students' reasoning skills. Students' inability to state Newton's second law correctly can be avoided if instructors revise the importance of dependent and independent variables. The results revealed of this study revealed that even after an introductory physics at university has been covered, students still have the misconceptions they had after instruction. This is consistent with [7] who indicated that the the majority of misconceptions remained unchanged. It can be concluded that majority of both B.Ed and B.Sc Ext students were incompetent on applying both first and second laws of motion but were competent in understanding the impact of friction on the moving object.

Acknowledgements
PM and MNK thanks UJ for financial support and all participants are acknowledged.

References

[1] Carson, R & Rowlands, S 2005 *Mechanics as the Logical point of Entry for the Enculturation into Scientific Thinking*. *Science & Education, 14(3-5). doi: 10.1007/s11191-004-1791-9*, (pp. 473-492).
[2] Hestenes, D, Wells, M, & Swackhammer, G 1992. Force concept inventory. *The physics teacher. 30(3)*, (pp. 141-158).
[3] Caballero, M D, Greco, E F, Murray, E R, Bujak, K R, Marr, M J, Catrambone, R, Kohlmyer, M A, & Scharz, M F 2012. Comparing large lecture mechanics curricula using the Force Concept Inventory: a five thousand student study. *American Journal of Physics*, 638-644.

[4] Fulmer, G W, Liang, L L, & Liu, X 2014. Applying a force and motion learning progression over an extended time span using the force concept inventory. International Journal of Science Education, http://dx.doi.org/10.1080/09500693.2014.939120.
[5] Alonzo, A C & Steedle, J T 2009. Developing and assessing a force and motion learning progression. Science Education, 93(3). doi: 10.1002/sce.20303, (pp. 389-421).
[6] Graham, T, Berry, J, & Rowlands, S 2012. Are 'misconceptions' or alternative frameworks of force and motion spontaneous or formed prior to instruction? International Journal of Mathematical Education in Science and Technology, 44(1), 84-103. doi: 10.1080/0020739X.2012.703333.
[7] Clement, J 1982. Students' preconceptions in introductory mechanics. American Journal of Physics, 50, 66–71.
[8] Gilbert, J K & Zylbersztajn, A 1985. A conceptual framework for science education: The case study of force and movement. *European Journal of Science Education*, 7(2), 107–120.
[9] Sadanand, N & Kess, J 1990. Concepts in force and motion. The Physics Teacher, 28 (8), 503–533.
[10]Bayraktar, S 2009. Misconceptions of Turkish pre-service teachers about force and motion. *International Journal of Science and Mathematics Education*, *7*(2), 273-291.

First year university physics students' understanding of units and measurements

S. Ramaila and L. Reddy

Department of Applied Physics and Engineering Mathematics, University of Johannesburg, P.O. Box 17011, Doornfontein, 2025, Johannesburg, South Africa

E-mail: samr@uj.ac.za

Abstract. Competency in units and measurements is a key skill required for undertaking studies in science. Ability to convert and manipulate both fundamental and derived units is a key requirement to achieve success in both theoretical and practical components of Physics courses. In light of this imperative, this investigation probed students' conceptual competence in units and measurements as crucial aspects associated with both theory and practical work in Physics. The sample in this research comprised students enrolled for diploma programmes in the Faculties of Engineering and Health Sciences at the University of Johannesburg. Key findings in this research strongly suggest that students' conceptual competence in units and measurements appears to be a function of the intrinsic requirements of the respective academic programmes.

1. Introduction

Students' conceptual competence in units and measurements is arguably of crucial significance for laying a solid foundation required to navigate other conceptual knowledge areas in Physics as an intellectually stimulating discipline. Hence, this investigation primarily focused on the assessment of students' conceptual competence in units and measurements as crucial aspects associated with both theory and practical work in Physics. The sample used in this inquiry comprised students enrolled for diploma programmes in Chemical Engineering and Electrical Engineering in the Faculty of Engineering and Chiropractic and Homoeopathy in the Faculty of Health Sciences at the Doornfontein Campus of the University of Johannesburg. In terms of the intrinsic requirements of the respective academic programmes, students are granted admission based on their admission point system (APS) scores as indicated in Table 1 below. The Physics modules for these programmes are structured to provide applied physics flavor for meaningful provision of tailor-made tuition. The Physics theory and practical modules are offered as separate entities for which students have to obtain pass credits. The assessment for the theory module is based on semester tests and a summative semester examination while continuous assessment is adopted for the practical module.

Table 1. Admission Point System (APS) scores for the two Faculties

Faculty	Qualification	Admission Point System Score
Health Sciences	Chiropractic Diploma	27
Health Sciences	Homoeopathy Diploma	27
Engineering	Chemical Engineering Diploma	24

2. Conceptual understanding and practical work

Meaningful practical work is a critical component of studies in science. It has been argued that it is necessary to introduce students to the relevant scientific concepts prior to their undertaking of any practical work if the task is to be effective as a means of enhancing the development of conceptual understanding [1]. At another pragmatic level, concerns have been expressed about whether the observation of specific phenomena within the context of a practical task can lead to the development of conceptual understanding unaided [2]. This discourse presents a complex dichotomy that ought to be unraveled in order to provide insightful elucidation on the relationship between meaningful practical work and the development of appropriate level of conceptual understanding. In this regard, it has further been maintained that the function of practical work might be better understood in terms of a link or bridge between previously taught scientific concepts and subsequent observations [3]. However, it is recommended that much more must be done to assist instructors in engaging students in science laboratory experiences in ways that optimize the potential of laboratory activities as a unique and crucial medium that promotes the learning of science concepts and procedures, the nature of science, and other important goals in science education [4].

3. Research design and methodology

A diagnostic conceptual assessment instrument was administered as part of a survey to assess students' conceptual competence in units and measurements. Specific conceptual areas covered by the diagnostic conceptual assessment instrument are depicted in Table 2 below.

Table 2. Conceptual areas covered by the diagnostic conceptual assessment instrument

Section A	Scientific notation
Section B	Elementary Conversions
Section C	Multiple conversions
Section D	Multiple conversions in dimensional formulae
Section E	Multiple conversions in graphical interpretations

4. Findings

The comparative performance of the three groups is provided in Figure 1 below. Chiropractic and Homoeopathy students demonstrated a better performance as compared to the Electrical and Chemical Engineering students. The performance disparity seems to suggest that competence in the conceptual areas investigated appears to be a function of the intrinsic requirements of the respective academic programmes. In terms of the required APS score, the admission criterion for the Faculty of Health Sciences is stringent as compared to the Faculty of Engineering and hence better quality students enroll for Chiropractic and Homoeopathy programmes. The nature of the students' performance may be attributed to the demands of the admission point system as a reflection of the quality of students admitted into each programme as well as their competence in units and measurements.

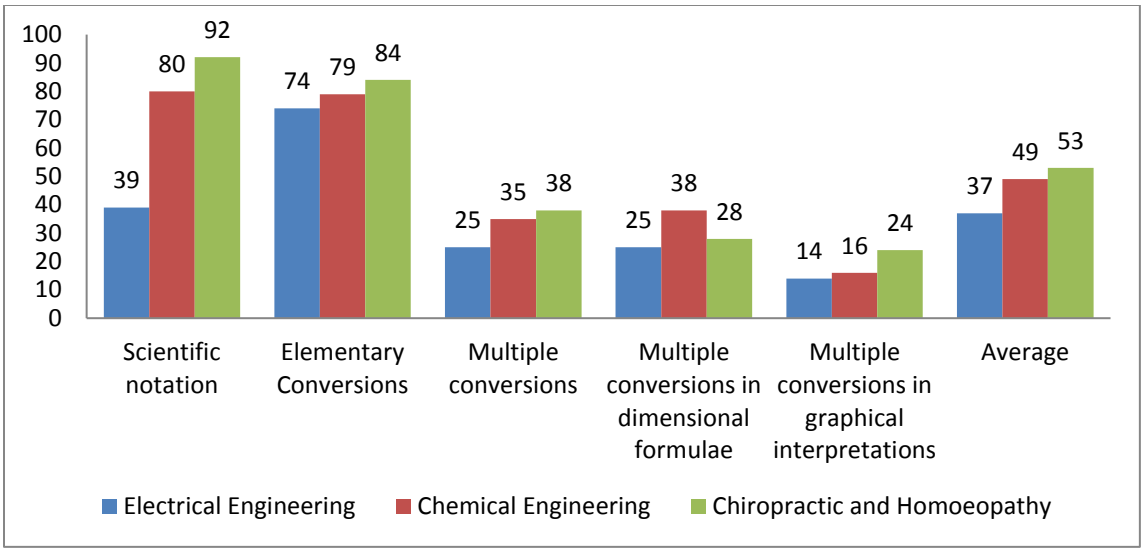

Figure 1. Comparative performance of the three groups

The overall academic performance in terms of the theory module appears to be consistent with the performance in units and measurements as indicated in Figure 2 below.

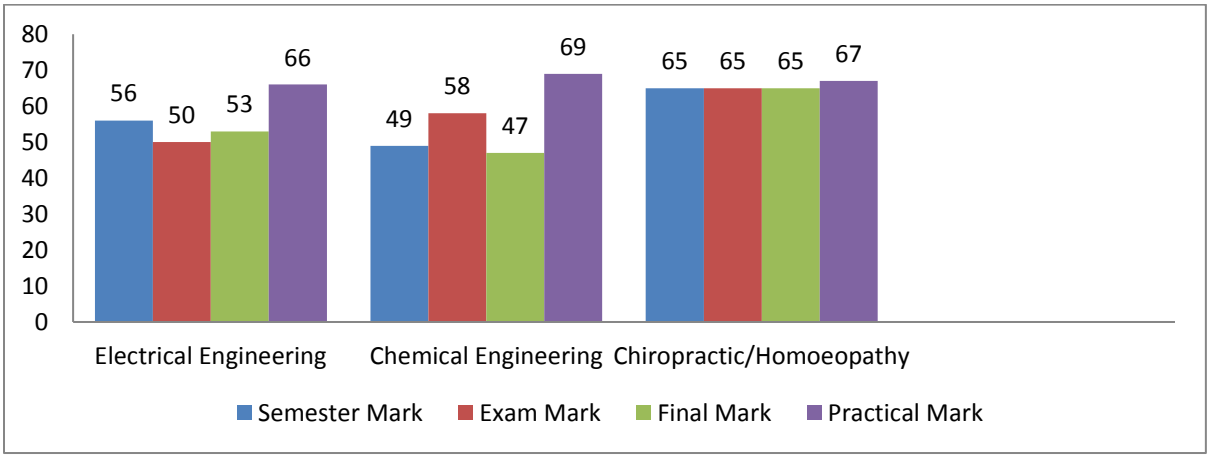

Figure 2. Comparison of academic performance in the theory module

Comparative analysis in terms of the pass rates and throughput rates [Figure 3] appears to reaffirm the fact that students enrolled for Chiropractic and Homoeopathy programmes demonstrated satisfactory performance.

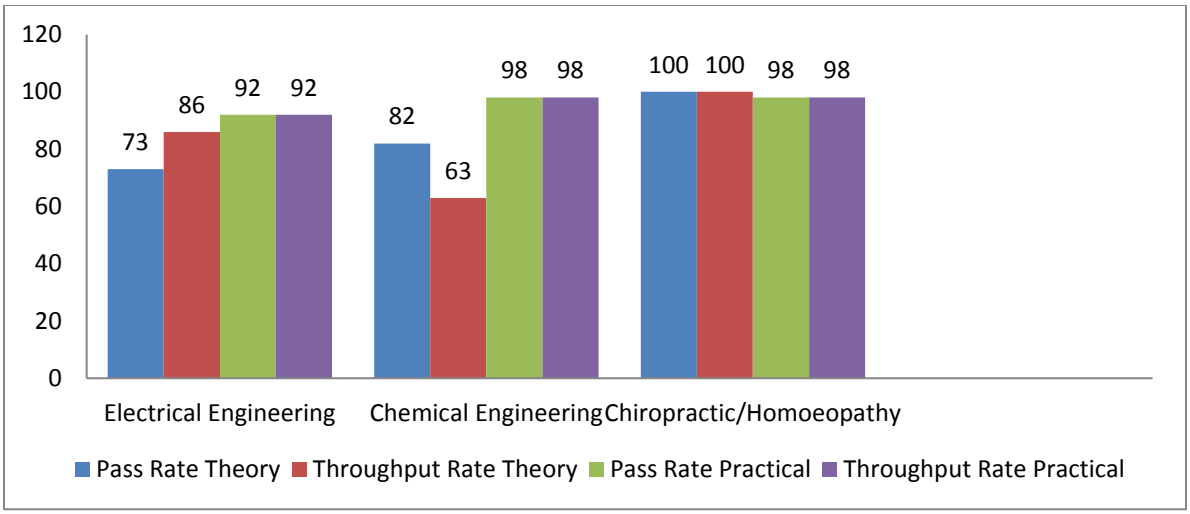

Figure 3. Comparison of pass rates and throughput rates

The pass rate is determined on the basis of the number of students undertaking the assessment while the throughput rate is based on the number of students initially enrolled for the specific module. The pass rate and the throughput rate for the practical module were evidently higher as compared to the theory module.

5. Discussion

Students in the three groups largely experienced difficulties when plotting graphs related to the experiments performed during their laboratory sessions. This inadequacy became evident when their experimental reports were evaluated. Yet, graphs play a highly significant role in providing visual means of presenting information that may be held in a functional relationship or a data set [5]. In addition, being too rigid with the prescription of graphical conventions for statistical data across the school years might stifle students' creativity in thinking of ways to tell the stories in their data sets [5]. The use of software applications to generate graphs is also accompanied by inherent difficulties for students although software applications are designed to enable students to visualize data to promote sense-making from the arrangement of information in space [5].

As an additional consideration, students have a tendency to use a spread of data and the measures of centre to compare data sets in later years of schooling but do not incorporate explicitly these notions with graph interpretation [6]. Within the context of this inquiry, other areas of difficulty for the students appeared to be multiple conversions and multiple conversions in dimensional formulae. These areas of difficulty require adequate attention for the sake of developing meaningful students' conceptual understanding as a key ingredient necessary for grappling with conceptual areas in Physics as well as solving application-type problems.

In a similar vein, practical work is largely viewed as essential part of teaching and learning Physics [3,7,8,9]. In addition, practical work is either considered as a central part of physics classes or its status is wished to be lifted to such a position in many countries [3,8] and South Africa is no exception. In fact, the importance of practical work and theoretical learning supporting each other has been accentuated [10]. However, it has been argued that experimental work is not effective as a tool for promoting understanding or learning the theoretical concepts of physics [3,11,12,13]. Suffice to indicate that although practical work is a somewhat effective tool in getting students to remember the practical aspects of an experiment, the ideas behind the

phenomena are rarely learned and even more so recollected later on [7]. Clearly, these contradictions present a complex scientific quagmire that ought to be fully unraveled.

6. Conclusion

The students' performance in semester tests as well as the final examination projects a reasonable correlation with competency levels in units and measurements. Key findings in this research strongly suggest that students' conceptual competence in units and measurements appears to be a function of the intrinsic requirements of the academic programme. Proficiency in units and measurements is a crucial skill necessary to study Physics and its ramifications as a fundamental science. This skill also forms an integral part of the technical expertise required for the performance of key tasks such as the calibration of instruments and equipments used in various scientific fields. In essence, this study has endeavored to provide valuable insights into some of the essential students' competency levels which are critical to becoming rounded professionals in a scientific sense.

References

[1] Hodson, D. (1991). Practical work in science: Time for a reappraisal. *Studies in Science Education*, **19**, 175-184.

[2] Millar, R. (1998). 'Rhetoric and reality: What practical work in science education is really for'. In J. Wellington (Ed.), *Practical Work in School Science: Which Way Now*? London: Routledge.

[3] Millar, R., Le Marèchal, J.F., & Tiberghien, A. (1999). 'Mapping' the domain: Varieties of practical work. In J. Leach & A. Paulsen (Eds), *Practical Work in Science Education – Recent Research Studies* (pp. 33-59). Roskilde/Dordrecht, The Netherlands: Roskilde University Press/ Kluwer.

[4] Lunetta, V.N., Hofstein, A., & Clough, M.P. (2007). Learning and teaching in the school science laboratory: An analysis of research, theory, and practice. In S.K. Abell & N.G. Lederman (Eds), *Handbook of Research on Science Education* (pp. 393-441). Mahwah, NJ.: Lawrence Erlbaum.

[5] Watson, J & Fitzallen, N. (2010). *The Development of Graph Understanding in the Mathematics Curriculum: Report for the NSW Department of Education and Training*. NSW Government.

[6] Australian Curriculum, Assessment and Reporting Authority. (2010). *Draft Consultation 1.0 Mathematics.* Canberra.

[7] Abrahams, I. & Millar, R. (2008). Does practical work really work? A Study of the effectiveness of practical work as a teaching and learning method in school science. *Journal of Science Education***, 30**(14), 1945-1969.

[8] Hodson, D. (2005). Towards research-based practice in the teaching laboratory. *Studies in Science Education*, **41**(1/2), 167-177.

[9] Jenkins, E.W. (1999). Practical work in school science – some questions to be answered. In J. Leach & A.C. Paulsen, (Ed.), *Practical Work in Science Research – Recent Research Studies* (pp. 19-32). Frederiksberg: Roskilde University Press.

[10] Solomon, J. (1999). Envisionment in practical work: Helping pupils to imagine concepts while carrying out experiments. In J. Leach & A.C. Paulsen, (Ed.), *Practical Work in Science Research – Recent Research Studies* (pp. 60-74). Frederiksberg: Roskilde University Press.

[11] Abrahams, I. (2011). *Practical Work in Secondary Science: A Minds-On Approach*. Continuun International Publishing Group, London.

[12] Hodson, D. (1990). A critical look at practical work in school science. *School Science Review*, **71**(256), 30-40.

[13] Wellington, J. (1998). Practical work in science: Time for a reappraisal. In J. Wellington (Ed.), *Practical Work in School Science: Which Way Now*? (pp. 3-15). London: Routledge.

First year university physics students' perceptions of teaching methods

S. Ramaila and L. Reddy
Department of Applied Physics and Engineering Mathematics, University of Johannesburg, P.O. Box 17011, Doornfontein, 2025, Johannesburg, South Africa
E-mail: samr@uj.ac.za

Abstract. Maximization of students' academic experience through meaningful pedagogic tasks is central to the improvement of instruction in various instructional settings. The effectiveness of various teaching methods through which instruction is provided remains a key imperative for the realization of meaningful student academic performance. As part of this inquiry, Physics students' perceptions of various teaching methods were established through the administration of a survey questionnaire after which interviews were conducted to corroborate the views expressed. Responses to the questionnaire appeared to gravitate towards the lecture method and group discussion as preferred instructional methods. Implications for the improvement of instruction are discussed.

1. Introduction

The improvement of instruction through the incorporation of meaningful pedagogic tasks remains a key goal underpinning the provision of quality education. The utilisation of various teaching methods as vital instructional tools ought to add pedagogic value to the enhancement of scientific literacy in particular. Various teaching methods elicit a wide variety of students' perceptions in terms of their effectiveness. It is imperative for instructors to present content and skills in ways that serve to enhance the opportunities for students to learn. It has been established that students are qualified sources to report on the extent to which the learning experience is productive, informative, satisfying, or worthwhile [1]. This inquiry explored university physics students' perceptions of various teaching methods within a formal instructional setting.

2. Student learning

Students' perceptions of the learning process play an increasingly significant role in the assessment of the learning experience. However, these perceptions cannot necessarily serve as direct measures of instructor or course effectiveness but can serve as legitimate indicators of students' satisfaction [1]. More specifically, student ratings of instructional methods tend to be reliable, valid, relatively unbiased and useful [2]. The need to assess the effectiveness of various teaching methods used within the higher education sector in particular is paramount. Instructors often grapple with student academic performance from various perspectives in an attempt to comprehend the social and cognitive dynamics associated with the learning process. The prevailing conundrum is that students have little experience to determine whether teaching methods adopted by individual instructors are appropriate or not [3].

The situation in this regard is exacerbated by the raging discourse about the definition of teaching or teaching effectiveness. Effective teaching is defined as teaching that produces beneficial and purposeful student learning through the use of appropriate procedures [4]. On the other hand, effective teaching is defined from another alternative intellectual perspective as the creation of situations in which appropriate learning occurs [5]. Adequate intellectual consensus on the definition of effective teaching is certainly required to provide appropriate critical basis for engaging with the dynamics associated with instructional setting in a constructive and meaningful manner.

3. Methodology

Physics students' perceptions of various teaching methods were established through the administration of a survey questionnaire after which interviews were conducted to corroborate the views expressed. The questionnaire was administered with first year university physics students enrolled for academic programmes in Chiropractic and Homoeopathy, Chemical Engineering and Analytic Chemistry. The students were drawn from the Faculties of Health Sciences, Engineering and Science. The study was conducted during the second semester after the students were adequately exposed to university instruction.

4. Findings

Chiropractic and Homoeopathy cohort demonstrated a general preference for lecture method, group discussion and assignments as instructional methods as depicted in Table 1 below. Conference and role-play were the least preferred instructional methods.

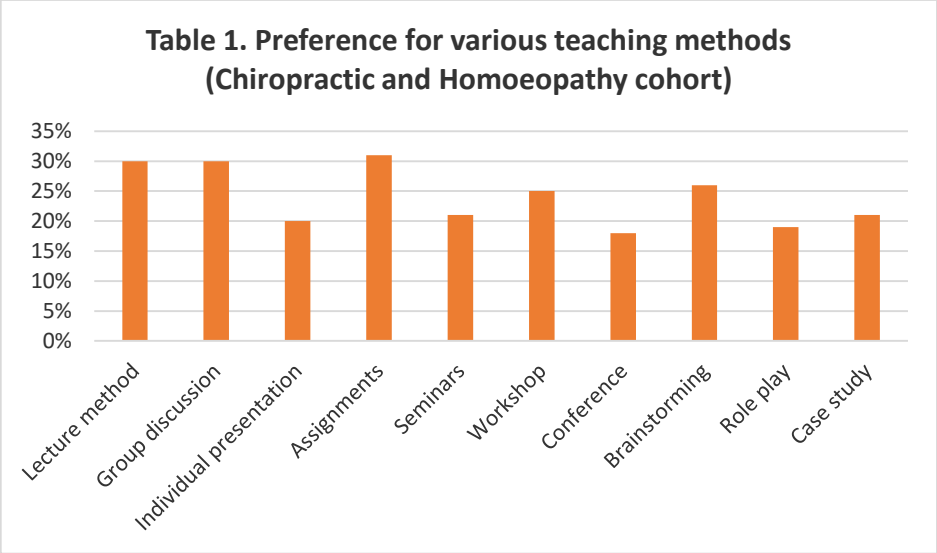

The Chemical Engineering cohort preferred lecture method, group discussion, workshop, and brainstorming as depicted in Table 2 below while the conference and role-play were the least preferred instructional methods.

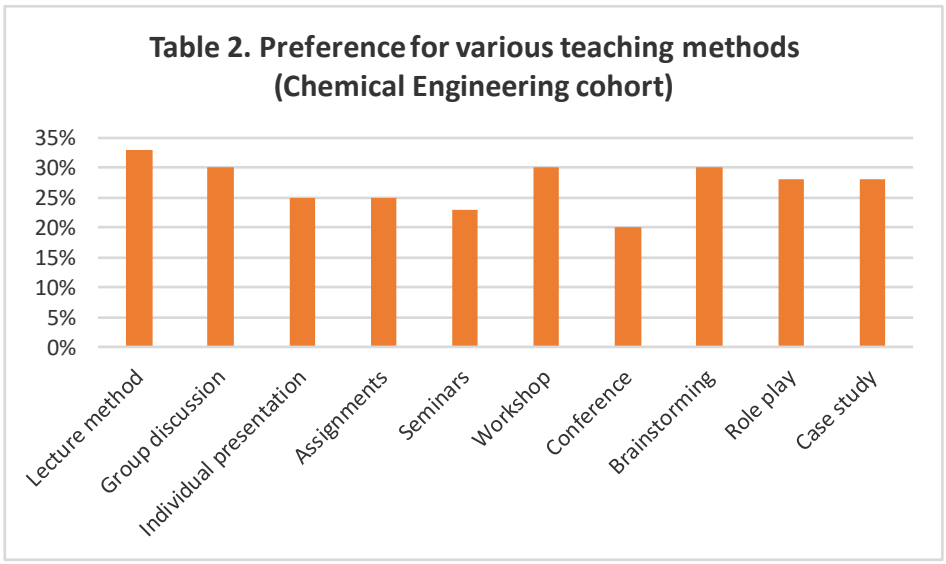

The Analytic Chemistry cohort (Table 3) mostly preferred lecture method, Group discussion and brainstorming. Individual presentation and conference were the least preferred instructional strategies in this case.

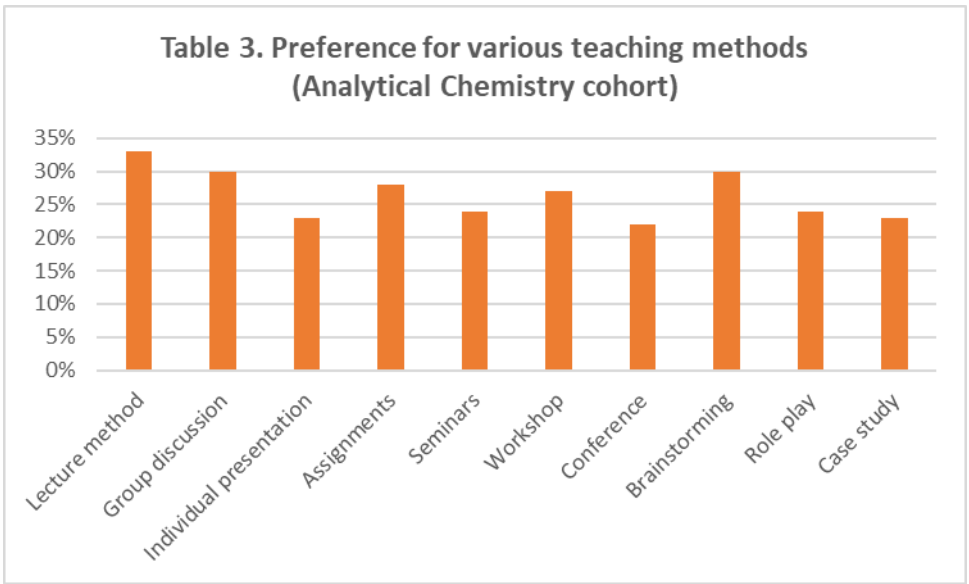

Students provided reasons which essentially captured their perceptions about their preference for particular instructional methods. Tables 4 and 5 below depict students' perceptions in relation to specific instructional methods.

Table 4. Students' perceptions of various teaching methods

Lecture method	**Group discussion**	**Individual presentation**	**Assignments**	**Seminars**
Provides opportunities for gaining knowledge	Provides opportunities to exchanging new ideas	Focused attention	Marks versus learning	Provides presentations which are sources of critical information
Provides opportunities for knowledge expansion	Interactions	Isolation	Reinforcement of knowledge	Interactions
Interactions with the instructor	Knowledge sharing	Focus on individual weaknesses and strengths	Research opportunities	Tedious
Provision of resource material	Alternative explanations	Lack of confidence a major impediment	Performance of intellectually challenging tasks	Gain deeper insight
Development of appropriate conceptual understanding through illustration	Development of conceptual clarity	Stressful	Sense of ownership	Require high levels of concentration
Reflection on key components of the course	Critical engagement with various perspectives	Intimidating	Difficult to complete demanding tasks properly	Provides orientation to learning
Provision of detailed explanations	Better understanding fostered	Opportunities for self-study	Requires determination	Research opportunities
Lack of individual attention	Development of problem-solving and analytical skills	Research opportunities	Requires work ethic	Critical engagement with various perspectives
Clarification of complex concepts	Active participation	Fear	Improves subject matter knowledge	Knowledge sharing
Opportunities for note taking	Stimulation of curiosity	Tedious	Lack of resources stifles task completion	Clarification of complex concepts
Little time to critically reflect on information	Development of thinking skills	Repetitive	Prolonged engagement duration	Knowledge sharing

Table 5. Students' perceptions of various teaching methods

Workshop	Conference	Brainstorming	Role play	Case study
Practical application of theoretical knowledge	Time consuming	Hard to get things done	Active participation	Active engagement with real-life situations
Gain deeper insight	Tedious	Opportunities to critically engage with various perspectives	Hard work	Active participation
Information sharing	Strenuous	Sharing of ideas	Requires determination	Practical application of theoretical knowledge
Revision opportunities	Require high levels of concentration	Deeper reflection	Requires work ethic	Source of information
Review opportunities	Source of key information	Facilitate learning	Development of critical understanding	Gain deeper insight
Good exam preparation	Interactions	Facilitate critical thinking	Active engagement with real-life situations	Interactions
Knowledge enhancement	Development of concrete understanding	Thought provoking	Intimidating	Thought provoking
Detailed explanations	Knowledge sharing	Knowledge sharing	Challenge to introverts	Knowledge sharing

5. Discussion

The most prominent instructional methods preferred by the students were lecture method, group discussion, workshop, as well as brainstorming. In particular, students demonstrated profound inclination to the lecture method. The lecture method is essentially a traditional instructional method widely utilised in various instructional settings. The characteristic features of each instructional method were explained to the students before the survey was conducted to ensure that the students were familiar with the nature of the various instructional methods under consideration. The survey was conducted at the end of the academic year. The differences between the three cohorts can partly be attributed to the teaching philosophies of the qualification offering faculties. It has been established that the lecture method leads to the development of the ability to recall facts while group discussion produces higher level of comprehension [6]. In addition, research conducted on the efficacy of group discussion revealed that group-oriented discussion methods produce favourable student performance outcomes and foster greater participation, self- confidence and leadership ability [7,8]. These notions are consistent with the views expressed by the students to justify their preference for prominent instructional methods. In terms of pedagogic innovation, a combination of instructional methods could facilitate the creation of sustainable opportunities for students to derive rich benefits to aid significant improvement of performance outcomes. Research conducted on the efficacy of the combination of the lecture method and group discussion revealed that the combination itself results in superior retention of material among students [9]. The need for active learning within the South African context is crucially important as a critical basis for fostering meaningful curriculum reform underpinned by constructivism as a contemporary educational perspective. By its very nature, constructivism provides opportunities for active engagement with the learning process through participation in discussions and collaborative activities [10]. The key findings of the study resonate with the notion that systemic exploration of the reform process offers the greatest promise for effective large-scale research-based reform [11].

6. Conclusion

Students expressed a wide variety of views about their preference for various instructional methods. For the benefit of coherent curriculum reform and the enhancement of pedagogic innovation, a conflation of instructional methods promoting active engagement with the learning process based on constructivist principles are advocated. The development of problem-solving and critical thinking skills in particular can be fostered through interventions of this nature. Students' perceptions about various teaching methods ought to be harnessed for meaningful improvement of instruction and sustained promotion of best professional practices.

References

[1] Theall M Franklin J 2001 *Looking for Bias in all the Wrong Places – A Search for Truth or a Witch Hunt in Student Ratings of Instruction?* In the student ratings debate: Are they valid? How can we best use them? Theall P Abrami L and Lisa Mets (Eds) New Directions in Educational Research, no 109 (San Francisco: Jossey-Bass)

[2] Murray H G 1994 *Can Teaching be Improved?* (Canada: Brock University)

[3] Doyle T 2008 *Evaluating Teachers Effectiveness*. Retrieved April 25, 2016, from http://www.ferris.edu/fctl/Teaching_and_Learning_Tips/.../Eva/TeachEffec.htm.

[4] Centra J A 1993 *Reflective Faculty Evaluation* San Francisco (CA: Jossey-Bass)

[5] Braskamp L A Ory J C 1994 *Assessing Faculty Work: Enhancing Individual and Instructional Performance.* (San Francisco CA: Jossey-Bass)

[6] De Caprariis P Barman C Magee P 2001 Monitoring the benefits of active learning exercises in introductory survey courses in science: An attempt to improve the education of prospective public school teachers *J. of Sch. of Teach. and Learn.* **1** 1-11

[7] Perkins D Saris N 2001 A jigsaw classroom technique for undergraduate statistics courses. *Teach. of Psych* **28**(2) 111-113

[8] Yoder J Hochevar C 2005 Encouraging active learning can improve students' performance on examinations *Teach. of Psych* **32** 91-95.

[9] Morgan R Whorton J Gunsalus C 2000 A comparison of short-term and long-term retention: Lecture combined with discussion versus cooperative learning *J. of Instr. Psych.* **27** 53-58.

[10] Fosnot C 1989 *Enquiring Teachers, Enquiring Learners* (New York: Teachers College Press)

[11] Henderson C Nancy M H 2011 Increasing the impact and diffusion of STEM education innovations. *A White Paper Commissioned for Characterizing the Impact and Diffussion of Engineering Education Innovations Forum*.

Soweto Science Centre as a flagship community engagement initiative

S. Ramaila and L. Reddy
Department of Applied Physics and Engineering Mathematics, University of Johannesburg, P.O. Box 17011, Doornfontein, 2025, Johannesburg, South Africa
E-mail: samr@uj.ac.za

Abstract. A flagship community engagement initiative is coordinated within the Faculty of Science at the University of Johannesburg. This initiative takes the form of a strategic and innovative instructional intervention which makes provision for tutoring of learners in the Further Education and Training (FET) band by providing tuition through contact sessions on Fridays, Saturdays and during school recess at the Soweto Science Centre. Learners are drawn from schools located within Soweto Township and the surrounding areas. Prior to the commencement of the mentoring intervention, learners' pre-entry characteristics in terms of the conceptual competence in various Physical Science knowledge areas covered at school were established through carefully structured knowledge, synthesis and application-type questions which formed an integral part of a diagnostic conceptual assessment instrument. In particular, the findings of this research revealed inadequacies in relation to the Physics content covered at schools as well as the competency of the FET teachers in the Physics conceptual knowledge areas investigated. Key findings that emerged from this investigation appear to be commensurate with documented research studies on Physical Science teachers' content knowledge and pedagogical content knowledge within the broader South African educational context. Implications for the coherent infusion of strategic and innovative instructional interventions in various educational settings are discussed.

1. Introduction

Skills development remains a key facet in terms of the realisation of sustainable growth in various sectors of the economy. This development hinges on the demonstration of competence in key knowledge areas such as science, mathematics, engineering and technology. However, South Africa's global ranking in terms of the quality of mathematics and science education as well as the quality of the overall education system paints a gloomy picture as compared to other developing countries [1,2]. Concerted efforts are required to bring about a fundamental transformative change that would serve to generate the desired appropriate quality leading to the restoration of public confidence in the South African education system.

In response to these crucial imperatives, the Soweto Science Centre (SSC) was established in 2010 as a flagship community engagement initiative located within the Faculty of Science at the University of Johannesburg. In terms of its key strategic mandate, the Soweto Science Centre provides tuition to Grade 10, 11 and 12 learners from schools located within Soweto Township and the surrounding areas. The key activities of the Soweto Science Centre include teaching theory lessons in Mathematics, Physical Science, Life Sciences and Environmental Sciences, conducting supervised laboratory and tutorial sessions, teaching English for scientific communication, provision of computer training, presentation of public lectures, participation in Science Expos, participation in the annual national science week, as well as the provision of career guidance and other science related activities [3]. Table 1 below provides learner enrolment information at SSC during the period 2013-2016.

Table 1. Learner enrolment at SSC during the period 2013-2016

Year	Subject	Grade 10	Grade 11	Grade 12	Total
2013	Mathematics	211	190	231	632
	English	211	190	231	632
	Life Sciences	143	140	135	418
	Physical Sciences	157	150	144	451
2014	Mathematics	169	201	198	568
	English	169	201	198	568
	Life Sciences	169	198	170	537
	Physical Sciences	186	192	191	569
2015	Mathematics	312	277	232	821
	English	312	277	232	821
	Life Sciences	62	57	40	159
	Physical Sciences	250	220	192	662
2016	Mathematics	255	319	196	770
	English	255	319	196	770
	Life Sciences	242	287	175	704
	Physical Sciences	251	317	194	762

2. Instructional approach

Evaluating the efficacy of instructional interventions is an inevitable and indispensable task requiring meticulous execution in order to ensure coherent achievement of envisaged outcomes. The instructional approach adopted and utilized by the Soweto Science Centre is underpinned by Peer-Mediated Instruction and Intervention (PMII) [4] as an instructional philosophy. In terms of theoretical clarity, PMII is an alternative classroom arrangement in which students take an instructional role with classmates. This approach makes provision for students to work in pairs or small cooperative learning groups. In addition, PMII provides alternatives to traditional arrangements of lecture, demonstrations and independent study. In essence, students are taught roles by the teacher for purposes of systematically instructing other students coupled with the provision of monitoring and facilitation of students' progress [4].

3. Research design and methodology

A survey was conducted through the administration of a conceptual assessment instrument probing students' conceptual knowledge in various knowledge areas in Physical Science. The conceptual assessment instrument was essentially administered as a pre-test in 2014 when the learners were in Grade 10 and as a post-test in 2016 when the same sample of learners were in Grade 12. The instrument consisted of 20 multiple choice items.

4. Findings

Figure 1 below illustrates Physical Science knowledge areas perceived to be difficult to comprehend by the learners. Mechanics as a vast conceptual area characterised by a myriad of alternative conceptions appeared to be the most difficult conceptual knowledge area for the learners as indicated by a higher percentage of students. This observation is commensurate with the notion that students come to the study of Physics with pre-conceived conceptions about how the world works [5]. In addition, Chemical Bonding as well as Waves were perceived to be abstract conceptual knowledge areas to grapple with by virtue of their complexity.

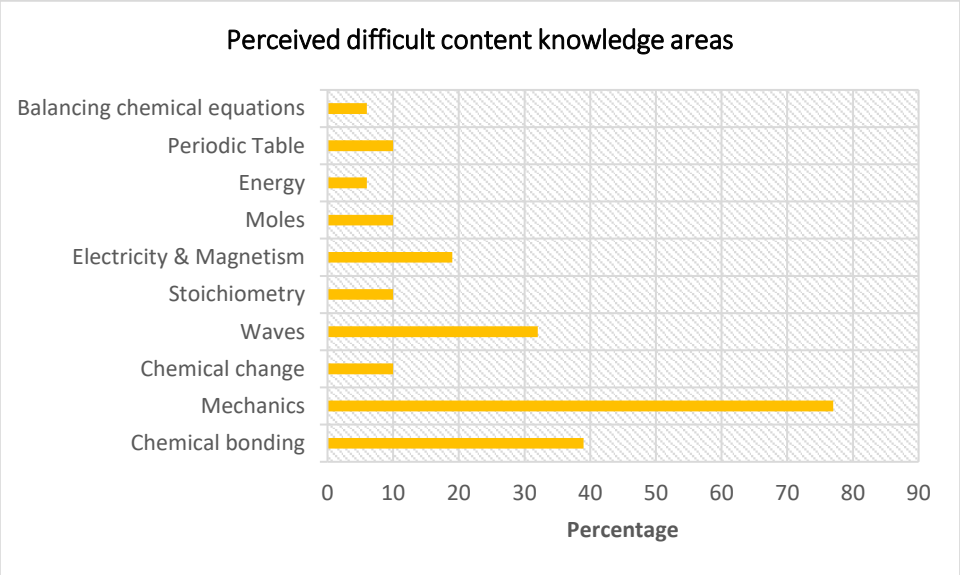

Figure 1. Perceived difficult content knowledge areas

Table 2 below depicts learners' pre-test and post-test performance.

Table 2. Grade 10 learners' pre-test and post-test performance

Percentages	Pre-test (Number of learners)	Post-test (Number of learners)
0 – 10%	67	0
11 – 20%	2	0
21 – 30%	0	1
31 – 40%	0	12
41 – 50%	0	15
51 – 60%	0	25
61 – 70%	0	14
71 – 80%	0	4
81 – 90%	0	0

The pre-test performance revealed that a substantial number of learners fell within the 0-10% performance range. However, the post-test scenario reflected a marked improvement in the overall learner performance which appears to be a positive shift in terms of the comparative performance. Pre-test and post-test numbers were slightly lower than the enrolment due to learner absenteeism. In addition, it is important to note that the same students were tracked over the period under review. As indicated in Figure 2 below, the learners largely expressed positive sentiments in relation to the mentorship opportunities provided by the Soweto Science Centre as compared to mentorship opportunities provided at school.

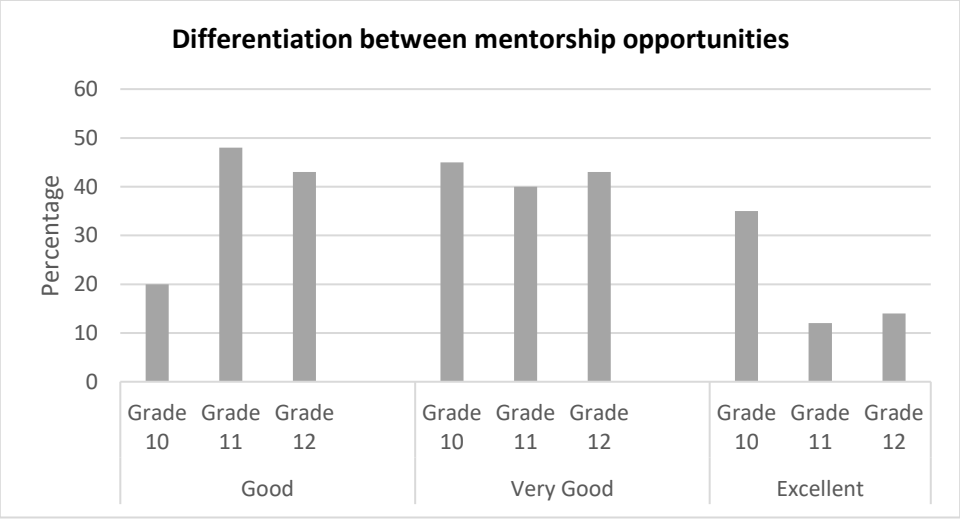

Figure 2. Overall differentiation between the mentorship opportunities provided by the SSC and mentorship opportunities provided at school

The mentorship opportunities provided by the Soweto Science Centre appear to provide the capacity to consolidate the maximisation of the learners' academic experience leading to an enriched learning environment. More specifically, a substantial number of learners who wrote National Senior Certificate (NSC) Examination during 2016 obtained bachelor (B) and diploma (D) passes as indicated in Table 3 below.

Table 3. SSC NSC examination results (2016)

Achievement level	Number of students
Level 6	102
Level 4	42
Level 2	14

Cognitive and affective factors associated with learning are central to meaningful learner performance in any instructional setting. Figure 3 below provides an array of content domains perceived to be intellectually stimulating as indicated by the learners.

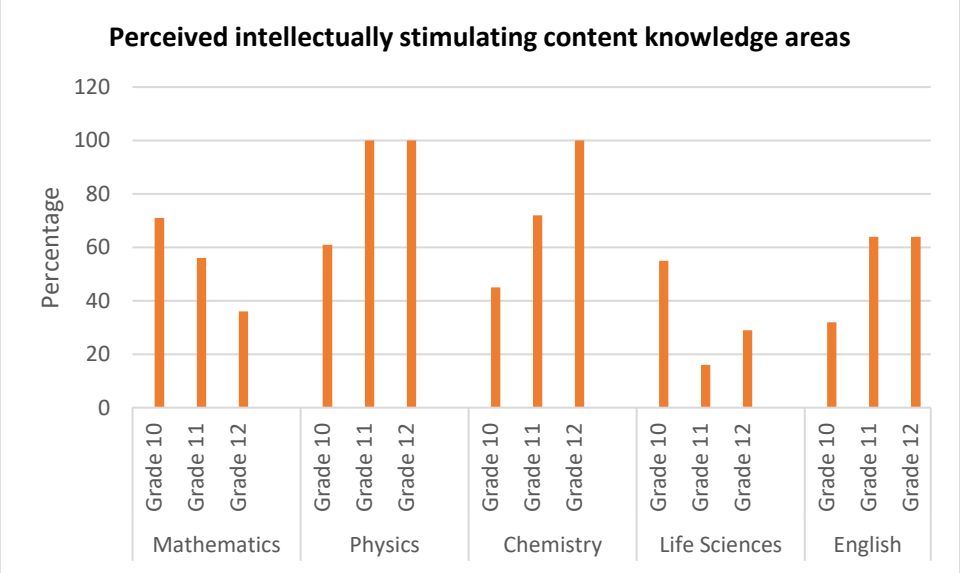

Figure 3. Perceived intellectually stimulating content knowledge areas

5. Discussion

Research on students' conceptual understanding remains a key strategic focus area of immense significance. Research into students' construction of scientific concepts concludes that most students exhibit creativity and intransigence in their quest to circumvent the construction of scientific concepts [6]. In addition, conceptual difficulties encountered by students in Newtonian Mechanics in particular have their origins in their understanding of kinematical concepts [5,7,8]. At another pragmatic level, deeply rooted alternative conceptions are associated with intuitive ideas or preconceptions acquired prior to learning at school [9]. It has also been established that these intuitive ideas are not just learned from experience but are built into the hardware of the brain [10]. The potential efficacy of the mentoring opportunities provided as part of the instructional intervention by the Soweto Science Centre resulted in a positive shift in terms of learner performance post instruction. Such interventions ought to be fully explored particularly within a broader South African context for purposes of adequately addressing conceptual knowledge gaps and conceptual inadequacies associated with various content domains.

6. Conclusion

Meaningful human capital development within the South African context requires effective and innovative instructional interventions geared towards the provision of appropriate mentorship opportunities. Mentorship opportunities provided as part of the instructional intervention by the Soweto Science Centre appear to have huge potential which ought to be harnessed for the benefit of learners in the medium to long term.

References

[1] Work Economic Forum – Global Competitiveness Report 2015-2016.
[2] Work Economic Forum – Global Competitiveness Report 2016-2017
[3] University of Johannesburg 2012 Faculty of Science Newsletter, Volume 02/2012.
[4] Hall T & Stegila RAS 2003 Peer-Mediated Instruction and Intervention *NCAC Classroom Practices* 1-19
[5] McDermott LC 1984 Research on conceptual understanding in mechanics *Physics Today* **37** 24-32.
[6] Loughran J & Derry N 1997 Researching teaching for understanding: The students' perspective *International Journal of Science Education* **19** 925-938.
[7] Trowbridge DE & McDermott LC 1980 Investigation of student understanding of the concept of velocity in one dimension *American Journal of Physics* **48** 1020-1028.
[8] Trowbridge DE & McDermott LC 1981 Investigation of student understanding of the concept of acceleration in one dimension *American Journal of Physics* **49** 242-253.
[9] Driver R 1988 Theory into practice: A constructivist approach to curriculum development IN: Fensham P. (Ed.) *Development and Dilemmas in Science Education* The Falmer Press, London.
[10] Preece PF 1984 Intuitive science: Learned or triggered *European Journal of Science Education* **6** 7-19.

How do undergraduate students respond to early research?

B M Sondezi

Highly Correlated Matter Research Group, Physics Department, University of Johannesburg, P. O. Box 524, Auckland Park 2006, South Africa

Abstract. Institutions of higher learning, particularly at the undergraduate level are driven by strategies used in teaching and learning. Students tends to attribute their performance on the teaching methods used in their academic terms. It is this measuring tool they use to determine their learning as exposed by their results. In the academic environment where the focus is to get an increased number of students who'll enrol for postgraduate degrees, methods of attracting students to stay longer in the system are sought out timely. In the field of Science, especially in Physics departments, where student numbers at postgraduate level are normally low, new and innovative methods are necessary to attract and retain students in the system. A study has been performed where students at the undergraduate level, were introduced to an early research environment, where the work they were exposed to is highly experimental and they had to be introduced to the fundamentals of research. At the end of the period, students were required to report back on their experiences. The second part of the study involved the analysis of scientific data obtained from our research laboratory where students had to do literature search, which also forced them to consult respective postgraduate students. In this report the responses and observations obtained from the students are reported.

1. Introduction

Most universities suffer from the reality of less postgraduate students which is as a result of a number of reasons. This scourge is normally prominent in the science faculty and also more so in some selected disciplines which amongst them Physics is included. Physics as a subject and a career is not famous due to the perceptions around it which includes scarcity of job opportunities' after studying as well as difficulty of the course itself. Students' experience in the field make them to quickly make up their minds about the course very early in their career. Lack of role models is one other factor that causes the reduced number of learners who gear up to postgraduate level.

As a result some interventions are a necessity if we aim to successfully deal with this national challenge. In her dissertation, Van Raden [1] states that of this list of interventions in trying to increase student numbers and to spark interest in postgraduate studies especially in Science, Technology, Engineering and Mathematics (STEM) careers, the one that was of interest was the influence of women role models. The presence of a professional woman scientists in a classroom can inform students about careers that they didn't know existed before. In some cases students can also see that anyone can be involved in research and be successful too.

Undergraduate research (UGR) is slowly becoming a vehicle for deeper, enhanced and engaged learning. In

his correspondence, Mathur [2] states that undergraduate research is something a student embarks upon of his/her own desires. The motivation for such an undertaking has a wide range from a genuine desire for research, to securing an early admission to a prestigious graduate programme, or perhaps to simply affect an improvement to the biodata. It has to be noted that most of our institutions in South Africa have scarcity or no such programs. With this observation, if these programs are established and well managed it is perceived that students will receive various opportunities for research and even internship during their undergraduate studies at institutions of higher learning. While we still explore undergraduate program, we'll continue ask questions like, what constitutes undergraduate research.

2. Experimental method

Within the perimeters of my daily program at the University of Johannesburg (UJ), a group of students were gathered with the aim of mentoring them with the aim of channelling them into their desired career paths. The selection of students was based on the interest of the students, as it was an open call done to students who were in their second year of their four year degree. Interested students availed themselves and were introduced to the program. Students had to learn fundamentals involved in research. These included literature search, as well as learning basic hands-on activities of experimental research. They had to take part in sample fabrication, starting from calculating masses of elements to use, weighing of respective elements (where they had to learn accuracy), cleaning (of elements, especially some rare-earths elements, where they had to learn to handle chemicals, and cleaning of apparatus). This was followed by characterization of samples (using powder X-ray diffraction), and subsequently report writing. This group of 10 students have been actively involved for 9 months prior to the survey that was done using questionnaires. Students had to spent at least 6 hours a week in the laboratory which was achieved over two allocated days in a week. The responses from some of the questions will be presented and discussed, and subsequently provide some conclusions and recommendations.

3. Results and discussion

The questions given in the questionnaires will be presented prior to giving students' responses which will be followed by discussions for respective questions.

Question 1: Briefly state the level of involvement in the research so far. **Responses: [To**
Note:- Each bulleted response is a selected response of an individual student]

- My involvement in the research includes:-
  - ✓ Being **hands on in basic stoichiometric calculations**, **weighing of various elements** in relation to the formation of the desired compounds and undergoing various scientific analysis - where through these analysis we shadow our mentor as she **uses numerous equipment in the low temperature laboratory**.
  - ✓ The research aids in being familiar with the general techniques of arc-melting and the usage of X-Ray Powder Diffraction instrument, electrical resistivity and magnetic susceptibility measurements by the use of relevant equipment available in the laboratory.

- The undergraduate research programme introduced me to another group of students involved in the research programme, where the actual research activities include:-
  - ✓ For now, we are still doing the basics of research. We learned about the **X-ray powder diffraction** and about the **diffraction patterns of different compounds.**

- ✓ We also **searched for publications that relate to research in Condensed Matter Physics so that we can have a better understanding of the field**. Recently we had a task to search for publications (literature search) about **gallium rich compounds which is the current research focus of our mentor.**

It is noteworthy that the activities undertaken in the program are well-known by students. Their ability to state them gives an impression that they are aware of every step undertaken in the program. Students are gradually absorbing the necessary basics, most of which are crucial in their progress.

Question 2: Do you think you are channelled to the right direction, with regards to your desires? Support your response?

- Yes. I always had a desire to do research at a postgraduate level. However, **I did not know which field to choose**. Through this guidance **I now know different research fields** available at UJ and I find the field of **Highly Correlated Matter** to be the most interesting.
- Yes, because **I highly value being in the field of sciences** - specifically studying Physics and Mathematics, as I enjoy working with numbers, laws and generally having to share my experience and applying my scientific knowledge to everyday problems.
- I am in a **process of finding myself**, **my strengths, my weaknesses**, **and my goals are near**, hence I believe I have channelled my studies in the right direction.

The experience of early involvement in undergraduate research seem to have given insight and encouragement to some students. Many times in scarce skills, which include STEM, and more so a career in Physics, see a huge negativity from students. These sources of negativity range from, the difficulty of the course, lack of exposure and role models and lack of facilities. While students struggle with the course, challenges related to lack of exposure dampen interest and they end up not considering postgraduate studies. It is evident that most of them get to universities not sure of what to do after their junior degrees, as one response alludes to the fact that he is still finding himself, in terms of strengths and weaknesses. Studies performed by other undergraduate student researchers, state that students' research experience clarified their career interests and increased their understanding and confidence in their major courses. Close to 70 percent of those surveyed said their interest in a STEM career increased due to their prior undergraduate experience, and 29 percent of students who had never considered getting a Doctorate degree now expected to. There appeared to be a positive effect of the duration of the research experience on how students viewed the experience [2].

Question 3: How is this involvement affecting your overall studies? **Responses:**

- This involvement in research **motivates me to work hard on my academics**. This is because our mentor monitors our progress and we are required to get good results to continue with the program. Furthermore, we are given time to work on our school work so our involvement in research doesn't have any bad effects on our academics.
- Actually **it supports my studies**, as it **elevates my interests** and supports my understanding of other courses.
- The research is helping **me improve on my scientific perspective of life itself**, the **methodology used in research helps me think critically** and respond to situation with a **proactive manner**.

Responses from students informs that they get motivated to even perform better in other courses in their curriculum. Students develop a scientific unction and they begin to develop different problem solving skills to even apply in their everyday life. An involvement of a mentor was seen as a crucial part, especially in guidance and approval of what they do. In their work Shellito at al [4] state that the amount of time a mentor and mentee are together is an important determinant of satisfaction. The most satisfied students spent 2.5 hours a week with their mentors, while those that were somewhat satisfied reported only spending 1.1 hours a week in contact with their mentors. Of the three models of mentors (project, career, and individual), 54 percent of the students felt the ideal mentor would emphasize project guidance, while 34 percent felt the ideal mentor would provide individual guidance. At this stage of inception of UGR, while students are encouraged to be involved in research, they were mostly pushed to perform well in their courses.
It is during the time spent with mentees that a mentor develops well defined projects, recognizing students' constraints outside of the laboratory. He/She will also be in a position to see needs and gaps and can make sure that, students have ample supplies of apparatus and good working equipment and whether they understand all that is communicated to them. Over and above these, spending time with and becoming acquainted with students, gives positive constructive feedback, being approachable, respecting students, progress toward student independence, encouraging reporting back, offering career advice timely, and providing continued mentorship [4] are crucial for their growth.

Question 4: Is the program of early research involvement recommended for undergraduate students? **Responses:**

- **Yes, it motivates students by stimulating interest and enjoyment**. It enhances the learning of scientific knowledge.
- Yes, it makes us **work on our own**. It makes **us explore** and find more information.
- Yes, because **undergraduate students get the opportunity to have hands-on experience** of what their careers will entail and to relate other knowledge to what we meet on a daily basis - as well as to have an **insight into the work involved in the Honours and Masters programs** offered.
- I do not know of any other research programs such as this one. In fact, I am convinced that it is the only undergrad research program in South Africa. **It is a good program** to be part of, we learn a lot and it **helps us prepare for postgraduate studies**. Therefore, I would recommend it to other undergrad students.

Students report enthusiasm about the program, as it also allows them opportunities that other students don't have, opportunities like, being in research lab, interacting with postgraduate students early in their curriculum, a certain level of freedom and independence, knowledge and various research options. Amongst other reported learning gains, were their confidence in their ability to do research and working like a scientist, as they spoke of hands-on experience. Gains were also reported in other skills (i.e., communication as they also wrote a scientific report as well as computer skills gained from writing and data manipulation), clarification of career goals, enhanced career preparation, and changes in attitudes [5].

Question 5: Is undergraduate research program a better tool for learning? Support your answer.
Responses:

- **Yes,** because with that experience, you learn how other students, including postgraduate students in the group, work and thus you follow their footsteps. At the same time research helps us to learn individually.
- **Yes**, it motivate students by stimulating interest and enjoyment. It enhance the learning of scientific knowledge.
- **Yes** it is a better tool for learning as the mentor gives guidance now and then, we are never in the dark.

Exposure to working with others in a group motivated students as they observe each other's commitment levels. Idling students also realised that there's no room for mediocre and they went on to do their part in making sure that they are at the same level of expectation. While students explore and learn new learning skills, it is important that the mentor monitors the whole process of learning and research.

4. Conclusions and Recommendations

The program UGR has been established with the aim of encouraging students to stay longer in the curriculum and subsequently get to PhD level. However, at this early stage, it is learnt that there are other goals that are being achieved over and above sparking interest and development of a deeper learning culture. Students get motivated as they also see their peers excelling in their work, that is, it creates positive competition amongst them.

It is recommended that a curriculum UGR project be made part of at least the students' laboratory activity, while more search continues on a broader scale and also on more students. This will help establish whether it can be taken or adopted as a requirement for the university syllabus of an UG (Bachelor) degree. It is believed that, we can solve most of our national challenges where we are faced with less numbers of students enrolment in STEM careers.

Acknowledgements
BMS thanks the help from students who participated in the program as well as help from P. Molefe. BMS also acknowledges NRF-Thuthuka grant (99231.

References

[1] Van Raden, Stephanie Justine, "The Effect of Role Models on the Attitudes and Career Choices of Female Students Enrolled in High School Science" 2011. *Dissertations and Theses.* Paper 370.
[2] Mathur D., 2017, *Current Science*, **112(8)**, 1613
[3] Russell SH, Hancock MP, McCullough J. 2007, *Benefits of undergraduate research experiences. Science,* **316**, 548-549.
[4] Shellito C, Shea K, Weissmann G, Mueller-Solger A , Davis W., 2001, *Successful mentoring of undergraduate researchers*: Tips for creating positive student research experiences. *Journal of College Science* Teaching; **30**, 460-465.
[5] Seymour E, Hunter A, Laursen S, DeAntoni T., 2003, *Establishing the benefits of research experiences for undergraduates: First findings from a three-year study, Science Education*, **88**, 493534.

DIVISION F – APPLIED PHYSICS

Simulation of Ground Level Spectral Solar Irradiance in Rwanda using LibRadtran.

MC Cyulinyana and H. Winkler

University of Johannesburg, Physics Department, PO Box 524, 2006 Auckland Park, Johannesburg, South Africa

E-mail: kamirwa@gmail.com

Abstract. Optimizing solar power development in Rwanda requires accurate knowledge of the spectral distribution of solar irradiation reaching the Earth's surface at different wavelengths. To characterize the effect of aerosols on surface solar irradiance, the simulation of a cloudless atmosphere is presented in this study. The irradiance spectrum is obtained by solving the radiative transfer equation for this aerosol distribution using established radiative transfer codes. The results show a spectral distribution simulated using LibRadtran, which is one such software package. Its main program, UVSPEC is a radiative transfer tool mainly used to compute radiances, irradiances, and actinic fluxes in the solar and thermal spectral regions. The aerosol properties are furthermore investigated through comparison with archival sunphotometry data from the region and their effect on the surface solar radiation. It is then shown how the outcome of this calculation may be used to estimate local energy yield.

1. Introduction

Solar radiation at the Earth's surface varies greatly due to the change in relative position of the Sun, both during the day and over the year, but also due to the change of atmospheric conditions [1, 2]. Cloud cover, air pollution, the latitude of a location, and time of the year all cause variations in solar irradiance at the Earth's surface [3]. The following types of solar radiation in the Earth's atmosphere are typically defined:(i) direct radiation, which comes direct from the Sun without any interaction; (ii) diffuse radiation, which comes from all over the atmosphere as a result of reflection and scattering by clouds and other atmosphere particles or molecules; and (iii) global horizontal radiation, which is the sum of direct and diffuse radiation on a horizontal surface [1, 4, 5]. In order to optimize locations for solar energy platforms, a ground level spectral solar irradiance distribution is desirable.

Good solar radiation data at ground level is also essential for a wide range of applications in engineering, meteorology, agricultural sciences, in health science, and other fields of natural science to name just a few [6]. The lack of widespread solar ground measurement equipment and meteorological stations leads to insufficient knowledge of solar energy potential in many developing countries. Solar radiation data would help to find solutions to energy shortage and environmental degradation in those areas [7]. This knoweldge helps decision and policy makers in energy sectors, especially for green energy technology implementation.

Even though many methods have been used to estimate and model solar radiation at ground level in the past [3, 4, 8], radiative transfer models have not been widely used, especially in a country like Rwanda where solar modelling was based on empirical and meteorological models

[7]. In this paper, the applicability of the LibRadtran computational code to model Rwanda's solar irradiance is being studied. The procedure could equally be extended to other countries.

This study determines the change of solar spectral irradiance and its relation with aerosols over a typical tropical area (Rwanda). A case study is made of three particular days (see table 1) representing various seasons in the country, using a standard or well-established radiative transfer code [10]. The results show a spectral distribution simulated using LibRadtran, which is a software package for radiative transfer calculations [9, 10].

2. Modelling the Interaction of the Solar Spectrum With the Atmosphere

2.1. Radiative Transfer Equation

The interaction of electromagnetic radiation as it propagates through a medium, is described by the radiative transfer equation (RTE). RTE is widely used to describe and understand the atmospheric radiative transfer of solar radiation [1, 5, 11]. As solar radiation at location (x, y, z) propagates through the atmosphere, it experiences absorption, emission, and scattering [9, 11].

To solve the RTE is non-trivial. It is usually not possible to obtain the solution in a simple analytical function. A common approach is to apply numerical computational methods to solve the RTE and compute the solar irradiance under specific circumstances [10]. The RTE gives the radiance field when solved with appropriate boundary conditions [3]. The solution of the RTE generally yields the diffuse irradiance and the direct irradiance, which in turn are added to give total irradiances or flux quantities [9, 10].

2.2. The Downward Spectral Irradiance

The downward spectral irradiance (the electromagnetic power per unit area received from the Sun radiation in a given wavelength range) $I_{\lambda\downarrow}$ is given by the sum of two components: the spectral direct $I_{\lambda\text{dir}}$ and spectral diffuse $I_{\lambda\text{diff}}$ irradiance.

$$I_{\lambda\downarrow} = I_{\lambda\text{dir}} + I_{\lambda\text{diff}} \tag{1}$$

Equation (1) can be rewritten in terms of direct transmittance (light fraction passing trough the atmosphere without being attenuated) $T_{\lambda\text{dir}\downarrow}$ and diffuse transmittance (transmitted light fraction after being scattered/attenuated) $T_{\lambda\text{diff}\downarrow}$ and becomes:

$$I_{\lambda\downarrow} = I_{E\lambda}\mu_0 \left(T_{\lambda\text{dir}\downarrow} + T_{\lambda\text{diff}\downarrow}\right), \tag{2}$$

where $I_{E\lambda}$ represents the extraterrestrial normal irradiance at an average wavelength λ and μ_0 is the cosine of solar incident angle (θ_z) (an angle that light ray makes with the normal to the surface at the point where the ray meets the surface). We use the approximation of a plane parallel atmosphere divided into two non-mixing layers. One consists of molecules modelled with Rayleigh scattering [12, 13], whose Rayleigh optical depth (the measure of molecules distributed within a column of air from the Earth's surface to the top of the atmosphere) $\tau_{r\lambda}$ and phase function $Re(\gamma)$ are given by the following equations, respectively:

$$\tau_{r\lambda} = 0.008735\lambda^{-4.08}\frac{P_s}{P_0}, \tag{3}$$

$$Re(\gamma) = \frac{3}{4}\left(1 + \cos^2(\gamma)\right). \tag{4}$$

where P_s and P_0 are site pressure and standard atmospheric pressure respectively and γ is the scattering angle.

The other layer is composed of aerosols. In order to model aerosols, the aerosol optical depth (AOD) $\tau_{a\lambda}$ and scattering phase function (Henyey-Greenstein) [13] are defined as follows:

$$\tau_{a\lambda} = \beta\lambda^{-\alpha} \simeq \beta\lambda^{-1.3} \tag{5}$$

$$HG(\gamma) = \frac{1-g^2}{(1+g^2-2g\cos(\gamma))^{3/2}}, \tag{6}$$

where β is the Angstrom turbidity coefficient, α is the Angstrom wavelength exponent, and λ is the wavelength in μm. β is related to the amount of aerosols present in the atmosphere, while α is proportional to the size distribution of aerosols [14]. g is the asymmetry parameter which describes the scattering angle distribution, and γ is the scattering angle. The combination of those two components gives us the total optical depth, τ_λ for the modelled atmosphere.

$$\tau_\lambda = \tau_{r\lambda} + \tau_{a\lambda}. \tag{7}$$

From equation (7), the total transmittance can be expressed in term of optical depth for each layer of this modelled atmosphere and is given by $T_{\text{tot}} = T_r T_a$. Where T_a and T_r refer to the total transmittance through the aerosol layer and molecule layer respectively.

Considering all those parameters, the downward solar irradiance expressed in equation (2) becomes

$$I_\lambda\downarrow = I_{E\lambda}\mu_0 T_{\text{tot}} \tag{8}$$

2.3. Model Description of Irradiance

Radiative transfer models (RTMs) use information about the optical properties of the Earth's atmosphere such as single scattering albedo (ω_0), aerosol optical depth ($\tau_{a\lambda}$), asymmetry parameter (g), aerosol models and different atmospheric profiles as input to determine a theoretical solar irradiance at the Earth's surface [5, 11]. To determine the degree to which incoming solar light is affected by aerosols we used libRadtran to simulate spectral irradiance. LibRatran is a library of radiative transfer routines and programs that includes a selection of twelve different radiative equation solvers, of which DISORT is most widely used. Its main function is the uvspec program which calculates the radiation field in the Earth's atmosphere [9, 15], which in turns determines irradiance, radiance, and actinic fluxes (the quantity of light available to molecules at a particular point in the atmosphere and which, on absorption, drives photochemical processes in the atmosphere)[1]. The inputs to the model are the constituents of the atmosphere including various molecules, aerosols, and clouds [10]. A tropical atmosphere profile and DISORT solver are used to evaluate the aerosol optical depth at a short wavelength range which is in visible - near infrared (VIS-NIR) region.

DISORT is based on discrete ordinates and allows users to compute irradiance in a plane-parallel geometry [10]. The AOD at several wavelengths of the solar spectrum (380, 440, 500, 675, 870 and 1020nm) and the Angstrom exponent at 440/870nm are retrieved from regional sunphotometry data [14].

By solving the RTE, a number of radiative quantities are simulated: the downward direct normal irradiance (DNI) and diffuse irradiance (DI) and the global horizontal irradiance (GHI). The irradiance is obtained by integrating the radiances, which is the radiative solar power per unit solid angle in a particular direction, weighted with the cosine of the viewing zenith angle over all viewing directions in the hemisphere (2π steradians) [9].

3. Results and Discussion

In this study, we estimate aerosols optical characteristics representing three typical atmospheric profiles in Rwanda. We did this by inspecting data from the nearest AERONET station

to Rwanda, which is in Bujumbura, Burundi (Latitude: 3.0°S and Longitude: 29.8°E), for which we assume the same atmospheric and weather profile as Rwanda (Latitude: 2.0°S and Longitude: 30.0°E). Table 1 shows the typical aerosol optical depth characterizing three

Table 1. Assumed AOD at 6 different wavelengths for Rwanda based on actual data retrieved from sunphotometry at Bujumbura.

Angstrom parameters (α, β)	$\tau_{1020\text{nm}}$	$\tau_{870\text{nm}}$	$\tau_{675\text{nm}}$	$\tau_{500\text{nm}}$	$\tau_{440\text{nm}}$	$\tau_{380\text{nm}}$	$\tau_{340\text{nm}}$
Low turbidity							
$\alpha = 2.0$, $\beta = 0.03$	0.03	0.04	0.07	0.12	0.15	0.20	0.25
Modarate turbidity							
$\alpha = 1.5$, $\beta = 0.16$	0.16	0.20	0.30	0.48	0.58	0.72	0.85
High turbidity							
$\alpha = 1.2$, $\beta = 0.44$	0.46	0.56	0.76	1.1	1.28	1.52	1.72

atmospheric scenarios in Rwanda. The data show the wavelengths dependence of AOD and characterizes certain conditions under study, for a site of altitude 1490m above sea level (corresponding to Kigali international airport). To test the sensitivity of solar irradiance change in AOD, the wavelength (500nm) was used to investigate three scenarios; low turbidity ($\tau_{500\text{nm}} = 0.12$, April/May 2014, rainy period in Rwanda), moderate turbidity ($\tau_{500\text{nm}} = 0.48$, October/November is a shorter rainy season) and high turbidity ($\tau_{500\text{nm}} = 1.1$, July/August, dry season in Rwanda). The simulation at two different solar positions (i.e., air mass (AM)) is also presented; AM=1.5 and AM=5 which represent roughly daytime and just before sunset respectively. To calculate AOD, we adopt typical values of the wavelength exponent α retrieved from AERONET data. $\tau_{a\lambda}$ was calculated using equations (5) and (9) [14]. In this study, $\tau_{a1\lambda_1} = \tau_{500}$ and $\lambda_1 = 500\text{nm}$.

$$\alpha = -\frac{\ln\frac{\tau_{a2\lambda_2}}{\tau_{a1\lambda_1}}}{\ln\frac{\lambda_2}{\lambda_1}}. \tag{9}$$

Under cloudless conditions, aerosols are the main atmospheric constituents responsible for the attanuation of solar radiation. The combination of aerosol scattering and atmospheric gas absorption are key players in the visible-near infrared (VIS-NIR) region. β values of less than 0.1 are associated with a relatively clear atmosphere, and values greater than 0.2 are associated with a relatively hazy atmosphere. The results show that AOD has a high impact on direct normal irradiance and the high attenuation is in the visible region (Figure 1, right). This effect has large uncertainties associated with aerosols characterization, aerosols properties (i.e. AOD, ω_0 and g) and their horizontal and vertical profiles.

3.1. Effect of AOD on Spectral Irradiance Components

We used a radiative transfer model to compute spectral irradiance for a cloudless sky. A remarkable reduction in total irradiance and the increase in diffuse light depending on aerosol particles distribution has been observed (Figure 1, left and middle).

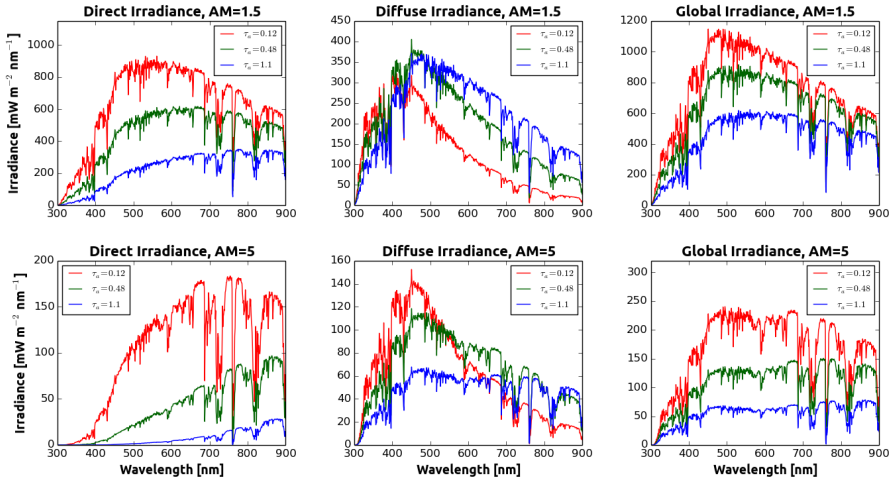

Figure 1. Spectral irradiance for a cloudless sky, AOD= 0.12, 0.48, 1.1. Top row represents an air mass (AM) of 1.5 used for characteristics of day time. The bottom row, represents an air mass (AM) of 5 (near sunset). Left, middle and right diagrams represent direct, diffuse and global surface irradiance.

In fact, when particle size to scatter wavelength is small, i.e. air molecules scattering visible wavelength (380-780nm), scattering is in Rayleigh regime in which short wavelengths (blues) are scattered more efficiently than long wavelengths (reds), giving the sky its blue color [3, 14]. When particles are similar in size to the scattered wavelength, scattering is more uniform across the visible spectrum. Thus, in the presence of an aerosol layer, diffuse irradiance at longer wavelengths (reds) increases more than the increase in shorter wavelengths (blues) [3, 14]. As scattering increases, the portion of diffuse light also increases, resulting in a brighter sky. Figure 1 gives more details for each solar irradiance component. The reduction of surface solar irradiance in the dry season is due to different human activities such as biomass burning while farmers are preparing for seeding season, charcoal preparation which is done by burning trees and the people movements from one place to another increase in such time, which are done by means of transport (i.e. vehicles). Those activities reproduce more atmospheric pollutants and dust particles to name few. These particles size grow due to water vapor presence in the atmosphere.

3.2. Effect of aerosols on Daily Solar Irradiance

Figure 2 shows the variation of surface solar irradiance on different days represented by different atmospheric conditions at 550 nm (visible light). The simulation was done from noon time when the Sun is overhead (SZA$\simeq 0°$ till the sunset time (SZA$\simeq 85°$) in a dry/rainy seasons. For example in figure 2, on a clear day when the Sun is overhead surface solar irradiance (global) is around 1200 Wm^{-2}nm^{-1} at and on a turbid day (figure 2 (bottom row)) it is slightly above 800 Wm^{-2}nm^{-1}, showing the effect on aerosol presence as expected. As the Sun changes position there is a remarkable reduction due to losses related to the optical path [3]. The increase in diffuse radiation and decrease in DNI are also observed and are represented in figure 2 (top row). The simulation results agree well with the actual recorded results. For example on a turbid day, when the Sun is overhead at Kigali international airport (3rd August 2014), surface solar irradiance varies between 875-980 Wm^{-2} which is in the same range with this study.

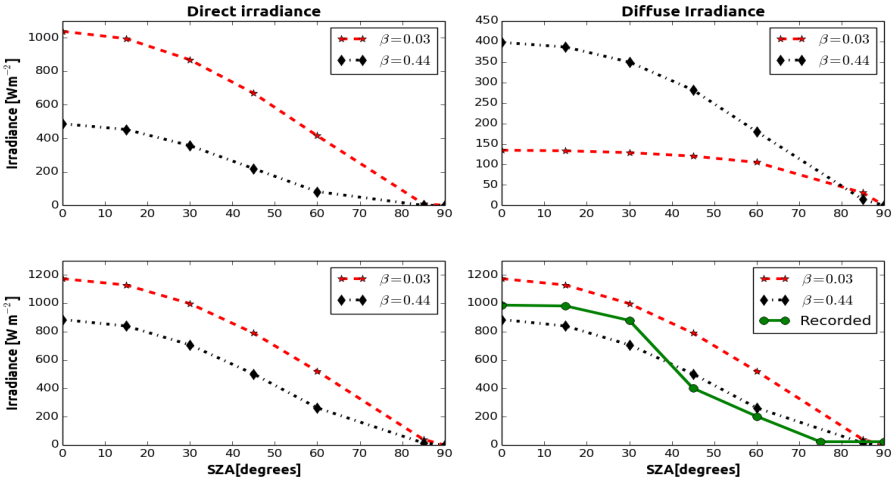

Figure 2. Diurnal effect of aerosol on surface irradiance at different days at $\lambda = 550$nm. The top row represents the variation of direct irradiance and diffuse irradiance on a clear day ($\beta = 0.03$) and on turbid day ($\beta = 0.44$) respectively. The bottom row represents the global irradiance variation on clear day and turbid day respectively and its comparison with recoded data

4. Conclusions

The present study reports the variation of solar spectral irradiance and its relation with aerosols over a turbid tropical region (specifically Rwanda). Considerable reduction in the VIS-NIR irradiances has been projected during the period of high aerosol loading. Our simulations show that aerosols substantially decrease downward shortwave irradiances at the surface, which then impacts solar energy availability on the Earth. High β and α values estimated on a turbid day are representative of urban environments which are similar to some reported previous studies.

This approximation of solar spectral irradiance distribution enables solar systems planners to develop more accurate technologies to estimate energy yield of photovoltaic panels and concentrated solar power plants.

Acknowledgements

Special thanks to Dr. Claudia Emde, for her useful assistance and discussion in developing this paper. This Ph.D. project is supported by University of Johannesburg, OWSD, and Sida.

References

[1] Liou K.N., 2002, *An introduction to atmospheric radiation*, vol.84 , *Academic press.*
[2] Gueymard C., 1993, *Solar Energy*, **51**, 121-138
[3] Muneer T., 2004, *Solar Radiation and Daylight Models*, *Elsevier Butterworth.*
[4] Benson R.B., et al., 1984, *Solar Energy*, **32**, 523-535
[5] Iqbal M., 2012, *An introduction to solar radiation*, *Elsevier.*
[6] Gueymard C., 2004, *Solar Energy*, **76** 423-454
[7] Safari B., Gasore J., 2009, *Asian Journal of Scientific Research*, **2**, 68-75
[8] Mi Zhou H., et al., 2005, *J.Geophys.Res*, **110**, 1-10
[9] Mayer B., 2009, *Eur.Phys.J.Conferences*, **1**, 75-99
[10] Emde C., et al., 2016, *Geosci. Model Dev*, **9**, 1647-1672
[11] Buglia J., 1986, NASA-RP-1156, L16068, NAS 1.61:1156
[12] Bucholtz A., 1995, *J.Ap.Opt*, **34** 2765-2773
[13] Prahl S., et al., 1989, *J. Dos. of. Las. Rad. in Med. and Bio.*, **5** 102-111
[14] Dubovik O., at al., 2002, *J.Atm.Sc*, **59**, 590-608
[15] Lorente J., et al., 1994, *J.Ap.Meteo*, **33**, 406-415

Trigger and data acquisition systems readout architecture of the Tile PreProcessor Demonstrator for the ATLAS Tile Calorimeter phase-II upgrades

D. Hlaluku[1], B. Mellado[2]

School of Physics, University of the Witwatersrand, Johannesburg 2050, South Africa

E-mail: D.Hlaluku@cern.ch, Bruce.Mellado@wits.ac.za

Abstract. The LHC has planned upgrades culminating in the High Luminosity LHC which will increase of order at least 5 times the LHC nominal instantaneous luminosity in order to increase the potential for discoveries. This major increase in luminosity presents significant challenges in the form of increased trigger rates and detector occupancy. The ATLAS trigger and data acquisition systems will be upgraded in order to cope with the increased luminosity foreseen with the LHC upgrades. The ATLAS Tile Calorimeter will be upgraded as well following the ATLAS detector developments. The readout electronics for the Tile Calorimeter will be redesigned, adopting a new readout architecture. A Demonstrator program has been initiated to evaluate and qualify the readout architecture before full installation in phase-II. In the Demonstrator, the on-detector electronics will transmit readout data for every bunch crossing to the off-detector Tile PreProcessor. This Tile PreProcessor stores the data in pipeline buffers and upon reception of an external trigger signal the event data is processed, packed and readout through the legacy system, the new ATLAS proposed FELIX system and an ethernet connection for monitoring all in parallel. A series of test with beam setup campaigns took place between 2015 and 2017 to evaluate the phase-II upgrade electronic prototypes in the lab and to help with estimate provisions for future commissioning efforts. The primary objective of this campaigns is to assess the status of the Demonstrator based on the modified 3-in-1 front-end board baseline option and to give some attention to QIE and the FATALIC. This contribution describes the various aspects of the proposed phase-II readout architecture..

1. Introduction

The hadronic Tile Calorimeter (TileCal) is the central region of the ATLAS experiment at the Large Hadron Collier (LHC) and is used for the energy and direction measurements of hadrons, jets and leptons. It is a large sampling calorimeter which makes use of steel as the absorber material and plastic scintillating plates readout by 9852 Photomultiplier Tubes (PMTs) through wavelength shifting (WLS) fibers [1]. The signals and data from the detector are processed by the Trigger and Data Acquisition (TDAQ) system. The trigger selects event fragments with distinguishing characteristics in real time. The DAQ receives event fragments, reads them out through the Readout System (ROS) and feeds them to the software based high level trigger. The DAQ also provides control, configuration and monitoring functionalities [2]. The High Luminosity LHC (HL-LHC) is a proposed upgrade project termed phase-II and is aimed at cranking up the performance of the LHC by increasing the luminosity to an order at least 5 times beyond the nominal value in order to increase the potential for discoveries after 2025 [3].

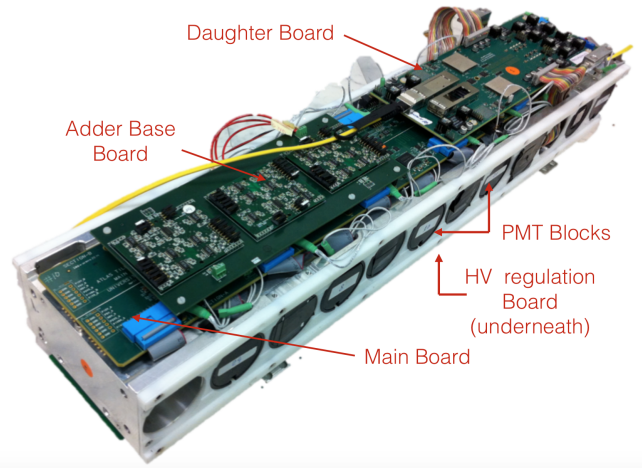

Figure 1: A rendering of a Tile Calorimeter mini-drawer and the components it comprises.

The large luminosity of course offers the opportunity for a wealth of physics measurements, but presents significant challenges to the detector and the TDAQ systems in the form of increased trigger rates and detector occupancy. This mandates an upgrade of the entire ATLAS TDAQ system in order to cope with the HL-LHC. TileCal plans to undergo upgrades as well following the ATLAS detector developments imposed by the HL-LHC. It is currently envisaged that the detector components (iron absorbers, scintillating tiles and optical fibers) will not be changed because they are still in good shape. The current readout architecture outputs digital data at a maximum rate of 100 kHz with a maximum latency of up to 3 μs and stores it in 6 μs pipelines , it is basically not compatible with the baseline trigger architecture of the HL-LHC. The detector readout electronics will be completely replaced to accommodate the new two-step Level-0/1 architecture: the higher trigger accept rates and the extended latencies at both Level-0 (L0) and Level-1 (L1). A new TDAQ architecture is to be adopted to provide full digital calorimeter granularity at the first level of trigger. The digitized data from every bunch crossing will be readout by the off-detector PreProcessors (PPr) [4]. In order to qualify the new proposed readout architecture and the first prototypes of the different components, TileCal has undertaken a series of tests with beam setup campaigns at the CERN accelerator facilities. TileCal prototype drawer modules termed Demonstrators have been instrumented with upgrade specific electronics together with other modules instrumented with current legacy system electronics were exposed to different particles (hadrons, electrons and muons) at different energies during 4 campaigns between 2015 and 2017.

2. TileCal Phase-II electronics Upgrade

For phase-II, the front-end (FE) electronics will be housed in independent mechanical structures called mini-drawers (see Fig. 1). Four mini-drawers comprise a super-drawer in contrast to the current configuration of 2 drawers. This particular stacking was done to improve reliability of the interconnections and to avoid single-point failures due to power distribution in particular. Each mini-drawer houses a total of 12 PMTs with FE amplifier cards for pulse conditioning and calibration, a main board (MB) that receives PMT signals and routes them to the Daughter Board (DB) which handles all communication with the back-end (BE) electronics, an adder base board which is only needed for analog trigger signals aggregation in the 3-in-1 Demonstrator, and lastly, a High Voltage (HV) regulation board to deliver the correct HV to the PMTs [5].

The proposed TileCal TDAQ architecture for phase-II is shown in Fig. 2. The readout is based on a continuous digitization and data transfer to the off-detector Tile PPr for very bunch

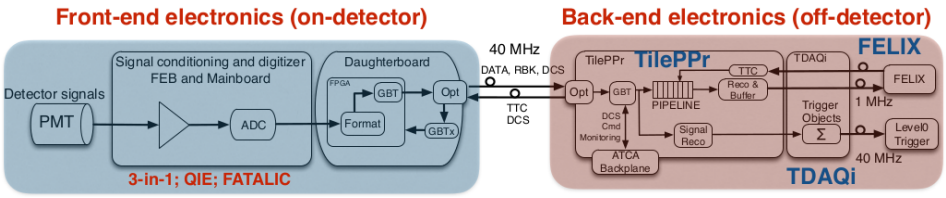

Figure 2: The TileCal phase-II upgrade readout architecture.

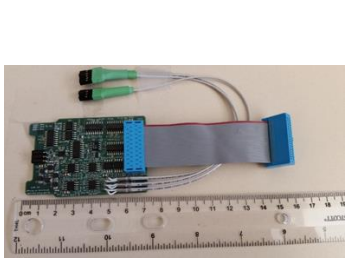

(a) 3-in-1 FEB.

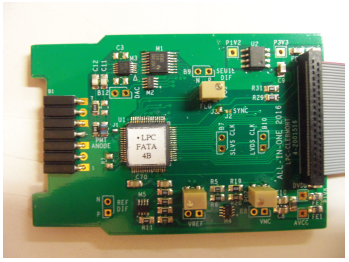

(b) FATALIC FEB.

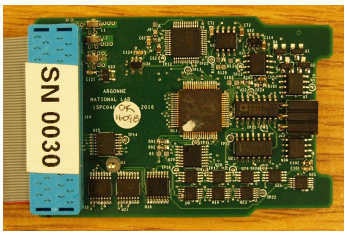

(c) QIE FEB.

Figure 3: The 3 Tile front-end cards under evaluation for phase-II.

crossing (40 MHz) of all readout channels. The design has fair emphasis on redundant optical transmission of the data, this means that no gain selection logic will be implemented in the FE electronics and the digitized signals of both gains will be transmitted. Pipelines and the de-randomizer are implemented by the PPr units located in a low radiation environment of USA-15. The PPr will further apply energy scale calibrations as in the current Readout Drivers (ROD) and prepare the L0/1 trigger information [6].

3. Changes and options

3.1. Front-End

TileCal R&D program includes three different front-end board (FEB) options for processing PMT signals as shown in Fig. 3. One of the options under consideration is an optimized redesign of the current 3-in-1 FEB that uses state-of-the-art discrete commercially off-the-shelf integrated circuits. The 3-in-1 signal processing approach uses a shaper circuit to transform a PMT pulse into an easy to digitize waveform/pulse whose amplitude is proportional to the total charge of the original PMT pulse. The shaped signal is then amplified in two separate ranges and sent to 12-bit ADCs on the MB [4].

Another approach is the Front-End ATLAS Tile Integrated Circuit (FATALIC) which uses shaping just like the 3-in-1 but with a different pulse. This ASIC chip is a new technology for TileCal and aims at integrating much of the 3-in-1 functionality into the FATALIC chip, this includes signal digitization. The ASIC design is based on a 130 nm CMOS process which has been already qualified in ATLAS for applications in other subsystems with much higher radiation doses [7].

The third option is the Charge Integrator and Encoder (QIE) ASIC developed by Argonne National Lab. The QIE circuit does not shape the PMT pulse to digitize at 40 MHz. Instead, it directly integrates the PMT anode current in 25 ns intervals. This chip has been designed to satisfy the radiation requirements tailored for TileCal. QIE offers a unique opportunity to reduce the impact of the out-of-time pileup measurements for TileCal [8].

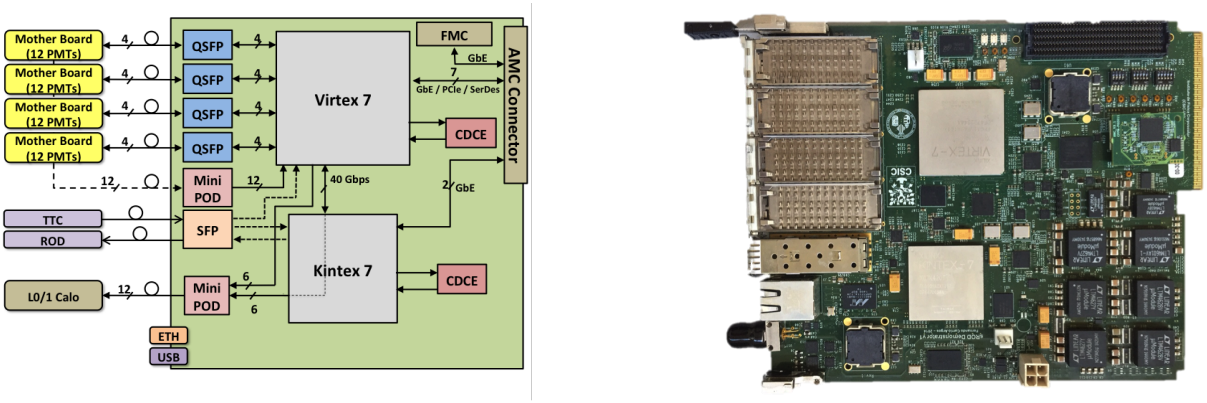

Figure 4: A sketch representation of the Tile PPr board (left), and the PPr AMC board (right).

3.2. Back-End, PPr

Figure 4 shows a sketch of the Tile PPr. The PPr is the core of the BE electronics system and provides benchmarks for investigating the different parts of the upgrade system. It is a high performance double advanced mezzanine board based on FPGA (Field Programmable Gate Array) resources and QSFP (Quad Small Form-Factor Pluggable) modules. This board has been designed in the framework of the ATLAS TileCal Demonstrator project for the phase-II upgrades as the first stage for the BE electronics. The data is received through four optical connectors and the internal hardware transceivers located in the main FPGA. This FPGA also contains the pipeline and de-randomizer memories, the synchronization of data with TTC (Timing, Trigger and Control) and the reconstruction of the events passing the L0/1 trigger. The L1 calorimeter (L1Calo) preprocessor module implements the algorithms to provide digital information to the L0/1 trigger of ATLAS. The new architecture of the read-out improves the precision and the granularity of the trigger information for the cluster and jet energy L1Calo processors. The increased granularity can be achieved in the radial direction, which would eventually allow the implementation of shower profile algorithms at L0/L1. The use of digital signals at the PPr for the L0/L1 trigger replaces the present analog L1 trigger preprocessors. The board transmits the data accepted by the L0/L1 trigger to the ROS. In addition, the board is the BE interface with the DCS (Detector Control System) and TTC of the FE electronics [9].

3.3. Demonstrator project

The Demonstrator project aims at testing the long term performance of the upgrade system without compromising the present data taking. This is to be achieved by developing an early version of the new digital calorimeter system that is compatible with the present analog trigger, DAQ, DCS and TTC. Digital transformation will translate TTC signals into upgrade specific commands and translate upgrade outputs to a format acceptable by the present RODs. The TileCal Demonstrator is a prototype phase-II super-drawer composed of 4 independent mini-drawers (see Fig. 1). If verified to perform according to requirements a Demonstrator drawer is to be inserted into the real ATLAS detector. If this is successful, three more additional Demonstrator modules will follow in one of the short end of year Christmas shutdowns [10]. This will allow thorough testing of the major functionality of a phase-II system before full installation in phase-II. The data is readout readout through the PPr board which formats and transmits to the legacy RODs for backward compatibility with current system and to the Front-End Link eXchange (FELIX) [11] as presented by Fig. 5.

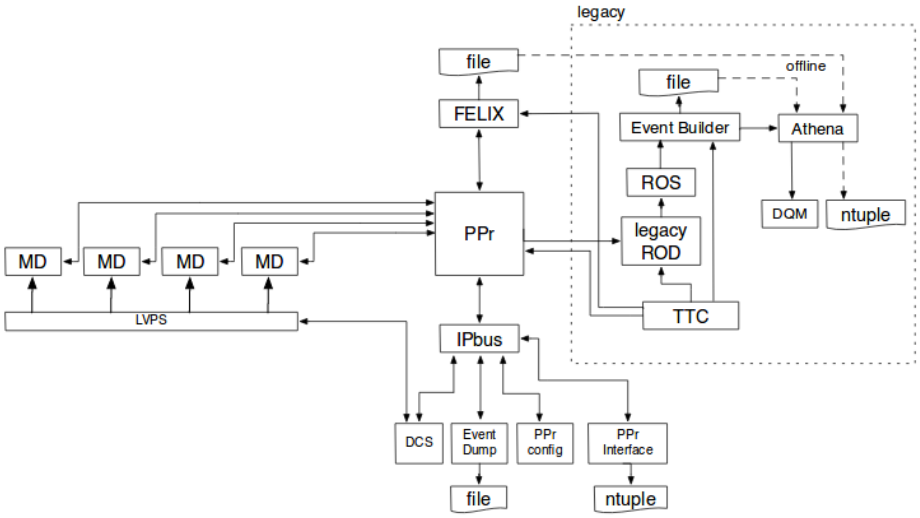

Figure 5: Demonstrator data acquisition architecture with PPr.

4. Test Beam campaigns

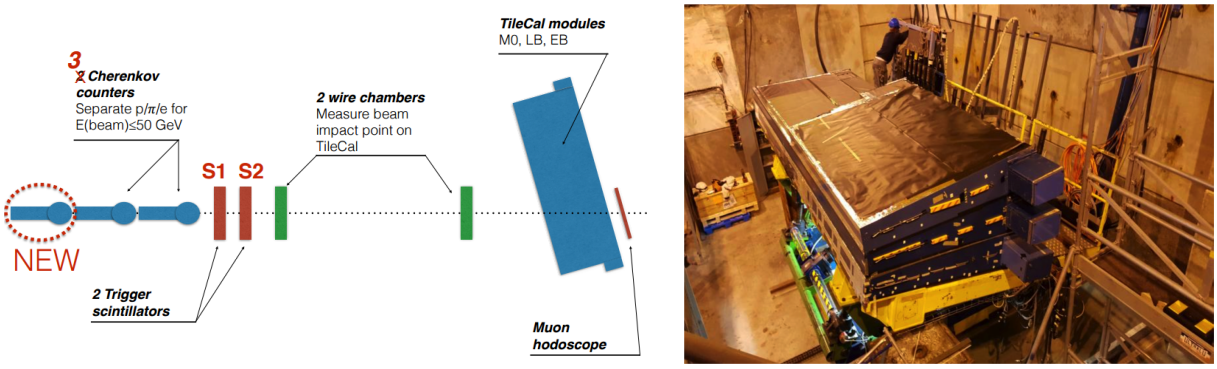

Figure 6: Diagram of the beam elements (left), and a picture of the TileCal modules mounted on a mobile table.

A series of test with beam setup campaigns took place between 2015 and 2017 to evaluate the phase-II upgrade electronic prototypes and to help with estimate provisions for future commissioning efforts. The primary objective is to assess the status of the Demonstrator based on the modified 3-in-1 FEB baseline option and to give some attention to QIE and FATALIC. A hybrid Demonstrator that uses the 3-in-1 option has been developed and is fully compatible with the current system providing both the analog trigger signals for the current L1 trigger and full digital information for the phase-II PPr prototypes. In parallel, one more TileCal module has been instrumented with the two other options, and three other modules equipped with current legacy system electronics were exposed to muons, electrons and hadrons at different energies during this test beam campaigns to assess their performance. The results from these campaigns provide the necessary performance analysis to aid the 2017 FEB option down-selection. Some preliminary results from the 2016 test beam campaigns are accessible here [5,12]. Figure 6 shows the module configuration for the tests with beam setup campaigns at the CERN beam facilities.

The prototype PPr was used during this campaigns since it can be operated in both legacy and upgrade modes as shown by Fig. 5. In legacy mode, the PPr emulates the legacy FE

electronics by receiving data samples at 40 MHz and stores it in pipeline memories and packs with the legacy L1A signals to be transmitted to the RODs through optical links. The ROD performs further processing and transmits to the ROS, and finally to the Event Builder which saves the data on disk. Synchronization of the Demonstrator data with the legacy system data is achieved using the clock and trigger information distributed by the legacy TTC modules. The PPr implements a trigger identification algorithm to the data packets and synchronizes the two systems. In upgrade mode, the PPr transfers the L1A data through dedicated high speed optical links to the FELIX system which then saves the data on local disk for offline reconstruction and analysis. There is a PPr specific package called the PPrInterface used for standalone system verification tests. The 3-in-1 Demonstrator was readout using both upgrade and legacy readouts, whilst the QIE and FATALIC are only readout using the upgrade specific FELIX readout [5,10].

5. Conclusions

The High Luminosity LHC project will increase the luminosity by an order at least 5 times beyond the Run 2 nominal luminosity (L = 5 x 10^{34} $cm^{-2}s^{-1}$) in order to reach the design center of mass energy ($\sqrt{s} = 14$ TeV). The ATLAS trigger and data acquisition architecture will undergo upgrades to cope with the High Luminosity LHC, TileCal will also undergo upgrades following ATLAS developments. TileCal Demonstrator modules have been instrumented with initial phase-II upgrade electronic prototypes and assessed with beam setup at the CERN beam facilities during 2015, 2016 and 2017. Preliminary results speak of a strong, efficient and mature upgrade system. The operation of the Demonstrators and data analysis have been used to gain experience and identify weak points in the system. The tests with beam will continue to test the maturity of the Demonstrator for insertion into the real ATLAS detector and to improve understanding of the physics performance of the current system. This will be followed by the production and installation of the new system during the LHC Long Shutdown scheduled for 2025-2026.

References

[1] ATLAS Collaboration (ATLAS Collaboration) 1996 *ATLAS Tile Calorimeter: Technical Design Report* Technical Design Report ATLAS (Geneva: CERN) URL https://cds.cern.ch/record/331062

[2] ATLAS Collaboration 2008 *Journal of Instrumentation* **3** S08003 URL http://stacks.iop.org/1748-0221/3/i=08/a=S08003

[3] CERN 2015 URL https://cds.cern.ch/record/2114693

[4] ATLAS Collaboration 2012 Letter of Intent for the Phase-II Upgrade of the ATLAS Experiment Tech. Rep. CERN-LHCC-2012-022. LHCC-I-023 CERN Geneva URL https://cds.cern.ch/record/1502664

[5] Hlaluku D R (ATLAS Collaboration) 2017 URL http://cds.cern.ch/record/2243316

[6] Valero A (ATLAS Collaboration) 2015 A new read-out architecture for the ATLAS Tile Calorimeter Phase-II Upgrade Tech. Rep. ATL-TILECAL-PROC-2015-025 CERN Geneva URL https://cds.cern.ch/record/2117093

[7] Royer L 2015 URL https://cds.cern.ch/record/2057101

[8] Drake G, Paramonov A, Proudfoot J, Stanek R and Chekanov S 2015 *ATLAS* URL https://cds.cern.ch/record/2058155

[9] Carrio F *et al.* 2015 The PreProcessors for the ATLAS Tile Calorimeter Phase II Upgrade Tech. Rep. ATL-TILECAL-PROC-2015-021 CERN Geneva URL http://cds.cern.ch/record/2104517

[10] Valero A (ATLAS Collaboration) 2017 Data acquisition and processing in the ATLAS Tile Calorimeter Phase-II Upgrade Demonstrator Tech. Rep. ATL-TILECAL-PROC-2017-001 CERN Geneva URL l{http://cds.cern.ch/record/2243768}

[11] Ryu S (ATLAS Collaboration) 2017 FELIX: The new detector readout system for the ATLAS experiment Tech. Rep. ATL-DAQ-PROC-2017-008 CERN Geneva URL http://cds.cern.ch/record/2253330

[12] Zakareishvili T 2017 Muon Signals at a Low Signal-to-Noise Ratio Environment Tech. Rep. ATL-COM-TILECAL-2017-003 CERN Geneva workshop BTTB starts at 24th of January, 2017 URL https://cds.cern.ch/record/2242000

A new D-T neutron facility at UCT

T. Hutton, A. Buffler

Department of Physics, University of Cape Town, Cape Town, 7701, South Africa

E-mail: tanya.hutton@uct.ac.za

Abstract. The Department of Physics at the University of Cape Town has recently installed a new fast neutron facility featuring a Sealed Tube Neutron Generator (STNG) to be used for applied nuclear physics research and education. The MP-320 neutron generator utilises a 90 kV accelerated deuteron beam impinging upon a tritium target, producing approximately 14 MeV neutrons via the $t(d,n)\alpha$ reaction. The long term aim of this facility will be to offer fully characterised neutron energy spectra, yield, and calibrated reference detectors. The potential use for such a facility is wide ranging, from nuclear data measurements to elemental analyses to detector development and calibration. This paper presents the design, building, and commissioning of this facility and proposes future uses. Radiation dosimetry and shielding data is presented for this facility, and initial beam characterisation using a calibrated scintillation detector.

1. Introduction

The MP-320 sealed tube neutron generator (STNG) from Thermo Fisher Scientific [1] produces neutrons of approximately 14 MeV via the deuterium-tritium fusion reaction. Deuterons are accelerated towards a solid target of titanium embedded with tritium. The MP-320 operates in pulsed or steady state mode, with variable beam current and accelerator voltage. The maximum production rate is 10^8 neutrons per second into 4π steradians at 60 μA and 80 kV [2]. Devices such as this are typically used in industrial settings for mining and oil logging, but here the STNG is used as part of the applied nuclear physics teaching and research program at the University of Cape Town (UCT). The STNG was purchased in 2010 and was relocated from iThemba LABS to the nuclear physics research laboratories within the UCT Physics department at the start of 2017.

This facility will complement the existing neutron facilities in South Africa increasing the footprint the fields of neutron physics and nuclear data measurements. One example is iThemba LABS, offering quasi-mono energetic neutrons from 30 MeV to 200 MeV in the D-line vault [3]. The use of this beamline is shared between many international research groups, and availability is limited. The smaller scale fast neutron facility at UCT aims to offer flexibility, availability and access to world-class expertise and equipment, offering neutron energies of 14 MeV and below.

2. Facility Overview

The STNG is installed in close proximity to accessible areas of the building, with the general layout shown in figure 1. The generator is well shielded in the neutron vault, with a beamline extending into the experimental area where neutron detectors and other experimental

components are mounted upon an optics table. The STNG and detectors are all managed from the control area, where experimental data is recorded, processed and analysed.

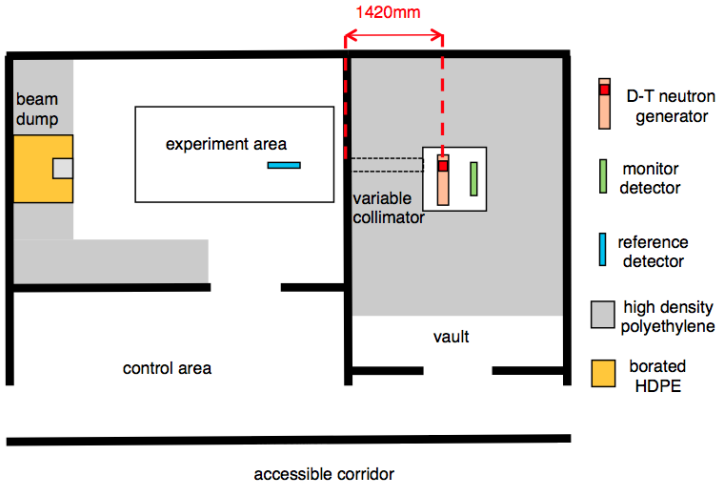

Figure 1. Layout of the fast neutron facility at UCT. The generator is installed within the vault, surrounded by HDPE shielding. Neutrons enter the experimental area via the variable collimator. Detector and generator controls are located in the control area. All areas are access controlled unless explicitly labelled.

The $t(d,n)\alpha$ fusion reaction requires an incident deuteron energy between 100 keV and 400 keV [4], and as such no neutrons will be produced when the device is switched off, or power is interrupted due to a fault. However, the fast neutrons produced during operation, and secondary radiation, can be extremely damaging when interacting with matter. Computational simulations were used as a design aid to ensure appropriate levels of radiation shielding for safe operation.

3. Neutron Vault Design

The Monte-Carlo radiation transport code, MCNP5 [5], was used to estimate the average behaviour of neutrons, and secondary photons, throughout the facility. From these simulations the effective dose was determined at key points and used to estimate safe operating parameters for the STNG and optimise the shielding design.

The simulations assume an isotropic point neutron source of 14 MeV at the centre of the tritium target and simulated the worst-case scenario, i.e. maximum neutron production rate. In reality the STNG will often be run at lower beam current and accelerator voltages, producing fewer than 10^8 neutrons per second. The shielding design was adapted until safe radiation levels were estimated in accessible areas for a run time of 100 hours per year. The device has a total usable lifetime of 1200 hours [1] at maximum production rates before refurbishment is required. A compromise was made between device longevity and useful research hours, allocating 100 hours of run time per year. Given the previous light use of the STNG, this gives an estimated accelerator lifetime of 11 years.

The ICRP (International Commission on Radiological Protection) dose limit for dose to members of the public is 1 mSv per above natural background levels per annum [6]. The ALARP (As Low As Reasonably Practicable) principle of shielding design was used to reduce dose levels below this level in controlled and accessible areas.

The estimated combined neutron and photon dose throughout the room, as calculated with MCNP5, can be seen in Figure 2. Plots ai) to aiii) are associated with an unshielded generator. The doses were calculated from the average particle behaviour, and multiplied by the ICRP-116 dose weighting factors [7].

The highest risk area for human accessibility was determined to be within the doorway to the neutron generator room (as indicated by the dashed lines in Figure 2), within the controlled area.

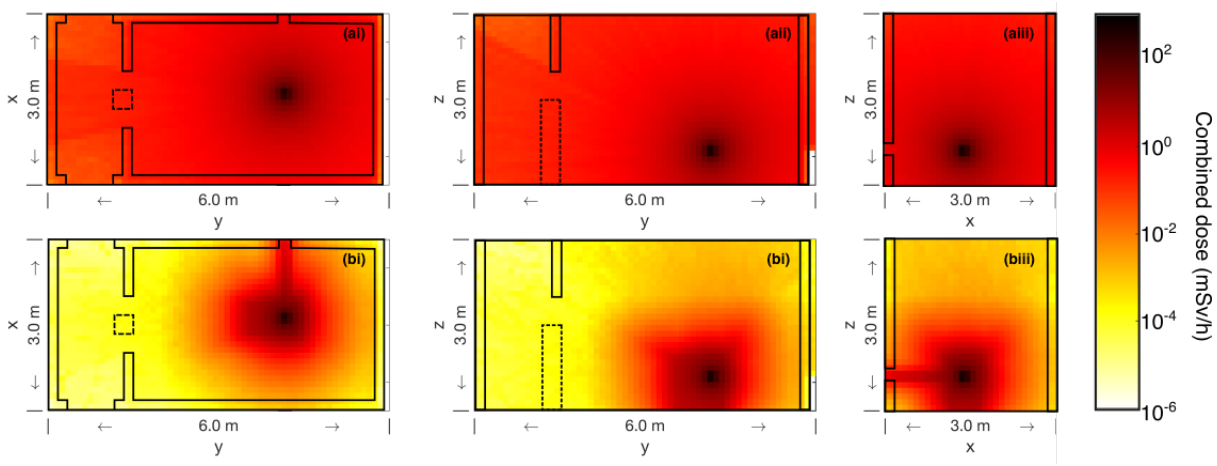

Figure 2. Combined neutron and photon dose maps for the (a) unshielded and (b) shielded geometries, as centred on the generator, i.e. the highest dose regions. The x-y plane is parallel to the floor and the z-axis is in the vertical direction. Solid lines indicate concrete walls, and the dashed region in (ai), (aii) and (bi), (bii) relates to the highest risk accessible area. Any regions with doses above 10^{-2} mSv per hour are considered unsafe for 100 operating hours per year.

The energy dependent doses for this region can be seen in figure 3 for both neutrons and photons. The neutron dose rate is peaked at 14 MeV, where uncollided neutrons pass through. The lower energy contributions are scattered from the surrounding walls. The estimated dose rate for the unshielded generator in this region is 17.7 ± 0.6 mSv per year, excluding any background contributions. If a member of the public were to occupy the doorway, annual dose limits would be exceeded within 5.5 ± 0.5 hours. This scenario is considered unsafe for the expected 100 operating hours per year. An additional 10% uncertainty has been included in the quoted estimates to compensate for additional nuclear data, model and geometry uncertainties[9]. These results confirm that even without shielding, it is safe to run the generator for long enough for a dosimetry survey to take place.

The shielding was constrained by the availability of materials and the room dimensions. A total volume of 5 m^3 High Density Polyethylene (HDPE) blocks was used to build the central component of the shielding. This was combined with close to 16 m^3 of recycled HDPE beads, which is 40% less dense than the blocks, to form the main body of the radiation shield. A central void was left for the generator and neutron monitor detector. The estimated doses associated with the final design can be seen in figures 2(bi) to (biii). The energy dependent dose rates in this region are shown in figure 3(b). The neutron component has reduced over all energy ranges, but most notably at 14 MeV. The high energy photon component has also diminished to zero, and the capture and inelastic scattering peaks from the shielding materials have become more apparent. The total dose rate in the doorway was reduced to 0.112 ± 0.008 mSv per year. In this case, the safe operating time was estimated to be 810 ± 80 hours per year, far exceeding the predicted runtime of 100 hours. By erring on the side of caution, model assumptions, errors or real-world differences in dose rates can be safely accommodated. The construction of the shielding was completed in April 2017, and a series of photos can be seen in figure 4.

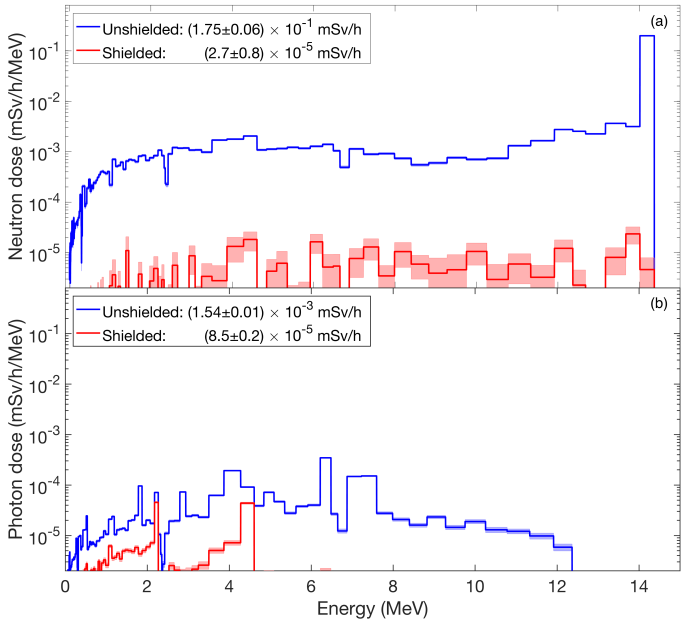

Figure 3. Energy dependent (a) neutron and (b) photon dose rates in the doorway as indicated by the dashed lines in figure 2. Blue lines relate to the unshielded simulation, and red lines relate to the shielded simulation. Statistical uncertainties are represented by the shaded bars, and integrated dose rates are given in the legend. Peaks at 2.2 MeV and 4.4 MeV in the photon spectrum are due to the radiative capture of thermal neutrons on hydrogen, and inelastic scattering of fast neutrons off carbon.

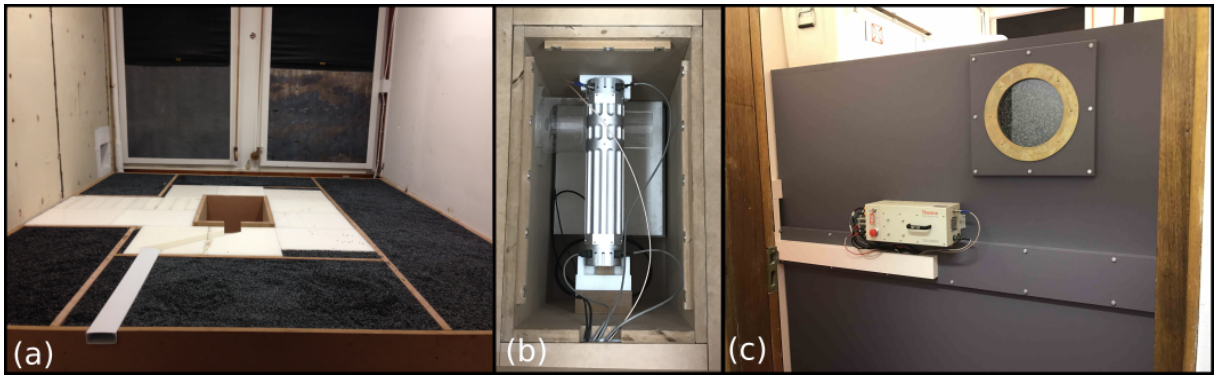

Figure 4. Photos of the neutron shielding (a) during and (c) after construction. The core component of the shielding are white blocks of HDPE, surrounded by the black HDPE beads. The neutron generator is situated in the central void as shown in photo (b). A neutron and gamma-ray sensitive monitor detector is installed underneath the STNG. The electronics have been separated from the generator and are installed outside the shielding as shown in photo (c). All generator and detector cables are routed into the control area. Note that the porthole visible in photo (c) serves no scientific function.

4. Experimental capabilities

Experiments can be run in two different modes, activation and narrow beam, by changing the variable collimator. Samples up to 17 cm diameter can be activated within the central cave. These samples can then be transported to the neighbouring low background HPGe detector facility for high precision gamma-ray measurements. Alternatively, narrow beam of nearly mono-energetic 14 MeV neutrons can be delivered to the experimental area using an 8 mm diameter HDPE collimator (with external dimensions of 17 cm diameter and 100 cm length). At the time of writing this paper, the RP survey process was ongoing, necessitating a conservative beam diameter, with the view to broaden this in the future. Further optimisation is expected in terms of beam divergence, and management of scattered neutrons entering the beam. Any un-collided neutrons will be incident upon a beam dump at the far end of the experimental room, where

they will be thermalised and captured. This is composed of borated HDPE (5% by mass), with a maximum thickness of 1.0 m.

Several neutron and gamma-ray sensitive detectors have been set-up within the experimental area. Of note is the organic liquid scintillator EJ-301 from Scionix, which is used as the reference detector for fast neutron detection. The excellent pulse shape discrimination properties of this scintillator is used to isolate the neutron events for further analysis [10]. Analogue and digital data acquisition systems are in place, both of which have pulse shape discrimination capabilities. The digital DAQ uses an open source software package, QtDAQ [11], with a Vx1761 CAEN digitiser [12].

Preliminary results are shown in figure 5 for neutron and gamma-ray pulse height spectra as recorded with the EJ-301 reference detector and digital DAQ. The gamma-ray pulse height spectra shows the two Compton edges associated with 2.2 MeV and 4.4 MeV gamma-rays from the shielding. The neutron pulse height spectra behaves as expected for a nearly mono-energetic beam of 14 MeV neutrons. The neutron energy spectra can be unfolded from the pulse height spectra with the GRAVEL and MAXED unfolding codes as part of the UMG package [13] provided the detector response is known. The facility includes a suite of additional detectors, sensitive to fast or thermal neutrons and/or gamma-rays.

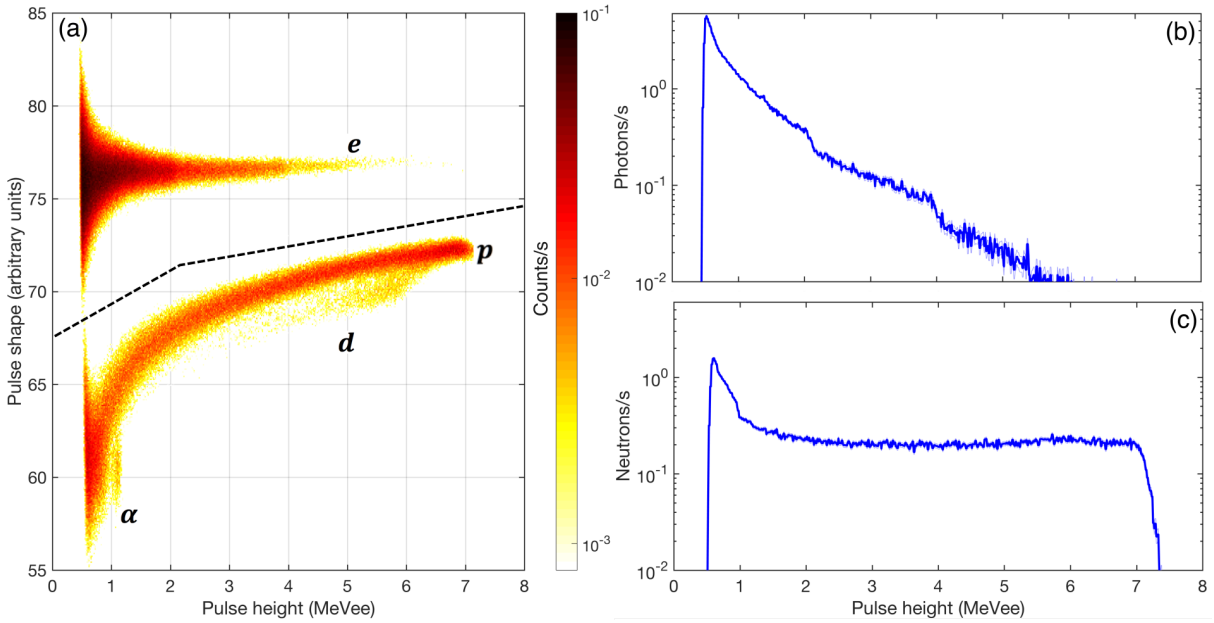

Figure 5. EJ-301 measured neutron and photon pulse height spectra with a narrow beam of 14 MeV neutrons. Figure (a) shows the pulse shape with respect to the detected light output, where the colour scale indicates the number of events per second. The detected light output is proportional to the energy and type of incident radiation. The different recoil particles are indicated, and the cut between gamma-ray induced events and neutron induced events is shown with the dashed line. The (b) gamma-ray and (c) neutron pulse height spectra are determined by integrating the number of events above/below the cut within each light output channel. The Compton edges related to the 2.2 MeV and 4.4 MeV gamma-rays are clearly visible.

5. Commissioning and Current Status

The STNG is operational, with RP measurements ongoing to confirm simulation results. The gamma-ray dose rate was measured to be $0.70 \pm 0.06\,\mu$Sv per hour in the vault doorway areas

when running the generator at maximum neutron yield, using the Thermo-Fisher Scientific RadEye B20 survey meter. The measured gamma-ray background dose has been subtracted. Thermal and fast neutron measurements were made in the same location. The thermal neutron rate was measured to be 0.39 ± 0.04 neutrons per second with a BF_3 detector. After efficiency corrections and worst-case dose weightings, the thermal neutron dose rate is estimated to be 0.9 ± 0.1 nSv per hour. The fast neutron rate was measured to be 0.85 ± 0.02 neutrons per second with the reference EJ-301 detector, equivalent to $0.076 \pm 0.002\,\mu$Sv per hour. The total measured dose rate was dominated by gamma-rays, and thermal neutron doses are negligible in comparison. The estimated dose from Monte-Carlo simulations was $0.112 \pm 0.008\,\mu$Sv per year, with measured values estimated at 0.121 ± 0.006 mSv per year. Initial measurements and simulations thus agree within one sigma. Dose rate calculations for the measured neutrons were deliberately conservative, so it is not unreasonable that the final dose rates exceed the simulated values. The measured values are still well within the safe operating limits for 100 hours per year when considering the ICRP guidelines [6]. Further measurements are expected to improve the agreement between simulation and measurement. Several undergraduate student projects are underway to characterise key aspects of the facility; including activation analyses to confirm the neutron production rate, detector characterisation and detector development.

6. Conclusion

The Department of Physics at the University of Cape Town is developing a flexible, fast neutron facility complementary to those currently available, with a focus on training the next generation of nuclear scientists in South Africa. The flexibility afforded by a university-run, in-house facility is key to offering a fast response to applied physics problems. The facility will offer well characterised energy spectra, backgrounds, detector responses, and data handling procedures. The areas of interest to which this facility may be applied includes, but is not limited to, detector calibration, fast neutron activation analysis (both prompt and delayed) and bulk materials analysis (both by activation and fast neutron scattering). Future measurement campaigns will aim to include fusion-relevant cross-section measurements, the development of nuclear data benchmarks and the provision of services to the nuclear engineering communities.

7. Acknowledgements

The authors would like to acknowledge several parties who have contributed to this facility. The STNG was purchased via an NRF grant, and HDPE blocks were donated from the PTB and NECSA. The construction of this facility has relied heavily on the contributions from the UCT mechanical and electrical workshop teams. The authors would also like to thank Dr Tom Leadbeater and Dr Steve Peterson from the University of Cape Town for their contributions.

References

[1] Thermo Fisher Scientific Inc, 2007. *Thermo Scientific MP 320: Product Specifications.*
[2] Thermo Fisher Scientific Inc, 2010. *MP320 Neutron Generator: Operation Manual.* Chapter 3, p 6.
[3] Mosconi M, Musonza E, Buffler A, Nolte R, Röttger S and Smit F D, 2010. *Characterisation of the high-energy neutron beam at iThemba LABS.* Radiation Measurements, Volume 45, Issue 10, Pages 1342-1345,
[4] Barschall H H, 1983. *Neutron sources: for basic physics and applications*, Volume 2 of Neutron physics and nuclear data in science and technology, OECD/NEA report, p57.
[5] X-5 Monte Carlo Team, 2003. *MCNP - Version 5, Vol. I: Overview and Theory.* Los Alamos National Laboratory.
[6] ICRP, 2007. *The 2007 Recommendations of the International Commission on Radiological Protection.* ICRP Publication 103. Ann. ICRP 37 (2-4).
[7] ICRP, 2010. *Conversion Coefficients for Radiological Protection Quantities for External Radiation Exposures.* ICRP Publication 116, Ann. ICRP 40(2-5).
[8] X-5 Monte Carlo Team, 2003. *MCNP - Version 5, Vol. I: Overview and Theory.* Los Alamos National Laboratory, p H-6.

[9] Morgan L W G and Packer L W, 2014. *A neutron poison tritium breeding controller applied to a water cooled fusion reactor model*. Fusion Engineering and Design, Volume 89, pp 1190-1194.
[10] Comrie A C, Buffler A, Smit F D and Wörtche H J, 2014. *Digital neutron/gamma discrimination with an organic scintillator at energies between 1 MeV and 100 MeV*. Nuclear Instruments and Methods in Physics Research A, Volume 772, pp 43-49.
[11] Comrie A C, 2015. *QtDAQ git repository,* [Online]. Available: https://bitbucket.org/veggiesaurus/qtdaq.
[12] CAEN, 2012. *Vx1761 user manual*. Technical Report.
[13] Matzke M, 1994. *Unfolding of Pulse Height Spectra: The HEPRO Program System*. Neutronenphysik, Volume 19, PTB-Bericht.

Testing the scattering distribution of a photon in a turbid medium using Monte Carlo simulations

T Mabhengu, MC Cyulinyana, and H Winkler

Department of Physics, University of Johannesburg, P. O. Box 525, Auckland Park 2006, South Africa

E-mail: thulanimabhengu@gmail.com

Abstract. The scattering distribution of a photon in a homogeneous turbid medium is too complex to be represented by an analytical expression, and therefore requires a numerical solution. Photon propagation may be treated as a stochastic process. In this study, a Monte Carlo simulation is used to reproduce the behaviour of photons in turbid media. The fraction of photons transmitted and reflected depends on the optical properties of a turbid medium as well as the angle of the incoming photon. We determine the transmission coefficients through several model atmospheres for three representative solar zenith angles. The fraction of the transmitted photons is further reduced depending on the angle of the incoming photons. The results presented in this study shows that the optical depth of the medium and the incoming angle of photons have a significant impact on the scattering distribution of photons in a turbid medium and on the amount of photons reaching the ground.

1. Introduction

Several studies done in the past show that photon propagation through scattering media can be solved by analytical expression only if there are few scattering events [1]. A photon experiences different kinds of scattering as it enters a homogeneous turbid medium. The propagation of light in such a medium may be analysed using either the wave model or photon model. This study uses the photon model.

The radiative transfer equation is often used to describe photon propagation through scattering media. However, the exact analytical solutions in turbid media are too complex and impractical [2]. Therefore, numerical methods based on the statistical Monte Carlo technique (which is one among other methods) are used to solve the radiative transfer equation in complex geometries [3]. The scattering distribution of a photon is influenced by the optical properties of a turbid medium, which is characterized by the absorption coefficient, scattering coefficient, as well as the scattering phase function. The absorption and scattering coefficients are determined by the probability of photon absorption and photon scattering per unit path length, respectively [4]. The scattering phase function describes the amount of scattered photons into a unit solid angle in a given direction.

Information about the optical properties of the turbid media such as the absorption coefficient, scattering coefficient as well as the asymmetry parameter of the medium are required in order to describe the scattering distribution of a photon through a homogeneous turbid medium. The new direction of a photon after each scattering event in a medium rich in aerosols can be randomly generated from a Henyey-Greenstein phase function [5, 6]. This function is appropriate for Mie scattering, where aerosols size is approximately equal to the incoming light wavelength. The Rayleigh

scattering phase function is used instead when particles have a small size compared to the wavelength of the incoming light.

This study uses a python code to model the scattering distribution of a photon in a turbid medium. The Monte Carlo program tracks scattered photons as they propagate through a turbid medium based on the scattering angles as well as the azimuthal angles in order to determine the scattering distribution.

2. Monte Carlo simulations

The Monte Carlo code developed to model the scattering distribution of a photon in a turbid medium is as per several studies done in the past for photon propagation through scattering media [1-8], except that in this study the focus is more on modeling the scattering distribution of photon propagation in a scattering and non-absorbing medium in which photons are scattered multiple times before reaching the receiver.

2.1. Set photons in motion

In this study, the first step was to launch photons (i.e. photon packet) through the turbid medium from the origin defined by the coordinates [*x*, *y*, *z*] and their path is followed until they are completely absorbed or exit the medium. The photon propagation direction was initially set along the *z*-direction pointing inside the medium defined by the coordinates system: [*x*, *y*, *z*] = [0, 0, 1] in units of airmass.

2.2. Photon step size

The photon travels along a straight line before it encounters the scattering center and is scattered in a random direction. When the photon propagates in a turbid medium, the path length ΔS, also known as the step size, is equal to the inverse of the extinction coefficient. This is the distance that a photon travels between two consecutive scattering events in the medium. It is calculated using random numbers between 0 and 1 generated by a random number generator as follows [5, 7]:

$$\Delta S = \frac{-\ln \xi}{\mu_t} \tag{1}$$

where μ_t is the total extinction coefficient obtained from scattering and absorption coefficients of a turbid medium, and ξ is the random number generated by the program which is distributed between zero and one.

The aerosol optical depth which characterizes the size and the amount of particles in a turbid medium is defined as the integral of the total extinction coefficient, μ_t over the photon path, ds:

$$\tau(s) = \int_0^s \mu_t ds \tag{2}$$

2.3. The new direction of a photon and scattering function

A single scattering model which is based on the Beer-Lambert law works very well on clear atmospheres, but is inappropriate for highly attenuating turbid media [9]. For our turbid medium we made the simplified assumption that scattering is dominated by aerosols, [10], and hence the Rayleigh scattering is not considered in this study. The redistribution of a photon in different directions is determined through the stochastic treatment of the multiple scattering events and corresponding phase function.

The Henyey-Greenstein phase function is used to describe the scattering phase function of the photon moving in the turbid media and this is used to calculate the photon scattering angle in different directions. This means that the scattering angle is derived from that phase function and it depends on the asymmetry parameter, g which is normally used to take care of the asymmetry in the scattering process [11]:

$$P(\theta)=\frac{1}{4\pi}\frac{1-g^2}{\left[1+g^2-2g\cos\theta\right]^{3/2}} \tag{3}$$

where $P(\theta)$ is a probability density function, the parameter g is the asymmetry factor for a homogeneous turbid medium, and θ is the scattering angle of the photon which here is generated stochastically using the expression [11]:

$$\cos\theta=\frac{1}{2g}\left\{1+g^2-\left(\frac{1-g^2}{1+g\xi}\right)^2\right\} \tag{4}$$

In addition to the scattering angle is a random azimuthal angle, Φ which is assumed to be uniformly distributed between 0 and 2π is also needed to describe statistically the direction of a photon:

$$\Phi = 2\pi\,\xi \tag{5}$$

3. Results and discussion

The propagation of a photon in a turbid medium is treated as a random walk using stochastic means. The histogram for the step size of photons in a turbid medium is illustrated in figure 1 with photons undergoing exponential attenuation. The total interaction coefficients values assumed to be of the medium under study were estimated from the aerosol optical depth provided by sun-photometer [12].

The total interaction coefficient of the medium used in this study is varied from 0.2 to 1. Photons can be scattered or absorbed as they propagate through the turbid medium. As shown in figure 1, photon movement through a turbid medium depends largely on the total interaction coefficient, which is inversely related to the step size, see equation (1). It is rather straight forward to see that photon step size depends solely on the total extinction coefficient encountered in various turbid media. As expected, by increasing the size of the total extinction coefficient from 0.2 to 1.0, photons travel a shorter distance.

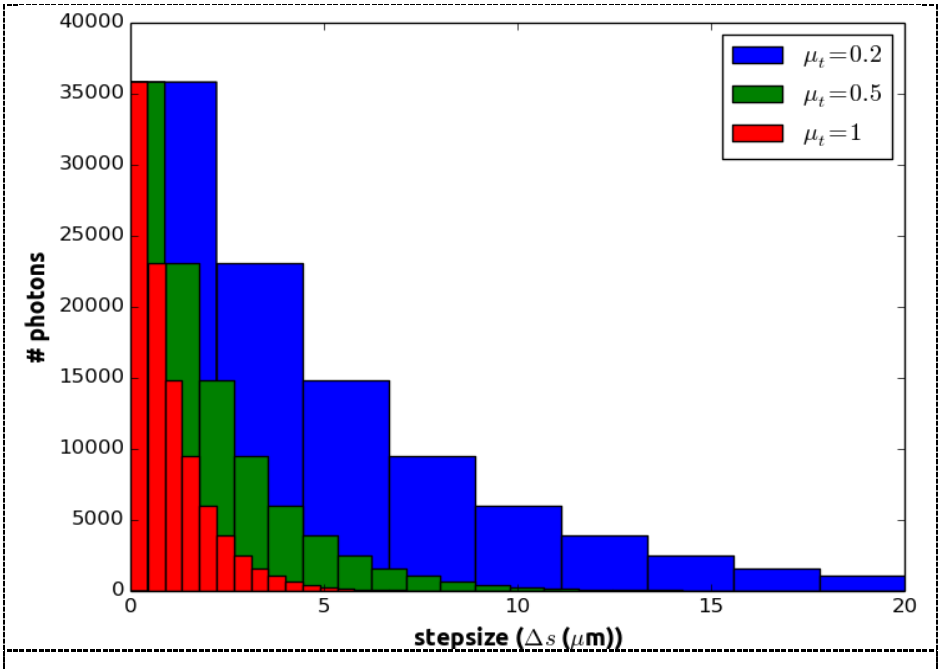

Figure 1. Histogram of the photon step size in a turbid medium

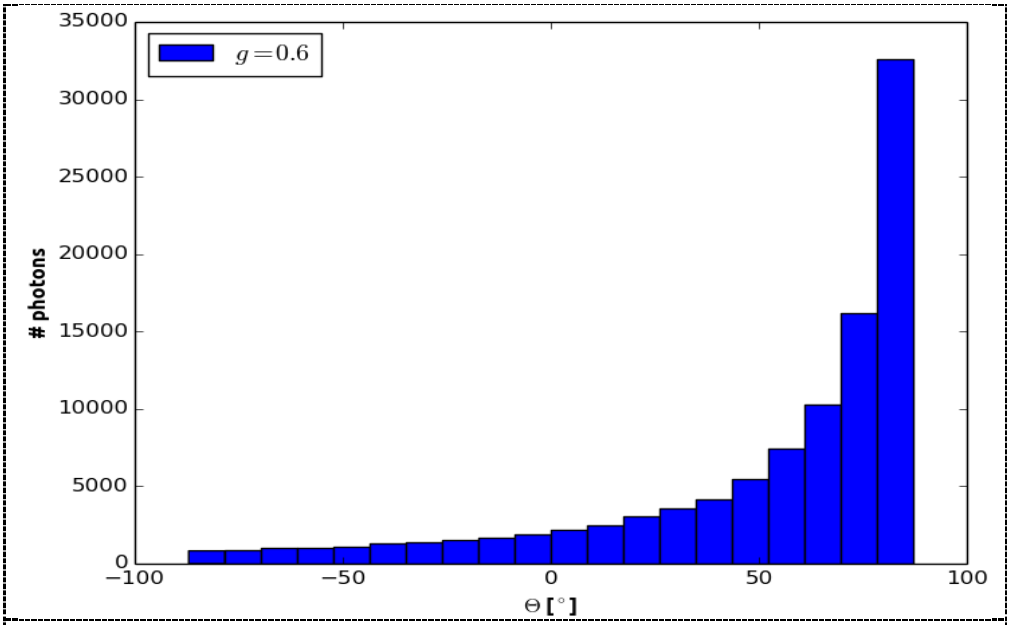

Figure 2. Scattering angles generated throughout the Monte Carlo simulation with the asymmetry parameter, g = 0.6

The above figure shows the histogram of the deflection angles, θ for g = 0.6. In this study, we used g = 0.6 as it appeared a suitable value to characterize aerosol scattering in the forward direction [13]. The focus was on modelling the aerosol scattering of photons. With anisotropy g equals to 0.6 indicates the forward directed scattering. Obviously from the formula, one can clearly see that more photons are scattered in the forward direction as the asymmetry parameter tends towards the positive value.

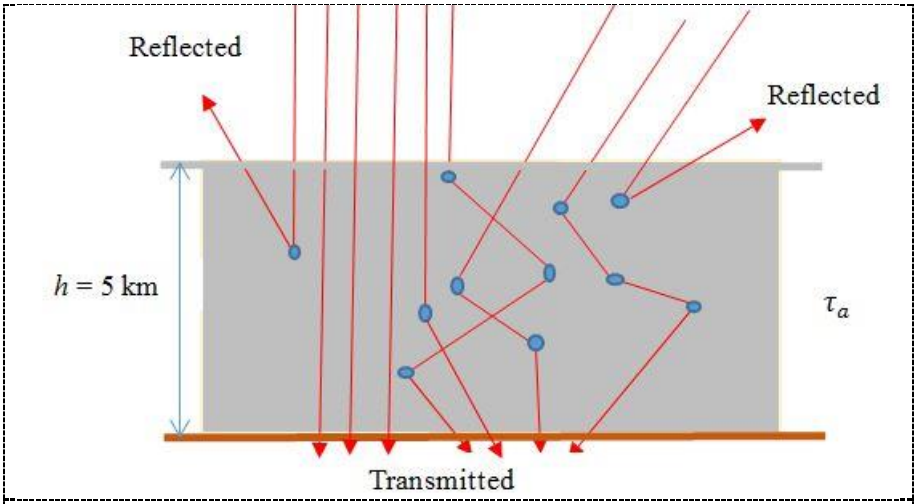

Figure 3. Schematic diagram of a photon movement through a plane parallel aerosol layer, h is the height above the ground level

Figure 3 shows examples of the photon propagation in a homogeneous turbid medium being scattered on its way to the ground level. Given the bias towards forward scatter, most photons reach

the ground after passing through a highly scattering medium. The scatter is determined by considering the optical properties of the atmospheric aerosol. Figures 4 and 5 illustrate the transmittance and reflectance of photons versus optical depth for three representative solar zenith angles. The aerosol optical depth as well as the incident angle of the photon have a significantly impact on the number of photons reaching the ground. Some photons are scattered back to the top of the atmosphere and their fraction to the total number of launched photons gives the reflection values of the turbid medium while the transmission values are given by the ratio of the transmitted ones to the total number of launched photons from the top of the atmosphere.

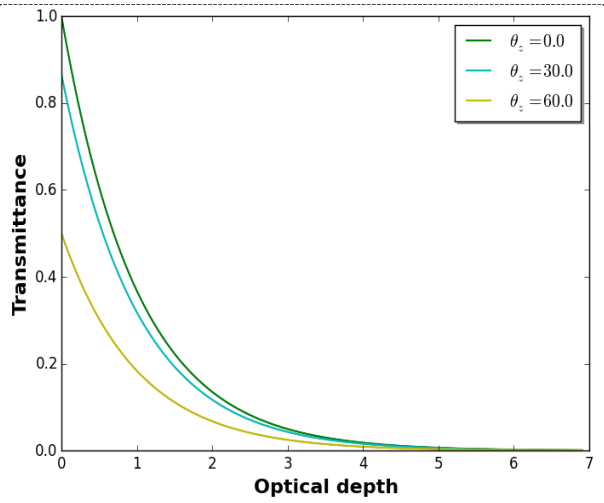

Figure 4. Transmittance of a turbid medium as function of the optical depth for three different solar zenith angles.

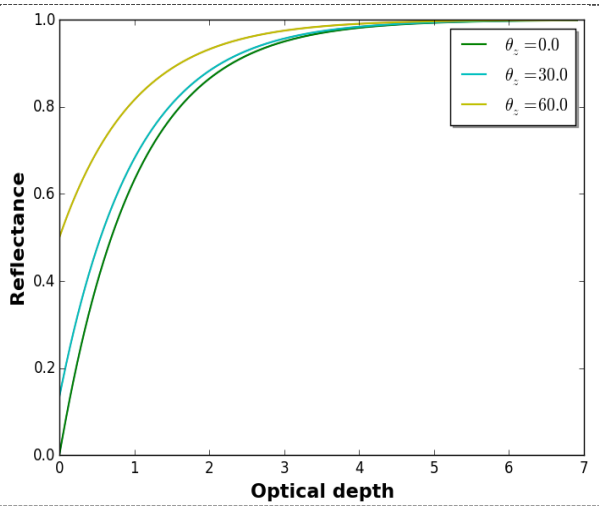

Figure 5. Reflectance as function of optical depth for three different solar zenith angles.

The three solar zenith angles, 0^o, 30^o, and 60^o used in this study were found to be representative of different sun's position and daily variation, i.e, 0^o is when the sun is overhead (airmass is one), 30^o is toward the afternoon, and 60^o is when the sun is approaching sunset. The aerosol optical depth of 1.5, 2.0, and 3.0 were chosen in order to examine the turbid medium.

Table 1: Transmission and reflection of a plane parallel aerosol layer for three different solar zenith angles at different aerosol optical depth for a wavelength of 440 nm [12].

θ_z (degrees)	τ_a	Transmission (T)	Reflection (R)
0	1.5	0.795	0.204
	2.0	0.737	0.262
	3.0	0.635	0.364
30	1.5	0.752	0.247
	2.0	0.692	0.307
	3.0	0.589	0.410
60	1.5	0.594	0.406
	2.0	0.529	0.471
	3.0	0.454	0.546

The results presented in the table above from stochastic simulations show the relation between the fraction of transmitted and reflected photons with an aerosol optical depth (AOD), for a wavelength of 440 nm, corresponding to blue light. Scattering at other wavelengths will be explored in a later publication. As seen in our results, the transmission and reflection depend on the optical properties of the aerosol layer as well as on the incident angle. The direct transmittance decreases exponentially with increasing AOD.

4. Conclusion

The Monte Carlo algorithm for simulating photon transport in turbid medium has been implemented in a 2-D code, where a scattering distribution of photons within a medium rich in aerosols has been tested in this study by changing the total interaction coefficients of the medium. A Monte Carlo Model was used to calculate the upward and downward solar photon flux characteristics based on different aerosols extinction coefficients. The results indicate that aerosol loading has a significant impact on the solar photons. Photon tracing through Monte Carlo simulation showed the true complexity of the scattering distribution of photons in turbid media. However, the Monte Carlo method was found to be suitable for multiple scattering events as well as for non-isotropic scattering. The redistribution of a photon in different directions in a turbid medium was determined.

5. Further study

The Monte Carlo method will be used to quantify the amount of solar radiation that is received by the Earth's surface under turbid atmosphere for the South African conditions. Future work also involves developing a statistical model to simulate the effect of high vapor concentration in the atmosphere on solar radiance, and the effect of heavy smoke-induced aerosols during winter dry seasons.

References

[1] Ramella-Roman J, Prahl A, and Jacques S 2005 *Optics Express* **13** 12
[2] Angelo A et al 1998 *Optical Society of America* **37** 31
[3] Berrocal E, Sedarsky D, Paciaroni M, Meglinski I, and Linne M 2007 *Optics Express* **15** 17
[4] Mourant J et al 1996 *Optics Letters* **21** 7
[5] Prahl S, van Gemert M, and Welch J 1993 *Appl. Opt*. **32** 559
[6] Binzoni T et al 2006 *Phys.Med.Biol*. **51** N313
[7] Wang L, Jacques S, and Zheng L 1995 *Comp. Methods Programs Biomed*. **47** 131
[8] Prahl S, Keijzer M, Jacques S, and Welch A 1989 *SPIE Institute Series* **5** 102
[9] Gardmer C, and Welch A 1985 *Appl.Opt* **33** 43
[10] Moosmuller H, and Ogren J 2017 *Atmosphere* **8** 133
[11] Henyey L, and Greenstein J 1941 *Astrophys* J. **93** 70
[12] Dubovik O et al 2002 *American Meteorological Society* **59** D05S04
[13] Andrews E et al 2006 *Journal of Geophysical Research* **111**
[14] Liou K 2002 *Elsevier science* 2nd ed
[15] Piskozub J, and Mckee D 2011 *Optics express* **19** 5
[16] Jones M, and Yamada Y 1998 *Optical Review* **5** 72

Computational comparison of a novel cavity absorber for parabolic trough solar concentrators

Khaled Mohamad, Philippe Ferrer
School of Physics, University of the Witwatersrand, Johannesburg 2001, South Africa

khaled@aims.edu.gh

Abstract Parabolic trough mirror plants are a popular design for conversion of solar energy to electricity via thermal processes. The absorber of concentrated solar radiation can reach high temperatures (> 500°C) and is responsible for efficiency losses mainly via thermal radiation. We build on our previous work on hot mirrors to study an absorber with a mirrored cavity. The cavity absorber for the parabolic trough receiver is designed to trap solar and thermal radiations by reflecting them back onto the absorber very efficiently, which would otherwise be lost. This paper shows simulation results indicating that the proposed design can exceed the heat transfer fluid temperature compared to existing alternatives. Using a theoretical model we developed, we can infer the temperature profile for the receiver unit, from which efficiency parameters can be derived.

1. Introduction

A parabolic trough solar thermal power plant consists of a series of parabolic mirrors concentrating solar radiation onto a linear focal line along which the receiver unit is positioned. The receiver heats up and in turn imparts a large portion of its heat to a heat transfer fluid circulating within. This heat transfer fluid can then be utilized in a steam cycle to generate electricity. The receiver is one of the most complex parts and the efficiency of the whole system largely depends on it. It has to be carefully designed in such a way so as to minimize the energy losses. Every part of the receiver unit is a topic of ongoing research, such as the working fluid that can be used, and also the optical, chemical, and thermal properties of the concerned material [1].

Typically, the receiver unit consists of a blackened absorber pipe (AP) encapsulated by the glass cover (GC), (See Fig. (1b)). There is a vacuum in between to minimize convective losses [2]. For the conduction losses, the thermal contacts between the receiver pipe and the glass cover are kept to a minimum. The heat transfer fluid (HTF) inside the receiver pipe is heated by the concentrated solar radiation. The hot HTF can be used in generating electricity through a steam cycle or in thermochemical applications [3]. The dominant heat losses at high temperatures are due to the thermal emission (IR) from the receiver pipe. There is a conventional method to minimize the IR by painting the receiver pipe with a spectrally selective coating, a dielectric film that absorbs well in the visible region of the solar spectrum and emits poorly in the IR region. Much work has been published in regard to the selective coating and their properties [4]. The main weakness of selective coating is that it prevents the receiver pipe from being heated to high temperature, since it thermally decomposes at about 680 K [5], [6].

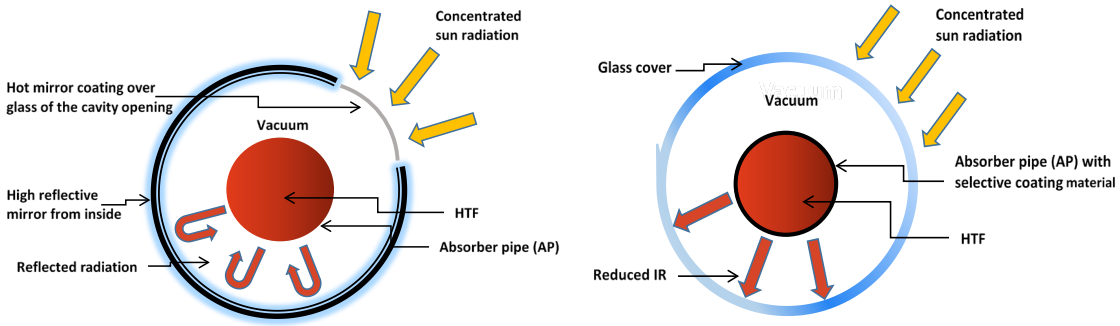

Figure 1. a) Receiver unit with the cavity design. b) Receiver unit with a selective coating.

An alternative option to the selective coating, which this work aims to discuss, is to reduce the thermal emission from the glass cover tube of a trough collector by trapping IR via a reflective surface on the part of the glass not facing the trough. The solar radiation inlet may be coated with a hot mirror type coating. The new aspect of this paper is applying the reflective cavity around the absorber, which is shown in Fig. (1a).
It consists of borosilicate glass over the opening, which is coated with a hot mirror film and the remaining circumference is a high reflective aluminium mirror.

Hot mirror coating films have been an active area of research in many applications, seeking to improve efficiency and reduce heat radiation losses [6,7]. It is often utilized in applications related to energy conservation and protection purposes, i.e., light bulb envelop, furnace windows, welding and laser goggles, and astronaut helmets [7]. The hot mirror coating for a solar collector must meet some performance specifications. It needs to be highly transparent (> 90 %) in the visible region and have high reflectivity in the IR region of the solar spectrum. There are two general types of hot mirror films: a semiconducting oxide with a high doping level and a very thin metal film sandwiched between two dielectric layers (see [7,8] for more details). The coating with a thin metal film shows some unavoidable losses. On the other hand, the semiconducting oxide with a high doping level shows more advantages, i.e., Indium-Tin-Oxide (ITO).

2. Theory and simulation study

We briefly review the total heat transfer of the system and the interaction between its components. The physical basis of the model that we are using starts with a complete description of the thermal interaction, which is shown in Fig. (2) and then applying energy conservation principles for the thermal interactions between the components of the receiver [9].

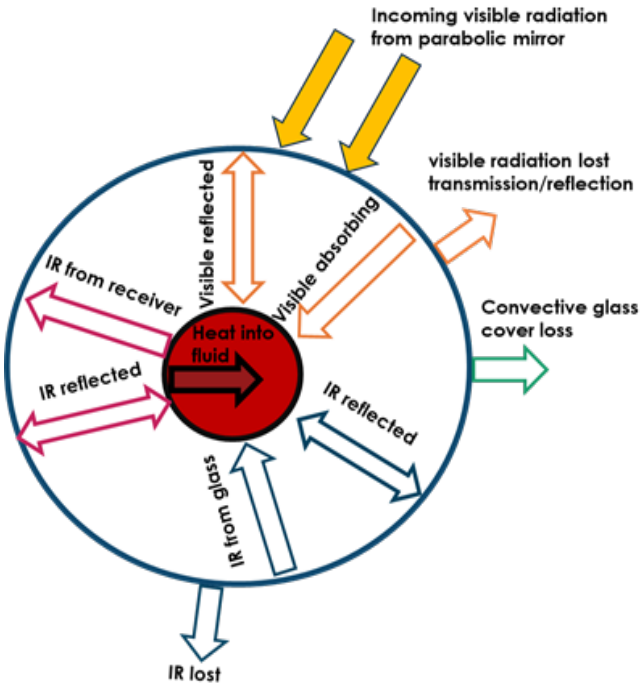

Figure 2. Schematic representation of the possible heat transfer modes.

The net heat flux due to solar radiation q'_{Sol}, convection q'_{Conv}, radiation q'_{Rad}, and conduction q'_{Cond} are computed under steady state conditions using the energy balance relationship

$$\left(\sum q'_{Sol} + \sum q'_{Conv} + \sum q'_{Cond} + \sum q'_{Rad}\right)_{ij} = 0. \quad (1)$$

The AP, the GC, and the HTF are discretized into control volumes (CV), using a finite volume method (FVM). The AP and GC are discretized along azimuthal Fig. (3b) and longitudinal directions Fig. (3a), but HTF is only discretized along the longitudinal direction Fig. (3a). Eq. (1) holds for every CV.

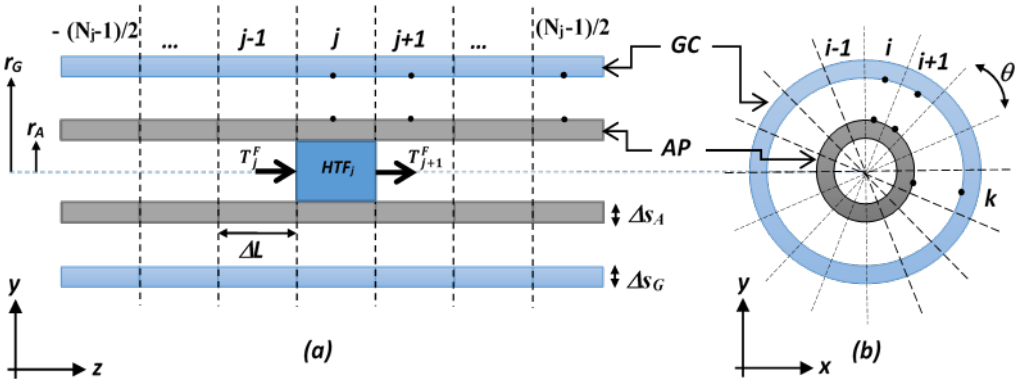

Figure 3. The discretization of AP and GC into control volumes [9].

The detailed theoretical calculations including the numerical solutions that have been implemented in a code are discussed in [9].

3. Results

The theoretical model of the solar receiver, taking hot mirror interactions into account, has been derived in [9]. For the purposes of this research, the simulation code presented in [9] is edited in order to fulfil the cavity requirements. A simulation validation for the work done in this paper was undertaken using two approaches. We selected simulation parameters for physical scenarios where the outcomes could be derived by other means. We used the zero irradiation case, zero conductivity in the materials, zero HTF convective coefficient, and zero emissivity on the absorber surface. The results conformed to theoretical expectations. Secondly, upon comparing the simulation results with existing experimental data for a selective coating, we found that the comparison was encouragingly close (less than 0.7% discrepancy), see [9].

The operating conditions and design parameters that were used simulate the SEGS LS2, the LS-2 is one of three generations of parabolic troughs installed in the nine SEGS (Solar Electric Generating System) power plants in California, [10]. They are shown in table 1.

Table 1. Design parameters of the SEGS LS2 used in our simulation [10]. * stands for the cavity design requirements.

Parameter	Value
Collector aperture (W)	5 m
Focal distance (f)	1.84 m
Absorber internal diameter	0.066 m
Absorber external diameter	0.07 m
Absorber emissivity (IR)	0.15
Glass internal diameter	0.109 m
Glass external diameter	0.115 m
Glass emissivity (IR)	0.86
Receiver absorptance (visible)	0.96
Glass transmittance (visible)	0.93
Parabola specular reflectance	0.93
Incident angle	0.0
Solar irradiance	933.7 W/m^2
HTF	Molten salt
Mass flow rate	0.68 Kg/s
Temperature HTF (inlet)	375.35 K
Temperature ambient	294.35 K
Wind speed	2.6 m/s
Reflectivity of the cavity mirror*	0.95
ITO reflectivity (IR)*	0.85
ITO transmittance (visible)*	0.875

The minimum cavity opening size is related to an upper limit to the possible concentration ratio of a parabolic mirror on its own, which is related to focal line width [11]. On the basis of that, the arc length of the minimum cavity opening is 4.8 cm for the design parameter in table 1.
In Figures (4, 5, 6), the results of the simulated temperature profiles for the AP, GC, and HTF are shown. In Fig. (4), the axial temperature variation for the HTF along the receiver is displayed, for HTF inlet temperatures of 375 K that enters the absorber at one end, and as a result of the flow rate of 0.68 kg/s along the length L (m) of the absorber tube under the concentrated solar irradiance, the HTF heats up. HTF temperature increases roughly linearly and then flattens out to approach the stagnation temperature (where solar energy input equals IR losses). The maximum HTF temperature for this design rises close to 1370 K.

Figure (5) shows the temperature profile around the AP circumference. The angle 180° points directly away from the sun (and towards the centre of the parabolic mirror). The temperature varies by approx. 200 K around the circumference. Three profiles are shown, each 50 m further along the AP. The temperature increase along the axial direction is relatively high. In order to make this simulation more realistic, finite sun-size effects will still be included. These will alter the solar radiation profile incident on the absorber pipe, and likely result in a more even temperature spread.

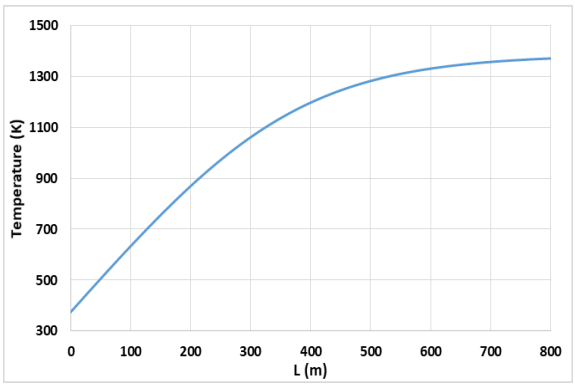

Figure 4. HTF temperature distribution for 375 K inlet temperature.

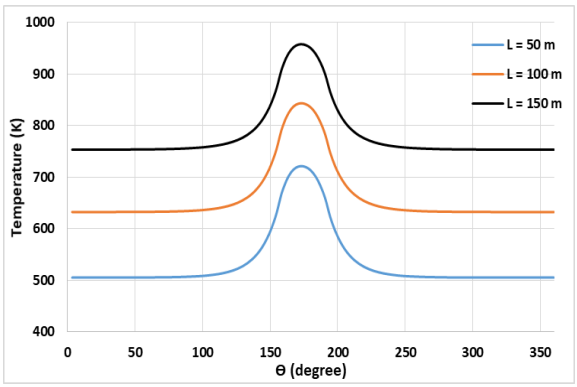

Figure 5. Temperature around AP circumference taken at different distances.

Figure (6) displays the temperature profile around the GC circumference. The temperature around the circumference varies by approx. 320 K and the temperature along the axial direction is very small. Hence most thermal losses will occur from the radiation entrance window.

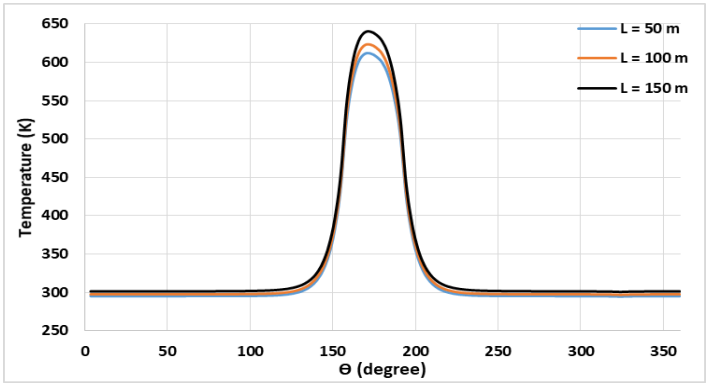

Figure 6. Temperature around GC circumference taken at different distances.

We evaluate the performance of the cavity design by comparing it to alternatives with bare and selective coating.

Figure (7) display the temperature profiles around the AP at 150 m. The temperature of the part of the AP surface that faces the parabolic mirror for the cavity design is higher than the selective coating. This is due to the more concentrated radiation incident on the AP.

The GC in Fig. (8) at 150 m, the part of the GC surface facing the parabolic mirror for the different designs indicates a higher temperature for the cavity design compared to the selective coating and bare. At the remaining circumference, the cavity design has a much lower temperature than the other designs along the entire length.

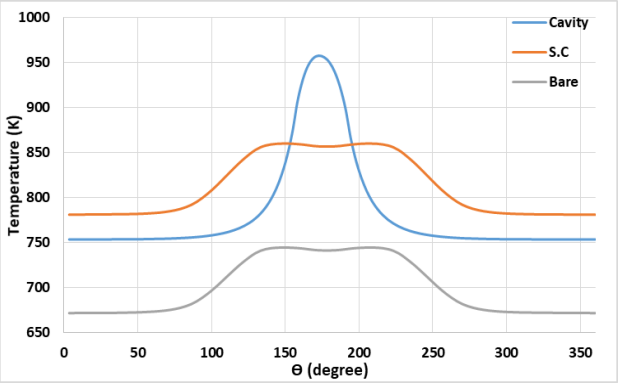

Figure 7. Temperature around AP circumference taken at 150 m receiver length for different designs.

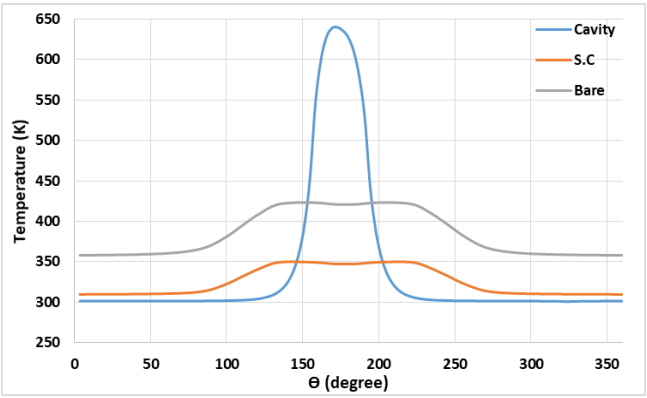

Figure 8. Temperature around GC circumference taken at 150 m receiver length for different designs.

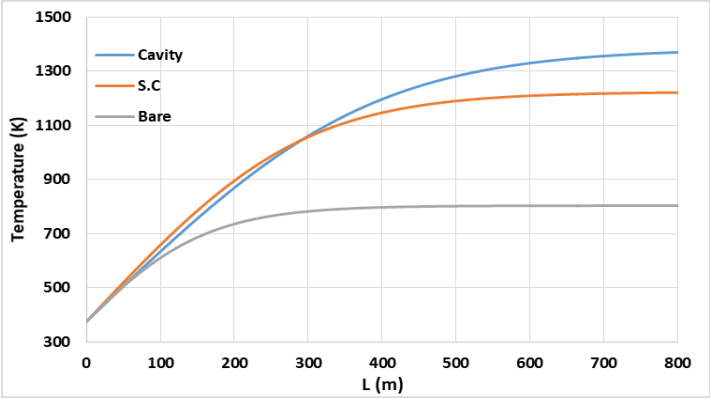

Figure 9. HTF outlet temp for 375 K inlet temperature of different designs.

Figure 9 shows the HTF temperature along the length, which is close to the surface temperature of the AP. The selective coating material on the AP will be chemically decomposed around 680 K, as previously mentioned and its length will be limited to < 100 m.

The HTF temperatures along the receiver unit in the cavity is capable of exceeding the selective coating temperature ceiling, as shown in Fig. (9).

4. Conclusion

We introduced a cavity concept to reduce thermal radiation losses for receivers for parabolic trough solar plants, and compared it to existing systems. The cavity design performs very well at higher temperatures and it theoretically capable of exceeding 1300 K, thus outperforming current technologies due to its thermal stability. This in turn can increase the overall (Rankine) efficiency of the entire plant. There are further important parameters that affect the temperature profile and the efficiency, such as the cavity opening size and the reflectivity of the cavity mirror. These will be shown in further communication.

References

[1] Cyulinyana M C and Ferrer P 2011 Heat efficiency of a solar trough receiver with a hot mirror compared to a selective coating *South Afr. J. Sci.* **107** 01–7

[2] Sargent and Lundy LLC Consulting Group 2003 *Assessment of Parabolic Trough and Power Tower Solar Technology Cost and Performance Forecasts* (Chicago, Illinois: DIANE Publishing)

[3] Lampert C M 1979 Coatings for enhanced photothermal energy collection I. Selective absorbers *Sol. Energy Mater.* **1** 319–41

[4] Burkholder F and Kutscher C 2008 *Heat-loss testing of Solel's UVAC3 parabolic trough receiver* (United States: National Renewable Energy Laboratory (NREL), Golden, CO.)

[5] Kennedy C E and Price H 2005 Progress in Development of High-Temperature Solar-Selective Coating *ASME Int. Sol. Energy Conf. Sol. Energy* 749–55

[6] Twidell J and Weir T 2015 *Renewable Energy Resources* (New York: Routledge)

[7] Kreith F and Kreider J F 1978 *Principles of solar engineering* (United States: Hemisphere Pub. Corp.)

[8] You Y and Hu E J 2002 A medium-temperature solar thermal power system and its efficiency optimisation *Appl. Therm. Eng.* **22** 357–364

[9] Kaluba V S and Ferrer P 2016 A model for hot mirror coating on solar parabolic trough receivers *J. Renew. Sustain. Energy* **8** 053703

[10] Hachicha A A, Rodríguez I, Capdevila R and Oliva A 2013 Heat transfer analysis and numerical simulation of a parabolic trough solar collector *Appl. Energy* **111** 581–92

[11] Ferrer P 2008 Enhanced efficiency of a parabolic solar trough system through use of a secondary radiation concentrator *South Afr. J. Sci.* **104** 383–388

Numerical modelling of control rod calibrations and fuel depletion at the OPAL research reactor

R. Mudau[1], D. Botes[1] and F.A. Van Heerden[1]

[1] The South African Nuclear Energy Corporation SOC Ltd (Necsa), P1900, P. O. Box 852, Pretoria, 0001, South Africa

E-mail: rotondwa.mudau@necsa.co.za

Abstract. The IAEA is currently administering an international Coordinated Research Project (CRP), the main purpose of which is to develop a set of research reactor benchmarks for the verification and validation of computational codes. The focus of the CRP in particular is the modelling of multi-cycle depletion. Necsa is developing a new calculational framework for performing nuclear reactor core calculations, which integrates both the stochastic and deterministic modeling methods in a consistent manner. In this work, the system is applied to the OPAL benchmark problem. The OPAL reactor is a modern research reactor with challenging aspects in neutronic design. In particular, the use of burnable poisons and a heavy water reflector pose modelling challenges. Analysis conducted on this benchmark includes control rod calibration experiments as well as the simulation of four actual operating cycles.

1. Introduction

Numerical modelling is often employed to support the safe and economic operation of nuclear reactors. Computer codes are used to calculate, amongst other things, the distribution of neutrons in space and time by solving the Boltzmann transport equation, or some approximation of it. Operational parameters such as power distribution, control rod position and fuel depletion can then be calculated using this information.

The International Atomic Energy Agency (IAEA) is conducting a CRP titled "Benchmarks of Computational Tools against Experimental Data on Fuel Burnup and Material Activation for Utilization, Operation and Safety Analysis of Research Reactors". Various institutions have submitted specifications of the research reactors they operate, as well as descriptions of experiments that were performed with the reactors and data gathered in the course of normal operations, to provide benchmarks against which reactor computational codes may be verified and validated [1].

Necsa developed a tool for creating detailed heterogeneous three dimensional models, which can be deployed to generate input for various reactor calculation codes such as Serpent 2 [2, 3], MCNP [4] and the OSCAR-4 [5] nodal diffusion solver, while maintaining the consistency of the model across these codes. In this work, the tool was used to prepare detailed models for the OPAL benchmark problem and generate input for Serpent, a criticality and burn-up code that employs a Monte Carlo solution method [3]. In this way Serpent and the unified model were validated against experimental data before they can be used to support operations.

2. Problem Description

The Open Pool Australian Lightwater (OPAL) reactor is a 20 MW research reactor that is operated by ANSTO (Australian Nuclear Science and Technology Organisation). It is heavy water reflected and light water moderated. A schematic representation of the model of the reactor, including the facilities around the core, is shown in Figure 1. There are a number of irradiation facilities, located mainly to the east and south of the core, for the production of radio isotopes, neutron activation analysis and silicon transmutation doping. A cold neutron source, which uses liquid helium to moderate neutrons to very low energies, is located to the north. There are five beam tubes that provide neutrons to various instruments, of which two are for thermal neutrons, two for cold neutrons, and one for hot neutrons.

The reactor consists of a compact core with 16 fuel assemblies, four control rods and a central, cruciform, regulating rod, which is used for fine-grained control of the critical state of the reactor as shown in Figure 2. It is divided into four quadrants by the control rods, with the regulating rod in the centre. The fuel is MTR (Material Testing Reactor) type assemblies, with 21 plates each. Three types of assemblies are used for the first cycle and are designated as type 1 fuel, type 2 fuel and standard fuel with 212 g U-235, 383 g U-235 and 484 g U-235 respectively. Only the standard fuel is used for reloading [6]. There are also burnable poisons in the form of cadmium wires slotted into every second fuel plate of the type 2 and standard fuel. Burnable poisons remove neutrons to limit the fission rate when fuel is fresh, and are removed by transmutation over time.

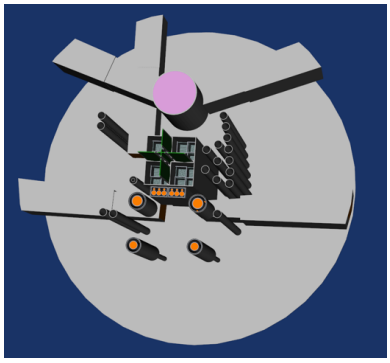

Figure 1: Schematic representation of the OPAL model and the reactor components

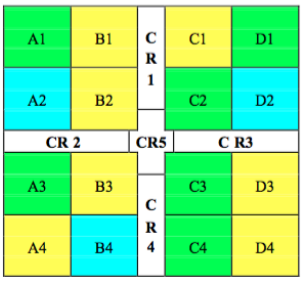

Figure 2: The numbering of control rods and fuel elements within the reactor core. Type 1 fuel is yellow, type 2 green and standard fuel is blue

The reactor operator submitted results from control rod calibration experiments that were performed at the start-up of the initial core, as well as data on the core state for the first 7 operating cycles [6].

Control rod calibrations start from a core that is critical, i.e. one in which the neutron production rate is balanced by the rate at which neutrons are lost due to capture or leakage from the system. They then proceed as follows: the core is made super-critical (neutron population is increasing) by withdrawing the control rod to be calibrated by a certain distance, and the resultant reactivity insertion is measured. One or more rods are then inserted to restore criticality. This process is repeated until the calibrated rod is fully extracted from the core. The reactivity change per unit movement of a rod is called the differential worth of the rod, and is dependent on insertion depth. The experiments for which data was made available are for control rod 1 compensated by rod 4, rod 2 compensated by rod 3, and rod 5 compensated by rod 2 and rod 3. The location of the rods within the core is demonstrated Figure 2.

The composition of fissionable materials within the core changes over time during operation, a process that is referred to as burn-up or depletion. No direct measurements of burn-up were provided, but data such as the reactor power and control rod positions at various points during reactor operation was made available. In this benchmark, cycles were between 30 and 40 days long and the core was reloaded with 3 fresh standard fuel assemblies after each cycle. Data was provided for the first 7 cycles of the reactor's operating life.

3. Calculational approach adopted and model description

The new pre and post processor tool was used to create heterogeneous model of the core and surrounding structures using the OPAL benchmark specification document, with as much detail as reasonably achievable. The specifications of certain structures were simplified or lacked full engineering detail. This was especially true for the cold neutron source and many of the irradiation facilities that surround the core.

The control rod calibration experiments were modelled using a modified version of Serpent 2.1.23 [3] and compared to the measured data. Additionally, core follow analysis was performed with Serpent for the first 4 reactor cycles to track the evolution of burnable elements in the core. It is known that a reactor is critical under normal operating conditions. Therefore, in the absence of depletion measurements, the deviation from criticality predicted by the model during operation may be used as a proxy for performance in tracking fuel depletion.

4. Results and Discussion

4.1. Control rod calibration

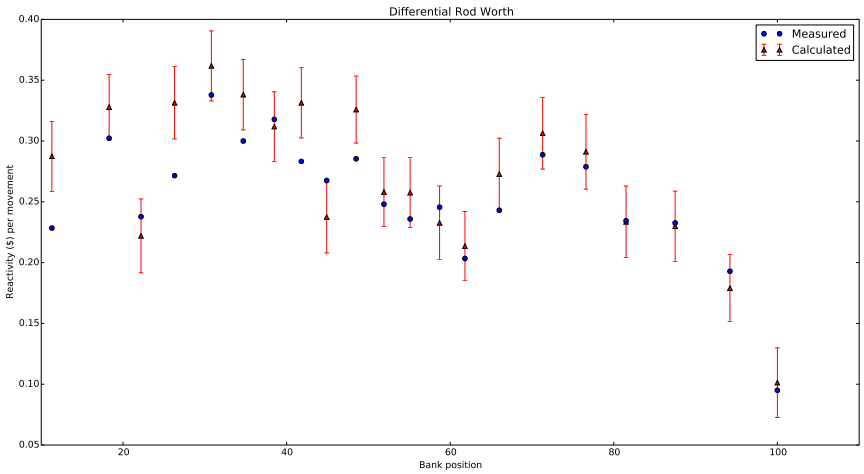

Figure 3: A comparison between the calculated and measured differential rod worth for control rod 1 compensated by rod 4

Figure 3 shows the calculated and measured differential rod worth curve for rod 1, which is measured in reactivity ($) inserted per unit bank movement (% of total rod travel distance), with rod 4 as the compensating rod. It is clear from Figure 3 that the model slightly overestimated the rod worth, especially in the lower and central parts of the core.

Figure 4 show the differential rod worth curves for the calibration of rod 2, which was compensated by rod 3. For these rods the model predicted the measured values very well.

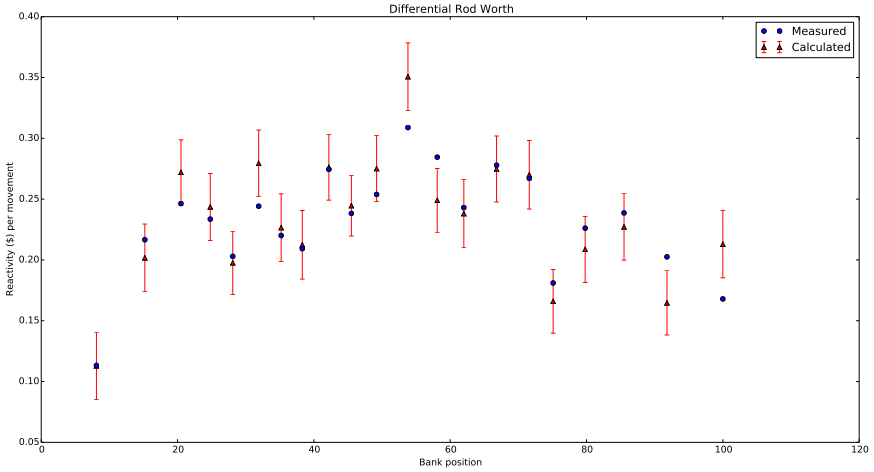

Figure 4: A comparison between the calculated and measured differential rod worth for control rod 2 compensated by rod 3

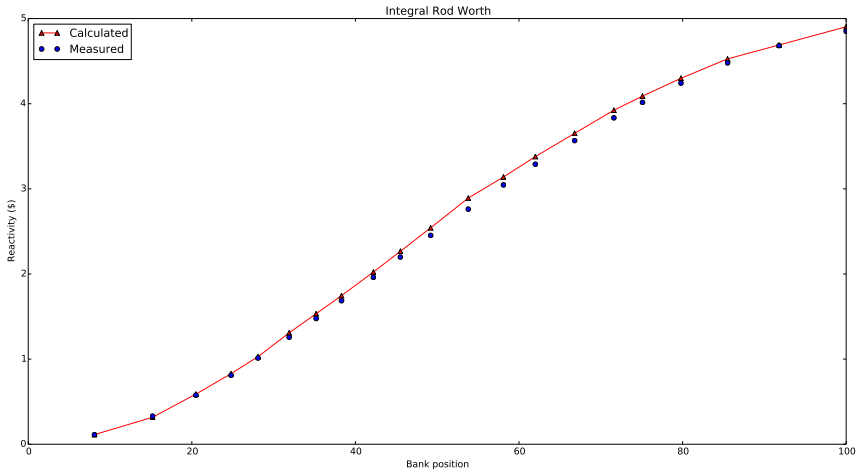

Figure 5: A comparison between the calculated and measured integral rod worth curves for control rod 2 compensated by rod 3

One can observe just how well the model performs by looking at the integral rod worth curve in Figure 5, which shows the cumulative worth of the rod over its total travel distance.

Figure 6 is the differential rod worth curve for rod 5, the regulating rod. It must be noted that the reactivity that was inserted by rod 5 was compensated for by both rod 2 and rod 3. The model again slightly overestimated the worth of this rod.

In general, good agreement between the measured control rod worth and the calculated control rod worth is observed. Since Serpent uses a Monte Carlo algorithm, it estimates the distribution of fissions in the system by continually re-sampling the distribution from an initial guess until balance is achieved. This creates a correlation between the critical estimates at

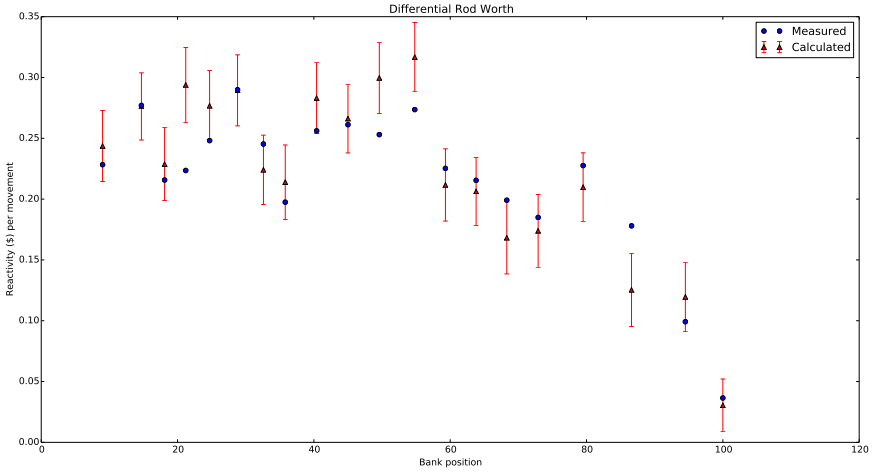

Figure 6: A comparison between the calculated and measured differential rod worth for control rod 5 compensated by rod 2 and rod 3

different rod positions, which will increase the variance, and hence the uncertainties on the estimates. That is, the displayed error bars should be larger. Currently, there is no built in measure of this additional source of uncertainty in Serpent. The effect would be particularly noticeable when a rod movement causes a large change in the fission distribution, either radially or axially. This, at least partly explains why the Serpent results seem more sensitive to large reactivity changes.

4.2. Core follow analysis

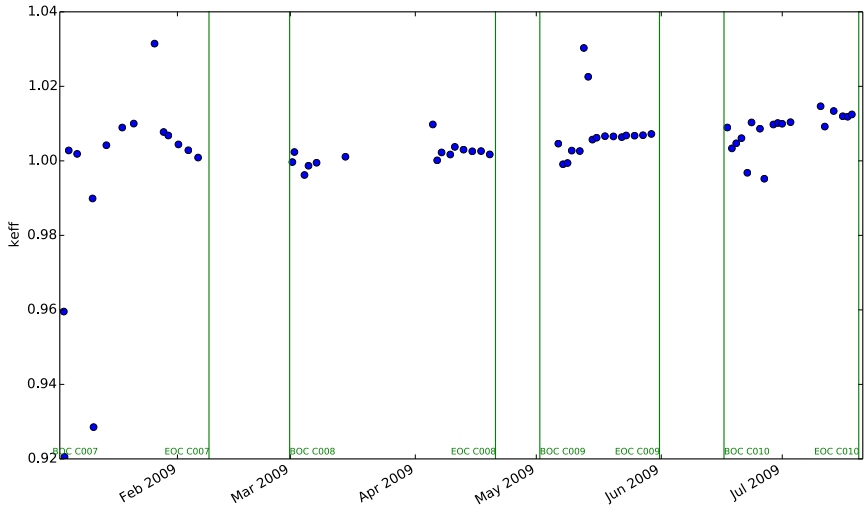

Figure 7: Calculated reactor k_{eff} for the first four cycles

Figure 7 shows the results of the core follow analysis for the first 4 of the 7 cycles for which

data was provided. A reactor in steady state operation is critical, with an effective neutron multiplication factor of $k_{\text{eff}} = 1$, which is the ratio between the number of neutrons produced by fission and the number of neutrons lost through absorption and leakage. In the absence of direct fuel depletion measurements, calculating k_{eff} with given operational data, such as control rod positions and core power, over the course of reactor operations gives a reasonable indication of the accuracy with which the depletion of fuel is modelled.

Overall the core follow calculation performed well, although there are some outliers in the data, which may be attributed to several shut-downs that the reactor experienced in the first few cycles for which data was not provided. Overall, however, the calculated k_{eff} is close to 1, although it increases gradually from cycle to cycle. There are a number of factors that can contribute to the rise in reactivity: The first is in the modelling of the burnable absorbers (cadmium wires) in the fuel assemblies. Since both the volume and surface of absorbing materials are important, when depleting the wires, absorbing materials near the surface of the wires should not be removed too quickly (the so called rim effect). Constraints on computing resources limit the number of depletion zones (rings) that can be used in the wires, and for this study only one inner and outer ring were employed. This can be refined in order to check if reactivity estimates improve.

The second factor contributing to a systematic reactivity increase is uncertainty in the provided core power levels. Reactor facilities have indirect measures of estimating core power, which must be carefully calibrated, since inlet and outlet temperature measurements can not directly account for loss of heat to the reflector pool and other structures. If the measured power is too low, fuel will be under depleted, which will cause reactivity to steadily rise until a new equilibrium mass distribution is reached. This estimated distribution will differ slightly from the real mass distribution in the system. Such a power sensitivity study is planned in future work.

5. Conclusion

The calculated control rod calibration results compared well with the measured results although there were some slight discrepancies. The discrepancies could be attributed to the constraints within the structure of Serpent especially in areas where the rod movement would cause a large change in the fission distribution. In the corefollow calculation the criticality estimates increased gradually from cycle to cycle. The gradual increase could be as a result of the uncertainties in the provided core power levels or the over burning of the burnable poisons.

Acknowledgements

The authors would like to acknowledge the computational resources provided by the Centre for High Performance Computing (CHPC) under research project INDY0788.

References

[1] IAEA CRP (T12029) *Benchmarks of Computational Tools against Experimental Data on Fuel Burnup and Material Activation for Utilization, Operation and Safety Analysis of Research Reactors* 2015

[2] Leppanen J *Serpent a continuous-energy Monte Carlo reactor physics burnup calculation code* 2013 VTT Technical Research Centre of Finland

[3] Leppanen J, Pusa M, Viitanen T, Valtavirta V and Kaltiaisenaho T *The Serpent Monte Carlo code: Status, development and applications in 2013* 2015 *Ann. Nucl. Energy* **82** 142-150

[4] X-5 Monte Carlo Team *MCNP - A General N-Particle Transport Code, Version 5 Volume I: Overview and Theory, LA-UR-03-1987* (2003, updated 2005) Los Alamos National Laboratory

[5] Prinsloo R H et al. *OSACR-4 system overview* 2012 RRT-OSCAR-REP-12002, Necsa Internal Report

[6] International Atomic Energy Agency *Research Reactor Benchmarking Database: Facility Specification and Experimental Data, Technical Reports* Series No. **480** 2015 IAEA Vienna

[7] Halton J H *A Retrospective and Prospective Survey of the Monte Carlo Method* January 1970 Society for Industrial and Applied Mathematics **2**

The proposed improvements of the hydrometer calibration system using Cuckow's method at NMISA

B Ndlovu [*], RT Mautjana and DJ Mabena

National Metrology Institute of South Africa, Private Bag X 34, Lynnwood Ridge, Pretoria, 0040, South Africa

[*] Email: bndlovu@nmisa.org

Abstract. Hydrometers are instruments that are used for measuring the density or specific gravity of liquids. NMISA uses Cuckow's method which is based on hydrostatic weighing to calibrate hydrometers. This involves weighing the dry hydrometer in air and then in liquid. The liquid level is aligned with the horizontal scale mark of the hydrometer point to be calibrated and the reference density is determined at that point to get the correction for the scale. The horizontal scale mark setting, vertical alignment and reference liquid density are some of the key factors that need to be set and measured accurately to ensure the quality of results. The horizontal scale mark (point to be calibrated) is set with the assistance of a computer software and a magnifying camera. This setting also depends on how well the vertical alignment is set as the hydrometer is suspended from underneath the balance. Distilled water (reference liquid) temperature is measured at three different depths and used to determine the liquid density at the time of measurement. This work discusses the setup of the hydrometer system at NMISA and also highlights the required improvements that need to be implemented to address all the uncertainty contributions associated with the system. We also report some results found for hydrometers calibrated at the minimum and maximum points of their respective scales using the current system. Three hydrometers with scale ranges of 0.600 – 0.700 g/ml, 0.700 – 0.800 g/ml and 0.800 – 0.900 g/ml were calibrated at a temperature of 20 °C. The uncertainty of measurement was found to be better than ±0.001 g/ml.

1. Introduction

The liquid's sugar contents, alcohol concentration or density are some of the important characteristics which need to be known for the liquid's specific use. For many applications, a simple measurement of dipping the hydrometer in the liquid and reading off the graduation mark is good enough. A hydrometer is a graduated glass hollow tube that is weighted at the bottom end to make it float upright inside a liquid. It is used to measure the specific gravity, concentration, percentage of salts or density of liquids between 0.5 g/ml and 20 g/ml [1]. Hydrometers are classified into constant-volume or constant-mass hydrometers. A constant-volume hydrometer is made to float in liquids of different densities by adding mass pieces such that the same scale mark is in line with the liquid level in each liquid which means the volume under each liquid remains constant. On the other hand, a constant-mass hydrometer on which this work focuses, floats at various levels for a variety of liquids with a range of densities and its mass is kept constant [2]. Over time, various liquids may result in slight drifts in the scale reading of the hydrometer due to mechanical stress, abrasion and ageing process of glass [2]. These slight changes need to be quantified to ensure the quality of measurement by a

hydrometer. This is done through regular calibration of hydrometers traceable to a relevant national standard.

Hydrometers have previously been calibrated in a range of reference liquids with different densities which is a bit expensive since a range of suitable liquids had to be made available and also time-consuming since the measurements had to be carried out in each of these liquids. A much cheaper method was introduced by Cuckow. In Cuckow's method, a single reference liquid is used for the calibration of the whole range of the hydrometer scale [3, 4]. This method is based on hydrostatic weighing where the hydrometer is first weighed in air and then in the reference liquid with a known density. The process involves immersing the hydrometer in the reference liquid and setting the scale mark to be calibrated to be aligned with the level of the reference liquid and then determining what would be the density of the reference liquid at that point. In the same way, other points can be calibrated by simply shifting the same liquid level vertically to align with the scale mark of the hydrometer without any additional mass pieces on the hydrometer. The correction to the calibrated hydrometer scale is then determined by subtracting the scale mark of the hydrometer from the measured reference liquid density at that point.

Cuckow's method for determining the reference liquid density is based on three scenarios which generate three equilibrium force equations [3]. In the first scenario, the hydrometer floats freely in a reference liquid. In the second scenario, the hydrometer is weighed in air. Thirdly, the hydrometer is weighed partially immersed to the same scale mark as in the first scenario [2]. After combining the equilibrium force equations that resulted from the three scenarios and some simplifications, the reference liquid density ρ_x is then given by

$$\rho_x = (\rho_L - \rho_a)\frac{\left[M_a\left(1-\frac{\rho_{a2}}{\rho_s}\right)+\pi D\gamma_x g^{-1}\right]}{\left[M_a\left(1-\frac{\rho_{a2}}{\rho_s}\right)-M_L\left(1-\frac{\rho_{a3}}{\rho_s}\right)+\pi D\gamma_L g^{-1}\right]}\left[1+\beta(T_3-T_0)\right]+\rho_{a2} \qquad (1)$$

where M_a, M_L : mass of the hydrometer in air and in reference liquid respectively,

ρ_L : liquid density at a measurement temperature T_3,

ρ_a : air density when the hydrometer scale is read,

ρ_s : density of the reference weights,

γ_x : surface tension of the liquid in for which the hydrometer is to be used,

g : local gravitational acceleration,

D : diameter of the hydrometer stem at the graduation mark to be calibrated,

ρ_{a2}, ρ_{a3} : air density while weighing in air and in liquid respectively,

γ_L : surface tension of the reference liquid,

β : volumetric thermal expansion coefficient [3].

The measuring equipment used to calibrate the hydrometer is the main contributor to the achieved measurement uncertainty and the quality of the measurement result [2]. In this work, we discuss the hydrometer calibration system setup at NMISA and some of the proposed improvements on the current system.

2. Experimental details

2.1. The hydrometer calibration system

The hydrometer calibration system used at NMISA is shown in Figure 1. This system consists of an electronic balance with a resolution of 0.01 mg. The thermostatic liquid bath (outer) contains tap water

that is used to maintain the temperature of distilled water (reference liquid) in the inner vessel at around the reference temperature of 20 °C. The inner liquid vessel contains three temperature sensors positioned at different depths (in case of any temperature gradient inside the reference liquid) to measure the temperature of distilled water at the time of weighing the hydrometer in liquid. A desktop computer has the software that is used for finer adjustments of the scale mark to the liquid level and for the collection of measurement data from the sensors (air temperature, relative humidity, pressure and water temperature) as well as from the balance. The image from the CCD camera is magnified and viewed on a computer monitor.

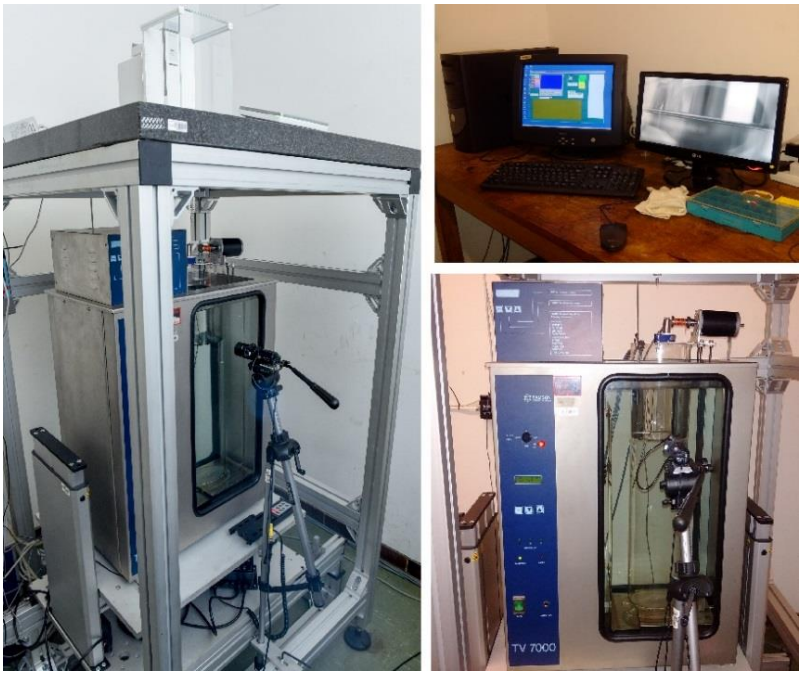

Figure 1: The hydrometer system at NMISA.

Figure 2 is a schematic representation of the hydrometer system which shows the connections of each component to another. The figure also shows a thermostat which regulates the water temperature in the thermostatic bath.

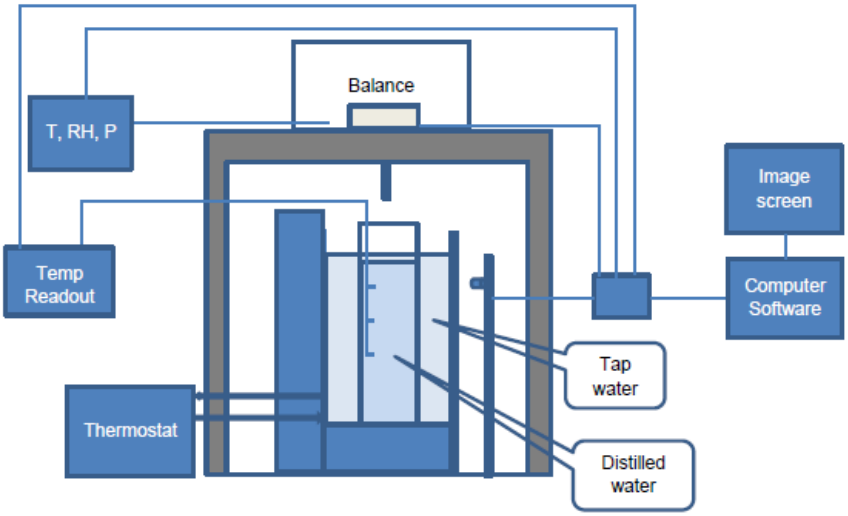

Figure 2: A schematic representation of the hydrometer system.

2.2. Weighing in the reference liquid

The clean and dry hydrometer is first weighed in air against the reference mass pieces. After completing a set of weighing measurements in air, the hydrometer is then weighed in the reference liquid by suspending it from the balance using a wire connected to two O-rings. This may somewhat make the hydrometer to be tilted slightly which also impacts on the graduation marks causing the scale to be at an angle to the horizontal position. Hydrometers with scale range of less than 1 g/ml require additional ring weights on the neck/stem so that they can be immersed to the desired scale mark for calibration since the density of water is close to 1 g/ml. This may further affect the vertical alignment of the hydrometer when the ring has a much bigger inner diameter than the hydrometer stem. Therefore, the suspension of the hydrometer from the balance should be performed carefully and the inner diameter of the additional ring weight should be such that the hydrometer stem just fits inside the ring to ensure proper vertical alignment of the hydrometer.

When weighing the hydrometer in the reference liquid, the scale mark to be calibrated is set to align with the level of the reference liquid by moving the fluid bath up until the liquid level just close enough to the calibration point. Then, some finer adjustments are required to get the meniscus correctly on the scale mark. This is performed with the assistance of the CCD camera and the computer software. The image from the camera is magnified by the software for a better view of the horizontal alignment of the scale mark and the liquid level. The software is also used to driving a step motor for finer vertical adjustments. When the alignment is completed, the apparent mass of the hydrometer is recorded when the balance reading is stable. Air temperature, pressure, humidity and liquid temperature are recorded for determining the air and liquid densities. The liquid density is mainly dependent on the liquid temperature and so this temperature needs be measured accurately as it has a direct impact on the resulting reference density at the scale mark of the hydrometer [4].

One of the biggest challenges of this system is the alignment of the hydrometer scale mark to the reference liquid level. Some institute(s) address this challenge by using a laser sheet (a horizontal laser beam which is in a form of a horizontal sheet) which is aligned to the hydrometer scale to be calibrated. By bringing the reference liquid towards the scale, the measured laser power increases once the laser sheet passes through the liquid instead of air due to more light being refracted towards the power meter on the opposite end [5]. The alignment of the liquid level and the hydrometer scale is determined to be somewhere within this measured laser power transition. Other institutes have developed software which automatically process the image of the scale and liquid level interface then adjusts the hydrometer to the correct liquid level [2]. NMISA plans to improve the software to automate the alignment of the scale to be calibrated and reference liquid level and to also use this software to check and confirm the vertical alignment of the hydrometer.

2.3. Surface tension

The reference liquid density determination is also affected by the surface tension γ which results in the liquid pulling the hydrometer downwards at its stem. γ, as per Equation (1), must be known at a measurement T_3 and reference T_0 temperatures. For this purpose, γ was measured using a tensiometer system in the temperature range 18.0 °C $\leq T \leq$ 22.0 °C in which the hydrometer calibrations are performed. In this temperature region, the mean surface tension of the reference liquid was found to be 71.11 mN/m ± 1.00 mN/m. Investigations of a more suitable reference liquid are also underway as distilled water (high density and high surface tension) is not ideally the best for this work. The meniscus of distilled water is also not reproducible in shape which results in a different surface tension force. Alkane liquids like nonane, tridecane, etc. are used by other institutes because of their better surface tension [2, 5].

3. Results

Three hydrometers with ranges of 0.600 – 0.700 g/ml, 0.700 – 0.800 g/ml and 0.800 – 0.900 g/ml were calibrated using Cuckow's method. The measurement results at a reference temperature of 20 °C are shown in Table 1. This table shows the calibrated hydrometer points against the measured reference

density at that point. The calculated measurement uncertainties were found to be better than ± 0.001 g/ml across the calibrated points.

Table 1: The hydrometer calibration results with their measurement uncertainties.

Number	Hydrometer Reading at 20 °C (g/ml)	Reference Density at 20 °C (g/ml)	Uncertainty of Measurement (g/ml)
1	0.600	0.599	± 0.001
	0.700	0.701	± 0.001
2	0.700	0.701	± 0.001
	0.800	0.799	± 0.001
3	0.800	0.801	± 0.001
	0.900	0.900	± 0.001

4. Conclusions

We have identified the improvements that are required on the current hydrometer system. The vertical and horizontal alignment of the hydrometer scale with the reference liquid level play a vital role in the quality of the measurement result and therefore will be incorporated accordingly in the analysis of results. The uncertainties may be improved by studying and quantifying each significant contributor in the uncertainty budget.

References

[1] Mohamed MH, Bayoumi MA, Eltawil AA and Abuelezz AE 2014 Design and validation of an automated hydrometers calibration system. *Int. J. Innov. Res. Sc*. **3**(5), 12735–41

[2] Lorefice S and Malengo A 2006 Calibration of hydrometers. *Measurement Sc. & tech.*, **17**(10), 2560

[3] Cuckow FW 1949 A new method of high accuracy for the calibration of reference standard hydrometers. *J. Chem. Tech. & Biotech.*, **68**(2), 44-49

[4] Akcadag ÜY and San SE 2001 Newly established hydrometer calibration set up at UM. *Proc. 17th Int. Conf. on Force, Mass, Torque and Pressure Measurements*, IMEKO TC3 (Istanbul, Turkey)

[5] Wright JD, Bean VE and Aguilera J 2010 NIST calibration services for hydrometers. *NIST Special Publication, **250***, 78

The MinPET diamond discovery technique

T Nemakhavhani[1], D Unwuchola[1], R C Andrew[1], M N H Cook[1], S H Connell[1] and S E Ballestrero[1], U Uggerhøj[2], S Pape Møller[2], P Aggerholm[2], N Hertel[2], J A Swartz[2]

[1]University of Johannesburg, Auckland Park, South Africa.
[2]University of Århus, Århus, Denmark.

E-mail: shconnell@uj.ac.za

Abstract. MinPET is a technology for diamond discovery in rock, specifically, the online, high throughput, quantitative, 3D imaging of local carbon concentration distributions in kimberlite. In the MinPET process, a high-energy photon beam of some tens of MeV irradiates a kimberlite rock stream, exciting the Giant Dipole Resonance. This transmutes especially some of the light stable isotopes within the kimberlite to become transient positron emitters, or Positron Emission Tomography (PET) isotopes. PET imaging of the rock is performed in an online run-of-mine scenario after a hold hopper, which delays detection for 20 minutes. After this time, ^{11}C, which has the longest PET isotope lifetime, is the dominant PET isotope. All non-diamond sources of carbon have a much lower carbon concentration than diamond, or they are diluted and finely dispersed within the kimberlite. Diamond is therefore evidenced by reconstructing the 3D quantitative carbon density distribution map. This contribution reviews the current status of the R&D towards a Mine Test Unit and concludes the technology is ready for deployment for such a unit in a full scale run-of-mine context. The expectation is that the technology is ready for deployment as a mine-test-unit operating in a full scale run-of-mine context

1. Introduction

The MinPET process has an activation and a detection stage, as depicted schematically in Figure 1 below [1, 2, 3, 4]. The activation stage consists of irradiation with a high-energy photon beam. This beam is produced by bremsstrahlung of a 40 MeV electron beam incident on a tungsten converter and then subsequently on the kimberlite rock stream. A shower develops as the mixed radiation field progresses through these materials. PET isotopes are produced primarily by the (γ,n) transmutation reaction, although there are several others, such as (γ,p(n)), (γ,α(n)) and (γ,xn) which also need to be considered. The (γ,n) reaction has a high cross section ($\sim$8 mb) in the region of the Giant Dipole Resonance ($E_\gamma \approx 20 - 30$ MeV). This transmutes various atomic species within the kimberlite to become transient positron emitters, or PET isotopes. PET stands for Positron Emission Tomography, as in the medical diagnostic technique for functional bio-imaging. It turns out that PET isotopes are the dominant sources of activity after several minutes. After about 20 minutes, ^{11}C is the dominant PET isotope. PET imaging of the rock after this time delay corresponds to a 3D quantitative imaging of the internal carbon distribution. All non-diamond sources of carbon have a much lower carbon concentration than diamond, or they are diluted and finely dispersed within the kimberlite.

This is then a technique on which to base the intelligent sensor-based sorting of barren from diamondiferous kimberlite. The contrast ratio is about 10:1 for diamond as compared to wood, rubber, large carbonate particles and so on. Kimberlite contains carbonates, usually quantified as an amount of CO_2. The fractional composition of this by weight is variable but a reference

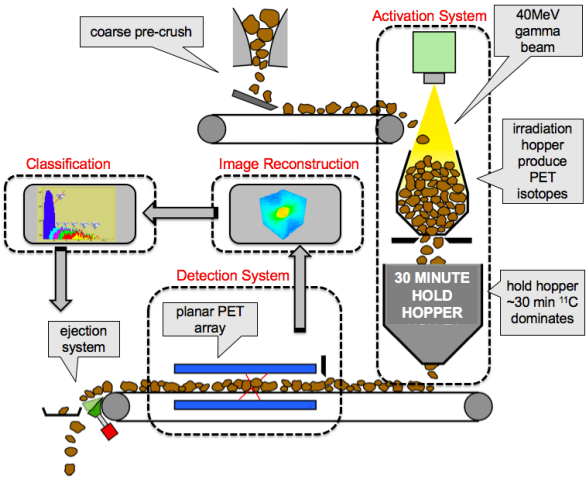

Figure 1. Schematic diagram of the MinPET process. Coarse crushed (<100 mm) kimberlite rock is irradiated with high energy photons. The hold hopper of ∼20 min allows non-carbon PET activity to decay out (mostly the ^{15}O), leaving ^{11}C as the main surviving PET isotope component. The planar PET detector array identifies diamond via hotspots in the 3D carbon concentrations.

case could be 5%. The contrast ratio for diamond in kimberlite would then be about 45:1. The concept is technologically demanding, as in a typical diamond mine, the rock throughput could be about 500 tons per hour, on a belt moving at 1 m/s, the detectors would have about 2 s to acquire the image, and the decision base on the quantitative visualisation of a diamond should be available within about 20 s. The concentration of diamond in kimberlite by weight varies from mine to mine, but typically it is just under a carat (0.2 g) per ton of kimberlite. Global production, as measured by the Kimberley Process Certification Scheme (KPCS), was 134-million carats in 2016 [5]. One therefore finds the crushing and processing of about 100 million tons of kimberlite rock per year, an unnecessary multi-billion dollar (barren) rock processing business. Normally the recovery of diamond is accomplished by a sequence of crushing and concentration operations. The concentration could be achieved by dense media separation, grease tables, dual energy X-ray transmission (XRT) and X-ray stimulated optical fluorescence (XRF). The early crushing to small rocks in these methods leads to diamond breakage. In addition they require substantial plant, they are not sufficiently efficient, they usually require a lot of water and lead to slimes dams. MinPET is therefore a potential disruptive technology. Diamond mining is expected to become more efficient, the recovered diamonds would suffer much less breakage, mining would be greener, mine life would be extended and sub-marginal mines could become competitive.

2. Full Dress Rehearsal, lab scale

A test of the performance of the MinPET technology requires the processes of activation, delay and then detection to be implemented on test samples of kimberlite rock spiked with diamond. Previous work has identified a benchmark dose for the case of a 40 MeV electron accelerator providing a beam current of 5 mA over a footprint of 1 m^2 to a belt of width 1 m moving at 1 m/s irradiating kimberlite rock with a throughput of 500 tons per hour. A detailed Geant4 [6, 7, 8] simulation is used to quantify the specific activity of various PET isotopes that is generated in this case for a reference kimberlite rock. In the simulation, the mixed radiation field that evolves is folded with the various nuclear cross sections for the processes mentioned above, in the evaluation of the specific PET activity. The benchmark dose producing this activity in a

reference sample of kimberlite leads to the definition of the MinPET dose and the MinPET specific activity. The benchmark MinPET detector here would be a planar detector array of 2 m × 1 m above and below the belt. The Geant4 simulation extends to detection and reconstruction of an event-by-event file of the lines of response (LoR). This then leads to the concept of the required MinPET detection capacity, which can successfully detect down to a given small diamond size within a given kimberlite rock size. The reference sizes here at the moment are a 4 mm diamond within a 100 mm particle of kimberlite containing 5% of carbon expressed as a weight percent of CO_2. It is necessary to specify these additional details as the first represents the signal activity, the second represents the amount of the systematic affects of scattering and attenuation for the annihilation 511 keV photons that affect the fidelity and number of the resulting LoRs, and the third relates to non-diamond carbon irreducible background.

When testing the performance of a lab-scaled MinPET system, it must be scaled in performance to a full run-of-mine MinPET system, which delivers an effective MinPET Dose, and generates the same specific activity in the kimberlite, and has a similar detection capacity, as the benchmark case described above. The differences in accelerator power and detection surface area are absorbed into adjustments to the throughput rate. In all, one seeks to have ultimately the same total number of LoRs that contribute to the image formation process, in the benchmark MinPET run-of-mine scenario as compared to the lab-scale Full Dress Rehearsal performance test scenario.

2.1. Activation

There are very few accelerators world-wide with a capacity for 40 MeV electrons, which can be re-purposed for general irradiations. Our full dress rehearsal experiments were recently carried out at the electron injector microtron of the ASTRID storage ring of the ISA, Centre of Storage Ring Facilities at the Department of Physics in Århus University, Denmark [9]. This injector microtron has an electron beam energy of 100 MeV. A 2.5 mm stainless steel degrader and a 5 mm copper degrader were used to soften the beam energy. The average beam current was 17 nA. This is a much weaker beam (about 3×10^5 times) than that envisaged in the benchmark MinPET specification. Irradiation times were increased from 1 s to 600 s to partially compensate for this effect. This can be considered a maximum irradiation time to avoid strong saturation effects considering the lifetimes of the relevant PET isotopes, specifically that of ^{11}C which is 20 minutes. The Geant4 simulations then allowed a scaling factor to be determined relating the specific activity produced in the lab-scale measurements at Århus to the benchmark MinPET scenario.

2.2. Detection

The MinPET lab-scale detection system has a dual planar array of BGO crystals set out with each plane comprising a matrix of 1024 pixels arranged in a 32 × 32 pixel square of dimension 20 cm × 20 cm. The light is collected into Hamamatsu H8500 photomultipliers (PMs). The read-out system has been specially designed and commissioned by Net Instruments for the MinPET application. This system will be described later elsewhere. The data acquisition system proceeds from front end FPGAs on each PM control board, to an FPGA on the planar array which does the event building for its side of the LoR. This system is controlled by an on-board PC. A coincidence determination is made with essentially no latency via a separate communication between the two planes. A trigger signal is generated to ensure that the two planar arrays publish only coincidence events to a fast network, containing their own data for their side of the LoR. The acquisition software can then build the LoRs after matching events from each plane. From there the data can be visualised using ROOT [10] and further analysed and also stored for additional off-line analysis. The rate of passage of the rock in a run-of-mine MinPET

system is 1 m/s for a 2 m × 1 m area of dual planar detectors. These lab-scale detectors have a fraction of this area. The rate of passage through the detector was determined to be 1 cm/s, as explained in the next section. This longer detection time would compensate the smaller detector size and part of the uncompensated component of the weaker accelerator beam, which was not fully compensated for by the longer irradiation time mentioned above. These compensations also included other systematic considerations which have been mentioned already.

2.3. Integration

The integration of the Activation-Detection system together, to represent a scaled version of the benchmark MinPET activation and detection system, considers both the lower accelerator beam current and the smaller capacity of the current lab-scale PET detection system, among other differences. Essentially the lower beam current with a different mixed radiation field profile is partially compensated for by a longer irradiation time. The smaller detector system and the remaining uncompensated factor for the irradiation stage is compensated for by a longer count time in the detectors. This corresponds to a slower passage of the rock through the MinPET detector array. More precisely, the considerations mentioned are modelled in Geant4, and the lab-scale test is compared to the benchmark MinPET scenario in the context of the net number of LoRs produced and detected in each of the cases. An approximate analytic calculation of the effects of the considerations mentioned leads to a similar conclusion to the detailed Geant4 modelling. The Geant4 modelling has also been bench-marked to careful experiments of ^{11}C activation by the same set-up as the Århus microtron, but where the activation was measured in absolute terms using efficiency-calibrated HPGe detectors. The Geant4 modelling of PET activity production by the Århus beam and the benchmark MinPET beam is therefore considered robust. In the results that follow, we therefore expect that the lab-scale experiments at Århus, with a weaker accelerator and small detector, but longer irradiation and count times, nonetheless correspond in terms of specific activation and detection efficiency to the benchmark scenario of a full run-of-mine MinPET scenario. That is to say, the results represent a test of MinPET corresponding to the throughput of a scaled up system capable of handling 500 tons per hour, and then discovering diamonds of a given size within a 100 mm particle of kimberlite where the carbon background as specified by CO_2 concentration by weight is 5%.

3. Reconstruction

The reconstructions that are shown later represent processing of the event-by-event LoR data to form 3D images using the CUDA-enabled ASTRA package [11, 12, 13]. The implemented algorithm is the iterative maximum likelihood method [14, 15] to find the most likely 3D source distribution for PET activity that best corresponds to a set of recorded 2D projections. The 2D projections used are obtained by binning the LoR event-by-event data based on a carefully chosen set of polar and azimuthal angles. This is effectively a higher dimensional sinogram. The reconstructed 3D image is treated to consider the systematic effects of the spatial non-uniformity of the Århus microtron beam compared to the spatial extent of the rock profile, and also for the "Compton Wind" effect of the depth dependence of softening of the mixed radiation fields energy distribution. In this data, there is not yet a correction for scattering and attenuation of the 511 keV annihilation photons. Such corrections would increase the detail seen in the reconstructions.

4. Results

The results are presented as reconstructed PET images, where only a sectional slice of the full 3D data-set is shown. The images should be interpreted as maps of the PET activity, where the dominant emitter is carbon. Hotspots in the image identify a buried diamond. The slice is chosen at the position that intersects the enclosed diamond. The slice form of presentation is

chosen as the full 3D image may only be visualised via a digital medium. Figures 2 and 3 show the MinPET discovery images for a 2.9 carat diamond in the middle of a 100 mm cube, and a 5.0 carat diamond buried in the middle of a 74 mm diameter cylinder respectively.

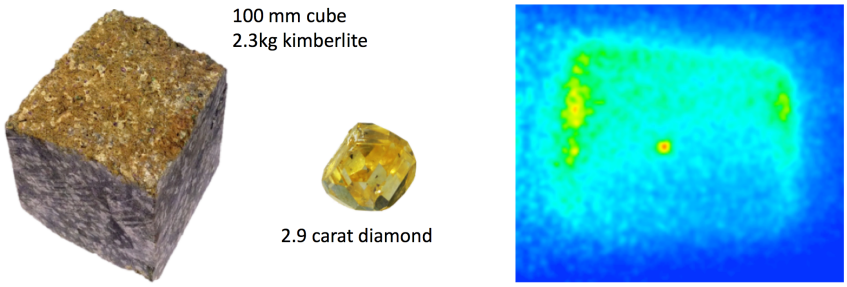

Figure 2. MinPET discovery image for a 2.9 carat diamond buried in the middle of cube of kimberlite of side 100 mm (2.3 kg).

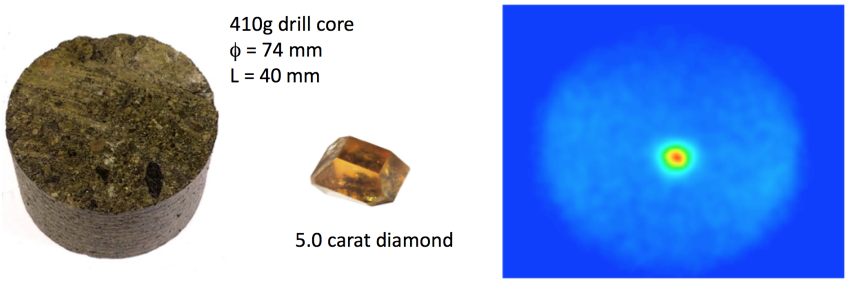

Figure 3. MinPET discovery image for a 5.0 carat diamond buried in the middle of cylinder of kimberlite of diameter 74 mm and length 40 mm (413 g).

Figure 4 shows the MinPET discovery image for a 10.3 carat diamond buried in the middle of calcite rock of length 150 mm. Calcite is a worst case scenario for MinPET as it has a high PET irreducible background. Its chemical formula is $CaCO_3$. The activation stage produces the PET isotopes $^{12}C(\gamma,n)^{11}C$, $^{16}O(\gamma,n)^{15}O$, $^{16}O(\gamma,n\alpha)^{11}C$ and $^{40}Ca(\gamma,np)^{38}K$. The PET activity of a possible diamond has to be visualised against a background of the PET activity of all the calcite constituent elements that could be activated too.

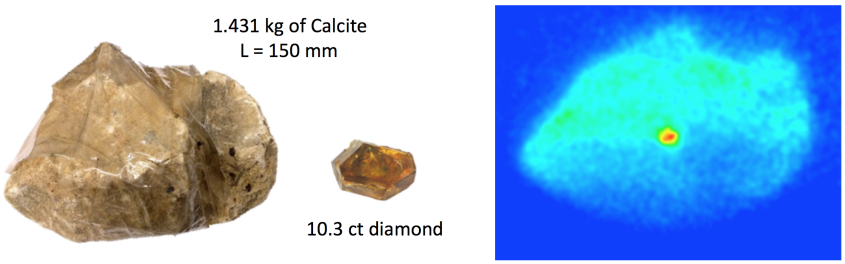

Figure 4. MinPET discovery image for a 10.3 carat diamond buried in the middle of calcite rock of length 150 mm (1.413 kg).

5. Conclusions

A Full Dress Rehearsal for the MinPET lab-scale technology demonstrator has been described. This means that the activation and detection stages are coupled and scaled to represent a

benchmark MinPET system capable of run-of-mine thoughputs (500 tph). The data shown represent PET reconstructions of essentially carbon 3D spatial concentrations. The sizes of diamonds buried within rocks of specified types and sizes is given for each image, and these are similar scenarios to those found in a mining context. The clarity with which a diamond may be recognised within the images therefore is an indication of the performance of the MinPET process in the specified conditions. Currently MinPET can discover at least a 4 mm diamond in a 100 mm kimberlite or a 2 mm diamond in a 40 mm kimberlite, under the conditions described above. The expectation is that the technology is ready for deployment as a mine-test-unit operating in a full scale run-of-mine context.

6. Acknowledgements

The authors acknowledge financial support of the National Research Foundation (NRF) and the IAEA TC CPF Programme, as well as provision of accommodation by Resolution Circle and iThemba LABS.

References

[1] TSA Patent 2006/08025, ARIPO Patent AP/P/2006/003753 (covers Botswana, Namibia, Lesotho and Zimbabwe), Canadian Patent 2,559,516, Australian Patent 2005220403, Russia Patent 2006135960, India Patent 5365/DELNP/2006F

[2] Ballestrero S et al 2010 *CERN-Proceedings-2010-001, Proceedings of the 12th INTERNATIONAL CONFERENCE ON NUCLEAR REACTION MECHANISMS Varenna (Italy), Villa Monastero, 15-19 June 2009* 589–602

[3] Tchonang M, Cook M, Bornman F, Connell SH and Ballestrero S 2014 *Proceedings of SAIP2013: the 58th Annual Conference of the South African Institute of Physics, edited by Roelf Botha, Thulani Jili, ISBN: 978-0-620-62819-8.* 502–506 URL `http://events.saip.org.za`

[4] Cook M, Tchonang M, Chinaka E, Bhamjee M, Bornman F and Connell SH 2015 *Proceedings of SAIP2014, the 59th Annual Conference of the South African Institute of Physics, edited by Chris Engelbrecht and Steven Karataglidis (University of Johannesburg, ISBN: 978-0-620-65391-6.* 479–484 URL `http://events.saip.org.za`

[5] Kimberley Process Certification Scheme 2016 *Annual Global Summary: 2016, Production, Imports, Exports and KPC Counts* URL `https://kimberleyprocessstatistics.org/static/pdfs/public_statistics/2016/2016GlobalSummary.pdf`

[6] Agostinelli S et al (GEANT4 Collaboration) 2003 *Nucl. Instrum. Meth.* **A 506** 250–303

[7] Agostinelli S et al (GEANT4 Collaboration) 2006 *IEEE Transactions on Nuclear Science* **53** 270–278

[8] Agostinelli S et al (GEANT4 Collaboration) 2016 *Nuclear Instruments and Methods in Physics Research* **A 835** 186–225

[9] Uggerhøj E 1994 *Le Journal de Physique IV* **4** C9–349

[10] Brun R and Rademakers F 1997 *Nuclear Instruments and Methods in Physics Research Section A: Accelerators, Spectrometers, Detectors and Associated Equipment* **389** 81–86

[11] van Aarle W, Palenstijn W J, Cant J, Janssens E, Bleichrodt F, Dabravolski A, De Beenhouwer J, Batenburg K J and Sijbers J 2016 *Optics express* **24** 25129–25147

[12] van Aarle W, Palenstijn W J, De Beenhouwer J, Altantzis T, Bals S, Batenburg K J and Sijbers J 2015 *Ultramicroscopy* **157** 35–47

[13] Palenstijn W, Batenburg K and Sijbers J 2011 *Journal of structural biology* **176** 250–253

[14] Dempster A P, Laird N M and Rubin D B 1977 *J. Roy. Stat. Soc., Ser. B* **39** 1–38

[15] Shepp L A and Vardi Y 1982 *IEEE transactions on medical imaging* **1** 113–122

Calculation of direct and diffuse solar irradiance components using a Slob Algorithm model in Gauteng conditions.

L.C. Nethwadzi and H. Winkler

University of Johannesburg, Physics Department, PO Box 524, 2006 Auckland Park, Johannesburg, South Africa

E-mail: thwadzi@gmail.com

Abstract. Most solar radiation measuring devices only determine the total irradiance on a horizontal surface, but for various applications diffuse and direct components are also needed. Because of this, several models have been developed to establish the correlations between the diffuse fraction and various predictors. This paper analyses the measured global irridiance at a Gauteng location as a function of the relative solar position. An equation is presented to estimate both components from the measured daily global solar irradiance only. In this equation, the diffuse component is related to the product of the cosine of the zenith angle and the Linke turbidity factor. The analysis attempts to reproduce the measured irradiance through basic modelling of the spectral opacity of the atmosphere in terms of the Linke Turbidity. This includes estimating direct beam attenuation and the diffuse component, which are then combined with the module spectral response in an attempt to match the measured and modelled energy yield. The performance of the model has been graphically and statistically analyzed by two established methods, namely; Mean Bias Error (MBE) and Root Mean Square Error (RMSE).

1. Introduction

Solar irradiance is abundant in South Africa. Therefore, reliable models predicting solar irradiance and the corresponding solar energy generated is of great importance. Modules utilize total irradiance, which consists of two components, direct and diffuse. Models are required for estimating both these components. In the past, many correlations between these quantities have been developed and the majority of these project the diffuse fraction using the clearness index ($K_T = G_h/I_0$), which is expressed by the ratio of global to extraterrestrial solar irradiance [1, 2, 3]. Some models also consider the effect of variables like solar zenith angle (θ_Z) (the angle the Sun makes with the zenith), air mass, Rayleigh optical thickness and the Linke turbidity factor. This study uses the Slob algorithm, which estimates the global irradiance component on a horizontal surface under cloud free conditions from the solar zenith angle in conjunction with the Linke turbidity factor [4]. In this study, new coefficients for this model have been found and then used to estimate solar irradiance over Gauteng.

2. Theory

When solar radiation traverse the Earth's atmosphere, some of its incident energy get absorbed and scattered, both this affects the solar spectrum reaching the ground level [5]. The radiation that reaches the surface consists of a direct normal component (B_N) from the Sun, i.e. the solar beam, and a diffuse component (D_h) from all other directions. The sum of these as measured by a horizontal surface is defined as the global horizontal irradiance.

The Linke turbidity factor (T_{LK}) quantifies the concentration of particles that reduce the incoming irradiance in cloud-free conditions. It is defined as the number of clear dry atmospheres necessary to produce the observed attenuation, and was introduced in 1922 [6] to quantify atmospheric aerosol [7]. It is a common parameter used to model the atmospheric absorption and scattering of solar irradiance under cloud free conditions. It may be expressed as follows:

$$T_{LK} = -\left(\frac{1}{\delta_R \times m_a}\right) \ln\left(\frac{B_N}{I_0}\right) \tag{1}$$

where δ_R is the Rayleigh optical thickness of a water and aerosol free atmosphere (clear and dry atmosphere), m_a is the relative optical airmass, B_N is the direct normal irradiance ($B_N = B_h/\cos\theta_Z$), and I_0 is the solar constant corrected for the Earth-Sun distance. The latter is given by $I_0 = I_{SC} \times [1 + 0.033 \times \cos\left(\frac{360\times n}{365}\right)]$, where $I_{SC} \approx 1367$ W/m^2 and n is the day number of the year, starting from 1 January [8]. Relative optical airmass is defined as the pathlength in terms of atmospheres along which solar irradiance travels through the Earth's atmosphere. It is given by $m_a = \sec\theta_Z$ if the Earth curvature and refraction are ignored, but it becomes more complex if those factors are considered [9]. Rayleigh optical thickness (δ_R) is a parameter used in solar energy research to determine the fraction of solar light able to traverse the atmosphere. In this study, the Linke turbidity factor will be determined using the classical method based on the Kasten and Young formulas [10] for the optical airmass and the improved Kasten formula for Rayleigh optical thickness as shown below:

$$\delta_{R1} = \frac{1}{[9.4 + 0.9 \times m_a]} \tag{2}$$

and

$$\delta_{R2} = \frac{1}{[a_0 + a_1 \times m_a - a_2 \times {m_a}^2 + a_3 \times {m_a}^3 - a_4 \times {m_a}^4]} \tag{3}$$

[9, 11], and where constants a_0, a_1, a_2, a_3 and a_4 are 6.6296, 1.7513, 0.1202, 0.0065 and 0.00013, respectively.

3. Method

The study proposes to analyze global irradiance in a typical Gauteng environment to determine the local Linke turbidity factor (T_{LK}) and then use this to estimate the solar irradiance. The global irradiance data were provided for several days collected by Sinetech in Randburg (latitude 26°5′11″S and longitude 27°58′28″E). The site is an urban and light industrial area which might experience moderate smog from traffic activities particularly during the morning and afternoon rush hour. These measurements were collected at intervals of 15 minutes on an ongoing basis from sunrise to sunset.

To improve the calculations of the Linke turbidibity values, irradiance data was linear interpolated for every minute. Global solar data for the dates 18 and 27 September, and 22 November 2015 are used in this work.

We have considered a NOAA [12] solar model to determine the relative position of the Sun at any particular time of the day using the latitude and longitude coordinates of the chosen site in Gauteng Province. To calculate the amount of solar energy delivered on the horizontal surface,

the solar zenith angle was calculated using $\theta_Z = \cos^{-1}[\cos(\phi) \times \cos(\sigma) \times \cos(\omega) + \sin(\phi) \times \sin(\sigma)]$. Here ϕ is the geographical latitude, σ is the solar declination angle and ω is the solar hour angle from the meridian in degrees expressed by: $\omega = (Solar\ Time\ (h) - 12) \times 15^\circ$, being negative in the morning and positive in the afternoon. The solar declination angle is defined as the angle between the equator and the direction of the Sun's rays, and is sufficiently accurately estimated by $\sigma = 23.45^\circ \times \sin[360(284 + n)/365]$.

In this adopted model, an extraterrestrial solar irradiance (I_0) corrected for the Earth-Sun distance and global solar irradiance (G_h) are used as an input to calculate the T_{LK} values for a site. The T_{LK} values were calculated using equation (1) with the use of standard (δ_{R1}) and adjusted (δ_{R2}) models of Rayleigh optical thickness defined by equations (2) and (3), respectively. While the estimation of the beam irradiance component is more precise, the key difference from various models presented in the writings distinguish themselves in the handling of the diffuse component [13].

To calculate the diffuse irradiance, the first step procedure consists of estimating the minute clearness index (K_T), followed by defining the diffuse fraction as predicted by one variable (K_T) not to be more than 1/3 [1] of the global irradiance. This is important because the turbidity specifically quantifies cloudless atmospheric environments. In view of the limited information available from our data, the following adopted linear equation proved to be reasonably good for prediction of the minute average daily diffuse solar irradiance over the chosen Gauteng location:

$$\frac{D_h}{G_h} = 0.331 - 0.2333K_T \tag{4}$$

[14, 15]. More importantly, the present model proposed by equation (4) does not require the clearness index to be classified into sub-intervals, which then allowed for greater flexibility when altering the relationship to accommodate for location differences, since it was tested in different locations with different altitudes. The calculations for the clearness index assumes that the terrain surrounding the site is a perfect horizontal surface meaning the incoming solar irradiance is unhindered by topographical structures. In the South African interior winter months usually exhibit clearer skies for most locations [16].

Through the ratio of D_h/G_h, it is possible to compute diffuse (D_h) and direct irradiance components on a minute-by-minute basis using $G_h = B_h + D_h$. The direct normal irradiance (B_N) component is evaluated from the difference between the G_h and D_h using the expression $B_N = B_h/\cos\theta_Z = (G_h - D_h)/\cos\theta_Z$. T_{LK} values can be calculated through equation (1) in every locality where G_h is measured [17]. Once the T_{LK} values of the atmosphere were known, they were then used to calculate the global solar irradiance components. Equation (1) was rearranged to become $B_h = I_0\ \cos\theta_Z\ \exp\ (-T_{LK}\ \delta_R\ m_a)$ so that the direct irradiance model associated with the T_{LK} could be approximated.

The diffuse component was estimated by the Slob Algorithm model expressed by $D_{h1} = X + Y\cos\theta_Z T_{LK}$ [4], which describes the diffuse irradiance component for cloudless conditions, where X and Y are coefficients found from linear regression fits for diffuse solar irradiance components applied to the above mentioned datasets obtained using equation (4). This was valid for the Linke turbidity factors less than 12.5. The formula was derived by making an assumption that the diffuse component is directly proportional to the product of $\cos\theta_Z T_{LK}$ ($=z$). However, the Slob Algorithm model results were improved with the use of quadratic function of the form $D_{h2} = az^2 + bz + c$. The figures below illustrate linear and quadratic fittings of the data:

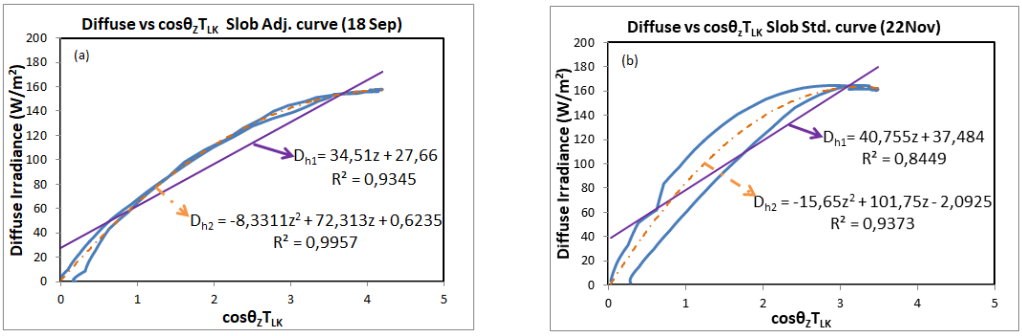

Figure 1. Represents the diffuse components D_{h1} (linear fit) and D_{h2} (quadratic fit) for (a) 18 September 2015 data and (b) 22 November 2015 data.

After the calculations of the direct and diffuse components, they were then added to give the global solar irradiance which was then compared with the measured global solar data. The performance of the model have been graphically and statistically analyzed by two established methods, namely; Mean Bias Error (MBE) and Root Mean Square Error (RMSE) [18]. The time varying errors were all analyzed for each minute of each hour, and then averaged within the same hour, over all days. The MBE describes the overall bias of a model and its value should be small. A percentage error between ±10% is considered acceptable [19]. In general, if this value is negative, the model underestimates compared to the observed values and percentage error. The RMSE is a good indicator of how accurate the model estimates the measured values [20]. The model performs best for the smallest possible values of RMSE. The latter are defined by the following expressions; $MBE = \frac{\sum_{i=1}^{N}(G_{(model)i} - G_{(meas)i})}{\sum_{i=1}^{N} G_{(meas)i}}$ and $RMSE = \frac{\sqrt{(1/N)\sum_{i=1}^{N}(G_{(model)i} - G_{(meas)i})^2}}{(1/N)\sum_{i=1}^{N} G_{(meas)i}}$, where $G_{(model)i}$ is the estimated value from a model, $G_{(meas)i}$ is the corresponding measured value and N is the number of values used in the series [18]. A greater positive RMSE means a huge deviation in the estimated value from the measured value and zero represents the ideal case.

4. Results and Discussion

The results of the measured and modelled global solar irradiance using Slob Algorithm (standard) model equation are shown in figures below

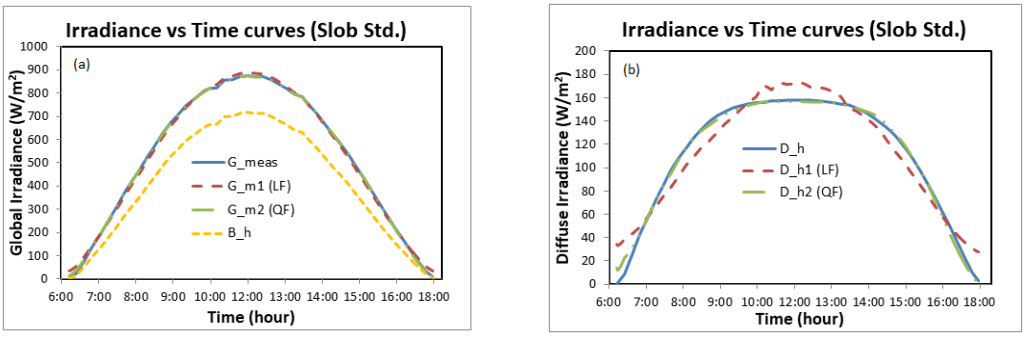

Figure 2. Represents results of Slob Algorithm standard model-measurements intercomparison. (a) global (G_{meas} (measured), G_{m1}(LF) (linear fit) and G_{m2}(QF) (Quadratic fit)) and direct (B_h), and (b) diffuse (D_h (model), D_{h1}(LF) (linear fit) and D_{h2}(QF) (Quadratic fit) irradiances with 18 September 2015 data.

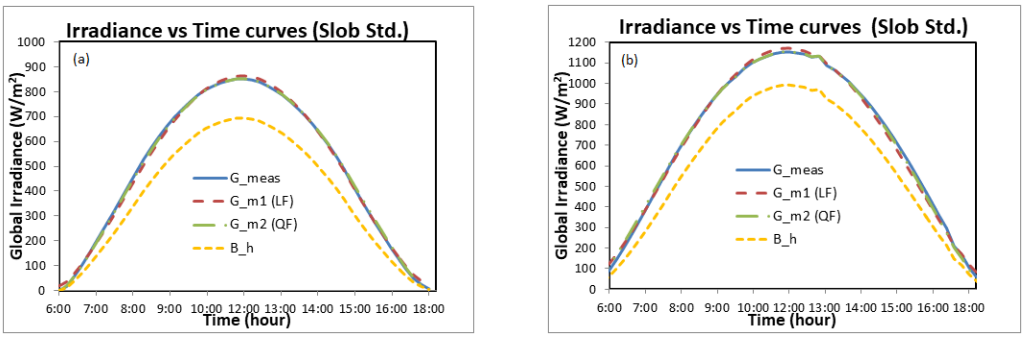

Figure 3. Represents results of Slob Algorithm standard model-measurements intercomparison of global (G_{meas} (measured), G_{m1}(LF) (linear fit) and G_{m2}(QF) (Quadratic fit)) and direct (B_h) irradiances with (a) 27 September and (b) 22 November 2015 data.

Figures 2 and 3 indicate that the total irradiance and modeled diffuse component are in agreement with the measurements performed at Randburg for clear sky conditions. While the measured and modeled daily global irradiance values have been equated through $G_h = B_h + D_h$, the corresponding values of global irradiance are not necessarily the same for each hour as illustrated in the figures. The quadratic fitting has improved the diffuse component as shown by D_{h2} and G_{m2} in figures 2 and 3. Hence, the quadratic relationship has caused the modeled global (G_{m2}) to be superimposed with the measured data. It is also found that diffuse fraction of the total irradiance is strongly correlated with the clearness index. This is consistent with the expectation that when the atmosphere is clearer, a smaller fraction of the radiation is scattered [21]. Using the standard model of Rayleigh optical thickness equation (2) resulted in higher values of T_{LK} compared to the values obtained using the adjusted model equation (3).

Table 1. The averaged performance evaluation by certain error parameters of the proposed Slob Algorithm standard model for each day considered.

n	G_{meas}(W/m^2)	G_{model}(W/m^2)	MBE(%)	RMSE(%)
261	531.1	532.6	0.007	2.35
270	500.1	500.1	-0.001	2.17
326	703.5	703.5	-0.0004	2.72

Table 2 shows the statistical performance of the model and the percentage values of MBE and RMSE are very low indicating a reasonably agreement between the modeled and measured data. The negative values of MBE indicate that the proposed model slightly underestimates the global irradiance. It was noted that there appear to be systematic discrepancies between the measured and computed values around sunrise and sunset. This may have resulted due to the model's intrinsic limitations, or of decreased measurement accuracy, which is expected when global solar irradiance is low. This analysis was done for the chosen days of the year to investigate seasonal variations in model error.

5. Conclusions

The diffuse irradiance versus the product of $\cos\theta_Z T_{LK}$ curves indicate that the quadratic relationship is the best fit for both diffuse and global solar irradiance results. The results of the model used here for the clear sky conditions over Randburg in Gauteng Province were

found to be in par with the measurements. The proposed model can be considered as consistent and efficient tool to estimate solar irradiance spatially and temporally. Future studies will try to test some irradiance models for the clear sky conditions and some models for diffuse irradiance in order to calculate the solar irradiance components. T_{LK} calculation and verification, and δ_R parameterization are key issue for further improvements in modelling performance.

Acknowledgment
The authors gratefully thank Sinetech Solar Company for making available their diurnal measured global solar irradiance data.

References

[1] Gama A, et al, 2010, Determination of atmospheric turbidity using solar radiation measurements for two Algerian sites, 2nd International conference on Nuclear and Renewable Energy Resources, 4-7 July 2010, Ankara Turkey, *ResearchGate*, 1-6.
[2] Liu B Y H, et al, 1960, The interrelationship and characteristics distribution of direct, diffuse, and total solar radiation, *Solar Energy*, **4**, 1-19.
[3] Gueymard C A, 2001, Parameterized Transmittance model for Direct Beam and Circumsolar spectral irradiance, *Solar Energy*, **71**, 325-346.
[4] Hinssen Y B L, 2006, Comparison of different methods for the determination of sunshine duration, *Scientific Report*, **WR-2006**, 1-76.
[5] Gard H P, et al, 1993, Fundamentals and characteristics of solar radiation, *Renewable Energy*, **3**, 305-319.
[6] Linke F, 1922, Transmissions-Koeffizient und Trübungsfaktor, *Beitr. Phys. fr. Atmos.*, **10**, 91-103.
[7] Bason F, 2004, Diffuse solar irradiance and atmospheric turbidity, In Eurosun 2004 conference proceedings, Freiburg, Germany, June 2004, 1-7.
[8] Iqbal M, 1983, An introduction to solar radiation, New York, USA, Academic Press, 2nd Edition.
[9] Winkler H, 2012, Appropriate air mass and solar radiation attenuation parameterization for Southern Africa, Proceedings of the 2012 South African Instute of Physics annual conference, 9-13 July 2012, UP, (events.saip.org.za), 1-6.
[10] Kasten F, et al, 1989, Revised optical air mass tables and approximation formula, *Applied Optics*, **28**, 4735-4738.
[11] Kasten F, 1996, The Linke turbidity factor based on improved values of the Integral Rayleigh Optical thickness, *Solar Energy*, **56**, 239-244.
[12] NOAA, 2011, National Oceanic and Atmospheric Administration solar calculations spreadsheet, NOAA, *Silver Spring*, MD, USA, (ftp://ftp.srrb.noaa.gov/pub/data/surfrad/).
[13] Perez R, et al, 1987, A new simplified version of the Perez diffuse irradiance model for tilted surfaces, *Solar Energy*, **39**, 221-231.
[14] Tiwari G, et al, 2015, Study and analysis of solar radiation models, *Internal Journal of Current Engineering and Technology*, **5**, 3544-3559.
[15] Aras H, et al, 2006, Estimating the horizontal diffuse solar radiation over the Central Anatolia Region of Turkey, *Energy Conversion and Management*, **47**, 2240-2249.
[16] Boland J, et al, 2001, Modelling the diffuse fraction of global solar radiation on a horizontal surface, *Environmetrics*, **12**, 103-116.
[17] Cucumo M, et al, 2000, A calculation method for the estimation of the Linke turbidity factor, *Renewable Energy*, **19**, 249-258.
[18] Badescu V, 1997, Verification of some very simple clear and cloudy sky models to evaluate global solar irradiance, *Solar Energy*, **61**, 251-264.
[19] Khalil S A, 2013, A comparative study of total, direct and diffuse solar by using different models on horizontal and inclined surfaces for Cairo, Egypt, *Renewable and Sustainable Energy Reviews*, **27**, 853-863.
[20] Hoff T E, et al, 2013, Reporting of irradiance modeling relative prediction errors, *Progress in Photovoltaics: Research and Applications*, **21**, 1514-1519.
[21] Erbs D G, et al, 1992, Estimation of the diffuse radiation fraction for hourly, daily, and monthly-average global radiation, *Solar Energy*, **28**, 293-302.

An investigation of synchronisation techniques for a handheld QKD device

S Pillay[1], M Mariola[1], F Petruccione[1,2]

[1] Quantum Research Group, School of Chemistry and Physics, University of KwaZulu-Natal, Private Bag X54001, Durban 4000, South Africa
[2]National Institute for Theoretical Physics (NITheP), KwaZulu-Natal, South Africa
Email: 206507614@stu.ukzn.ac.za

Abstract. The importance of cryptography has become more prevalent in contemporary communication and the commercial use of Quantum Key Distribution (QKD) is now a realistic option for fibre networks. Long-range, free-space QKD and miniaturised, personal QKD devices are emerging fields of research aiming towards future commercial use. Previously, a handheld QKD device was developed using the Coherent One-Way (COW) protocol to exchange the encryption key between the transmitter and receiver. An optical synchronisation system was developed for the handheld device establishing real time synchronisation between the transmitter and receiver. This paper will investigate the viability of other synchronisation techniques appropriate for a handheld QKD device. The first technique will use asynchronous communication to establish communication between the transmitter and receiver. The second technique will use a radio channel to establish synchronisation, based on Binary Phase-Shift Keying. The radio channel also serves as the public channel for the QKD system.

1. Introduction

Quantum Key Distribution (QKD) provides an unconditionally secure method to share an encryption key between two authenticated parties [1]. QKD does not rely on the complexity of mathematical algorithms in order to protect sensitive data. Instead, quantum 2-level systems are used to distribute binary data from the transmitter to the receiver [2]. The use of QKD facilitates the long-term security of sensitive data, since QKD is not vulnerable to increasing computing power in decryption technology. Quantum particles necessarily follow the laws of quantum physics which govern their behavior. The No Cloning theorem [3] and Heisenberg's Uncertainty principle [4] ensure that any eavesdropping attempts on the transmission are detected. The most commonly used quantum 2-level system is a single photon of light, encoded using its polarisation state or phase. This method of encoding is used in most prepare-and-measure schemes, such as the BB84 protocol [5] and the SARG04 protocol [6].

Commercial applications of QKD have been well developed for metropolitan fibre networks [7]. Free-space QKD is a technology that is still undergoing research but is rapidly gaining commercial relevance [8]. Another emerging QKD technology are handheld, portable QKD devices which are designed to be used by individual users over a short range [9]. Handheld devices can be implemented with either a free-space or a fibre link and allow a user to share and store a set of secret keys with a central node for personal use at a later time. An application of this technology is the sharing of a secret One-Time Pin between a bank and a customer. The keys can also be used as authentication tools for workplace security or other applications. The handheld device must be integrated into a network using shared nodes to connect users with a central mainframe. The user can top up on One-Time Pins at

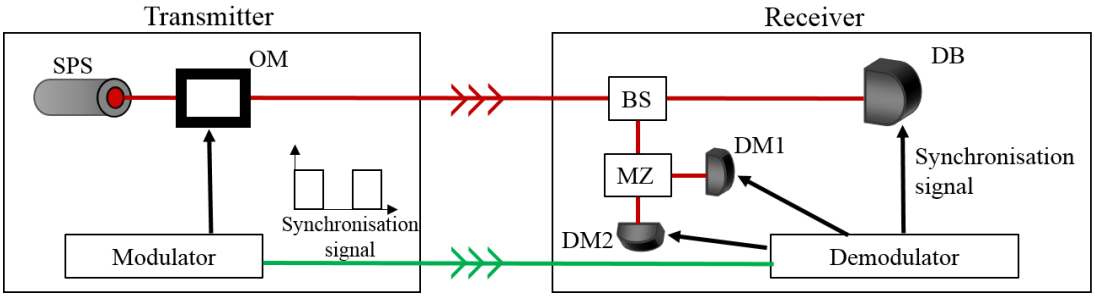

Figure 1. A schematic of the COW protocol detailing the transmitter and receiver modules. The transmitter includes a faint, coherent laser source, SPS, coupled with an external optical modulator, OM, used to create the bit encoding. The transmitter also includes a synchronisation modulator and additional electronics and on-board memory required for post-processing. The receiver module requires a beam splitter, BS, to create two separate optical paths from the incoming bit stream. The first path serves as the detection line and requires a single photon detector, DB, which measures incoming photons to create the raw key. The second path of the beam splitter serves as the monitoring line. This path consists of a Mach-Zehnder interferometer, MZ, and single photon detectors at each output of the interferometer, DM1 and DM2. The purpose of the interferometer is to confirm the coherence between two consecutive decoy pulses. A break in coherence infers the presence of an eavesdropper. The demodulator receives the synchronisation signal and commands the gates of the single photon detectors DB, DM1 and DM2.

a node, such as an ATM machine. The ATM, in turn, distributes this key with a central mainframe using a long-range fibre or free-space QKD channel. The user can then use the stored pins for secure communication with the central mainframe. This paper will discuss the application of the COW protocol in handheld devices in Section 2. Section 3 will detail the existing optical synchronisation system that was built for the device. Section 4 and 5 will discuss other potential methods of synchronisation, including asynchronous transmission and radio synchronisation.

2. Coherent One-Way Protocol

Current implementations of handheld devices use the BB84 protocol with polarisation encoding but a four-state protocol such as BB84 requires more components and post-processing algorithms after the key distribution. The Coherent One-Way (COW) protocol [10] provides a simpler alternative for smaller QKD devices. The COW protocol is suitable for use in fibre networks since coherence between laser pulses will deteriorate in a turbulent, free-space channel. Since a handheld device transmits over a short range, free-space channel, the pulses will not be affected by turbulence, allowing for a COW protocol implementation. The bit encoding implemented in the COW protocol is distributed over two consecutive pulses. One pulse contains a photon and the other is empty. The order of these two pulses creates the 2-level system used for the encoding as follows,

$$|0_k\rangle = \left|\sqrt{\mu}\right\rangle_{2k-1}|0\rangle_{2k} \quad \text{and} \quad |1_k\rangle = |0\rangle_{2k-1}\left|\sqrt{\mu}\right\rangle_{2k}, \tag{1,2}$$

where μ is the mean photon number and k is the time bin index. A portion of the pulses are also encoded as decoy pulses. In this case, both the pulses contain a photon. Figure 1 shows a schematic of the COW protocol and discusses its implementation.

3. Optical synchronisation system

As with all QKD systems, the transmitter and receiver must be initially synchronized before the key distribution begins. The synchronisation of the devices is necessary to ensure that the single photon detectors open at precisely the time of arrival of the photon pulses. If the detectors make a measurement

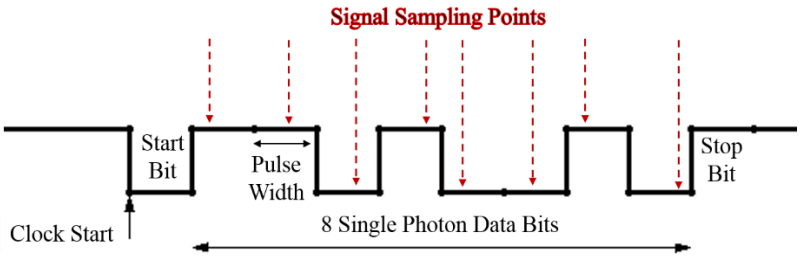

Figure 2. Asynchronous transmission begins with a Start bit which serves as the synchronisation indicator. The pulse width of each bit is agreed upon before the transmission begins and the receiver is able to measure the 8 data bits following the Start bit. The Stop bit indicates that the data has stopped, pending the transmission of another Start bit.

at the wrong time, the system will register a high loss rate. The COW protocol particularly requires precise synchronisation since the transmitter and receiver must compare their bits at specific time bins.

The previous synchronisation system designed for the handheld COW protocol device used an additional light source to synchronise the transmitter and the detectors of the receiver [11]. A 532 nm LED was installed in the transmitter as the synchronisation source. The LED was aligned to pass through the pulse modulator without being influenced by the bit encoding. The LED signal was measured by the receiver using a photodiode. The signal from the photodiode was squared using a Smith trigger and transmitted to a microcontroller. The microcontroller triggered the single photon detectors, commanding the detector gates to open only when a pulse was incident on the detector. It is important to note that, due to the varying bit encoding or the losses in the channel, some of the pulses did not contain a photon, but the detector must still measure these pulses in order to register an empty pulse.

4. Asynchronous Transmission

Asynchronous transmission intersperses the data signal with a synchronisation sequence using the same light source [12]. The advantage of aligning just one light source makes this method simpler to implement than a synchronous method such as the optical synchronisation mentioned above. The bit rate of the signal is established before the transmission begins and it is, therefore, only necessary for the transmitter to indicate when the receiver should start to take measurements. The bit sequence for asynchronous transmission must begin with an indicative “Start” bit followed by 8 bits of data. A “Stop” bit indicates the end of the data and the beginning of another synchronisation iteration, as seen in Figure 2. The key generation rate of the system will decrease when using asynchronous transmission since the start and stop indicators do not contribute to the key. However, the COW protocol produces a higher bit rate compared to other QKD protocols, therefore compensating for the large overhead.

In order to implement asynchronous transmission for a handheld QKD device, the pseudo-single photon source in the transmitter must be controlled by a variable attenuator so that the mean photon number of each pulse can be adjusted. It is necessary for each start and stop pulse to be measured by the single photon detectors. Since single photons can be lost during transmission, the mean photon number of the start and stop pulses should be increased to increase the probability of detection. Should the start and stop pulses not be measured, the receiver will not open the detector gates to receive a new set of bits, thus resulting in high losses in the channel. The mean photon number can be decreased to one during the transmission of the data bits.

5. Radio Synchronisation using BPSK

A radio signal can serve as a simple method to synchronise QKD modules. A similar system using a radio signal and BPSK encoding was proposed in [13]. A radio transmitter and receiver are easier to align in comparison to an optical signal. The radio signal can also be used for initial authentication between the modules, as well as the public channel used for post processing of the quantum signal, making a radio signal versatile and robust. Generally, free-space QKD modules use a GPS signal for

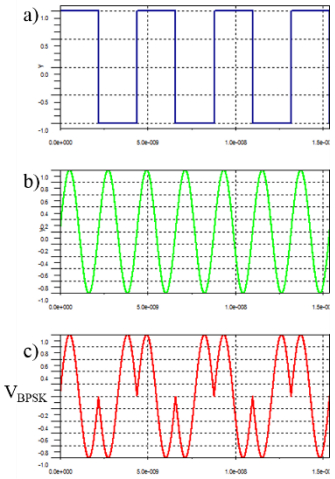

Figure 3. Diagram a) shows the modulating signal which represents the information to be transmitted over the public channel. The carrier signal, shown in b), is a sinusoidal radio signal which will be used for synchronisation. The modulated signal V_{BPSK}, shown in c), carries general binary data through the public channel.

tracking and synchronisation [8]. A radio signal is a reliable alternative which will work in the absence of a GPS signal. Since QKD is an unconditionally secure means to share encryption keys, it can be useful for both the banking and defense sectors. A reliable synchronisation system is therefore necessary to facilitate the key exchange. A radio signal can be encoded with a binary string using Binary Phase-Shift Keying (BPSK) [14]. Phase-Shift Keying refers to the phase modulation of a sine or cosine wave, where BPSK specifically modulates the wave by 180°, creating a binary code, as seen in Figure 3. BPSK is more resistant to errors compared to other types of Phase-Shift Keying since the binary values are 180° apart. An erroneous phase-shift will have to be greater than 90° to change the binary bit value.

5.1. The Costas Loop

The coherent demodulation and the carrier recovery can be performed by using a Costas loop [15]. The Costas loop is based on a phase-locked loop and can be used to recover the carrier frequency of a phase-modulated signal, such as BPSK. A circuit diagram of the Costas loop is shown in Figure 4. In the Costas loop, the Voltage Controlled Oscillator (VCO) is a free oscillator centered on the error frequency ω_0, that can change the frequency in function of an applied voltage, named V_{CON}. The output signal can be synthesized by the equation

$$V_{\mathrm{VCO}}(t) = cos\left[\omega_0 t + \int_0^t kv\, V_{\mathrm{CON}}(\tau)d\tau\right], \tag{4}$$

where *kv* is the sensitivity expressed in *rad/V*. A BPSK signal can be represented according to the following function:

$$V_{\mathrm{BPSK}}(t) = AS_{\mathrm{p}}(t)\cos(\omega_0 t)\,, \tag{5}$$

where ω_0 is the angular frequency of the carrier, $S_p(t)$ contains the bit to transmit and A is the amplitude of the received carrier. The angular frequency ω_0 is the frequency of the local oscillator of the VCO. The timing frequency for the QKD device is extracted from the carrier frequency.

Suppose that the signal from the VCO is

$$V_{\mathrm{VCO}}(t) = \cos(\omega_0 t + \varphi_e)\,, \tag{6}$$

where φ_e represents the difference in phase between V_{BPSK} and V_{VCO}. The VCO signal in Equation (6) is sent to analog multiplier 1 and a -90° phase shifter. The signal at the output of the analog multiplier is

$$V_1(t) = V_{\mathrm{BPSK}} \cdot V_{\mathrm{VCO}} = \frac{AS_p}{2}[cos\varphi_e + \cos(2\omega_0 t + \varphi_e]\,.$$

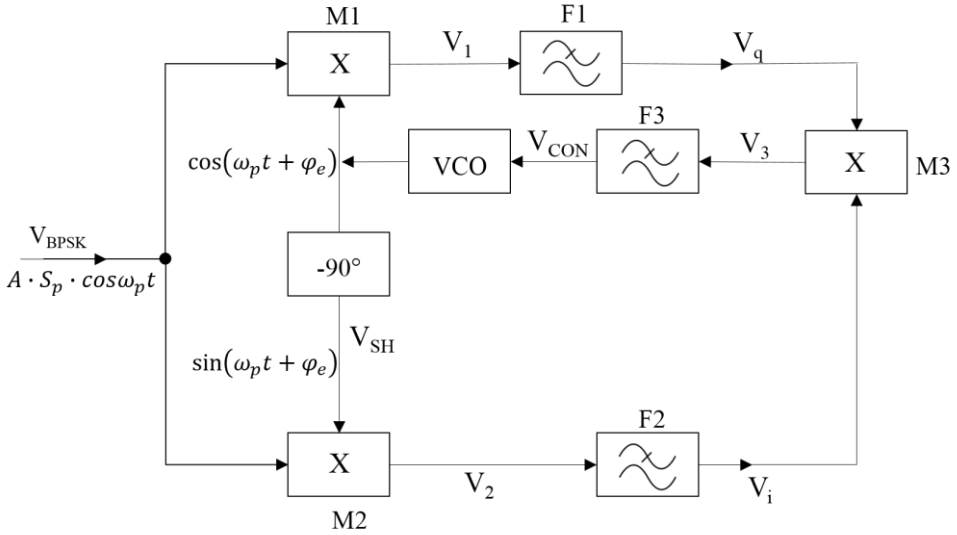

Figure 4. A diagram of the Costas loop, used to demodulate the BPSK signal. VCO is a voltage controlled oscillator which oscillates with the same frequency as the received V_{BPSK} signal. Any phase difference between the signals must be resolved. V_{BPSK} is multiplied by VCO at multiplier M1. VCO undergoes a -90° phase shift and is multiplied to V_{BPSK} at M2. Both signals are passed through respective low pass filters F1 and F2 and are multiplied at M3. The resultant signal is passed through low pass filter F3 in order to remove any noise and is then applied to VCO to correct the phase difference. The signal from VCO can then be used to synchronise the receiver module.

It is possible to attenuate the components cos ($\omega_p t + \varphi_e$) of the signal $V_1(t)$ through the low pass filter F1. The signal at the output of F1 is:

$$V_q = \frac{AS_p}{2} cos\varphi_e \ . \tag{7}$$

V_q is not dependent on the frequency ω_0. When V_{VCO}, crosses the phase shifter, the signal $V_{SH}(t)$ is

$$V_{SH}(t) = \cos(\omega_0 t + \varphi_e - 90°) = \sin(\omega_0 t + \varphi_e) \ .$$

V_{SH} multiplied by V_{BPSK} is

$$V_2(t) = \frac{AS_p}{2}[\cos(90° - \varphi_e) + \cos(2\omega_0 t + \varphi_e + 90°)] \ .$$

Since the signal has double frequency components, the signal can be filtered to obtain a signal $V_i(t)$,

$$V_i(t) = \frac{AS_p}{2}\cos(90° - \varphi_e) = \frac{AS_p}{2}\sin(\varphi_e) \ . \tag{8}$$

The signals V_q and V_i are multiplied to obtain the voltage control of the VCO, V_{CON},

$$V_{CON} = V_q \cdot V_i = \frac{A^2 {S_p}^2}{32}\sin(2\varphi_e) \ . \tag{9}$$

From Equation (4), it is possible to observe that V_{CON} changes the frequency V_{VCO} proportionally to the phase φ_e. If φ_e increases, V_{CON} and V_{VCO} increase in order to follow the signal V_{BPSK} received. When φ_e=0, V_{VCO} is 0 and the signal V_{VCO} is in phase with V_{BPSK}. The synchronisation signal for the handheld QKD device is now obtained from the V_{VCO} signal.

6. Conclusion

Handheld QKD devices are an emerging field of research with future commercial applications. An optical synchronisation system was previously developed for a handheld device implemented with the COW protocol. An investigation of other synchronisation methods was done. Asynchronous transmission using the single photon source provided the advantage of aligning only one laser source to use for both synchronisation and bit encoding. A radio channel between the transmitter and receiver can also provide a reliable synchronisation link, as well as a public channel used for the QKD authentication and post processing. The radio signal can be encoded using BPSK and demodulated by the receiver using a Costas loop.

Acknowledgements

This work is based on research supported by the South African Research Chair Initiative of the Department of Science and Technology and National Research Foundation.

References

[1] Lo H K and Chau H F, 1999 Unconditional security of quantum key distribution over arbitrarily long distances *Science* **283**(5410) 2050-2056.
[2] Gisin N, Ribordy G, Tittel W and Zbinden H 2002 Quantum Cryptography *Review of Modern Physics* **74** 145.
[3] Wooters W K and Zurek W H 1982 A single quantum cannot be cloned *Nature* **299**(5886) p802.
[4] Zettili N 2009 *Quantum mechanics: Concepts and applications* (John Wiley & Sons Inc.) p.28.
[5] Bennett C and Brassard G 1984 Quantum Cryptography: Public key distribution and coin tossing *Proceedings of IEEE International Conference on Computers, Systems and Signal Processing* pp 175-179.
[6] Scarani V, Acin A, Ribordy G and Gisin N 2004 Quantum cryptography protocols robust against photon number splitting attacks for weak laser pulse implementations *Physical Review Letters* **92**(5) 57901.
[7] Gobby C, Yuan Z L and Shields A J 2004 Quantum key distribution over 122 km of standard telecom fiber *Applied Physics Letters* **84** pp 3762-3764.
[8] Schmitt-Manderbach T, Weier H, Furst M, Ursin R, Tiefenbacher F, Scheidl T, Perdigues J, Sodnik Z, Kurtsiefer C, Rarity J G, Zeilinger A and Weinfurter H 2007 Experimental Demonstration of Free-Space Decoy-State Quantum Key Distribution over 144 km *Physical Review Letters* **98**(1) 010504.
[9] Duligall J L, Godfrey M S, Harrison K A, Munro W J and Rarity J G 2006 Low cost and compact quantum key distribution *New Journal of Physics* **8**(10) 249.
[10] Gisin N, Ribordy G, Zbinden H, Stucki D, Brunner N and Scarani V 2004 Towards practical and fast quantum cryptography *arXiv preprint quant-ph/0411022.*
[11] Pillay S, Mariola M, Mirza A and Petruccione F 2015 Handheld QKD device using the COW protocol, in The Proceedings of the 60th Annual Conference of the South African Institute of Physics (SAIP2015)(ADDENDUM), edited by Makaiko Chithambo (RU) and André Venter (NMMU) pp 29 - 35. ISBN: 978-0-620-70714-5.
[12] [online] Asynchronous and Synchronous Communication http://www.pccompci.com/Asynchronous%20and%20Synchronous%20Communication.html.
[13] Mariola M, Mirza A and Petruccione F 2011 Quantum cryptography for satellite communication, in Proceedings of SAIP2011, the 56th Annual Conference of the South African Institute of Physics, edited by I. Basson and A.E. Botha (University of South Africa, Pretoria) pp 403 - 408. ISBN: 978-1-86888-688-3.
[14] Bernardini A 2008 *Lezioni del corso di sistemi di comunicazione satellitari* Vol 1 ed Edizioni Ingegneria 2000 (Rome) pp 251-256.
[15] Kostopoulos A 1995 *Corso di telecomunicazioni. Dai sistemi di comunicazione ai servizi telematici* ed 2 (Petrini) pp 466-467.

System control applications of low-power radio frequency devices

R M van Rensburg[1], **B Mellado, C J Sandrock**

School of Physics, University of the Witwatersrand, Johannesburg 2050, South Africa

E-mail: roger.vanrensburg@wits.ac.za

Abstract. This paper realizes a wireless network development for application deployment to reduce theft of portable computer devices utilized in educational institutions. The study aims to develop a low-cost, low-power and reliable wireless network that can eradicate the accessibility of a device human interface. A portable computer device which is operated in a field perimeter where device communication in the network is restricted, indicating a possible theft scenario, will initiate a shutdown of its operating system that renders the device unusable. Design outcomes thus far indicate that a robust wireless network, using low-power embedded hardware, is feasible for anti-theft applications. Preliminary results indicate the reliable performance of data communications between interconnecting nodes in a harsh indoor building environment using the Thread networking protocol.

1. Introduction

In 2015 the South African government spent billions of rands in modernizing learning institutions with the goal of fully digitizing schools by the year 2020. It was reported that a substantial amount of tablets were lost due to theft that consequently jeopardized the project because of the significant financial loss incurred by the government [1]. This led to more than 88000 tablets being recalled and fitted with an anti-theft technology in order to protect the investment. The upgrade of the devices enabled the government to involve investigative authorities in the tracking of stolen tablets [2]. The tracking systems, however, appeared only operational with the device powered-on to communicate with global positioning satellites in outdoor environments.

With deficits currently present in the protection of such devices, there is a need to improve the security of these devices by taking advantage of the wireless technologies today. This paper presents a preliminary performance analysis of a low-power wireless network for application deployment to protect a Portable Computer Device (PCD) such as a tablet against theft in indoor building environments. A PCD operated in a perimeter outside the wireless network may initiate a shutdown of its operating system by using a polling algorithm to communicate to the wireless network located at a educational institution.

2. Methodology

An embedded system with a multiprotocol radio and advance processor capabilities was fully utilized during the inception phase of the development of the network. An ad-hoc wireless

[1] Present address: School of Physics, University of the Witwatersrand, Johannesburg 2050, South Africa.

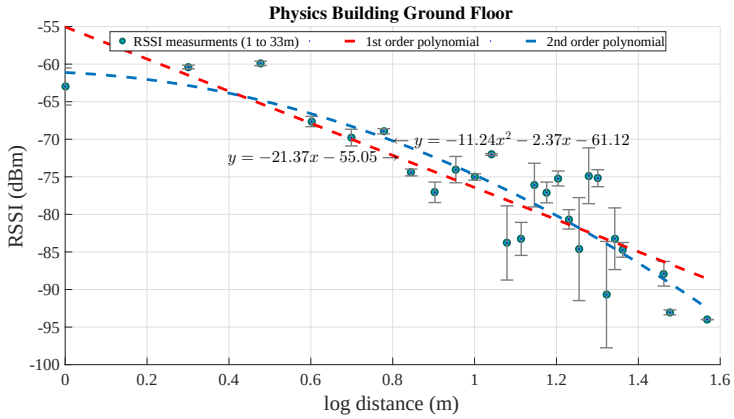

Figure 1: $RSSI$ versus $log_{10}(d)$ at Tx = 0 dBm.

network consisting of ten nodes was developed in an indoor building environment. Field measurements of each node's quality of service from a remote indoor location were recorded.

3. Experimental Study

The Physics building at the University of the Witwatersrand was used as an indoor testing environment where radios were distributed at specific areas located on the ground floor. The building consists of many obstacles or what is termed as shadow regions that may inadvertently affect radio transmissions between nodes in the network. In this section, an experiment is set up which determined the Radio Frequency (RF) path loss at a specific area of the building. Finally, the network performance and reliability is analyzed and results concluded.

3.1. Received Signal Strength (RSS) versus Distance Estimation

Path losses are signal attenuations of electromagnetic wave propagations due to reflection, diffraction and scattering in indoor environments which may be modelled to determine the RF range [3]. In the Physics building ground floor hall area, signal strength measurements between two nRF52840 transceivers were taken at various distances to determine the RF coverage area. The nRF52840 from Nordic Semiconductor integrates a miniature radio and Micro-Controller Unit (MCU) for use in ultra-low power applications. Multiple 2.4 GHz protocol stacks can be run on the System-on-Chip (SoC) concurrently. The nRF52840 (hereafter referred to the SoC) is a 7 mm x 7 mm chip that houses a 32-bit 64 MHz ARM Cortex-M4F MCU with 1 MB flash and 256 kB of RAM. Utilizing two tranceivers, the RF path loss is determined from the Log Distance Path Loss Model [3]:

$$RSSI = 10n \log_{10}(d) + E \tag{1}$$

where $RSSI$ is the received signal strength indicator in dBm, n is the path loss exponent, E is an environmental constant and d is the distance of the $RSSI$ measurement from transceivers in meters. Parameter n is determined using polynomial least-squares regression of the logarithmic distances and averaged RSS measurements. With reference to Eq.1 and depicted in Fig.1, the path loss exponent n is estimated at 2.137 ($m = 10n$) and the environmental constant E at 55.05. In free space, $n = 2$ and where obstacles are present, $n > 2$. [3].

The fit demonstrated a 87.58 % of the total variation in the data about the average. By running similar experiments, nodes may be optimally distributed to cover a wide range of areas in the building. RF attenuation due to obstacles may be determined experimentally through similar field measurements. To aid in indoor propagation modelling, researchers have accumulated huge

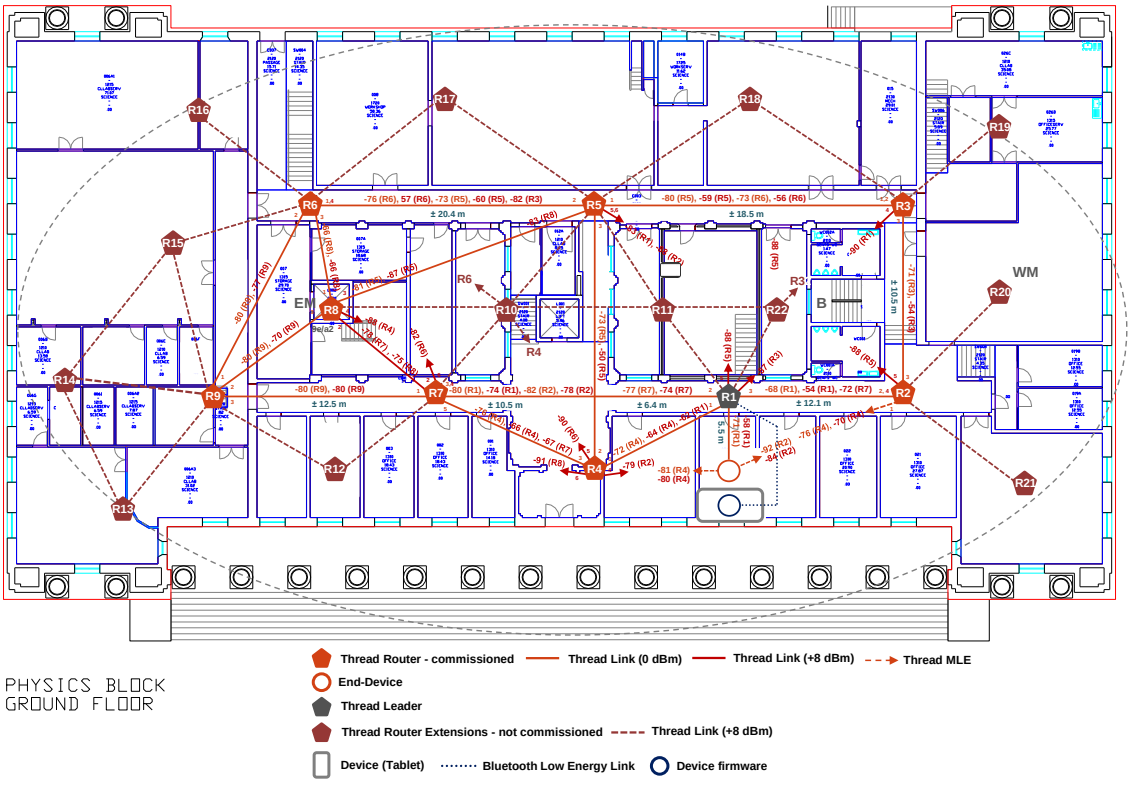

Figure 2: Experimental development of Thread network.

amounts of signal loss measurement data of building material in indoor environments [3]. With reference to Fig.1, further analysis indicates reliable data transmissions should be expected between transceivers not exceeding $\log_{10}(20)$ line-of-sight distances or $RSS \geq -80\ dBm$ in both directions for the SoC radio transmitter outputting power at Tx = 0 dBm. With the radio transmitting at Tx = +8 dBm, more than double the RF distances may be covered for reliable data transmissions but with an increase in SoC power consumption.

3.2. Development of the network

OpenThread, which is a relatively new wireless technology developed by Nest, is an open-source implementation of the Thread networking protocol. Nordic Semiconductor and several hardware platforms from other manufacturers are contributing members to the development of Thread. OpenThread (hereafter referred as Thread) is a Thread certified component which adheres to all the features defined in the Thread 1.1.1 specification [4].

The Thread network contains *border-routers*, *routers* and *end-devices*. *Border-routers* are *routers* that connect the IEEE 802.15.4 Thread network to WiFi or Ethernet networks for remote monitoring and control. *Routers* are nodes in the network that provide communications services between nodes. The Thread networking protocol provides autonomous mesh connectivity between all *routers* in the network by continuously checking the reliability of links between nodes in both directions using the Distance Vector Routing (DVR) protocol and Trickle algorithm [9]. An *end-device*, also known as a *sleepy child*, is a low-power device which operates under small duty cycles. The child device may only communicate directly with its *router* parent to other *routers* in the network. The Thread networking layer also ensures automatic reallocation of an *end-device* to a parent *router*. When the *end-device* is moved to a different area and coverage to the existing parent route is lost or a parent *router* fails, a new parent *router* will be allocated

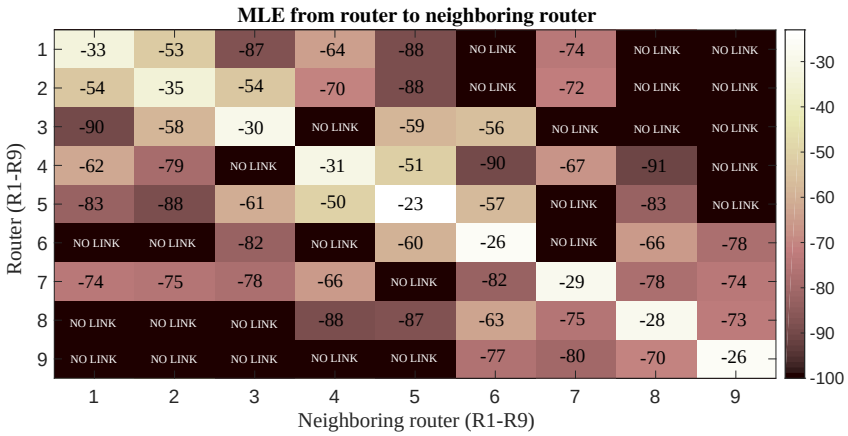

Figure 3: Mesh Link Establishment (MLE) by RSS at Tx = +8 dBm .

to the *end-device* based on the quality of alternative links in the network. One of the *routers* is always selected as a leader and is responsible for joining other *routers* in the network. All *routers* in the network share persistent data of the leader. If the leader fails, another *router* node will be selected as leader, therefore ensuring no single point of failure [5].

Nordic Semiconductor's Thread Application Programming Interface (API) consists of programming functions to interface with the Thread stack. The Thread stack is flashed as binary files to the MCU using the GCC compiler and SEGGER-link programmer tools. The API was used to configure a Thread network by programmatically setting node roles and testing the performance of the network.

As depicted in Fig.2, the development of the Thread network consisted of nine *routers* (R_1 to R_9) distributed on the ground floor. Routers R_8 and R_9 were mounted at a mezzanine area where walls obstructed the propagation of RF waves but sufficient links were established with neighboring routers. An *end-device* was used to send Internet Control Message Protocol (ICMP) packets to individual *routers* from a remote location to test the performance of the network. In Fig.2, R_{10} to R_{22} illustrate potential *router* installations in the building ground area which may add additional redundancy in links connectivity between nodes in the mesh network. Thread allows up to a maximum of 32 *routers* and 511 *end-devices* per parent *router* to be connected to a single network provided ample MCU processing and memory are allocated to run the Thread stack. MLE periodically sends multicast messages defined by the DVR protocol to estimate the quality of the links from neighboring *routers* in the network [4]. Advertisements or messages are sent periodically by the Trickle algorithm to determine the rate of change of network traffic in order to update routers [9]. The quality of the *router* links of the network is presented in Fig.3 where the link information was used to determine the mesh topology in Fig.2. The diagonal elements from left to right represent the *end-device* link quality placed within one meter to a *router* followed by the link quality of the *router* with neighboring routers displayed in the rows. As an example, depicted in Fig.2 and displayed in Fig.3, R_1 established five potential links with neighboring routers R_2, R_3, R_4, R_5 and R_7 at Tx = +8 dBm. The DVR protocol will ensure that a link is established with a neighboring *router* in both directions with the best link quality, in this example R2 at -53 dBm (R_1, R_2) and -54 dBm (R_2, R_1). If for some reason R_2 fails, the next best available link is $R4$ for data transmissions at -64 dBm (R_1, R_4) and -62 dBm (R_4, R_1). As expected, results indicate more links with neighboring *routers* are established at Tx = +8 dBm which may provide better reliability of data transmissions over longer multi-hopping distances. For more information on Thread and MLE, a comprehensive specification is available on the Thread Group website at [4]. The OpenThread software stack can be found at [8].

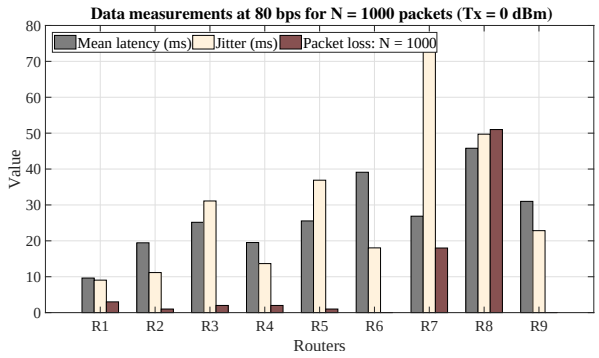

Figure 4a: Performance at Tx = 0 dBm.

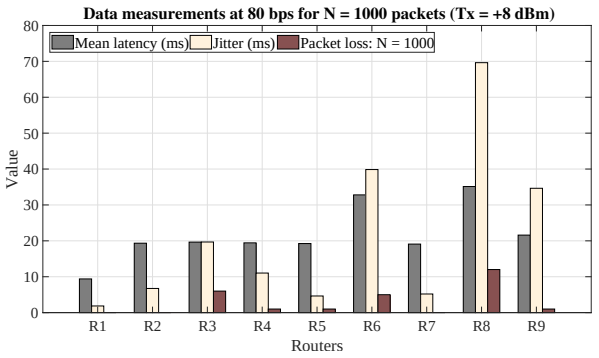

Figure 4b: Performance at Tx = +8 dBm.

3.3. Data Collection and Analysis

In this section, the reliability and performance of the network are evaluated. A loop containing 1000 samples of data packets was sent at a throughput of 80 bps from the *end-device* to a *router* and echoed back to the *end-device* where the latency measurements were recorded. A statistical approach was followed whereby the distributions and probabilities of the latency measurements were computed. The following figures are analyzed:

- In Fig.4a and Fig.4b, the test results concerning the network reliability and performance are presented from *end-device* to each *router* in the network for each node programmed at Tx = 0 dBm and Tx = +8 respectively.
- In Fig.5, latency measurements concerning the network performance from the *end-device* to R_1 through to R_9 are combined in a single data vector. The latency distribution and probability plot are shown at Tx = 0 dBm and Tx = +8 dBm respectively.

Assuming a constant packet loss, the reliability of the network is computed by the packet delivery ratio $PDR = packets\ recieved\ \times (total\ number\ of\ packets\ send)^{-1}$ which indicate reliable packet transmissions for both Tx = 0 dBm and Tx = +8 dBm field measurements. However, there does exist a variation of latency delay known as jitter which may be caused by obstacles in the RF propagation region, especially routers R_7 and R_8 because of their location in a mezzanine area. At a throughput of 80 bps, the latency data in Fig.5 lies approximately on the straight lines and therefore the data is approximately lognormal distributed. The lognormal distributions provides a reasonable model for analyzing the the performance of the network:

- Fig.5a reveal a 99 % confidence interval of $\mu = 26.80 \pm 0.31$ and $\sigma = 11.49 \pm 0.22$. There exist a 1 % probability that latency delay are ≥ 60 ms.
- Fig.5b reveal a 99 % confidence interval of $\mu = 21.72 \pm 0.2357$ and $\sigma = 8.66 \pm 0.17$. There exist a 1 % probability that latency delays are ≥ 50 ms.

The measurements in the above figures indicate that the latency data are multimodal and positively skewed. The skewness indicates greater latency delays in some of the multi-hopping routes and therefore causes some performance degradation in the network. The degradation may be caused by CCMA-CA operations and/or retransmissions of packets due to acknowledgements not received caused by obstructions in the environment. Outliers may be caused by CSMA-CA retransmissions, substandard link quality or packet relays/transmissions over greater multi-hopping distances.

3.4. Conclusion

In this paper, a low-power network based on the Thread networking protocol was developed. By installing an *end-device* securely onto the PCD, hundreds of *end-devices* representing tablets

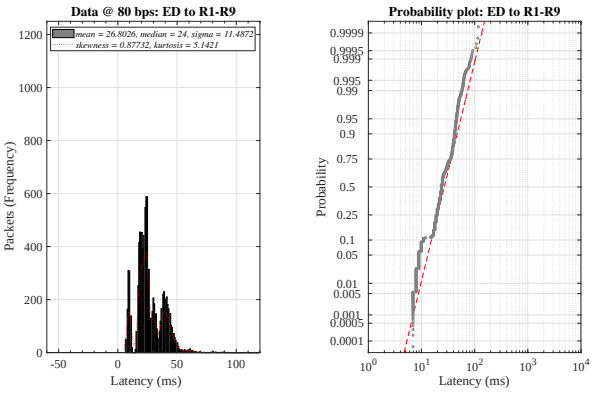

Figure 5a: Distribution at Tx = 0 dBm.

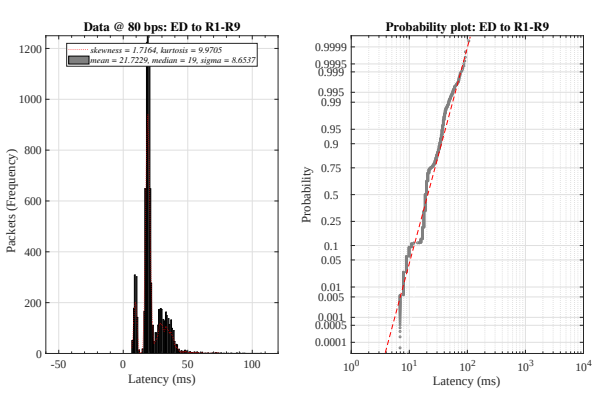

Figure 5b: Distribution at Tx = +8 dBm.

my be connected to a single router. However, by omitting the *end-device* in the network design, the PCD may communicate directly with the nearest router by using Bluetooth-Low Energy (BLE) to communicate to a router where a router runs BLE and Thread concurrently. Nordic Semiconductor provides both wireless technology solutions on their SoCs.

A simple path loss propagation model was implemented to determine the RF ranges of the SoC at Tx = 0 dBm. The estimated RF line-of-sight distance or averaged RSS value aided in the distribution of *router* nodes (R1-R9) in the building ground floor area. Additional MLE were discovered with greater RF ranges with the radio set at a higher transmitting output power. For this particular building environment, an *end-device* will mostly have at least one stable link ($RSSI > -80\ dBm$) to a parent *router* when placed at any location inside the building perimeter. However, some areas in the building do cause a high decrease in signal propagation due to obstacles and shadowing caused by concrete walls ($RSSI < -80\ dBm$). To compensate for this, the network coverage and additional MLE redundancy may be greatly improved by incorporating additional *routers* in the network development as depicted by R_{10} to R_{22}. Finally, a statistical approach was followed to represent field measurements. Results indicate acceptable latency delays and PDR between point to multipoint node communications.

3.5. Future Work

Similar latency confidence intervals are assumed if field measurements are taken for an *end-device* located at a different location inside the building perimeter, provided the *end-device* has a reliable link to its parent *router*. A comprehensive multipoint to multipoint node field measurements and analysis will be conducted. The *end-device* may be omitted from ther design by incorporating a multiprotocol wireless system using BLE of the PCD to communicate to the Thread network. A proprietary PCD firmware solution is needed from a reputable tablet manufacturer to render a device inoperable.

References

[1] Phaladi B 2015 http://citizen.co.za/news/news-national/382489/schools-tablet-theft-shock
[2] Writer S 2015 https://businesstech.co.za/news/government/87334/gauteng-withdraws-88000-tablets
[3] Rappaport T 2002 *Wireless communications principles and practice* 1st ed (New York: Prentice Hall) p 69-127
[4] Thread Group 2017 http://threadgroup.org/ThreadSpec
[5] Thread Group 2017 https://threadgroup.org/ourresources
[6] IEEE Standards Association 2017 https://standards.ieee.org/findstds/standard/802.15.4-2006.html
[7] Nordic Semiconductor 2017 https://infocenter.nordicsemi.com/index.jsp
[8] OpenThread 2014 https://github.com/openthread/openthread
[9] Trickle Algorithm 2011 https://tools.ietf.org/html/rfc6206

DIVISION G – THEORETICAL AND COMPUTATIONAL PHYSICS

How quantum is bird migration: A review

B Adams[1], I Sinayskiy[1] and F Petruccione[1]

[1]Quantum Research Group, School of Chemistry and Physics, University of KwaZulu-Natal Durban, KwaZulu-Natal, 4001, South Africa and National Institute for Theoretical Physics (NITheP), KwaZulu-Natal, 4001, South Africa

E-mail: betony@gmail.com

Abstract. In the decades since it was first suggested as a mechanism for avian magnetoreception, the radical pair model has generated both theoretical and experimental interest. This proceedings aims to give some idea of what progress has been made and to what extent the phenomenon of bird migration can be considered an integral part of the research field of quantum biology. Evidence that birds use quantum mechanics to navigate is still not absolutely established. The radical pair mechanism is, however, strongly supported by behavioural elements of the avian compass such as the fact that it is a light dependent, inclination compass and is disrupted by radiofrequency magnetic fields. Work has also been done to show that it is structurally possible for a molecule in the eye of a bird to be influenced in a measurable way by the weak geomagnetic field. Cryptochrome, the biological molecule proposed as the site of magnetoreception, has also been investigated and found to be compatible with much of the theory. That cryptochromes might mediate magnetic responses in animals has also been documented for the case of fruit-flies. Recently, interest in the effects of radiofrequency fields has been reignited by the experimental confirmation that birds are disoriented by low intensity anthropogenic electromagnetic radiation across a broad range of radio frequencies. Current theoretical research suggests that a possible explanation for this disorientation could be a quantum needle effect which slots the avian compass more firmly into the category of quantum biology.

1. Introduction

1.1. Bird migration

Throughout recorded history there have been attempts to explain the seasonal appearance and disappearance of certain species of birds. More than 4000 years ago Egyptians exploited the extraordinary navigational skills of birds, domesticating certain species to serve as messengers. [1]. But for a long time migration was open to misinterpretation. It was only in the nineteenth century that a more rigorously scientific approach to avian migration grew out of methods such as bird-banding. Nowadays it is generally agreed that birds use a two-step process that entails first mapping their geographical position to ascertain a theoretical direction then applying a compass to locate this direction [1, 2]. Early experiments with displaced homing pigeons suggested the use of a sun compass, however this is most effective over shorter distances rather than seasonal migration [1, 3]. Experiments show that nocturnal migrants use cues related to sunset as well as a star compass, while both mature birds as well as fledglings use a magnetic compass. Although the navigational skills of mature birds differ somewhat from fledglings, with the former able to compensate for a marked displacement during autumn migration while the latter only learn to correct this displacement on their return spring migration [1, 4, 5, 6] this built-in ability to

perceive the earth's magnetic field forms the base of birds' navigational system, providing a first means for navigation and homing [1, 7].

1.2. The magnetic compass

The discovery of earth's magnetic field and its use in navigation by humans, led to the belief that this field might also play a role in avian navigation. This hypothesis was given experimental heft by tests done on European robins, *Erithacus rubecula*, from the 1960s [8, 9]. There are two main theories for how birds use the geomagnetic field to orientate themselves; although the possibility of a third magnetoreceptor in the inner ear lagena of various animals is a recent development [10, 11]. The magnetite model of avian magnetoreception, first proposed by Kirschvink and Gould in 1981 [12] built on the fact that certain bacteria use magnetite to orientate themselves. Magnetite particles, a specific form of iron oxide, located in the birds' beaks align themselves in the magnetic field [13]. An alternate theory of avian magnetoreception is the radical pair model, which suggests that a light-activated molecule in the eye gives rise to a radical pair, the dynamics of which allow the bird to 'see' the magnetic field. While there is limited evidence that the magnetite model provides compass information in fields as weak as the geomagnetic field it has been suggested that birds might use a combination of both magnetite and radical pair models [14], the former to detect differences in magnetic intensity and the latter for directional information [13]. This combination could also offer a way of explaining the phenomenon of fixed responses. Fixed responses are migratory trajectories that do not follow the accepted north-south migratory direction and appear to combine elements of both models, being dependent on specific light regimes as well as being disrupted by anaesthetic applied to the beak [15]. While these responses raise interesting questions, and while it is clear that different animals seem to employ different orientation mechanisms [16, 17], it is solely with the radical pair mechanism that this review will be preoccupied [7]. It is this radical pair theory that puts avian magnetoreception into the category of quantum biology.

1.3. Quantum biology

Until fairly recently it was generally accepted that quantum effects would be unlikely to be found in the warm, wet and messy environments that characterise biological systems. However, the emerging field of quantum biology incorporates a number of mechanisms that might be understood to be quantum phenomena in processes as diverse as photosynthesis, migration, olfaction, anaesthesia and even cognition. One of these is the radical pair mechanism. The radical pair mechanism is implicated in many biological processes. In photosynthetic reaction centres it plays a role in polarisation and protection mechanisms [18, 19]. Radical pairs observed in flavoproteins such as cryptochrome might offer an explanation for the mechanism controlling the circadian clock in some organisms [20] - [22]. In addition to this, the role of radical pair mediated magnetic field effects in enzyme reactions is still being investigated [23] - [25]. This review will focus on the role that the radical pair mechanism is hypothesised to play in avian magnetoreception, it will examine the evidence for this hypothesis and how firmly it can be said that the extraordinary navigational prowess of birds can truly be called a quantum phenomenon.

2. The radical pair mechanism (RPM)

Investigation into the magnetic field modulation of chemical reactions and the formalisation of the radical pair mechanism began as long ago as the 1960s [26, 27, 28]. Application of radical pair theory to avian magnetoreception began not long after this, first proposed by Schulten *et al* in the 1970s [26]. A simple radical-pair mechanism that may be utilised as a compass is depicted in Figure 1 and can be described briefly in the following three steps. First a photon incident on the molecule in question transfers sufficient energy to excite an electron. This extra energy means that it is favourable for the electron to be transferred from donor molecule to acceptor

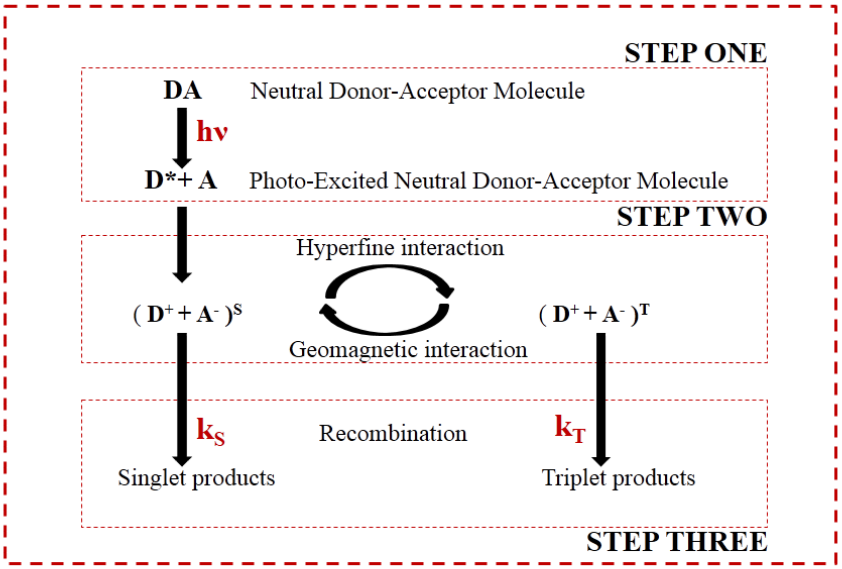

Figure 1. Radical pair schematic. A photon of energy *hv* excites an electron in the magnetoreceptor molecule causing the electron to move from donor **D** to the acceptor **A** part of the molecule. The result is a spatially separated, spin correlated electron pair: the radical pair. Hyperfine interactions between each electron and its surrounding nuclear environment cause singlet–triplet oscillations, aided by the Zeeman effect of the earth's magnetic field. On recombination singlet and triplet states give rise to different chemical products with rates k_S and k_T respectively [7].

molecule, forming a radical, or unpaired electron. The simultaneous production of two such radicals results in the spin correlated pair. Step two involves interaction with the surrounding nuclear environment and the external magnetic field, which drives interconversion of spin states between singlet and triplet states. The third and final step involves recombination by reverse electron transfer and the transformation of spin states to the specific, possibly chemical, signals which allow the bird to perceive the magnetic field [7].

2.1. Behavioural evidence

The radical pair theory of avian magnetoreception is strongly supported by the behavioural evidence of migrating birds. The avian compass is light dependent, as would be expected from the photo-activation necessary for the first stage of the mechanism. It has been demonstrated that not only are birds disoriented in darkness but their compass is also, more specifically, wavelength dependent [13]. The compass is also an inclination compass, it is not disrupted by switching poles [29]. Further evidence for the viability of the radical pair compass came in 2004 when Ritz *et al.* showed that the avian compass was disrupted by radiofrequency radiation, specifically radiation at the Larmor frequency, which led to speculation that one of the radicals in the pair had no hyperfine interaction [30]. More evidence for the radiofrequency disruption of the avian compass came in 2014. However, rather than identifying a specific frequency at which this disruption occurred the research suggested that birds were disoriented under the influence of

low intensity electromagnetic radiation across a very broad range of frequencies [31]. According to a very recent study, however, the strongest evidence that the radical pair theory of avian migration is a truly quantum phenomenon is the incredible accuracy that birds achieve in their navigation. It has been shown that birds can attain a directional precision to within 5° and Hore *et al.* attribute this to the avoided crossings of the radical pair's spin energy levels. They go on to conclude that this effect, which has no classical correlation, places the avian compass firmly in the category of quantum biology [32].

2.2. Structural evidence

Progress has also been made into clarifying the structure of the avian compass and whether this might support the radical pair theory. The molecule that has been proposed as the most likely to be the site of the compass is the flavoprotein cryptochrome [33]. Four different types of cryptochrome have been confirmed in the eyes of migratory birds [34]. Plant cryptochromes have also been shown to have enhanced responses to weak magnetic fields, while the magnetic responses of fruit flies are also mediated by cryptochrome [35]. More specifically, flavin-tryptophan radical pairs in an initial singlet state have been identified in cryptochrome [36] and cryptochrome in the eye of the migratory garden warbler has been observed to form radical pairs with the long (millisecond) lifetime necessary for the dynamics of the radical pair [37].

3. Conclusion

The radical pair theory of avian magnetoreception is not a new theory, having been acknowledged as a viable one for more than a few decades. Despite this it has not yet established itself as firmly a quantum phenomenon as, for example, certain elements of photosynthetic reactions. However the recent hypothesis that the accuracy shown by birds during their migrations might be explained by avoided crossings theory could afford the mechanism a more rigorously quantum status. A good understanding of the radical pair mechanism and its possible application in the case of avian magnetoreception is important, particularly since it has been shown that birds are disoriented by weak electromagnetic radiation that is 'well below the guidelines for human exposure proposed by the International Commission on Non-Ionizing Radiation Protection (ICNIRP) and adopted by the World Health Organization' [31]. The magnetic sensitivities of chemical reactions as described by radical pair theory is a phenomenon that is not specific to birds, but implicated in a number of different processes in living systems. Indeed it has been shown that cryptochromes found in humans display light-dependent magnetosensitivity [38] and it would serve us well to know how the human body interacts with the technology that plays such an integral part in our lives.

References

[1] Wiltschko W and Wiltschko R 2003 *Animal Behaviour* **65** 257–272
[2] Collett TS and Graham P, 2004 *Current Biology* **14** R475–R477
[3] Gould JL *Current Biology*, **14:6** R221–R224
[4] Perdeck AC 1958 *Ardea* **46** 1–37
[5] Perdeck AC 1967 *Ardea* **55** 194–202
[6] Mouritsen H and Larsen ON 1998 *Journal of Experimental Biology* **201** 2927–2934
[7] B. Adams 'An open quantum systems approach to avian magnetoreception' Masters thesis 2015
[8] Wiltschko W and Merkel F 1966 *Verh. dt. zool. Ges.* **59** 362–367
[9] Wiltschko W 1968 *Zeitschrift fur Tierpsychologie* **25** 536–558
[10] Harada Y, Taniguchi M, Namatame H and Iida A 2001 *Acta Otolaryngol* **121** 590–595
[11] Wu L and Dickman JD 2011 *Current Biology* **21** 418–423
[12] Kirschvink JL and Gould JL 1981 *Biosystems* **13**, 181–201
[13] Wiltschko W and Wiltschko R 2005 *J Comp Physiol A* **191** 675–693
[14] Yan L and Tao S 2012 *Chin. Phys. B* **22: 4** 048701
[15] Wiltschko R and Wiltschko W 2009 *Communicative & Integrative Biology* **2:2** 100–103

[16] Wiltschko R, Stapput K, Ritz T, Thalau P and Wiltschko W 2007 *HFSP Journal* **1:1** 41–48
[17] Thalau P, Ritz T, Burda H, Wegner RE and Wiltschko R 2006 *J. R. Soc. Interface* **3** 583–587
[18] Kominis IK 2013 *New Journal of Physics* **15** 075017
[19] Marais A, Sinayskiy I, Petruccione F and van Grondelle R 2015 *Scientific Reports* **5**
[20] Biskup T, Schleicher E, Okafuji A, Link G, Hitomi K, Getzoff E D and Weber S 2009 *Angewandte Chemie International Edition* **48** 404–407
[21] Yoshii T, Ahmad M and Helfrich-Frster C 2009 *PLoS Biology* **7** 813–9
[22] Fedele G, Edwards MD, Bhutani S, Hares JM, Murbach M, Green EW, Dissel S, Hastings MH, Rosato E and Kyriacou CP 2014 *PLoS Genetics* **10** e1004804
[23] Buchachenko AL and Kuznetsov DA 2008 *J. Am. Chem. Soc.* **130** 12868–12869
[24] Messiha HL, Wongnate T, Chaiyen P, Jones AR and Scrutton NS 2015 *J. R. Soc. Interface* **12** 20141155
[25] Crotty D, Silkstone G, Poddar S, Ranson R, Prina-Mello A, Wilson MT and Coey JMD 2012 *Proceedings of the National Academy of Sciences* **109** 1437–1442
[26] Schulten K, Staerk H, Weller A, Werner HJ and Nickel B 1976 *Z. Phys. Chem.* **101** 371
[27] Haberkorn R and Michel-Beyerle M 1979 *Biophys. J.* **26** 489–498
[28] Steiner UE and Ulrich T 1989 *Chem. Rev.* **89** 51–147
[29] Stapput K, Thalau P, Wiltschko R and Wiltschko W 2008 *Current Biology* **18** 602-606
[30] Thalau P, Ritz T, Stapput K, Wiltschko R and Wiltschko W 2004 *Naturwissenschaften* **92** 86-90
[31] S. Engels *et al.* 2014 *Nature* **509** 353-356
[32] Hiscock HG, Worster S, Kattnig DR, Steers C, Jin Y, Manolopoulos DE, Mouritsen H and Hore PJ 2016 *PNAS* **113:17** 4634–4639
[33] Ritz T, Adem S and Schulten K 2000 *Biophysical Journal* **78** 707–718
[34] Mouritsen H and Hore PJ 2012 *Current Opinion in Neurobiology* 22 343-352
[35] Yoshii T, Ahmad M and Helfrich-Forster C 2009 *PLoS Biology* **7** 813-9
[36] Maeda K *et al.* 2012 *PNAS* **109:13** 47744779
[37] Liedvogel M *et al.* 2007 *PLoS ONE* **2:10** e1106
[38] Foley LE, Gegear RJ and Reppert SM 2011 *Nature Communications* **2** 356

Entanglement and gravity

JM Hartman[1], SH Connell[1], C Engelbrecht[1] and F Petruccione[2]

1. University of Johannesburg, Johannesburg, South Africa
2. University of Kwa-Zulu Natal, South Africa

E-mail: hartman.jonathan2@gmail.com

Abstract. Entanglement in quantum mechanics leads to a non-local correlation between two particles. This is the conclusion that one comes to from Bell's theorem in light of the experimental verification of the prediction that the Bell inequality is actually violated in quantum mechanics. Previous authors have found that the Bell correlations are modified in relativistic frames such that at first sight it appears as though the Bell inequality may no longer be violated. However, maximal violation of the Bell inequality is still preserved in a different set of directions, one has to rotate one of the detectors in a potential experiment through an angle, called the Wigner angle in order to detect the maximal violations. We argue that if such an effect can be observed between two inertial frames moving with constant velocity with respect to each other then a precessional effect, called the Thomas precession, should be observed in the Bell observables when the particles are accelerating. We specifically discuss accelerations which relate directly to motion as a result of a force, namely gravity.

1. Introduction

Quantum entanglement is a phenomenon in quantum mechanics whereby two particles are correlated in such a way that when the state of one is measured, then the state of the other is always known (in the case of a maximally entangled system). The concept goes back to the famous EPR paradox, initially put forth by Einstein, and it set off a flurry of debates over it's nature. The ideas as to it's nature, and that of the EPR paradox, only became empirically testable, however, in 1964 when John Bell published a paper on an argument now known as Bell's theorem. In the paper, Bell derived an inequality, Bell's inequality, which would hold if the correlations could be described by classical local realism. In essence, Bell's theorem says that no physical theory that incorporates local realism can reproduce all the predictions of quantum mechanics as quantum mechanics itself predicts a violation of Bell's inequality. Bell calculated this for the case of non-relativistic quantum mechanics though and it's only recently that people have started investigating how Bell's inequality changes when relativistic effects are considered.

The first to investigate a relativistic Bell inequality was Czacor in 1997 [1], who found that the relativistic effects of entangled massive particles affect the correlations between them in the special case where both are moving in the same direction. The origin of this deviation from the non-relativistic Bell's inequality is the length contraction when measuring the spin correlations in the laboratory frame, though Bell's theorem is still valid as the maximal violation of Bell's inequality is still obtained when the spins are measured with respect to a basis which has a compensating rotated direction.

Later, in 2003, Terashima and Ueda [2] investigated a similar situation to Czacor but from the perspective of an observer moving perpendicular to the motion of the entangled particles,

moving in opposite directions, with opposite spins. Like, Czacor, they found that there would be a degradation of the entanglement correlations as opposed to an observer that is in the frame of the source. They similarly also concluded that maximal violation of Bell's inequality could still be obtained when the spins are measured in in a basis with compensating directions. In 2004, Lee and Chang-Young [3] combined Czacor's result with Terashima and Ueda's to derive a more general case for the special relativistic Bell theorem.

Later, some authors investigated quantum communication in accelerated frames [4] [5], and others investigated quantum entanglement in curved space-times [6] [7].

In our own previous work [8], we have explored the effect of accelerated motion on entanglement in a relativistic kinematical context. This current work takes the matter further, exploring this effect for accelerations as a result of central potentials such as gravity.

2. The Bell inequality and Thomas precession

Consider a source of entangled particles of opposite spins with detectors on either side that measures their spins in the longitudinal direction of their spin orientations. If local realism is assumed then the Bell inequality is given by

$$\left|P\left(\vec{a},\vec{b}\right)-P\left(\vec{a},\vec{c}\right)\right|\leqslant 1+P\left(\vec{b},\vec{c}\right), \tag{1}$$

where $\vec{a}$ and $\vec{b}$ are unit vectors of the detector settings (defining the basis) for measuring the spin projections, $\vec{c}$ is any other arbitrary unit vector and $P\left(\vec{a},\vec{b}\right)$ etc are the average products of the results of the spin projections as measured by the detectors. It can easily be shown that the quantum mechanics violates this inequality. For example, given that quantum mechanics predicts that $P\left(\vec{a},\vec{b}\right)=-\vec{a}\cdot\vec{b}$, then if we take $\vec{a}$ and $\vec{b}$ to perpendicular to each other and $\vec{c}$ to be at a 45 degree angle to each, then $P\left(\vec{a},\vec{b}\right)=0$ and $P\left(\vec{a},\vec{c}\right)=P\left(\vec{b},\vec{c}\right)=-0.707$, giving the left hand side of (1) as 0.707. As the right hand side evlaluates to $1-0.707=0.293$, we have a violation of the Bell inequality.

The original formulation of the Bell inequality is not practical for experiment, however, as it is restricted to the special case in which outcomes of the spin measurements are always anti-correlated whenever the detectors are parallel. A more general inequality that was more suitable to experiment was given in 1969 by Clauser, Horn, Shimony and Holt. It is now called the CHSH inequality [9] and is given by

$$C(a,a',b,b')\equiv\left\langle\hat{a}\otimes\hat{b}\right\rangle+\left\langle\hat{a}\otimes\hat{b'}\right\rangle+\left\langle\hat{a'}\otimes\hat{b}\right\rangle-\left\langle\hat{a'}\otimes\hat{b'}\right\rangle\leqslant 2, \tag{2}$$

Here, $\vec{a}$ and $\vec{a}'$ are two detector settings on side A and $\vec{b}$ and $\vec{b}'$ are two detector settings on side B. This is violated in non-relativistic quantum mechanics since quantum mechanics predicts a maximal violation as

$$C(a,a',b,b')=2\sqrt{2}. \tag{3}$$

Now let's look at the relativistic case where two particles are moving apart from each other in their combined rest frame, while an observer is moving perpendicular to the two particles. This could correspond, for example, to an observer noting the decay of a moving parent particle into two daughters. As said before, this situation was investigated by Terashima and Ueda [2]. The adding of two velocities (the motion of the particle and the motion of the observer) together in special relativity is not commutative. In fact, when you combine two boosts together that are not parallel, you do not simply get a new boost in a new direction but a boost plus a rotation. This rotation as observed in the lab frame with respect to the rest frame of the decaying particle,

or the centre of mass frame (CoM) is called the Wigner angle. This Wigner angle showed up in Terashima and Ueda's calculation of the maximal violation of Bell's inequality as

$$C(a, a', b, b') = 2\sqrt{2}\cos^2\delta, \tag{4}$$

where the Wigner angle, δ, in the case of a perpendicular boost is given by

$$\tan\delta = \frac{\sinh\xi \sinh\chi}{\cosh\xi + \cosh\chi} \tag{5}$$

where ξ and χ are the rapidities of the particles in the CoM frame and the observer frame with respect to the CoM frame respectively given by $\frac{v_1}{c} = \tanh\xi$ and $\frac{v_2}{c} = \tanh\chi$.

We have previously shown [8] that if the two particles are accelerating away from each other, then the Wigner angle δ as seen in the moving frame can be said to be changing with respect to time, so that it looks like a precession. This precession is called the Thomas precession. By considering an acceleration as a sequencing of infinitesimal changes in velocity, we have shown that the Thomas precession can be written as

$$\tan(\delta_0 + \Delta\delta(t)) = \frac{\sinh(\xi + \Delta\xi(t))\sinh\chi}{\cosh(\xi + \Delta\xi(t)) + \cosh\chi} \quad \text{with} \quad \Delta\xi(t) = \int_0^\tau a_P(\tau)d\tau. \tag{6}$$

This links the acceleration a explicitly to the change in the rapidity $\Delta\xi(t)$ and hence to the Thomas precession. Here a_P and τ are the proper acceleration and proper time.

The acceleration induced Thomas precession would have the effect of gradually weakening the violation of the Bell or CHSH inequality. One can imagine however that the unit vectors describing the orientation of the detectors can be adjusted to compensate the effect of the Thomas precession, so that the maximal violation can be restored. The acceleration is the result of a force. In this way an entanglement witness (the CHSH, or some other incarnation) is sensitive to the force environment for the decaying system. Put alternatively, entanglement can be used to measure the force (for example local gravity) of the entangled system.

We now turn to how one could apply this to, in principle, the use entanglement to detect small forces between particles.

3. Thomas precession for the Newtonian gravitational force between two entangled particles

In order to consider the two body problem, let's consider the that the decay products are of different masses m_1 and m_2 and velocities, v_{p1} and v_{p2} with respect to the lab frame. In this case, the CoM frame is the one where the sum of the momenta of the two particles is zero, or $\vec{p}_1 = m_1\vec{v}_{p1} = -m_2\vec{v}_{p2} = -\vec{p}_2 = \mu\vec{v}_1$, where $\mu = \frac{m_1 m_2}{m_1+m_2}$ is called the reduced mass and $\vec{v}_1 = \vec{v}_{p1} - \vec{v}_{p2}$ is the relative velocity between the particles. This reduces the number of variables so that we can treat it as a one-particle system. Let's also assume that there is a gravitational attraction between the two particles. Then if we assume conservation of mechanical energy, we have

$$E = K + V = \frac{1}{2}\mu {v_1}^2 - \frac{Gm_1m_2}{r}, \tag{7}$$

for the kinetic energy and the gravitational potential energy and where r is the distance between the two particles and G is Newton's gravitational constant. Therefore, the relative speed v_1 is given by

$$v_1 = \sqrt{\frac{2\left(Gm_1m_2 + Er\right)}{\mu r}}. \tag{8}$$

Referring back to equations 5 and 6, we find that the Thomas precession is given by

$$\tan\left(\delta_0 + \triangle\delta\right) = \frac{v_1 v_2}{c\left(\sqrt{c^2 - {v_1}^2} + \sqrt{c^2 - {v_2}^2}\right)}, \tag{9}$$

by applying the hyperbolic identities $\sinh\left(\text{artanh } x\right) = \frac{x}{\sqrt{1-x^2}}$ and $\cosh\left(\text{artanh } x\right) = \frac{1}{\sqrt{1-x^2}}$ and where v_2 is the speed of the lab frame with respect to the CoM frame. Substituting (8) into (9) gives

$$\tanh\left(\delta_0 + \triangle\delta\right) = \frac{v_2\sqrt{2\left(Gm_1m_2 + Er\right)}}{c\left(\sqrt{c^2\mu r - 2\left(Gm_1m_2 + Er\right)} + \sqrt{\mu r\left(c^2 - {v_2}^2\right)}\right)}. \tag{10}$$

So substituting (10) into (4) provides a possible application of quantum entanglement and the relativistic Bell inequality to detect a small gravitational force between two particles. If this were possible, it would be useful because normally gravity as a force is too weak to detect on the scale of individual particles. One of the reasons one would want to do this is that some theories of quantum gravity predict a deviation from the standard inverse square law of Newton's law of gravity. For example, in string theory, if large extra dimensions are present, then the gravitational potential would be modified as (see [10] and [11])

$$V_g = -\frac{\Gamma\left(\frac{d-2}{2}\right) l^{d-3} G\mu}{\pi^{\frac{d-2}{2}} r^{d-2}}, \tag{11}$$

where d is the total number of spacial dimensions and l is the compactification size of the extra dimensions. There is a problem with the above equations though, in that this potential for Newtonian gravity is non-relativistic. One would have to apply general relativity, or some approximation of general relativity. We tackle this in the next section.

4. Calculation for the relativistic gravitational force between two entangled particles

Whenever one has to go beyond the Newtonian gravitational force to make it compatible with special relativity, one has to use Einsteins theory of general relativity instead (the most accurate theory known concerning non-quantum gravity). General relativity claims that the gravitational force is not a "force" as such but a curvature in the space-time background generated by matter and energy. The relationship between mass-energy and the amount of curvature is given by a tensor equation called Einstein's field equation which related a measure of the space-time curvature to the stress-energy tensor (the tensor which encodes the matter content of the equation). For our purposes we do not need to use the full Einstein field equation though. Just note that Newton's force law can be recovered from it if we assume that the gravitational field strength is very weak and when the speed of the source is much slower than that of light. Interestingly, if we make the same approximation that the gravitational field is very weak but we allow for relativistic speeds then we obtain an equation very similar to the Lorentz force law for electromagnetism instead. At this level there are some similarities between the gravitational force and the electromagnetic force, [12]

$$\vec{a} = -\vec{E}_g - 4\vec{v} \times \vec{B}_g, \tag{12}$$

where E_g and B_g have the same definitions as the electric and magnetic fields in electromagetism, $\vec{E}_g = -\vec{\nabla}\phi$ and $B_g = \nabla \times \vec{A}$. From the general solution of the linearised approximation of Einstein's field equation, the scalar and vector potentials are given by

$$\phi = \frac{G}{c^2}\int \frac{\rho_0}{|\vec{x}-\vec{x}'|}\frac{1}{(1-\frac{{v_s}^2}{c^2})^{\frac{1}{2}}}dx'^3 \tag{13}$$

and

$$\vec{A} = \frac{G}{c^4}\int \frac{\rho_0\vec{v}_s}{|\vec{x}-\vec{x}'|}\frac{1}{(1-\frac{{v_s}^2}{c^2})^{\frac{1}{2}}}dx'^3, \tag{14}$$

where $\vec{v}_s$ is the velocity of the source and ρ_0 is the mass density of the source. For a point mass, we can take $\rho_0 = m\delta(\vec{x}')$, where $\delta(\vec{x}')$ is the Dirac delta function. Substituting this into (13) and (14), we get

$$\phi = \frac{1}{c^2\left(1-\frac{{v_s}^2}{c^2}\right)^{\frac{1}{2}}} \quad \text{and} \quad \vec{A} = \frac{1}{c^4\left(1-\frac{{v_s}^2}{c^2}\right)^{\frac{1}{2}}}\frac{Gm\vec{v}_s}{r}. \tag{15}$$

Substituting these back into equation (12) and utilising the definitions of E_g and B_g, we get

$$\vec{a} = -\frac{1}{\left(1-\frac{{v_s}^2}{c^2}\right)^{\frac{1}{2}}}\frac{Gm}{r^2}\hat{r} \quad \text{or} \quad \vec{a} = -\frac{G}{r^2}\left(\frac{m_1}{\left(1-\frac{{v_1}^2}{c^2}\right)^{\frac{1}{2}}} + \frac{m_2}{\left(1-\frac{{v_2}^2}{c^2}\right)^{\frac{1}{2}}}\right)\hat{r}. \tag{16}$$

for the case of our two particle system.

This expression for the acceleration can then be deployed in equation (6) to determine the Thomas precession as a result of the treatment of gravity at this mostly classical level of approximation.

5. Quantum mechanical description of the gravitational force

We can also model the decay into two particles in a gravitational field in quantum mechanics by modelling it as a scattering solution similar to Coulomb scattering, given the similarities of Newton's law of gravitation to Coulomb's force law in electrostatics. In the quantum mechanical description of the two particle system, the Hamiltonian in the CoM frame is given by

$$\hat{H} = \frac{1}{2\mu}\hat{p}^2 + V(\vec{r}) \quad \text{with} \quad V(\vec{r}) = -\frac{Gm_1m_2}{\mu r} = -\frac{G(m_1+m_2)}{r} \tag{17}$$

for the gravitational potential so that

$$\hat{H}\psi = -\frac{1}{2\mu}\hbar^2\nabla^2\psi - \frac{G(m_1+m_2)}{r}\psi. \tag{18}$$

The solution to Schrödinger's equation in (18) is given by

$$\psi = \exp(ikr\cos\theta)\ {}_1F_1\left(in', 1, ikr\,(1-\cos\theta)\right), \tag{19}$$

where ${}_1F_1(a,b,c)$ is the hyper-confluent geometric function and $n' = \frac{Gm_1m_2}{\hbar^2 k}$. It would be useful to compare our result to the Rutherford scattering cross section far away from the "scattering centre" in order to validate our numerical results. We plotted our scattering solution on the same axes as that of Rutherford scattering on a logarithmic scale in figure (1). Since for our purposes we are interested in small radii, we want to see if it approaches the Rutherford scattering at large radii. We see that it does according to the right part of figure (1). The procedure is then to extract the expectation value for the acceleration a from this solution (19) in the standard way, and then deploy this as well in the calculation of the Thomas precession.

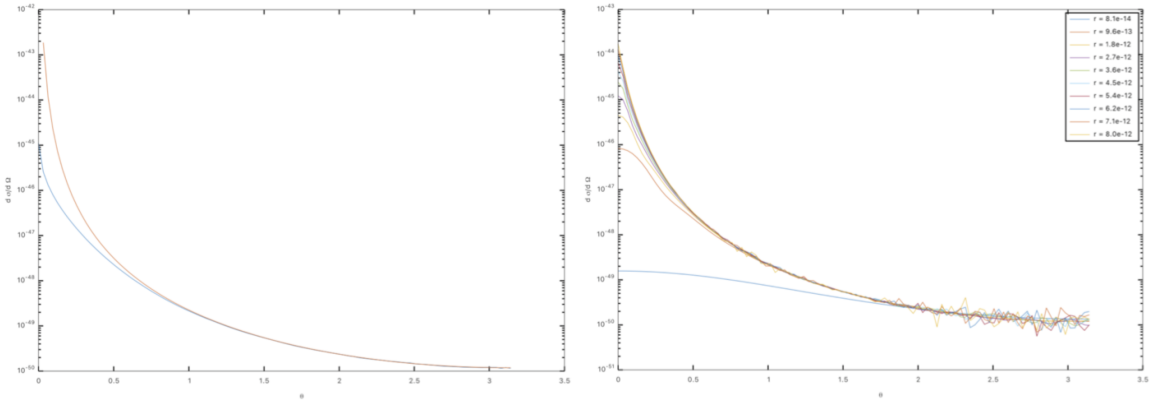

Figure 1. Left : Scattering cross section compared with Rutherford scattering. Right : Comparison of the cross sections at different distances between the particles.

6. Conclusion

We have reviewed some literature on relativistic entanglement and the Bell-type inequalities. In the second section on Bell's theorem, we used the work on relativistic entanglement by Terashima and Ueda [2] to show how one could use entanglement to detect small accelerations between particles by measuring the Thomas precession. In the following section we developed the idea further and suggested how one could use the result to detect weak forces between entangled particles and explained how it could be extended to also detect large extra dimensions. The calculation of the Thomas precession required the calculation of the change in rapidity of the particles in the CoM frame. Given that Newton's law of gravitation is not compatible with special relativity, the next section was devoted to a relativistic description of the gravitational force between the two particles, utilising the weak field approximation of general relativity. This section showed explicitly at a mostly classical level of approximation how the desired rapidity could be calculated. A subsequent section introduced a non-relativistic quantum approach to calculating the same rapidity. Future work would extend the calculations to more accurate treatments. In particular, a more accurate treatment should be given to the relativistic scenario. It would also evaluate the size of the effects in a range of plausible scenarios. Given that previous lower limits for extra dimensions are measured down to nanometre scale, an experiment as we have described, if successful, could could constrain it even further to the femtometre scale.

7. Acknowledgements

The authors acknowledge financial support of the National Research Foundation (NRF) as well as provision of accommodation by Resolution Circle.

References

[1] Czachor M 1997 *Phys. Rev. A* **55**(1) 72–77
[2] Terashima H and Ueda M 2003 *Quantum Information & Computation* **3** 224–228
[3] Lee D and Chang-Young E 2004 *New Journal of Physics* **6** 67
[4] Van Enk S J and Rudolph T 2003 *Quantum Info. Comput.* **3** 423–430 ISSN 1533-7146
[5] Alsing P M and Milburn G J 2003 *Phys. Rev. Lett.* **91**(18) 180404
[6] Terashima H and Ueda M 2004 *Phys. Rev. A* **69**(3) 032113
[7] Ralph T C, Milburn G J and Downes T 2009 *Phys. Rev. A* **79**(2) 022121
[8] Hartman J M, Connell S and Petruccione F 2015 *Proceedings of the 60th Annual Conference of the South African Institute of Physics (SAIP2015)* ed Chitambo M and Venter A pp 499–504
[9] Clauser J F, Horne M A, Shimony A and Holt R A 1969 *Phys. Rev. Lett.* **23**(15) 880–884 URL `https://link.aps.org/doi/10.1103/PhysRevLett.23.880`
[10] Arkani-Hamed N, Dimopoulos S and Dvali G 1998 *Physics Letters B* **429** 263 – 272 ISSN 0370-2693
[11] Zwiebach B 2004 *A first course in string theory* (Cambridge: Cambridge Univ. Press) URL `https://cds.cern.ch/record/789942`
[12] Wald R M 1984 *General Relativity* 1st ed (University Of Chicago Press) ISBN 0226870332

Heavy flavor tagged photon bremsstrahlung from AdS/CFT

W. A. Horowitz

Department of Physics, University of Cape Town, Private Bag X3, Rondebosch 7701, South Africa

E-mail: wa.horowitz@uct.ac.za

Abstract. We compute for the first time the near-side photon bremsstrahlung spectrum associated with open heavy flavor propagating through a strongly-coupled quark-gluon plasma. We expect that this observable will show measurably distinguishable differences between the soupy slowdown in AdS/CFT compared to the sporadic stiff smacks from a weakly-coupled pQCD plasma gas. Assuming the heavy quark loses energy from the usual AdS/CFT drag setup we find that small angle photon radiation is suppressed in medium compared to vacuum while wide angle radiation is enhanced.

1. Introduction

Experimental indications give a mixed picture of the relevant dynamics of the quark-gluon plasma (QGP) created at the Relativistic Heavy Ion Collider (RHIC) and the Large Hadron Collider (LHC). In particular, measurements of the distribution of low transverse momentum ($p_T \lesssim 2$ GeV/c) particles can be understood through near perfect viscous hydrodynamics with a rapid hydrodynamization time [1–7] or from parton cascades [8–13]. Similarly, observables related to single partons at high transverse momentum ($p_T \gtrsim 15$ GeV/c) can also be qualitatively described using energy loss models based on either strong-coupling AdS/CFT [14–22] or weak-coupling pQCD [23–39].

We therefore seek novel experimental handles to provide insight into the relevant dynamics of the quark-gluon plasma (QGP) produced at the temperatures $T_{QGP} \sim 400$ MeV accessible at RHIC and LHC. In particular with the massive increase in luminosity and detector sensitivity that will come to the LHC after upgrades, the study of rare observables becomes possible.

A natural observable of potential interest is the measurement of the *photon* bremsstrahlung associated with open heavy flavor propagation in QGP. Presumably the radiation pattern for photons will differ depending on whether the heavy quark undergoes rare hard scattering events as one expects from pQCD or if it rather is plowing through a strongly-coupled soup as described by AdS/CFT. (Note that photon tagged heavy flavor production is different and refers to the $2 \to 2$ or $2 \to 3$ prompt hard photon production at heavy ion collision time $t = 0$ that is clearly well described by standard perturbative field theory methods [40, 41].)

We provide here quantitative predictions for the photon bremsstrahlung produced by an open heavy quark strongly-coupled to a strongly-coupled plasma. In this exploratory study we use leading order heavy quark drag as derived from a steady state string setup in AdS/CFT [42, 43].

The influence of fluctuations [44–46] in the momentum loss experienced by the heavy quark may be an important contribution, but we leave it to future work.

2. Setup

We treat the heavy quark–anti-quark pair produced at the initial nuclear overlap at $t = 0$ and moving in opposite directions as a classical current [47]

$$j^\mu(x) = Q\,e\,\theta(t)\left[v^\mu(t)\delta^{(3)}(\vec{x}-\vec{x}(t)) - \tilde{v}^\mu(t)\delta^{(3)}(\vec{x}+\vec{x}(t))\right] \tag{1}$$

coupled to the electromagnetic field

$$\mathcal{L} = -\frac{1}{4}F_{\mu\nu}F^{\mu\nu} + j_\mu A^\mu. \tag{2}$$

In Eq. 1, Q is the fractional electric charge carried by the heavy quark, $\theta(t)$ is the usual Heaviside step function, and

$$\begin{aligned} v^\mu(t) &= (1, \vec{v}(t))^\mu \\ \tilde{v}^\mu(t) &= (1, -\vec{v}(t))^\mu \\ \vec{x}(t) &= \vec{x}_0 + \int_0^t dt'\vec{v}(t'). \end{aligned} \tag{3}$$

For any generic current coupling to the electromagnetic field given by Eq. 2, one finds [16, 48] that the momentum differential energy distribution of the emitted electromagnetic radiation is given by

$$\frac{dE}{d^3k} = -\frac{1}{2}\frac{1}{(2\pi)^3}\tilde{j}^\mu(k)\tilde{j}_\mu(-k), \tag{4}$$

where

$$\tilde{j}^\mu(k) \equiv \int d^4x\, e^{-ik\cdot x} j^\mu(x). \tag{5}$$

2.1. Hard Production Electromagnetic Radiation

Since we will ultimately wish to compare to pQCD-based energy loss calculations for which there are usually non-trivial UV and IR catastrophes associated with the factorization of the hard production and subsequent dynamics, we wish to compute the *difference* in the radiated energy in medium as compared to the vacuum. For the vacuum case, we have that, in the soft radiation approximation, the heavy quark pair does not lose momentum after it is produced. In this case we then take $\vec{v}(t) \equiv \vec{v}_0$ and $\vec{x}(t) = \vec{v}_0 t$ in Eq. 1. To perform the Fourier transform in Eq. 5 one must insert a small convergence factor η. Evaluation of Eq. 5 then yields

$$\begin{aligned} \tilde{j}^\mu_{vac}(k) &= \lim_{\eta\to 0}\int d^4x\, e^{-i[(\omega - i\,\eta)t + \vec{k}\cdot\vec{x}(t)]}\, j^\mu(x) \\ &= \lim_{\eta\to 0} Q\,e\left[\frac{v_0^\mu}{i\,\omega - i\,\vec{k}\cdot\vec{v}_0 + \eta} - \frac{\tilde{v}_0^\mu}{i\,\omega + i\,\vec{k}\cdot\vec{v}_0 + \eta}\right] \\ &= -i\,Q\,e\left[\frac{v_0^\mu}{\omega - \vec{k}\cdot\vec{v}_0} - \frac{\tilde{v}_0^\mu}{\omega + \vec{k}\cdot\vec{v}_0}\right]. \end{aligned} \tag{6}$$

After some manipulation and taking the motion of the quarks to be along the z direction, with $\vec{k}\cdot\vec{v}_0 = \omega\, v_0\cos\theta$, $\omega \equiv k^0$, and $v_0 \equiv |\vec{v}_0|$, we find Eq. 4 yields for the differential energy radiated in vacuum

$$\frac{dE_{vac}}{d^3k} = \frac{2}{(2\pi)^3}(Q\,e)^2\frac{1}{\omega^2}\frac{v_0^2\sin^2\theta}{(1 - v_0^2\cos^2\theta)^2}. \tag{7}$$

As is usual, we see that the total integrated energy radiated by the vacuum current grows linearly with an artificially imposed UV cutoff ω_{max}. Interestingly, the inclusion of the *pair* of quarks has tamed the usual IR divergence: the long wavelength physics knows that the total charge remains 0 as the $q\bar{q}$ pair separates.

2.2. AdS/CFT Induced Electromagnetic Radiation

The leading order energy loss of a heavy quark in a strongly-coupled $\mathcal{N} = 4$ SYM plasma is given by [42, 43]

$$\frac{d\vec{p}}{dt} = -\mu\,\vec{p}, \quad \mu = \frac{\pi\sqrt{\lambda}}{2}\frac{T^2}{M_Q}, \tag{8}$$

where $\lambda = g^2 N_c$ is the 't Hooft coupling, T is the temperature of the plasma, and M_Q is the mass of the heavy quark.

From Eq. 8, and assuming motion is only in one dimension, we may solve for

$$\begin{aligned} p(t) &\equiv |\vec{p}(t)| = p_0 e^{-\mu t} \\ E(t) &= \sqrt{m^2 + p^2(t)} \\ v(t) &= p(t)/E(t) \\ x(t) &= \frac{1}{2\mu}\ln\left[\frac{E_0 + p_0}{E_0 - p_)} \times \frac{E(t) - p(t)}{E(t) + p(t)}\right]. \end{aligned} \tag{9}$$

We may plug in our results from Eq. 9 into our equation for the Fourier transform of the current, Eq. 5, to find the Fourier transform of the current when the heavy quarks are subject to the AdS/CFT heavy quark drag. Unfortunately, the result cannot be evaluated analytically.

3. Results

Once we have the Fourier transform of the current associated with a heavy quark pair separating in a strongly-coupled AdS/CFT plasma, we may compute the difference in energy radiated by the heavy quark in medium minus the energy radiated in vacuum. We show in Fig. 1 (left) the result for $m_c = 1.5$ GeV/c^2 charm quarks and (right) $m_b = 4.75$ GeV/c^2 bottom quarks. Not surprisingly, the biggest medium modification to $\omega^2 dE/d^3k$ is centered at $\theta_{max} \sim m_Q/p_T$; one can show numerically that the depth of the difference at θ_{max} is a function of $(m_Q/p_T)^2$.

One can understand the reduction in emitted photon radiation shown in the plot as follows. In vacuum, the quarks are accelerated from rest to some non-zero velocity v_0 associated with the initial p_T of the particles. The quarks in medium, on the other hand, immediately begin decelerating due to the presence of the plasma. The produced photons will always have some non-zero formation time. For the photons produced in-medium, the effective acceleration of the quark is smaller than that for the quark in vacuum because of the immediate deceleration. Therefore there is less radiation emitted from the in-medium quarks, and thus the suppression observed in the subtracted spectrum.

4. Conclusions and Outlook

We presented the first prediction of photon bremsstrahlung for heavy quarks produced in a strongly-coupled $\mathcal{N} = 4$ SYM plasma. We derived the spectrum of emitted QED radiation dE/d^3k for a classical point current of given (potentially) time-dependent velocity in Eq. 4. We then focused on the trajectory of a heavy quark strongly coupled to a strongly coupled plasma as predicted by leading order AdS/CFT, in which case the momentum of the heavy quark is modified according to the usual drag result $dp/dt = -\mu p$, where $\mu = \pi\sqrt{\lambda}T^2/m_Q$. We plotted the difference in the spectra of the photons produced in medium compared to those produced

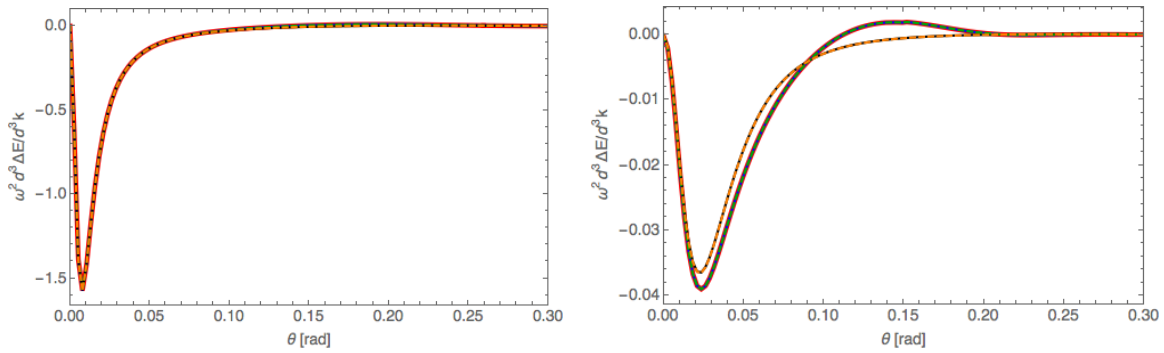

Figure 1: (Colour online) $dE/d^3k|_{med} - dE/d^3k|_{vac}$ for $T = 400$ MeV strongly-coupled $\mathcal{N} = 4$ SYM plasma for (left) $m_c = 1.5$ GeV/c^2 charm quarks and (right) $m_b = 4.75$ GeV/c^2 bottom quarks. For both plots the quarks have $p_T = 200$ GeV/c, the photon has energy 20 GeV, and $\lambda = 12$. In both plots, the thicker red curve corresponds to both quarks traversing an infinite length plasma, the thick blue curve to both quarks traversing up to 5 fm of plasma, and the thick black curve to both quarks traversing up to 1 fm of plasma. For the dashed green curve, the quark moving in the z direction traverses a distance of up to 5 fm while the away side quark traverses a 1 fm thick plasma; for the dashed orange curve, the distances are reversed.

in vacuum, $\omega^2 dE/d^3k|_{med} - \omega^2 dE/d^3k|_{vac}$, in Fig. 1. The presence of the medium suppresses the radiation emitted by heavy quark compared to that in the vacuum. Given the very small angle at which the modification is significant, $\theta_{max} = m_Q/p_T \ll 1$, it is currently unclear whether the current experiments at the LHC could distinguish between a modification to the production bremsstrahlung as shown here or a potential modification to the photons generated in the hadronization process in which the heavy quarks become heavy mesons.

Acknowledgments
The authors wish to that the South African National Research Foundation and the SA-CERN Collaboration for generous support.

References

[1] Teaney D 2003 *Phys. Rev.* **C68** 034913 (*Preprint* nucl-th/0301099)
[2] Chesler P M and Yaffe L G 2011 *Phys. Rev. Lett.* **106** 021601 (*Preprint* 1011.3562)
[3] Song H, Bass S A, Heinz U, Hirano T and Shen C 2011 *Phys. Rev. Lett.* **106** 192301 [Erratum: Phys. Rev. Lett.109,139904(2012)] (*Preprint* 1011.2783)
[4] Gale C, Jeon S, Schenke B, Tribedy P and Venugopalan R 2013 *Phys. Rev. Lett.* **110** 012302 (*Preprint* 1209.6330)
[5] Bernhard J E, Moreland J S, Bass S A, Liu J and Heinz U 2016 *Phys. Rev.* **C94** 024907 (*Preprint* 1605.03954)
[6] Alqahtani M, Nopoush M, Ryblewski R and Strickland M 2017 (*Preprint* 1705.10191)
[7] Weller R D and Romatschke P 2017 (*Preprint* 1701.07145)
[8] Molnar D and Gyulassy M 2002 *Nucl. Phys.* **A697** 495–520 [Erratum: Nucl. Phys.A703,893(2002)] (*Preprint* nucl-th/0104073)
[9] Lin Z w and Ko C M 2002 *Phys. Rev.* **C65** 034904 (*Preprint* nucl-th/0108039)
[10] Bzdak A and Ma G L 2014 *Phys. Rev. Lett.* **113** 252301 (*Preprint* 1406.2804)

[11] Orjuela Koop J D, Adare A, McGlinchey D and Nagle J L 2015 *Phys. Rev.* **C92** 054903 (*Preprint* 1501.06880)

[12] He L, Edmonds T, Lin Z W, Liu F, Molnar D and Wang F 2016 *Phys. Lett.* **B753** 506–510 (*Preprint* 1502.05572)

[13] Lin Z W, He L, Edmonds T, Liu F, Molnar D and Wang F 2016 *Nucl. Phys.* **A956** 316–319 (*Preprint* 1512.06465)

[14] Horowitz W and Gyulassy M 2008 *Phys.Lett.* **B666** 320–323 (*Preprint* 0706.2336)

[15] Akamatsu Y, Hatsuda T and Hirano T 2009 *Phys.Rev.* **C79** 054907 (*Preprint* 0809.1499)

[16] Horowitz W A 2010 (*Preprint* 1011.4316)

[17] Horowitz W and Gyulassy M 2011 *J.Phys.* **G38** 124114 (*Preprint* 1107.2136)

[18] Horowitz W 2012 *AIP Conf.Proc.* **1441** 889–891 (*Preprint* 1108.5876)

[19] Morad R and Horowitz W A 2014 *JHEP* **11** 017 (*Preprint* 1409.7545)

[20] Horowitz W A 2015 *Phys. Rev.* **D91** 085019 (*Preprint* 1501.04693)

[21] Hambrock R and Horowitz W A 2017 AdS/CFT predictions for azimuthal and momentum correlations of $b\bar{b}$ pairs in heavy ion collisions *8th International Conference on Hard and Electromagnetic Probes of High-energy Nuclear Collisions: Hard Probes 2016 (HP2016) Wuhan, Hubei, China, September 23-27, 2016* (*Preprint* 1703.05845) URL https://inspirehep.net/record/1518153/files/arXiv:1703.05845.pdf

[22] Brewer J, Rajagopal K, Sadofyev A and van der Schee W 2017 Holographic Jet Shapes and their Evolution in Strongly Coupled Plasma *26th International Conference on Ultrarelativistic Nucleus-Nucleus Collisions (Quark Matter 2017) Chicago,Illinois, USA, February 6-11, 2017* (*Preprint* 1704.05455) URL https://inspirehep.net/record/1592399/files/arXiv:1704.05455.pdf

[23] Gyulassy M, Levai P and Vitev I 2002 *Phys. Lett.* **B538** 282–288 (*Preprint* nucl-th/0112071)

[24] Vitev I and Gyulassy M 2002 *Phys. Rev. Lett.* **89** 252301 (*Preprint* hep-ph/0209161)

[25] Wang E and Wang X N 2002 *Phys. Rev. Lett.* **89** 162301 (*Preprint* hep-ph/0202105)

[26] Majumder A, Wang E and Wang X N 2007 *Phys. Rev. Lett.* **99** 152301 (*Preprint* nucl-th/0412061)

[27] Dainese A, Loizides C and Paic G 2005 *Eur. Phys. J.* **C38** 461–474 (*Preprint* hep-ph/0406201)

[28] Armesto N, Cacciari M, Dainese A, Salgado C A and Wiedemann U A 2006 *Phys. Lett.* **B637** 362–366 (*Preprint* hep-ph/0511257)

[29] Wicks S, Horowitz W, Djordjevic M and Gyulassy M 2007 *Nucl. Phys.* **A784** 426–442 (*Preprint* nucl-th/0512076)

[30] Majumder A, Nonaka C and Bass S A 2007 *Phys. Rev.* **C76** 041902 (*Preprint* nucl-th/0703019)

[31] Zhang H, Owens J F, Wang E and Wang X N 2009 *Phys. Rev. Lett.* **103** 032302 (*Preprint* 0902.4000)

[32] Vitev I and Zhang B W 2010 *Phys. Rev. Lett.* **104** 132001 (*Preprint* 0910.1090)

[33] Schenke B, Gale C and Jeon S 2009 *Phys. Rev.* **C80** 054913 (*Preprint* 0909.2037)

[34] Young C, Schenke B, Jeon S and Gale C 2011 *Phys. Rev.* **C84** 024907 (*Preprint* 1103.5769)

[35] Majumder A and Shen C 2012 *Phys. Rev. Lett.* **109** 202301 (*Preprint* 1103.0809)

[36] Horowitz W A and Gyulassy M 2011 *Nucl. Phys.* **A872** 265–285 (*Preprint* 1104.4958)

[37] Buzzatti A and Gyulassy M 2012 *Phys. Rev. Lett.* **108** 022301 (*Preprint* 1106.3061)

[38] Horowitz W A 2013 *Nucl. Phys.* **A904-905** 186c–193c (*Preprint* 1210.8330)
[39] Djordjevic M and Djordjevic M 2014 *Phys. Lett.* **B734** 286–289 (*Preprint* 1307.4098)
[40] Stavreva T, Arleo F and Schienbein I 2013 *JHEP* **02** 072 (*Preprint* 1211.6744)
[41] Huang J, Kang Z B, Vitev I and Xing H 2015 *Phys. Lett.* **B750** 287–293 (*Preprint* 1505.03517)
[42] Herzog C, Karch A, Kovtun P, Kozcaz C and Yaffe L 2006 *JHEP* **0607** 013 (*Preprint* hep-th/0605158)
[43] Gubser S S 2006 *Phys.Rev.* **D74** 126005 (*Preprint* hep-th/0605182)
[44] Gubser S S 2008 *Nucl. Phys.* **B790** 175–199 (*Preprint* hep-th/0612143)
[45] Casalderrey-Solana J and Teaney D 2007 *JHEP* **0704** 039 (*Preprint* hep-th/0701123)
[46] Moerman R W and Horowitz W A 2016 (*Preprint* 1605.09285)
[47] Adil A, Gyulassy M, Horowitz W A and Wicks S 2007 *Phys. Rev.* **C75** 044906 (*Preprint* nucl-th/0606010)
[48] Peskin M E and Schroeder D V 1995 *An Introduction to quantum field theory* ISBN 9780201503975, 0201503972 URL http://www.slac.stanford.edu/spires/find/books/www?cl=QC174.45%3AP4

Matrix logarithmic quantum wave equation

Miloslav Znojil[1,2] **and Konstantin G. Zloshchastiev**[1]

[1] Institute of Systems Science, Durban University of Technology, 4000 Durban, South Africa
[2] Nuclear Physics Institute of the CAS, Hlavní 130, 250 68 Řež, Czech Republic

E-mail: znojil@ujf.cas.cz

Abstract. Quantum wave equations with logarithmic nonlinearity are motivated by the conventional (linear) quantum formalism and theory of quantum liquids. The matrix generalization of the logarithmic equation is introduced, which is expected to complement and extend the existing range of physical applications of the conventional ("single-channel") logarithmic wave equation; its properties and possible applications are studied.

1. Introduction

We consider the nonlinear logarithmic Schrödinger equation (LSE)

$$i\partial_t\psi(\vec{x},t) = (-\Delta + V_{LSE})\,\psi(\vec{x},t)\,, \quad V_{LSE} = -b\,\ln|\psi(\vec{x},t)|^2, \tag{1}$$

where Δ is the d-dimensional Laplacian, b is a nonlinear coupling assumed to be a positive constant here; the equation has the wavefunction solutions $\psi \in L^2(\Re^d)$. This equation, as well as its relativistic analogue (which is obtained by replacing the derivative part with the d'Alembert operator), finds numerous applications in extensions of quantum mechanics [1, 2], physics of quantum fields and particles [3, 4, 5, 6, 7], optics and transport or diffusion phenomena, nuclear physics, theory of dissipative systems and quantum information [8, 9], theory of superfluidity [10, 11, 12] and effective models of physical vacuum and classical and quantum gravity [13, 14, 15, 16].

The physical meaning of the solutions ψ and proper interpretation of their dynamics are determined by a phenomenological background of a given application. Still, the generic mathematical features of Eq. (1) (and, first of all, the logarithmic form of its nonlinearity) can be shared. For the purposes of illustration one can select, as a starting point, the context of a linear quantum wave equation. In the Schrödinger picture, the evolution of quantum systems is commonly described by the Schrödinger equation

$$i\partial_t\psi(\vec{x},t) = \hat{H}\psi(\vec{x},t)\,, \qquad \hat{H} = -\Delta + V(\vec{x}), \tag{2}$$

which is linear by construction. In this equation, the choice of the potential $V(\vec{x})$ is usually determined by a number of considerations. Let us consider as an example the exactly solvable (ES) harmonic oscillator $V_{(HO)}(\vec{x}) \sim |\vec{x}|^2$, which has the equidistant, purely vibrational spectrum of the low-lying bound-state energies $E_{(HO)}$ and the localized wavefunctions of the form:

$$\psi_{(HO)}(\vec{x},t) \sim \exp(-iE_{(HO)}t)\,\exp\left(-|\vec{x}|^2/2 + \mathcal{O}(\ln|\vec{x}|)\right), \tag{3}$$

which can be regarded as a natural realization of the above-mentioned Madelung decomposition. The other choices of a potential can be considered on grounds of either the formal relevance of $V(\vec{x}) \neq V_{(HO)}(\vec{x})$ or its capability of describing the variability of the dynamics (by adding perturbations to $V_{(HO)}(\vec{x})$).

Such an asymptotic behavior of wavefunctions may be perceived as related to a certain equivalence-class property of potentials,

$$V_{(initial)}(\vec{x}) = |\vec{x}|^2 + \mathcal{O}(\ln|\vec{x}|) \sim \ -\ln[\psi^*(\vec{x},t)\psi(\vec{x},t)] = V_{(generalized)}(\vec{x}). \tag{4}$$

It is thus not too surprising that the logarithmically nonlinear Schrödinger equation (1) was proposed as a "minimal" generalization of its linear predecessor in quantum theory [1].

2. Logarithmic wave equation in theory of quantum liquids

If one accepts that strongly correlated helium atoms can form a bound state characterized by a single macroscopical wavefunction then the wave equation describing such object cannot be of the Gross-Pitaevskii (GP) type, also known as the cubic Schrödinger (in the relativistic field theory, its analogue would be the quartic scalar field theory ϕ^4). There exist at least two reasons for this. Firstly, the GP approach is a perturbative approach, which takes into account only two-body interactions and neglects anomalous contributions to self-energy, which is a robust approximation for dilute system like cold gases. However, it is unlikely to be sufficient for more dense objects like liquids: according to aforesaid quantum liquid's atoms are delocalized and thus nothing prevents them from getting involved into multiple-body interactions. One example of why multi-body (three and more) interactions are very important for forming bound states of bosons at low temperatures is the Efimov state, which has been experimentally observed in helium. The second issue is that the ground-state wavefunction of the GP BEC model in absence of an external potential trap does not describe a localized object. Instead, the free GP condensate tends to occupy all available volume - as such one needs to apply some kind of a trap, in order to confine the condensate and stabilize the system. This feature is more pertinent to gases than to liquids.

Luckily, there exists another candidate where the above-mentioned issues simply do not occur in the first place. This is nonlinear Bose liquid defined by virtue of the logarithmic Schrödinger equation of the type (1), except that the condensate wavefunction is normalized not to one but to a total amount of condensate particles, see Refs. [14, 10, 11, 12]. The logarithmic Bose liquid has a number of features suitable for our objectives: it implicates not only binary but also multiple-body interactions (when three or more bodies can scatter simultaneously), and its ground state is the so-called gausson – a spherically-symmetric object which is localized and stable even in absence of a trapping potential, with the interior density obeying the Gaussian law

$$\rho = |\psi(\vec{x},t)^2| \sim \exp\left(-|\vec{x}|^2/a^2\right), \tag{5}$$

where a is a characteristic size. Notice that this object is different from the classical droplet because it does not have border in a classical sense: its stability is supported by nonlinear quantum effects in the bulk, rather than by surface tension.

In the work [11], an analytical theory of structure and excitations in superfluid helium was proposed, which elaborates on above-mentioned microscopical aspects and goes beyond the GP approximation. It consists of two nested models which act on different length scales, but are connected via the parametric space: quantities and values of parameters in the long-wavelength model are derived from the short-wavelength part. The short-length model justifies appearance of collective degrees of freedom that can be used for describing the volume elements (fluid parcels) of the quantum liquid. Thus, an intrinsic structure of a fluid parcel is described using

the non-perturbative approach based on the logarithmic wave equation: one can show that the interior density of the element obeys the Gaussian distribution.

The fact that the logarithmic model was so instrumental in describing one of the realistic quantum Bose liquids we know of, gives us a hope that it can be also useful in a theory of physical vacuum. According to the latter, the physical vacuum is described by an essentially non-relativistic superfluid, while the Lorentz symmetry and relativistic gravity emerge in the linearized ("phononic") regime. This can be shown, independently, by means of the modular group approach [13], fluid/gravity correspondence [14], Bogoliubov method [10], and Arnowitt-Deser-Misner formalism [16]. Furthermore, there already exist some experimental data suggesting a connection between the phenomena of superfluidity and gravity [17, 18]. As a matter of fact, the superfluid vacuum paradigm allows us to explore a border of the relativity's applicability range, which is crucial for truly understanding of the spacetime approach, as well as to go beyond it [15].

3. Analytical solutions

In this section we pay our attention to the possible simulations of the interaction between a system and its environment which would be based on the logarithmic type of the interaction's nonlinearity. Let us, therefore, start from the choice of the first nontrivial case and consider solutions of the matrix LSE with $\mathcal{A}$ being a 2×2 matrix. For the sake of simplicity let us also limit our attention to the case of the single spatial dimension replacing vector $\vec{x}$ by scalar x. Then we can write

$$i\partial_t \mathcal{A} + \partial_{xx}\mathcal{A} + b\ln(\mathcal{A}^\dagger\mathcal{A})\mathcal{A} = 0, \tag{6}$$

and we also impose that

$$\int_{x_0}^{x_1} \mathrm{tr}(\mathcal{A}^\dagger\mathcal{A})dx = \mathcal{N}, \tag{7}$$

assuming that the system is confined to the interval of $x \in [x_0, x_1]$. The latter formula comes from the normalization condition $\int d\vec{x}\,\mathrm{tr}(\mathcal{A}^\dagger\mathcal{A}) \equiv \langle\mathcal{A}|\mathcal{A}\rangle = \mathcal{N}$, where integration is taken over a spatial volume taken by the system, $\mathcal{N}$ being a constant usually interpreted as a number of particles inside such a volume, while tr here is the standard matrix-trace operation.

Furthermore, below we consider the cases when we managed to obtain exact analytical solutions of Eq. (6).

3.1. Diagonal case

We shall start our analysis from the simple yet nontrivial case of the two coupled LSEs, $\mathcal{A}$ being a diagonal matrix

$$\mathcal{A} = \begin{pmatrix} \psi_1(x,t) & 0 \\ 0 & \psi_2(x,t) \end{pmatrix}, \tag{8}$$

where $\psi_a(x,t)$ are complex-valued functions. In this model the auxiliary cross-coupling terms are neglected. Considering this case enables us to contemplate, more easily, a pair of uncoupled logarithmic Schrödinger equations in a way which would emphasize also certain parallelism with the concept of the coupled channels in the linear-theory setting. Moreover, in the language of phenomenology, any pair of similar individual equations, linear or nonlinear, may be perceived as mimicking a fully separated evolution of an isolated system $\mathcal{S}_1$ (of our immediate interest) and of its remote and irrelevant, "switched-off" environment $\mathcal{S}_2$.

In the more realistic situations one can only rarely neglect the possible cross-interaction between subsystems $\mathcal{S}_1$ and $\mathcal{S}_2$ completely. Still, the most immediate reward of the study of such a mutual interaction usually comes when one assumes that the resulting "perturbation" of the relevant subsystem $\mathcal{S}_1$ remains weak.

The ground-state solution of Eq. (6) can be found exactly. In a rest frame, it has the form of the gausson, i.e., by the Gaussian packet modulated by the de Broglie plane wave,

$$\psi_a(x,t) = C_a \exp\left(-\frac{1}{2} b\, x^2 + \nu_a x - iE_a t\right), \tag{9}$$

where $a = 1$, 2 and where

$$E_a = b(1 - \ln C_a^2) - \nu_a^2 \tag{10}$$

is energy of a wave in the ath channel. Quantities C_a and ν_a are integration constants related, together with b, to the mean and variance of the Gaussian packet.

If one imposes also the normalization condition (7) then one obtains an additional constraint for the integration constants

$$F_1(x_0) - F_1(x_1) + F_2(x_0) - F_2(x_1) = 2\sqrt{\frac{b}{\pi}}\mathcal{N}, \tag{11}$$

where we denoted $F_a(x) = C_a^2 \exp\left(\frac{\nu_a^2}{b}\right) \mathrm{erf}\left(\frac{\nu_a - bx}{\sqrt{b}}\right)$. For instance, when x_1 and x_0 are set to plus and minus infinity then this constraint takes a simple form $\sum_{a=1}^{2} C_a^2 \exp\left(\frac{\nu_a^2}{b}\right) = \sqrt{\frac{b}{\pi}}\mathcal{N}$.

Note that due to the Galilean symmetry of LSE, from solution (9) one can always obtain gausson solutions whose center of mass propagates with velocity v_a, independently for each channel. For instance, one can check that the following function

$$\psi_a(x,t) = C_a \exp\left[-\frac{1}{2}\,(x - v_a t)\,(b(x - v_a t) - 2\nu_a - iv_a)\right], \tag{12}$$

is also a solution of Eqs. (6), (9), provided

$$(v_a/2)^2 + \nu_a^2 = b(1 - \ln C_a^2), \tag{13}$$

v_a being another real-valued integration constant.

3.2. Off-diagonal case

Contrary to the previous case, let us assume that it is the channel-coupling terms which are dominating now. Therefore, one can assume $\mathcal{A}$ being an off-diagonal matrix

$$\mathcal{A} = \begin{pmatrix} 0 & \bar{\psi}_1(x,t) \\ \bar{\psi}_2(x,t) & 0 \end{pmatrix}, \tag{14}$$

where $\bar{\psi}_a(x,t)$ are complex-valued functions.

Still, the ground-state solution of Eq. (6) can be found exactly. In a rest frame, it also has the form of the Gaussian packet modulated by the de Broglie plane wave,

$$\bar{\psi}_a(x,t) = C_a \exp\left(-\frac{1}{2} b\, x^2 + \nu_a x - i\bar{E}_a t\right), \tag{15}$$

where $a = 1$, 2, and

$$\bar{E}_a = \nu_a^2 - b(1 - \ln C_a^2) \tag{16}$$

is energy of a wave, C_a and ν_a are integration constants related, together with b, to the mean and variance of the Gaussian packet. If one imposes also the normalization condition (7) then one obtains an additional constraint for the integration constants, which is identical to Eq. (11).

Comparing the solution (15) with its diagonal analogue (9), one can see an interesting feature: two solutions can be transformed from one another by a simple time inversion

$$\psi_a(x,t) = \bar{\psi}_a(x,-t), \quad E_a = -\bar{E}_a, \tag{17}$$

which can indicate that the diagonal and off-diagonal terms of the matrix $\mathcal{A}$ describe the processes happening in opposite directions of time, or, alternatively, having opposite signs of their energy eigenvalues.

4. Conclusion

The logarithmically nonlinear quantum wave equation, both in its original and matrix forms, is introduced and discussed based on motivations coming from different areas of quantum physics. We also considered some special cases and analytical solutions, for the case of 2×2 matrices. The solutions seem to have a general feature of possessing a Gaussian wave packet shape modulated by the de Broglie plane waves. Besides, the diagonal and off-diagonal components of the matrix turn out to be describing the waves with opposite signs of energy or, alternatively, moving in opposite directions of time. Other types of matrix solutions can be a subject of future studies.

Acknowledgments

Research of K.Z. is supported by the National Research Foundation of South Africa under Grants No. 95965, 98083 and 98892. Research of M.Z. is supported by Grants GAČR 16-22945S and IRP RVO61389005, and his visit to Durban University of Technology was funded by the National Research Foundation of South Africa under Grant No. 98892.

References

[1] Bialynicki-Birula I and Mycielski J 1976 *Annals Phys.* **100** 62
[2] Bialynicki-Birula I and Mycielski J 1979 *Phys. Scripta* **20** 539
[3] Rosen G 1969 *Phys. Rev.* **183** 1186
[4] Dzhunushaliev V and Zloshchastiev K G 2013 *Central Eur. J. Phys.* **11** 325
[5] Gulamov I E, Nugaev E Y and Smolyakov M N 2014 *Phys. Rev.* D **89** 085006
[6] Gulamov I E, Nugaev E Y, Panin A G and Smolyakov M N 2015 *Phys. Rev.* D **92** 045011
[7] Dzhunushaliev V, Makhmudov A and Zloshchastiev K G 2016 *Phys. Rev.* D **94** 096012
[8] Yasue K 1978 *Annals Phys.* **114** 479
[9] Brasher J D 1991 *Int. J. Theor. Phys.* **30** 979
[10] Avdeenkov A V and Zloshchastiev K G 2011 *J. Phys.* B: *At. Mol. Opt. Phys.* **44** 195303
[11] Zloshchastiev K G 2012 *Eur. Phys. J.* B **85** 273
[12] Bouharia B 2015 *Mod. Phys. Lett.* B **29** 1450260.
[13] Zloshchastiev K G 2010 *Grav. Cosmol.* **16** 288
[14] Zloshchastiev K G 2011 *Acta Phys. Polon.* B **42** 261
[15] Zloshchastiev K G 2011 *Phys. Lett.* A **375** 2305
[16] Scott T C, Zhang X, Mann R B and Fee G J 2016 *Phys. Rev.* D **93** 084017
[17] Tajmar M, Plesescu F and Seifert B 2009 *J. Phys. Conf. Ser.* **150** 032101
[18] Tajmar M and Plesescu F 2010 *AIP Conf. Proc.* **1208** 220